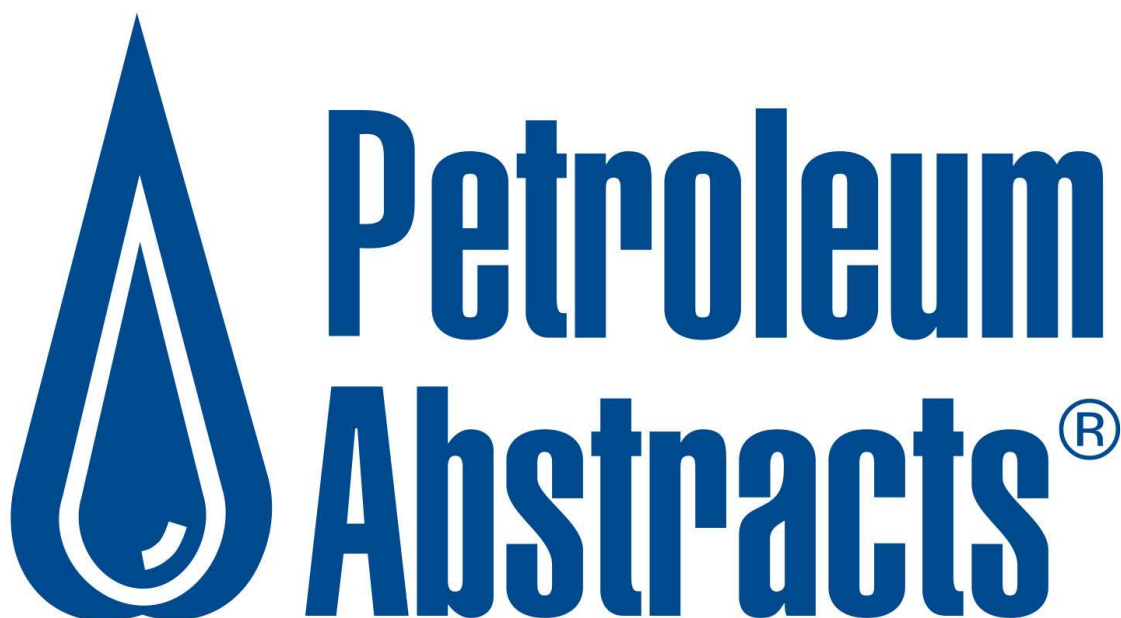


Volume 63, Number 01
January 7, 2023
Abstract Nos. 1,561,095—1,561,894



Document Delivery

Photocopies of most articles and patents abstracted for Petroleum Abstracts can be obtained from Petroleum Abstracts Document Delivery Service, 800 S. Tucker Dr., MLIC 1520, Tulsa, Oklahoma 74104. Phone: 918-631-2231. E-mail: padds@utulsa.edu

PETROLEUM ABSTRACTS®

Volume 63, Number 01

January 7, 2023

Abstract Nos. 1,561,095—1,561,894

TABLE OF CONTENTS

	Page	Abstract Number
GEOLOGY	3	1,561,095
GEOCHEMISTRY	78	1,561,382
GEOPHYSICS	87	1,561,415
DRILLING (WELL)	115	1,561,555
WELL LOGGING & SURVEYING.....	121	1,561,592
WELL COMPL SERV & WORKOVER	121	1,561,595
PRODUCING OIL & GAS	129	1,561,640
RESERVOIR ENG & REC METHOD	149	1,561,741
PIPELINING, SHIP & STORAGE	159	1,561,792
ALT FUELS & ENERGY SOURCES	166	1,561,826
BUSINESS & ECONOMICS	167	1,561,832
HEALTH, SAFETY & ENVIRON	168	1,561,839
SCIENCE & ENGINEERING	176	1,561,874
AUTHOR AND AFFILIATION INDEX	181	*****

©2023 Energy Abstracts LLC

ISSN 0031-6423 (print)

ISSN 2153-1471 (online)

No part of this bulletin may be reproduced or quoted without written permission from Petroleum Abstracts, a division of Energy Abstracts. A subscriber may not make use of the abstracts for the purpose of furnishing any information to any other person, firm or corporation, or in any way which would violate the Copyright Act as amended, without Petroleum Abstracts' written permission.

GEOLOGY

ADELAIDE GEOSYNCLINE

1,561,095

NEARSHORE ENVIRONMENTS BEFORE THE EVOLUTION OF LAND PLANTS

B.O'Connell, M.W.Wallace, A.S.Hood, M.A.Lechte and E.M.Mahon (Melbourne Univ; McGill Univ). *PRECAMBRIAN RESEARCH* v.382, Nov. 2022. (ISSN 0301-9268; Article no.106883)

The long-term evolution of the biosphere has caused fundamental shifts in environmental conditions and sedimentation at Earth's surface. While effects of the evolution of terrestrial vegetation on river systems have been explored in detail, facies models and possible shifts in sedimentation in pre-vegetation nearshore marine settings have not been sufficiently explored. The circa 800-million-year-old Burra Group, exposed in the Adelaide Fold Belt of South Australia, is a terrestrial to nearshore transgressive sedimentary succession associated with rifting. The Burra Group provides a record of marginal and shallow marine environments before the evolution of land plants. Environments are interpreted to record deposition in low energy fine-grained tidal flat, lagoon, tidal inlet, and beach-barrier environments (a beach-barrier system). The thick mudflats (up to 30 m) of the studied units indicate that vegetation is not essential for mudflat accumulation, contrary to some models. The fluvial-marine transition and the back-barrier-tidal inlet-beach-barrier transition is highly regular and there is little interbedding of units. The Tonian beach-barriers of the Burra Group do not backstep into the back-barrier region and aggrade much like stable modern systems backed by peat. These observations are suggestive of a stable barrier system in the absence of land plants. The high mud percentage and/or early carbonate cementation (including microbialite and stromatolite deposition during transgression) may have contributed to the stability of this beach-barrier system. (c2022 Elsevier B.V.)

ADRIATIC PLATFORM

1,561,096

NEW CONSTRAINTS ON THE PETM RECORD IN SHALLOW-MARINE CARBONATES FROM THE ADRIATIC CARBONATE PLATFORM, NE ITALY

M.Sabbatino, M.Franceschi, J.Dell'Anno, G.Frija, L.Consorti, E.Petranich, N.Barago, A.Corradetti, S.Covelli et al. (Trieste Univ). *21ST INTERNATIONAL SEDIMENTOLOGICAL CONGRESS [ISC] (Beijing, China, 8/22-26/2022) ABSTRACT BOOK* pp.184-185, 2022. (Available at <http://www.isc2022.org.cn> as of 9/22/2022; Abstract only)

The Paleocene-Eocene Thermal Maximum (PETM; ca 56 Ma) was an interval of extreme transient climate change, associated with global warming and a massive perturbation of the global carbon cycle (e.g., Zachos et al., 2003). This latter is testified by a sharp Negative Carbon Isotope Excursion (N-CIE) in the global marine and terrestrial $\delta^{13}\text{C}$ records, linked to the injection of large volumes of isotopically light carbon into the ocean-atmosphere system. The source of such ^{13}C -depleted carbon is still a matter of debate. The emplacement of the North Atlantic Igneous Province (NAIP) with the release of huge amounts of CO_2 is suspected to be one of the factors that may have caused such a relevant change in the composition of the atmosphere/ocean carbon reservoirs and the associated abrupt climate perturbation. Research is increasingly exploring mercury (Hg) anomalies as tracers of volcanism during the Paleocene-Eocene interval mostly in deep-water and subordinately in shallow-water settings (e.g., Tremblin et al., 2022 and references therein), arguing about their possible relationship to the NAIP emplacement and its impact on the PETM onset and duration. The aim of this contribution is to present an integrated study of sedimentology, stratigraphy (bio and chemo), and geochemistry of the deposits belonging to the Adriatic Carbonate Platform cropping out in the Classical Karst area of Friuli Region (NE Italy), encompassing the PETM event. In particular, here we show paired new carbon- and oxygen-isotope data combined with Hg concentrations and TOC analyses from two shallow-water marine carbonate sections across the Paleocene-Eocene boundary. The two investigated sections were deposited during the migration

of the foreland basin related to the Dinaric orogeny and are today exposed in the Classical Karst area near Trieste (Italy) for about 50 and 300 meters, respectively, of Paleocene-Eocene platform carbonates evolving upward to hemipelagic marls and then to siliciclastic deposits. Vertical facies evolution of the carbonate platform indicates that an initial inner- to mid-ramp setting underwent a relative deepening and then was followed by multiple emersion episodes intercalated by proximal marine deposition (i.e., innermost to inner ramp environments). This latter was followed by a return to open marine facies which then persisted until the final drowning of the Adriatic platform that in our study area occurred in the late early Eocene. Our results show in both sections a negative excursion in the carbon-isotope record that, associated with biostratigraphic data, can be correlated with the PETM N-CIE and is comparable to other coeval $\delta^{13}\text{C}$ records, both in shape and amplitude.

AFAR DEPRESSION

1,561,097

ANALOG AND NUMERICAL MODELING OF RIFT-RIFT-RIFT TRIPLE JUNCTIONS

D.Maestrelli, S.Brune, G.Corti, D.Keir, A.A.Muluneh and F.Sani (IGG-CNR; Helmholtz Centre Potsdam; Firenze Univ). *TECTONICS* v.41, no.10, Oct. 2022. (ISSN 0278-7407; ISSN 1944-9194; Article no.e2022TC007491)

Rift-Rift-Rift triple junctions are key features of emergent plate boundary networks during fragmentation of a continent. A key example of such a setting is the Afar triple junction where the African, Arabian and Somalian plates interact. We performed analog and numerical models simulating continental break-up in a Rift-Rift-Rift setting to investigate the resulting structural pattern and evolution. We modified the ratio between plate velocities, and we performed single-stage (with all plates moving at the same time) and two-stage (where one plate first moves alone and then all the plates move simultaneously) models. Additionally, the direction of extension was changed to induce orthogonal extension in one of the three rift branches. Our models suggest that differential extension velocities in the rift branches determine the localization of the structural triple junction, which is located closer to the rift branch experiencing slower extension velocities. Furthermore, imposed velocities affect the deformation resulting in end-member fault patterns. The effect of applying similar velocities in all rift arms is to induce a symmetric fault pattern (generating a Y-shaped geometry). In contrast, a faster plate generates structures trending orthogonal to dominant velocity vectors, while faults associated with the movement of the slower plates remain subordinate (generating a T-shaped pattern). Two-stage models reveal high-angle faults interacting at the triple junction, confirming that differential extension velocities strongly affect fault patterns. These latter models show large-scale similarities with fault patterns observed in the Afar triple junction, providing insights into the factors controlling the structural evolution of this area.

ANADARKO BASIN

1,561,098

LATE PALEOZOIC EVOLUTION OF THE ANADARKO BASIN: IMPLICATIONS FOR LAURENTIAN TECTONICS AND THE ASSEMBLY OF PANGAEA

N.F.Hobbs, J.W.van Wijk, R.Leary and G.J.Axen (New Mex Inst Mining Technl). *TECTONICS* v.41, no.10, Oct. 2022. (ISSN 0278-7407; ISSN 1944-9194; Article no.e2021TC007197)

Interplay between marginal and intraplate late Paleozoic tectonics in southeastern Laurentia is a subject of debate. In southern Laurentia, intraplate deformation has been attributed to combinations of compressive forces from orogenic belts in the west, southwest, and southeast. While left-lateral transpression is generally an accepted mechanism for formation of uplifts in the Southern Oklahoma Aulacogen (SOA), to date no studies have explained the driving mechanisms of these kinematics. Here, we analyze the Southern Oklahoma Transpressional System (SOTS), a ca. 500-km long ca. 50-km wide fault zone that extends from the southeastern Laurentian margin into the plate interior along Cambrian lithospheric weaknesses inherited from the SOA. We use a compilation of published studies to present detailed, time-integrated sedimentary thickness maps of SOTS-related basins. We

combine these maps with a new interpretation of three 2D seismic reflection lines to constrain timing and kinematics of all major late Paleozoic SOTS fault zones. We show that the SOTS kinematics evolved from contraction to left-lateral strike-slip during Mississippian-Pennsylvanian time. Tectonic activity and fault kinematics in the SOTS are explained by a model in which a remnant ocean basin closed diachronously from northeast to southwest along the Southern Appalachian and Ouachita-Marathon orogens. Left-lateral transpression during diachronous closure of the Rheic oceanic basin along the Ouachita-Marathon margin is related to rotation of the stress field due to changes in slab-pull and eastward drift of Laurentia toward Gondwana. We speculate that the SOTS acted in part as a STEP (subduction-transfer edge propagator) fault that followed the pre-existing SOA.

ANHUI

1,561,099

SYNCHROTRON-AIDED RECONSTRUCTIONS OF THE OZARKODINID CONODONT APPARATUSES, SCYTHOGONDOLELLA AND HADRODONTINA, FROM THE LATE SMITHIAN (OLENEKIAN, EARLY TRIASSIC) OF EAST CHINA

S.Liu, Z.Sun, C.Ji and D.Jiang (Beijing Museum; Peking Univ; Nanjing Inst Geol Palaeont). *5TH INTERNATIONAL CONODONT SYMPOSIUM [ICOS] (Wuhan, China and Online, 6/24-27/2022) PROGRAM AND ABSTRACTS* pp.60-61, 2022. (Abstract only)

Although natural conodont assemblages are extremely rare, they record direct morphological, compositional, and homological evidence as well as the architectural arrangement of the elements. They thus serve as excellent material for reconstructing a conodont apparatus. We here report on exceptionally preserved natural assemblages of the gondolelloid *Scythogondolella milleri* and the prioniodinin *Hadrodontina aequabilis* from the end Smithian (Olenekian, Early Triassic) of the South Majiashan section, Chaohu City, Anhui Province and the Longtan section, Nanjing City, Jiangsu Province, East China. These materials were scanned using non-destructive synchrotron radiation X-ray tomographic microscopy (SRXTM), which reveals the original three-dimensional architectures of the apparatuses and then allows us to test the architectural models for gondolelloids and prioniodinins. Accordingly, the best characterized architectural models further constrain the functional interpretations of the 15-element ozarkodinid apparatuses. Six conodont natural assemblages with various degrees of preservation were ascribed to the superfamily Gondolelloidea (Ozarkodinina, Ozarkodinida) based on the occurrence of enantiognathiform elements in the S2 position (i.e., the S1 position proposed by Orchard, 2005) and further identified as *Scythogondolella milleri* due to their broad segminiplanate P1 elements with strong marginal denticles.

APPALACHIAN BASIN

1,561,100

BLACK SHALE-GRAY SHALE TRANSITIONS IN A LATE DEVONIAN SHALE SUCCESSION, CENTRAL APPALACHIAN BASIN (NORTHERN OHIO): SEDIMENTARY AND GEOCHEMICAL EVIDENCE FOR TERRESTRIAL ORGANIC MATTER INPUT DRIVING ANOXIA EVENTS

C.A.Dunkel, A.Vazquez-Ortega and J.E.Evans (Bowling Green State Univ). *PALAEOGEOGRAPHY, PALAEOCLIMATOLOGY, PALAEOECOLOGY* v.608, 12/15/2022. (ISSN 0031-0182; Article no.111271)

In a 140 m-thick sediment core through Upper Devonian shale units in the Central Appalachian Basin, gray shale units (TOC \leq 1%) and black shale units (TOC \leq 9%) are separated by "intercalated zones" (ICZs) of thinly interbedded gray and black shales. In accordance with Walther's law of facies successions, ICZs imply environments producing black shales were coeval and adjacent to environments producing gray shales. To understand these facies transitions, we studied event layer sedimentology, organic geochemistry, and trace elements. This study found black shales to be shallow-water deposits (with tempestites and wave-modified turbidites), associated with significant terrestrial input (with abundant hyperpycnites, and terrestrial-derived humic and

fulvic acids). The shales were deposited under varying redox conditions, with extensively bioturbated intervals alternating with intervals preserving intact micro-lamination, and demonstrating significant variations in trace element V/Cr, Ni/Co, and Th/U ratios. These observations are reconciled by attributing shale TOC values to sediment dynamics of deltas draining the Neo-Adacian Highlands. Progradation of individual delta distributary lobes resulted in localized offshore regions receiving increased terrestrial nutrient input and causing freshwater-induced water column stratification and oxygen stress (similar to the "dead zones" of many modern deltas), producing black shales. In contrast, gray shales formed between deltas or after delta distributary lobe abandonment. The intercalated black shale-gray shale transition intervals (ICZs) are interpreted to represent dynamic water and sediment conditions during the time interval of delta distributary lobe avulsion events. This model contrasts with previous models calling for basin-wide anoxia or assigning black shales to basinal deposits. (c2022 Elsevier B.V.)

AQUITAINE BASIN

1,561,101

ONSET OF IBERIAN-EUROPEAN PLATE CONVERGENCE: LATE CRETACEOUS FLEXURAL RESPONSE OF A HOT LITHOSPHERE (AQUITAINE BASIN, FRANCE)

B.Issautier, E.Lasseur, N.Saspiturry, P.Angrand, S.Andrieu and O.Serrano (Bureau Rech Geol Min (Fr); Montpellier Univ; Geosciences Envir Toulouse). *TECTONOPHYSICS* v.843, 11/20/2022. (ISSN 0040-1951; Article no.229504)

The Aquitaine Basin is closely linked to the evolution of the Pyrenees, providing precious evidence of the early stages of the Pyrenean orogeny in the Late Cretaceous. Although the timing and geometry of the Early Cretaceous rifting stage is well constrained in the Pyrenees and surrounding north Pyrenean basins, the subsequent early inversion stage has resisted characterization. In this study, we used well log correlations and interpretation of seismic reflection profiles to determine the Late Cretaceous evolution of the sedimentary record in the Aquitaine Basin, spanning the transition from the postrift stage to the beginning of convergence. We identified two main deformation stages during the Late Cretaceous with radically different basin geometries in the western and eastern portions of the Aquitaine Basin. The western part appears to remain under a thermal subsidence regime, inherited from the postrift stage initiated in the Turonian, with little to no deformation. In contrast, the eastern part records early inversion, as indicated by the presence of a well-defined Campanian flexural basin. Between them, Coniacian and Santonian strata indicate a sharply increasing distinction between a very slowly subsiding North Aquitaine Domain (condensed sedimentation) and a strongly subsiding South Aquitaine Domain. We interpret this development as a consequence of lithospheric buckling resulting from far-field compressive strain between the Eurasia and Africa plates. During the Campanian, northward convergence of the Iberia plate led to the formation of a flexural basin with a narrower, steeper geometry than the subsequent Eocene basin that formed in nearly the same region during the Pyrenean orogeny. We attribute this difference to the development of the foreland over a lithosphere that was not thermally reequilibrated in Campanian time, roughly 10 Myr after rifting. This thermal inheritance resulted in lithosphere of very low rigidity. Sedimentary basins formed during both the Coniacian-Santonian and Campanian to early Maastrichtian were thus accommodated by short-wavelength flexural deformation of the lithosphere, a distinctive deformation pattern that represents an immediate response to the onset of compressive strain. (c2022 Elsevier B.V.)

ARCTIC AREA

1,561,102

BIOSTRATIGRAPHY AND SEQUENCE STRATIGRAPHY OF THE JURASSIC-CRETACEOUS TRANSITION IN THE CANADIAN HIGH ARCTIC, INFERRED FROM PALYNOMORPHS AND MACROFAUNA

S.Ingrams, D.W.Jolley and S.R.A.Kelly (Aberdeen Univ; CASP). *65TH ANNUAL PALAEOONTOLOGICAL ASSOCIATION MEETING (Manchester, UK, 12/18-20/2021) PROGRAMME AND ABSTRACTS* pp.71-72, 2021. (Available at <http://www.palass.org> as

of 11/1/2022; **Abstract only**)

The Rollrock Section in Arctic Canada offers one of the best-exposed, most continuous high-latitude sedimentary and palaeontological archives of the Jurassic-Cretaceous transition. Nine out of 15 macrofossil horizons correlate to Pan-Boreal schemes for the Tithonian-Berriasian interval. Dinoflagellate cyst assemblages from 200 samples, taken at intervals of 1.5 m or greater over a 560-meter succession, conform to seven Oxfordian to early Valanginian biozones. Statistical analysis of the same assemblages reveals long-term trends as well as short-term, cyclic shifts in community structure driven by dinoflagellate palaeoecology. In particular, abundances of proximochorate and chorate dinocysts are utilized as proxies. While the former prefer proximal, high-energy, nutrient-rich settings, the latter dominate in distal, low-energy, nutrient-depleted environments. They thus can be linked to regressive and transgressive systems tracts, respectively, and are useful for inferring fourth-order sequence stratigraphy. Altogether, the studied succession spans two entire and two partial third-order transgressive-regressive sequences, and its upper portion is subdivided into ten fourth-order sequences. By integrating the results from macrofossil and palynological analysis, a greatly improved stratigraphy is now available for the Jurassic-Cretaceous boundary interval in Arctic Canada that will be used in subsequent studies to reconstruct the palaeoenvironmental dynamics at high latitudes in greater detail.

ASIA

1,561,103

MESOZOIC MAGMATIC ARC IN EAST ASIAN CONTINENTAL MARGIN TRIGGERED BY PALEO-PACIFIC PLATE SUBDUCTION: CONSTRAINTS FROM GRAVITY AND MAGNETIC ANOMALIES

D.Weil, S.Jiang, J.Liu, S.Li, L.Guo, I.Somerville, X.Guan, Y.Liu and Y.Chen (China Ocean Univ). *TECTONOPHYSICS* v.844, 12/5/2022. (ISSN 0040-1951; Article no.229625)

The Mesozoic East Asian Continental Margin (EACM) is generally considered as a continental magmatic arc triggered by Paleo-Pacific Plate subduction. However, the magmatic arc was not evident for a long time. This paper tries to use the gravity and magnetic responses along the magmatic arc to deeply explore its spatio-temporal distribution. Based on the gravity and magnetic anomalies of the Mesozoic magmatic arc on the EACM and combined with the integration of previous geological and geochronological studies, it is found that the tectonic features of the magmatic arc are more obvious in the fourth-order approximation/detail gravity anomaly fields by using wavelet multi-scale analysis. Furthermore, the residual crustal gravity anomalies containing the medium-wavelength components of the complete Bouguer gravity anomalies are analyzed for the identification of the Jurassic magmatic arcs. Finally, line-drawing analysis is performed on the fourth-order detail gravity anomaly field to explore the response of the Mesozoic magmatic arcs to Paleo-Pacific subduction on the EACM. Our results support that the magmatic arcs on the EACM mainly developed in the Late Triassic-Early Cretaceous Andean Active Continental Margin and in the late Early Cretaceous-Eocene transtensional continental margin. Our study contributes to the formation and refinement of the Paleo-Pacific Plate subduction mechanism and the Mesozoic tectonic evolutionary model of the EACM, and also provides geophysical evidence for the reconstruction of dynamic processes of the EACM. (c2022 Elsevier B.V.)

AZERBAIJAN

1,561,104

GRADUAL WARMING PRIOR TO THE END-PERMIAN MASS EXTINCTION

J.Gliwa, M.Wiedenbeck, M.Schobben, C.V.Ullmann, W.Kiessling, A.Ghaderi, U.Struck and D.Korn (Berlin Museum; GeoForschungsZentrum). *PALAEONTOLOGY* v.65, pt.5, Sept./Oct. 2022. (ISSN 0031-0239; ISSN 1475-4983; Article no.e12621)

The biggest known mass extinction in the history of animal life occurred at the Permian-Triassic boundary and has often been linked to global warming. Previous studies have suggested that a geologically rapid (< 40 kyr) temperature increase of more than 10°C occurred simultaneously with the main extinction pulse. This

hypothesis is challenged by geochemical and palaeontological data indicating profound environmental perturbations and a temperature rise prior to the main extinction. Using secondary ion mass spectrometry (SIMS), we measured oxygen isotope ratios from Changhsingian (late Permian) ostracods of north-western Iran. Our data show that ambient seawater temperature began to rise at least 300 kyr prior to the main extinction event. Gradual warming by approximately 12°C was probably responsible for initial environmental degradation that eventually culminated in the global end-Permian mass extinction.

BAJA CALIFORNIA

1,561,105

THE TIMING OF FOREST FIRE AT THE K-Pg BOUNDARY: EVIDENCE FROM THE PACIFIC MARGIN OF BAJA CALIFORNIA, MEXICO

B.Kneller, A.Santa Catharina, J.C.Marques, A.D.McArthur, S.R.S.Cevallos-Ferriz, T.Theurer, D.Muirhead and I.A.Kane (Aberdeen Univ; Rio Grande Sul Fed Univ). *21ST INTERNATIONAL SEDIMENTOLOGICAL CONGRESS [ISC] (Beijing, China, 8/22-26/2022) ABSTRACT BOOK* p.203, 2022. (Available at <http://www.isc2022.org.cn> as of 9/22/2022; **Abstract only**)

Impact of the Chicxulub bolide that brought the Mesozoic to a close is widely recorded by a layer of highly distinctive deposits, including the products of catastrophic sedimentation around the Gulf of Mexico and the North Atlantic, as well as globally-distributed bolide- and target-sourced ejecta from the impact site itself. These deposits also include soot, the origin of which has ascribed either to combustion of inorganic material at the target site, or to wild fires occurring at or close to the time of impact, or subsequently due to ignition of forest killed by the immediate after-effects of the impact (Morgan et al., 2022, and references therein). We describe a section from a mid-slope succession on the Pacific margin of Mexico, about 2500 km from the impact site, which on the basis of faunal and floral changes, radiometric dating, and an iridium anomaly, clearly represents a Cretaceous-Palaeogene (K-Pg) boundary section. The deposit consists largely of debrites that contain not only re-sedimented shallow marine faunas but also large sections of silicified tree trunks with charred bark and cambium but pristine xylem, and no evidence of decay or bio-erosion (Cevallos-Ferriz et al., 2021). Raman spectroscopy of the charcoal indicates temperatures up to more than 1000 C. The presence of fossil wood within deepwater deposits implies its incorporation into a debris flow whose matrix yield strength exceeded the buoyancy of the wood. The adjacent slope and coastal succession shows widespread and large-scale sliding at the K-Pg boundary. We interpret the presence of shallow marine and terrestrial material within debrite of the K-Pg boundary section to indicate resedimentation by the back-wash of a slide-generated -1 tsunami. Adopting upper crustal P wave velocities of 6 to 8 km s (e.g. Rosalia et al., 2019) depending on the ray path, arrival times of the first seismic shocks from the impact would have been no more than 5 to 7 seconds post-impact. Based on historic seismogenic mass failures (e.g. Lovholt et al., 2019), sliding would have occurred almost immediately, and the associated tsunami would have arrived within minutes to tens of minutes. Since the trees incorporated into the debris flow by the tsunami were already charred, the high-temperature event responsible must already have occurred by this time, i.e. within minutes to tens of minutes of the impact. This rules out secondary burning of dead trees in the days to months following impact. This rules out secondary burning of dead trees in the days to months following impact.

BAYANHOT BASIN

1,561,106

CHARACTERISTICS OF LATE REFORMATION AND PETROLEUM PROSPECT OF CARBONIFEROUS STRATA IN THE BAYANHOT BASIN, N. CHINA

H.Zhao, C.Liu, Y.Zhou, X.Shao, J.Wang, Z.Peng, L.Huang, Z.Ruan, H.Guo et al. (Northwest Univ, China). *GEOLOGICAL JOURNAL* v.57, no.10, pp.4183-4193, Oct. 2022. (ISSN 0072-1050; ISSN 1099-1034)

The Bayanhot Basin is located at the intersection of the Alxa Block, Ordos Basin, and Corridor Transitional Zone. Although the

Carboniferous palaeo-sedimentary and tectonic features are of great significance in discovering the scientific issues of the influential range of the Qinlin-Qilian Ocean and palaeo-Asian Ocean and the relationship of the North China Block and Alxa Block, as well as in evaluating hydrocarbon prospects, it is difficult to restore the Carboniferous features because of intense late reformation. It is necessary to systematically discuss the late reformation characteristics. It is shown in this paper that Carboniferous strata have mainly experienced two extensive tectonic movements during the Late Hercynian-Indosinian and Yanshanian periods and had four reformation types: structural compression, uplift to erosion, superimposed and deep burial, and thermodynamic reformation, based on comprehensive analysis of seismic profiles, wells, aeromagnetic data and tectonic characteristics of the surrounding regions. Carboniferous strata were partly eroded by the compressional folding during Late Hercynian-Indosinian movement, and were forcefully eroded by thrusting and uplift during Yanshanian movement, especially movement in the Late Jurassic, which determined the present thickness of the Carboniferous strata. The deep overlap of the overlying Jurassic, Lower Cretaceous, Palaeogene, and Neogene rocks in different areas was beneficial to the maturation of Carboniferous source rocks. The magmatic rocks exposed by well drilling and shallow aeromagnetic anomaly belts show heating reformation, which accelerated the maturation of source rocks to some extent. The total strength of the Carboniferous late reformation was stronger in the western area than in the eastern area and greater in the northern area than in the southern area. The multiple periods and various types of reformation were closely related to the regional closure of the Palaeo-Qinling-Qilian Ocean in the south, Palaeo-Asian Ocean, and Mongolia-Okhotsk Ocean in the north and the subduction of the Palaeo-Pacific Plate in the east. The Carboniferous strata in eastern and southern basins will be the prospective favourable areas for the petroleum exploration.

BEIBU GULF**1,561,107****DEVELOPMENT OF EXTENSIONAL DECOLLEMENT STRUCTURE AND ITS PETROLEUM IMPLICATION IN THE WUSHI EAST SUBSAG, BEIBUWAN BASIN**

Z.Wang, D.Tong, M.Gao and J.Yu (China Univ Geosci, Wuhan). *21ST INTERNATIONAL SEDIMENTOLOGICAL CONGRESS [ISC] (Beijing, China, 8/22-26/2022) ABSTRACT BOOK* p.344, 2022. (Available at <http://www.isc2022.org.cn> as of 9/22/2022; **Abstract only**)

Wushi Sag is located in the central part of the Beibuwan Basin, northwestern continental margin of the South China Sea. From the early Paleocene to the end of the Oligocene, it experienced multiple phases of extension. Based on the new high-quality 3-D seismic data obtained in the process of petroleum exploration, this study conducted an in-depth analysis of the extensional decollement faults in the Wushi east subsag, established the growth and linkage model of decollement faults and discussed the meaning to oil and gas exploration. The results show that there are 7 extensional decollement faults (Fa-Fg) in the Wushi east subsag, which are distributed in the near E-W or NE-SW direction. These decollement faults together with north-dipping No.7 boundary fault, controlled sedimentation from the 1st Member of Liushagang Formation to the 1st Member of Weizhou Formation, which formed a huge rollover anticline. In terms of evolution, during the Early-Middle Eocene, the basin is a graben or half-graben controlled by the NE-SW No.7 boundary fault and other local small basement faults. The 3rd member of Liushagang Formation strata are discretely distributed and were overlaid by thick layer of the 2nd member of Liushagang Formation. From the late Eocene to the late Oligocene, the basin deposited 1st Member of Liushagang Formation to the 1st Member of Weizhou Formation, controlled by the oppositely dipping extensional decollement faults and the No.7 boundary fault. From the early Miocene to the present, the basin changed into a sag basin. This study depicted the geometry of extensional decollement structure which formed during the second rifting rift phase of Wushi east subsag, analyzed the growth and linkage pattern of decollement faults, proposed the decollement faults upslope-ward migration model, which has a great significance for solving the problems of oil and gas migration, storage and preservation.

BEIKANG BASIN**1,561,108****FORMATION AND IMPLICATION OF COLD-SEEP CARBONATES IN THE SOUTHERN SOUTH CHINA SEA**

W.Zhang, C.Chen, P.Su, Z.Wan, W.Huang, J.Liang, J.Liang, J.Feng, W.Zhou et al. (Guangzhou Marine Geol Surv). *JOURNAL OF ASIAN EARTH SCIENCES* v.241, Jan. 2023. (ISSN 1367-9120; Article no.105485)

Southern South China Sea (SCS), rich in oil and gas resources, can provide a favorable condition for the formation and development of cold seeps. However, the geochemical effect of cold seep activities and the carbon cycle in the SCS are not well understood. Cold-seep carbonates as a window to exploration of gas hydrate are of great significance to investigate the material circulation in cold-seep system and to reconstruct the paleo-climate environment in the SCS. In this research, eight cold-seep carbonates collected from the Beikang Basin, southern SCS, are generally presented as yellow-black irregular column, crust and block, and mainly composed of high magnesium calcite (HMC), indicating they probably formed inside the deep fluid migration pathway. The middle rare earth element (MREE) enrichment with no or positive Ce anomaly in the carbonates from BH-CL37A suggests that they precipitated in anoxic pore water, while heavy rare earth element (HREE) enrichment in BH-CL32A carbonate shows great effect of seawater and they were formed in shallower depth. Different enrichments of redox sensitive trace elements and (Mo/U) EF indicate the strong anoxic environment. It is concluded that the difference of fluid environment could affect the enrichment degree and precipitation rate of trace elements by the relations between trace elements and Al. Extremely depleted ^{13}C , slightly enriched ^{18}O and the variation of Sr isotopes have archived the main biogenic methane source and the co-effect of seawater and seep fluid driven from a deep source (possibly containing the water from hydrate dissociation). The unique and complex geological conditions in the southern SCS will lead to the distinct regional specificity of the cold seep, which is different from the cold seep system in the northern SCS. This study plays an essential role in fulfilling the understanding of the activities of cold seeps in the SCS, revealing the element migration and transformation in cold seeps and their influencing factors. (c2022 Elsevier Ltd.)

BENGAL BAY**1,561,109****DRIVERS OF LATE MIOCENE TROPICAL SEA SURFACE COOLING: A NEW PERSPECTIVE FROM THE EQUATORIAL INDIAN OCEAN**

C.Martinot, C.T.Bolton, A.C.Sarr, Y.Donnadieu, M.Garcia, E.Gray and K.Tachikawa (Aix Marseille Univ). *PALEOCEANOGRAPHY AND PALEOCLIMATOLOGY* v.37, no.10, Oct. 2022. (ISSN 2572-4525; Article no.e2021PA004407)

During the late Miocene, global cooling occurred alongside the establishment of near-modern terrestrial and marine ecosystems. Significant (3°C – 5°C) sea surface cooling from 7.5 to 5.5 Ma is recorded by proxies at midlatitudes to high latitudes, yet the magnitude of tropical cooling and the role of atmospheric carbon dioxide (pCO_2) in driving this trend are debated. Here, we present a new orbital-resolution sea surface temperature (SST) record spanning the late Miocene to earliest Pliocene (9–5 Ma) from the eastern equatorial Indian Ocean (International Ocean Discovery Program Site U1443) based on Mg/Ca ratios measured in tests of the planktic foraminifer *Trilobatus trilobus*. Our SST record reveals a 3.2°C decrease from 7.4 to 5.8 Ma, significantly increasing previous estimates of late Miocene tropical cooling. Analysis of orbital-scale variability shows that before the onset of cooling, SST variations were dominated by precession-band (19–23 kyr) variability, whereas tropical temperature became highly sensitive to obliquity (41 kyr) after 7.5 Ma, suggesting an increase in high-latitude forcing. We compare a revised global SST database with new paleoclimate model simulations and show that a pCO_2 decrease from 560 to 300 ppm, in the range suggested by pCO_2 proxy records, could explain most of the late Miocene sea surface cooling observed at Site U1443. Using our new Site U1443 record as representative of tropical SST evolution, estimated meridional SST gradients suggest a much more modest increase over the late Miocene than previously suggested, in agreement with modeled meridional SST gradients.

BENTHONIC ORGANISM

1,561,110

ECOLOGICAL INSIGHTS INTO EDIACARAN EVOLUTION

E.G.Mitchell (Cambridge Univ). *65TH ANNUAL PALAEOONTOLOGICAL ASSOCIATION MEETING (Manchester, UK, 12/18-20/2021) PROGRAMME AND ABSTRACTS* p.16, 2021. (Available at <http://www.palass.org> as of 11/1/2022; **Abstract only**)

Ediacaran fossils include some of the earliest animals known from the fossil record (572-550 Ma). However, understanding Ediacaran evolution is hampered by the lack of clear morphological analogues between Ediacaran and extant organisms. Fortunately, Ediacaran preservation is exceptional, with thousands of soft-bodied, sessile organisms preserved in their in-life positions. This in situ preservation means that the position of the specimens on their bedding planes captures their entire life history: how they reproduced and interacted with each other and with their local environment. As such, spatial analyses can be used to reconstruct Ediacaran eco-evolutionary dynamics. We have systematically mapped Ediacaran palaeocommunities using LiDAR, photogrammetry and a laser line probe, and used spatial analyses to infer the underlying processes governing community dynamics. We found a lack of influence of the local environment on the older deep-water organisms, which suggests that early metazoan diversification may not have been driven by systematic adaptations to the local environment, but instead may have resulted from stochastic demographic differences. This pattern shifts for younger, shallow-water communities, which were heavily influenced by local environmental patchiness. Our results provide quantitative support for the "Savannah" hypothesis for early animal diversification, whereby Ediacaran diversification was increasingly driven by patchiness in the local benthic environment.

BETIC CORDILLERA

1,561,111

REFINED TECTONIC EVOLUTION OF THE BETIC-RIF OROGEN THROUGH INTEGRATED 3-D MICROSTRUCTURAL ANALYSIS AND Sm-Nd DATING OF GARNET PORPHYROBLASTS

D.Aerden, T.P.Farrell, E.F.Baxter, E.M.Stewart, A.Ruiz-Fuentes and M.Bouybaouene (Granada Univ; Boston Coll; Boston Univ; Rabat Univ). *TECTONICS* v.41, no.10, Oct. 2022. (ISSN 0278-7407; ISSN 1944-9194; Article no.e2022TC007366)

High-resolution microstructural analysis of porphyroblast inclusion trails integrated with Sm-Nd garnet geochronology has provided new insight into the tectonic history of the Betic-Rif orogen. Three principal age groups of porphyroblasts are demonstrated with distinctly oriented inclusion-trails. Inclusion-trail curvature axes or "FIA" (Foliation Inflexion/Intersection Axes) are shown to represent "fossilized" crenulation axes from which a succession of different crustal shortening directions can be deduced. The regional consistency of microstructural orientations and their geometric relationship with multiple sets of macroscopic folds reveal the composite character of the Gibraltar Arc formed by a superposition of different folding directions and associated lineations. Bulk-garnet ages of 35-22 Ma obtained from five micaschist samples of the Alpujarride-Sebide complex (ASC) and of 35-13 Ma from four micaschists of the Nevado-Filabride complex (NFC) allow to deduce NNE-SSW directed shortening in the Late Eocene changing to NW-SE shortening in the early Oligocene, alternating with suborthogonal NE-SW shortening during the Miocene. These directions can be related to a major swing in the direction of relative Africa-Iberia plate-motion known from kinematic modeling of magnetic seafloor anomalies, and subsequent dynamic interference between plate convergence and suborthogonal "tectonic escape" of the Alboran Domain. Coupled to previously established P-T-t paths, the new garnet ages support a common tectono-metamorphic evolution of the ASC and NFC as laterally equivalent orogenic domains until, in the Miocene, the second became re-buried under the first.

BETIC CORDILLERA

1,561,112

COMPLEX ENVIRONMENTAL PERTURBATIONS RELATED THE EARLY APTIAN OAE 1A - INSIGHTS FROM A PELAGIC SUCCESSION FROM THE WESTERN TETHYS**(SUBBETIC ZONE, SE SPAIN)**

C.Sequero, J.M.Castro, M.L.Quijano, R.Aguado, G.A.de Gea, B.D.A.Naafs and R.D.Pancost (Jaen Univ; Bristol Univ). *21ST INTERNATIONAL SEDIMENTOLOGICAL CONGRESS [ISC] (Beijing, China, 8/22-26/2022) ABSTRACT BOOK* p.174, 2022. (Available at <http://www.isc2022.org.cn> as of 9/22/2022; **Abstract only**)

The early Aptian Oceanic Anoxic Event (OAE 1a) represents a major perturbation in the global carbon cycle associated with a light-carbon input into the climate system, from volcanogenic (Ontong-Java Plateau) and/or methanogenic sources, originating significant environmental, biotic and sedimentary changes. The global signature of this event is a negative followed by a positive carbon stable isotope excursion (CIE), which correlates with the widespread massive accumulation of organic matter in all major ocean basins. Besides the global environmental perturbation that characterizes the OAE 1a, local factors are a key aspect to take into account when discussing the global signals on marine successions. Here, we combine new biomarker and elemental data with published high-resolution C-isotope stratigraphy, TOC content and biostratigraphy from an early Aptian pelagic succession in the western Tethys, La Frontera section (Subbetic basin, SE Spain), in order to provide new insights into the relative roles of variations in terrestrial inputs, primary productivity and degree of oxygenation of marine waters during and after the OAE 1a. This section is further compared with a published equivalent record from a nearby succession deposited on a slightly different palaeogeographic context (Carbonero section), in order to discuss the local vs. global controls on the geochemical signal. In La Frontera section, analyses of the distribution of selected biomarkers (n-alkanes, acyclic isoprenoids, steranes and hopanes) together with the record of redox-sensitive trace elements, has revealed three intervals of accelerated environmental change that correlate with those previously observed in the Carbonero section. These episodes occurred during intervals of rapid change in the C-isotope values. In La Frontera section, the first episode, which coincides with the negative C-isotope excursion at the onset of the OAE 1a (isotope segment C3), is characterized by a weak deoxygenation and environmental stress. The second episode, which took place at the end of the positive shift globally assigned to the C4 segment, represents the major environmental and biotic perturbation of the succession, with development of anoxia/dysoxia and increased continental inputs and productivity. The third interval of rapid perturbations during the OAE 1a occurred in the lower part of C6 segment, in this case showing a moderate increase in marine productivity, weak development of anoxia/dysoxia and no evidences of increased continental inputs. Despite the correlation of these episodes with those observed in the Carbonero section, interesting differences can be noticed regarding the magnitude of these perturbations. At Carbonero, the three intervals have similar intensity in the geochemical signal, whereas at La Frontera the second episode (C4) shows a signal clearly stronger than the others.

BIODIVERSITY

1,561,113

LOCATING THE BASE OF THE CAMBRIAN: GLOBAL CORRELATION OF THE EDIACARAN-CAMBRIAN BOUNDARY

T.P.Topper, M.J.Betts, D.Dorjnamjaa, G.Li, L.Li, G.Altanshagai, B.Enhkbaatar and C.Skovsted (Northwest Univ, China; Inst Paleontol (Mongolia)). *65TH ANNUAL PALAEOONTOLOGICAL ASSOCIATION MEETING (Manchester, UK, 12/18-20/2021) PROGRAMME AND ABSTRACTS* p.96, 2021. (Available at <http://www.palass.org> as of 11/1/2022; **Abstract only**)

The emergence and diversification of animals during the Cambrian is one of the most significant evolutionary events in Earth's history. However, the sequence of events leading to the origin of "modern" ecosystems and the exact temporal relationship between Ediacaran and Cambrian faunas are uncertain, as identification of the Ediacaran-Cambrian boundary and global correlation through this interval remains problematic. The base of the Cambrian has been the source of constant conjecture due to the drawbacks of *Treptichnus pedum* and the lack of secondary markers at the GSSP. Because of this we suggest that the GSSP be redefined elsewhere, in a new section that contains secondary markers that

permit global correlation. We propose the nadir of the Basal Cambrian carbon isotope Excursion (BACE) as the favoured candidate to define the base of the Cambrian. It is essential, however, that the BACE be complemented with secondary markers such as the protoconodont *Protohertzina* and *Treptichnus pedum*. These taxa provide essential biostratigraphic control on the BACE and increase potential for effective global correlation. We also recommend that an auxiliary boundary stratotype section and point (ASSP) be simultaneously established in order to incorporate additional markers that will aid global correlation of the Ediacaran-Cambrian boundary.

.....
BLUE RIDGE MT AREA **1,561,114**

DEFINING THE TIMING, EXTENT, AND CONDITIONS OF PALEOZOIC METAMORPHISM IN THE SOUTHERN APPALACHIAN BLUE RIDGE TERRANES OF TENNESSEE, NORTH CAROLINA, AND NORTHERN GEORGIA

J.R.Thigpen, D.P.Moehler, H.H.Stowell, A.Mersch, R.D.Hatcher, N.E.Powell, B.M.Spencer, C.A.Mako, E.M.Bollen et al. (Kentucky Univ). *TECTONICS* v.41, no.10, Oct. 2022. (ISSN 0278-7407; ISSN 1944-9194; Article no.e2022TC007406)

The tectonometamorphic evolution of the southern Appalachians, which results from multiple Paleozoic orogenies (Taconic, Neocadian, and Alleghanian), has lacked a consensus interpretation regarding its thermal-metamorphic history. The Blue Ridge terranes have remained the focus of the debate, with the interpreted timing of regional Barrovian metamorphism and associated deformation ranging from early (Taconic) to late Paleozoic (Alleghanian). New monazite U-Pb geochronology and thermobarometric data are integrated with previously reported geo- and thermochronology to delimit the Paleozoic thermal-metamorphic evolution of these terranes. Monazite compositional, textural, and U-Pb age systematics are remarkably consistent for all samples, yielding a single dominant age mode for each sample. The western, central, and eastern Blue Ridge terranes yield weighted mean monazite U-Pb ages of 450-441, 459-457, and 458-453 Ma, respectively. Thermodynamic modeling using mineral assemblages yields peak conditions of 600°C-650°C and 5.8-8.9 kbar for staurolite and kyanite grade western Blue Ridge units, including the stratigraphically youngest unit in the Murphy syncline, which also yields a weighted mean monazite U-Pb age of 441 Ma. The Taconic metamorphic core of the central Blue Ridge yields peak conditions of 775°C and ca. 11.5 kbar. Combined, these ages indicate that the relatively intact Barrovian metamorphic progression mapped across the Blue Ridge of Tennessee, North Carolina, and northern Georgia is solely of Ordovician (Taconic) age. Synthesis of this new data with existing geo- and thermochronology support a model of Barrovian metamorphism resulting from construction of a Taconic accretionary wedge and subduction complex, followed by post-Taconic unroofing during Neocadian and Alleghanian thrusting.

.....
BOHAI GULF **1,561,115**

QUANTITATIVE CHARACTERIZATION OF CLASTIC RESERVOIR ARCHITECTURE BASED ON ENVELOPE SURFACE: A CASE STUDY OF P OILFIELD IN BOHAI SEA

X.Ye, X.Liu, S.Wang, L.Zhang and C.Huo (Bohai Oilfield Res Inst). *21ST INTERNATIONAL SEDIMENTOLOGICAL CONGRESS [ISC] (Beijing, China, 8/22-26/2022) ABSTRACT BOOK* p.1562, 2022. (Available at <http://www.isc2022.org.cn> as of 9/22/2022; **Abstract only**)

In order to solve the problems existing in conventional grid-based clastic reservoir architecture modeling methods, such as low model accuracy and non-convergence of reservoir numerical simulation, a quantitative characterization method of clastic reservoir architecture based on envelope surface was proposed. This method achieves the fine geology modeling and reservoir numerical simulation of clastic reservoir architecture through the prototype modeling of reservoir architecture envelope surface, envelope surface reconstruction based on discrete architecture data and equivalent characterization of envelope surface. In P oilfield of Bohai Sea, this method was applied to quantitatively characterize the braided river reservoir architecture units. Firstly, the 3D

surface-based prototype model of braided river architecture units was established based on the geological knowledge base. Then, under the constraints of the prototype model, the envelope surfaces of each level architecture units were constructed by using the reservoir architecture data of different dimensions, such as 1D well point data, 2D boundary data, etc. Finally, an equivalent characterization method based on the conductivity of grid interface was used to realize the quantitative characterization of the envelope surface in conventional grid-based reservoir numerical simulation, which provided a model basis for fine remaining oil prediction and potential exploitation in the middle and late stage of oilfield development. Reservoir numerical simulation results of P oilfield show that the historical fitting coincidence rate of the new model based on the proposed method is 12 percent higher than that of the old model, and the overall prediction accuracy of remaining oil is more than 85%. In addition, this method has been successfully applied in many meandering river and delta oilfields in Bohai Sea, showing a good application prospect.

.....
BOREHOLE IMAGING **1,561,116**

SINGLE-WELL LITHOFACIES IDENTIFICATION BASED ON LOGGING RESPONSE AND CONVOLUTIONAL NEURAL NETWORK

Z.Li, P.Li, Z.Liu and Y.Cui (Northeast Petroleum Univ). *JOURNAL OF APPLIED GEOPHYSICS* v.207, Dec. 2022. (ISSN 0926-9851; Article no.104865)

To address lithofacies identification of single-well, we proposed two solutions based on logging response and convolutional neural network. Firstly, the lithofacies types are obtained according to the coring well data, and then the logging response characteristics of different lithofacies are obtained by associating the lithofacies with some logging responses. Finally, the mapping relationship between logging responses and lithofacies types is established by convolutional neural network. The trained network can be used for single-well lithofacies identification. In the first scheme, we employed a deep residual network based on transfer learning. This network receives three-dimensional image as input and use two-dimensional convolution to extract pattern characteristics. Hence, it needs to plot the logging responses of each lithofacies into an image in advance. In the second scheme, we employed a parallel model composed of residual network and long short-term memory network, which can directly receive the sequence data of logging response without transforming them into images. The lithofacies identification results of 2 test single-wells show that the identification accuracy of the two schemes is more than 92%, which provides a new way for lithofacies identification in oil and gas exploration and development. (©2022 Elsevier B.V.)

.....
BOSNIA HERZEGOVINA **1,561,117**

PERMIAN-TRIASSIC BIOFACIES OF THE TEOCAK SECTION, BOSNIA AND HERZEGOVINA

T.Kolar-Jurkovsek, H.Hrvatovic, D.Aljinovic, G.P.Nestell, B.Jurkovsek and F.Skopljak (Slovenia Geological Survey; Bosnia Academy Sci & Arts; Zagreb Univ; Texas Univ, Arlington). *5TH INTERNATIONAL CONODONT SYMPOSIUM [ICOS] (Wuhan, China and Online, 6/24-27/2022) PROGRAM AND ABSTRACTS* p.56, 2022. (**Abstract only**)

The Teocak section in Bosnia and Herzegovina (Sava-Vardar Zone) is composed of the Upper Permian Bellerophon Formation and the Lower Triassic Werfen Formation, including the transitional beds. The section was studied sedimentologically and micropaleontologically by using foraminifers and conodonts. The Bellerophon Formation was deposited in a shallow, biota-rich subtidal lagoon characterized by typical Changhsingian foraminiferal species. Deposition on a shallow epicontinental ramp with pronounced long-term transgression is proposed for the Lower Triassic strata. The recovered conodont faunas are assigned to the Late Permian *praeparvus* (Changhsingian) and to the Early Triassic *isarcica-staeschei* (Griesbachian), *costatus* (latest Dienerian-early Smithian) and *hungaricus* (early Spathian) Zones. The studied strata include the Permian-Triassic Boundary as well as the Induan-Olenekian Boundary. The results contribute to the knowledge of the aftermath end-Permian mass extinction and the

recovery of conodonts in the Early Triassic. The introduced conodont biozonation in the Teocak section is for the first time proposed for the region. The acquired data are a valuable source of paleontological evidence that provides an important contribution to the paleobiogeography of the western Tethys. For the time being, the Teocak section is the only locality comprising the Permian-Triassic Boundary strata in Bosnia and Herzegovina, and because of its relevance, the Teocak geological profile is proposed for admission to the Natural Heritage Registry.

BOWEN BASIN**1,561,118****NEW INSIGHTS INTO THE TERRESTRIAL END-PERMIAN BIOTIC CRISIS FROM EASTERN AUSTRALIA**

C.Fielding, T.Frank, S.McLoughlin, V.Vajda, C.Mays, A.Winguth, C.Winguth, R.Nicoll, M.Bocking et al. (Connecticut Univ). *21ST INTERNATIONAL SEDIMENTOLOGICAL CONGRESS [ISC] (Beijing, China, 8/22-26/2022) ABSTRACT BOOK* p.195, 2022. (Available at <http://www.isc2022.org.cn> as of 9/22/2022; **Abstract only**)

This talk summarises results from a multi-disciplinary project that aimed to elucidate responses of lowland terrestrial settings in high paleolatitudes to end-Permian environmental stresses. The study focused on an extensive, north-south-elongate basin system in eastern Australia that preserves a stratigraphically complete succession of late Permian to Middle Triassic age. A suite of high-precision, CA-IDTIMS U-Pb ages from zircons in tuffs provides tight constraints on the timing of events. The succession accumulated on a broad, coastal alluvial plain in a retroarc foreland basin. The Permian succession preserves abundant coal. Abrupt extirpation of the *Glossopteris* flora is recorded at the top of the uppermost coal seam in the succession, but this event took place some 200-600 kyr before the marine extinction event as determined at the Meishan Permo-Triassic boundary GSSP. Above the uppermost coal is a distinctive dark grey shale ("Marker Mudstone" in the Bowen Basin of Queensland, Frazer Beach Member in the Sydney Basin of New South Wales) that preserves mainly algae, fungi, amorphous organic matter and charcoal fragments. Elements of a new macro- and microflora then become apparent gradually through the overlying strata. These strata are initially drab grey like the underlying Permian succession, but progressively change to stronger hues upward. Chemical Index of Alteration data indicate a major increase through the Permian-Triassic transition, $\delta^{13}\text{C}_{\text{org}}$ values describe a negative excursion, and there are transient spikes in nickel concentrations in mudrocks across the boundary. Climate models suggest a shift towards warmer and more seasonal climates across the boundary, and this is supported by sedimentological data that indicate fluvial sediment dispersal under increasingly flashy discharge regimes. Deep tetrapod burrows were found subtending from the base of a sharp-bounded sandstone bed at one locality. No significant, long-term change in overall depositional environment, average grain-size, or sediment dispersal direction is recorded across the boundary, with mobile fluvial systems active both before and after the floral extirpation. However, the Marker Mudstone/Frazer Beach Member record widespread ponding of surface water caused by an excess of water availability following demise of the *Glossopteris* flora. Presence of charcoal indicates abundant wildfires, and the proliferation of algae and fungi indicates that lakes became eutrophic and were inhospitable to aerobic life. Above this, stratal color changes and together with the deep tetrapod burrows, suggest that the Early Triassic climate entailed periods of drought and/or seasonal drying of the landscape. Geochemical and modelling data indicate a change to a warmer, seasonal, and more humid climate. Floral extirpation was likely caused by climate and fire regimes passing a tipping point, possibly in conjunction with poisoning by airborne volcanogenic heavy metal toxins.

BOWEN BASIN**1,561,119****PROXY RECORDS OF TERRESTRIAL CLIMATIC AND ENVIRONMENTAL CHANGE THROUGH THE END-PERMIAN EXTINCTION IN THE HIGH PALAEO-LATITUDES OF SOUTHEASTERN GONDWANA**

T.D.Frank, C.Fielding, A.Winguth, K.Savatic, C.Winguth,

S.McLoughlin, V.Vajda, C.Mays, R.S.Nicoll et al. (Connecticut Univ, Storrs). *21ST INTERNATIONAL SEDIMENTOLOGICAL CONGRESS [ISC] (Beijing, China, 8/22-26/2022) ABSTRACT BOOK* p.197, 2022. (Available at <http://www.isc2022.org.cn> as of 9/22/2022; **Abstract only**)

Rapid climatic and environmental change were major contributors to the End-Permian Extinction (EPE). Although well-constrained for the marine realm, relatively few records document the pace, nature, and magnitude of climatic and environmental change across the EPE in terrestrial environments. The Bowen and Sydney basins in eastern Australia were major depocenters within a narrow, north-south-elongate basin system that stretched along the southeastern margin of Gondwana. These basins preserve a stratigraphically complete, upper Permian to Middle Triassic succession, which accumulated on a broad, coastal alluvial plain in a retroarc foreland basin setting. A continental volcanic arc produced numerous zircon-bearing tuff beds, which has facilitated the development of a high-resolution chronostratigraphic framework. We generated geochemical proxy records for pCO₂, chemical weathering, and land surface temperature (LST). Regional climate simulations provide additional context. Through the latter half of the Changhsingian, Chemical Index of Alteration (CIA) profiles show increases from long-term averages of c. 70 in the Bowen Basin and c. 75 in the Sydney Basin to 80-85 regionally, suggesting an increase in LSTs from 12-14°C and 14-16°C, respectively, to 20-21°C along the entire continental margin. Consistently humid, temperate, broad-leafed *Glossopteris* forest-mire ecosystems thrived through this interval, despite gradual warming and increasingly seasonal climate. The EPE horizon, evident as the abrupt disappearance of coal-forming forest communities and elevated levels of charcoal in sediments, is marked by a peak in CIA and LST values of 85-90 and 22-23°C, respectively, indicating that the extinction coincided with an episode of intense chemical weathering and peak warmth. These results suggest that a tipping point was reached, which crossed a tolerance threshold for the forest-mire ecosystems that had long dominated the landscape. CIA profiles indicate that erosion following the collapse of vegetation was relatively short-lived in what was a low-gradient landscape. Although the post-EPE climate was 10-14°C warmer and landscapes were no longer persistently wet, results point to overall higher but more seasonal precipitation consistent with an intensification of a monsoonal climate regime in southeastern Gondwana. Aridification, often linked to the EPE, developed gradually in this region, perhaps facilitating the persistence of refugia for moisture-loving terrestrial flora. In the immediate aftermath of the extinction, the region was dominated by flora indicative of more open vegetation with adaptations to periodic water stress. Consistently humid conditions supporting coal-forming vegetation only re-established in the region some 5-10 million years later, during the Middle Triassic.

BRACHIOPODA**1,561,120****DECIPHERING BRACHIOPOD ORIGINS: THE CAMBRIAN EXPLOSION, SMALL SHELLY FOSSILS AND EARLY EVOLUTIONARY HISTORY OF LOPHOTROCHOZOA**

A.D.Butler, M.Streng, Z.Zhang, R.Garwood and L.E.Holmer (Uppsala Univ; Northwest Univ, China; Manchester Univ). *58TH ANNUAL PALAEOONTOLOGICAL ASSOCIATION MEETING (Leeds, UK, 12/16-19/2014) ABSTRACTS* p.23, 2014. (Available at <http://www.palass.org> as of 11/15/2022; **Abstract only**)

The fossil record of life on Earth is strongly biased towards organisms composed of hard parts--biomineralized tissues such as shells or skeletons. The Cambrian explosion, once considered as the initial appearance of life, in fact partially results from the evolution of hard parts and their seemingly sudden appearance in the fossil record. This event is predated by the appearance of a group of problematic microfossils known as the small shelly fauna (SSF). A consensus has emerged that many of the taxa comprising the SSF are stem-group representatives of extant phyla that emerged during the Cambrian, although this is not without controversy. We provide a review of the current synthesis of tommotioid research including novel data retrieved using SEM and CT scanning techniques that strengthen the purported link of a tommotioid sub-group, the tannuoliniids, with stem-group brachiopods such as

Mickwitzia and the acrotretids. Generation of a comparative dataset based on broad high-resolution CT sampling of these enigmatic animals has also allowed investigation of patterns of growth and development in these early Cambrian organisms. Determining suites of homologous characters through such a comparative approach allows us to unravel the pattern of tommotiid inter-relationships and their affinities to extant Lophotrochozoa.

.....
BRAIDED STREAM DEPOSIT 1,561,121

SANDBODY ARCHITECTURE AND RESERVOIR HETEROGENEITY OF SANDY BRAIDED RIVER: AN INSIGHT FROM OUTCROP AND SUBSURFACE DATA

B.Chen, Z.Shi, L.Xue, L.Ma and L.Wang (Res Inst Petrol Explor Dev). *21ST INTERNATIONAL SEDIMENTOLOGICAL CONGRESS [ISC] (Beijing, China, 8/22-26/2022) ABSTRACT BOOK* p.1559, 2022. (Available at <http://www.isc2022.org.cn> as of 9/22/2022; **Abstract only**)

As an important oil/gas reservoir, sandy braided river sandstone is characterized by thick thickness, well continuity and good physical properties. However, muddy barrier-intercalation is developed inside the sandy braided river, there are few systematical study have been carried out on reservoir heterogeneity of this type of reservoir. On the basis of outcrops in Yungang Formation of Datong Basin, Shanxi and study in sandy braided river in Jimidi Formation of Melut Basin, according to fine observation of outcrops and cores, measurement for outcrops, inter-well correlation, experimental analysis, and logging interpretation, the results show that sandy braided river deposit is dominated by seven typical litho-facies and five litho-facies assemblages, where three types of muddy barrier-intercalations with different sedimentologic genesis were recognized, flooding mud (Fm) with large thickness and wide distribution, and lateral accretion draping mud (Lm) and abandoned-channel filling mud (Am and Em) with restricted distribution inside single channel. Four typical sandbody architecture units are common to be found, including channel (CH), Channel bar (CB), Point bar (PB) and overfall deposits (OF), where distribution frequency of channel and channel bar is the highest and reservoir quality of channel bar is the best. According to the case study in Jimidi Formation in Ruman area of Melut Basin, channel and channel bar architecture units that are characterized with high porosity and permeability controlled the enrichment of heavy oil, especially the channel bar architecture units, with higher charging of heavy oil, is the major reservoir type for remaining oil.

.....
BRAZIL 1,561,122

EARLY DEVONIAN ORGANIC-WALLED PHYTOPLANKTON FROM THE PONTA GROSSA FORMATION, PARANA BASIN, BRAZIL

V.J.Garcia Muro, C.V.Rubinstein, E.Pereira and P.Steemans (IANIGLA-CONICET; Rio de Janeiro State Univ; Liege Univ). *REVIEW OF PALAEOBOTANY AND PALYNOLOGY* v.307, Dec. 2022. (ISSN 0034-6667; Article no.104777)

The depositional succession of the Ponta Grossa Formation (Parana Basin) corresponds to a wave-dominated shallow-marine environment, represented by four coarsening-upwards cycles, limited by flooding surfaces. Previous studies on a well-preserved and diverse assemblage of miospores indicated a late Pragian to possibly middle Emsian age. The palynological analysis of the Jaciara section is completed herein with the analysis of the marine fraction, composed of highly abundant and diverse organic-walled phytoplankton, with 222 species recognized. Preservation and abundance of some species, that were previously informally described or mentioned, are here formally described. Additionally, two new species are instituted: *Pterospermella jaciarensis* sp. nov. and *Florisphaeridium brasiliensis* sp. nov. The phytoplankton species, such as *Bimerga paula*, *B. sp. aff. B. bensonii*, *B. nuda*, *Cordobesia orientalis*, *C. uruguayensis*, *Palacanthus ledanoisii*, *Pyloferites escobaides*, *P. paranaensis* and *Winwaloeusia distracta*, recorded in the lower part of the section, indicate a late Pragian age, in coincidence with the miospore age. *Navifusa* spp. and *Pterospermella pernambucensis* first appear in the middle part of the studied section, suggesting an Emsian age, as do the miospores.

The diversity and preservation quality of the phytoplankton tend to decrease towards the top of the section, probably related to a general shallowing trend. (c2022 Elsevier B.V.)

.....
BRAZIL 1,561,123

OBLIQUE COLLISION AND ACCRETIONARY PROCESSES IN THE SOUTH BORBOREMA PROVINCE: INSIGHTS FROM STRUCTURAL GEOLOGY AND GEOPHYSICAL DATA

G.M.Almeida, R.A.Fuck, E.L.Dantas and S.S.Lima (Brasilia Univ; Pernambuco Federal Univ). *TECTONOPHYSICS* v.844, 12/5/2022. (ISSN 0040-1951; Article no.229607)

During orogenesis, the forming structures vary according to several factors such as the nature of rocks, geological environment, P-T conditions, and type of collision. Deformational styles play a significant role in orogenic processes. While thin-skinned tectonics comprise only supracrustal deformation, in thick-skinned tectonics both supracrustal rocks and the basement are deformed reaching Moho depths. Both styles may coexist in a single orogenic system and the recognition of different sectors may help to unravel the nature of the orogen. In this paper, we apply the definition of tectonic styles to the São Miguel do Aleixo Shear Zone, a major transpressive shear zone in the Sergipano Belt, NE Brazil. It separates domains with different structural and metamorphic grades and provides evidence for understanding the tectonic implications of this structure and its role in the evolution of the orogen. We suggest that the São Miguel do Aleixo Shear Zone is a major crustal boundary formed during the oblique collision with and a possible transitional region between areas with dominant thin-skinned and thick-skinned tectonics. The presence of both tectonic styles together with metamorphic grade and geological environment lead to suggest that accretionary processes had a key role in the evolution of the Sergipano Belt. (c2022 Elsevier B.V.)

.....
BRAZIL 1,561,124

LATE TONIAN EXPLOSIVE VOLCANISM AND HYALOCLASTITES IN NORTHERN PARAGUAY BELT, CENTRAL BRAZIL: A RECORD OF RODINIA BREAK-UP IN WESTERN GONDWANA

M.F.Silva, E.L.Dantas, M.Matteini and R.I.Trindade (CPRM; Brasilia Univ; Sao Paulo Univ). *PRECAMBRIAN RESEARCH* v.382, Nov. 2022. (ISSN 0301-9268; Article no.106862)

Explosive volcanism and oceanic crust generation are key aspects to understanding the break-up history of the Rodinia. Its impact on the extreme glaciations of the Cryogenian was marked by ocean chemistry fluctuations in these times, which are still poorly known and preserved in western Gondwana. Here we describe in detail and provide a series of U-Pb ages for the Nova Xavantina Metavolcanosedimentary Sequence, where extrusive rocks, such as hyaloclastite and metabasalts, as well as mafic and ultramafic intrusive rocks and ignimbrites, are associated with diamictites, limestones, and iron formations in the Paraguay belt, Central Brazil. Two styles of pyroclastic eruptions were identified in the studied area. Basic-ultrabasic Surtseyan eruption was enhanced by magma-water interaction and is represented by hyaloclastites and incorporated bombs of scoria. Felsic Plinian eruption, in its turn, was formed by violent explosions in a subaerial environment and is represented by widely exposed acidic tuffs and ignimbrites. Shallow subaqueous environments, such as lakes, salt lakes, and possibly proto-oceans, developed in this precursor basin concomitant with bimodal volcanism. High resolution U-Pb geochronology results indicate they were formed in at least three magmatic events, starting with the formation of ca. 745 Ma seafloor metabasalts and felsic volcanics dated at ca. 735 Ma, and intrusive gabbros at ca. 714 Ma. Alkaline ultramafic rocks of ca. 577 Ma intrude the region and may be associated with similar rocks that crop out regionally as the Planalto da Serra Alkaline Complex. Our results from Nova Xavantina volcanism explain the main Neoproterozoic source until now unrecognized and previous recorded in detrital zircons from the Paraguay belt sediment provenance. (c2022 Elsevier B.V.)

CARLIN CANYON FM

1,561,125

EVOLUTION ON MY MIND: LOWER PERMIAN SWEETOGNATHUS LINEAGES

C.M.Henderson (Calgary Univ). 5TH INTERNATIONAL CONODONT SYMPOSIUM [ICOS] (Wuhan, China and Online, 6/24-27/2022) PROGRAM AND ABSTRACTS pp.54-55, 2022. (Abstract only)

Sweetognathus is a shallow-marine hyper-diverse predator or scavenger that evolved by exhibiting recurrent parallel morphologies (Petryshen et al., 2020). As a shallow-water conodont taxon, the stratigraphic record of this genus tends to be episodic. The combination of recurrent morphologies and episodic occurrences creates a challenge for biostratigraphy. The solution to this challenge lies in innovative morphometrics, sampling strategies in long sections comprising multiple transgressive-regressive sequences, and an open mind. The "normal" mindset for *Sweetognathus* evolution begins with an uninterrupted pavement of pustulose micro-ornament (*Sw. expansus*) that breaks up into rounded nodes (*Sw. binodosus*). These nodes then extend laterally into dumbbell shapes (*Sw. asymmetricus*) before starting to separate (*Sw. clarki*). The completion of this evolutionary trajectory leads to pustulose bearing nodes on both parapets separated by a sulcus (*Neostreptognathodus pequopensis*). These taxa occur in succession at Carlin Canyon, Nevada where detailed mapping and carbonate sedimentology reveal a series of prograding carbonate platforms separated by transgressive facies (Beauchamp et al., 2022). However, at Carlin Canyon, another neostreptognathodiform taxon (*Sw. obliquidentatus* or *Sw. aff. ruzhencevi* or *N. aff. pequopensis*) occurs in association with *Sweetognathus binodosus*. In addition, in Wyoming and Kansas, a homeomorph of *Sw. asymmetricus* called *Sweetognathus whitei* occurs in association with late Asselian species of *Streptognathodus*; for a long time these two sweetognathid taxa were one (Mei et al., 2002). Opening up our minds allows us to now recognize two distinct lineages (Henderson, 2018; Petryshen et al., 2020), including one with irregular pustulose micro-ornament on sloped nodes (*Sweetognathus*) and a second with regular pustulose micro-ornament on steep margined nodes (*Sweetognathus-too* or maybe *Wardlawella*). Innovative morphometric analyses demonstrate these patterns and many more details await the next generation to reveal. Geochronology, carbonate sedimentology, sequence stratigraphy and even mapping all support these evolutionary trends. We are sometimes a stubborn species and often slow to adopt change, but these distinctions tell us that *Sweetognathus whitei* lived alongside *Streptognathodus* during the late part of the Late Paleozoic Ice Age (P1 phase) while *Sweetognathus asymmetricus* lived about 5 million years later during a time of major sea-level and CO₂ rise. The first appearance of the latter defines the base Artinskian stage in our new geologic time scale. These distinctions also highlight that these shallow-water taxa evolved rapidly and in some cases, new phenotypes were short-lived. Getting the right samples will sometimes reveal timelines in otherwise controversial successions. For example, Gao et al., (2005) named *Xuzhounathus monoridgosis* (*Diplognathodus*) in association with *Sweetognathus whitei* and *Sw. binodosus* from the upper Taiyuan Formation of north China. I recently found a comparable form from the upper Community Pit Formation of New Mexico, USA.

CENTRAL ASIA

1,561,126

DETERMINATION OF AN INTRACONTINENTAL TRANSFORM SYSTEM ALONG THE SOUTHERN CENTRAL ASIAN OROGENIC BELT IN THE LATEST PALEOZOIC

J.Zhang, J.Qu, B.Zhang, H.Zhao, R.Zheng, J.Liu, J.Hui, P.Niu, L.Yun et al. (Chinese Academy Geol Sci). AMERICAN JOURNAL OF SCIENCE v.322, no.7, pp.851-897, Sept. 2022. (ISSN 0002-9599; ISSN 1945-452X)

Intracontinental transform structures are important forms of continental deformation, such as the Altyn Tagh fault on Tibetan Plateau. Although many intracontinental transform structures have developed throughout geological history, their identification is relatively difficult due to later deformation and sedimentary covering. Strike-slip faults played an important role in the

formation and subsequent transformation of the Central Asian orogenic belt (CAOB). In this study, a group of nearly EW-trending dextral shear zones along the southern CAOB in the Beishan, Alxa, northern margin of the North China Craton and the Great Xing'an Mountains to the east, is reported. Regional strike-slip duplex systems were developed and strongly superimposed on the CAOB in the Beishan and Alxa regions. Meanwhile, to the west of the Beishan, coeval ductile shear zones with the same kinematics also developed along the CAOB. The ages of the shear zones range from 280 Ma to 230 Ma and become younger to the east. This megashear system may also connect with the shortening in the Ural Orogenic belt to the west and the convergence along the eastern margin of the Eurasian continent, which is approximately more than 9000 km long in the Asian continent and consists of an intracontinental transform structure in the central Pangea continent. Further west, the dextral shear system may also connect with the coeval shear zones with the same kinematics along the southern Variscan orogenic belt in Europe and even the South Appalachian Orogenic Belt in the southeastern North America, which we call the Intra-Pangean Megashear (IPM) after Irving (2004). The rotation and approach of the Baltic Craton and Siberian Craton and the northern Pangean lithosphere heated by mantle plumes and its lateral (eastward) spreading may have caused the development of the IPM and intracontinental deformation from Pangea B to Pangea A.

CEPHALOPOD

1,561,127

DECOUPLED MORPHOLOGICAL DISPARITY TRENDS DURING THE EARLY DIVERSIFICATION OF AMMONOIDS

N.Allaire, S.Ginot, N.Goudemand, K.De Baets, C.Monnet and C.Cronier (Friedrich Alexander Univ; Lyon Ecole Normale Super; Lyon Univ). 65TH ANNUAL PALAEOONTOLOGICAL ASSOCIATION MEETING (Manchester, UK, 12/18-20/2021) PROGRAMME AND ABSTRACTS p.18, 2021. (Available at <http://www.palass.org> as of 11/1/2022; Abstract only)

Ammonoids constitute an invaluable fossil record for documenting macroevolutionary patterns. Our study investigates the morphological evolution of ammonoids during their initial radiation through the Early and Middle Devonian. Previous morphological disparity analyses were restricted to conch geometry; here we have also explored the evolutionary patterns of the suture lines using the exceptional early ammonoid record from Morocco. We quantified the conch geometry and the suture line shape by classical, linear morphometrics and by geometric morphometrics, respectively. These morphometric data enabled the reconstruction of ammonoid empirical morphospaces, for which standard disparity indices were computed. These metrics enabled us to quantify the changes in morphological disparity through time, using the ammonoid biozonation as a temporal scale. The results reveal important fluctuations in morphological disparity. Despite a well-known covariation relationship (i.e., the second Buckman's rule, the more compressed conchs displaying more frilled sutures), the evolution of disparity in respectively conch geometry and suture lines, respectively, are temporally decoupled: conch geometry reached the maximum disparity at the end of the Early Devonian, while suture line disparity climaxed much later, at the end of the Middle Devonian, when multilobate sutures first appeared. This decoupling may reflect the influence of distinct ecological tasks (e.g., buoyancy, hydrodynamics) associated with these different traits.

CEPHALOPOD

1,561,128

EXCEPTIONALLY PRESERVED SOFT TISSUES OF VAMPYRONASSA RHODANICA PROVIDE INSIGHTS ON THE EVOLUTION AND PALAEOECOLOGY OF VAMPYROTEUTHIDS

A.Rowe, I.Kruta, H.J.Hoving, N.H.Landman, L.Villier and I.Rouget (Sorbonne Univ; GEOMAR Helmholtz-Zentrum; American Museum). 65TH ANNUAL PALAEOONTOLOGICAL ASSOCIATION MEETING (Manchester, UK, 12/18-20/2021) PROGRAMME AND ABSTRACTS pp.42-43, 2021. (Available at <http://www.palass.org> as of 11/1/2022; Abstract only)

The soft tissues of coleoid cephalopods record key evolutionary

adaptations, although they are rarely preserved in the fossil record. This prevents meaningful comparative analyses between extant and fossil forms, and the development of a relative timescale for morphological innovations. However, unique 3D soft tissue preservation of *Vampyronassa* (Vampyromorpha, Incertae sedis) from the Jurassic Lagerstätten of La Voulte sur Rhone (Ardèche, France) provides unparalleled opportunities for the observation of these tissues in the supposed oldest-known relative of extant *Vampyroteuthis infernalis*. Synchrotron microtomography and reconstruction of *Vampyronassa* allowed, for the first time, a high-resolution reexamination of external and internal morphology and a comparison with other fossil and extant species, including *Vampyroteuthis*. The new data obtained demonstrate that key *Vampyroteuthis* characters, such as sucker attachments, were already present in Jurassic taxa. Nonetheless, compared with the detritivorous extant forms, many characters in *Vampyronassa* indicate a pelagic predatorial lifestyle. The contrast in trophic niches between the two taxa is consistent with the hypothesis, suggesting a habitat shift towards a deep-sea environment prior to the Oligocene.

CEPHALOPOD 1,561,129

DISPARITY TRENDS IN THE SHELL SHAPE OF NON-HETEROMORPH AMMONOIDS (CEPHALOPODA)

M.E.Clapham (Calif Univ, Santa Cruz). *58TH ANNUAL PALAEOONTOLOGICAL ASSOCIATION MEETING (Leeds, UK, 12/16-19/2014) ABSTRACTS* p.24, 2014. (Available at <http://www.palass.org> as of 11/15/2022; **Abstract only**)

The shape of non-heteromorph ammonoid shells can be described by simple geometric parameters, enabling quantification of conch shape and assessment of trends in disparity during successive replacements of dominant taxonomic groups, across mass extinctions, and with changes in prey, competitors, or predators. I collated measurements of shell diameter, whorl width and height, and umbilical diameter from published papers, totaling more than 8,200 Emsian-Maastrichtian specimens from over 2,500 species. I performed principal components analysis on dimensions normalized to shell diameter and quantified the disparity of shell shapes by the sum of variances. Shell-shape disparity peaked in the Early and Middle Permian, dropping precipitously with the shift to ceratite-dominated faunas in the Late Permian. Despite the high diversity of Mesozoic ammonoids, disparity never recovered to Paleozoic values. High Permian disparity partly resulted from the coexistence of prolecanitid and goniatite lineages, which had different shell shapes. However, goniatites alone had much more disparate shell shapes than ceratites or ammonites. Non-heteromorph ammonites rarely re-occupied morphospace characterized by high width:diameter ratio shells, previously occupied by goniatites, perhaps because that ecological niche was instead filled by heteromorph ammonites, by non-ammonoid competitors, or was unfeasible at the larger body sizes typical of ammonites.

CHADAMU BASIN 1,561,130

CHARACTERISTICS OF JURASSIC SOURCE ROCKS AND OIL AND GAS EXPLORATION DIRECTION IN THE PIEDMONT ZONE BETWEEN THE SOUTHWESTERN QAIMAM BASIN AND ALTUN MOUNTAIN

X.Zeng, B.Wang, Q.Cao, A.Wang, P.Jia, P.Zhang and B.Qiao (Res Inst Petrol Explor Dev; Qinghai Oilfield Co). *GEOLOGICAL JOURNAL* v.57, no.10, pp.4152-4166, Oct. 2022. (ISSN 0072-1050; ISSN 1099-1034)

The Jurassic petroleum system in the piedmont zone between Qaidam Basin and Altun Mountain is rich in oil and gas resources. Based on the sedimentary environment, geochemical analysis, and distribution prediction of the Middle-Lower Jurassic source rocks in the piedmont zone between the south-western Qaidam Basin and Altun tage region, the Jurassic oil and gas exploration potential in the area was systematically evaluated. The Jurassic source rocks in the study area are mainly coal, dark mudstone, and carbonaceous mudstone developed in the Lower Jurassic fan delta facies, as well as, oil shale, and mudstone in the Middle Jurassic of lacustrine facies, and coal measure strata of braided river delta facies. The

thickness of Middle Jurassic source rocks is relatively thicker. Through restoration and weathered source rock samples analysis, the average TOC of the Middle Jurassic source rocks in the area can reach 4.19%, and the average chloroform bitumen "A" is 0.5915%, meeting the criteria for a good source stone. Every index is close to the Yuka Jurassic source rock, the highest quality found in the basin so far. At the same time, the distribution range of Jurassic source rocks in the study area is meticulously described through seismic facies identification and prediction analysis. Several Jurassic hydrocarbon generating centers in the area, such as Honggouzi - Yueyashan, Nanyishan - Xiaoliangshan, Pingxi, and Dafengshan, with thicknesses ranging from 200 to 400 m, indicating that the Jurassic source rocks have the material basis for large oil and gas fields formation.

CHADAMU BASIN 1,561,131

EFFECTS OF QINGHAI-TIBET PLATEAU UPLIFT ON PALEOGENE-NEOGENE SEDIMENTARY EVOLUTION IN THE SOUTHWESTERN MARGIN OF QAIMAM BASIN

W.Y.Qing and S.G.Yong (PetroChina Research Inst). *21ST INTERNATIONAL SEDIMENTOLOGICAL CONGRESS [ISC] (Beijing, China, 8/22-26/2022) ABSTRACT BOOK* p.290, 2022. (Available at <http://www.isc2022.org.cn> as of 9/22/2022; **Abstract only**)

The stages and spatial differences of the uplift of the Qinghai-Tibet Plateau have important scientific significance for further understanding the uplift mechanism of the Qinghai-Tibet Plateau, discussing the effects of climate and environment, and guiding oil and gas exploration. This paper takes the Qaidam Basin located in the northeastern part of the Qinghai-Tibet Plateau as the research object, and conducts a comprehensive analysis of the distribution, evolution characteristics and differences of sedimentary systems. Combined with the research results on the uplift of the Qinghai-Tibet Plateau in recent years, this paper discusses the control effect of the Qinghai-Tibet Plateau uplift on the Paleogene-Neogene sedimentary differences in the Qaidam Basin. The research results show that five major provenance sedimentary systems developed in the Paleogene in the western Qaidam Basin, i.e., NBZL braided delta, QHQ-YYs fan delta, ALE-TMLK braided delta, QMTA-DCS braided delta and GS braided delta. While four major provenance sedimentary systems developed in the Neogene, i.e., NBZL braided delta, QHQ-YYs fan delta, Aral braided delta, and Gs braided delta. The NBZL braided delta sedimentary system exhibits the evolutionary characteristics of retrogression, the ALE-TMLK fan delta sedimentary system exhibits retrogression to progression, the ALE-TMLK braided delta sedimentary system exhibits regression to strong progression, and the GS braided delta sedimentary system shows the evolution characteristics of regression-progression. The QMTA-DCS braided delta sedimentary system developed in the Paleogene and not developed in the Neogene. It can be seen that due to the influence of the uplift of the Qinghai-Tibet Plateau, the distribution and sedimentary evolution of each provenance system in the western Qaidam Basin showed obvious differences. The uplift of the Qinghai-Tibet Plateau in the Paleogene was relatively small, and the ancient Kunlun Mountains in the southwestern margin of the basin provided provenance, forming the QMTA-DCS large-scale braided delta deposits. The Mantage Mountains blocked the direct flow of the ancient Kunlun Mountains water system into the Qaidam Basin, but went westward along the mountain through the Kunlun Mountain Pass, and merged into the Qaidam Basin along the Alar River and the Timurik River, forming the largest Alar braided delta sedimentary system in the region. In the KB and DCS areas, the petroleum exploration was suggested to focus on the Paleogene braided delta reservoirs and the Neogene shallow lake beach-bar reservoirs. It supports the discovery of the Paleogene braided delta oil reservoirs in the KB area and the Neogene coastal shallow lake beach-bar oil reservoirs in the ZHQ-WN area. In conclusion, the detailed first-hand data in this paper are of great significance for restoring the lithofacies and paleogeography of the Qaidam Basin, understanding the stages and spatial differences of the uplift of the Qinghai-Tibet Plateau, and guiding oil and gas exploration in the Qaidam Basin.

CHAIDAMU BASIN

1,561,132

SEDIMENTARY SEQUENCE AND ARCHITECTURE ANALYSIS BY INTEGRATING MULTI-DISCIPLINE DATA - AN EXAMPLE OF A SANDY CONGLOMERATE RESERVOIR IN QIE12 BLOCK, Q AidAM BASIN, NW CHINA

Q.Gong (PetroChina). *21ST INTERNATIONAL SEDIMENTOLOGICAL CONGRESS [ISC] (Beijing, China, 8/22-26/2022) ABSTRACT BOOK* p.1570, 2022. (Available at <http://www.isc2022.org.cn> as of 9/22/2022; **Abstract only**)

Understanding the sedimentary sequence and architecture is important for planning the development strategy. We illustrate a case study of analyzing the sequence and architecture of a sandy conglomerate reservoir by integrating geology, petrophysics, seismic, and development data. The analysis indicates that the depositional environment of the target lower part of the Ganchaigou Formation is an alluvial fan. We defined eight lithofacies according to the core analysis and five sedimentary microfacies by integrating the core and petrophysical data. We next propose four sedimentary architectural models by integrating the lithofacies result, microfacies analysis, and high frequency sequence models. The four architecture models include the extensively connecting body sandwiched with intermittent channels, the composite channel formed by the overlapping and separation of stable channels, the lateral alternated braided channel and sheet flow sediment, and the runoff channel inlaid in flood plain mudstone. We finally build an architecture model for the alluvial fan. The model of the alluvial fan overall shows an upward-fining grain-size features and this feature indicates that the alluvial fan belongs to a retrograding sequence. The built model consists of six alluvial fan bodies that migrates from north.

CHAOSHAN DEPRESSION

1,561,133

THE EVOLUTION OF THE CHAOSHAN DEPRESSION CONTROLLED BY MULTISTAGE SUBDUCTION OF THE PALEO-PACIFIC PLATE

K.Feng, W.Zhu, M.He, Q.Zhang, J.Zheng and X.Fu (Tongji Univ; CNOOC Ltd). *21ST INTERNATIONAL SEDIMENTOLOGICAL CONGRESS [ISC] (Beijing, China, 8/22-26/2022) ABSTRACT BOOK* p.329, 2022. (Available at <http://www.isc2022.org.cn> as of 9/22/2022; **Abstract only**)

The South China Block is characterized by giant and multistage magmatic belt associated with the subduction of the Paleo-Pacific plate in the Mesozoic. In contrast to the extensive research on this magmatic belt, the associated fore-arc basins are still poorly known, in particular the tectono-sedimentary evolution of fore-arc basins in response to the Paleo-Pacific plate subduction. Chaoshan Depression (CSD), one of a Mesozoic basin in northern South China Sea, was a typical fore-arc basin associated with the subduction of the Paleo-Pacific plate from the Jurassic to the Early Cretaceous. Thick Mesozoic sediments with precise stratigraphic age frame that determined by micropaleontology and zircon U-Pb ages of volcanic interlayers have been revealed in CSD and thus provide a great opportunity to investigate the evolution of fore-arc basin in response to complex subduction processes. In this study, we compiled a large number of zircon U-Pb ages of the arc-related magmatic rocks to trace the magmatic belt, combined with well and seismic reflection of CSD to explore the sedimentation changes. The exposure of early Jurassic magmatic belt was possibly very limited, which was insufficient to provide great detritus to the CSD and shallow marine environment was inferred for the CSD. From the middle Jurassic, quick subsidence occurred in CSD and followed by rapid increase in the sea water characterized by Radiolarian siliceous rock that continued to the late Jurassic. This scenario was possibly caused by landward migration of the arc resulted from the flat subduction of the Paleo-Pacific plate. Since the Cretaceous, there was a prominently tilted denudation with NW increasing in erosion thickness and followed by a dramatic change of sedimentary environment in the CSD. These changes were consistent with the seawards migration of the magmatic zone in response to the rollback of the subduction slab. The plenty detritus eroded from this magmatic belt facilitated large deltas in the CSD. Our study shows how the migrating arc resulting from the changing pattern of the subduction plate controlled the evolution of

fore-arc basin and provide new insights into the evolution of the Paleo-Pacific plate subduction.

CHIAPAS

1,561,134

PROVENANCE, AGE CONSTRAINTS AND METAMORPHISM OF EDIACARAN METASEDIMENTARY ROCKS FROM THE EL TRIUNFO COMPLEX (SE CHIAPAS, MEXICO): EVIDENCE FOR RODINIA BREAKUP AND IAPETUS ACTIVE MARGIN

R.Gonzalez-Guzman, B.Weber, R.Manjarrez-Juarez, A.C.de Leon, L.Hecht, J.C.Herguera-Garcia (CICESE; Mexico Nac Auton Univ; Humboldt Univ). *INTERNATIONAL GEOLOGY REVIEW* v.58, no.16, pp.2065-2091, 2016. (ISSN 0020-6814; ISSN 1938-2839)

Metasedimentary rocks from the El Triunfo Complex (Jocote Unit) in the southern Chiapas Massif (SE Mexico) are constituted mainly by sillimanite-rich micaschist, locally intercalated with marble and calc-silicate rocks. Mafic rocks (now amphibolite) intruded the sequence prior to deformation and folding. Peak metamorphic conditions are estimated by geothermobarometry at approximately 6.0 kbar and approximately 650°C. The timing of the metamorphic event is dated by LA-MC-ICPMS analysis on zircon rims at 438±23/12 Ma. Furthermore, detrital zircon grains yield mainly Stenian-Tonian and minor early Mesoproterozoic ages, indicating provenance from Grenville-type orogens (such as Oaxaquia) and some older cratonic sources. The 87Sr/86Sr values of 0.70775-0.70777 and the δ13C values from +1.9 per mil to +2.7 per mil in associated calcite marble define the time of deposition between 600 and 580 Ma. Geochemical markers from metapelite samples (such as La/Th > 3.94, La/Sc > 3.72, Th/U > 8.19, Th/Co > 0.42 and CIA = 74 to 83), as well as Sm-Nd isotope data (εNdi = -8.1 to -4.0, TDM(Nd) = 1.651.32 Ga) suggest weathering of Mesoproterozoic felsic rocks during temperate to warm climate. Furthermore, Zr/Sc values (9.121.0), chondrite-normalized REE patterns [La/Yb]N = 10.323.3, Eu/Eu* < 0.64, and ΔHf values (1.98-10.02) are indicative of pelagic and zircon-depleted sediments of a passive margin. The results suggest that the Jocote Unit was deposited during the opening of the Eastern Iapetus Ocean in the Ediacaran Period. This is the first evidence for Rodinia breakup in southern Mexico. Besides that, the Ordovician tectonothermal event is probably related to compression during subduction and accretion along the western margin of Gondwana.

CHINA

1,561,135

ARE MORPHOLOGICAL CHARACTERISTICS OF PARROTIA (HAMAMELIDACEAE) POLLEN SPECIES DIAGNOSTIC?

B.Adroit, F.Grimsson, J.P.Suc, G.Escarguel, R.Zetter, J.M.Bouchal, S.Fauquette, X.Zhuang and M.Djamali (Swedish Museum). *REVIEW OF PALAEOBOTANY AND PALYNOLOGY* v.307, Dec. 2022. (ISSN 0034-6667; Article no.104776)

Parrotia persica is one of the most notable endemic relict tree species growing in the Hyrcanian forest at the southern Caspian Sea. The recent discovery of sibling species *Parrotia subaequalis*, occurring in the temperate forests of south-eastern China, offers the opportunity to compare their morphology and ecological preferences and to dig deeper into the paleophytogeographic history of the genus from a perspective. Since pollen morphology of these species would be essential to unravel the origin and evolution of these Arcto-Tertiary species, the present study aimed to investigate whether it is possible to segregate pollen from these two species. Therefore, a detailed combined light- and scanning electron microscopy-based pollen-analysis of each taxon was conducted, the pollen was described, measured, and compared using statistical approaches and principal component analyses to establish unbiased results. The correlation-based principal component analysis achieved for each species shows an overall good superposition of pollen grains measured in equatorial and polar views in the first principal plane, revealing that the *P. persica* pollen is morphometrically as homogeneous as that of *P. subaequalis*. Then, the significant difference, mainly driven by lumen density, has been highlighted between the two species. Ultimately, the cross-validation of the resulting two-species linear discriminants classifier shows that based upon this reference dataset, (sub)fossil

pollen grain can now be confidently assigned to either of the two species with an 85.8% correct-assignment rate. This opens new doors in the affiliation of fossil *Parrotia* pollen and suggests that previous pollen records need to be revised. (c2022 The Authors. Elsevier B.V.)

CHU SARYSYI BASIN

1,561,136

INCREASED RIVER DISCHARGE ACROSS THE PETM RECORDED IN COASTAL-PLAIN STRATA OF SOUTHERN KAZAKHSTAN

A.Dillinger, E.Chanvry, Y.Bolat, A.Tileugabylov and M.Fustic (Nazarbayev Univ; Orano; Katco JV LLP). *21ST INTERNATIONAL SEDIMENTOLOGICAL CONGRESS [ISC] (Beijing, China, 8/22-26/2022) ABSTRACT BOOK* p.177, 2022. (Available at <http://www.isc2022.org.cn> as of 9/22/2022; **Abstract only**)

The lower Paleogene sedimentary record of the uraniumiferous Chu-Sarysu Basin preserves a complex succession of coarse fluvial channel-belt deposits interstratified with finer floodplain and delta-plain strata that were deposited on a large subtropical coastal plain at the eastern margin of the Turan Platform. Two laterally extensive, approximately 25 m-thick sandstone bodies floored by prominent erosion surfaces are recorded below and above the Paleocene-Eocene boundary, respectively, and reflect laterally amalgamated channel fills partitioned by local abandonment mudstone facies. Sedimentary analysis indicates that sandstone bodies consist of multi-storey channel fills exhibiting a variety of architectural elements. The lower sandstone body comprises fining-upward grain-size trends and an abundance of rippled, organic-rich levee deposits characteristic of meandering-channel fills. In contrast, the upper sandstone body is dominated by stacked tabular cross-sets of coarser lithologies suggestive of braided-river deposits. This abrupt geomorphic change from meandering to braided fluvial style suggests a widespread increase in river discharge on the coastal plain arguably controlled by allogenic forcing. Base-level changes linked to a fluctuating water table are unlikely during greenhouse conditions of the early Paleogene, whereas the south Kazakh domain of the Turan Platform had been peneplained and uniformly subsiding since the Late Cretaceous. It is herein proposed that Paleocene-Eocene fluvial systems in the Chu-Sarysu Basin predominantly responded to intensified rainfall and runoff associated with extreme global warming. This study comes within a growing body of sedimentological evidence indicating that the PETM induced increased atmospheric humidity and an enhanced hydrological cycle. These rapid climatic changes led to increased channel-discharge regimes and sediment fluxes that are reflected in coeval sedimentary records worldwide and, for the first time, showcased in coastal-plain deposits of central Asia.

CLAY IRONSTONE

1,561,137

PALEOZOIC IRONSTONE SUGGESTS REDOX STRATIFICATION PLAYED A ROLE IN ORDOVICIAN AND SILURIAN BIOTIC CRISES

E.J.Matheson, P.K.Pufahl and J.B.Murphy (Queen's Univ, Kingston; St Francis Xavier Univ). *21ST INTERNATIONAL SEDIMENTOLOGICAL CONGRESS [ISC] (Beijing, China, 8/22-26/2022) ABSTRACT BOOK* p.199, 2022. (Available at <http://www.isc2022.org.cn> as of 9/22/2022; **Abstract only**)

Variable oceanic redox and expanding shelfal anoxia have been increasingly invoked as the causal mechanism in several biotic crises (extinctions) and contemporaneous isotopic excursions that occurred during the early and middle Paleozoic. However, the exact drivers of these anoxic events remain poorly constrained. In this study, sedimentologic, stratigraphic, and geochemical analyses of five Ordovician and Silurian ironstone-bearing successions are used to provide insights into the oceanic redox structure during the early Paleozoic. Eu anomaly and $87\text{Sr}/86\text{Sr}$ data indicate that ironstone formed from marine fluids with a component of mid-ocean ridge hydrothermal waters that remained largely unmixed during transport over thousands of kilometers to continental margins and epeiric seas. These results suggest that areas of the deep oceans must have been oxygen deficient, thereby supporting the buildup of hydrothermal fluids. Thus, ironstone provides novel evidence that

redox stratification, with oxygenated surface oceans above anoxic deep waters, must have at least transiently existed through the Ordovician and Silurian. Furthermore, these data suggest that ironstone is a previously unrecognized proxy of Paleozoic oceanic oxygenation, one that supports the hypothesis that Paleozoic oceans did not become as well ventilated as modern oceans until at least the Devonian. The interpretation of protracted deep-ocean oxygenation and open-ocean redox stratification has important implications for the co-evolution of the biosphere. We propose that widespread transport of deep anoxic water, and with it both toxic and bioessential trace elements, onto oxygenated continental shelves represents a previously unrecognized driver of, or contributor to, numerous Ordovician-Silurian biotic crises and anoxic events. If sub-redoxcline, anoxic, trace-element-rich waters spread from deep oceans onto outer continental shelves, the expected effects would have included elevated primary productivity, expanded neritic oxygen minimum zones, benthic oxygen deficiency, enhanced organic matter burial, modified regional biologic pumps, abrupt facies changes, locally ferruginous or euxinic bottom water leading to sedimentary metal enrichment (e.g., ironstone or elevated pyrite burial), and resultant $\delta^{13}\text{C}$ and $\delta^{34}\text{S}$ excursions. Each of the aforementioned effects is widely documented for many of the Late Ordovician (i.e., Hirnantian) and Silurian biotic crises (e.g., the Ireviken, Lau, Klomk). Furthermore, the oceanographic and climatic shifts (i.e., glacioeustasy, intensified upwelling, changes in circulation patterns, etc.) interpreted as coincident with these early Paleozoic extinction events are all means by which sub-redoxcline waters could have readily spread into shallower environments. This spread would have occurred either directly through upwelling or indirectly through shoaling of the redoxcline such that it impinged above the shelf-slope break.

CLEVELAND BASIN

1,561,138

RAPID REDOX VARIATIONS IN A LOWER JURASSIC BLACK SHALE: A PALAEOONTOLOGICAL AND GEOCHEMICAL PERSPECTIVE

C.O'Keeffe, C.T.S.Little, F.L.Gill, C.Marz, J.B.Riding, L.Schwark and S.W.Poulton (Leeds Univ; British Geological Survey; Christian Albrechts Univ). *65TH ANNUAL PALAEOONTOLOGICAL ASSOCIATION MEETING (Manchester, UK, 12/18-20/2021) PROGRAMME AND ABSTRACTS* p.84, 2021. (Available at <http://www.palass.org> as of 11/1/2022; **Abstract only**)

The Toarcian oceanic anoxic event (T-OAE) occurred in the Lower Jurassic (ca. 183 Ma) and is associated with the deposition of black shales across much of Europe, including in the Cleveland Basin (Yorkshire, UK). Despite extensive geochemical evidence for severe oxygen depletion in the Toarcian Mulgrave Shale Member, the presence of thin "pavements" of bivalves (predominantly *Pseudomytiloides dubius*) indicates that oxygen levels were more dynamic than low-resolution geochemistry suggests. This dynamism is further implied by the presence of a thin black shale unit (the Lower Sulphur Band, LSB) in an otherwise oxygenated shale unit stratigraphically below the Mulgrave Shale. Here, we present the results of an ongoing, high-resolution, combined geochemical - palynological - macropalaontological study of the LSB and bivalve pavements. We document the occurrence of bioturbation (*Chondrites*) closely associated with the deposition of the LSB and the presence of a mixed marine-terrestrial palynofacies, and we consider the implications of both of these palaeobiological observations for geochemical studies of condensed black shale intervals. Our study of the LSB in particular highlights the sensitivity of this Jurassic marine system to changes in the exogenic carbon cycle and carries implications for the future trajectory of modern marine systems exposed to anthropogenic oxygen depletion.

COELENTERATA

1,561,139

THAUMAPTILON WALCOTTI AND THE EARLY EVOLUTION OF THE CNIDARIA

J.B.Antcliffe (Oxford Univ). *58TH ANNUAL PALAEOONTOLOGICAL ASSOCIATION MEETING (Leeds, UK, 12/16-19/2014) ABSTRACTS* p.18, 2014. (Available at <http://www.palass.org> as of 11/15/2022; **Abstract only**)

The Cambrian Burgess Shale from British Columbia, Canada, has provided generations of palaeontologists with new and wonderful puzzles concerning the early evolution of animal life. *Thaumaptilon* is one of the most intriguing of these, as it links to two major problems in early animal evolution. First is the possible connection between enigmatic Ediacaran age (ca. 565 Ma) taxa such as *Charnia* and their possible successors, such as *Thaumaptilon* from the Cambrian. It has been thought that if we could understand the relationships of *Thaumaptilon* to modern animals, then by inference we could understand the relationship of the critically important Ediacaran biota. Second is that *Thaumaptilon* has been interpreted as an early soft-bodied cnidarian. The early evolution of the Cnidaria is poorly understood as Cambrian cnidarians are rare and often poorly preserved. This is particularly problematic, as the bilateria appear in the fossil record at the same time, if not even before, the earliest reliable cnidarian fossils. Here, new ontogenetic, anatomic, and decay data are presented that aims to resolve these major questions with implications for the earliest evolution of the Cnidaria and the battle between convergent and contingent patterns of evolution in the Cambrian Explosion.

.....
CONCRETION 1,561,140

SEDIMENT PERMEABILITY AND EXCEPTIONAL PRESERVATION WITHIN CONCRETIONS

V.E.McCoy, R.T.Young and D.E.G.Briggs (Yale Univ; Clark Energy Group). *58TH ANNUAL PALAEOLOGICAL ASSOCIATION MEETING (Leeds, UK, 12/16-19/2014) ABSTRACTS* p.37, 2014. (Available at <http://www.palass.org> as of 11/15/2022; **Abstract only**)

Concretions are an important source of soft-bodied fossils. In order to determine the controls on exceptional fossilization within concretions, we scored 88 concretion-bearing sites for different states of 11 variables and analyzed their effects on the presence/absence of soft-tissue preservation using qualitative logistic regression. Fine-grained host lithology correlates with the presence of soft-tissue preservation, suggesting that low permeability sediments promote soft tissue fossilization within concretions by: (1) inhibiting decay; and (2) promoting the precipitation of authigenic minerals. We tested these two effects with decay experiments on fish tissue in glass beads of three different sizes and therefore of different permeability. We measured decay using infrared gas analysis and mineral precipitation using micro-CT scanning. The results showed that decay is inhibited and mineral precipitation enhanced in lower permeability sediments. Thus a process of positive feedback promotes exceptional preservation during concretion formation where decay is inhibited and early cementation results in a rapid decrease in permeability.

.....
CONODONT 1,561,141

PHYSICAL CHARACTERIZATION OF THE CONODONT WHITE MATTER TISSUE

C.M.Perez, A.Atakul-Ozdemir, X.Warren, P.G.Martin, M.Guizar-Sicarios, M.Holler, F.Marone and P.C.J.Donoghue (Valencia Univ; Bristol Univ). *65TH ANNUAL PALAEOLOGICAL ASSOCIATION MEETING (Manchester, UK, 12/18-20/2021) PROGRAMME AND ABSTRACTS* p.35, 2021. (Available at <http://www.palass.org> as of 11/1/2022; **Abstract only**)

Conodont elements are phosphatic tooth-like microfossils that comprised the dentition of an extinct clade of primitive vertebrates that thrived in marine environments from the Cambrian to the Triassic, and are commonly exploited as mineral archives of past ocean chemistry. The elements are histologically differentiated into a base and a crown, the latter comprised of lamellar crown tissue and the white tissue matter that has been the focus of geochemical assays. However, the nature of the white matter has been the subject of controversy, including claims that it is macrocrystalline, microcrystalline or even non-crystalline. Concerns have also been raised that its porous structure may reflect permeability and, as such, it has been considered an imperfect geochemical archive. Using electron backscatter diffraction (EBSD), pychographic X-ray computed nanotomography (PXCT), and pore network analysis, we demonstrate that white matter is crystalline, as it is comprised of a

single crystal that is typically tens of microns in dimension. PXCT and pore network analysis reveals that while the tissue is extremely porous, the pores are unconnected. Combining these data reveals that conodonts enlarged their dentition through syntactic growth of their denticles and provides support for the exploitation of conodont white matter as a closed geochemical system suitable for inferring the changing chemistry of Cambrian-Triassic oceans and atmospheres.

.....
CONODONT 1,561,142

QUANTIFYING CONODONT CRYSTALS: CONTROLS OF BIOMINERALIZATION IN EARLY VERTEBRATES

B.Shirley, I.Leonhard, J.E.Repetski and E.Jarochowska (Friedrich Alexander Univ; US Geological Survey). *65TH ANNUAL PALAEOLOGICAL ASSOCIATION MEETING (Manchester, UK, 12/18-20/2021) PROGRAMME AND ABSTRACTS* p.44, 2021. (Available at <http://www.palass.org> as of 11/1/2022; **Abstract only**)

The emergence of mineralized skeletons in vertebrates is one of the most impactful events in the history of life. Conodonts are the first of this clade to have evolved tooth-like structures known as elements and provide a unique insight into these early stages of biomineralization. We can use crystal properties such as size, shape and orientation to quantify an organism's control on biomineralization by evaluating the relative organization of multiple crystals. A better alignment of these crystals' c-axes would be beneficial, as this would reduce episodes of breakage during feeding via better dispersal of stress throughout the material. We hypothesize that more derived conodonts will have a higher degree of organization in the alignment of crystals due to feeding adaptations. Here we test this with the application of electron backscatter diffraction (EBSD) to directly compare these crystal properties in situ, across multiple taxa, in order to compare crystal texture through time. We propose a new method of quantifying and comparing crystal organization using three phylogenetically distinct conodont taxa: two simple cone-like elements, *Proconodontus muelleri* and *Panderodus equicostatus*, and one complex blade-like element of *Wurmiella excavata*. This novel approach proposes a new measure of skeletal adaptation in early vertebrates.

.....
CONODONT 1,561,143

PARALLEL EVOLUTION IN THE DENTAL ELEMENTS OF SWEETOGNATHUS CONODONTS

W.Petryshen, C.M.Henderson, K.De Baets and E.Jarochowska (Calgary Univ; Friedrich Alexander Univ). *5TH INTERNATIONAL CONODONT SYMPOSIUM [ICOS] (Wuhan, China and Online, 6/24-27/2022) PROGRAM AND ABSTRACTS* p.53, 2022. (**Abstract only**)

Disentangling patterns of diversification throughout Earth's history is fundamentally important if we hope to understand the mechanisms that lead to adaptive radiations. The conodont genus *Sweetognathus* provides an outstanding opportunity to test the evolutionary patterns that may have facilitated conodont adaptive radiation in shallow marine settings during the Permian. The repeated emergence of similar morphologies in the dental elements of Permian *Sweetognathus* conodonts has been hypothesized as an example of parallel evolution. To test if morphologic parallelisms occur between isolated *Sweetognathus* lineages, this study used two-dimensional-based geometric morphometrics combined with a revised and expanded phylogeny of Permian *Sweetognathus* species to quantify dental element trait distributions and compare phenotypic trajectories between lineages. A hierarchical clustering method was used to identify recurrent species pairs based on principal component scores describing their morphologic variation, with the further incorporation of widely used ecologic metrics such as limiting similarity and morphologic overlap. Our research implies that a major contributor to conodont diversity in Paleozoic marine trophic networks is the emergence of recurrent parallel morphologies via disruptive and directional selection. An interesting avenue for future research is the incorporation of landmark-free, three-dimensional shape descriptors like relief index, average slope and angularity, orientation patch count, and Dirichlet normal energy. These techniques provide opportunities to

compare aspects of morphology that lack biologically homologous points, assuming elements had similar functions and that dental element shape correlates to variations in diet. As in traditional landmark-based methods, three-dimensional shape descriptors calculated from a small subset of *Sweetognathus* lineage endmembers displayed similar patterns of morphologic change through time. This may illustrate that a similar mechanism operated throughout the Permian driving parallel adaptations between recurrent species pairs. Conodont dental elements may respond quite strongly to dietary changes and thus changes to the environment, helping them to achieve their status as hyper-diverse predators and scavengers, contributing substantially to the complexity of Paleozoic marine communities.

CONODONT

1,561,144

PHYLOGENY OF THE CONODONT FAMILY ANCHIGANATHODONTIDAE, SWEETOGNATHIDAE AND IDIOGNATHODONTIDAE FROM CARBONIFEROUS TO TRIASSIC

C.Xue and Y.Chen (Northwest Univ, China). *5TH INTERNATIONAL CONODONT SYMPOSIUM [ICOS] (Wuhan, China and Online, 6/24-27/2022) PROGRAM AND ABSTRACTS* p.63, 2022. (Abstract only)

Conodonts, as elements of the feeding apparatus of marine agnathan vertebrates, are extensively preserved in marine sediments and are important for correlating strata from the Paleozoic to the Triassic. Carminiscaphate conodonts evolved quickly and have high morphological diversity in the geological record, and thus they are ideal material to reveal the phylogeny and evolutionary pattern of the conodont animal. Sixteen genera belonging to the families *Anchiganathodontidae*, *Sweetognathidae* and *Idiognathodontidae* were analyzed here to reveal its evolutionary relationships. The genus *Hindeodus* is chosen as outgroup, and each genus is represented by the oldest species of the genus, as the oldest species can cover primitive characters. The collected data matrix includes 51 Pl discrete morphological characters. Characters from multi-element apparatuses are not collected, as apparatus data from previous publications are insufficient. The strict consensus phylogenetic tree depicted several possible lineages: *Isarcicella-Sweetohindeodus*, *Sweetognathus-Xuzhounathus*, and *Adetognathus-Neognathodus-Streptognathodus*. The cladogram also shows that *Rabeignathus*, *Neostreptognathodus*, *Pseudosweetognathus*, *Meiognathus* and *Iranognathus* are a paraphyletic group, which combines with *Sweetognathus* and *Xuzhounathus* to constitute a polyphyletic array. This phylogenetic hypothesis explains the evolution of conodonts in this lineage from the Carboniferous to the Triassic.

CONODONT

1,561,145

THE CONODONT DATABASE (CONODATA): A GUIDE TO CONODONT SYSTEMATICS

G.Silverio (Evora Univ). *5TH INTERNATIONAL CONODONT SYMPOSIUM [ICOS] (Wuhan, China and Online, 6/24-27/2022) PROGRAM AND ABSTRACTS* pp.64-65, 2022. (Abstract only)

Conodonts are among the most common, diverse and biostratigraphically useful groups in the fossil record. Their rapid evolution and long age range (as a group) resulted in such a high diversity of forms that it makes it difficult for researchers to gather all already published information regarding conodont systematics. Database creation has, therefore, been of great value to researchers. The first conodont database was published by Holmes (1928), following the work of Ulrich & Bassler (1926), which significantly increased the number of conodont species at that time. Soon after, in the 1930s, conodont taxonomy saw a drastic increase accompanying the high frequency of publications on the matter (Ellison Jr., 1962). Ultimately, a new database, called the Catalogue of Conodonts, was created by Fay (1952). Successive databases were published in the following decades to gather all information regarding conodont taxonomy and maintain systematic coherency (Ash, 1961; Ellison Jr., 1962; Collier, 1971). In a combined effort of several distinguished conodont researchers, a five-volume remake of the Catalogue of Conodonts was made during the 1970s up until the 1990s. It was the most detailed work in subgeneric conodont

taxonomy (Ziegler, 1973; 1975; 1977; 1981; 1991). After the publication of the last volume in 1991, compendium articles became more specific to certain periods or ages, thus focusing the efforts of conodont systematics on particular age ranges. To the knowledge of the author, the last compendium of all conodont taxa was made by Sweet (1988), whose work refers to the existence of almost 5000 conodont species, although these are not fully listed in his work. With such a high number of species, the performance of conodont systematics represents a great effort for researchers, with no conodont collection being big enough to house specimens of all known species, and original diagnoses being of difficult access, depending upon the funding of the institutions to which these researchers belong. The Conodont Database (ConoData) is meant to facilitate the work of conodont researchers by compiling all published data regarding conodont systematics (genera and species diagnoses, author and year of classification, synonymy, geographical occurrences, age range, holotype identifiers, references and figures) into a complete, intuitive and yearly updated online portal with open access to both experts and non-experts. In its current preliminary phase, the database contains detailed information on 31 genera, 205 species and 14 invalid taxa. The database should be completed after all of the generic and subgeneric taxa have been assessed.

CONODONT

1,561,146

DID YOU SAY "LITTLE WHATZITS"? CURRENT AND FUTURE KNOWLEDGE OF CONODONT PALAEOBIOLOGY

P.Guenser (Bordeaux Univ). *5TH INTERNATIONAL CONODONT SYMPOSIUM [ICOS] (Wuhan, China and Online, 6/24-27/2022) PROGRAM AND ABSTRACTS* p.66, 2022. (Abstract only)

What have we learned so far about conodonts? The image of these "fascinating little whatzits" (Sweet, 1985) has changed a lot since their first description in 1856. From disarticulated "fish teeth" to an entire class of marine stem-vertebrates that represent 300 million years of existence, conodonts are not whatzits anymore. They are a golden mine of information: (1) to understand early vertebrate evolution; (2) to constrain biochronology of Palaeozoic and early Mesozoic time intervals; and (3) to track Paleozoic-early Mesozoic environmental changes and their consequences for biodiversity. Indeed, conodonts are a super model for palaeontologists thanks to their biostratigraphic attributes (i.e., abundance; disparity; sub-continuous record; global distribution) because there are few comparable extinct taxa that recorded the past for such a long time interval. Nevertheless, their huge stratigraphic range and abundant material is as a weakness as a strength: how to synthesize 300 million years of existence? The beginning of the answer lies in collectively gathering and sharing our current knowledge about conodonts with state-of-the-art techniques such micro-CT scanning and online collaborative platforms. In this keynote, I will sum up current knowledge on conodont palaeobiology and evolution (i.e., growth patterns, phylogeny, biodiversity, habitat, diet, and biogeography) and show how this knowledge is deeply related to the different taxonomical methodologies applied through the last century. Based on the earliest developments, I will propose future research directions. I will focus on two main subjects: the importance of the quantification of P1 element shape and taxonomy in evolutionary studies. Understanding all the facets of conodont evolution requires, on one hand, distinguishing realized vs. unrealized morphologies of P1 elements to evaluate evolutionary drivers (i.e., intrinsic vs. extrinsic). On the other hand, we need to constrain (specific) conodont classification by synthesizing the descriptions of all known taxa with a unique tool. Elaborating on a clear consensus will then bring stability to the understanding of morphological variability and will help researchers to compare patterns from distant taxa in time and phylogeny. The combination of a global morphological view and a standardized taxonomy of P1 elements will allow a better understanding of conodont evolution through their function, their diet, their position in trophic network, and their role in past environments.

CONODONT 1,561,147**ECCENTRIC CONODONTS FROM EXTREME ENVIRONMENTS: SPECIALIZED BIOTA OF LATE WENLOCK (SILURIAN) SABKHAS**

E.Jarochowska and A.Munnecke (Friedrich Alexander Univ). *58TH ANNUAL PALAEOONTOLOGICAL ASSOCIATION MEETING (Leeds, UK, 12/16-19/2014) ABSTRACTS* p.30, 2014. (Available at <http://www.palass.org> as of 11/15/2022; **Abstract only**)

Conodonts are one of the key groups in Palaeozoic biostratigraphy and fossil-based geochemistry. Although biofacies models are well established for late Palaeozoic conodonts, they are nearly lacking for Silurian conodont faunas, resulting in sea-level and facies control over local conodont diversity being underappreciated. We show an example from the latest Wenlock. The conodont record of this time is dominated by taxa representing highly specialized biofacies, characteristic for restricted, upcratonic settings. The Ustya Formation, in Podolia, Ukraine, and the Rootsikuella Formation in Estonia represent hypersaline tidal carbonate settings dominated by dolomite-precipitating microbial mats. These evaporitic, periodically-emerged environments were hostile to most skeletal organisms except for rare eurypterids and ostracods. The only organisms to thrive in these conditions were stromatoporoids, porostromate problematica, and calcifying cyanobacteria. These extreme environments are associated with a distinct conodont fauna dominated by diverse species of *Ctenognathodus* characterized by large and robust elements. Conodont diversity estimates for the late Wenlock indicate a major drop in the taxonomic richness and shift towards low-diversity assemblages, followed by slow recovery at the Wenlock/Ludlow boundary. These estimates appear to be biased by the coincident eustatic sea-level fall resulting in a wider spread of shallow-water depauperate conodont biofacies and, in extreme cases, monospecific *Ctenognathodus* faunas.

CONTINENTAL CRUST 1,561,148**A THREE-BILLION-YEAR HISTORY OF CONTINENTAL WEATHERING**

G.Li, R.Yang, J.Hartmann and J.Chen (Nanjing Univ; Hamburg Univ). *21ST INTERNATIONAL SEDIMENTOLOGICAL CONGRESS [ISC] (Beijing, China, 8/22-26/2022) ABSTRACT BOOK* p.215, 2022. (Available at <http://www.isc2022.org.cn> as of 9/22/2022; **Abstract only**)

Chemical weathering has profound influence on the Earth's habitability because it releases vital nutrients to sustain the biosphere and regulates climate through interaction with carbon cycle. However, reconstructions of continental weathering through the Earth's history are scarce. Based on a novel big-data algorithm applied to the O-U-Pb-Hf isotopic compositions of over 5,000 grains of globally distributed detrital zircons, this work deconvolves a three-billion-year history of continental weathering rate from the time-integrated weathering-alteration of crustal $\delta^{18}\text{O}$ registered by detrital zircons with varying temporal and spatial coverage. Zircon can record the oxygen isotopic composition ($\delta^{18}\text{O}$) of its parent crust at the time of crystallization, the value of which principally reflects the time-integrated effect of crustal alteration. The Hf isotopes and U-Pb isotopes of zircon constrain the alteration history between crust generation and zircon crystallization. A new algorithm is introduced to reconstruct the average $\delta^{18}\text{O}$ alteration rate of continental crust ($R\delta^{18}\text{O-CC}$) through time by solving a set of linear equations based on a large population of detrital zircons with varying temporal coverage across the history of crustal alteration. The reconstructed $R\delta^{18}\text{O-CC}$ shows an overall bell-shape long-term evolution centered at 2 Ga superposed with variations that are coupled with supercontinental assembly cycles. The long-term evolution of the reconstructed $R\delta^{18}\text{O-CC}$ seems to be correlated with solid-earth CO_2 degassing expected from the age distribution of deleted mantle and the supercontinental cycles. Thus, the $R\delta^{18}\text{O-CC}$ is interpreted to reflect weathering considering the control of solid-earth CO_2 degassing on the total weathering flux of continental crust. This work demonstrates the great potential that weathering history may have in reconstructing the operation of the Earth system across deep-time.

CYANOBACTERIA 1,561,149**CYANOBACTERIA AND THE GREAT OXIDATION EVENT: EVIDENCE FROM GENES AND FOSSILS**

B.E.Schirmer (Bristol Univ). *58TH ANNUAL PALAEOONTOLOGICAL ASSOCIATION MEETING (Leeds, UK, 12/16-19/2014) ABSTRACTS* p.16, 2014. (Available at <http://www.palass.org> as of 11/15/2022; **Abstract only**)

Cyanobacteria are among the oldest organisms on this planet and are unique among prokaryotes regarding their age, morphology and fossil record. Their ability to gain energy via oxygenic photosynthesis transformed Earth's atmosphere and redefined the evolutionary boundaries of life. They caused one of the most dramatic environmental changes in the history of our planet, the Great Oxidation Event (GOE). Yet, the origin of cyanobacteria and their morphological disparity, as well as their causal association with the rapid accumulation of atmospheric oxygen, is not resolved. Previous phylogenetic studies I have conducted suggest that the origin of multicellular cyanobacteria might be associated with the GOE. In the fossil record, unequivocal cyanobacterial fossils are not found before 2 Ga. Fossil findings from the Archean and early Proterozoic failed to provide enough taxonomic information using traditional methods. To resolve the occurrence of multicellular cyanobacteria during the early Precambrian, I have combined novel data on morphotype disparity and abundance from Synchrotron Radiation X-ray tomographic microscopy, with phylogenetic analyses of all major prokaryotic taxa. Results suggest that multicellular fossils from the Archean/early Proterozoic can only be compared to modern Cyanobacteria, Chloroflexi, or Actinobacteria among the Eubacteria.

DAGANG OIL FIELD 1,561,150**A STUDY ON THE SINGLE SAND BODY ARCHITECTURE MODEL OF GRAVITY FLOW CHANNEL IN BAN 1 OIL FORMATION IN BANQIAO OILFIELD**

L.Bao, J.Hou, Y.Liu and P.Liu (China Univ Petroleum). *21ST INTERNATIONAL SEDIMENTOLOGICAL CONGRESS [ISC] (Beijing, China, 8/22-26/2022) ABSTRACT BOOK* p.1557, 2022. (Available at <http://www.isc2022.org.cn> as of 9/22/2022; **Abstract only**)

The Ban 1 oil group is the main oil-bearing of the second member of the Shahejie Formation in Banqiao Oilfield. This layer is a lacustrine gravity flow deposition, and is mainly composed of channel deposition. In this paper, through the in-depth study of the gravity flow channel in the Ban 1 oil group, the sedimentary architecture characteristics of the gravity flow channel under different influencing factors such as channel stage, scale and swing stability are analyzed, and different channel architecture patterns are summarized, which provides model guidance for the subsequent development of reservoirs in the area. Combined with coring data, the sedimentary background and sand body distribution characteristics of the study area were analyzed, and it was determined that the study area developed lake bottom gravity flow channel deposits. In this paper, by selecting key blocks with dense well net and high development level, combined with dynamic information such as tracers and injection-production relationship, the channel architecture boundary is determined, and the results of the thin layer-level single water channel division are obtained, and finally the scale of the waterway is quantitatively analyzed. The research results show that there are two complex channels in the study area, and there are multiple single water channels in each complex. The water channel complex is mainly developed in the north area of Banqiao, and the water channel gradually bifurcates into the lobe in the middle area of Banqiao. The average thickness of a single channel is 7.2m, the plane width of the channel is 664m, and the width-thickness ratio is between 120:1 and 172:1. Statistical analysis of the size of a single sand body shows that the width and thickness are positively correlated ($w = 182.79h_{\text{max}} - 237.7$). On the basis of studying the single sand body configuration and geometric characteristics of the gravity flow channel in the study area, the three-dimensional architecture of the gravity flow channel in this area is summarized according to the channel stage, channel size and swing stability. The model provides a geological basis for the subsequent determination of the remaining oil distribution and well location deployment.

DALAZI FM

1,561,151

STUDY ON RESERVOIR CHARACTERISTICS IN EASTERN SAG OF YANJI BASIN

D.Wang and J.Zhu. *21ST INTERNATIONAL SEDIMENTOLOGICAL CONGRESS [ISC] (Beijing, China, 8/22-26/2022) ABSTRACT BOOK* pp.278-279, 2022. (Available at <http://www.isc2022.org.cn> as of 9/22/2022; **Abstract only**)

Reservoir characteristics are the key factors affecting the distribution and accumulation of oil and gas, which are of great significance to the exploration and development of oil and gas reservoirs. This paper analyzes and evaluates the reservoir characteristics of Tongfosi-Dalazi Formation in eastern Yanji Basin. Through thin-section observation and analysis, the contact relationship, morphological change and content of diagenesis products of rock debris were analyzed for various types of diagenesis in the study area to study the distribution and development of secondary pores; Combined with the existing physical property data, the distribution law and correlation of porosity and permeability in the study area are analyzed to find the layers with better physical property conditions; Based on the characteristics of mercury injection curve, the pore types and structure of different layers are analyzed, and the reservoir performance in the study area is judged by combining with the physical property data. The heterogeneity of the study area is evaluated by using the characterization parameters of permeability heterogeneity, and then the connectivity of sand bodies is studied to reveal the law of oil-water movement. The results show that the sandstone reservoir rocks in the study area are feldspathic sandstone, lithic feldspathic sandstone and feldspathic lithic sandstone. The main diagenesis types include compaction, cementation and dissolution. The physical property of reservoir is characterized by low porosity and low permeability. The pore type is dominated by secondary pores with strong heterogeneity. This paper makes an objective and general expression of the overall reservoir capacity, and correct reservoir evaluation is of great significance to oil and gas exploration.

DATONG BASIN

1,561,152

SEDIMENTARY ARCHITECTURE MODELS OF FLUVIAL SUCCESSIONS IN RESPONSIBLE FOR VARIABLE ACCOMMODATION TO SEDIMENT SUPPLY RATIO

W.Li, D.Yue and S.Wu (China Univ Petroleum). *21ST INTERNATIONAL SEDIMENTOLOGICAL CONGRESS [ISC] (Beijing, China, 8/22-26/2022) ABSTRACT BOOK* p.1565, 2022. (Available at <http://www.isc2022.org.cn> as of 9/22/2022; **Abstract only**)

Fluvial rivers are common landforms of continental environments, and sedimentary architecture models of their successions are variable with the change of accommodation to sediment supply ratio (A/S ratio). However, few published research documents proposed variable sedimentary architecture models of fluvial successions in responsible for conditions of A/S ratio. Therefore, this work aims to establish variable sedimentary architecture models of fluvial successions that are responsible for the conditions of A/S ratio, based on the outcropping fluvial successions located in the Datong Basin, China. The used fluvial outcrop is composed of 8 outcrop sections, and the used dataset mainly includes (i) outcrop photomosaics, (ii) data obtained from analyses of rock samples, consisting of measurements of grain size, porosity, and bulk and skeletal density, (iii) impregnated thin sections. Outcrop fluvial strata is divided into 9 short-term and 2 medium-term depositional (A/S ratio) cycles based on mudstone (sandstone) percent, paleosol maturity, and ancient river depth. The results indicate that fluvial rivers transit between different patterns following the sequence, i.e., braided rivers, wandering rivers, transiting rivers between braiding and meandering, and to meandering rivers. Sedimentary architecture models are different significantly for their succession in different river pattern or conditions of A/S ratio. For example, erosion/incise surfaces and chutes show a heavy density in braided river successions whereas decrease sharply in wandering river successions. Also, mid-channel bars in wandering rivers are commonly composed of a set of vertical accretion sandbodies, which are separated by thin silt layers.

Generally, variable sedimentary architecture models that are responsible for different conditions of A/S ratios are proposed in this work.

DEAD SEA FAULT

1,561,153

SEISMICITY INDUCED AT THE NORTHERN DEAD SEA TRANSFORM FAULT, KINNERET (SEA OF GALILEE) BASIN, BY SHALLOW CREEP INVOLVING A SALT BODY

O.B.Cohen, S.Cesca, T.Dahm, A.Hofstetter, Y.Hamiel and A.Agnon (Jerusalem Hebrew Univ; GeoForschungsZentrum Potsdam; Israel Geological Survey). *TECTONICS* v.41, no.10, Oct. 2022. (ISSN 0278-7407; ISSN 1944-9194; Article no.e2022TC007247)

In October 2013 and July-August 2018, two extensive earthquake swarms shook the northern reaches of Lake Kinneret (Sea of Galilee). Former studies explored the swarms, resulting in discrepant depths and mechanisms. Here, we attempt to settle the discrepant interpretations using alternative seismological methods and some unpublished data from borehole seismometers. We propose a hypothesis for the faulting phenomenon focusing on the interaction of the two plate boundary segments that step-over the northern Kinneret depocenter: a creeping segment in the south and a locked segment in the north. The energy accumulated from the interaction induces earthquake swarms from time to time. A shallow fault patch (from the surface down to 1.5 ± 1.0 km) south of the swarms is thought to creep in association with a salt formation underlying some of the basin fill. We use regional seismograms, including two near-source borehole stations, to refine the characteristics of the swarms. We test hypocentral and centroid depths using several methods and different velocity models and corroborate shallow ruptures: the majority are shallower than 6 km (all shallower than ≤ 10 km). The hypocentral locations and focal mechanisms suggest shallow NW-SE normal faults splaying from the tip of the creeping segment in a horseshoe pattern. We test the hypothesis by Coulomb stress calculations that show stress concentration at the step-over interaction zone, consistent with focal locations and mechanisms of the earthquake swarms.

DELTAIC DEPOSIT

1,561,154

EFFECTS OF BASINAL WATER DEPTH ON BAR FINGER ARCHITECTURE IN THE DELTAIC ENVIRONMENT

Z.Xu, S.Wu and C.Zhang (Yangtze Univ; China Univ Petroleum). *21ST INTERNATIONAL SEDIMENTOLOGICAL CONGRESS [ISC] (Beijing, China, 8/22-26/2022) ABSTRACT BOOK* p.1555, 2022. (Available at <http://www.isc2022.org.cn> as of 9/22/2022; **Abstract only**)

Bar finger is the significant sand body in the digitate delta, consisting of mouth bar, distributary channel and levee deposits. It is common seen in modern deposits, as well as ancient hydrocarbon reservoirs, formed by fine-grained, cohesive river. Bar finger could be developed in both shallow-water and deep-water deltas, which exhibits distinctive architectures. Basinal water depth play critical roles on their architecture. However, it is still unclear that effects of basinal water depth. We utilize Delft3D simulations and model deposits to quantify the effects of basinal water depth on bar finger geometric and internal architectures, and recognize criteria for shallow-water and deep-water deltas. The results show that (1) bar finger is almost straight if basinal water depth is larger than distributary channel depth, otherwise, bar finger is sinuous, and the sinuosity of bar finger positively scales to the basinal water depth; (2) bar finger width and length is negatively related to the basinal water depth; (3) basinal water depth determines distributaries-mouth bar combination style, high basinal water depth accompanies with thin mouth bars and relatively deep distributaries, low basinal water depth accompanies with thick mouth bars and relatively shallow distributaries with many avulsed distributaries; (4) basinal water depth influence the existence of point bar, if basinal water depth is smaller than distributary channel depth, sinuous bar finger could develop point bars at inner bank of distributary channel, resulting in distinct internal architecture with straight bar finger. As results, the ratio of basinal water depth to distributary channel depth is a crucial parameter to determine whether shallow-water or deep-water delta. And three morphologic criteria for digitate shallow-water and

deep-water delta is recognized: Sinuosity, the ratio of distributary channel depth to mouth bar thickness, the existence of avulsed distributaries, the existence of point bars. This work provides insights into natural and artificial digitate delta growth and provides new quantitative facies models for shallow-water digitate delta reservoirs.

DHARWAR REGION

1,561,155

MAJOR, TRACE ELEMENT, AND Nd ISOTOPIC COMPOSITIONS OF BANDED IRON FORMATION AND SHALES FROM THE SIRSI SHELF, DHARWAR CRATON, INDIA: IMPLICATIONS FOR PALEO-SEAWATER CHEMISTRY, POST-DEPOSITIONAL ALTERATION, AND PROVENANCE

P.Basu, C.Ishwar-Kumar, S.Chaudhary, R.Chakrabarti, M.Satish-Kumar and K.Sajeev (Indian Inst Science; IIT Kanpur; Niigata Univ). *PRECAMBRIAN RESEARCH* v.382, Nov. 2022. (ISSN 0301-9268; Article no.106882)

We report geochemical and Nd isotopic data for ca. 2.5 Ga old Banded Iron Formation (BIF) and associated clastic rocks which include red- and purple-coloured shales, mudstone, and sandstone from the Sirsi shelf of the Dharwar Craton. Based on lanthanide and non-lanthanide (yttrium) rare earth element (REE) concentration patterns, the Sirsi BIF samples are sub-divided into two groups. The group-1 BIF samples show low shale-normalized (SN) ratios of (La/Yb)SN (0.37-0.53) and (Pr/Yb)SN (0.29-0.34), and superchondritic Y/Ho (41–52); these samples also show insignificant negative Ce anomaly ((Ce/Ce*)SN = 0.83-1.22) compared to modern seawater and seawater-derived precipitates. In contrast, the group-2 BIF samples show strong light REE (LREE) enrichment with high (La/Yb)SN (1.73-18.48) and (Pr/Yb)SN (1.50-7.58), negative Ce anomaly ((Ce/Ce*)SN = 0.02-0.16), and mostly subchondritic Y/Ho (19-39). The group-1 BIF displays modern-day seawater-like REE patterns and their initial ϵ_{Nd} at 2.5 Ga overlaps with contemporaneous global BIF, suggesting their precipitation from Archean seawater. The REE compositions of the group-2 Sirsi BIF cannot be explained by contribution of detritus and are best explained by alteration by a LREE-enriched and Ce-depleted fluid. The Sm-Nd isotopic compositions suggest that this alteration event took place approximately 0.5 Ga ago. The timing of the alteration event coincides with the Pan-African orogeny, which had regionally affected the Greater Dharwar Craton. Among the associated clastic rocks, red and purple shales show group-2-BIF-like REE signatures with negative Ce anomaly, and display high Chemical Index of Alteration (CIA) values (78–98), which suggest high degree of chemical alteration. The enrichment factors (calculated as [(Xelement/XTi)sample/(Xelement/XTi)reference-1] relative to the Archean Upper Continental Crust) of La, Pr, and Ce, in the Sirsi red shales further confirm post-depositional modifications by a LREE-enriched and Ce-depleted fluid, and indicate that negative Ce anomaly in ancient sedimentary rocks could be generated by post-depositional fluid overprint. Geochemical compositions of the Sirsi clastic rocks suggest a felsic provenance, while Nd isotopic compositions of selected shale samples indicate that these sediments were most likely derived from granitoids in the Goa-Dharwar Sector. (c2022 Elsevier B.V.)

DIAGENESIS

1,561,156

SIMULATION OF DIAGENESIS EVENTS BASED ON DIGITAL ROCK TECHNIQUES

Y.Wu, K.Liu, C.Lin and C.Dong (China Univ Petroleum). *21ST INTERNATIONAL SEDIMENTOLOGICAL CONGRESS [ISC] (Beijing, China, 8/22-26/2022) ABSTRACT BOOK* p.231, 2022. (Available at <http://www.isc2022.org.cn> as of 9/22/2022; **Abstract only**)

Sedimentary rocks form after the sediments experience a series of diagenesis events, such as deposition, cementation, and dissolution. It is of great difficulty to quantitatively simulate the diagenesis events using computationally numerical techniques since these events involve chemical and physical reactions between the fluids and minerals. In this paper, some novel methods based on digital rock techniques are presented to address the issues. The discrete element method is used to simulate the packing of mineral

particles, and the dilation operation and quartet structure generate set algorithms are utilized to simulate the cementation and dissolution. The new digital rocks are generated after the original rock undergoes a diagenesis event. Besides, the effects of diagenesis events and diagenesis pathways on rock properties are comprehensively analyzed. The results show that cementation can decrease the porosity, fractal dimension, pore/throat radius, coordination number, correlation of pore space, permeability, and velocity values of the rocks and increase the tortuosity and formation factor of pore space. Comparing the cementation, the dissolution makes a reverse effect on rock properties. The diagenesis pathway also has an impact on the physical properties of digital rocks. In a word, the study will present a comprehensive simulation workflow about deposition and diagenesis and help us to better understand the variations of the flow and mechanical properties of rocks without conducting extensive experiments if rocks experience different diagenesis processes along different pathways.

DINOFLAGELLATE

1,561,157

GLOBAL DINOFLAGELLATE DIVERSITY AND TEMPERATURE PREFERENCE COMPARED TO NEOGENE CLIMATE DEVELOPMENT

J.L.Boyd, M.J.Pound, J.B.Riding, A.M.Haywood and R.F.Ivanovic (Leeds Univ; Northumbria Univ; British Geological Survey). *58TH ANNUAL PALAEOONTOLOGICAL ASSOCIATION MEETING (Leeds, UK, 12/16-19/2014) ABSTRACTS* pp.22-23, 2014. (Available at <http://www.palass.org> as of 11/15/2022; **Abstract only**)

The Neogene (23.03-2.59 Ma) is a period of progressive global cooling, interrupted by the Middle Miocene Climatic Optimum, that led to the glacial-interglacial cycles of the Pleistocene. We have tested the role of Neogene climate change on the evolution, diversity and biogeography of dinoflagellates. Using the Tertiary Oceanic Parameters Information System (TOPIS) database, 500 globally distributed sites and 28,100 dinoflagellate occurrences from the Neogene have been synthesized. We found that during the Neogene, the number of warm-water species (WWS) was reduced in the higher latitudes, but the global diversity of both WWS and cold-water species (CWS) increased. These results suggest that dinoflagellate evolution, diversity, and biogeography were, in part, controlled by climate. The WWS migrated away from the poles due to the cooling climate and narrowing warm water zone, but because more species are thought to originate in the tropics than the poles, we still see a rise in the diversity in the WWS, even as their habitat decreases. This suggests that some of the CWS of today may have originated in tropical regions and then expanded into the higher latitudes.

DOLOMITES MT

1,561,158

CLAY MINERALS AS WEATHERING AND PALEOCLIMATIC PROXIES ACROSS THE CARNIAN PLUVIAL EPISODE (LATE TRIASSIC): A COMPOSITE SECTION FROM THE DOLOMITES (ITALY)

M.Pecorari, P.Gianolla, G.Cruciani, F.Tateo and M.Caggiati (Ferrara Univ; Natl Res Council (Italy)). *21ST INTERNATIONAL SEDIMENTOLOGICAL CONGRESS [ISC] (Beijing, China, 8/22-26/2022) ABSTRACT BOOK* p.218, 2022. (Available at <http://www.isc2022.org.cn> as of 9/22/2022; **Abstract only**)

Clay minerals are weathering products par excellence and their formation can be linked to the climate; thus they could be helpful in paleoclimatic reconstructions. The Carnian Pluvial Episode (CPE) is a multi-pulses climatic perturbation associated with almost four negative Carbon isotopic shifts (Dal Corso et al., 2020). The CPE triggered many important consequences on the sedimentary, environment and global ecosystem evolution of the Late Triassic. Several sedimentological, geochemical and paleontological features have been studied to detect changes related to the climatic episode, and the Dolomites have been representing a helpful source of data on this topic (Dal Corso et al., 2018). Nevertheless, through more than 20 years of studies in the Dolomites, clay minerals were not considered yet. Here we provide the first paleoclimatic study of clay sediments based on mineralogical data (bulk and clay fraction) and

geochemical analysis for Dolomites successions, which encompass not only the syn-CPE succession, but also the pre- and post-event stratigraphic intervals. We sampled clayey beds and interbeds from the San Cassiano Fm., Heiligkreuz Fm. and Travenanzes Fm., obtaining a composite section which covers the earliest (Julian) to late (Tuvallian) Carnian time span. Collected samples were XRD-analysed both as "bulk" powders and oriented mounts. Diffraction patterns of the "bulks" were Rietveld-fitted to achieve phase quantitative analyses while oriented mounts allowed complete identification of clay minerals. ICP-OES analyses were conducted for major, minor and trace elements. This approach combines complementary data from mineralogy and geochemistry, allowing to provide a complete picture on the weathering processes and rate occurred across the CPE. Obtained analyses have been integrated to sedimentological and palynological data to improve the paleoclimatic reconstruction. Interestingly, the samples from the uppermost San Cassiano Fm. and the first two members of the Heiligkreuz Fm. (Alpe di Specie and Borca mbs.) displayed the same clay assemblage, dominated by Illite-Smectite mixed-layer (I/S), followed by Illite, Kaolinite and also Chlorite in several samples. Within this interval, we observed a maximum in the ratio of clay minerals vs. carbonates located few meters above the first Negative Carbon Isotope Excursion (NCIE) detected by Dal Corso et al. (2018), suggesting that clays might record the environmental change connected to the first pulse of the CPE later than other proxies (e.g., palynomorphs). Samples from the overlying Dibona Mb. (above the second NCIE) show a higher dominance of siliciclastics/carbonates ratio (confirmed also by geochemistry) and contain two different species of mixed-layer phase: the disordered I/S and the regular mixed-layer (Reclorite). In suborder, we found Illite and Kaolinite while Chlorite is absent.

DONGPU DEPRESSION 1,561,159

DEVELOPMENT-ORIENTED FINE DESCRIPTION TECHNOLOGY OF SEDIMENTARY MICROFACIES IN FLUVIAL RESERVOIR: A CASE STUDY OF Ng IN BLOCK LZ9 OF LINFANJIA OILFIELD

M.Zhu, Z.Yang, L.Chen, W.Lue, S.Qian, H.Jiao and Y.Leng (Sinopec; Shengli Oilfield Technol Ltd). *PETROLEUM GEOLOGY AND RECOVERY EFFICIENCY (YOUQI DIZHI YU CAISHOULU)* v.29, no.6, pp.39-48, Nov. 2022. (ISSN 1009-9603; In Chinese)

[Full article and English abstract available from P.A.]

DONGPU DEPRESSION 1,561,160

BIO-ENVIRONMENTAL INTERACTIONS AND ASSOCIATED HYDROCARBON GENERATION IN A SALINE LAKE BASIN: A CASE STUDY OF THE PALAEOGENE INTERVAL IN THE DONGPU SAG, EASTERN CHINA

Y.Liu, S.Yao, J.Cao, C.Xu, X.Ma and B.Zhang (Nanjing Univ). *JOURNAL OF ASIAN EARTH SCIENCES* v.241, Jan. 2023. (ISSN 1367-9120; Article no.105465)

Saline lake basins are important Cainozoic petroliferous basins in China. There are significant differences in the palaeoenvironments of these basins. Different biological assemblages resulted in varying hydrocarbon generation characteristics and potential. Therefore, the bio-environmental interactions are key to understanding the oil generation from terrestrial organic matter. In this study, we investigated the organic petrology and geochemistry of the Palaeogene Shahejie Formation in the Dongpu Sag, Bohai Bay Basin, China. The depositional palaeoenvironment varied from saline to freshwater. Cyanobacteria and coccolithophores were deposited in the saline environment, and green algae and higher plant debris were deposited in the freshwater to brackish water environments. The algal biomass in the sediments increased with salinity. Thermal and pyrolysis experiments revealed differences in the hydrocarbon generation potential of the source rocks deposited in different sedimentary environments. The source rocks deposited in the saline water environment have a high hydrocarbon generation potential. Two immature to low-mature oil generation peaks were observed, which are mainly due to the pyrolysis of coccolithophores, cyanobacteria, and dinoflagellates. Only one oil generation peak was observed for source rocks deposited in the freshwater environment, which is

mainly due to the pyrolysis of dinoflagellates and green algae. The hydrocarbon generation potential and two stages of oil generation of the source rocks deposited in the saline environment may be due to the type of hydrocarbon-generating organisms and the catalytic effect of the high-salinity diagenetic environment. The results show that the sedimentary environment of saline lake basins affects the hydrocarbon-generating organisms and hydrocarbon generation process. (c2022 Elsevier Ltd.)

DUVERNAY LIMESTONE 1,561,161

CONTROLS ON EAST SHALE BASIN RESERVOIR DISTRIBUTION WITHIN THE UPPER DEVONIAN DUVERNAY FORMATION, WESTERN CANADA SEDIMENTARY BASIN

A.M.Thorson, E.G.Rau, S.C.Atchley and D.W.Yeates (Matador Resources Co; Baylor Univ). *THE MOUNTAIN GEOLOGIST* v.59, no.4, pp.295-314, Oct. 2022. (ISSN 2327-2945)

The Duvernay Formation accumulated as an organic-rich basinal mudrock concurrent with shallow marine platform carbonates of the Leduc and Grosmont formations. Historically classified as a major source rock to conventional hydrocarbon production, the Duvernay evolved into an unconventional shale reservoir across Alberta, Canada much like other source rock intervals worldwide. Distributions of the Duvernay Formation are partitioned into the West and East Shale basins by a narrow, linear Leduc Formation reef complex known as the Rimbey-Meadowbrook trend. Since 2011, development has focused on the West Shale Basin, but thermal maturity trends suggest the potential for expanded shale reservoir development within the southern portion of the East Shale Basin. This study characterizes sedimentologic and stratigraphic controls on Duvernay reservoir potential to identify development "sweet spots" within the East Shale Basin. Duvernay geologic attributes mapped within this study include: oil thermal maturity, thick restricted basin facies association occurrence (at least 5-10 m thick), high average TOC values (greater than 2.0 wt.%), and high net carbonate thickness (greater than 40 m). The geologic attributes are predictive of production potential within horizontal wells, and the distribution of their co-occurrence suggests the potential for expanded development within the southern portion of the East Shale Basin.

EAGLE FORD FM 1,561,162

MULTI-SCALE ORBITALLY AND SUB-ORBITALLY DRIVEN CLIMATIC AND ENVIRONMENTAL CONTRIBUTIONS TO SOURCE ROCK FORMATION ACROSS THE CENOMANIAN AND TURONIAN, TEXAS, USA

J.S.Eldrett, C.Ma, S.C.Bergman, D.Minisini, L.Kennan, S.R.Meyers and L.Hinnov (Shell Global Solut Int BV; Chengdu Univ Technology; Shell Int Explor & Prod). *21ST INTERNATIONAL SEDIMENTOLOGICAL CONGRESS [ISC] (Beijing, China, 8/22-26/2022) ABSTRACT BOOK* p.165, 2022. (Available at <http://www.isc2022.org.cn> as of 9/22/2022; **Abstract only**)

Modelling source rock petroleum potential requires an understanding of organic matter content, type and geographic extent. These parameters are generally constrained by abundant well and core data in heavily explored and developed basins. However, in frontier basins with sparse data, or in the search of source rock sweet spots in unconventional tight oil and gas plays, prediction of source rock character and extent away from data points is critical. To predict multi-scaled vertical and horizontal source rock heterogeneities (decimeter to micro-meter) away from well control, we need to understand the impact of the primary forcing mechanisms for source rock formation and preservation. We present an integrated multidisciplinary study from a continuously cored section of the entire Eagle Ford Group (Boquillas Formation) from the Shell Iona-1 and other research boreholes and surface sections (Texas, USA). The Eagle Ford Group is a prolific source rock along the US Gulf Coast and Gulf of Mexico and was deposited during the Cenomanian to Turonian Stages of the Late Cretaceous, a Greenhouse Climate state period characterized by extreme warmth. The sedimentary succession is characterized by sub-meter scale limestone-marlstone couplets which preserve unambiguous

primary environmental signals. Integrated sedimentological, paleobiological and geochemical analyses support greater water-mass ventilation and current activity promoting increased silica/carbonate productivity during the deposition of limestone beds compared to deposition of marlstone beds which reflect greater organic matter productivity and preservation. Astrochronological analysis indicates that these environmental variations occur on multiple orbital timescales. In particular, we propose that obliquity and precession forcing on the latitudinal distribution of solar insolation are consistent with the observed lithological and environmental variations in this mid-latitude epicontinental sea setting. We also present a conceptual model that illustrates the geographic variation in orbital expression on sedimentary successions and associated impact on organic matter type and quality prediction. As part of the multi-scaled understanding of source rock deposition, we also analyzed exceptionally well-preserved, millimeter-scale laminations from the organic-rich marlstone beds of the lower Eagle Ford. Sedimentological, geochemical, and micropaleontological data indicate that individual pairs of light-dark laminae record alternations in the extent of water-column mixing and oxygenation with sub-orbital periodicities (80-100 yr, 200-230 yr, 350-500 yr, 1650 yr, 4843 yr and 10,784 yr periodicities). The centennial to millennial variations are reminiscent of those found in Holocene total solar irradiance variability, and the 10,784 yr anoxia cycle may be a manifestation of semi-precession-influenced Tethyan oxygen minimum zone waters entering the seaway.

EAST AFRICA 1,561,163

SEDIMENTARY ARCHITECTURE CHARACTERISTICS OF SUBMARINE FAN LOBES UNDER GRAVITY FLOWS AND BOTTOM CURRENTS - INSIGHTS FROM DEEP-WATER RESEARCH IN EAST AFRICA

M.Chen, S.Wu and J.Zhang (China Univ Petroleum). *21ST INTERNATIONAL SEDIMENTOLOGICAL CONGRESS (ISC) (Beijing, China, 8/22-26/2022) ABSTRACT BOOK* p.1571, 2022. (Available at <http://www.isc2022.org.cn> as of 9/22/2022; **Abstract only**)

Submarine fan deposits have great potential for oil and gas resources, and the study of their sedimentary architecture is essential for the development of deep-water reservoirs. At present, the influence of bottom currents on submarine fan channel architecture has been widely recognized. Whereas, for submarine fan lobes, the current study only found that bottom currents can modify the entire lobe system distribution and deposit architecture under gravity flows and bottom currents, and no research has been carried out on the effect of bottom currents on different hierarchical lobe architecture under this deep-water environment. In this paper, we study on a deep-water area in East Africa under gravity flows and bottom currents, including architecture of the submarine lobe, and different stacking patterns and connectivity features of different hierarchy lobes by using well core, logging and seismic data. Then, the sedimentary architecture pattern of submarine lobes under gravity flows and bottom currents is established. The main conclusions include: (1) the lobe complex and the single lobe show unidirectional southward stacking pattern, which is opposite to the direction of bottom currents, and the single lobe presents an asymmetric shape with thicker lobe margin on bottom currents; the mudstone between the lobe complex is thick and continuous, and the mudstone between the single lobe is thin and discontinuous. (2) The lobe layers in a single lobe display vertical accumulation, which shows no obvious relationship with bottom currents; there are few mudstone interlayers in a single lobe, and the mudstone interlayers gradually increase from the proximal the distal of the lobe. (3) The influence of the bottom currents on the lobes is mainly manifested in the fact that the single lobe in the early stage deposited thicker vertically of the lobe margin along the bottom currents side, so that the followed single lobe deposit on the lower position of the previous topography, showing the migration opposing bottom currents. For the effects of the bottom current on the channel, their migration directions are all opposite to bottom currents. For the submarine lobe, there is no obvious asymmetry with large-scope horizontal drift deposits on the bottom currents side. Instead, the single lobe margin is thicker vertically on the

bottom currents side, which shows the asymmetry that the main body of the lobe is biased to the bottom currents side. The research is of great significance to improve the theory of deep-water sedimentary architecture and development of reservoir.

ENGLAND 1,561,164

GIANT ARTICULATED ARTHROPLEURA REMAINS FROM THE MISSISSIPPIAN OF NORTHERN ENGLAND

N.S.Davies, R.J.Garwood, W.J.McMahon, J.Schneider and A.P.Shillito (Cambridge Univ; Manchester Univ; Freiberg Tech Univ; Oxford Univ). *65TH ANNUAL PALAEOONTOLOGICAL ASSOCIATION MEETING (Manchester, UK, 12/18-20/2021) PROGRAMME AND ABSTRACTS* p.21, 2021. (Available at <http://www.palass.org> as of 11/1/2022; **Abstract only**)

Newly discovered partial remains of the giant millipede-like organism, *Arthropleura*, are reported from the Serpukhovian (Pendleian) aged Stainmore Formation in the Northumberland Basin of northern England. The reported specimen is a rare example of its kind, as only two other partially articulated giant *Arthropleura* fossils are previously known. Measuring 76 x 36 cm, the specimen is remarkable as one of largest arthropod fossils known from the global geological record, and the largest arthropleurid, from an interval pre-dating Palaeozoic oxygen peaks. The specimen is preserved in three dimensions within fine sandstone and exhibits a number of unusual taphonomic characteristics due to its moderate deformation by syndimentary tectonics. Sedimentological evidence for a lower delta plain environment supports the contention that *Arthropleura* preferentially occupied open woody habitats rather than swampy environments, and shared such habitats with tetrapods. The new datapoint for *Arthropleura* remains is compared with other global evidence to show that the organism was closely associated with the location of the palaeoequator and relatively unaffected by climatic events in the late Carboniferous prior to its extinction in the early Permian.

ENGLAND 1,561,165

"COMATULID CRINOIDS" ON THE MORNING NEWS: PRELIMINARY OBSERVATIONS AND IMPLICATIONS OF A NEW BATHONIAN (MIDDLE JURASSIC) LAGERSTÄTTE IN WILTSHIRE, UK

T.A.M.Ewin, S.Hollingworth, C.J.Underwood, D.J.Ward, A.E.M.Ward, C.G.Miller, S.Stukins, A.R.Lord, J.R.Young et al. (London Museum). *65TH ANNUAL PALAEOONTOLOGICAL ASSOCIATION MEETING (Manchester, UK, 12/18-20/2021) PROGRAMME AND ABSTRACTS* p.65, 2021. (Available at <http://www.palass.org> as of 11/1/2022; **Abstract only**)

A new UK Bathonian (Middle Jurassic) Lagerstätte has revealed one of the most important Jurassic echinoderm localities in the world. Excavation of the site has produced large numbers (thousands) of exceptionally preserved articulated echinoderms including at least 18 species belonging to all five extant echinoderm classes. Other significant fossils include plants and Radiolaria, the latter being rarely seen in UK onshore Jurassic rocks. The fossils are preserved in indurated packstone horizons (at least two) within a unit of interbedded buff siltstones and dark grey un lithified mudstones that vary rapidly in thickness and lateral extent. The well-preserved echinoderm fossils are preserved in various orientations, indicating brief transportation prior to rapid burial (obstruction). Other shelly faunas are more disarticulated and suggest greater residency within the environment and greater transportation prior to burial. The echinoderm fossils are dominated by the true comatulid crinoid *Palaeocomaster* sp., represented by over 3,000 individuals, and the stalked crinoid *Isocrinus* sp. This is the earliest incidence of true comatulid crinoids dominating a marine environment. It is significant, as "comatulid meadows," important areas of biomass and diversity in several modern soft seafloor ecosystems (such as at continental shelf margins), are unknown in the fossil record before the Cretaceous.

FAULT BLOCK

1,561,166

FINE DIVIDED METHOD OF ACTIVE TECTONIC BLOCKS BASED ON ADAPTIVE DENSITY PEAK CLUSTERING AND IMPROVED EULER MODEL, REVEALED BY GNSS VELOCITIES IN SOUTHWEST JAPAN

W.Qu, J.Wang, Y.Yang, Y.Gao, J.Li, Y.Wang, Q.Zhang and M.Hao (Chang'an Univ; Chengdu Univ Technology). *TECTONOPHYSICS* v.844, 12/5/2022. (ISSN 0040-1951; Article no.229635)

The rational division of active tectonic blocks is an important premise for distinguishing active faults, discovering hidden faults, and an in-depth understanding of regional crustal deformation characteristics, seismicity, and tectonic dynamics. In recent years, clustering algorithms have been widely used in active block division owing to their high efficiency and reliability. However, the classical clustering algorithm sensitivity to the block boundary under different conditions is inconsistent. Additionally, the Euler model constraint (EMC) process involved in the classical clustering algorithm ignores the influence of the boundary points and gross error points of the active block. Therefore, in this study, a new active block division method based on adaptive density peak clustering (ADPC) and an improved Euler model constraint (IEMC) is proposed. The simulation test results show that compared with the traditional clustering algorithm, the mean error rate of the new method can be reduced by up to 40% in the simple single-fault model and by 10% in the complex three-segment model. The new method was further applied to an actual case of an active block division in southwest Japan. The results further show that the new method is less affected by the regional environmental conditions. Compared with previous results in southwest Japan, the proposed method has higher accuracy and higher reliability of the active block division results. The new method for active block division proposed in this study can be used to accurately explore the location and quantity of block boundaries. (c2022 Elsevier B.V.)

FORAMINIFERA

1,561,167

A NEW TECHNIQUE FOR OBSERVING THE INTERNAL MORPHOLOGY OF FORAMINIFERAL TESTS IN TRANSMITTED LIGHT

C.M.McCauley, G.P.Nestell and M.K.Nestell (Texas Univ, Arlington). *MICROPALEONTOLOGY* v.68, no.6, pp.587-599, 2022. (ISSN 0026-2803; ISSN 1937-2795)

The technique proposed herein reveals the internal morphology of calcareous and agglutinated foraminifers in transmitted light, aiding in taxonomic identifications. It involves eliminating air bubbles inside tests through the application of a vacuum or high heat during oil immersion, and the subsequent mounting of the oil-clarified tests in compatible QSM thermoplastics. The technique is rapid, non-destructive, allows internal viewing of large tests and is especially useful for small tests that are difficult to thin section. The technique has been used for mounting other microfossils, such as polycystine radiolarians.

FORAMINIFERA

1,561,168

IMPLICATIONS FOR THE FORAMINIFERA OVER THE TOARCIAN (EARLY JURASSIC) OCEANIC ANOXIC EVENT (TOAE), FOLLOWING DEVELOPMENT OF THE FREEZE-THAW EXTRACTION TECHNIQUE

A.E.Kennedy and A.L.Coe (Open Univ). *58TH ANNUAL PALAEOONTOLOGICAL ASSOCIATION MEETING (Leeds, UK, 12/16-19/2014) ABSTRACTS* p.31, 2014. (Available at <http://www.palass.org> as of 11/15/2022; **Abstract only**)

The Toarcian Oceanic Anoxic Event (TOAE) is marked by the widespread deposition of organic-rich mudrocks and pronounced changes in palaeoenvironmental conditions. The interval between the Pliensbachian/Toarcian boundary and the TOAE is associated with a mass extinction. Microfossils, including foraminifera, are highly sensitive to the environment around them and therefore suitable as a proxy for examining the impacts of palaeoenvironmental change. This study has investigated a range of processing techniques for the extraction of foraminifera from organic-rich mudrocks, using samples from the TOAE on the North Yorkshire coast. These included the widely-used hydrogen peroxide

H2O2 and a modification of the freeze-thaw technique. Those processed with H2O2 contained fewer foraminifera, lower diversity and damaged tests (Kennedy and Coe, 2014). In this presentation we will show the results from our modified freeze-thaw technique (Kennedy and Coe, 2014) which call into question the previously observed changes in foraminifera: including size decrease, lower diversity and barren interval associated with the TOAE that may be an artefact of sampling and processing. Our study highlights the importance of high resolution sampling and careful extraction techniques and has implications for other microfossil groups when they are in low abundance.

FRANCE

1,561,169

EPIBIOSES OF FOSSIL CRUSTACEANS: INSIGHTS ON SPECIFIC PALAEOECOLOGY AND TRUE PALAEOSYMBIOSES

N.Robin, S.Charbonnier, B.Van Bakel, S.Bernard, J.Miot and G.Petit (Paris Museum; Boxtel Museum; Pierre & Marie Curie Univ). *58TH ANNUAL PALAEOONTOLOGICAL ASSOCIATION MEETING (Leeds, UK, 12/16-19/2014) ABSTRACTS* pp.41-42, 2014. (Available at <http://www.palass.org> as of 11/15/2022; **Abstract only**)

Because their study may reveal possible palaeosymbioses, organisms fossilized in direct association deserve a true consideration. However, their syn-vivo or post-mortem nature is not always obvious. Focusing on decapod crustaceans as hosts, we report here two studied kind of epibioses: a case of post-mortem meeting that brings insights about the palaeoecology of associated organisms, and a true palaeosymbiosis. The first epibiosis involves one of the earliest brachyuran crabs of the world and two bryozoan colonies fixed on its dorsal side. We described this precious Bathonian crab (Sarthe, France) and placed it within the Homolodromioidea. Systematic sizes and structures of the bryozoan colonies demonstrate their post-mortem settlement on the crab, enabling us to conclude that the thickness of the carapace of Homolodromioidea was greater in the past than today. A cohabitation of hermit crabs in the palaeoenvironment of this crab may also be presumed. The second epibiosis, described in both fossil (La Voulte Lagerstaette, France) and extant record, involves calcifying bacterial colonies living on Penaeoidea shrimps. This association has been identified as a syn-vivo one, and shows even parasitic features. These studies show the ability of punctual fossil epibioses to reveal aspects of both palaeoenvironments and life habit of associated organisms.

FUJIAN

1,561,170

DISRUPTION OF TERRESTRIAL PLANT ECOSYSTEM IN MIOCENE (SUB) TROPICS: A PALYNOLOGICAL PERSPECTIVE FROM FOTAN FORMATION, SOUTHEAST CHINA

Y.Yang and W.M.Wang (PetroChina; Nanjing Inst Geol Palaeont). *21ST INTERNATIONAL SEDIMENTOLOGICAL CONGRESS [ISC] (Beijing, China, 8/22-26/2022) ABSTRACT BOOK* p.196, 2022. (Available at <http://www.isc2022.org.cn> as of 9/22/2022; **Abstract only**)

The palynological records on "fern spike", i.e., forest was transiently replaced by fern-dominant vegetation and then rapidly recovered, were documented in the geological past around the world, especially following the massive extinction (e.g. Triassic/Jurassic and Cretaceous/Tertiary boundaries). Fern spikes represent the initial colonization by pioneer species following massive destruction of vegetation. Here, two fern spikes were recognized in the palynological sequences of MP-1 section (late Early-early Middle Miocene) and HK section (late Middle-Late Miocene) from the Fotan Formation in Zhangpu County, Fujian Province, Southeast China, which is the first report about fern spike events in this area. Based on the appearances of fern spikes and the law of vegetation succession, we found that at least two catastrophic events occurred in our study area during the Miocene, which are considered to be caused mainly by the contemporaneous flood basalt volcanism. Along with the fern spikes we observed the increased runoff and the bloom of *Concentricystes* (algae) as a result of enhanced nutrient inputs after the ecosystem disturbances.

Besides, in comparison with MP-1 section, the fern spike in HK section is characterized by (1) the higher abundance and diversity in terms of the composition of fern spores, (2) the appearance of fungal spike, (3) the longer time of duration, and (4) the much higher degree of prosperity of *Concentricystes*, suggesting that the severity of the catastrophic event occurred during the deposition of HK section is greater than that of MP-1 section.

GEOLOGIC MODEL

1,561,171

METHOD FOR ESTIMATING THE GEOLOGICAL MODEL (VMATRIX) AND EFFECTIVE POROSITY FROM STRATIGRAPHIC INVERSION [PROCEDE D'ESTIMATION DU MODELE GEOLOGIQUE (VMATRIX) ET DE LA POROSITE EFFECTIVE A PARTIR D'UNE INVERSION STRATIGRAPHIQUE]

N.Ouabed and A.Lekam. World 2022/199,778A1, p. 9/29/2022, f. 3/23/2022 (Appl. 2,250,006), pr. DZ 3/24/2021 (Appl. 021,139) (G01V-0001/30; G01V-0001/40). (Assigned to N.Ouabed and A.Lekam; **In French**)

The invention relates to the fields of characterizing heterogeneous and anisotropic reservoirs at the well, on the seismic scale and on the laboratory scale. More particularly, the present invention relates to a novel method for quantitatively evaluating, in heterogeneous and anisotropic oil reservoirs, the volume of the matrix [V_{matrix}] and the effective porosity [ϕ_e], irrespective of the lithology, at the well using the acoustic logs of the respective slowness of the longitudinal [ΔT_p] and transverse [ΔT_s] waves, as well as on the seismic scale using the acoustic impedances of the longitudinal [I_p] and transverse [I_s] waves from stratigraphic inversion.

GLOBAL WARMING

1,561,172

ASTRONOMICALLY FORCED WARMING EVENTS AND ORGANIC CARBON BURIAL

C.Huang and Z.Wang (China Univ Geosci, Wuhan). 21ST INTERNATIONAL SEDIMENTOLOGICAL CONGRESS [ISC] (Beijing, China, 8/22-26/2022) ABSTRACT BOOK p.164, 2022. (Available at <http://www.isc2022.org.cn> as of 9/22/2022; **Abstract only**)

Stratigraphic records are essential for deciphering past climate variability and understanding causality of climate events in Earth history. Some geological records during warming events such as the ocean anoxic events (OAEs), Early Eocene Climatic Optimum (EECO), and Middle Eocene Climate Optimum (MECO) reveal a close relationship between increased surface temperatures and enhanced organic carbon burial in sedimentary basins driven at orbital eccentricity time scales. There are some evidences reveal that the organic carbon burial occurred at the minima of the 405 kyr and approximately 2.4 Myr long eccentricity cycles and approximately 1.2 Myr long obliquity cycle with global cooling and decline of atmospheric CO₂. However, how the orbitally forced climate changes and driven the carbon cycle variations and what is the mechanisms of the organic carbon burial and source rock formation that remain poorly understood. Here, we present an example of EECO and MECO events recorded at North China oil-bearing basins that reveal the relationship between the astronomically forced climate changes and source rock formation, feedback of carbon cycle on climate changes.

GORU FM

1,561,173

THE FIRST RECORD OF OAE2 AND HIGH RESOLUTION INTEGRATED STRATIGRAPHY OF THE CENOMANIAN-TURONIAN SUCCESSION, SULAIMAN RANGE, PAKISTAN

M.Hanif, M.Sabba, I.Omer Yilmaz and M.Mohibullah (Peshawar Univ; Middle East Technical Univ; Balochistan Univ). 21ST INTERNATIONAL SEDIMENTOLOGICAL CONGRESS [ISC] (Beijing, China, 8/22-26/2022) ABSTRACT BOOK p.181, 2022. (Available at <http://www.isc2022.org.cn> as of 9/22/2022; **Abstract only**)

High-resolution planktonic foraminiferal and calcareous nannoplankton biostratigraphy is provided for the pelagic

succession of the Goru Formation from Murree Brewery Section of the Sulaiman Range, Pakistan. The Goru Formation in the studied section spans over the Middle Albian (*Biticinella breggiensis*; CC8 Zone) to Late Turonian stages (*Marginotruncana sigali*; CC12 Zone). Lithologically, the Goru Formation is predominantly composed of the carbonate-rich mudstones and a 0.5 m black shale interval representing OAE2 followed by red colored marl/limestones (potentially Cretaceous Oceanic Red Beds, CORBS). Biostratigraphically, The Cenomanian/Turonian (C/T) boundary is identified based on the First Appearance Datum (FAD) of calcareous nannoplankton *Quadrum gartneri* and the FAD of the planktic foraminifera *Helvetoglobotruncana helvetica*. The Carbon and oxygen isotopic analysis on the carbonate fraction is also presented. A prominent negative $\delta^{13}\text{C}$ isotopic excursion of 6‰ occurs at the bottom of the black shale interval, this is followed by a positive isotopic excursion of 5.8‰ representing the Cenomanian-Turonian boundary (CTB) immediately above the black shale interval. A change to more negative $\delta^{18}\text{O}$ values from the uppermost Cenomanian into the lowermost Turonian may be the result of warming. Similar to other Tethyan sections, the onset of the OAE2 predates the CTB in Murree Brewery Section as recorded in many European sections. A major turnover in the deep-dwelling planktonic foraminifera (*Rotaliporas*) occurred during the Cenomanian-Turonian boundary Interval. The single-keeled *Rotaliporas* was succeeded by the double-keeled *Globotruncanids*. Three dissolution resistant calcareous nannoplankton taxa are dominant i.e. *Watznaueria barnesae*, *Eiffelithus turrisseiffelii*, *Eprolithus floralis* within the studied interval. High species richness and high abundance of the tropical species *Watznaueria barnesae*, suggest warm tropical waters. The two abundant species, tropical *W. barnesae* and cool water *E. floralis* alternate in abundance in the early and middle Turonian, suggesting changing climatic conditions.

GREENLAND

1,561,174

MORPHOMETRIC ANALYSIS OF SKIAGIA-PLEXUS ACRITARCHS: TOWARDS A MEANINGFUL EVALUATION OF PHENOTYPIC PLASTICITY

E.Wallet, S.Willman and B.J.Slater (Uppsala Univ). 65TH ANNUAL PALAEOONTOLOGICAL ASSOCIATION MEETING (Manchester, UK, 12/18-20/2021) PROGRAMME AND ABSTRACTS p.97, 2021. (Available at <http://www.palass.org> as of 11/1/2022; **Abstract only**)

The Cambrian evolutionary radiations are marked by spectacular biotic turnovers and the establishment of increasingly tiered food chains. At their base are primary producers, which in the Cambrian fossil record are chiefly represented by an informal category of incertae sedis called "acritarchs." The form-taxonomic subdivisions of acritarchs have been not only intensively used in biostratigraphy, but also in large-scale studies of phytoplankton diversity. However, both prospects are challenged by cases of taxonomic inconsistencies and over-splitting arising from the significant phenotypic plasticity evident in these microfossils. Here we apply a multivariate approach to investigate the morphological variation among the biostratigraphically significant acritarch genus *Skiagia*. Using an assemblage sourced from the Buen Formation (Cambrian Series 2, Stage 3-4) of North Greenland, our analysis showed that the current specific-level classification of *Skiagia* discretizes a continuous spectrum of morphologies, likely encompassing a mixture of various ontogenetic stages and ecophenotypes. These findings shed light on important taxonomic and biostratigraphic hurdles, and question the reliability of currently used measures of ancient phytoplankton diversity. This study demonstrates the value of using morphometric tools to explore acritarchs' phenotypic plasticity and their potential ontogenetic and palaeoecological drivers in Cambrian ecosystems.

GUADALUPE MT

1,561,175

CHITONS OF THE PERMIAN CAPITAN REEF AND THE NATURE OF LATE PALAEOZOIC POLYPLACOPHORA

M.J.Vendrasco, R.D.Hoare, G.L.Bell and J.M.Hearst (Granada Univ; Bowling Green State Univ; Guadalupe National Park). 58TH ANNUAL PALAEOONTOLOGICAL ASSOCIATION MEETING

(Leeds, UK, 12/16-19/2014) ABSTRACTS p.51, 2014. (Available at <http://www.palass.org> as of 11/15/2022; **Abstract only**)

A diverse assemblage of exceptionally preserved chiton shell plates has been extracted from the Permian Bell Canyon Formation in the Guadalupe Mountains, west Texas, USA. The chitons were found in thin debris shed from the massive Capitan Reef. These fossils show fine details of tegmental sculpture and configuration of aesthete canals, and they add to the already high diversity of chitons known from the Permian of Texas. Rarefaction analysis of these assemblages indicates that the diversity of late Palaeozoic chitons was probably much higher than recorded. The fossils show high variability in overall shape, tegmental coverage and sculpture, as well as shape and extent of incisions in insertion plates. Mesozoic chitons, in contrast, are sparse and morphologically uniform. Thus, it seems that many chiton lineages died out during the end Permian mass extinction, and along with diversity went disparity. The Capitan fossils confirm convergent evolution in the Polyplacophora of both tegmentum reduction as well as incisions in the articulamentum. Otherwise, the presence of such slits in insertion plates might provide an upper bound for the origin of the chiton crown group. In either case, the crown group Polyplacophora probably originated during the late Palaeozoic, by which time some chitons had shell plate morphology very similar to modern forms.

GUIZHOU

1,561,176

PROVENANCE AND DEPOSITIONAL ENVIRONMENT IN SHUICHENG AREA, WESTERN GUIZHOU PROVINCE, CHINA - EVIDENCE FROM PALEONTOLOGY AND GEOCHEMISTRY

Y.Shen and Z.Dang (China Univ Mining Technol). *21ST INTERNATIONAL SEDIMENTOLOGICAL CONGRESS [ISC] (Beijing, China, 8/22-26/2022) ABSTRACT BOOK* pp.221-222, 2022. (Available at <http://www.isc2022.org.cn> as of 9/22/2022; **Abstract only**)

Well-developed marine carbonate of the the Late Permian Changhsingian in the Shuicheng area of western Guizhou, with abundant biological fossils such as calcareous algae, foraminifera, brachiopods, gastropods, bivalves, cephalopods, crinoids, echinoids, sponges and ostracods. Based on the systematic paleontological and geochemical analysis, we studied the water medium conditions, palaeoclimate, paleoceanography and provenance background of the late sedimentary period of Changxing Formation in the area. The results show that six fossil assemblages can be delineated from the bottom to top in the Changhsingian vertical sedimentary sequence: the Foraminifera-Calcareous algae-Brachiopoda assemblage, the Foraminifera-Brachiopoda-Bivalve assemblage, the Bivalve-Gastropoda-Crinoida assemblage, the Foraminifera-Calcareous algae-Bivalve assemblage, and the Foraminifera-Bivalve-Brachiopoda and Foraminifera-Calcareous algae-Ostracoda assemblages. Among them, calcareous algae and planktonic foraminifera are the most abundant and diverse. The trace elements of Rb, Cs, Ba and Tl are relatively depleted, while the Trace elements of Nb are relatively enriched. The trace elements abundance of Li, Be, Sc, V, Cr, Co, Ni, Cu, Zn, Ga, Sr, Zr, Sn, Hf, Ta, Pb, Th and U are closer the average of the upper crust. Chondrite-normalized REE patterns show that the rocks are enriched in LREE and relatively depleted in HREE, with Eu weak negative anomaly and Ce no anomaly. Study area Changxing Formation main sedimentary period was mainly in warm humid climate paralic sedimentary environment and anoxic environment thus in favor of abundant calcareous algae and foraminifera growing. A sudden dry and hot climate in the late period, with a sudden rise in the water column, an increase in salinity and temperature, and the emergence of clusters of relatively heat-tolerant ostracods, while other organisms declined sharply or even disappeared. Σ REE-La/Yb discrimination diagram indicate that the Provenance is mainly influenced by volcanism during the Emeishan stage, diagenetic parent material is basalt. According to discrimination diagrams of La-Th-Sc, Th-Sc-Zr/10 and Th-Co-Zr/10 source materials of the Changxing Formation was mainly deposited in a continental island arc setting and clastic materials from an oceanic island arc were partly added during the late depositional period.

HAILAR BASIN

1,561,177

JURASSIC VOLCANISM AND SEDIMENTATION ALONG THE DERBUGAN AND ERGUNA FAULTS, WESTERN HAILAR BASIN

D.Zhao, G.Shi, C.Shen, Y.Hou, L.Wu, X.Zeng, R.Sun, C.Zheng, Y.Peng et al. (China Univ Geosci, Wuhan). *21ST INTERNATIONAL SEDIMENTOLOGICAL CONGRESS [ISC] (Beijing, China, 8/22-26/2022) ABSTRACT BOOK* p.342, 2022. (Available at <http://www.isc2022.org.cn> as of 9/22/2022; **Abstract only**)

Derbugan and Erguna faults are the two important structures in the northeastern Asia. Recent studies suggest that the two fault belts control Jurassic volcanic eruptions, basin subsidence and sedimentary filling. The western Hailar Basin lies between the Derbugan and Erguna faults. Based on 2D/3D seismic data and field observation, this study aimed to characterize volcanic edifices, identify the lithofacies distribution of volcano-sedimentary rocks, and reconstruct volcanic paleogeography in the western Hailar Basin. The volcanic rock belt distributed along the NNE-trending Derbugan and Erguna faults is about 50 km wide and hundreds of kilometers long. The volcanic edifices show multi-center eruption patterns as the typical features of composite volcanoes, and they predominantly distribute along the NE-trending faults that are the secondary faults of the Derbugan and Erguna faults. The spatial distribution of the volcanoes is controlled by typical fault patterns, for example, parallel-fault assemblage, antithetical-fault assemblage, fault-transition zone and echelon-fault assemblage. Sedimentation usually takes place between volcanic edifices and the boundary faults of basin, and the fault-related structures and volcanic paleogeomorphology jointly impact the distribution of sedimentary rocks. The dip angle of boundary faults controls the range of sediment accommodation. The volcanic eruptions occur almost simultaneously with basin rifting and occupy a considerable part of the accommodation space. The sedimentary facies are developed in the accommodation space limited by volcanic edifices and faults. A detailed anatomy suggests that the volcanics in Bayanhushu depression mainly belong to effusive facies and explosive facies composed of tuffs. The Chagannuor depression is predominated by shallow lacustrine sediments, and the explosive facies and volcano-sedimentary facies mainly distribute in the south. Fan deltas and offshore sedimentary fans are generally developed in the gentle slope zone away from volcanic disturbance. The Derbugan and Erguna faults serve as a pathway for magma migration and affect the emplacement of volcanic edifices and the distribution of volcano-sedimentary rocks.

HEBEI

1,561,178

MICROSCOPIC AND GEOCHEMICAL ANALYSES OF THE TONIAN LONGFENGSHAN BIOTA FROM THE LUOTUOLING FORMATION (HEBEI PROVINCE, NORTH CHINA) WITH TAPHONOMIC IMPLICATIONS

Y.Jing, Z.Q.Chen, R.P.Anderson, X.Wang, Z.Zheng and X.Feng (China Univ Geosci, Wuhan; Oxford Univ). *PRECAMBRIAN RESEARCH* v.382, Nov. 2022. (ISSN 0301-9268; Article no.106899)

The Tonian Longfengshan biota is among the earliest known fossil assemblages with a predominance of the benthic macroalgal fossil *Longfengshania* Du, 1982, which is well known for its blade, stipe, and holdfast differentiation. However, the microstructure and geochemical composition of these fossils are poorly understood. We documented the microscopic characteristics, mineralogy, and geochemistry of 29 fossil specimens from the Luotuling Formation at the Longfengshan locality of Hebei Province, North China using scanning electron microscopy (SEM), energy dispersive X-ray spectroscopy (EDS), micro X-ray fluorescence spectroscopy (μ -XRF), Raman spectroscopy, and X-ray Diffraction (XRD). SEM-EDS revealed that all fossil specimens are preserved as two-dimensional compressions that are composed of carbonaceous patches and also have high calcium content. Iron-rich clay minerals were additionally detected in association with the fossils. μ -XRF mapping confirmed the fossils' high calcium content. Raman spectroscopy showed that carbonaceous patches are comprised of disordered organic carbon that has been altered by low grade metamorphism (<300 °C). XRD showed a homogenous mineralogy

(dominated by quartz, feldspar, and muscovite with other minor e.g., kaolinite, smectite). Petrographic analysis revealed that microbial mats existed in the fossil-bearing shale, implying that benthic macroalga *Longfengshania* attached its holdfast in a sticky microbial mat that encrusted the sea-bed. Integration of these data suggested that the fossil-bearing silty shale was deposited in the subtidal zone below storm wave base. Iron-replete but sulfate-depleted porewater within sediments may have inhibited the degradation process of the Longfengshan macroalgae. (c2022 Elsevier B.V.)

HEILONGJIANG

1,561,179

A NEW STUDY OF THE LATE TRIASSIC CONODONT FAUNA FROM RAOHE, HEILONGJIANG, NORTH-EASTERN CHINA

X.Wu, H.Jiang, Y.Chen and X.Lai (China Univ Geosci, Wuhan). *5TH INTERNATIONAL CONODONT SYMPOSIUM [ICOS] (Wuhan, China and Online, 6/24-27/2022) PROGRAM AND ABSTRACTS* p.48, 2022. (Abstract only)

The Nadanhada terrane of northeastern Heilongjiang, northeastern China comprised the Late Triassic marine succession (Shengli Fm.) of North China. The Shengli Fm. consists of the wackestone to packstone with abundant planktonic radiolarians and foraminifers, which indicated the toe of slope environment. Four conodont genera and eight species have been recovered from Shengli Fm. in the Minnan section, Raohe, Heilongjiang, including: *Neocavitella cavitata*, *Norigondolella* sp., *Epigondolella triangularis*, *Epigondolella vialovi*, *Epigondolella* sp., *Carnepigondolella tualica*, *Carnepigondolella samueli*, and *Mockina postera*. In Minnan section, two Carnian conodont zones have been recognized, in ascending order, they are: *C. samueli* Zone and *E. vialovi* Zone. Three conodont genera and six species are obtained from Shengli Fm. in the Minzhu section, whereas 1.5 km northeast of the Minnan section, including: *Norigondolella* sp., *Epigondolella quadrata*, *Epigondolella rigoi*, *Epigondolella* sp. and *Mockina postera*, two Norian conodont zones have been also recognized at the Minzhu section, in ascending order, they are: *Epigondolella quadrata-Epigondolella rigoi* Zone and *Mockina postera* Zone. *Neocavitella cavitata*, *Epigondolella vialovi*, *Carnepigondolella tualica*, and *Epigondolella triangularis* are firstly reported in the study area. The new findings enrich the conodont fauna of Nadanhada terrane, which allows the comparisons to be made with the North-west Pangaea (North America), Tethyan realm (Europe), Panthalassa Ocean (Japan). The conodont assemblage from the Nadanhada terrane is included in the Tethyan Late Triassic conodont fauna, but the diversity and abundance are much less than the latter one. Only four species, *Carnepigondolella samueli*, *Epigondolella quadrata*, *Epigondolella triangularis* and *Mockina postera* from Nadanhada have been observed at North-west Pangaea (North America), and only 2 species, *Epigondolella quadrata* and *Mockina postera* at Panthalassa Ocean (Japan). In general, the conodont faunas from the Nadanhada terrane, north-eastern China are closely similar to those from the Tethyan realm (Europe). It indicates that the Nadanhada terrane is closely related to the Western Tethyan realm during the Late Triassic.

HELLENIDES TECTONIC COMPLEX

1,561,180

QUATERNARY E-W EXTENSION UPLIFTS KYTHIRA ISLAND AND SEGMENTS THE HELLENIC ARC

G.de Gelder, D.Fernandez-Blanco, N.Ogretmen, S.Liakopoulos, D.Papanastassiou, C.Faranda, R.Armijo and R.Lacassin (ISTerre; Globe Inst Physique). *TECTONICS* v.41, no.10, Oct. 2022. (ISSN 0278-7407; ISSN 1944-9194; Article no.e2022TC007231)

Several crustal and lithospheric mechanisms lead to deformation and vertical motion of the upper plate during subduction, but their relative contribution is often enigmatic. Multiple areas of the Hellenic Forearc have been uplifting since Plio-Quaternary times, yet spatiotemporal characteristics and sources of this uplift are poorly resolved. The remarkable geology and geomorphology of Kythira Island, in the southwestern Hellenic forearc, allow for a detailed tectonic reconstruction since the Late Miocene. We present a morphotectonic map of the island, together

with new biostratigraphic dating and detailed analyses of active fault strikes and marine terraces. We find that the Tortonian-Pliocene stratigraphy in Kythira records ca. 100 m of subsidence, and a wide coastal rasa marks the ca. 2.8-2.4 Ma maximum transgression. Subsequent marine regression of ca. 300-400 m and minor E-W tilt are recorded in ca. 12 marine terrace levels for which we estimate uplift rates of ca. 0.2-0.4 mm/yr. Guided by simple landscape evolution models, we interpret the coastal morphology as the result of initial stability or of slow, gradual sea-level drop since ca. 2.8-2.4 Ma, followed by faster uplift since ca. 1.5-0.7 Ma. Our findings on- and offshore suggest that E-W extension is the dominant mode of regional active upper crustal deformation, and N-S normal faults accommodate most, if not all of the uplift on Kythira. We interpret the initiation of E-W extension as the result of a change in plate boundary conditions, in response to either propagation of the North Anatolian Fault, incipient collision with the African plate, mantle dynamics or a combination thereof.

HELMSTEDT AREA

1,561,181

THE HELMSTEDT LIGNITE MINING DISTRICT IN NORTHERN GERMANY - AN IMPORTANT ARCHIVE FOR THE PALEOGENE GREENHOUSE

O.K.Lenz, V.Wilde, W.Riegel and A.Mulch (Forschungsinstitut Senckenberg; Senckenberg Res Center). *21ST INTERNATIONAL SEDIMENTOLOGICAL CONGRESS [ISC] (Beijing, China, 8/22-26/2022) ABSTRACT BOOK* p.171, 2022. (Available at <http://www.isc2022.org.cn> as of 9/22/2022; Abstract only)

Long-term effects of present global warming on ecosystems on timescales beyond those covered by the human record are mostly a matter of speculation. However, the reaction of ecosystems to global warming on different timescales can be inferred from detailed studies of long-term greenhouse periods and short-term warming events repeatedly known from the geologic past. The Early Eocene Climatic Optimum (EECO) and its superposed short-term warming events such as the Paleocene-Eocene Thermal Maximum (PETM) represent the last greenhouse period before today. It is especially suited for comparisons to the presently developing greenhouse since fauna and flora already reached an evolutionary state similar to today. The Paleogene succession of the former Helmstedt Lignite Mining District in northern Germany is situated in an estuary at the southern edge of the proto-North Sea. It includes the late Paleocene to lower Eocene Schoeningen Formation and the middle Eocene Helmstedt Formation, thus uniquely covering the entire Paleogene greenhouse phase and its gentle demise. Due to the interaction between changes in sea level, salt withdrawal in the subsurface and climate-related changes in runoff from the hinterland the area was subject to frequent changes between marine and terrestrial conditions, repeatedly leading to peat formation. The more than 200 m thick succession with about 13 lignite seams of up to 15 m thickness offers the rare opportunity to study late Paleocene-middle Eocene near-coastal sedimentary systems and to trace the long-term changes and short-term perturbations of the climate on the diversity and composition of plant communities across 10 million years by using pollen and spores as proxies. Changes in vegetation concur with strong differences in petrologic composition of the lignite seams between the two formations, especially with regard to charcoal content. In the Schoeningen Formation fusain layers and dispersed fusain are common whereas the lignites of the Helmstedt Formation are nearly devoid of fusain. In both formations the lignite seams are separated by more or less marine interbeds in the lower part while they are associated mainly with fluvial sediments in the upper part. Bulk organic carbon isotopic data from the Schoeningen Formation show different negative carbon isotope excursions reflecting massive short-term carbon cycle perturbations, which can be related to long- and short-term hyperthermals of the early Eocene such as the EECO and the PETM. Palynological analysis proved that shifts in $\delta^{13}C_{TOC}$ values are correlated with changes in the peat forming wetland vegetation. Rapidly changing palynofloras at the PETM may be attributed to the thermal event.

HELVETIC NAPPE

1,561,182

4D RECONSTRUCTION OF THE DOLDENHORN NAPPE-BASEMENT SYSTEM IN THE AAR MASSIF: INSIGHTS INTO LATE-STAGE CONTINENT-CONTINENT COLLISION IN THE SWISS ALPS

F.Musso Piantelli, D.Mair, A.Berger, F.Schlunegger, M.Wiederkehr, E.Kurmann, R.Baumberger, A.Mori and M.Herwegh (Bern Univ). *TECTONOPHYSICS* v.843, 11/20/2022. (ISSN 0040-1951; Article no.229586)

The inversion of passive margins and their transportation into fold-and-thrust belts is a critical stage of mountain-building processes. In this study, we selected the Doldenhorn Nappe and Aar/Gastern Massifs (Central Swiss Alps) system as an ideal laboratory to document the impact of inherited structures, their along-strike variations, and basement tectonics on the evolution of a fold-and-thrust belt. Three-dimensional geological modelling and cross-section restoration allowed us to reconstruct the 4D evolution of the investigated area during the late-stage Alpine orogeny (30 to 0 Ma). Our results demonstrate that: (i) the Doldenhorn Nappe is the product of the inversion of an asymmetric half-graben basin; (ii) variations in incipient basin sediment thicknesses correlate directly with the along-strike variation of the deformation of the Doldenhorn Nappe; and (iii) the multiphase thick-skinned deformation that overprinted the Doldenhorn Nappe from 22 Ma until today changed the shape of the Doldenhorn Nappe and Aar/Gastern Massifs. This reconstruction shows how thin-skinned nappe formation mechanisms and the nappe geometries are controlled by the initial basement geometry and by the rheological strength contrasts between basement and cover sediments. Basement-involved uplift and shortening controls then the late-stage collisional 3D overprint and mechanics of the fold-and-thrust belts. (c2022 The Authors. Elsevier B.V.)

HIMALAYA MT AREA

1,561,183

A SULFUR-ISOTOPE RECORD OF LONG-TERM OCEANIC ANOXIA IN THE TOARCIAN AND POSSIBLE PROTRACTED CEASE OF GYPSUM DEPOSITION

Z.Han (Chengdu Univ Technology). *21ST INTERNATIONAL SEDIMENTOLOGICAL CONGRESS [ISC] (Beijing, China, 8/22-26/2022) ABSTRACT BOOK* p.179, 2022. (Available at <http://www.isc2022.org.cn> as of 9/22/2022; **Abstract only**)

The early Toarcian of the Early Jurassic saw a long-term positive carbon-isotope excursion (CIE) abruptly interrupted by a significant negative shift, associated with rapid global warming and an oceanic anoxic event (T-OAE, 183 Ma). However, the detailed processes and mechanisms behind ocean deoxygenation are unclear. Here, we present high-resolution carbonate-associated sulfate-sulfur isotope data ($\delta^{34}\text{SCAS}$), from the Tibetan Himalaya, spanning the Toarcian interval. The $\delta^{34}\text{SCAS}$ record shows a large positive shift from approximately +20‰ to approximately +40‰ which persists to nearly the end of the Toarcian. This confirms that the oceans were spatially heterogeneous with respect to their sulfate-sulfur isotope composition and suggests major pyrite burial associated with widespread development of anoxic/euxinic bottom waters during the early Toarcian. Box modelling results and sedimentary evidence suggest that large amounts of pyrite burial likely occurred in the near-equatorial deep-sea floor of the Panthalassa/Tethys. Additionally, the high-resolution $\delta^{34}\text{S}$ data presented here provide strong evidence for two major phases of the early Toarcian ocean deoxygenation and this process was likely terminated around the end of the T-OAE nCIE. Box modelling also indicates that the persistent positive $\delta^{34}\text{S}$ of seawater in the aftermath of the event was likely maintained by a long term downwards shift in the relative proportion of gypsum burial. This was likely driven by the forcing of seawater to below gypsum saturation point driven by a combination of massive evaporite burial of sulfate prior to the event and increased pyrite burial during it.

HONSHU ISLAND

1,561,184

DETRITAL ZIRCON U-Pb AGES OF THE MIOCENE CLASTIC SEDIMENTARY SUCCESSION IN THE SHIDARA BASIN, CENTRAL JAPAN: IMPLICATIONS FOR PROVENANCE CHANGES AND TIMING OF COLLISION BETWEEN THE IZU-OGASAWARA AND HONSHU ARCS

S.Yabuta, M.Takeuchi and Y.Asahara (Nagoya Univ). *JOURNAL OF ASIAN EARTH SCIENCES* v.241, Jan. 2023. (ISSN 1367-9120; Article no.105463)

Collision of the Izu-Ogasawara and Honshu arcs occurred during the Miocene. The Miocene Hokusetsu Subgroup in the western part of the Izu collision zone is considered to be a key formation that might record the timing of the initial collision. To clarify the timing, we conducted provenance analysis based on detrital zircon U-Pb ages of the Hokusetsu Subgroup. Zircon ages show a Late Cretaceous peak in the strata below the Umedaira Sandstone Member and a peak around 100 Ma in the lower Umedaira Sandstone Member. Furthermore, the proportions of Jurassic to Proterozoic ages increase in the upper part of the sandstone member and the overlying horizons. The zircon ages and the petrographical characteristics of detritus suggest that the formations below the lower Umedaira Sandstone Member were derived from the Ryoke Plutonic Rocks, but the formations above the upper Umedaira Sandstone Member were derived from a Jurassic accretionary complex. Deposition of the Umedaira Sandstone Member suggests uplift of the provenance areas, which are inferred to have been the 100 Ma Ryoke Plutonic Rocks to the northeast and east of the Shidara Basin and Jurassic accretionary complexes farther to the northeast and east. The provenance change during deposition of the Umedaira Sandstone Member was caused by collision of the Izu-Ogasawara and Honshu arcs. Therefore, the collision is considered to have begun around 17.4 ± 0.7 Ma constrained by depositional age of the Umedaira Sandstone Member. (c2022 Elsevier Ltd.)

HUANGHEKOU DEPRESSION

1,561,185

SEDIMENTARY CHARACTERISTICS AND ARCHITECTURE MODEL OF RIVER-DOMINATED SHALLOW WATER DELTA FRONT

Q.Wu, S.Wang, G.Sun, H.Yue and D.Zhao (Bohai Oilfield Res Inst). *21ST INTERNATIONAL SEDIMENTOLOGICAL CONGRESS [ISC] (Beijing, China, 8/22-26/2022) ABSTRACT BOOK* p.1569, 2022. (Available at <http://www.isc2022.org.cn> as of 9/22/2022; **Abstract only**)

Based on the comprehensive application of modern sedimentary, core, logging and dynamic data, the sequence stratigraphy and sedimentary characteristics of oilfield A in Huanghekou Sag are studied in detail, and the architecture model of distal fine-grained shallow water delta is established. The study shows that the lower Ming member of Neogene in A oilfield in the Huanghekou sag is divided into two complete third-order sequences and seven fourth-order sequences, that is, the bottom third-order sequences composed of IV and V oil groups are dominated by low-stand and transgression domains, and the top third-order sequences composed of I, II and III oil groups are dominated by low-stand and high-stand domains. Slow slope and far away from provenance are necessary conditions for the development of fine-grained shallow-water deltas. Fine sedimentary particle size, scale of sedimentary structure and small thickness of single genetic unit sand body are obvious sedimentary characteristics. The high frequency fluctuation of lake level controls the sedimentary model of distal fine-grained shallow water delta. Flake shallow water deltas are mostly developed in the lowstand period, with underwater distributary channel sand body as the main body, and channel migration and swing frequently. Dendritic shallow water deltas are developed in the early stage of transgression and highstand, and underwater distributary channels are striped and isolated. In the late high-level region, lobed shallow water deltas were developed, overbank deposits are mostly developed between single distributary channels and some distributary channels were transformed into bar and sheet sand by lake waves in the distal. The research results provide a basis for the exploration and development of shallow water delta in the Huanghekou Sag.

HUANGHUA DEPRESSION

1,561,186

ANALYSIS ON VOLCANIC DEVELOPMENT MODEL AND MAIN CONTROLLING FACTORS OF FAVORABLE RESERVOIR IN THE 3RD MEMBER OF SHAHEJIE FORMATION IN ZAOYUAN OILFIELD

L.Bao, Y.Liu, J.Hou and Z.Xia (China Univ Petroleum). *21ST INTERNATIONAL SEDIMENTOLOGICAL CONGRESS [ISC] (Beijing, China, 8/22-26/2022) ABSTRACT BOOK* p.332, 2022. (Available at <http://www.isc2022.org.cn> as of 9/22/2022; **Abstract only**)

The volcanic oil reservoir of the third member of the Shahejie Formation in the Zao35 fault block of Dagang Oilfield is located in the Cangdong Sag of the Huanghua Depression, Bohai Bay Basin. It is a fracture-porous dual medium oil reservoir. Based on well logging, and 3D seismic data, the characteristics of volcanic rock reservoirs, volcanic eruption patterns and volcanic eruption stages were studied, and the influence of different volcanic rock factors on reservoir distribution was explored, which provided the geological basis for subsequent development of volcanic rock reservoirs. The research results show that there are two development modes of volcanoes in this area, the fractured eruption with the Litanmu fault as the channel and the string beaded central eruption. The volcanic rocks are divided into 3 main eruption cycles based on the comprehensive seismic response characteristics. Combined with the stable mudstone intervals drilled by wells, the volcano can be further subdivided into 8 eruption stages. Affected by the two eruption modes and the distribution of fractures, the favorable reservoirs in the volcanic rock are distributed between the Litanmu fault and the central eruption channel. Lithology is also the main reason for controlling volcanic rock reservoirs in this area. Basalt is developed on a large scale in this area, so it is more likely to be communicated by fractures to form favorable reservoirs. In addition, due to the different eruption stages, there are 3 different basalt reservoir types in the overflow facies reservoirs in each stage, namely thick and tight basalt without pores, basalt with pores develop at the top and dense at the bottom, and basalts with pores developed at the top and tight in the middle, so the oil reserves are mostly distributed on the top and bottom of the thick basalt, among which the volcanic rock reservoirs of stage III4 and III5 have the greatest oil reserves and development potential.

HUBEI

1,561,187

A LATE EARLY TRIASSIC SHALLOW MARINE CONODONT COMMUNITY FROM THE YING'GOU SECTION OF THE NANZHANG-YUAN'AN FAUNA, HUBEI PROVINCE, SOUTH CHINA

K.Wu, Y.Zou, H.Li, S.Wan, L.Yang, I.Metcalf, Y.Cui, J.Li and L.Cheng (Hubei Geological Bureau). *5TH INTERNATIONAL CONODONT SYMPOSIUM [ICOS] (Wuhan, China and Online, 6/24-27/2022) PROGRAM AND ABSTRACTS* p.46, 2022. (**Abstract only**)

The largely stagnant marine ecosystem following the Permian-Triassic mass extinction (PTME) was superseded by the appearance of marine reptiles. One of the most abundant Early Triassic (Spathian) marine reptile faunas occurs in the Nanzhang-Yuan'an area of Hubei Province, South China, and provides remarkable information for understanding biotic recovery after the PTME. Situated on the north edge of the Middle Yangtze Platform in South China, the well-exposed Ying'gou stratigraphic succession in Yuan'an County represents one of the most productive sections yielding abundant marine reptiles. Intensive sampling of this section reveals a unique conodont community that belongs to a shallow marine facies. This conodont community consists of abundant Ellisoniidae characterized by ramiform P1 elements, and *Neostrachanognathus tahoensis* here reported from South China for the first time and characterized by coniform P1 elements. Foraminifers and fish found together with the conodont elements form other low-level parts of the local food web. Other temporally coincident sections nearby, for example, the Yanduhe section of western Hubei Province, yield only rare conodonts. The unique conodont community from the Ying'gou section suggests that the Nanzhang-Yuan'an area might be a "refuge area" for the Early Triassic marine ecosystem, or at least for the marine reptiles and the conodont communities.

HUNGARY

1,561,188

PALAEOECOLOGY OF BENTHIC MARINE COMMUNITIES IN THE WAKE OF THE LATE PERMIAN MASS EXTINCTION EVENT

W.J.Foster, R.J.Twitchett and S.Danise (Plymouth Univ; London Museum). *58TH ANNUAL PALAEONTOLOGICAL ASSOCIATION MEETING (Leeds, UK, 12/16-19/2014) ABSTRACTS* pp.26-27, 2014. (Available at <http://www.palass.org> as of 11/15/2022; **Abstract only**)

The Late Permian extinction event was the largest biotic crisis of the Phanerozoic and is associated with an extreme climate warming event. Here, we use multivariate analyses to investigate the temporal and environmental distribution of fossil benthic invertebrates from the Lower Triassic succession of the Aggtelek Karst, Hungary, which was deposited in a mixed siliciclastic-carbonate ramp setting on the northwestern margin of the Palaeotethys Ocean. There were no significant changes in α diversity or community structure through the Induan of the study site, and only minor differences with the Smithian. The Spathian communities, however, show significant increases in α diversity and the re-establishment of deep infaunal and erect tiers. Furthermore, the Spathian biofacies show a strict environmental control: siliciclastic inner ramp settings are characterized by low diversity assemblages whereas mixed carbonate-siliciclastic shoal to outer ramp settings show the greatest α diversity. Ecologically most of the Early Triassic assemblages were dominated by infaunal suspension feeders, apart from the mid-ramp setting during the Spathian which is characterised by slow-moving grazers. Our data, therefore, demonstrate the importance of the depositional environment in the restructuring of benthic communities following the late Permian mass extinction event.

IBERIAN MASSIF

1,561,189

OROGENIC REWORKING AND REACTIVATION IN CENTRAL IBERIA: A RECORD OF VARISCAN, PERMIAN AND ALPINE TECTONICS

D.Moreno-Martin, R.D.Fernandez, G.de Vicente, C.Fernandez and J.G.Barreiro (Madrid Complutense Univ; Inst Geol & Min Espana; Salamanca Univ). *TECTONOPHYSICS* v.843, 11/20/2022. (ISSN 0040-1951; Article no.229601)

Interference between orogenic systems and deformation phases within them may lead to reworking and reactivation of previous structures. The eastern sector of the Spanish-Portuguese Central System holds evidence of two orogenic systems, Variscan and Alpine, plus a stage of Permian extension. We perform an integrated structural analysis to identify reworking and reactivation processes throughout the geological record. The Variscan record starts with crustal thickening (D1; E-verging overturned folds). A second phase features the intra-orogenic collapse of an overthickened crust (D2; top-to-the-SE ductile extensional shear zone), which produced intense structural reworking at the core of the shear zone and moderate reworking at its hanging wall. During subsequent strike-slip tectonics, crustal thickening parted transpressional deformation into a dextral shear zone and upright folds (D3). Variscan deformation did not reactivate previous structures, but exploited a weak rheological boundary defined by contrasted lithologies (sedimentary versus igneous rocks) to accommodate D2 shearing. Reactivation played a role afterwards: Variscan strike-slip shear zone acted as a transfer fault to accommodate Permian extension (post-orogenic collapse), and then Alpine contraction. The Permian extension record is blurred by Alpine inversion, although the trend of Alpine structures in Central Iberia, and the Spanish-Portuguese Central System, may result from Permian structural inheritance. (c2022 The Authors. Elsevier B.V.)

ILLINOIS BASIN

1,561,190

TRACING ANOXIC EVENTS ACROSS MUD-DOMINATED EPICONTINENTAL SEAS DURING THE MIDDLE TO UPPER DEVONIAN IN THE ILLINOIS BASIN, NORTH AMERICA

M.N.Remirez, G.Gilleaudeau, C.H.Lau, M.Elrick and T.Algeo

(George Mason Univ; New Mexico Univ; Cincinnati Univ). *21ST INTERNATIONAL SEDIMENTOLOGICAL CONGRESS [ISC] (Beijing, China, 8/22-26/2022) ABSTRACT BOOK* p.201, 2022. (Available at <http://www.isc2022.org.cn> as of 9/22/2022; **Abstract only**)

Anoxic conditions in epicontinental water masses have been implicated as one of the key drivers for deposition of black shales in the geologic record. However, there are several mechanisms that can trigger anoxia, and distinguishing among them is a significant challenge for the reconstruction of depositional conditions in ancient mud-dominated systems. In this study, we reconstructed the general evolution of water mass conditions through deposition of the organic-rich Late Devonian New Albany Shale (NAS) in the Illinois Basin, USA. Through a detailed sedimentological and geochemical characterization of three cores, we establish a general sequence evolution of the NAS that we extrapolate to 50 wells across the basin using gamma ray logs. The three studied cores have been divided into three stages based on detrital proxies (Zr, Al), carbonate proxies (Ca), and redox-sensitive proxies (Mo, U). Moreover, each stage is characterized by a distinctive facies association arrangement. Our results suggest that deposition of the NAS occurred in three stages (two prograding, and one retrograding), characterized by the occurrence of four variably-related anoxic pulses. The first anoxic pulse was triggered by initial flooding of the basin at the base of a depositional sequence. The second anoxic pulse occurs in the middle of this prograding sequence and is likely related to the Lower Kellwasser Event based on scarce available biostratigraphy. The third anoxic pulse is related to basin flooding at the base of a second prograding sequence and can be confidently assigned to the Upper Kellwasser Event based on biostratigraphy and the presence of a positive carbon isotope excursion in organic matter. The fourth anoxic pulse occurs in a general retrogradational context when black shale deposition reached its maximum areal extent in the basin. This signal matches the expression of the global Hangenberg Event in the Williston Basin (North Dakota, USA), but further bio- and chemostratigraphic constraints are needed to confirm the placement of this event in the Illinois Basin. Overall, we find that anoxia in the epicontinental Illinois Basin was triggered by a variety of different mechanisms through deposition of the NAS. In some cases, anoxia is a local response to changes in relative sea level and, in other cases, basin anoxia is related to global anoxic events with no change in relative sea level. In some instances, however, these two mechanisms are related likely because anoxia in multiple epicontinental seas worldwide is triggered by the same eustatic forcings. We suggest that a similar approach may be useful in reconstructing the conditions that led to black shale deposition in other epicontinental seas of the geologic past.

INDIA

1,561,191

U-Pb ZIRCON GEOCHRONOLOGY OF A PYROCLASTIC ROCK FROM THE PARSOI FORMATION, MAHAKOSHAL GROUP: IMPLICATIONS TOWARDS AGE AND TECTONICS OF THE BASIN IN CENTRAL INDIAN TECTONIC ZONE

A.Sharma, K.Das, P.P.Chakraborty, F.Shiraishi and M.Kayama (Delhi Univ; Hiroshima Univ; Hiroshima Inst; Tokyo Univ). *GEOLOGICAL JOURNAL* v.57, no.10, pp.4122-4138, Oct. 2022. (ISSN 0072-1050; ISSN 1099-1034)

The Mahakoshal Group of rocks in the Central Indian Tectonic Zone (CITZ) holds the key to documenting the early events in the CITZ evolution and initiation of collision/accretion between the North and South Indian cratons (NIC, SIC). Centimetre to decimetre-thick conformable pyroclastic beds, sandwiched within the siltstone-argillite metasedimentary succession of the Parsoi Formation allows us to generate (i) a robust depositional age, which otherwise is bracketed based on basement and intrusive age, and (ii) track the earliest record of accretion at the plate margin of NIC. A magmatic origin for the inferred pyroclastic unit is established from petrographic signatures and, in particular, the CL response of quartz grains. The dominance of the Dauphine twin in fine-grained (ca.100 μ and <20 μ) quartz fraction implies sub-aquatic fast-cooling across the phase transition temperature (573°C) of quartz within the pyroclastic rock. A volcanic arc to syn-collisional granite affinity is suggested for the pyroclastic unit based on (i) dacitic to

ryholitic composition, (ii) LILE-enrichment, (iii) HFSE depletion, and (iv) enrichment of Th, U, and Pb. The 207Pb/206Pb 1894.3 \pm 9.4 Ma age of crystallization is estimated from the youngest and most prominent peak of near-concordant oscillatory zoned zircon grain with a high Th/U ratio. The age data is important in documenting the earliest accretion event at the plate margin in the collisional history of NIC and SIC.

INDIA

1,561,192

A FRESHWATER BIVALVE SUPERFAMILY DECCANOIDEA NOV., FROM THE SAURASHTRA DECCAN INTERTRAPPEAN, WESTERN INDIA: AN EXAMPLE OF VICARIANCE PALAEOBIOGEOGRAPHY

N.Shah and S.Patel (Maharaja Sayajirao Univ). *65TH ANNUAL PALAEOBIOGEOGRAPHICAL ASSOCIATION MEETING (Manchester, UK, 12/18-20/2021) PROGRAMME AND ABSTRACTS* p.92, 2021. (Available at <http://www.palass.org> as of 11/1/2022; **Abstract only**)

The Deccan large igneous province (DLIP) of India marks geological, biogeographical, climatic and extinction events on the rapidly migrating Indian plate over the Reunion hotspot across the Cretaceous-Palaeogene. The waning phase of the DLIP is characterized by intermittent lava flows emanating into fossiliferous intertrappean rocks, chiefly of the continental realm. The Saurashtra Peninsula, on the western part of the Indian plate, comprises thick, grey to rusty brown fossiliferous sandy/muddy shale studded with freshwater bivalve shells (mussels) of the order Unionida. These are fragile and disarticulated in preservation, mostly occurring as moulds or casts and occasionally calcified; the fissility of the shale obstructs their complete retrieval. High-resolution photography and X-radiography revealed various morphological features, which enabled specimens to be distinguished, suggesting new stocks of Unionida. A new superfamily-level category, Deccanoidea nov., is proposed; morphological and morphometric analysis led to further subdivision, which includes family Deccanoidea nov. and subfamilies Deccanoidea nov. (two genera, four species) and Chotiloidea nov. (one genus, three species). After the break-up from Gondwanaland and subsequent separation from Madagascar, the Indian plate exhibited island biogeography within a volcano-prone environment, which might have led to isolation-forced localized radiation in freshwater bivalves, suggesting evidence of vicariance palaeobiogeography.

INDIA

1,561,193

DETRITAL ZIRCON AGES AND Hf-ISOTOPE CHARACTERISTICS OF THE NEOPROTEROZOIC-CAMBRIAN MARWAR SUPERGROUP SEDIMENTS, NW INDIA: IMPLICATIONS ON THE EAST GONDWANA ASSEMBLY

M.K.Pandit and W.Wang (Rajasthan Univ). *21ST INTERNATIONAL SEDIMENTOLOGICAL CONGRESS [ISC] (Beijing, China, 8/22-26/2022) ABSTRACT BOOK* p.325, 2022. (Available at <http://www.isc2022.org.cn> as of 9/22/2022; **Abstract only**)

The Precambrian-Lower Paleozoic sedimentary successions in northwest India have been investigated to evaluate the assumption that they record the collision between Western and Eastern Gondwana continental blocks and contain detritus derived from the East African Orogen. The detrital zircon U-Pb age distribution patterns and Hf-isotopic characteristics of Marwar Supergroup (Pc-C transition) sedimentary rocks, together with paleocurrent analysis, suggest a proximal provenance within the Eastern Gondwana. The time equivalent successions from the Qiangtang terrane and the northern margin of Neoproterozoic India display similarity in the provenance record, along with additional input of late Mesoproterozoic and Neoproterozoic detritus from East Antarctic-Eastern India and Western Australia. Detritus from the uplifted East African Orogen are abundant in the north African sedimentary deposits, which constitute part of the Western Gondwana, but are absent in the equivalent successions in the Indian Eastern Gondwana. The consistency in sedimentary provenance of the late Neoproterozoic to early Palaeozoic strata in

NW India, combined with the lack of evidence for deformation/metamorphism since at least ca. 760 Ma, argues against collision between eastern and western segments of Gondwana in this northern domain of the supercontinent. These domains remained as passive continental margins, separated by a large-scale embayment of the proto-Tethys ocean, until the late Paleozoic fragmentation of the continental blocks.

IOWA

1,561,194

THE WINNESHIEK LAGERSTAETTE (MIDDLE ORDOVICIAN, DARRIWILLIAN) OF IOWA YIELDS THE OLDEST KNOWN EURYPTERIDS

J.C.Lamsdell, D.E.G.Briggs and H.P.Liu (Yale Univ; Iowa Univ). *58TH ANNUAL PALAEOONTOLOGICAL ASSOCIATION MEETING (Leeds, UK, 12/16-19/2014) ABSTRACTS* p.33, 2014. (Available at <http://www.palass.org> as of 11/15/2022; **Abstract only**)

The Winneshiek Lagerstaette, which occurs in the Decorah meteorite impact crater in northeast Iowa, has yielded a diverse fauna including conodont assemblages, early vertebrates, brachiopods, phyllocarids, and large eurypterids. The eurypterids are preserved as carbonaceous cuticle and probably represent exuviae. They are the oldest recorded members of the group, predating the previously known earliest occurrence by about eight million years. Preliminary study of approximately 300 specimens has revealed the presence of at least two species. The ornamentation of the large body segments of the more common species and the nature of fragments of cercal blades indicate an affinity with *Megalograptus*. The prosomal doublure and posterior appendages, however, more closely resemble those of Carcinosomatidae, suggesting that the species is a basal megalograptid or intermediate between the two groups. The second species appears related to *Orcanopterus*, another Ordovician predatory form known from Canada. These taxa are relatively derived within eurypterid phylogeny, and their presence in the Middle Ordovician hints at an explosive radiation earlier in the Ordovician or a cryptic Cambrian radiation. Early North American eurypterids appear to be limited to members of two clades and may represent successful immigrants from less well-sampled palaeobiogeographic regions.

IRAN

1,561,195

HIGH-RESOLUTION OF THE CHANGHSINGIAN SUCCESSION IN IRAN AND CORRELATION WITH CHINA

D.Korn, A.Ghaderi, L.Leda and M.Schobben (Berlin Museum; Ferdowsi Univ). *58TH ANNUAL PALAEOONTOLOGICAL ASSOCIATION MEETING (Leeds, UK, 12/16-19/2014) ABSTRACTS* p.32, 2014. (Available at <http://www.palass.org> as of 11/15/2022; **Abstract only**)

We investigated the Changhsingian Stage in six sections in the area of Julfa (Aras Valley) for their lithology (petrography and carbonate facies), geochemistry (stable isotopes), conodonts and ammonoids. Revision of the biostratigraphy led to the separation of ten Changhsingian conodont zones and eight ammonoid zones. This refined scheme serves as a basis for studies on the proximate causes of the end-Permian mass extinction. The detailed subdivision of the Changhsingian by means of ammonoids has some potential for the correlation of sections within the Tethyan realm. However, ammonoids have only rarely been used for the correlation of the Transcaucasian/Iranian with the Chinese sections, but nevertheless they played a role in discussions about the completeness or incompleteness of the central Tethyan sections. This resulted in the statement that the Iranian assemblages represent only the lower part of the Changhsingian. Correlation of the Late Permian ammonoid successions in Iran and China reveals major problems, which are rooted in the significant differences of the assemblages on the family level. The morphological differences demonstrate that, in terms of sutural development (notching of individual lobes), the Tethyan forms are even more advanced than the Chinese forms.

IVORY COAST

1,561,196

ARCHEAN TO PALEOPROTEROZOIC CRUSTAL EVOLUTION IN THE SASSANDRA-CAVALLY DOMAIN (COTE D'IVOIRE, WEST AFRICA): INSIGHTS FROM Hf AND U-Pb ZIRCON ANALYSES

A.Y.Koffi, N.Thebaud, A.N.Kouamelan, L.Baratoux, O.Bruguier, O.Vanderhaeghe, P.Pitra, A.I.Kemp and N.J.Evans (Houphouët-Boigny Univ). *PRECAMBRIAN RESEARCH* v.382, Nov. 2022. (ISSN 0301-9268; Article no.106875)

Crustal evolution in the south West African Craton is dominated by a significant input of juvenile material into the crust at ca. 2.1 Ga and it remains unclear how much of the Paleoproterozoic continental mass was influenced by the presence of pre-existing Archean crustal domains. The Sassandra-Cavally (SASCA, Cote d'Ivoire) domain is strategically located east of the Sassandra shear zone at the transition of the Paleoproterozoic and Archean terranes of the Leo-Man shield. Combined U-Pb and Lu-Hf isotopic analyses by LA-(MC-)ICP-MS were acquired on zircon grains extracted from migmatitic gneisses, metasedimentary rocks and a granitic intrusion. The migmatitic gneisses, yield Archean ages between ca. 3330 and 2810 Ma with δHf ranging from -9.4 to +3.3 and a metamorphic age at 2076 ± 6 Ma. They are tentatively interpreted as orthogneisses extracted from the mantle during the Paleoproterozoic and reworked substantially in the Mesoarchean. Detrital zircon grains from metasedimentary units adjacent to the Archean migmatitic gneisses yield ages ranging from ca. 2213 to 2088 Ma with δHf ranging from +0.0 to +5.5, indicating derivation from juvenile Paleoproterozoic source rocks. A granite intrusion was dated within uncertainty of the metamorphic age at 2084 ± 6 Ma. It exhibits a hybrid isotopic signature with δHf forming two distinct clusters between -4.9 and -8.5, and between +2.2 and +6.5 for inherited zircon grains dated between ca. 2343 to 2100 Ma. The near continuous U-Pb age record from this early Mesoarchean event to the Neoproterozoic is associated with constant initial $176Hf/177Hf$ suggesting for an ancient lead loss event at ca. 2800 Ma or a prolonged period of zircon dissolution/precipitation and/or crystallization. This early period is followed by peaks of zircon dates highlighting crustal extraction during the Eoeburnean (ca. 2250 to 2150 Ma) and Eburnean orogenies (ca. 2140 to 2100 Ma). The absence of detrital zircon of the ages similar to those of migmatitic gneisses (ca. 3200-2800 Ma) in Paleoproterozoic metasediments suggests their deposition distal from the Archean terranes followed by a tectonic assemblage of the SASCA domain during the later stages of the Eburnean orogeny. (c2022 Elsevier B.V.)

JAPAN

1,561,197

WIDESPREAD PALAEOBIOGEOGRAPHICAL SIGNALS OF THE SILURIAN ENCRINURID TRILOBITES OF JAPAN

C.P.Stocker, D.J.Siveter, P.D.Lane, M.Williams, T.Oji, T.Komatsu and G.Tanaka (Leicester Univ; Oxford Univ; Keele Univ). *65TH ANNUAL PALAEOONTOLOGICAL ASSOCIATION MEETING (Manchester, UK, 12/18-20/2021) PROGRAMME AND ABSTRACTS* p.94, 2021. (Available at <http://www.palass.org> as of 11/15/2022; **Abstract only**)

Encrinurid trilobites are geographically widespread in the Silurian strata of Japan, occurring in all three of its lower Palaeozoic terranes. Previous revisions of other Japanese trilobite groups have extended the palaeobiogeographical ranges of several taxa, but have not signalled a consistent palaeogeographical affinity. Here we present a revision of all previously described encrinurids from Japan (approximately 10 species). These show strong biogeographical links between all three Japanese terranes and with the Australian segment of East Gondwana, Indochina, and the North China palaeo-plate. They also show weaker biogeographical links with the South China palaeo-plate, Sibumasu, Laurentia, and possibly Baltica. These biogeographical signatures partly overlap those of illaenid and scutellid trilobites, but more broadly represent a pan-tropical signal that climate was a significant control on trilobite distribution.

JIYANG DEPRESSION

1,561,198

PORE EVOLUTION CHARACTERISTICS AND SHALE OIL ENRICHMENT MODEL OF SANDSTONE BEARING SHALE SERIES

X.We, S.Zhang and H.Liu (Sinopec Research Inst; Sinopec). *21ST INTERNATIONAL SEDIMENTOLOGICAL CONGRESS [ISC] (Beijing, China, 8/22-26/2022) ABSTRACT BOOK* p.275, 2022. (Available at <http://www.isc2022.org.cn> as of 9/22/2022; **Abstract only**)

In recent years, China has found huge shale oil resources in sandstone bearing shale series, which has greatly increased China's shale oil production. This kind of shale oil has attracted the attention of academic and industrial circles. We found shale series with the same characteristics in the north of Dongying Sag, Bohai Bay Basin, and analyzed its mineral composition, reservoir physical properties and oil characteristic. The result shows that this kind of lithofacies is mainly developed in the ancient steep slope area in Dongying sag. Although the sandstone layer is close to the organic-bearing or organic-rich shale, some sandstone layers didn't storage oil in a priority fashion. This is because the intergranular pore cementation in the diagenetic evolution process is earlier than the generation of oil. The shale series in the deep-water area is more rich in organic matter and clay mineral, the number of micropores and mesopores is greater than that of shallow water shale series. Sandstone provides limited porosity, so although more sandstone is developed in shallow water shale series, deep water shale series has higher porosity. However, sandstone significantly improves the permeability. Due to the development of more macropores, shallow water shale oil has high gas oil ratio and free hydrocarbon content. Therefore, the shale oil in shallow water shale series has higher fluidity than that in deep water shale series. On this basis, the pore evolution model and shale oil enrichment model of sandstone bearing shale in this area are proposed.

JIYANG DEPRESSION

1,561,199

DEEP STRUCTURAL CHARACTERISTICS AND FORMATION AND EVOLUTION OF DONGYING DEPRESSION

C.We and J.Yang. *21ST INTERNATIONAL SEDIMENTOLOGICAL CONGRESS [ISC] (Beijing, China, 8/22-26/2022) ABSTRACT BOOK* pp.326-327, 2022. (Available at <http://www.isc2022.org.cn> as of 9/22/2022; **Abstract only**)

The deep structure of Dongying depression has always been the research focus of many scholars. This paper mainly studies the deep structure of the fourth member of Shahejie formation from Kongdian formation to Shahejie Formation in Dongying depression, including the section style and plane style of deep structure. It is found that the structural styles are mostly extensional structural styles and extensional strike slip structural styles, such as "Y" shaped structure, flower like structure, warped fault block, graben Horst structure, salt mud diapir structure and so on. In addition, the distribution of regional tectonic belts and their horizontal and vertical differences in Dongying sag are also a research scope of this paper. Dongying depression is located in Jiyang depression of Bohai Bay basin. It has experienced the influence of multi-stage tectonic movement and plate movement, forming a unique structural pattern and multi-stage faults. With the evolution of the profile, combined with the large tectonic movement at that time, the tectonic evolution history can be reasonably deduced, and the key "red bed" strata in this study have experienced basin rifting expansion stage, regional uplift stage, secondary rifting stage and so on.

JIYANG DEPRESSION

1,561,200

PALEOCLIMATE EVOLUTION RECORDED BY THE PALEOCENE-EOCENE SALT-LAKE SEDIMENTS IN EASTERN CHINA AND ITS DRIVING MECHANISM

J.Wang (China Univ Petroleum). *21ST INTERNATIONAL SEDIMENTOLOGICAL CONGRESS [ISC] (Beijing, China, 8/22-26/2022) ABSTRACT BOOK* p.238, 2022. (Available at <http://www.isc2022.org.cn> as of 9/22/2022; **Abstract only**)

The Paleocene-Eocene with complex paleoclimate changes is a

key period for understanding the evolution of the Paleogene paleoclimate in East Asia. Previous studies focused on this period were mainly based on sedimentological data from Central and Western Asia, the sediments of the Dongying Depression in Eastern China provide a stratigraphic sequence of red-bed clastic rocks, gypsum-salt rocks and shallow-semi-deep lacustrine mudstones with abundant sporopollen fossils and stratigraphic data during the Paleocene-Eocene, which was a period highly sensitive to paleoclimate changes. Selecting the Kongdian Formation (Ek)-the third member of the Shahejie Formation (Es3) of the Dongying Depression as the study object, the evolutionary characteristics and the Driving Mechanism of the Paleocene-Eocene climate are investigated by a comprehensive analysis of sedimentological data, geochemical indicators, paleontological data and Milankovitch cycle analysis. The results indicate that the paleoclimate evolution during the period of the Ek-Es3 member in the Dongying Depression can be divided into eight stages, in which the trends of paleoclimate change in stages 1-4 were similar to those in Central and Western China. The paleoclimate reached the hottest period in the Cenozoic after warming and drying during the first stage, and then showed a long-term drying and cooling trend with the Middle Eocene Climate Optimum (MECO) in the fourth stage. Affected by the uplift of the Tibetan Plateau and the regression of the Tarim Sea, the trends in stages 5-8 are clearly distinct from those in Central and Western China. In the fifth stage, although the paleoclimate in the study area was dry during stage 5, the paleoclimate in eastern East Asia began to evolve towards humid condition. In the sixth stage, the paleoclimate in the study area became oscillatory humid, and the latitudinal zonal paleoclimate pattern started to fall apart. The paleoclimate pattern changed from latitudinal zonation to east/humid and west/arid during stages 7-8, suggesting that the East Asian summer monsoon became prevalent and dominated the climate in eastern China from that time. Based on the investigation of Paleocene-Eocene global atmospheric evolution and tectonic activities, and the analysis of sedimentary cycles at different scales, it is found that the driving mechanism for the paleoclimate evolution in the study area can be divided into two categories. The dominant mode of eccentricity under the background of planetary wind system during the 1-6 stages and the short eccentricity and precession control mode under the background of East Asian monsoon during the 7-8 stages. The paleoclimate is relatively dry and mainly controlled by the planetary wind system during stages 1-6, and the climatic characteristics reflected by meter scale sedimentary cycle is mainly driven by the eccentricity cycle.

KARANJ OIL FIELD

1,561,201

ADSORPTION BEHAVIOUR OF KARANJ OIL SURFACTANT - ROLE OF DIFFERENT ADSORBENT SURFACES

H.Kesarwani and S.Sharma (Rajiv Gandhi Inst Technol). *83RD ANNUAL EAGE CONFERENCE (Online and Madrid, Spain, 6/6-9/2022) ABSTRACTS* 2022. (Abstract no.619; Available at <http://www.earthdoc.org> as of 7/7/2022; 5 pp; **Abstract only**)

The present work focuses on the behavioral analysis of the Karanj oil surfactant (KOS) on different adsorbent surfaces (sand, bentonite shale, carbonate). Adsorption experiments were performed to evaluate the amount of KOS loss on the rock surfaces. Highest amount of surfactant loss of 44.85 mg/g was observed for carbonate surface whereas KOS was proved to be the most efficient for sand particle surface with a minimum of 3.78 mg/g of surfactant losses. However, due to the complex charge distribution and layered structure, greater loss was obtained for shale. The results elucidate that the Coulombic force of attraction plays a major role when two oppositively charged entities are involved. Moreover, surface area available for adsorption also plays a key role in quantifying the amount of surfactant loss. Based on the higher adsorption losses, it can be concluded that the KOS would effectively perform for sandstone reservoir whereas for carbonate reservoir some additives would be required to cut down the adsorption losses.

KARROO BASIN

1,561,202

NETWORK-BASED BIOSTRATIGRAPHY FOR THE LATE PERMIAN TO MID-TRIASSIC BEAUFORT GROUP (KAROO SUPERGROUP) IN SOUTH AFRICA ENHANCES BIOZONE APPLICABILITY AND STRATIGRAPHIC CORRELATION

P.A.Viglietti, A.Rojas, M.Rosvall, B.Klimes and K.D.Angielczyk (Field Museum (Chicago); Umea Univ; Roosevelt Univ). *PALAEONTOLOGY* v.65, pt.5, Sept./Oct. 2022. (ISSN 0031-0239; ISSN 1475-4983; Article no.e12622)

The Permo-Triassic vertebrate assemblage zones (AZs) of South Africa's Karoo Basin are a standard for local and global correlations. However, temporal, geographical and methodological limitations challenge the AZs reliability. We analyze a unique fossil dataset comprising 1408 occurrences of 115 species grouped into 19 stratigraphic bin intervals from the *Cistecephalus*, *Daptocephalus*, *Lystrosaurus declivis* and *Cynognathus* AZs. Using network science tools we compare six frameworks: Broom, Rubidge, Viglietti, Member, Formation, and one suggesting diachroneity of the *Daptocephalus*/*Lystrosaurus* AZ boundary (Gastaldo). Our results demonstrate that historical frameworks (Broom, Rubidge) still identify the Karoo AZs. No scheme supports the *Cistecephalus* AZ, and it probably comprises two discrete communities. The *Lystrosaurus declivis* AZ is traced across all frameworks, despite many shared species with the underlying *Daptocephalus* AZ, suggesting that the extinction event across this interval is not a statistical artefact. A community shift at the upper Katberg to lower Burgersdorp formations may indicate a depositional hiatus which has important implications for regional correlations, and Mesozoic ecosystem evolution. The Gastaldo model still identifies a *Lystrosaurus* and *Daptocephalus* AZ community shift, does not significantly improve recent AZ models (Viglietti), and highlights important issues with some AZ studies. Localized bed-scale lithostratigraphy (sandstone datums), and singleton fossils cannot be used to reject the patterns shown by hundreds of fossils, and regional chronostratigraphic markers of the Karoo foreland basin. Metre-level occurrence data suggests that 20-50 m sampling intervals capture Karoo AZs, unifying the use of metre-level placements of singleton fossils to delineate biozone boundaries and make regional correlations.

KERKENNAH PLATEAU AREA

1,561,203

MILANKOVITCH CYCLES TO DETECT THE RELATION BETWEEN THE ABUNDANCE OF NUMMULITES AND THE MIDDLE EOCENE PEAK WARMING: CYCLOSTRATIGRAPHY OF THE CARBONATE OIL RESERVOIR, SIOUF MEMBER, IN CENTRAL TUNISIA

J.Haj Messaoud (King Abdullah Univ). *21ST INTERNATIONAL SEDIMENTOLOGICAL CONGRESS [ISC] (Beijing, China, 8/22-26/2022) ABSTRACT BOOK* pp.169-170, 2022. (Available at <http://www.isc2022.org.cn> as of 9/22/2022; **Abstract only**)

The middle Eocene witnessed several episodes of rapid warming, leading to changes in the sedimentary facies and microfossils content. These changes culminated during the Middle Eocene Climatic Optimum (MECO), an episode of global warming that led to the widespread deposition of nummulitic limestone of the Reneiche/Siouf member (Mb.) in central and NE Tunisia. The Siouf Mb. is a lateral equivalent to the Reneiche Mb., both are the leading oil reservoirs in central Tunisia, Kerkennah, and the Gulf of Gabes. This early Bartonian nummulitic limestone member has yielded exceedingly well-developed oil reservoir properties. However, the potential links between the occurrences of these exceptionally developed nummulites and the MECO remain poorly investigated. We have used a multi-proxy approach (Sedimentology, biostratigraphy, stable isotopes, and cyclostratigraphy) to place our findings in a well-defined temporal context. We constrain the factors that led to the fast change toward a short-lived nummulitic limestone shelf. The MECO interval is unambiguously identified here at the Reneiche/Siouf Mb. by the biostratigraphic age (lower SBZ17 and E12) and a 3‰ negative $\delta^{18}O$ excursion in the shallow-water carbonate platform. We interpret the coincidence between the MECO and the Reneiche/Siouf Mb. as an indication for a link between the re-appearance of nummulites and the intense warming

event. Nummulites appear in low abundance during the Lower Reneiche Limestone unit (LRL, Bey et al., 2015) from 40.52 to 40.18 Ma, then show transient increase reaching maximum abundance at the Upper Reneiche Limestone unit (URL, 40.11 to 40 Ma). Our data show that the abundance peak of nummulites and the negative values of $\delta^{18}O$ in the URL post-dated the Middle Eocene third-order maximum flooding surface by 350 kyr, took place during the MECO peak warming from 40.07 to 40 Ma. Our results indicate that the development of the nummulitic limestone oil reservoir is directly related to the onset of the MECO warming event rather than to the sea level. Mesotrophic environment and arid to semi-arid climate during the MECO with a correspondingly high eustatic sea level favored the deposition of the Siouf/Reneiche Mb. in central and NE Tunisia from 40.54 Ma to 39.8 Ma.

KNIPOVICH RIDGE

1,561,204

CRUSTAL AND THERMAL HETEROGENEITIES ACROSS THE FRAM STRAIT AND THE SVALBARD MARGIN

M.A.Dumais, L.Gernigon, O.Olesen, A.Lim, S.E.Johansen and M.Bronner (Norwegian Univ Sci Technol; Norway Geological Survey). *TECTONICS* v.41, no.10, Oct. 2022. (ISSN 0278-7407; ISSN 1944-9194; Article no.e2022TC007302)

The lithospheric structure of the Fram Strait and the extent from the Knipovich Ridge to the Barents Sea shelf and Svalbard are poorly understood. Several multi-geophysical investigations from various campaigns since the 90s along the Western Barents Sea margin and the Northeast Greenland margin resulted in insufficient and contradicting interpretations of the crustal and upper mantle settings in the oceanic and continental domains. New airborne magnetic data across the Knipovich Ridge and west of Svalbard provide new insights, reveal the complexity of the seafloor spreading history of the Arctic Atlantic Ocean, and indicate a European-Eurasian continent-ocean boundary located ca. 150 km farther west than previously suggested. This new location of the continent-ocean boundary prompted to revise the existing 2-D seismic interpretations in terms of crustal domains and tectono-stratigraphic setting. This is tested using joint 2-D gravity and magnetic field modeling to derive an improved crust-mantle model of the study. One recently acquired combined 2-D controlled source electromagnetic/magneto-telluric (CSEM/MT) profile across the Mohs Ridge was also modeled with potential field data and provided new insights into the tectonic settings of the crust and the mantle thermal anomalies. This study proposes to unify the various seismic and CSEM/MT interpretations using the new aeromagnetic compilation.

KONGDIAN FM

1,561,205

CHARACTERISTICS AND DISTRIBUTION LAW OF THE LITHOFACIES ASSEMBLAGES OF FINE-GRAINED SEDIMENTARY ROCKS IN THE EK2 IN THE CANGDONG SAG, BOHAI BAY BASIN, EASTERN CHINA

N.Ji and S.Chen (China Univ Petroleum). *21ST INTERNATIONAL SEDIMENTOLOGICAL CONGRESS [ISC] (Beijing, China, 8/22-26/2022) ABSTRACT BOOK* p.281, 2022. (Available at <http://www.isc2022.org.cn> as of 9/22/2022; **Abstract only**)

The thick fine-grained sedimentary rocks in the second member of the Kongdian Formation (Ek(2)) in the Cangdong sag, Bohai Bay Basin, eastern China, are typical lacustrine source rocks and have recently been regarded as the main target for shale oil exploration. Fine-grained sedimentary rock with strong heterogeneity and poor plane continuity, is the basis for the accumulation of shale oil and gas. Therefore, it is of great significance to strengthen the study of lithology, lithofacies and lithofacies assemblages of fine-grained sedimentary rocks. Based on the observation and description of cores from Well G108-8, Well GD12, and Well GD14, combined with analysis of thin sections and X-ray diffraction data, lithofacies of the Ek(2) fine-grained sedimentary rocks can be divided into six types, including laminated felsic fine-grained sedimentary facies according to mineral compositions and sedimentary structures, massive felsic fine-grained sedimentary rocks, laminated mixed fine-grained sedimentary rocks, massive mixed fine-grained sedimentary rocks, laminated carbonate fine-grained rocks, and

massive carbonate fine-grained sedimentary rocks. Due to the vertical frequent alternation of lithofacies, lithofacies assemblages are proposed to describe the distribution law of the Ek(2) fine-grained sedimentary rocks, which can be named felsic lithofacies assemblages, felsic bedded with carbonate lithofacies assemblages, mixed lithofacies assemblages, carbonate bedded with felsic lithofacies assemblages, and carbonate lithofacies assemblages. The mineral compositions, sedimentary structures, and containing lithofacies types show significant differential among these lithofacies assemblages, which can be consisted with the evolution of sedimentary environment. The method of combining the acoustic travel time (AC) log and density log is established to identify lithofacies assemblages in the study area, which can be used to study the distribution law. Lithofacies assemblages transformed from mixed to felsic bedded with carbonate in the lower part of the Ek(2)1, while from felsic to carbonate in the upper part of the Ek(2)1. From the margin to center of the lacustrine basin, lithofacies assemblages have two trends during the sedimentary period of Ek(2)1. Lithofacies assemblages present felsic, felsic bedded with carbonate, and mixed from the margin to center with the humid climate and strong detrital input. Furthermore, lithofacies assemblages present mixed, carbonate bedded with felsic, and carbonate from the margin to center with the arid climate and weak detrital input.

KUCHE BASIN

1,561,206

COMPOSITIONAL ZONING IN CALCITE CEMENTS RECORDS TRANSGRESSIONS: CRETACEOUS TERRESTRIAL SANDSTONES, KUQA DEPRESSION, NW CHINA

Z.Li, J.Wang, Y.Cao, T.Mo, W.Zhu and S.Wang (China Univ Petroleum; Tarim Oilfield Co). *21ST INTERNATIONAL SEDIMENTOLOGICAL CONGRESS [ISC] (Beijing, China, 8/22-26/2022) ABSTRACT BOOK* p.282, 2022. (Available at <http://www.isc2022.org.cn> as of 9/22/2022; **Abstract only**)

Concentric compositional zones of early calcite cements can reflect changes in fluid properties and are further indicative of changes in sedimentary environments. Concentric compositional zoning revealed by cathodoluminescence is common in early non-ferroan calcite cements in Cretaceous sandstones of the Kelasu thrust belt within the Kuqa Depression. Optical microscopy, cathodoluminescence (CL), LA-ICP-MS and stable-isotope analysis were used to investigate the petrographic and chemical characteristics of these calcite cements. In cathodoluminescence, the zoned cements consist of alternating brightly luminescent zones and non-luminescent zones. Concentrations of Fe²⁺ are both low in non-luminescent and brightly luminescent zones (< 200 ppm). Mn²⁺ Concentrations in brightly luminescent zones (880 ca. 3020 ppm) are higher than Non-luminescent (< 620 ppm). Non-luminescent zones show negative $\delta^{13}\text{C}$, while brightly luminescent zones show positive $\delta^{13}\text{C}$. These data imply that non-luminescent zones precipitated in oxidizing diagenetic environments, and brightly luminescent zones precipitated in reductive environments. The $\delta^{13}\text{C}$ values of non-ferroan calcite cements range between -4.8 per mill and 0.8 per mill PDB, while the $\delta^{18}\text{O}$ values are between -14.9 per mill and -6.6 per mill PDB, which is interpreted to indicate precipitation from meteoric water. Kuqa Depression experienced multiple transgression-regression of Tethyan seawater from the Early Paleocene to Late Eocene. During transgression, seawater inundated the unconformity and prevented meteoric water from recharging the Cretaceous sandstone aquifer, causing the pore waters to tend to stagnate and become more reductive, and resulting the brightly luminescent zones to precipitate. During regression, oxygen-rich meteoric water from the Southern Tien Shan dissolved the surface-deposited carbonates and continuously recharged the sandstone aquifer along the unconformity, and causing non-luminescent zones to precipitate. Thus, a cycle from brightly luminescent zone to non-luminescent zone records once transgression-regression (The last cycle only includes a brightly luminescent zone). Four zoning cycles can be observed in Cretaceous sandstones of Dabe 12 well, which indicates that transgression may have occurred four times in this area. Three zoning cycles can be observed in Cretaceous sandstones of Bozi 9 well, implying that transgression may have happened three times

in this area. Two zoning cycle can be identified in Cretaceous sandstones of Keshen 10 well, so this region may have experienced twice transgression.

KUNSAN BASIN

1,561,207

DEVELOPMENT OF REGIONAL UPLIFT AND UPLIFT-RELATED STRATA IN GUNSAN BASIN, YELLOW SEA: IMPLICATIONS FOR CENOZOIC CRUSTAL EXTENSION

C.Lee, Y.J.Shinn and I.C.Ryu (Kyungpook National Univ; Korea Inst Geosci Min Rscs). *INTERNATIONAL GEOLOGY REVIEW* v.58, no.16, pp.2029-2045, 2016. (ISSN 0020-6814; ISSN 1938-2839)

The Mesozoic-Cenozoic Gunsan Basin is the northeastern part of the Northern South Yellow Sea Basin between eastern China and the Korean Peninsula. On the basis of seismic interpretation, this study presents and interprets geologic features of regionally uplifted structures, the Haema Arch, located in the central western part of the basin. The Haema Arch is defined as dome-shaped uplift complexes, 95 km long and 60 km wide. It is characterized by prominent basement uplifts along its margin and plunging syncline inside the arch. The marginal large-scale uplifts are bounded by outward-dipping faults. The uplift-related strata are identified on the hanging wall block of the bounding faults and within the Haema Arch, which can be divided into pre-, syn-, and post-uplift units. The pre-uplift unit rests on the acoustic basement and shows an upturned stratal pattern near the marginal large-scale uplift. The syn-uplift unit locally occurs on the hanging wall block of the bounding faults along the northern and southern margins. The uplift of the Haema Arch and its coeval fault-controlled subsidence possibly occurred during the late Oligocene. The post-uplift unit initially formed on remnant topographic lows during the early Miocene and subsequently covered the overall area of the Haema Arch and the Gunsan Basin. The late Oligocene uplifting of the Haema Arch can be interpreted as an isostatic response to tectonic unloading by the arch-bounding faults that possibly extend to detachment faults. We suggest that the Gunsan Basin underwent crustal thinning and extensional deformation during the late Oligocene, which accounts for the coeval uplifting and fault-controlled subsidence in the study area.

KUNYANG GR

1,561,208

NEOPROTEROZOIC GEODYNAMICS OF SOUTH CHINA AND IMPLICATIONS ON THE RODINIA CONFIGURATION: THE KUNYANG GROUP REVISITED

L.Sun and W.Wang (China Univ Geosci, Wuhan). *21ST INTERNATIONAL SEDIMENTOLOGICAL CONGRESS [ISC] (Beijing, China, 8/22-26/2022) ABSTRACT BOOK* p.291, 2022. (Available at <http://www.isc2022.org.cn> as of 9/22/2022; **Abstract only**)

The late Mesoproterozoic to early Neoproterozoic strata in the Yangtze Block hold a key position in deciphering the tectonic evolution of the South China Block and implicate upon the reconstruction of the Rodinia supercontinent. The sedimentological, geochronologic, and geochemical data on the Kunyang Group, southwestern Yangtze Block, were evaluated for a better understanding of the regional geodynamics and refinement in its paleo-position in the Rodinia supercontinent. Our findings constrain the deposition of the Kunyang Group sediments occurring during 1152 Ma and 1000 Ma, under a stable environment with alternating neritic and littoral facies sedimentation. In contrast, deposition of the Meidang Formation, traditionally thought to represent the upper part of the Kunyang Group, continued up to 866 Ma in an active setting at varying basin depths and hydrodynamic conditions. Moderate to high SiO₂ contents (57.7-95.4 wt%), highly variable K₂O/Na₂O ratios (0.01-55.8), and critical trace element abundances (Zr: 57.6-578 ppm, Th: 1.95-28.3 ppm, Sc: 0.75-24.3 ppm), detrital zircon age distribution, sedimentological characteristics, and bimodal magmatism cumulatively underline a transition from continental rift to passive continental margin setting, followed by an active continental margin setting. The onset of oceanic subduction below the SW-NW margin of the Yangtze Block caused a hiatus in sedimentation, marked by an unconformity between the Kunyang Group and Meidang Formation. Paleocurrent data, zircon U-Pb ages, and Lu-

Hf isotopic characteristics indicate that the Kunyang Group received detritus from some interior sources and exotic terranes, such as the Gawler Craton in Australia, the Transantarctic Mountains in East Antarctica, and the Ongole domain in the Eastern Dharwar Craton of India. The Yangtze Block was likely located to the west of Australia and East Antarctica and north of India in the Rodinia supercontinent. Paleocurrent data also confirm an external location for the Yangtze Block in the Rodinia paleogeographic configuration.

LIAOHE BASIN

1,561,209

CENOZOIC INTERMEDIATE AND MAFIC IGNEOUS ROCKS IN THE EASTERN SAG OF LIAOHE DEPRESSION - LITHOLOGY, LITHOFACIES AND CONTROLLING FACTORS OF RESERVOIRS

B.Zhang (PetroChina Research Inst). *21ST INTERNATIONAL SEDIMENTOLOGICAL CONGRESS [ISC] (Beijing, China, 8/22-26/2022) ABSTRACT BOOK* p.335, 2022. (Available at <http://www.isc2022.org.cn> as of 9/22/2022; **Abstract only**)

On the basis of 110 wells with 1100 meters drilling cores and 500 wells with 107000 meters long sections of igneous rocks in the Eastern sag of Liaohe Depression, lithologic and lithofacies of the Cenozoic intermediate and mafic igneous rocks and controlling factors of reservoirs were studied by means of description and slice identification of cores, reservoirs physical property data and oil reservoirs analysis. Based on these data, 16 types of volcanic, intrusive rocks and volcanic sedimentary rocks are recognized, basaltic lava and basaltic volcanoclastic rocks have the greatest thickness and the most widely distributed 91%. The volcanic lithofacies are mainly divided into 6 lithofacies and 16 subfacies during which Effusive lithofacies accounts for about 63%. The reservoirs space can be grouped into 4 types and 9 sub-types, secondary porosity and fracture are most developed in the study area. Trachytic lava and Trachytic volcanoclastic rocks, basaltic volcanoclastic rocks, extrusive dome facies, volcanic conduit facies and explosive facies are the most favorable reservoirs. Three factors including Lithology, lithofacies and faults are thought related to the porosity and permeability of igneous rocks reservoirs. Lithology determines types and microscopic characteristics of reservoirs; lithofacies controls the development of primary pores and distribution of reservoirs; faults control the range of igneous rocks, position of vent lithofacies and proximal lithofacies, and effectiveness of reservoirs. The areas of favorable petroleum accumulation are near oil sources, structural highs adjacent to faults, and advantage of lithology and lithofacies.

LIAONING

1,561,210

DETRITAL ZIRCON U-Pb AGE CHARACTERISTICS OF THE CAMBRIAN JIACHANG FORMATION IN EASTERN LIAONING, NORTH CHINA CRATON AND ITS GEOLOGICAL SIGNIFICANCE

Z.Wu, L.Qiu, C.Lu and H.Wang (China Univ Petroleum). *21ST INTERNATIONAL SEDIMENTOLOGICAL CONGRESS [ISC] (Beijing, China, 8/22-26/2022) ABSTRACT BOOK* p.289, 2022. (Available at <http://www.isc2022.org.cn> as of 9/22/2022; **Abstract only**)

The Jichang Formation (F) in eastern Liaoning is mainly distributed in Benxi area and Dalian. The Jichang F. overlies the Kangjia F. or Qiaotou F. of the Late Mesoproterozoic-Early Neoproterozoic, in Benxi, and a layer of sandstone with a thickness of nearly 2 m developed at the bottom, which is obviously different from the Dalian area. Scholars have mostly explored the relationship between the NCC and the two supercontinents, Rodinia and Gondwana, by analyzing the detrital zircon ages in the Precambrian strata of the NCC. In order to find more information, we collected sandstone samples from the sandstone at the bottom of the Jichang F., which had never been studied before, and carried out a zircon LA-ICP-MS U-Pb chronology study. The dating results show that the detrital zircon ages in the sandstone of the Jichang F. have 5 peaks of 2490 Ma, 2145 Ma, 1824 Ma, 1178 Ma and 517 Ma. It is worth noting that the above-mentioned age peaks greater than 1000 Ma have been reported in the Xihe Group strata in the eastern Liaoning (Zhang et al., 2020; Zhao, 2020), indicating that

many parts of the Precambrian zircon in the sandstone in the Jichang F. should have inherited the Xihe Group. These zircon ages are interpreted as being partly from the North China Craton itself, and other part comes from cratons such as Laurentia, Siberia, Baltica, Sao Fransico, etc (Zhao et al., 2020; Wang et al., 2021). The age of the youngest zircon is 513.4 ± 12.9 Ma, which limits the lower limit of the deposition of the Jianhang F., and its age is determined at Stage 4 of the Cambrian Second Series. At the same time, it also shows that the NCC had the mixing of new biological sources close to the age of stratigraphic deposition in the Cambrian. Some scholars have suggested that there may be at least two periods of magmatic activity at 520 Ma and 430 Ma in the deep part of the NCC, and 520 Ma coincides with the aggregation peak of the Gondwana supercontinent. Therefore, we speculate that the age peak of 517 Ma found in the Jiachang F. indicates a key node in the Early Paleozoic evolution of the NCC, probably related to a global tectonic event controlled by its deep processes. In addition, the age of 700-1000 Ma is not found in the detrital zircon ages of the Jiancahg F., but these ages have been found in the Jinxian Group and Early Cambrian strata in the Dalian area. Therefore, after the deposition of the Xihe Group and before the second Cambrian, the Benxi area began to expose the surface and did not accept deposition, while the Jinxian Group and the Early Cambrian strata were deposited in the Dalian area. Therefore, the magmatism during this period may not have affected the Benxi area, resulting in the sandstone provenance of the Jiachang F. have no such information.

LONGZHONG BASIN

1,561,211

TERRESTRIAL CARBONATE OXYGEN ISOTOPES CONSTRAINTS ON THE INTERPLAY BETWEEN WESTERLIES AND MONSOONAL RAINS MODULATING THE CENOZOIC CLIMATE ON THE NORTHEASTERN TIBETAN PLATEAU

Y.Yang, X.Fang, W.Han, Y.Wang and A.Galy (Chinese Academy Sciences; Linyi Univ; Lorraine Univ). *PALAEOGEOGRAPHY, PALAEOCLIMATOLOGY, PALAEOECOLOGY* v.608, 12/15/2022. (ISSN 0031-0182; Article no.111289)

The relative contribution of the westerlies and the Asian monsoon has played a critical role in regulating the evolution of the Cenozoic Asian interior environment in response to regional tectonic uplift and global climate change. Here, we reconstruct a long-term record of atmospheric moisture oxygen isotopes in the Asian interior using the oxygen isotopic composition of authigenic carbonates in terrestrial sediments from the Xining Basin on the northeastern Tibetan Plateau spanning the last 52 Myrs. On the VPDB scale, the average carbonate $\delta^{18}\text{O}$ is characterised by a long-term decrease from -1.5‰ at ca. 43 Ma to -7.5‰ at 33 Ma and smaller variations from -7‰ to -8.5‰ after 33 Ma, with the exception of one period that contains samples with higher $\delta^{18}\text{O}$ values at -6‰ at 17–14 Ma. At the same time, there is a corresponding long-term rise in average carbon isotope $\delta^{13}\text{C}$ values from -9.5‰ at ca. 43 Ma to -3.5‰ at 33 Ma, followed by a less variable but similar variation in $\delta^{18}\text{O}$ values after 33 Ma. The oxygen and carbonate isotopic compositions are negatively correlated before 33 Ma and positively after, suggesting a transition at ca 33 Ma in the context of atmospheric circulation coupled with regional aridity. The $\delta^{18}\text{O}$ record can be explained by a simple binary mixing model of the atmospheric moisture between the recycling moisture with a positive $\delta^{18}\text{O}$ value in the westerlies-dominated region and the monsoon rainfall or related moisture with a negative $\delta^{18}\text{O}$ value from the Indo-Pacific Ocean. In that case, the first-order carbonate $\delta^{18}\text{O}$ decrease from ca. 43 Ma to 33 Ma was primarily controlled by the retreat of the Para-Tethys Sea, which induced a remarkable decline in westerly rainfall relative to the monsoon. After ca 33 Ma, the contribution from the westerlies could be constant and the lower limits of the carbonate $\delta^{18}\text{O}$ values are modelled by episodic increases in monsoon rainfall corresponding to enhanced Asian monsoon periods at 26–24 Ma, 17–14 Ma, and 9–8 Ma induced by the tectonic uplift of the Tibetan Plateau and the global climate. Our study, also, suggests that the Oligocene was a transitional stage of moisture sources from the dominance of Eocene westerlies to the Miocene-Quaternary monsoon in continental Asian environments. (c2022 Elsevier B.V.)

LOWER CONGO BASIN

1,561,212

THE LATE CRETACEOUS-MIOCENE SUPRA-SALT STRUCTURES IN BLOCK M, LOWER CONGO BASIN (CONGO, WEST AFRICA) AND THE CONTROLS ON CHANNEL DEVELOPMENT

C.Liang, W.Ding, Y.Liu and M.Li (China Univ Geosci, Beijing; Res Inst Petrol Explor Dev). *GEOLOGICAL JOURNAL* v.57, no.10, pp.4167-4182, Oct. 2022. (ISSN 0072-1050; ISSN 1099-1034)

The Lower Congo Basin is a typical passive continental margin basin of West Africa and is currently the focus and hot spot of deep-sea oil and gas exploration. Previous studies have focused on the deformation process and mechanism of the salt rock itself, but have ignored the interaction process between the faults and salt diapirs. The direct influence of the interaction process between the faults and salt diapirs on oil and gas exploration is reflected in the control of the reservoir distribution. In recent years, most of the oil and gas discovered in the Lower Congo Basin have been concentrated in the Oligocene–Miocene turbidite reservoirs, and the distribution of channel sand bodies is largely affected by supra-salt tectonic activity. In this study, Block M in the Lower Congo Basin was selected for study. Based on the 3D seismic, drilling, and logging data, the typical structural styles and stress mechanisms were analysed. The 2D Move software was used to restore the tectonic evolution history and, based on this, established the interaction model of salt diapirs and faults, and summarized the action modes of diverse types of sedimentary channels. The research results are expected to lay the foundation for follow-up studies on the laws of hydrocarbon accumulation.

LOWER CONGO BASIN

1,561,213

A MULTI-POINT STOCHASTIC BASED TURBIDITE LOBE ARCHITECTURE MODELING OF L OILFIELD, LOWER CONGO BASIN, WEST AFRICA

R.Xue, W.Zhang, W.Lu and M.Li (Sinopec). *21ST INTERNATIONAL SEDIMENTOLOGICAL CONGRESS [ISC] (Beijing, China, 8/22-26/2022) ABSTRACT BOOK* pp.1563-1564, 2022. (Available at <http://www.isc2022.org.cn> as of 9/22/2022; **Abstract only**)

Deep-water turbidite is a specific field of current exploration and development because of its considerable petroleum potential. As a significant composite of turbidite deposition system, internal architectural and 3D characterization of turbidite lobe has been technical tacking difficulty as consequence of its complex depositional environment and strong heterogeneity. Based on a large number of cores, logging, field outcrop and high-frequency three-dimensional seismic data, using the research ideas of well-seismic combination and progressive constraint, taking Miocene reservoir developed turbidite lobe of L Oilfield in the Lower Congo Basin of West Africa as an example, detailed architecture analysis and three-dimensional geological modeling were carried out. Firstly, the standard of lobe architecture level was clarified and the three-dimensional architecture model was established based on multi-dimensional and multi-scale data. Secondly, according to the middle-high frequency seismic data of the target layer in the study area and the high frequency seismic data of shallow layer, seismic RMS attribute slices were used to obtain the lobe deposition samples. The length, width and thickness of the turbidite lobe system were quantitatively analyzed to establish empirical function of geometric parameters and as a quantitative knowledge base to provide parameter guidance for multi-point statistical simulation. Lastly, the lobe training image is established by means of seismic multi-attribute and seismic volume carving technology, and 3D architecture model of turbidite lobe in the target layer M8 sand group is established by multi-point geostatistics method. The simulation results generally followed the lobe architecture model and were highly consistent with the actual drilling inspection well. This study has formed a set of detailed modeling technology for deep-water turbidite lobes, and enriched the geological knowledge base of deep-water turbidite lobes, which has practical significance for efficient development of lobe reservoirs.

LUANPING BASIN

1,561,214

EARLY CRETACEOUS PALYNOLOGICAL ASSEMBLAGES FROM THE DABEIGOU FORMATION AT YUSHUXIA IN THE LUANPING BASIN, NORTHERN HEBEI PROVINCE, CHINA AND THEIR STRATIGRAPHIC SIGNIFICANCES

M.Lin, J.Li and Y.Wu (Nanjing Inst Geol Palaeont). *REVIEW OF PALAEOBOTANY AND PALYNOLOGY* v.307, Dec. 2022. (ISSN 0034-6667; Article no.104751)

Late Jurassic–Early Cretaceous strata in western Liaoning and northern Hebei provinces are famous for yielding the Yanliao and Jehol biotas. However, there are great disputes over the stratigraphic division and correlation and chronology between the two regions, which will surely affect our understanding of the origin and evolution of the Jehol Biota. The Dabeigou Formation in the Luanping Basin is among the most argued. Palynostratigraphy, as an effective approach to stratigraphic correlation within or between basins, has been studied relatively preliminary on the formation. Our new material recovered from a well excavated section at Yushuxia, Luanping County, provides a fairly good, continuous, and complete succession for the pollen and spore study of this formation. Plenty of pollen and spores are obtained from the section, encompassing a palynological succession of three assemblage zones. These fossils provide a solid Early Cretaceous or middle Valanginian–early Hauterivian age for the Dabeigou Formation. This material found at Yushuxia, Luanping County allows us to build up a correlation between the northern Hebei and western Liaoning for the Upper Jurassic–Lower Cretaceous strata. A combined palynostratigraphic sequence is established, namely the *Classopollis*, *Classopollis-Densoisporites-Cicatricosisporites*, *Perinopollenites-Crybelosporites* and *Bisaccates* assemblages in ascending order. Our research implies that the Dabeigou Formation in northern Hebei is very likely to correlate with the Third Member of the Tuchengzi Formation and the lowermost part of the Yixian Formation in western Liaoning and the palaeoenvironment was diversified between the two sites during the early Early Cretaceous. (c2022 Elsevier B.V.)

LUFENG FIELD

1,561,215

ARCHITECTURE ANALYSIS OF SHALLOW WATER BRAIDED RIVER DELTA RESERVOIRS - TAKING ENPING 420 OIL GROUP IN LUFENG A OILFIELD, PEARL RIVER MOUTH BASIN AS AN EXAMPLE

X.Liang, Z.Wang, T.Niu, F.Chen, X.Wu, H.Fan and Z.Ge (State Key Laboratory China; CNOOC Research Inst Co Ltd; CNOOC China Ltd). *21ST INTERNATIONAL SEDIMENTOLOGICAL CONGRESS [ISC] (Beijing, China, 8/22-26/2022) ABSTRACT BOOK* p.1560, 2022. (Available at <http://www.isc2022.org.cn> as of 9/22/2022; **Abstract only**)

Braided river delta sand bodies are widely developed in Enping formation of Eocene in Lufeng sag, Pearl River Mouth Basin, which is the key target area for CNOOC's 14th Five-Year Plan. The unclear relationship between reservoirs and the complex internal structure are the bottlenecks restricting the planning of such oilfields. Combining well-seismic and carrying out the anatomy of composite sand body is the key to solving the problem. Taking the Enping 420 Oil Group in Lufeng A Oilfield as an example, under the guidance of the theory of sequence stratigraphy, seismic sedimentology and regional big data pattern, combined with core-logging facies, paleogeomorphology analysis and seismic inversion volume edge detection technology, clarified the internal structural characteristics of the sand body. The results show that: (1) the geomorphology of the Enping 420 oil group was relatively flat during the depositional period, but there were structural slope breaks in some parts, which was the shallow-water braided river delta deposition dominated by the channel; (2) it was subdivided into three periods vertically, among which the early sand The sand body is small in scale, poor in physical properties, and limited in distribution; in the middle stage, the sand body is large in scale and is the concentrated section of the main oil layer; in the late stage, the sand body is in limited distribution. (3) On the plane, it is characterized by divergent interweaving channels, the width of the main channel is 300m-600m, with good connectivity. The above achievements have effectively guided the well pattern deployment

and well type selection of Lufeng A Oilfield, and promoted the rapid production of the oilfield.

LUSITANIAN BASIN 1,561,216

THE ULTRASTRUCTURE OF IN SITU ARAUCARIAN POLLEN FROM THE MALE CONE CALLIALASTROBUS SOUSAI, LOWER CRETACEOUS OF CATEFICA, LUSITANIAN BASIN, WESTERN PORTUGAL

M.Tekleva, M.M.Mendes and J.Kvacek (Russian Academy Sciences; Coimbra Univ; Prague National Museum). *REVIEW OF PALAEOBOTANY AND PALYNOLOGY* v.307, Dec. 2022. (ISSN 0034-6667; Article no.104782)

Pollen morphology and ultrastructure are described for fossil pollen of the *Araucariacites* and *Callialasporites* types extracted from a *Callialastrobus sousai* pollen cone previously reported from the Lower Cretaceous Almargem Formation near the village of Catefica, in the Estremadura region, western Portugal. Pollen grains were studied with transmitted light and scanning and transmission electron microscopy. The pollen grains are medium-sized, being smaller and with a thicker exine in the *Callialasporites* type. Both pollen types appear inaperturate, although both polar regions are represented by a thinner exine. The exine sculpture (granulate/microechinate) and ultrastructure (granular sexine and lamellate/homogeneous endexine) are generally the same in *Araucariacites*- and *Callialasporites*-type grains. Saccus-like structures in the *Callialasporites*-type pollen are formed by loosely arranged endexine lamellae, while *Araucariacites*-type pollen is asaccate. The exine structure of the *Araucariacites*- and *Callialasporites*-type grains also agrees well with that of known araucariaceous pollen. (c2022 Elsevier B.V.)

MAANTANG FM 1,561,217

THE CARNIAN PLUVIAL EPISODE IN THE WESTERN SICHUAN BASIN (SOUTH CHINA)

X.Jin, Z.Shi, P.Mietto, P.Gianolla, M.Franceschi, M.Rigo, M.Caggiati, G.Roghi, Y.Du et al. (Chengdu Univ Technology). *21ST INTERNATIONAL SEDIMENTOLOGICAL CONGRESS [ISC] (Beijing, China, 8/22-26/2022) ABSTRACT BOOK* p.187, 2022. (Available at <http://www.isc2022.org.cn> as of 9/22/2022; **Abstract only**)

The Carnian Pluvial Episode (CPE; early Late Triassic) was a global perturbation of the C-cycle associated with a marked enhancement of the hydrological cycle, and consequent increase terrigenous sediment and freshwater input to the shallow marine sedimentary environments. Within the CPE interval, negative shifts in the $\delta^{13}\text{C}$ of marine and terrestrial organic matter and marine carbonates testify to multiple injection of large amounts of CO_2 into the atmosphere-ocean system, likely linked to the emplacement of the Wrangellia Large Igneous Province. The CPE coincided with a crisis of shallow water carbonate production and with a major biological turnover both in the marine and terrestrial realms. The environmental effects of the CPE have been widely documented in the western Tethys, but much less data are available from other areas. In the last decade, the western Sichuan Basin (China) became a reference locality for the study of the effects of the CPE in the eastern Tethys. However, research has also given rise to debate on the bio-, magneto- and chemostratigraphy of the Carnian successions. To resolve the existing controversies on this key CPE study area, we review the current knowledge on biostratigraphy, petrology and geochemistry of the successions in the Sichuan Basin, and provides an updated bio- and chronostratigraphic framework. Furthermore, we highlight the open questions and outline future research directions about the CPE in the area.

MARINE ORGANISM 1,561,218

AN AGGLUTINATED EARLY CAMBRIAN ACTINOTROCH-LIKE PHORONID FROM THE CHENGJIANG LAGERSTÄTTEN AND ITS IMPLICATIONS

Z.Zhang and L.E.Holmer (Northwest Univ, China; Uppsala Univ). *58TH ANNUAL PALAEOONTOLOGICAL ASSOCIATION*

MEETING (Leeds, UK, 12/16-19/2014) ABSTRACTS p.53, 2014. (Available at <http://www.palass.org> as of 11/15/2022; **Abstract only**)

The lophophorates are united by the presence of a fan of ciliated tentacles surrounding the mouth. Although considerable advances have recently been made in unveiling the Cambrian morphology and diversity of brachiopods, and other lophophorate animals, the most conspicuous phylogenetic gap in the Cambrian fossil record is for the Phoronida. *Iotuba* (= *Eophoronis* (Chen)) was proposed as a phoronid candidate, but it has more recently been considered as a sipunculid. New, abundant, well-preserved material of *Archisaccophyllia kunmingensis* (Hou et al.) from the Cambrian (Series 2) Chengjiang deposits is here reinterpreted as a stem-group phoronid with actinotroch-like larval characters. The phoronid affinity is supported by the sessile body plan and interior soft anatomy. The body consists of an upper agglutinated calyx and a lower stout stalk with a distal holdfast. The soft anatomy includes a U-shaped gut with a mouth surrounded by a fan of flexible tentacles. *Archisaccophyllia kunmingensis* differs from extant phoronid actinotroch larvae in being much larger with a sessile lifestyle, as well as in having the calyx covered by agglutinated quartz grains that is reminiscent of agglutination that is known in both extant adult phoronid and the stem-group brachiopod *Yuganotheca* recently reported from the Chengjiang fauna.

MARYLAND 1,561,219

SHELF ECOSYSTEMS ALONG THE U.S. ATLANTIC COASTAL PLAIN PRIOR TO AND DURING THE PALEOCENE-EOCENE THERMAL MAXIMUM: INSIGHTS INTO THE STRATIGRAPHIC ARCHITECTURE

M.Doubrawa, P.Stassen, M.M.Robinson, T.L.Babila, J.C.Zachos and R.P.Speijer (Leuven Katholieke Univ; US Geological Survey; Southampton Univ; Calif Univ, Santa Cruz). *PALEOCEANOGRAPHY AND PALEOCLIMATOLOGY* v.37, no.10, Oct. 2022. (ISSN 2572-4525; Article no.e2021PA004475)

The Paleocene-Eocene Thermal Maximum (PETM) is the most pronounced global warming event of the early Paleogene related to atmospheric CO_2 increases. It is characterized by negative $\delta^{18}\text{O}$ and $\delta^{13}\text{C}$ excursions recorded in sedimentary archives and a transient disruption of the marine biosphere. Sites from the U.S. Atlantic Coastal Plain show an additional small, but distinct $\delta^{13}\text{C}$ excursion below the onset of the PETM, coined the "pre-onset excursion" (POE), mimicking the PETM-forced environmental perturbations. This study focuses on the South Dover Bridge core in Maryland, where the Paleocene-Eocene transition is stratigraphically constrained by calcareous nannoplankton and stable isotope data, and in which the POE is well-expressed. The site was situated in a middle neritic marine shelf setting near a major outflow of the paleo-Potomac River system. We generated high-resolution benthic foraminiferal assemblage, stable isotope, trace-metal, grain-size and clay mineralogy data. The resulting stratigraphic subdivision of this Paleocene-Eocene transition is placed within a depth transect across the paleoshelf, highlighting that the PETM sequence is relatively expanded. The geochemical records provide detailed insights into the paleoenvironment, developing from a well-oxygenated water column in latest Paleocene to a PETM-ecosystem under severe biotic stress-conditions, with shifts in food supply and temperature, and under dysoxic bottom waters in a more river-dominated setting. Environmental changes started in the latest Paleocene and culminated at the onset of the PETM, hinting to an intensifying trigger rather than to an instantaneous event at the Paleocene-Eocene boundary toppling the global system.

MASS MORTALITY 1,561,220

OCEAN DEOXYGENATION ACROSS THE END-TRIASSIC MASS EXTINCTION

T.The (Leeds Univ). *21ST INTERNATIONAL SEDIMENTOLOGICAL CONGRESS [ISC] (Beijing, China, 8/22-26/2022) ABSTRACT BOOK* p.189, 2022. (Available at <http://www.isc2022.org.cn> as of 9/22/2022; **Abstract only**)

The role of ocean deoxygenation as a cause of the end-Triassic

marine mass extinction is widely debated. Here we present multi-redox proxy data (carbonate-associated sulfate $\delta^{34}\text{S}$, I/(Ca+Mg), Fe speciation and trace metals) at sections across the shallow to deep-water marine realms of the western Tethys and eastern Panthalassa. Results show local dissolved oxygen decline in the near-surface ocean of low-latitude Tethys across the extinction, synchronous with the global-scale spread of deeper anoxic waters on continental shelves and slopes. Further, persistent euxinic conditions prevailed across the Triassic-Jurassic boundary in many semi-enclosed basins of the NW European epicontinental sea, coinciding precisely with the major phase of benthic faunal loss at the regional scale. Hence, the coincidence of extreme redox shifts with the extinction losses on a global scale implicates oxygen scarcity as an important factor in the crisis.

MASS MORTALITY**1,561,221****THE ROLE OF MICROBIAL ANAEROBIC RESPIRATION IN THE END-PERMIAN MASS EXTINCTION**

M.Schobben, A.Stebbins, A.Ghaderi, H.Strauss, D.Korn, R.Hannigan and C.Korte (Berlin Museum; Mass Univ, Boston; Ferdowsi Univ). *58TH ANNUAL PALAEOONTOLOGICAL ASSOCIATION MEETING (Leeds, UK, 12/16-19/2014) ABSTRACTS* p.43, 2014. (Available at <http://www.palass.org> as of 11/15/2022; **Abstract only**)

Changes in plankton productivity have been connected with the end-Permian mass extinction. A box-model-proxy data comparison suggests that an increase of microbial sulfate reduction (MSR) can explain excursions in $\delta^{34}\text{SCAS}$ and $\delta^{18}\text{OCAS}$. These fluctuations are contemporaneous with the biodiversity crisis and are probably related to enhanced availability of organic substrates. This caused MSR to increase proportionally and induce the observed positive $\delta^{18}\text{OCAS}$ excursion. The scenario would only require an increase in the oceans' organic carbon inventory--a suggestion that can be linked to the climate warming and elevated continental weathering at that time. These physical processes are linked to the short-term carbon cycle, as ocean fertilization by nutrient input stimulated primary productivity. Enhanced microbial activity can be regarded as the killing agent because of increased oxygen consumption (aerobic respiration) and H_2S (MSR) production. This caused a rapid global expansion of euxinic water and resulted in iron limitation in the ocean water. This, together with decreased iron supply due to a change in fluviate regimes, reduced pyrite burial, explaining a negative $\delta^{34}\text{SCAS}$ excursion. This suggests that the latest Permian ocean was not dead ("Strangelove Ocean") but rather alive, and that microbial life can create adverse conditions for eukaryotic organisms.

METAZOA**1,561,222****BURGESS SHALE-TYPE PRESERVATION OF "SHELLY" METAZOANS**

M.M.Mus (Extremadura Univ). *58TH ANNUAL PALAEOONTOLOGICAL ASSOCIATION MEETING (Leeds, UK, 12/16-19/2014) ABSTRACTS* pp.35-36, 2014. (Available at <http://www.palass.org> as of 11/15/2022; **Abstract only**)

Most studies of Burgess Shale-type preservation have understandably focused on soft-bodied organisms, but "shelly" metazoans are also preserved as carbonaceous films. Common examples include brachiopods, trilobites, spiculate sponges and hyolithids. In such cases, the carbonaceous films are usually interpreted as coherent organic layers that were originally present in the mineralized elements, mostly external sheaths or periostacal layers. Using the example of hyolithids it is shown that these films do not represent original cuticular "layers". Instead, they are a composite carbonaceous compression resulting from the coalescence of all the preservable organic matter originally present in the skeletal element. The diagenetic processes that led to Burgess Shale-type preservation (which involve the polymerisation of organic matter and the loss of original internal structure and chemical integrity of the original tissues) are compatible with, and can account for, the characteristics observed in the fossil films of hyolithid skeletal elements. These observations have general implications for the interpretation of other mineralized organisms, such as the diverse and often problematic Cambrian sponges. The

observations summarised in this work suggest that all sponge spicules, regardless of their original mineralogy or precise phylogenetic affinities, could be preserved as carbonaceous films.

MONGOLIA**1,561,223****A LATE PALEOZOIC EXTENSION BASIN CONSTRAINED BY SEDIMENTOLOGY AND GEOCHRONOLOGY IN CENTRAL INNER MONGOLIA, EASTERN CAOB**

Y.Wang (Sinopec Research Inst). *21ST INTERNATIONAL SEDIMENTOLOGICAL CONGRESS [ISC] (Beijing, China, 8/22-26/2022) ABSTRACT BOOK* p.324, 2022. (Available at <http://www.isc2022.org.cn> as of 9/22/2022; **Abstract only**)

According to sedimentary structure, petrology and sequence analysis from seven sections (S1S7) across the West Ujimqin basin, the late Carboniferous to Permian sedimentary facies have been recognized and summarized as four sedimentary systems, i.e. the late Carboniferous-early Permian sedimentary system (SA) comprising the alluvial fan-delta-littoral facies, the late Carboniferous sedimentary system (SB) including the littoral facies-delta facies-platform margin facies, the early Permian sedimentary system (SC) characterized by delta front and prodelta facies, and the middle Permian sedimentary system (SD) with alternations of littoral and delta facies. According to the spatial and temporal distribution of the four sedimentary systems, the basin filling process can be divided into three stages. The first stage (324-290 Ma) is dominated by bidirectional terrigenous sediments containing the SA from alluvial fan to delta and littoral facies in the northwestern and the SB from littoral-delta to platform margin facies in the southern, respectively. The second stage (290-270 Ma) is characterized by delta front and prodelta facies of the SC marked by thick-bedded matrix-supported conglomerate, rapid accumulation of terrigenous sediments and volcanic debris, syn-sedimentary deformation and slump. The third stage (270-255 Ma) formed the SD with the alternations of littoral and delta facies, which is represented by complex terrigenous clasts and intra-basin carbonate. These shallow and proximal sedimentary systems from fan delta to littoral facies indicate that there was not oceanic sedimentary system in the eastern CAOB during the late Carboniferous to Permian except for some small red sea basins, which provides convictive evidence that the Paleo-Asian Ocean (PAO) had closed before the late Carboniferous. Detrital zircon dating reveals bidirectional provenances of the West Ujimqin basin, indicating that it was a limited basin between two uplifts, which implies presence of the late Paleozoic "basin and uplift" tectonic framework that developed on the eastern CAOB during the late Paleozoic.

MONTAGNE NOIRE**1,561,224****3D TOPOGRAPHY AS TOOL FOR SHAPE DISCRIMINATION OF CONODONT ELEMENTS**

A.Assemat, G.Thiery, T.Lieffroy and C.Girard (Montpellier Univ; UMR-CNRS). *5TH INTERNATIONAL CONODONT SYMPOSIUM [ICOS] (Wuhan, China and Online, 6/24-27/2022) PROGRAM AND ABSTRACTS* p.59, 2022. (**Abstract only**)

The flourishing of conodont diversity through the Paleozoic is evidenced by the strong diversification of the shape of the elements composing their feeding apparatus. Among the different elements that compose the feeding apparatus, the platform elements (P1) are the most robust. The qualitative analysis of their diversity of shape has been the corner stone of conodont taxonomy and Paleozoic biostratigraphy. However, the P1 elements also represent the most posterior dental elements of the apparatus, performing therefore the ultimate stage of food processing before ingestion of the food bowl. Thus, characterizing the shape of these elements across various species of conodonts could be relevant to decipher the diversity of feeding behavior among this group as well. Here we use topographic indices initially developed for the description of teeth relief (RFI, Slope), orientation (OPCr) and sharpness (ARC, DNE) to discriminate quantitatively P element shapes among conodont communities of the Late Famennian (Late Devonian) from the Montagne Noire Area (south France). We evidence methodological considerations that should be imperatively considered before conducting these methods on conodonts. Under several

homogeneous conditions, topographic analyses appear to be relevant for the study of taxonomic, ontogenetic and occlusal aspects of platform elements as they allow to segregate shapes independently of the phylogenetic relationship between taxa. Moreover, this quantification of shape diversity could bring new clues for understanding P element kinematics and feeding strategies among conodonts.

MOROCCO

1,561,225

SYSTEMATIC EXCAVATION IN THE LOWER ORDOVICIAN FEZOUATA LAGERSTAETTE (ZAGORA AREA, MOROCCO)

E.L.O.Martin, N.Allaire, A.Azizi, K.El-Hariri, K.Kourais, J.C.Gutierrez-Marco, B.Lefebvre, R.Lerosey-Aubril, A.Hafid et al. (UMR-CNRS). *58TH ANNUAL PALAEOONTOLOGICAL ASSOCIATION MEETING (Leeds, UK, 12/16-19/2014) ABSTRACTS* p.36, 2014. (Available at <http://www.palass.org> as of 11/15/2022; **Abstract only**)

The Lower Fezouata Formation (Lower Ordovician, Morocco) has yielded a remarkably diverse exceptionally-preserved biota, which provides unique insights into the transition between the Cambrian and Palaeozoic Evolutionary Faunas. Until recently, fossils from these deposits were collected from small isolated excavations, the stratigraphic positions of which relative to one another were poorly constrained. These collections were also biased by a greater interest for non-biomineralized fossils. This approach has been fruitful for documenting the diversity of the biota, but it does not permit exploration of the spatial and stratigraphic evolution of fossil assemblages. To address this question, we initiated a long-term systematic excavation at Bou Izargane, a locality exposing an 18-m-thick section within one of the two stratigraphic intervals with exceptional preservation recently identified within the Lower Fezouata Formation. Our first campaign has shown that exceptional preservation occurs in three discrete horizons within the section, each preserving an abundant but weakly diverse fauna. These characteristics are suggestive of episodes of environmental stress, as are the presence of abnormally small trilobites or the abundance of stylophorans. Ongoing sedimentological and geochemical studies will provide new data on the environmental context that facilitated soft-tissue preservation in these deposits.

MOROCCO

1,561,226

A NEW PROBLEMATIC COLONIAL ORGANISM FROM THE CAMBRIAN OF MOROCCO

C.Skovsted and S.Clausen (Swedish Museum; Lille Univ). *58TH ANNUAL PALAEOONTOLOGICAL ASSOCIATION MEETING (Leeds, UK, 12/16-19/2014) ABSTRACTS* p.44, 2014. (Available at <http://www.palass.org> as of 11/15/2022; **Abstract only**)

A large number of minute colonial fossils have been found in the Cambrian Brececa Micmacca Limestone at Lemdad in the High Atlas Mountains, Morocco. The fossils are formed by replacement and/or infill of iron oxides and most specimens are represented by internal moulds of the cone-shaped internal cavity of individual elements, often with triangular or quadratic cross-sections. Individual elements were closely juxtaposed and arranged in sub-parallel or radiating bundles that were attached to larger skeletal elements (e.g. trilobites or archaeocyathans). The largest composite specimens contain more than 20 individual elements. The new fossils resemble some poorly known Cambrian colonial organisms, such as *Labyrinthus* (Kobluk, 1979) and *Rosellatana* (Kobluk, 1984), which have been compared to corals. However, the Moroccan specimens are preserved in a fundamentally different way compared to previous accounts, allowing for better resolution of important internal structures. These include potential connecting structures between individual elements and the origination of the colony as well as the addition of new elements during growth, which can be studied in three dimensions. Thanks to the new data, it is possible to evaluate the suggested affinity of these problematic fossils to corals and to elucidate their potential role in the early evolution of the Anthozoa.

NAMIBIA

1,561,227

PRIAPULID TRACE FOSSILS FROM THE LATE EDIACARAN OF NAMIBIA

K.A.Turk, K.M.Maloney, M.Laflamme and S.A.F.Darroch (Vanderbilt Univ; Toronto Univ). *65TH ANNUAL PALAEOONTOLOGICAL ASSOCIATION MEETING (Manchester, UK, 12/18-20/2021) PROGRAMME AND ABSTRACTS* p.48, 2021. (Available at <http://www.palass.org> as of 11/1/2022; **Abstract only**)

Latest Ediacaran to earliest Cambrian trace fossils preserve evidence for the early evolution of metazoan complexity and behaviours as well as the onset of critical geobiological changes that continued into the Palaeozoic (the "agronomic revolution"). Here we present an unusual suite of trace fossils from the late Ediacaran Nasep-Huns transition (Nama Group, Namibia) potentially referable to *Archaechinnum haughtoni* (Glaessner 1963), and which bear strong resemblance to priapulid burrows from the lower Cambrian Haidar Formation of Sweden. Of particular note are the two distinct surface patterns present on this material that exhibit both distal longitudinal striations consistent with scalidophoran proboscides and transversely annulated proximal sections reminiscent of priapulid caudal anatomy. Furthermore, these traces appear to dip below the sediment surface and re-emerge consistent with the directions of motion, similar to modern priapulid burrows produced under experimental conditions. Attribution of these traces to priapulids would thus represent among the oldest records of crown group Ecdysozoa, pushing their first appearance beneath the base of the Cambrian. Furthermore, this finding would illustrate that complex bioturbative--and perhaps predatory--animal behaviours evolved prior to the Ediacaran-Cambrian boundary and may have played a prominent role in structuring benthic communities over the Ediacaran-Cambrian transition.

NANPU DEPRESSION

1,561,228

STRUCTURAL STYLES AND EXTENSION-STRIKE SLIP FAULT SYSTEM: A CASE FROM NANPU SAG, BOHAI BAY BASIN, NE CHINA

Y.Wang and F.Yu (China Univ Petroleum). *21ST INTERNATIONAL SEDIMENTOLOGICAL CONGRESS [ISC] (Beijing, China, 8/22-26/2022) ABSTRACT BOOK* p.333, 2022. (Available at <http://www.isc2022.org.cn> as of 9/22/2022; **Abstract only**)

Nanpu sag is located in the northeast of Huanghua depression in the Bohai Bay Basin (BBB), and the northern part is the first-order boundary fault of the depression: Baigezhuang fault (BGZ) and Xi'nanzhuang fault (XNZ) form the depression boundary together. It is a continental dustpan sag with the characteristics of north Fault and south superstructure. The research data show that the shallow reservoirs (Nm, Ng, Ed) in the Nanpu sag have the characteristics of shallow burial depth, good physical properties and high production capacity. In order to clarify the way in which the staged tectonic deformation affects the fracture spreading of hydrocarbons, this paper systematically summarizes the stress field transformation in the Nanpu sag region, the spatial spreading characteristics of the No. 4 structure belt and the zonation characteristics of the main fracture of the shallow Cenozoic layer system through detailed interpretation of 3D seismic data, and clarifies the structure deformation mechanism of the No. 4 belt. The established spatio-temporal evolution process combined with the paleotectonic geometry of the No. 4 structure belt is then used to design physical analogue experiments to recover the deformation process and simulation results. Research shows that: (1) the Cenozoic No. 4 structure belt and the surrounding areas mainly have the characteristics of superposition of anisotropic extensional deformation in phases, and there are several groups of NW and NE trending faults, which mainly form the style of strike-slip stacked fan and horst-ground combination in the plane, and the style of compound "y" combination, conjugate combination and negative flower combination in the section; (2) The Cenozoic No. 4 structure belt has the deformation characteristics of planar zoning and sectional staging, forming a strong slip-weak extension zone at the southern section of the No. 3-4 structure belt, and a conjugate strong extension-weak slip zone at the northwest end where the slip component gradually decreases; (3) The "strike-slip stacked fan

structure" in the No. 4 structure belt is the result of the diagonal boundary extension due to the near north-south extension under the pre-existing basement conditions, and there is no significant combination of pure strike-slip deformation, and specific boundary faults, basement inhomogeneity and preexisting fractures have a controlling effect on the tectonic pattern of the fault system; (4) The mudstone at the base of Ed3 is both the main hydrocarbon source rock and the controlling material factor in the formation of the extensional-slip transition zone in No. 4 structure belt.

NANPU DEPRESSION

1,561,229

THE DEVELOPMENT CHARACTERISTICS, GENESIS AND FORMATION ENVIRONMENT OF IGNEOUS ROCKS IN NANPU SAG OF BOHAI BAY BASIN

J.Yu and F.Yu (China Univ Petroleum). *21ST INTERNATIONAL SEDIMENTOLOGICAL CONGRESS [ISC] (Beijing, China, 8/22-26/2022) ABSTRACT BOOK* p.337, 2022. (Available at <http://www.isc2022.org.cn> as of 9/22/2022; **Abstract only**)

Nanpu Sag is located in the northern end of Bohai Bay Basin. There are two types of volcanic rocks, intrusive rocks and exhalative rocks. The intrusive rocks include diabase, diabase porphyrite, quartz diorite, etc. Ejected rocks can be divided into volcanic lava and volcanic clastic rocks. The former mainly includes basalt, andesite, rhyolite, and the latter includes volcanic breccia, tuff, tuffaceous sandstone, etc. Nanpu depression volcanic formation period can be divided into Shahejie, Dongying and Guantao three periods. The distribution characteristics of volcanic rocks: (1) Distribution direction deflection. In the early Shahejie period, the volcanic rocks were distributed in NE direction, and in the middle Dongying period, they were NW-SE direction, and in the late Guantao period, they were NE-SW direction, indicating that the regional stress changed; (2) Spatial distribution. The early volcanic rocks were distributed in the southwest of the sag, and the middle and late volcanic rocks extended to the middle and north; (3) Increased intensity of activities. From the early stage to the late stage, it is generally the expansion depression, and the expansion intensity increases. The weighted average age of zircon U-Pb dating is 34.1 ± 0.5 Ma, so it is determined to be formed in Shahejie period. On the primitive mantle normalized spider diagram of trace elements, the curve generally tilts to the right, showing a zigzag jumping decreasing distribution, Enriched Rb, Ba, Sr and LREE, depleted Zr, Th; in the REE distribution pattern map of chondrite, the curve was right-leaning, enriched LREE and depleted HREE; the mean value of δEu is 0.97, indicating weak negative Eu anomaly. The (Th/Ta) PM and (La/Nb) PM of the sample data are less than 1, suggesting no obvious crustal contamination. In the Huck plot with MgO as the abscissa, Ni, CaO and Al₂O₃ were positively correlated with MgO, TiO₂ and P₂O₅ were negatively correlated with MgO. Sm-Sm/Yb diagram shows that the mantle source is composed of garnet, spinel and lherzolite, and 3% ca. 16% partial melting is speculated. The sample data have high Ta/Yb and Th/Yb values. The Th/Yb-Ta/Yb diagram, $\delta Nd-87Sr/86Sr$ diagram and 208Pb/204Pb-206Pb/204Pb diagram show that the magma originates from the mixed source area of EMI and depleted mantle. In the 2Nb-Zr/4-Y diagram, TiO₂-MnO-P₂O₅ diagram and Th/Hf-Ta/Hf discrimination diagram, it is shown that the formation environment is active rift expansion in continental plate.

NENJIANG FM

1,561,230

OBLIQUITY-FORCED AQUIFER-EUSTASY DURING THE LATE-CRETACEOUS GREENHOUSE WORLD

Z.Zhang, Y.Huang, C.Wang, M.Li, P.Ju and X.Li (China Univ Geosci, Beijing; Peking Univ; Northwest Univ, China). *21ST INTERNATIONAL SEDIMENTOLOGICAL CONGRESS [ISC] (Beijing, China, 8/22-26/2022) ABSTRACT BOOK* pp.284-285, 2022. (Available at <http://www.isc2022.org.cn> as of 9/22/2022; **Abstract only**)

The mechanism of short-term and high-magnitude sea-level oscillation has long been debated between glacio- and aquifer-eustasy (Miller et al., 2005; Haq, 2014), largely due to the sparse robust evidence for the aquifer-eustasy, and the little knowledge about hydrological dynamics behind it. Non-marine/continental

greenhouse archives (e.g. lake level) and their temporal correlation to marine successions (e.g. sea level) could give clue to aquifer-eustasy (Wagreich et al., 2014). The Songliao Basin (SLB), in Northeast China, is one of the largest Mesozoic terrestrial inland basins and has deposited the near whole Cretaceous successions (Wang et al., 2013). The greenhouse Late Santonian-Early Campanian Lower Nenjiang Formation (K(2)n 1+2), recovered from three boreholes in SLB provides a unique opportunity for validating and decoding the aquifer-eustasy. Initially the cyclostratigraphy of logging gamma ray (GR) and Thorium (Th) series from three boreholes was implemented, which in junction with the radioactive ages renewed the chronology framework of SLB. Using the astronomically tuned GR and Th series, the lake level of SLB, which is recovered from sedimentary noise modeling (Li et al., 2019) and presents the water table of groundwater reservoir, shows a clear out-of-phase relationship with the coeval sea level, validating the aquifer-eustasy hypothesis. The lake level shows prominent ca. 1.2 Myr cycles and a well-coupled relationship with sea level and obliquity modulation, indicating that the orbital obliquity drove the lake level and modulated the water exchange between ocean and continent during the Cretaceous greenhouse period. The strong precipitation indicated by the negative excursion of Ostracods $\delta 18O$ (Chamberlain et al., 2013) well correlates to the high lake level, high obliquity, and low sea level, suggesting that during obliquity modulation maxima, more moisture was precipitated into the high-latitude continents, consequently recharging the aquifer and raising the lake level while drawing down the sea level and vice versa. The close correspondence between reported marine incursion layers (Hu et al., 2015) and lowstand of sea level casts a doubt on marine incursion hypothesis in the SLB, more work is needed to reconcile this paradox. Overall, this study gives robust geological evidence for aquifer-eustasy and firstly decodes its role on Cretaceous short-term eustasy.

NEWFOUNDLAND

1,561,231

THE ECOLOGICAL IMPORTANCE OF EDIACARAN STEMS

N.Barnes, C.G.Kenchington and E.G.Mitchell (Bristol Univ; Cambridge Univ). *65TH ANNUAL PALAEOANTHROPOLOGICAL ASSOCIATION MEETING (Manchester, UK, 12/18-20/2021) PROGRAMME AND ABSTRACTS* p.52, 2021. (Available at <http://www.palass.org> as of 11/1/2022; **Abstract only**)

The Ediacaran-aged Avalonian Assemblage of Newfoundland, Canada (ca. 565 million years old) hosts some of the oldest known multicellular life. Preserved as in situ census communities, spatial analyses can be utilized to better understand these unique assemblages. In this study, random labelling analyses (RLA) were used to investigate how morphological characteristics and taxonomic affinities impact the spatial distribution of taxa on the Lower Mistaken Point (LMP) surface. LMP is particularly well suited for these analyses because there are two abundant rangeomorph taxa—*Beothukis* and *Culmofrons*—that share many similar branching characters, but *Culmofrons* has a stem while *Beothukis* does not. Fossil specimens present on the surface were categorized according to their morphology (i.e., stem or not) and by their broad taxonomy (i.e., rangeomorph or not). In general, the spatial distribution of those morphologically and taxonomically defined was similar in all situations examined. However, small-scale differences are evident in the distribution of stemmed and non-stemmed rangeomorphs on the LMP surface; it is more likely that a stemmed rangeomorph individual will be located near another stemmed individual rather than a non-stemmed individual. This suggests that different ecological processes are operating on stemmed vs. non-stemmed rangeomorphs and demonstrates an underlying importance to broad morphological traits.

NEWFOUNDLAND

1,561,232

HYDRODYNAMICS OF THE RANGEOMORPH EDIACARAN ORGANISM *PECTINIFRONS ABYSSALIS*

H.Masaki, B.M.Gibson, I.A.Rahman, F.S.Dunn, E.G.Mitchell and S.A.Farroch (Vanderbilt Univ; Oxford Univ; Cambridge Univ). *65TH ANNUAL PALAEOANTHROPOLOGICAL ASSOCIATION MEETING (Manchester, UK, 12/18-20/2021) PROGRAMME AND*

ABSTRACTS p.79, 2021. (Available at <http://www.palass.org> as of 11/1/2022; **Abstract only**)

Late Ediacaran fossil surfaces at Mistaken Point (ca. 574–564 Ma) preserve some of the oldest complex macroscopic communities and are dominated by "fractal" rangeomorph organisms whose relationships to extant animal groups are unknown. Among the least well-understood of these is *Pectinifrons abyssalis*—a fence-like organism consisting of a curved basal pedicle rod and two upright rows of rangeomorph fronds. Like other rangeomorphs, *Pectinifrons* is widely believed to have been a sessile osmotroph, feeding via the direct absorption of dissolved organic compounds; however, this model has yet to be objectively tested. In this project, we used computational fluid dynamics (CFD) modelling to examine simulated flow patterns around *Pectinifrons* under a range of realistic palaeoenvironmental conditions. The patterns were compared with those computed for other Ediacaran organisms and with a range of potential modern analogues. These data allowed us to critically assess the palaeobiology of *Pectinifrons*, including the establishment of their likely feeding mode, as well as to examine a range of potential interactions with co-occurring rangeomorph organisms. Ultimately, this work sheds new light on a little-studied Ediacaran organism and tests the hypothesis that *Pectinifrons* formed part of a unique biocenosis that disappeared prior to the base of the Cambrian.

NEWFOUNDLAND

1,561,233

RECOGNIZING THE REPRODUCTIVE MODE OF *FRACTOFUSUS* THROUGH SPATIAL ANALYSIS

E.G.Mitchell, A.G.Liu, C.G.Kenchington and N.J.Butterfield (Cambridge Univ). *58TH ANNUAL PALAEOONTOLOGICAL ASSOCIATION MEETING (Leeds, UK, 12/16-19/2014)* ABSTRACTS p.39, 2014. (Available at <http://www.palass.org> as of 11/15/2022; **Abstract only**)

Fractofusus is one of the most distinctive members of the Rangeomorpha, a clade of fractally branching Ediacaran macroscopic fossils that has defied palaeobiological resolution. *Fractofusus* positions were mapped out on three bedding planes ("D" and "E" Surfaces, Mistaken Point and H14 surface, Bonavista Peninsula) in Newfoundland, Canada (565-570 Ma), allowing spatial distributions to be analyzed and shedding light on their reproductive biology. For each bedding plane, the spatial patterns of fossils were described using pair correlation functions and the patterns were compared with different types of clustering models. All three of the *Fractofusus* populations were found to exhibit recurrent, species-specific spatial clustering indicative of reproductive processes. On "E" and H14, we identified three generations of *Fractofusus*, but only two on "D". On H14, where body size was recorded, *Fractofusus* specimens in the smallest class preferentially cluster around those in the medium class, which preferentially cluster around those in the largest class. Comparing pair correlation functions, cluster directionality and mean cluster radius suggests that *Fractofusus* grew via a process of stolon-like reproduction, similar to that seen in plants that propagate via asexual runners. The identification of this reproduction strategy represents a fundamental new level of palaeobiological understanding of rangeomorphs.

NEW ZEALAND

1,561,234

GEOLOGY OF NEW ZEALAND'S SUB-ANTARCTIC ISLANDS

J.M.Scott and I.M.Turnbull (Otago Univ). *NEW ZEALAND JOURNAL OF GEOLOGY AND GEOPHYSICS* v.62, no.3, pp.291-317, 2019. (ISSN 0028-8306; ISSN 1175-8791)

New Zealand's remote five Sub-Antarctic island groups are the only sub-aerial exposures of the approximately 800,000 km² Campbell Plateau portion of Zealandia. An up-to-date geological map, a summary of the current geological knowledge and a geological interpretation is presented for each island group. The oldest rocks are Early Paleozoic metasediments on Campbell Island/Motu Ihupuku. Granitoids dominate the Bounty Islands/Moutere Hauriri (Early Jurassic) and Snares Islands/Tini Heke (Early Cretaceous), form a small part of the Auckland Islands/Motu Maha (Late Cretaceous), and occur as rare

Cretaceous xenoliths in tuffs on the Antipodes Islands/Moutere Mahue. The Campbell Island/Motu Ihupuku metasedimentary rocks are overlain by Late Cretaceous-Cenozoic basin sediments, which are in turn overlain by tuff and lava resulting from emergent intraplate volcanism. The Auckland Islands/Motu Maha and Antipodes Islands/Moutere Mahue stratigraphies are also related to emergent intraplate volcanism. Limited radiometric dating indicates that the Auckland Islands/Motu Maha breached the Southern Ocean in the Early-Middle Miocene, Campbell Island Volcano formed in the Late Miocene, and the Antipodes Volcano formed in the last 300,000 yrs. Basaltic dikes on the Snares Islands/Tini Heke are undated, and mafic dikes on the Bounty Islands/Moutere Hauriri are Mesozoic; it is unclear when these two island groups formed. The Auckland Islands/Motu Maha and Campbell Island/Motu Ihupuku have cirques, terminal and lateral moraines, till deposits and glacially carved fjords, and near-shore bathymetry indicates that all island groups exposed significantly larger areas during glacial periods. More work is required to understand the geological formation of these islands and their Southern Ocean climatic records.

NIGER DELTA AREA

1,561,235

DEPOSITIONAL ARCHITECTURES OF TECTONICALLY FORCED DEEP MARINE CHANNEL BENDS: NIGER DELTA OFFSHORE

M.Bouchakour and X.Zhao (Southwest Petroleum Univ). *21ST INTERNATIONAL SEDIMENTOLOGICAL CONGRESS [ISC] (Beijing, China, 8/22-26/2022)* ABSTRACT BOOK p.1566, 2022. (Available at <http://www.isc2022.org.cn> as of 9/22/2022; **Abstract only**)

Throughout the past decades, submarine channels have been one of the most relevant hydrocarbon prospects in continental slopes. The detailed descriptions of channel architectures and the connectivity of sand bodies have aided hydrocarbon production in terms of reservoir heterogeneity and connected oil. Nevertheless, the ranges of these stacked channels within tectonically complex slopes remain poorly understood, in part because their sedimentary records diverge. Two submarine channel systems have been investigated in the Agbada formation, within the southern Niger Delta offshore, to help understand and depict the distribution of submarine channel architectures around growing structures. A critical examination of these channels including stratigraphic subdivision has led to the identification of several vertically-stacked channel complexes, revealing a number of channel bends around structural reliefs. These latter have been mapped using seismic attributes, including variance, RMS, and spectral decomposition. The cross sections analysed along these bends, have permitted the characterization of channel stacking patterns, consisting of lateral offsets, vertical amalgamations, and oblique amalgamations. The integrated seismic profiles and platforms, have been further used to assess several parameters around the bends, such as channel TWT-thickness, width, sinuosity, bend amplitudes, and channel shift distances. This has allowed the classification of the deflected bends throughout the opposition of tectonic forcing against channel autogenic processes. The tectonic forcing reflects the high amplitude bends growing with dominantly lateral offsets. In addition, the seismically-defined channel chute cut-offs are as well believed to form on stepwise tilting of channel floor. Where the channel encounters orthogonal ridge, the deflected bend has been associated to overwhelming sands "swept" into structural lows making up "ladle-shaped" architectures with bars and channel cuts, and significant amounts of upstream sediment reflections. While, the opposite autogenic influence is shown by levee confinements, which dramatically restricted the bend growth and were favorable to downstream translation of channel pathways. These channel relief constrictions have comprehensively resulted oblique and vertical channel trajectories within bend apices. Besides, where channel sedimentation is dominantly mud-rich debrites, the deflected bends were particularly kinked, showing up a poor development of channel lateral shifting. Such architecture is believed to emerge under the influence of downstream surge flows surpassing the tectonic drift. These observations demonstrate the pivotal role of channel sedimentary processes altering the architectures of tectonically influenced bends, establishing a new

outlook for future investigations on structurally controlled submarine channels.

NINGKUO FM 1,561,236

CONODONT BIOSTRATIGRAPHY OF THE LATEST CAMBRIAN AND THE EARLIEST ORDOVICIAN IN THE HUANGNITANG-GSSP SECTION, SOUTH CHINA

R.Fan, Y.Zhang, S.Deng, X.Fang, Y.Lu, X.Ma, S.Zhou, Y.Huang, Y.Sun et al. (Res Inst Petrol Explor Dev). *5TH INTERNATIONAL CONODONT SYMPOSIUM [ICOS] (Wuhan, China and Online, 6/24-27/2022) PROGRAM AND ABSTRACTS* p.74, 2022. (Abstract only)

The Huangnitang section located in Changshan County, Zhejiang Province, is widely known as the global boundary stratotype for the Darriwilian Stage of the Ordovician System. The base of the Darriwilian is within the Ningkuo Formation, below which develop the Yinchufu Formation and the Siyangshan Formation successively. The interval of these two latter formations contains the Cambrian-Ordovician boundary. Conodont fauna of 14 species and 10 genera are recovered from the samples collected from this interval. It mainly includes *Coelocerodontus trigonius* (Ethington, 1959); *Eoconodontus notchpeakensis* (Miller, 1969); *Proconodontus muelleri* (Miller, 1969); *Teridontus nakamurai* (Nogami, 1967); *Cordylodus proavus* (Muller, 1959); *Cordylodus intermedius* (Furnish, 1938); *Cordylodus lindstromi* (Druce & Jones, 1971); *Cordylodus deflexus* (Bagnoli, Barnes & Stevens, 1987); *Cordylodus lenzi* (Muller, 1973); *Cordylodus angulatus* (Pander, 1856); *Utahconus utahensis* (Muller, 1969); and *Hirsutodontus simplex* (Druce & Jones, 1971). Although the primary marker species *Iapetognathus fluctivagus* (Nicoll et al., 1999) for the Cambrian-Ordovician boundary is absent from it, just as with the other conodont fauna recovered from the coeval interval in South China, the fauna basically correlates well with those from the GSSP section in Canada and especially with the ASSP section in North China.

NIUBAO FM 1,561,237

A COMPARATIVE STUDY OF LAKE LEVEL FLUCTUATION BASED ON SEDIMENTARY FACIES AND HYDROGEN INDEX: A CASE FROM THE CENOZOIC NIMA BASIN IN TIBET

K.Tian, H.Yi and G.Xia (Chengdu Univ Technology). *21ST INTERNATIONAL SEDIMENTOLOGICAL CONGRESS [ISC] (Beijing, China, 8/22-26/2022) ABSTRACT BOOK* pp.267-268, 2022. (Available at <http://www.isc2022.org.cn> as of 9/22/2022; Abstract only)

Lake level fluctuations are extremely sensitive to regional and even global climate and environmental changes. Meanwhile, the source rocks are mostly developed and distributed during the lake-flooding period. Identifying the level fluctuations of ancient lakes is beneficial to the prediction and search of source rocks, and promotes the exploration and development of oil and gas resources. Therefore, it is significant to restore the indicators that record the level change of ancient lakes. In modern lakes, lake shorelines and lakeside terraces can directly reflect the fluctuation of lake levels. However, these geomorphological signatures are generally difficult to preserve in ancient lake deposits. Lake level fluctuations derived from traditional sedimentary facies changes are more intuitive, but the resolution is low. As an indicator of the redox environment, the hydrogen index can make up for the shortcomings of the above methods. The Niubao Formation of Paleogene in the Nima Basin, Tibet, with clear outcrops, rich lithology, and fossils, is suitable for studying lake level fluctuations. Investigated the development horizon of source rocks in this section, this study discussed the relationship between source rocks and lake level and the superiority of hydrogen index in studying paleo-lake level fluctuations. We discuss lake level and its controlling effect on source rocks by comparing the lake level fluctuation curves based on sedimentary facies and hydrogen index respectively. Through the research of sedimentary petrology, kerogen type, hydrogen index, and organic matter maturity of the samples, it was found that deep lacustrine facies has higher TOC compared to shallow and semi-deep lakes. The increase of lake paleo-depth plays a

leading role in the quality of source rocks. However, when the lake level rises to a certain extent, the TOC of source rocks is mainly controlled by paleoproductivity. Compared with the lake level curve based on sedimentary facies, the hydrogen index also identifies lake level changes in similar lithologies. This more detailed method of describing the level fluctuations of ancient lakes is of great significance for guiding oil and gas exploration.

NIUTITANG FM 1,561,238

ANALYSIS OF PROVENANCE AND TECTONIC BACKGROUND OF LOWER CAMBRIAN BLACK SHALE IN WESTERN HUNAN AND HUBEI

21ST INTERNATIONAL SEDIMENTOLOGICAL CONGRESS [ISC] (Beijing, China, 8/22-26/2022) ABSTRACT BOOK p.276, 2022. (Available at <http://www.isc2022.org.cn> as of 9/22/2022; Abstract only)

Based on the geochemical analysis of the black shale of Niutitang Formation in Gucheng Village (GCC) section and Yanwutan (YWT) section in Western Hunan and Hubei, the provenance and tectonic background of the black shale of Lower Cambrian in Western Hunan and Hubei are discussed. According to the combination ratio characteristics of major, trace and rare earth elements, the provenance background of the two sections is of mixed origin. The tectonic background is dominated by passive continental margin in GCC section and continental island arc in YWT section. There are great differences in sedimentary and mineral characteristics between the two sections. Niutitang Formation in GCC section is stratified. Niu1 member is siliceous shale and argillaceous shale, Niu2 member is micritic limestone, and Niu3 member is limestone and mudstone. The Niutitang Formation of YWT section is not stratified, mainly developing carbonaceous tabular shale, and the lower part is enriched with pyrite, nickel, cobalt, vanadium and other metals and phosphorus nodules. The quartz mineral content in YWT section is much higher than that in GCC section, and pyrite is also more developed than that in GCC section. The main reason for the difference of characteristics is the different tectonic background, followed by the influence of hydrothermal activities and the different depth of water body.

NORTH AFRICA 1,561,239

MORPHOLOGICAL DISPARITY TRENDS IN DEVONIAN TRILOBITES FROM NORTH AFRICA

V.Bault, C.Cronier and C.Monnet (Lille Univ). *PALAEONTOLOGY* v.65, pt.5, Sept./Oct. 2022. (ISSN 0031-0239; ISSN 1475-4983; Article no.e12623)

The Devonian was a time of drastic environmental change that shaped the morphology of trilobites. This study aims to investigate their morphological evolution and to show the influence of some abiotic and biotic factors (bathymetry, feeding habits and visual abilities) on their shape. A dataset was compiled to investigate the shape of three structures (cephalon as a whole, central part of the cephalon, and pygidium) of Devonian trilobites from North Africa, using a geometric morphometric approach. Based on empirical morphospaces, the morphological changes were quantified through the Devonian stages. The results reveal important variations in the morphological disparity of the glabella shape, the facial suture location, the pygidial length and the presence of spines. In the Lochkovian, morphological disparity was low, subsequently increased in the Pragian with numerous innovations, and reached a maximum in the Emsian. If the morphospace occupancy remained until the Eifelian, a severe loss of disparity occurred in the Givetian, a time known for important environmental changes. Disparity then remained low in the Late Devonian. The shapes inherited from the Silurian persisted throughout the Devonian whereas Pragian novelties were most affected by losses. These persistent shapes were more versatile for environmental adaptation, helping those trilobites to survive the environmental events. Similarly, the trilobite orders that survived Devonian events had a wide morphological spectrum and were better adapted to withstand environmental change.

NORTH CHINA PLATFORM

1,561,240

TIMING OF THE KAIYUAN-JIAPIGOU SHEAR ZONE IN THE NORTHERN MARGIN OF THE NORTH CHINA CRATON: IMPLICATIONS FOR CLOSURE OF THE MONGOL-OKHOTSK OCEAN

S.Q.Huang, S.W.Dong, F.Zhang, Y.Q.Zhang, W.Shi and W.E.G.Mueller (Chinese Academy Geol Sci; Chinese Academy Sciences; Johannes Gutenberg Univ). *TECTONOPHYSICS* v.844, 12/5/2022. (ISSN 0040-1951; Article no.229626)

The ductile Kaiyuan–Jiapigou Shear Zone (KJSZ) is located within the eastern part of the northern margin of the North China Craton (NCC). The foliation within the shear zone generally dips at 55° towards N20° and contains a lineation that plunges at 40° towards N30°. Field and thin section observations and quartz c-axis fabrics of the KJSZ indicate that this zone records top-to-the-SSW shearing associated with a NNE–SSW regional compression event. Muscovite, biotite, and hornblende 40Ar/39Ar step-heating ages constrain the timing of shearing and the tectonothermal history of the KJSZ. Quartz c-axis fabrics and mineral deformation features indicate the deformation within the KJSZ occurred at temperatures of 400°C–450°C, which are lower than the Ar–Ar closure temperature of hornblende but higher than the closure temperatures of muscovite and biotite. Samples from the KJSZ yield 40Ar/39Ar step-heating ages from 164.6 ± 0.5 to 165.2 ± 0.6 Ma for hornblende samples and from 161.4 ± 0.4 to 163.1 ± 0.4 Ma for mica samples. Combining these ages with the temperature of deformation within the KJSZ indicates that this shear zone most likely formed between 165.2 ± 0.6 and 161.4 ± 0.4 Ma. Linking these new data with the tectonics and geochronology of the eastern part of the northern margin of the NCC suggests that the deformation within this region was most likely controlled by a nearly N–S compressional event associated with the far field effect of the Mongol–Okhotsk Ocean closure during the Middle–Late Jurassic. (c2022 Elsevier B.V.)

NORTH CHINA PLATFORM

1,561,241

ZINC ISOTOPIC EVIDENCE FOR ENHANCED CONTINENTAL WEATHERING AND ORGANIC CARBON BURIAL DURING THE LATE CAMBRIAN SPICE EVENT

C.Yuan, S.A.Liu, J.Chen and L.Fang (China Univ Geosci, Beijing; Nanjing Inst Geol Palaeont; China Univ Petroleum). *PALAEOGEOGRAPHY, PALAEOCLIMATOLOGY, PALAEOECOLOGY* v.608, 12/15/2022. (ISSN 0031-0182; Article no.111302)

The globally recognized late Cambrian Steptoean Positive Carbon Isotope Excursion (SPICE; ca. 497–494 Ma) is one of the most prominent carbon isotope excursions during the Phanerozoic eon, yet its primary cause remains debatable. To provide new insights into this issue, here we investigate zinc stable isotopes (expressed as $\delta^{66}\text{Zn}$) on two coeval carbonate successions spanning the Miaolingian–Furongian transition in North China. Similar stratigraphic $\delta^{66}\text{Zn}$ trends are observed in the two sections, indicating a widespread perturbation to the marine Zn cycling. An abrupt decline of $\delta^{66}\text{Zn}$ values by up to 0.4‰ and a concomitant increase of Zn/Ca ratios are observed at the pre-SPICE to the early SPICE interval, which can be best explained by the enhanced influx of isotopically light Zn from continental weathering. Enhanced continental weathering increased the inputs of terrestrial-sourced nutrients to the oceans, promoting the primary productivity and burial fluxes of organically bound Zn. At the middle stage of the SPICE, the coupled positive shifts of $\delta^{66}\text{Zn}$ and $\delta^{13}\text{C}_{\text{carb}}$ indicate a phase of marine Zn cycling fluctuations driven by massive organic matter burial. Enhanced sequestration of organic carbon caused a rise in atmospheric oxygen levels, favoring the remobilization of previously buried Zn at shallower marine settings. With the development of muted continental weathering during the falling limb of the SPICE, the return of $\delta^{66}\text{Zn}$ to initial background values marks the reestablishment of the stable seawater chemistry condition. Our results constrain the important roles of enhanced continental weathering and organic matter burial in micronutrient fluctuations during the SPICE, which were most likely the primary trigger for the SPICE. (c2022 Elsevier B.V.)

NORTH CHINA PLATFORM

1,561,242

MICROFABRICS AND ORGANOMINERALS AS INDICATOR OF MICROBIAL DOLomite IN DEEP TIME: AN EXAMPLE FROM THE MESOPROTEROZOIC OF NORTH CHINA

Y.Yuan, X.Shi, D.Tang, Q.Shi and Y.Li (China Univ Geosci, Beijing). *PRECAMBRIAN RESEARCH* v.382, Nov. 2022. (ISSN 0301-9268; Article no.106881)

Both laboratory experiment and modern environment studies show that primary dolomite can precipitate at low temperature ($\leq 60^\circ\text{C}$) only when microbes were involved. Vast dolostones in mid-Proterozoic have long been suspected to be the results of microbial mediation, but direct evidence is rare. To reveal their origin, an integrated study was conducted on the Mesoproterozoic Wumishan Formation (ca. 1.48 Ga) of North China using multiple techniques. The results show that the Wumishan dolostone contains abundant multiscale organominerals that are closely associated with fossilized remnants of extracellular polymeric substances (EPS) and putative bacteria fossils. These microfabrics are strikingly similar to those in dolomite precipitates produced in laboratory culture and modern sabkha environment, suggesting microbial origin. Nanoglobules (60–200 nm) preferentially attach to fossilized EPS filaments, and tend to merge into polyhedrons (3–8 μm) that in turn coalesce into microspheres (20–50 μm). EDS analysis revealed a successive decrease in carbon from nanoglobules to microspheres with the increases of Mg and Ca contents, implying an increased mineralization. Nanoglobules may have derived from EPS degradation during nucleation, and served as seeds for subsequent growth of carbonate polyhedrons. Microsphere, as a basic building block in dolostone, can transform into rhombohedral crystal via neomorphogenesis during early diagenesis. Petrographic and XRD analyses show that the dolostone is dominated by ordered dolomite and was largely formed in peritidal environment with thriving microbial community. Geochemical analyses of iodine species, redox sensitive elements, Ce anomalies, and C–O isotopes in the Wumishan dolostone suggested an environment predominated by anoxic to suboxic conditions, with low P but high Si contents in seawater. Our study offered direct evidence of microbial origin for the Mesoproterozoic dolostone, providing new insights into the “Dolomite Problem”. The massive development of microbial dolostone in Mesoproterozoic points to a specific ocean chemistry, where low oxygen and active bacterial metabolisms may have played crucial roles in precipitating dolomite. The co-existence of abundant microbial components and multiscale organominerals may be taken as textural evidence for microbial dolomites and signatures of life-environment interactions in deep time. (c2022 Elsevier B.V.)

NORTH CHINA PLATFORM

1,561,243

MESOPROTEROZOIC EARTH ORBITAL PERIOD AND THE EVOLUTION OF THE EARTH-MOON SYSTEM

X.Wang, S.Zhang and H.Wang (Res Inst Petrol Explor Dev). *21ST INTERNATIONAL SEDIMENTOLOGICAL CONGRESS [ISC]* (Beijing, China, 8/22-26/2022) *ABSTRACT BOOK* pp.162-163, 2022. (Available at <http://www.isc2022.org.cn> as of 9/22/2022; **Abstract only**)

The periodic variation of earth orbit parameters results in a multi-scale rhythm of sediment by controlling the surface climate and sea level changes. The identification of sediment cycle period can also be used to calculate the orbital parameters of geological history and to establish astronomical chronology scales with a resolution of 100,000 or even 10,000 years. There is relatively good astronomical time tuning for the Cenozoic strata and Mesozoic strata (Hinnov, 2018), while there are not so much evidences for Paleozoic studies, even scarce for Precambrian. North China holds the most continuous Mesoproterozoic strata (Wang et al., 2017). The deposition time from Changchanggou Formation to Xiamaling Formation is 1.65 to approximately 1.35 billion year in the Yanliao Basin, and the stratum has good rhythmic characteristics, covering nearly 8000 m, providing an excellent case for the study of Mesoproterozoic astronomical chronology. The periodic astronomical cycle of Milankovitch signal of eccentricity, obliquity and precession is identified from the studies of Hongshuizhuang, Tieling and Xiamaling formation, confirming the earliest

Milankovitch cycle and its controlling on the climate changes. The long eccentricity is 405 kyr, short eccentricity is 128 kyr, obliquity and precession is 28 kyr and 14 kyr by the spectral analysis of magnetic susceptibility, greyscale data, Cu/Al, Si, Zr/Al, and Ti/Al for Xiamaling Formation sedimentation, recording all of the major periods expected from the orbital forcing of solar insolation on Earth like today and much of the Phanerozoic Eon (Zhang et al., 2015). The Tieling formation records the same long eccentricity of 405 kyr, eccentricity from 86 to approximately 130 kyr, and the obliquity of 22.5 kyr (Lyu et al., 2021), and Hongshuizhuang formation holds a same long and short eccentricity, obliquity of 20-28.5 kyr and precession of 14-16 kyr (Cheng et al., 2020). Meyers and Malinverno (2018) got dominant climatic precession cycles of 14 kyr and eccentricity cycles of 131 kyr by using a Bayesian inversion approach to quantitatively link astronomical theory with Xiamaling geologic data, almost similar with data of Zhang et al (2015). So the short eccentricity is short than the modern of 100 kyr, and the obliquity and precession obtained from the Mesoproterozoic were obviously smaller than modern of 42 kyr and 23 kyr, which might reflect the closer distance between the earth and the moon and the shorter daytime (Meyers and Malinverno, 2018). Anyway, the Mesoproterozoic climate changes cause the same organic matter burial heterogeneity with Phanerozoic by affecting seawater circulation, seasonal/trade wind intensity and terrigenous input.

NORTHEAST CHINA REGION 1,561,244

THE EARLY PERMIAN ASSEMBLY OF THE JIAMUSI MASSIF AND KHANKA MASSIF: EVIDENCE FROM SEDIMENT SOURCES

Z.J.Xu, N.C.Sun, J.B.Zhou, J.T.Kong, R.H.Cheng and G.Li (Jilin Univ). *GEOLOGICAL JOURNAL* v.57, no.10, pp.4325-4344, Oct. 2022. (ISSN 0072-1050; ISSN 1099-1034)

The Jiamusi-Khanka Massif is an important tectonic unit of the Central Asian Orogenic Belt in North-east China. Its Late Palaeozoic tectonic properties and the timing of assembly have restricted the understanding of the tectonic evolution process at the eastern segment of the Central Asian Orogenic Belt for a long time. Based on the study of clastic rock petrology and zircon U-Pb chronology of the Early Permian Erlongshan Formation in Mishan, it is clear that the zircon age of the Early Permian Erlongshan Formation in Mishan is mainly Late Palaeozoic, with a major age peak at 300 ± 3 Ma and secondary age peaks at 356 ± 7 Ma and 475 ± 10 Ma. The provenance mainly comes from the magmatic arc source area, and Early Palaeozoic (500–420 Ma) detrital zircons mainly come from the south-east margin of Jiamusi Massif, Late Palaeozoic (400–270 Ma) detrital zircons mainly come from the eastern margin of Jiamusi Massif and the northern margin of Khanka Massif. Among them, detrital zircons of a special age group 330–310 Ma come from the north of Khanka Massif, while 490–470 Ma detrital zircons which are common in the Early-Middle Permian strata of Khanka Massif come from Jiamusi Massif. Combined with the evidence of petrology and palaeontology, this paper believes that the Early Permian Jiamusi Massif and Khanka Massif should be a unified Massif, that is, Jiamusi-Khanka Massif.

NORTH ISLAND 1,561,245

GENETIC LINK BETWEEN MIOCENE SEAFLOOR METHANE SEEP LIMESTONES AND UNDERLYING CARBONATE CONDUIT CONCRETIONS AT ROCKY KNOB, GISBORNE, NEW ZEALAND

C.S.Nelson, K.A.Campbell, S.L.Nyman, J.Greinert, D.A.Francis and S.D.Hood (Waikato Univ; Auckland Univ; Christian Albrechts Univ). *NEW ZEALAND JOURNAL OF GEOLOGY AND GEOPHYSICS* v.62, no.3, pp.318-340, 2019. (ISSN 0028-8306; ISSN 1175-8791)

Methane-derived authigenic carbonates (MDACs) in Miocene bathyal mudstones in North Island, New Zealand are typically expressed as either sub-seafloor conduit concretions or as seafloor seep limestones, but rarely are both types exposed in outcrop at one locality. Consequently, any potential genetic link between them is usually inferred. This also appears to be the case for global occurrences of MDAC. At the Rocky Knob seep complex near

GISBORNE both seep limestones and conduit concretions co-occur. The petrography and stable carbon ($\delta^{13}\text{C}$) and oxygen ($\delta^{18}\text{O}$) isotope compositions of their various authigenic carbonate components (automicrite, fibrous aragonite crystals, and granular, blocky and bladed calcite crystals) show that distinctive isotope and petrographic groupings for precipitates within the conduit concretions match or "correlate" with several of those in the seep limestones. This corroborates their genetic tie and derivation from the same fluids, albeit in different parts (i.e. sub-seafloor vs. seafloor) of the seep complex.

NORTH ISLAND 1,561,246

DECOLLEMENT STRENGTH AND MECHANICAL SEGMENTATION ALONG THE FRONTAL WEDGE OF THE HIKURANGI CONVERGENT MARGIN (NEW ZEALAND): INSIGHTS FROM CRITICAL TAPER ANALYSIS

C.O.Schwarze and N.Kukowski (Friedrich Schiller Univ). *TECTONOPHYSICS* v.844, 12/5/2022. (ISSN 0040-1951; Article no.229622)

To better understand the mechanics of outer forearcs, which is influenced to a large degree by the frictional properties of the plate interface, is a pre-requisite to address topics like natural hazard such as large earthquakes and slumping. Previous research including geodetic and geophysical measurements as well as critical taper analyses (CTA) has revealed that the mechanics of the Hikurangi margin (HM) offshore New Zealand may vary along the margin. However, the relationship between the morphology of the submarine margin and effective décollement strength of the Pacific-Australian plate boundary is not fully understood. From areal gridded data of surface slope (α) and plate dip (β) we characterise the central HM as an intermediate accretionary wedge and the northern HM as a non-accretionary wedge sensu Lallemand et al. (1994). Our areal CTA, comprising the entire region of the submarine margin from the transition to strike-slip faulting in the south to subduction erosion in the northernmost part of HM reveals significant variation of the effective décollement strength of the Pacific-Australian plate boundary. Altogether the décollement strength shows significant regional variability along the HM (0.02 to 0.21), increasing to the toe of the accretionary wedge, and in regions with seamount subduction. Furthermore, mean values of the décollement strength are increasing from the central (0.05) to the northern HM (0.09). Also, our CTA suggests moderate to high fluid overpressure along the plate interface. Finally, our approach of an areal computation of the décollement strength provides a low-effort and on the same hand helpful tool to characterise convergent margin mechanics. (c2022 Elsevier B.V.)

NORTHWEST TERRITORIES 1,561,247

OXYGEN, AGE AND FACIES CONTROLS ON THE APPEARANCE OF EDIACARAN AND CRYOGENIAN MACROSCOPIC FOSSILS IN THE MACKENZIE MOUNTAINS, NORTHWEST TERRITORIES, CANADA

E.A.Sperling, C.Carbonate, D.T.Johnston, G.M.Narbonne and F.A.Macdonald (Harvard Univ; Queen's Univ, Kingston). *58TH ANNUAL PALAEONTOLOGICAL ASSOCIATION MEETING (Leeds, UK, 12/16-19/2014) ABSTRACTS* pp.46-47, 2014. (Available at <http://www.palass.org> as of 11/15/2022; **Abstract only**)

The causes behind the appearance of abundant macroscopic fossils at the end of the Neoproterozoic remain debated. Iron geochemical analysis of fossiliferous Ediacaran successions in Newfoundland suggested that first appearances there were correlated with an oxygenation event. A similar relationship was claimed to exist in the Mackenzie Mountains, Canada, although recent stratigraphic studies indicate the sections analyzed for geochemistry were incorrectly correlated with those hosting the fossils. To directly connect fossils with geochemistry, we conducted a multi-proxy iron, carbon, sulfur, and trace element geochemical analysis of the sections hosting the Cryogenian "Twitya discs" at Bluefish Creek and Ediacaran fossils at Sekwi Brook. There is no oxygenation event correlated with the appearance of macroscopic body fossils in either section, or simple bilaterian burrows in the Blueflower Formation, although partial oxygenation appears

correlated with increasing burrow width higher in the Blueflower. Data from Sekwi Brook suggest that these organisms were periodically colonizing a predominantly anoxic basin, requiring assumptions of differing timescales between redox proxy data and ecological responses in order to reconcile fossil and geochemical data. Thus, hypotheses directly connecting ocean oxygenation with the appearance of macrofossils may be too simplistic or not apply to all areas of a heterogeneous Ediacaran ocean.

OMAN

1,561,248

THE AGE, ORIGIN AND CONTEXT OF RESERVOIR SANDSTONES UNDERLYING THE LOWERMOST SILURIAN "HOT" SHALES IN THE WEST OF THE SULTANATE OF OMAN

A.S.M.Al-Ghafri, A.P.Heward, G.A.Booth and I.A.Abbasi (OQ Explor & Prod LLC; Sultan Qaboos Univ). *JOURNAL OF PETROLEUM GEOLOGY* v.45, no.4, pp.345-362, Oct. 2022. (ISSN 0141-6421; ISSN 1747-5457)

The age and origin of reservoir sandstones which underlie the lowermost Silurian "hot" shales of the Sahmah Formation in the west of Oman is controversial. Here we describe one such sandstone which was cored and interpreted based on geological well evidence, and which then had to be re-interpreted when definitive palynological results became available. The findings are enhanced when interpreted along with other deep wells in the area which have consistent palynological data. The western part of the Sultanate of Oman is a tectonically stable intra-basinal high with low regional dips. In this area, the relief on the base-Silurian unconformity of >250 m appears to be greater than that beneath the Permo-Carboniferous unconformity which is well known for being highly erosive. The sandstones preserved beneath the base-Silurian unconformity vary in depositional environment and reservoir quality from well to well, depending on their age, degree of erosion and differences in regional subsidence. There has been little evidence for the presence of Hirnantian-aged deposits in Oman to date. However, some of the erosion and deep incisions which affect deposits of the Upper Ordovician Hasirah Formation are almost certainly related to falling sea levels accompanying the Hirnantian glaciation, just as the presence of the "hot shale" source rocks in the overlying Sahmah Formation are likely to be related to rising sea-levels and anoxic conditions during the later deglaciation. Deformed strata in the Upper Ordovician deposits may reflect the instability of valley-sides cut into weakly-consolidated strata exposed during changes in sea-level. The Sahmah oil play underlying the basal Silurian "hot" shales in Oman carries significant risks relating to the presence or absence of closures and reservoir, and the character, continuity and cementation of reservoir sandstones.

OMAN MT

1,561,249

MIXED DELTAIC AND CARBONATE DEPOSITION IN A TECTONICALLY RESTRICTED BASIN: AN EXAMPLE FROM THE LOWER AND MIDDLE MEMBERS OF THE EOCENE MUSAWA FORMATION, ABAT BASIN, SOUTH-EASTERN OMAN MOUNTAINS

I.Ahmed Abbasi, E.Ozcan, M.A.K.El-Ghali, O.S.Hersi, A.Al-Harthy and A.Ali (Sultan Qaboos Univ; Istanbul Technical Univ; Regina Univ; Petroleum Develop Oman Co). *GEOLOGICAL JOURNAL* v.57, no.10, pp.4242-4261, Oct. 2022. (ISSN 0072-1050; ISSN 1099-1034)

Mixed siliciclastic and carbonate sediments of the Eocene Musawa Formation were deposited in the Abat Basin in the south-eastern part of the Oman Mountains when the rest of the Arabian Plate was experiencing extensive carbonate sedimentation. The Musawa Formation was deposited as mixed siliciclastic and carbonate sediments in the Abat Basin bounded by the Ja'alan and Qalhat strike-slip faults. Movements along these bounding faults and extensive deformation in the source area provided an enormous amount of clastic sediments in a laterally restricted basin undergoing strong tectonic-related subsidence and was fed by basin axis parallel drainage system. The lithofacies assemblage represents fluvial and wave-dominated deltaic sediments that accumulated as a local siliciclastic feature in a carbonate-

dominated subtropical environment. The Musawa Formation is divided into three members, the lower, middle, and upper, based on lithological characteristics; however, this study focuses on the lower and middle members of the formation. The lower Musawa member is about 350 m thick, comprising laterally confined conglomerate (lithofacies GL) beds interbedded with Alveolina-bearing sandstone in the lowermost part of the formation. These beds were deposited as fan-delta on top of the underlying Ypresian limestone of the Abat Formation. The conglomerate beds grade up-section into over 170 m thick medium- to thick-bedded channelized sandstone lithofacies (lithofacies CSL), occasionally interbedded with mudstone and peat streaks. The sandstone sequence northwards of the study area passes into fine-grain lithofacies of siltstone and mudstone (lithofacies ML). The sandstone (CSL) was deposited in a delta-plain setting with coastline shifting northwards. The enormous thickness of the sandstone sequence is due to the location of the depocenter around Wadi Musawa area, from where the streams entered the basin and deposited their sediment load. The upper part of the lower Musawa member comprises interbedded clay, siltstone, and thin-bedded fine-grain sandstone (lithofacies association LFA3) deposited as mud-flat accumulations. The middle Musawa member is about 650 m thick, comprising both carbonate (LFA4) and siliciclastic (LFA2 and LFA3) lithofacies associations. The carbonate lithofacies association (LFA4) was deposited during flooding events. The marl lithofacies (CM) comprising branching corals, gastropods, and oysters was deposited in a lagoonal setting, whereas thick-bedded limestone lithofacies (CL) comprising *Nummulites* was deposited in open-marine conditions. Occasional coarse siliciclastic influx resulted in the deposition of mouth bar and shoreface lithofacies association (LFA2), especially in the upper part of the middle Musawa member. The mouth bar and shoreface sandstone interbedded with occasional chert-bearing conglomerate are laterally persistent across the Abat Basin outcrops.

ONTARIO

1,561,250

A NEW MARRELLOMORPH ARTHROPOD FROM SOUTHERN ONTARIO AND THE POTENTIAL FOR SOFT TISSUE PRESERVATION ON LATE ORDOVICIAN OPEN MARINE SHELVES

J.Moysiuk, A.Izquierdo-Lopez, G.E.Kampouris and J.B.Caron (Toronto Univ). *65TH ANNUAL PALAEOONTOLOGICAL ASSOCIATION MEETING (Manchester, UK, 12/18-20/2021) PROGRAMME AND ABSTRACTS* pp.37-38, 2021. (Available at <http://www.palass.org> as of 11/1/2022; **Abstract only**)

Post-Cambrian open marine Lagerstätten are rare and widely dispersed, producing a patchy picture of the diversity and biogeography of non-mineralized marine organisms and challenging our understanding of the fate of Cambrian groups. We report new soft-bodied fossils—including a marrellomorph arthropod, fragmentary carapaces and macroalgae—from the late Ordovician (Katian) Upper Member of the Kirkfield Formation near Brechin, Ontario, Canada. The non-mineralized elements are associated with an exceptionally preserved shelly biota that was entombed rapidly in storm deposits that smothered the shallow, carbonate-dominated shelf. The marrellomorph is remarkable for its ornate, curving cephalic spines and pair of hypertrophied appendages, suggesting a slow-moving, benthic lifestyle. Re-evaluation of marrellomorph phylogeny using new data favours an arachnomorph affinity, but internal relationships are robust to differing outgroup selection. Clades Marrellida and Acercostraca are recovered, but the monophyly of Marrellomorpha is uncertain. The new taxon is recovered as sister to the Devonian *Mimetaster* and, as the second-youngest known marrellid, bridges an important gap in the evolution of this clade. Taken together, the Kirkfield biota represents a rare window into Ordovician open marine shelf environments in Laurentia, representing an important point of comparison with contemporaneous Lagerstätten from other palaeocontinents with great potential for further discoveries.

ORDOS BASIN

1,561,251

SOURCE ROCK POTENTIAL OF THE UPPER TRIASSIC CHANG 7 MEMBER IN THE WESTERN ORDOS BASIN, CHINA

G.Chen, N.Wang, S.Yang, X.Li, P.Zhang and Y.Su (Yangtze Univ; PetroChina; Jiangsu Oilfield Co; Shandong Univ Sci Technol). *JOURNAL OF PETROLEUM GEOLOGY* v.45, no.4, pp.395-415, Oct. 2022. (ISSN 0141-6421; ISSN 1747-5457)

The Chang 7 member of the Upper Triassic Yanchang Formation is an important source rock in the Ordos Basin, NW China. Previous studies of the unit have in general focused on the relatively deep-water (ca 25 m) anoxic, OM-rich lacustrine mudstones which form the main Mesozoic source rock at fields in the south of the basin. However, this paper presents an integrated geochemical investigation of the relatively shallow-water Chang 7 facies in a study area around Jiyuan field in the western part of the basin in order to evaluate its source rock potential. The results show that the Chang 7 source rock in the study area has a high content of Type II OM, and is interpreted to have been deposited in a suboxic-anoxic lacustrine setting with a mixed input of aquatic and terrigenous organic matter. The results of 1D modelling of a well in the study area showed that the Chang 7 member entered the oil generation window from the Middle Jurassic. Oil-oil correlations based on hierarchical cluster analysis and correspondence analysis showed that crude oils generated by deep-water Chang 7 source rocks from wells in the south of the basin can be distinguished from Soxhlet-extracted petroleum from reservoir sandstones in the study area. The compositional differences are inferred to be due to variations in source rock facies compositions. An oil – source rock correlation study showed that the shallower-water Chang 7 source rock in the western part of the basin generated the hydrocarbons in core extracts of reservoir sandstones from wells in this area. The shallow-water Chang 7 facies may therefore constitute an effective oil-prone source rock in the western Ordos Basin.

ORDOS BASIN

1,561,252

DEVELOPMENTAL CHARACTERISTICS OF ORGANIC MATTER AND ITS ENRICHMENT MODEL IN SHALE RESERVOIRS OF CHANG7(3) MEMBER IN YANCHANG FORMATION OF SOUTHEAST ORDOS BASIN

G.Du, Z.Yang, H.Yin, F.Wang, Y.Chen and Y.Cui (Xi'an Shiyou Univ; PetroChina Research Inst). *PETROLEUM GEOLOGY AND RECOVERY EFFICIENCY (YOUQI DIZHI YU CAISHOULU)* v.29, no.6, pp.1-11, Nov. 2022. (ISSN 1009-9603; In Chinese)

[Full article and English abstract available from P.A.]

ORDOS BASIN

1,561,253

TECTONIC AND DEPOSITIONAL EVOLUTION OF MESO-NEO PROTEROZOIC IN ORDOS BASIN AND ITS PERIPHERY

Z.Ouyang, J.Feng and W.Li (Lanzhou City Univ; Xi'an Univ Sci & Technol; Northwest Univ, China). *21ST INTERNATIONAL SEDIMENTOLOGICAL CONGRESS [ISC] (Beijing, China, 8/22-26/2022) ABSTRACT BOOK* pp.270-271, 2022. (Available at <http://www.isc2022.org.cn> as of 9/22/2022; **Abstract only**)

The tectonic and sedimentary evolution of Meso-Neo Proterozoic in Ordos Basin and its periphery is ascertained in order to restore the original tectonic and sedimentary pattern and to explore oil and gas. In this paper, based on geological, seismic and logging data, the tectonic and depositional evolution of Meso-Neo Proterozoic have been studied in Ordos Basin and its periphery. The research shows that the Ordos Basin and its periphery underwent four tectonic and sedimentary evolutionary stages in Changchengian, Jixianian, Qingbaikou and Sinian Period of Meso-Neo Proterozoic. They are rift, passive continental margin, marginal subsidence and marginal depression, respectively. The Changchengian System was mainly composed of a set of terrestrial-littoral facies quartz sandstone, and developed braided river, delta, littoral shallow sea, shallow sea and deep sea sedimentary facies. The Jixianian System was mainly epeiric sea sedimentary facies with shallow water, including sand flat, dolomitic flat, flint dolomitic flat, open platform and shallow sea facies. Within Qingbaikou Period, the sedimentary environment of Ordos Basin and its periphery was retention marine basin and continental slope. There was glacial deposits in the Sinian System developed continental glacier, littoral sediment and shelf sedimentary facies.

ORDOS BASIN

1,561,254

GENESIS AND SEDIMENTATION OF THE MIDDLE PROTEROZOIC EN ECHELON RIFT IN THE WESTERN MARGIN OF THE NORTH CHINA PLATE

M.Li, X.Yan, Y.Guo and W.Zhang (Sinopec Research Inst). *21ST INTERNATIONAL SEDIMENTOLOGICAL CONGRESS [ISC] (Beijing, China, 8/22-26/2022) ABSTRACT BOOK* p.288, 2022. (Available at <http://www.isc2022.org.cn> as of 9/22/2022; **Abstract only**)

The en echelon rift located at the margin of continental plates is rare in the world, and its genetic mechanism has not been widely concerned. In the western margin of the North China Plate, a series of Mesoproterozoic rifts are developed in the Ordos Basin, which are characterized by en echelon distribution in the NE direction. At present, there are still different understandings about the genetic mechanism of this rift zone. This paper reviews the research progress of Columbia supercontinent, studies the characteristics of middle Proterozoic rift in Hangjinqi area, and puts forward a new interpretation scheme. Under the tectonic background of the Columbia supercontinent cracking, the western margin of the North China Plate moved relative to adjacent plate, resulting in the formation of boundary transform faults. Under the action of the translation shear, the localized extensional (T) faults developed in en echelon style, and a series of NW trending rift belts developed continuously. At the strike turning point at the end of the boundary transform fault, the associated T rupture strike shows NNE-NS-NNW deflection from east to west, and finally forms the diverging rift in the Hangjinqi area. The boundary transform fault is related to the spreading of the mid-ocean ridge within the supercontinent and is also subjected to the counterclockwise rotation of the North China plate. In this paper, the tectonic origin of the boundary shift fault is proposed, which explains the formation mechanism of the middle Proterozoic en echelon rift and the northern divergent rift on the western margin of the North China Plate. The Middle Proterozoic Yanlian rift in Ordos basin plays an important role in controlling stratigraphic deposition and hydrocarbon accumulation.

ORDOS BASIN

1,561,255

SEDIMENTARY RESPONSE TO ABRUPT CLIMATE CHANGE ACROSS THE HYPERTHERMAL PERMIAN-TRIASSIC BOUNDARY ON LAND, NORTH CHINA

Z.Zhu, Y.Liu, H.Kuang, A.J.Newell and M.J.Benton (Chinese Academy Geol Sci; British Geological Survey; Bristol Univ). *21ST INTERNATIONAL SEDIMENTOLOGICAL CONGRESS [ISC] (Beijing, China, 8/22-26/2022) ABSTRACT BOOK* p.200, 2022. (Available at <http://www.isc2022.org.cn> as of 9/22/2022; **Abstract only**)

The Permian-Triassic boundary (PTB, ca 252 Ma) witnessed the largest hyperthermal event ever, with the most drastic environmental changes and the most severe biotic extinction worldwide, both on land and in the oceans. The climate heated rapidly in low-latitude areas, caused by a huge and sharp input of greenhouse gases related to large igneous province volcanism (Siberia LIPs) and synchronous massive volcanism worldwide. This study investigates the sedimentary response to environmental changes across the terrestrial PTB in the eastern Ordos Basin, North China. The PTB is indicated by the die-off of tetrapods and plants, decreased bioturbation levels in the uppermost Sunjiagou Formation, and the bloom of microbially-induced sedimentary structures (MISS) in the Liujiagou Formation, supported by the sharp negative shift of carbon isotope and synchronous geochemical proxies. The abrupt sedimentary transition from Lopingian meandering rivers to Induan braided river-aeolian facies to Olenekian shallow lacustrine setting documents palaeoenvironmental changes from semi-arid to arid and then to semi-humid conditions, which is synchronous with the collapse and delayed recovery in palaeoecosystems and is likely to be one of the direct causes. Similar sedimentary responses to extreme climate crises on land have been reported elsewhere worldwide at the PTB (e.g. South Africa, Russia, NE Spain) and across other similar deep-time hyperthermal events (e.g. Paleocene-Eocene Thermal Maximum). Exploring their common features could test the idea that there is a "hyperthermal blueprint" or common pattern to such

events through geological time, but at different magnitudes that could inform our understanding of the current, Anthropocene climate crisis. Such a sedimentary response under a regime of warming, aridity and intermittent heavy precipitation on land may not only accumulate or amplify the signals of abnormalities and consequences in shallow marine settings but also connect the land and ocean.

ORDOS BASIN

1,561,256

NEW INSIGHTS INTO DEEP-LACUSTRINE ARCHITECTURAL ELEMENTS: EXAMPLES FROM THE UPPER TRIASSIC YANCHANG FORMATION, ORDOS BASIN

G.Bozetti, X.Li, Z.Yang, H.Liu, J.Huang, Z.Li and J.Xu (Southern Univ Sci Technol; Res Inst Petrol Explor Dev). *JOURNAL OF ASIAN EARTH SCIENCES* v.241, Jan. 2023. (ISSN 1367-9120; Article no.105431)

Deep-lacustrine systems are considerably less studied than their marine counterparts, mostly due to the low number of large and continuous outcrops worldwide. This study details outcrops and cores from Chang 7, Ordos Basin, China, which are composed dominantly of fine-grained deposits interbedded with amalgamated sandstones. Thick sandstone deposits, previously described as massive sandstones and interpreted as sandy debrites, are here re-interpreted as amalgamated sandstones, deposited by high-density turbidity currents associated with deep-lacustrine slope channels. Two outcrops composed of these deposits, which form intervals ranging from 6 to 20 m thick, laterally ranging from 600 to 1200 m, preserving evidence of sediment bypass such as erosional features and abundant trough cross-bedding, have been interpreted as lacustrine slope channels. Deposits composed dominantly of interbedded thin-bedded normal-graded sandstone and mudstone, with common occurrences of ripple cross-lamination (>70 % of the beds), interbedded with sporadic amalgamated medium-bedded sandstones have been interpreted as levee deposits. These deposits outcrop laterally to slope channel deposits, supporting the interpretation they are genetically and architecturally related. Similar deposits are also described in core, overlying channelised sand-prone deposits. Interbedded thin- to medium-bedded normal-graded sandstones and mudstones, which are not associated with a confining surface (non-channelised), nor an adjacent slope channel, have been interpreted as terminal splays. The re-interpretation of the sandstone-prone deposits of the Yanchang Formation as slope channel-levees to terminal splays provides a different approach to lateral and temporal distribution of architectural elements in intracratonic lacustrine basins, and therefore hydrocarbon exploration and production. (c2022 Elsevier Ltd.)

ORDOS BASIN

1,561,257

OUTCROP MODELING OF FLOW UNITS AND REDUCTANT WITHIN A SANDSTONE URANIUM RESERVOIR IN THE ZHILUO FORMATION, EASTERN ORDOS BASIN: IMPLICATIONS FOR THE URANIUM MINERALIZATION MECHANISM

Z.Tao, Y.Jiao, L.Wu and H.Rong (Huanggang Normal Univ; China Univ Geosci, Wuhan). *21ST INTERNATIONAL SEDIMENTOLOGICAL CONGRESS [ISC] (Beijing, China, 8/22-26/2022) ABSTRACT BOOK* p.1567, 2022. (Available at <http://www.isc2022.org.cn> as of 9/22/2022; **Abstract only**)

The spatial distribution of flow units and reductant within a sandstone uranium reservoir is very beneficial for exploring the uranium mineralization mechanism; however, such studies have been almost neglected. As such, this paper aims to provide the sedimentological interpretation and heterogeneity models of the sandstone of the Middle Jurassic Zhiluo Formation at Shiwan outcrop area, in the eastern Ordos Basin. The outcrops are sandstone-dominated subaqueous distributary channel successions, in which five distinct architectural elements are identified and interpreted: channel units (CU), downstream accretion elements (DA), lateral accretion elements (LA), sandy bedforms (SB) and non-channelized fine-grained sediments (NFS). Within the sandstone succession, six flow units are present in the middle and lower parts of CU, or the lower parts of DA and SB elements, with their

geometry to be controlled by the fourth- or third-order bounding surfaces. Moreover, the carbonaceous debris-rich zones (CDZ) are places with the highest abundance of reductant and preserve exclusively upon the basal erosional surfaces of CU and DA elements. Based on those results, a prediction model is established and shows that the formation of interlayer oxidation zone is strongly selective and confined within the CU and DA elements. The favorable sites of uranium mineralization are preferentially distributed in the transition zone between the front of flow unit and the CDZ.

ORDOS BASIN

1,561,258

SEDIMENTOLOGICAL RESPONSE OF LATE TRIASSIC CARNIAN PLUVIAL EPISODE (CPE) IN LACUSTRINE BASIN: A CASE STUDY FROM YANCHANG FORMATION OF ORDOS BASIN

X.Li (NWGI). *21ST INTERNATIONAL SEDIMENTOLOGICAL CONGRESS [ISC] (Beijing, China, 8/22-26/2022) ABSTRACT BOOK* p.232, 2022. (Available at <http://www.isc2022.org.cn> as of 9/22/2022; **Abstract only**)

The Carnian Pluvial Episode (CPE event) is one of the most significant climate abrupt events on Earth in the Triassic, and the abrupt climate environment has an important control effect on the sediment characteristics of inland lake basins. In this paper, the most important petroliferous basin on land in my country: the Triassic Yanchang Formation in the Ordos Basin is taken as an example. Based on the latest research progress on global paleoclimate, event sedimentation, source rock development mechanism and heterogeneous integration surface in terrestrial basins, based on full reference at home and abroad, and through rethinking and researching some sedimentation and accumulation problems of the Yanchang Formation, the following three points of understanding have been obtained: The Carnian period of the Middle-Upper Triassic Yanchang Formation in the basin has been redefined, and the sedimentary response to the CPE event of the Yanchang Formation has been clarified. The top boundary is equivalent to the stratigraphic boundary between the Chang 4 + 5 member and the Chang 3 member, and the CPE event roughly corresponds to the deposition of the "Chang 7 member black shale event"; During the Carnian and CPE events, the Yanchang Formation sedimentary lake basin showed the characteristics of "rapid lacustrine transgression and oscillating slow retreat", which is very conducive to the development of high-quality source rocks; Affected by the paleo-climate and CPE events in the Carnian period, the Yanchang Formation developed two upper and lower xenconformity formed due to abrupt climate and environment, and they both had a significant control effect on the distribution of oil and gas. This research is of positive significance for in-depth discussion of the formation and evolution mechanism of Yanchang Formation lake basin, sedimentary sequence filling and evolution characteristics, and guiding the practice of oil and gas exploration.

PABDEH FM

1,561,259

ENHANCED STORM-INDUCED TURBIDITIC EVENTS DURING EARLY PALEOGENE HYPERTHERMALS (ARABIAN CONTINENTAL MARGIN, SW IRAN)

J.Jiang, X.Hu, E.Garzanti, J.Li, M.K.BouDagher-Fadel, G.Sun and Y.Xu (Nanjing Univ; Milano-Bicocca Univ; London Univ Coll). *21ST INTERNATIONAL SEDIMENTOLOGICAL CONGRESS [ISC] (Beijing, China, 8/22-26/2022) ABSTRACT BOOK* p.182, 2022. (Available at <http://www.isc2022.org.cn> as of 9/22/2022; **Abstract only**)

Early Paleogene hyperthermal episodes including the Paleocene-Eocene Thermal Maximum (PETM) have long been viewed as analogues of the Anthropocene global warming. Few studies, however, have analyzed the environmental consequences of such climatic anomalies in deep-water turbidite-rich successions. This integrated sedimentological, biostratigraphic, and stable-isotope study of the Paleogene Pabdeh Formation, deposited along the Arabian continental margin of southwestern Iran, allowed us to document the geological response of hyperthermal events in deep Neo-Tethyan Ocean. The late Thanetian event (Pre-Onset Excursion or long-term late Paleocene climatic perturbation), the

Early Eocene Climate Optimum, and the Middle Eocene Thermal Maximum were successfully identified within the Pabdeh Formation. The PETM event could not be documented because the Paleocene/Eocene boundary corresponds to a prolonged non-depositional hiatus marked by a glauco-phosphorite interval. Based on high-resolution microfacies analysis, three different processes in a carbonate slope to basin-margin environment were distinguished including pelagic settling, upwelling-condensation-reworking, and storm-induced turbiditic deposition. Detailed sedimentological analysis revealed an anomalous abundance of storm-induced proximal to distal turbidites represented by packstones with deep-water and reworked shallow-water bioclasts occurring during the hyperthermal intervals. A close causal link between climate warming and tropical storms during the early Paleogene hyperthermal events is thus envisaged. As a principal mechanism, we propose that rapid warming in response to massive carbon release triggered pronounced sedimentological changes along low-latitude tropical margins, leading to generation of storm-induced calciturbidite and re-deposition in the deep sea during hothouse stages.

PALEOECOLOGY

1,561,260

ANCIENT LIFE IN MOVING FLUIDS: USING COMPUTER FLOW SIMULATIONS TO RECONSTRUCT THE PALAEOECOLOGY OF THE FIRST ANIMAL COMMUNITIES

S.G.Diaz, E.G.Mitchell, F.S.Dunn, B.M.Gibson, R.A.Racicot, S.A.F.Darroch and I.A.Rahman (London Museum; Cambridge Univ; Oxford Univ). *65TH ANNUAL PALAEOONTOLOGICAL ASSOCIATION MEETING (Manchester, UK, 12/18-20/2021) PROGRAMME AND ABSTRACTS* p.69, 2021. (Available at <http://www.palass.org> as of 11/1/2022; **Abstract only**)

The Ediacaran biota (ca. 571-539 Ma) represents the first radiation of complex macroscopic life on Earth. This period ushered in an extraordinary diversity of benthic forms, including the first animals. The Ediacaran-Cambrian transition--the biotic turnover that corresponds with the emergence of animal-dominated ecosystems--remains poorly understood in part due to uncertainties surrounding the palaeoecology of Ediacaran organisms, most of which lack modern analogues. In recent years, computational fluid dynamics (CFD) has emerged as a powerful tool to aid functional inference in these enigmatic organisms, enabling rigorous hypothesis-testing relating to feeding in individual Ediacaran taxa. Here we applied CFD for the first time to Ediacaran multi-organismal arrays. We used R to simulate virtual communities based on in situ fossil beds from the Avalon assemblage (ca. 571-560 Ma), recreating Earth's oldest Ediacaran communities using 3D computer modelling software. We then carried out CFD simulations for different virtual communities from this assemblage. Results from these analyses allow us to elucidate the impact of community structure and composition on vertical mixing. Ultimately, assessing how these patterns changed through time will shed light on the evolution of ecosystem engineering during the Ediacaran and its role in the emergence of the modern marine biosphere.

PALEOPROTEROZOIC

1,561,261

TECTONIC QUIESCENCE TRIGGERED THE EARLY PALEOPROTEROZOIC GLACIAL CLIMATE AND THE ONSET OF THE GREAT OXIDATION EVENT

X.Ma and G.Luo (China Univ Geosci, Wuhan). *21ST INTERNATIONAL SEDIMENTOLOGICAL CONGRESS [ISC] (Beijing, China, 8/22-26/2022) ABSTRACT BOOK* p.212, 2022. (Available at <http://www.isc2022.org.cn> as of 9/22/2022; **Abstract only**)

The Great Oxidation Event (GOE), a milestone event in the evolutionary history of habitable Earth, generally coincided with the Paleoproterozoic glacial climate. However, the causal-effect relationships between these two events remain controversial. Here, we investigate the continental chemical weathering, which is the critical link between these two events, by compiling a global data set of the chemical index of alteration (CIA) in this interval from 2600 to 2000 Ma. Our results demonstrate that the time period

from ca 2430 to 2340 Ma is generally characterized by limited continental chemical weathering, coinciding with the glacial climate and tectonic quiescence revealed by the compiled data of U-Th-Pb ages of zircons and volume of the large igneous province (LIP). The limited continental chemical weathering suggests that the nutrients fluxed into the ocean would be very low, which would restrict O₂ production. Therefore, we proposed that both the glacial climate and onset of the GOE were attributed to tectonic quiescence, which decreases the CO₂ and reducing gases released into the atmosphere. The resurgence of the tectonic activity ca 2340 Ma could trigger the termination of glacial climate, result in a significant increase in the continental chemical weathering, and, consequently, promote the large increase in pO₂ indicated by the high $\delta^{13}C$ values in the interval from ca 2250 to 2060 Ma.

PAMIR MT AREA

1,561,262

MESOZOIC TECTONIC EVOLUTION IN THE KURGOVAT-VANCH COMPLEX, NW PAMIR

Y.Li, A.C.Robinson, M.Zucali, M.Gadoev, I.Oimuhammadzoda, T.J.Lapen and B.Carrapa (Houston Univ; Tajikistan Academy Science; Arizona Univ). *TECTONICS* v.41, no.10, Oct. 2022. (ISSN 0278-7407; ISSN 1944-9194; Article no.e2021TC007180)

Different crustal deformation histories between Tibet and the Pamir reflect along-strike variations in geodynamics of the Tethys orogen. To investigate the less well-documented deformation history of the Pamir, which has been a barrier in understanding the nature of these differences, we conducted an integrated study in the Kurgovat-Vanch region, NW Pamir. The lithologies are primarily Ediacaran-to-Carboniferous metasedimentary rocks intruded by Carboniferous plutons, which then experienced Late Triassic to Early Jurassic regional metamorphism. Structural mapping and analyses document a low-angle NW-directed thrust fault, the Poshkharv thrust, separating the overlying upper-greenschist facies Poshkharv complex from the underlying amphibolite facies Kurgovat complex. Regional geologic maps indicate the Poshkharv thrust continues for ca. 300 km across the NW Pamir. Our study also documents another regional thrust fault, the top-to-the-SE Vanch thrust that juxtaposes the Southern Kurgovat complex above the lower-grade Vanch complex in the south. Biotite ⁴⁰Ar/³⁹Ar thermochronology indicates Early Cretaceous movement on all structures with ca. 135–125 Ma exhumation along the NW-directed Poshkharv thrust and ca. 125–115 Ma exhumation along the SE-directed Vanch thrust. Regional crustal deformation in the Northern Pamir was formed in a Cretaceous retro-arc setting, unrelated to the Cenozoic India-Asia collision. Cretaceous deformation in the NW Pamir was broadly coeval with the NE Pamir, but preceded Cretaceous shortening and coeval arc magmatism in the Southern Pamir. We interpret Early Cretaceous thrusting and crustal thickening followed by southward migration of shortening and magmatic flare-up in the Pamir to have resulted from a transition of Neotethys subduction from northward flat-slab advancing to southward retreating.

PATAGONIA

1,561,263

TECTONIC SUBSIDENCE MODELING OF DIACHRONOUS TRANSITION FROM BACKARC TO RETROARC BASIN DEVELOPMENT AND UPLIFT DURING CORDILLERAN OROGENESIS, PATAGONIAN-FUEGIAN ANDES

R.A.VanderLeest, J.C.Fosdick, M.A.Malkowski, B.W.Romans, M.C.Ghiglione, T.M.Schwartz and Z.T.Sickmann (Connecticut Univ, Storrs; Texas Univ, Austin; Virginia Tech). *TECTONICS* v.41, no.10, Oct. 2022. (ISSN 0278-7407; ISSN 1944-9194; Article no.e2021TC006891)

Backstripped tectonic basin subsidence histories are critical for interpreting phases of lithospheric deformation and paleoenvironmental change from the stratigraphic record. This study presents new subsidence modeling of the Rocas Verdes Backarc Basin (RVB) and Magallanes-Austral retroarc foreland basin (MAB) of southernmost South America to evaluate along-strike changes in tectonic subsidence related to the Late Jurassic through Miocene history of the Southern Andes. We compiled composite stratigraphic sections for seven basin localities that span 47°–54°S from published sedimentological records of

paleoenvironment, paleobathymetry, and geochronology. Modeling results resolve regional trends in basin tectonic subsidence, uplift, and sedimentation rate that influenced the depositional environment during five broad phases of RVB-MAB development: (a) Late Jurassic tectonic subsidence and basin deepening associated with rift-related backarc extension that postdated regional diachronous rift-related magmatism. (b) Southward younging of Early to Late Cretaceous pronounced acceleration in tectonic subsidence interpreted as the initiation of flexural loading and development of the MAB foreland basin system. (c) Late Cretaceous (ca. 85-70 Ma) tectonic uplift within the central foredeep ca. 49° to 52°S, coeval with a shift from slope to shelf deposition at these latitudes. (d) A protracted period of low-magnitude basin uplift and relative tectonic quiescence during the Paleogene, with the exception of southernmost localities; and (e) Synchronous latest Oligocene-early Miocene tectonic subsidence linked to basin deepening and transgression across the northern and central basin sectors. Backstripped tectonic subsidence analysis corroborates existing interpretations for orogenic development in the RVB-MAB and sheds new light on complex polyphase basin histories where extension precedes convergence.

PATAGONIA

1,561,264

EARLY CRETACEOUS TO CENOZOIC GROWTH OF THE PATAGONIAN ANDES AS REVEALED BY LOW-TEMPERATURE THERMOCHRONOLOGY

G.Ronda, M.C.Ghiglione, J.Martinod, V.Barberon, M.E.Ramos, I.Coutand, D.Grujic and R.Kislitsyn (Buenos Aires Univ; Savoie Univ). *TECTONICS* v.41, no.10, Oct. 2022. (ISSN 0278-7407; ISSN 1944-9194; Article no.e2021TC007113)

The Southern Patagonian Andes at the latitude of the Chile Triple junction in Argentina and Chile (46°–47.5°S) are the object of an ongoing discussion regarding their orogenic evolution in terms of tectonic crustal thickening and exhumation. Recent works point to an Early Cretaceous onset of shortening according to observations in foreland sequences. The ensuing Cenozoic thermal history of the region was influenced by increased shortening, oceanic-ridge collision and formation of asthenospheric windows in a dynamic subduction setting. Furthermore, the onset of Patagonian glaciations after 7 Ma added increased complexities to the analysis of the main drivers of crustal cooling in this region. We applied zircon (U-Th)/He and apatite fission track thermochronometry, and inverse thermal modeling to unravel the thermal history throughout different structural domains of the Patagonian Andes. New thermochronological data and thermal models showed a previously unrecognized set of Cretaceous cooling ages (120-80 Ma) toward the foreland, that we relate to the onset of contraction during initial tectonic inversion. Toward the hinterland, Cenozoic cooling ages predominate, and are related to Oligocene-Miocene contraction in response to increased subduction velocities. Based on the regional distribution of thermochronological ages and on results from thermal modeling, a resetting of the zircon (U-Th)/He and apatite fission track systems in response to crustal heating related to the formation of an asthenospheric window after 16 Ma appears unlikely. After 7 Ma cooling rates increased in response to enhanced glacial erosion.

PELECYPOD

1,561,265

A GLOBAL PERSPECTIVE OF THE TRIGONIIDA (BIVALVIA: PALAEOHETERODONTA), WITH A FOCUS ON THEIR MESOZOIC AND CENOZOIC REPRESENTATIVES

S.Schneider and S.R.Kelly (CAS). *58TH ANNUAL PALAEOONTOLOGICAL ASSOCIATION MEETING (Leeds, UK, 12/16-19/2014) ABSTRACTS* pp.42-43, 2014. (Available at <http://www.palass.org> as of 11/15/2022; **Abstract only**)

The Trigoniida (Dall, 1889) are a globally important group of dominantly marine Bivalvia that peaked during the Mesozoic, when they played an influential role in shallow marine communities. The anticipated revision of the bivalve volumes of the Treatise has fostered the authors' attempt to make a global genus-level systematic arrangement for the Mesozoic and Cenozoic Trigoniida. Currently, classification is not based on rigid phylogenetic analysis, but on qualitatively defined apomorphies.

Nevertheless, it allows us to identify several palaeogeographically and stratigraphically well-constrained clades. Other clades—in particular the Myophorellidae and Pterotrioniidae—are considerably less resolved and their subdivision is controversially discussed, mainly due to conflicting genus-level concepts. A circum-Pacific origin seems obvious for most of the Triassic clades of the Trigoniida. Subsequently, the break-up of Pangaea and later Gondwana created space for global expansion across shelf seas. At the same time, isolation forced more localized radiations of several groups. We present chronostratigraphic range charts for the genera currently recognized as valid, supplemented by palaeogeographic distribution maps for selected taxa. We further exemplarily discuss difficulties of generic assignment in the Myophorellidae. Finally, we propose a revised classification for the Trigoniida that is put up for discussion.

PELECYPOD

1,561,266

RUDIST MYOPHORES: CONSTRUCTIONAL CONSTRAINTS AND PHYLOGENETIC INFORMATIVENESS

P.W.Skelton (Open Univ). *58TH ANNUAL PALAEOONTOLOGICAL ASSOCIATION MEETING (Leeds, UK, 12/16-19/2014) ABSTRACTS* pp.43-44, 2014. (Available at <http://www.palass.org> as of 11/15/2022; **Abstract only**)

Molluscan muscle/shell attachment is mediated by adhesive epithelium, which secretes a collagenous "tendon sheath" bonded to the shell by embedded fibres. Serial detachment and re-attachment of muscle fibres allows growth migration of the muscles across the epithelium. But tendon sheath adhesion to the shell constrains normal growth of the latter. Hence, for the adductors to maintain their relative positions in the shell during growth, the insertion surfaces must remain coplanar with their growth trajectories. In most bivalves, muscle scars thus lie flush on the inner valve surfaces, tracking the radial growth of the valve margins. Primitive rudists maintained this pattern, albeit with the posterior adductor migrating helicospirally along myophoral ledges that limited the muscle's length. With further muscle shortening the myophores became flat extensions of the hinge plates. But with the onset of uncoiled valve growth accompanying ligamentary invagination, the adductor insertions had to tilt away from the commissural plane to allow them to track the now orthogonally growing valve margins. Different clades of uncoiled rudists followed contrasting options for such myophoral tilting. Each re-arrangement proved virtually irreversible, however, so imparting a reliable phylogenetic signal, as illustrated for example by contrast between the caprinoid families Caprinidae and Caprinuloideidae.

PENGLAI FIELD

1,561,267

PORE-THROAT CHARACTERISTIC RESPONSE OF DIFFERENT SEDIMENTARY MICROFACIES OF SHALLOW-WATER BRAIDED RIVER DELTA RESERVOIRS IN GUANTAO FORMATION, BOHAI BAY BASIN, CHINA

Z.Wang and H.Tang (Southwest Petroleum Univ). *21ST INTERNATIONAL SEDIMENTOLOGICAL CONGRESS [ISC] (Beijing, China, 8/22-26/2022) ABSTRACT BOOK* p.1553, 2022. (Available at <http://www.isc2022.org.cn> as of 9/22/2022; **Abstract only**)

The Guantao Formation Reservoir in the Penglai Oilfield is a loose sandstone with high porosity and high permeability. The reservoir diagenesis is weak and is dominated by compaction diagenesis. However, insufficient research into the relationship between sedimentary microfacies and pore structure characteristics, which restricts the prediction of favorable reservoir distribution and the scientific implementation of development plans. In this paper, the loose sandstone reservoir of Neogene Guantao Formation in Penglai Oilfield are targeted to clarify and estimate the sensitivity of pore structure characteristics to sedimentary microfacies and the main controlling factors affecting the microscopic pore structure of the reservoir are quantitatively analyzed by grey correlation analysis. Firstly, the main sedimentary microfacies types of Guantao formation reservoir are identified based on core and logging data. Then, the reservoir characteristics of different sedimentary microfacies, such as reservoir space types, pore size distribution, fractal dimension,

grain size characteristics and mineral distribution were revealed by means of high-pressure mercury injection, laser grain size analysis, core analysis and scanning electron microscopy. Finally, after the above parameters are extracted, grey correlation analysis is applied to quantitatively analyze the main controlling factors affecting the pore structure characteristics. The results show that the pore structure of various sedimentary microfacies is comprehensively influenced by the sedimentary texture and differences in mineral distribution. Characterized by more abundant hard siliceous minerals, positive skewness, and lower pore sorting coefficients, the arenaceous microfacies possess larger pore-throat radius and lower pore fractal dimensions than argillaceous microfacies. Using the grey correlation method, it is clarified that the order of importance affecting the pore structure characteristics is the mean grain size > median grain size > potassium feldspar > plagioclase > kaolinite > sorting > mix-layer illite/smectite > skewness > quartz > chlorite > illite. These results provide new insights for studying the control mechanism of microfacies controls on reservoir quality.

PHOSPHATE MINERAL 1,561,268

AN EARLY CAMBRIAN WINDOW INTO MECHANISMS FOR PHOSPHATIZATION OF LABILE SOFT TISSUES

M.L.Nielsen, P.R.Wilby, M.Lee, A.T.Nielsen, T.Y.S.Park and J.Vinther (Bristol Univ; British Geological Survey; Korea Polar Research Inst; Copenhagen Univ). *58TH ANNUAL PALAEOLOGICAL ASSOCIATION MEETING (Manchester, UK, 12/18-20/2021) PROGRAMME AND ABSTRACTS* pp.38-39, 2021. (Available at <http://www.palass.org> as of 11/1/2022; **Abstract only**)

Phosphatization has the potential to preserve labile soft tissues in exquisite detail, providing a wealth of otherwise unavailable information. However, previous studies and laboratory experiments suggest that the process is highly biased, ultimately affecting our view of the fossil record. The scarcity of phosphatized fossils at any given locality prevents a comprehensive synthesis of the relationship between depositional environments and taxon-specific anatomy/composition, giving rise to phosphatized tissues. Here we explore the lower Cambrian Sirius Passet Lagerstätte (North Greenland) where phosphatized fossils are abundant. The work is based on both qualitative and quantitative (phosphatized $n > 700$) data. The depositional environment is characterized by frequent depositional events with dense accumulations of fossils (on average about 77 specimens per 1,000 cm³) and organic fragments, and occasional microbial mats. There is a strong bias both between and within taxa, explained by size, diet and anatomy. Organisms with high phosphorus content are favoured (e.g., large muscle volume, carnivorous diet). Muscle phosphatization is generally less frequent in small specimens (juveniles?) and species. Muscles phosphatize more readily in the axial region and near phosphorous-rich tissues (e.g., gut diverticula and ganglia). Gut diverticula phosphatize more frequently than the gut tract. Closed local environments, exemplified by enrolled arthropods, favour extensive phosphatization.

PHOTOSYNTHESIS 1,561,269

PHOTOSYNTHESIS IN PROTEROZOIC OCEANS: EVOLUTIONARY AND ECOLOGICAL INNOVATIONS

N.J.Butterfield (Cambridge Univ). *58TH ANNUAL PALAEOLOGICAL ASSOCIATION MEETING (Leeds, UK, 12/16-19/2014) ABSTRACTS* p.14, 2014. (Available at <http://www.palass.org> as of 11/15/2022; **Abstract only**)

Oxygenic photosynthesis has been driving the global carbon cycle for at least the past three billion years, but the manner in which it has been packaged, and the associated geobiological feedbacks have changed radically over this time. The body-fossil record documents effectively modern cyanobacterial mat biotas in sunlit settings since at least the mid-Palaeoproterozoic, imparting a pervasive sedimentary fabric and accompanying taphonomic signatures. Eukaryotic microfossils are also known from at least the late Palaeoproterozoic, most likely representing benthic photosynthesizers. By the late Mesoproterozoic and early Neoproterozoic these have been joined by a range of unicellular and multicellular plant-protists, though sedimentological and molecular

biomarker data point to the continued ecological dominance of cyanobacteria. Eukaryotes were not contributing significantly to ecosystem function until the middle Neoproterozoic, documented by the first quantitative occurrence of testate eukaryotic steranes. Along with the coincident appearance of testate amoebae and biomineralized scale microfossils, these biomarker data identify a major reorganization of the biological pump--with important implications for interpreting the redox geochemistry and climatic perturbations of the later Neoproterozoic. Full eukaryotic control of marine productivity was achieved during the Ediacaran and Cambrian radiations, establishing the default Phanerozoic condition. The belated shift to a eukaryote-dominated carbon cycle is best explained as a co-evolutionary byproduct of early animal evolution.

PHOTOSYNTHESIS 1,561,270

ENVIRONMENTAL INSTABILITY FOLLOWING THE RISE OF OXYGENIC PHOTOSYNTHESIS

S.Poulton (Leeds Univ). *58TH ANNUAL PALAEOLOGICAL ASSOCIATION MEETING (Leeds, UK, 12/16-19/2014) ABSTRACTS* p.15, 2014. (Available at <http://www.palass.org> as of 11/15/2022; **Abstract only**)

The evolution of oxygenic photosynthesis irrevocably changed the course of chemical and biological evolution on Earth. Yet, despite this significance, the timing of the evolution of oxygenic photosynthesis is extremely poorly constrained, as are the resultant dynamics and consequences of biospheric oxygenation. Over recent years a wealth of geochemical and geological data has been produced, which in general converges on an environmental signal of oxygenic photosynthesis by at least 2.7 Ga, although more speculative data suggests a much earlier origin. Thus, it appears likely that oxygenic photosynthesis evolved at least several hundred million years before the Great Oxidation Event at ca. 2.3 Ga. The evolution of oxygenic photosynthesis essentially threw the Earth into a state of turmoil, and it took more than two billion years to achieve the (more or less) stable levels of oxygenation experienced during the Phanerozoic. As well as providing a broad overview of Earth's oxygenation history, this presentation will include new data that questions both the timing of persistent atmospheric oxygenation, and the concept of an irreversible rise in oxygen after the rise of oxygenic photosynthesis.

PHYLOGENY 1,561,271

DOES TIME MATTER IN PHYLOGENY? A PERSPECTIVE FROM THE FOSSIL RECORD

P.Guenser, R.C.M.Warnock, W.Pett, D.De Vleeschouwer, P.C.J.Donoghue and E.Jarochowska (Friedrich Alexander Univ; Iowa State Univ; Bremen Univ; Bristol Univ). *65TH ANNUAL PALAEOLOGICAL ASSOCIATION MEETING (Manchester, UK, 12/18-20/2021) PROGRAMME AND ABSTRACTS* pp.27-28, 2021. (Available at <http://www.palass.org> as of 11/1/2022; **Abstract only**)

The role of time (i.e., taxa ages) in phylogeny has been a source of intense debate within palaeontology for decades, and the debate has not yet been fully resolved. The fossilized birth-death range process is a model that explicitly accounts for information about species through time. It presents a fresh opportunity to examine the role of stratigraphic data in phylogenetic inference of fossil taxa. Here, we apply this model in a Bayesian framework to an exemplary dataset of well-dated conodonts from the Late Devonian. We compare the results to those obtained using traditional unconstrained tree inference. We show that the combined analysis of morphology and stratigraphic data under the FBD range process reduces the overall phylogenetic uncertainty compared to unconstrained tree inference. We find that previous phylogenetic hypotheses based on parsimony and stratophenetics are closer to trees generated under the FBD range process. However, the results also highlight that irrespective of the inclusion of age data, a large amount of topological uncertainty will remain. Thus, Bayesian inference provides the most intuitive way to represent the uncertainty inherent in fossil datasets, and new flexible models increase opportunities to refine hypotheses in palaeobiology.

PILBARA CRATON

1,561,272

SUB-MICROMETRE 2D-3D INVESTIGATION OF THE HYDROTHERMAL MINERALIZATION OF EARTH'S OLDEST STROMATOLITES (CA. 3.5 GA)

K.Hickman-Lewis, B.Cavalazzi, K.Giannoukos, L.d'Amico, S.Vrbaski, G.Saccomano, D.Dreossi, G.Tromba, F.Foucher et al. (London Museum). *65TH ANNUAL PALAEOONTOLOGICAL ASSOCIATION MEETING (Manchester, UK, 12/18-20/2021) PROGRAMME AND ABSTRACTS* pp.69-70, 2021. (Available at <http://www.palass.org> as of 11/1/2022; **Abstract only**)

Palaeoarchaeon stromatolites are among the oldest compelling evidence for life. Here we present advanced 2D-3D reconstructions of the morphology, mineralogy, trace element geochemistry and taphonomy of permineralized stromatolites from the lowermost ca. 3.5 Ga North Pole Chert, Dresser Formation, Pilbara, Western Australia. These stromatolites comprise syndepositional silica and baryte, and recent iron oxides. Rare earth element compositions suggest marine deposition; this contrasts with younger Dresser stromatolites, which are interpreted to have developed around hot springs. The intimate association of stromatolites with chert-barite veins and strong Eu anomalies in chert denote pervasive, syndepositional hydrothermal activity, promoting exceptionally high-fidelity microstructural preservation. Although no primary kerogen is preserved, numerous 2D-3D morphological characteristics are consistent with a biogenic origin. Phototrophic growth is evidenced by non-isopachous laminations with crestal thickening, fine-scale undulatory laminations, ragged and laminoid fenestrae, and sub-vertical fabric elements resembling microbial palisade structure. 3D reconstructions using laboratory and synchrotron approaches highlight the utility of tomography for non-destructive, high-resolution analyses of fossil microbialites. The correlated micro-analytical strategy used cements the Dresser stromatolites as the oldest convincing microbial fossils and could be applied to samples returned from Mars, where extracting large amounts of geochemical information from small amounts of potentially fossiliferous materials will be essential.

PLANKTONIC FORAMINIFERA

1,561,273

EVOLVING ECOLOGY AND MORPHOLOGY OF NEOGENE PLANKTONIC FORAMINIFERA

G.Lamyman and T.Aze (Leeds Univ). *65TH ANNUAL PALAEOONTOLOGICAL ASSOCIATION MEETING (Manchester, UK, 12/18-20/2021) PROGRAMME AND ABSTRACTS* p.75, 2021. (Available at <http://www.palass.org> as of 11/1/2022; **Abstract only**)

Planktonic foraminifera are marine microorganisms that have the most complete fossil record of the Cenozoic era. As such, they are widely employed to generate palaeoceanographic proxy data and to address evolutionary questions at the species level. In this work, we use a high-resolution direct sampling approach to investigate the paired morphological and ecological evolution of a group of enigmatic clavate planktonic foraminifera: the *Globigerinella* and *Beella* lineages. This high-resolution analysis has allowed the speciation of *G. siphonifera*, *G. calida*, *G. adamsi* and *B. megastoma* and the extinction of *G. praesiphonifera* to be studied in detail. Paired individual-level morphometric and geochemical data have allowed investigation into the relationships between chamber size, body size, and increasing ocean depth habitat through time.

POLECAT BENCH FM

1,561,274

CLAY MINERAL CONSTRAINS ON GLOBAL CONTINENTAL WEATHERING DURING THE PALEOCENE-EOCENE THERMAL MAXIMUM

K.Ji, C.Wang, H.Hong, K.Yin, C.Zhao, Y.Xu, B.Song, L.J.Lourens, P.D.Gingerich et al. (China Univ Geosci, Wuhan). *21ST INTERNATIONAL SEDIMENTOLOGICAL CONGRESS [ISC] (Beijing, China, 8/22-26/2022) ABSTRACT BOOK* p.173, 2022. (Available at <http://www.isc2022.org.cn> as of 9/22/2022; **Abstract only**)

The Paleocene-Eocene Thermal Maximum (PETM), approximately 56 million years ago, is a geologically short-term greenhouse gas-induced global warming event. The drawdown

mechanisms and rates of the high CO₂ concentrations in the atmosphere-ocean system during the event remain enigmatic. Continental chemical weathering is thought to be an important process removing CO₂ from the atmosphere, although the rates of weathering and drawdown change remain unknown. World-wide, enhanced physical weathering is observed during the event, while evidence for enhanced chemical weathering remains scarce. Here, we test chemical weathering and physical weathering changes in the PETM interval in a proximal continental setting using high-resolution clay mineralogy measurements in floodplain strata. The records from the Bighorn basin, Wyoming, a Laramide foreland basin, reveal a 30-kyr lagged increase of smectites during the body of the PETM that is prolonged for at least 50-kyr after the event. Altogether, this increase can only be explained as the result of an increase of physical weathering and erosion of smectite-rich Cretaceous bentonites in the catchments. The lagged response after the PETM onset most likely relates to the time it takes before the signal fully propagates through the catchments and upstream, basal channel and floodplain sediments. We observe significant grain-size sorting smectites with smectites enriched in coarse-grained sediments. However, sedimentation rates and average grain sizes remain similar in the PETM. Therefore, the smectite increase cannot be explained by grain size sorting. In-situ pedogenesis after deposition at the study site was insignificantly different in the PETM from pre-PETM soils, also not being able to explain the observed trends. Global warming during the PETM could have generated enhanced climate seasonality with contrasting precipitation regimes during the different seasons. This may have led to drier summers causing lower vegetation covers reducing cohesiveness of catchment laterites and basinal soils. More frequent rainstorms then likely intensified the denudation of smectite-rich sediments, which at the same enhanced sediment recycling within the source-to-sink system. The prolonged nature of the smectite enhanced after the PETM event may again relate to post-PETM signal propagation times, which are even lower than after the onset of the PETM due to lower recycling rates after the event. Our result suggest that chemical weathering rates are not significantly altered during transient hyperthermal events of less than 200 kyr or are overruled by physical weathering and erosion changes. Our data therefore suggest that chemical weathering changes might not play as a strong additional role as negative feedback mechanism to reduce greenhouse-gas warming.

PYRITIZATION

1,561,275

AN EXPLORATION OF SOFT-TISSUE PYRITIZATION THROUGH EXPERIMENTAL DECAY AND COMPUTED TOMOGRAPHY

M.Waskom, S.R.Losso and J.Ortega-Hernandez (Harvard Univ). *65TH ANNUAL PALAEOONTOLOGICAL ASSOCIATION MEETING (Manchester, UK, 12/18-20/2021) PROGRAMME AND ABSTRACTS* p.97, 2021. (Available at <http://www.palass.org> as of 11/1/2022; **Abstract only**)

Pyritization represents one of the most common modes of exceptional preservation in the fossil record and has the potential to capture highly detailed morphological information of both animal and plant macrofossils. The preservation of delicate morphological detail in pyritized Palaeozoic animal macrofossils suggests that this process likely took place during early diagenesis, before the loss of information by extensive decay. Despite its palaeobiological significance and a working understanding of the pyritization process, there is much that remains unresolved. Although the fossilization of soft-tissues indicates that pyritization must happen rapidly, pyritization is microbially mediated, and mineralization is typically a longer process. Experimental taphonomy can be employed to better understand the complex dynamics between the short- and long-term diagenetic processes and to establish a timeline for the formation of pyritized remains in the fossil record. By optimizing experimental conditions through biogeochemical methods, we followed pyritization in *Triops* using organic-poor sediment with sulfur-reducing bacteria, which recreated realistic conditions. We employed micro-computed tomography to track differences in density in the experimental vials, where we could observe the precipitation of minerals and density decrease in decaying specimens, providing a non-invasive and non-destructive

method to investigate the timeline of pyritization and fossil formation.

QIANGTANG BASIN**1,561,276****ORGANIC MATTER ACCUMULATION MECHANISM UNDER GLOBAL/REGIONAL WARMING: INSIGHT FROM THE LATE BARREMIAN CALCAREOUS SHALES IN THE QIANGTANG BASIN (TIBET)**

Y.Nie, X.Fu, X.Liu, H.We, S.Zeng, F.Lin, Y.Wan and C.Song (Southwest Petroleum Univ; Chengdu Univ Technology). *JOURNAL OF ASIAN EARTH SCIENCES* v.241, Jan. 2023. (ISSN 1367-9120; Article no.105456)

The Late Barremian (Early Cretaceous) is a global/regional warming interval. Deciphering the mechanism of organic matter (OM) accumulation in this interval could cast lights on OM accumulation mechanism under global/regional warming. This study presented high-resolution geochemical data of the Late Barremian marls and calcareous shales in the Qiangtang Basin to unravel the effect of paleoclimate and hydrothermal activity on OM enrichment, and to further discuss OM enrichment mechanism under warming climates. Our work revealed that the Late Barremian calcareous shales in the Qiangtang Basin showed high total organic carbon contents and were deposited under an anoxic-euxinic condition, high bioproductivity, and relatively stable high-salinity water mass. Hydrothermal activity was intense during this calcareous shale interval deposition. Hydrothermal fluids not only released reducing gas to increase the reducibility of water column, but also provided sufficient nutrients to enhance bioproductivity, thus facilitating the preservation and accumulation of OM. A climate transition from cold-arid to warm-humid occurred at the onset of calcareous shale deposition. A warming climate evidences in the late Barremian succession in the Qiangtang Basin suggested at least a regional warming event. The OM enrichment in the Late Barremian calcareous shales in the Qiangtang Basin was caused by the combined effect of regional (warming climate) and local (hydrothermal activity) factors. Accelerated hydrological cycle under warming climates promoted fluvial delivery of nutrients to sedimentary basins, and thus flourished bioproductivity. Local factors (e.g., hydrothermal activity and water-column stratification) facilitated OM accumulation and preservation under a warming setting. (c2022 Elsevier Ltd.)

QINLING RANGE**1,561,277****COMPARATIVE STUDY OF UPPER PERMIAN TO LOWER TRIASSIC CONODONTS AND CARBON ISOTOPE RECORDS FROM QINLING AND THE SOUTH CHINA BLOCK**

H.Li, P.B.Wignall, H.Jiang, M.Zhang, Z.Ouyang, X.Wu and X.Lai (China Univ Geosci, Wuhan; Leeds Univ). *5TH INTERNATIONAL CONODONT SYMPOSIUM [ICOS] (Wuhan, China and Online, 6/24-27/2022) PROGRAM AND ABSTRACTS* p.45, 2022. (Abstract only)

The Qinling Sea was a funnel-shaped seaway developed between the South China and North China blocks that faced westwards to the Paleo-Tethys Ocean during the end Permian to Early Triassic interval. Ten Early Triassic conodont zones have been established at the shallow-water Yiwagou Section of the South Qinling Platform. In ascending order, they are the: *Hindeodus parvus*, *H. postparvus*, *Neospathodus dieneri*, *Eurygnathodus costatus* and *E. hamadaei*, *Novispathodus waageni-Scythogondolella mosheri*, *Pachycladina-Parachirognathus* assemblage, *Triassospathodus hungaricus*, *Ns. robustispinus* and *T. clinatus* zones. In South China, a large number of palaeontological and palaeoenvironmental studies have been undertaken on this interval, especially focused on the Northern Yangtze Platform and Nanpanjiang Basin, which allow comparisons to be made with the South Qinling Platform. Thus, the conodont faunas from Yiwagou closely resemble those from the Northern Yangtze Platform (100% at genus level, 90.9% at species level), but are less comparable to the fauna from the Nanpanjiang Basin (71.0% at genus level, 54.5% at species level). The $\delta^{13}\text{C}$ carb records from the South Qinling Platform is also similar to that from the North Yangtze Platform in showing a larger amplitude positive excursion (7.7-11.9 per mill)

across the Smithian-Spathian boundary than is seen in the Nanpanjiang Basin (3.1-7.0 per mill). The South Qinling Platform is also similar to the North Yangtze Platform: both record red, bioclastic limestone in the middle-late Smithian, testimony to well-oxygenated conditions at this time. In contrast, anoxic deposition prevailed in the Nanpanjiang Basin during this period. The compilation of global conodonts show that all Smithian conodont species became extinct during the Smithian-Spathian transition, a level that is younger than the extinction level seen in other groups, such as the ammonoids. The early Spathian saw the radiation of new conodont species. Hence, we infer that conodont animals with high motile ability had more chance to move to refuges (e.g., deeper water, higher latitude regions) than other taxa with lower motile ability when environmental deteriorated. Finally the survivors became extinct or evolved into new species in the new habitats. The extinction and evolution patterns of conodonts in the mass extinctions deserve further research.

QINLING RANGE**1,561,278****AN IMPORTANT TECTONOTHERMAL EVENT OCCURRED IN THE MIDDLE AND LATE PALEOZOIC IN THE QINLING OROGENIC BELT**

Z.Jiang, J.Luo, Z.Zhang and Z.Li (Qinghai Univ; Northwest Univ, China; Res Inst Petrol Explor Dev). *21ST INTERNATIONAL SEDIMENTOLOGICAL CONGRESS [ISC] (Beijing, China, 8/22-26/2022) ABSTRACT BOOK* p.336, 2022. (Available at <http://www.isc2022.org.cn> as of 9/22/2022; Abstract only)

The Permian in the Liuyehe Basin of the North Qinling, the Lintan area of the West Qinling, the Zhen'an Basin of the South Qinling in the Qinling Orogenic Belt (QOB) and the Permian in the southern Ordos Basin on the north side of the QOB contain a large amount of ca. 350 ca. 260 Ma detrital zircons. Although the studies believe that the ca. 350 ca. 260 Ma detrital zircons come from the QOB, there are a few public reports of the magmatic/metamorphic age records of this period in the QOB. Only a small amount of reliable magmatic/metamorphic zircon age records of ca. 350-260 Ma have been found in the Jiangligou and Zhongchuan granites in the Western Qinling and the metamorphic rocks of the Wuguan Group in Danfeng County in the eastern North Qinling. Based on the existing work, we put forward the scientific hypothesis for the first time that "there is an important tectonothermal event that has not been fully revealed and recognized in the QOB during ca. 350 ca. 260 Ma". Through the research on the Jiangligou and Zhongchuan granites, and the metamorphic rocks of the Wuguan Group in Danfeng County (front side) by means of petrology, petrography, rock geochemistry, zircon U-Pb isotope dating and in situ Lu-Hf isotope. Through the study on the provenance, genesis and source area attribute of the ca. 350 ca. 260 Ma detrital zircons in the Permian of the southern Ordos Basin, the Liuyehe basin, the Lintan area, the Zhen'an basin (reverse side) by means of paleocurrent direction, sandstone composition, debris composition and heavy mineral characteristics analysis, sedimentary geochemical analysis, zircon U-Pb isotope dating and Lu-Hf isotope tracing. We combined with direct demonstration and indirect inversion, fully demonstrate the hypothesis from both pros and cons, and discuss the nature, tectonic evolution characteristic and tectonic setting of this tectonothermal event in the QOB during ca. 350 ca. 260 Ma. The research results are of great significance to further reveal the Late Paleozoic tectonic evolution history and plate tectonic attributes of the QOB, clarify the Qinling orogenic process and its control over the filling history of peripheral basins, and broaden the exploration fields and ideas of various mineral resources in the QOB and surrounding sedimentary basins.

RECONCAVO BASIN**1,561,279****RESERVOIR CHARACTERIZATION OF MARACANGALHA SANDSTONE USING MEASUREMENTS ON OUTCROPS AND WELL LOGS**

J.C.Batista, O.A.L.Lima and A.Boligon (Bahia Federal Univ). *JOURNAL OF APPLIED GEOPHYSICS* v.207, Dec. 2022. (ISSN 0926-9851; Article no.104843)

In this research, we performed petrophysical measurements using conventional techniques (Pycnometer and gas permeameter),

resistivity and chargeability electrical, besides nuclear magnetic resonance (NMR), on 122 shale sandstone samples collected from outcrops of the Maracangalha Formation in Frades Island, Bahia Brazil. This Formation is an of the main hydrocarbon reservoirs in the Reconcavo Basin in Brazil, but little petrophysical information is available. Electrical measurements were performed using a sample holder build with four-electrode, two for current injection and two for electrical potential measurements, where the rock samples were inserted under condition 100% saturated with multiples salinity solutions. NMR measurements were also obtained with saturated samples and under the condition of partial saturation. The conventional, electrical, and NMR data were analyzed together, resulting in important petrophysical parameters for the lithological characterization of the Maracangalha Formation sandstones. These samples were characterized according to your effective porosity, cementation exponent, volumetric-solid conductivity, clay content, mean grain, and pore-throat sizes. Such laboratory results allowed developing an integrated approach to interpret geophysical well logs of the Maracangalha reservoir. These logs, including gamma-ray, porosity (density, sonic and neutron) and electrical data, were interpreted in terms of shaliness, effective porosity, and partial water saturation, supported by our experimental petrophysical results. In particular, to complete this interpretation was used a combination of electric logs was used to describe the true resistivity at the invaded and in the virgin zone of this reservoir. Taking into account the effects of weathering in the samples used, these results contributed to the formation of a petrophysical database for the Maracangalha Formation, as well as its use as guide values for new interpretations in geophysical profiles in this region. (c2022 Elsevier B.V.)

RED SEA 1,561,280

GEOPHYSICAL EVIDENCE FOR MAGMATISM SOUTHWEST OF THE BROTHERS ISLANDS, NORTHERN RED SEA (OFFSHORE QUSEIR, EGYPT)

M.Ali, M.Ligi, A.Ceriani, F.Bouchaala, W.Bosworth and A.Decarlis (Khalifa Univ Sci & Technol; Istituto Scienze Marine; Apache Egypt Companies). *TECTONICS* v.41, no.10, Oct. 2022. (ISSN 0278-7407; ISSN 1944-9194; Article no.e2022TC007228)

The Red Sea formed as a consequence of Cenozoic rifting between the African and Arabian plates. While continuous oceanic spreading is active in the southern and central sectors, in the northern Red Sea, exposure of oceanic crust is limited to a few along-axis isolated deeps. However, several off-axis magmatic edifices have been recognized in this sector, their description in terms of relative age and architectural features remains vague. One of these, offshore Quseir corresponding to a kilometer-size structural high, was studied in detail using 3D industrial seismic data. This structure is interpreted as due to the coalescence of different volcanic edifices developed on the footwall of a major rift-related normal fault. Magnetic and gravity data and forward modeling suggest a volcanic nature of the substratum underlying the morphological relief. A similar volcanic origin is proposed for other neighboring basement hills that show a similar magnetic signal. Relationships with the imaged seismo-stratigraphic sequences point to a Pleistocene age for the magmatic event. Arabian alkali-basalts, at the same latitude as Quseir, show ages comparable to those inferred for the volcano edifice studied, suggesting a similar tectonic context. In the western Arabian plate, large alkali-lava fields (Harrats) developed along rift-related faults since the early stages of the Red Sea rift (Late Oligocene). They display a significant northward rejuvenation trend that may be explained by the progressive propagation of the Afar mantle plume.

REEF BUILDER 1,561,281

DIVERSITY PARTITIONING IN PHANEROZOIC REEF-BUILDING COMMUNITIES

M.Khan (Cambridge Univ). *65TH ANNUAL PALAEOLOGICAL ASSOCIATION MEETING (Manchester, UK, 12/18-20/2021) PROGRAMME AND ABSTRACTS* p.73, 2021. (Available at <http://www.palass.org> as of 11/1/2022; **Abstract only**)

Biodiversity can be partitioned into three hierarchical concepts.

Alpha diversity assesses intra-habitat diversity, beta diversity looks at the compositional variation between assemblages, and gamma diversity assesses the richness within the entire observed system. Unweighted by-list sampling standardization of tropical reef builders and other Phanerozoic marine invertebrates reveals important differences in their diversity trajectories. Reefs--defined as laterally confined structures built by the growth and/or metabolic activity of sessile benthic organisms in an aquatic environment--are ecologically important ecosystems. Alpha diversity for both systems increases over time, indicating increasing habitat complexity, but in almost all instances, reef builders are comprised of more genera than other marine organisms. Gamma diversity trajectories show differing pathways--generic richness in reefs has declined over time, whereas the rest of the invertebrate taxa have exponentially increased. This result is an important deviation from earlier studies, which discovered that reefs and the rest of the marine taxa share congruent extinction patterns. Reef beta diversity declines significantly over time, while other invertebrates show no temporal trend. Reef beta decline may be attributed to the increasing dominance of corals as reef builders. Diversity partitioning of reef builders provides empirical support for the statement that reefs are "cradles of biodiversity."

RESERVOIR CHARACTERIZATION 1,561,282

RESERVOIR CLASSIFICATION AND EVALUATION BASED ON FRACTAL THEORY AND FACTOR ANALYSIS

H.Cheng, Z.Jin and R.Zhu (China Univ Petroleum; Res Inst Petrol Explor Dev). *21ST INTERNATIONAL SEDIMENTOLOGICAL CONGRESS [ISC] (Beijing, China, 8/22-26/2022) ABSTRACT BOOK* pp.1551-1552, 2022. (Available at <http://www.isc2022.org.cn> as of 9/22/2022; **Abstract only**)

With the development of exploration and development of oil and gas resources, the early reservoir description methods based on physical parameters can no longer meet the requirements of guiding the development and production of modern oil and gas fields. The pore structure of the reservoir is an important factor affecting reservoir properties and seepage properties, and its fine characterization has gradually become an important content of reservoir description. The reservoir pore structure is complex and affected by many factors, so it is difficult to describe quantitatively. Katz, Wong, and Pfeifer later discovered and confirmed that the pore structure of sedimentary rocks has fractal characteristics, which can be used as an effective means to characterize reservoir physical properties, pore structure, and heterogeneity. The concept of fractal was put forward by Mandelbrot in 1977, which is a mathematical-statistical theory to study the self-similarity of objects. It is a more accurate quantitative representation of the inhomogeneity of the distribution of the basic properties of the stratum in three-dimensional space. The theory has been mature and widely used in architecture, physics, geology, and other industries. In geology, it is mainly used in the quantitative characterization of reservoir pore structure, joint or fracture, microscopic image observation, etc., and is mostly used to describe geological body structure. It can also be used as a measure of the irregularity of complex geologic bodies at the microscopic scale, reflecting the order and complexity of geologic body microscopic morphology.

RESERVOIR CHARACTERIZATION 1,561,283

MULTITASKING PHYSICS-INFORMED NEURAL NETWORK FOR DRILLSTRING WASHOUT DETECTION

A.Jan, F.Mahfoudh, G.Draskovic, C.Jeong and Y.Yu (Schlumberger). *83RD ANNUAL EAGE CONFERENCE (Online and Madrid, Spain, 6/6-9/2022) ABSTRACTS 2022*. (Abstract no.607; Available at <http://www.earthdoc.org> as of 7/7/2022; 5 pp; **Abstract only**)

Various types of anomalies are frequently observed during drilling operations. Drillstring washout is one of the most serious problems, which involves the presence of holes or cracks in the drillstring and downhole drilling tools. In this abstract, we propose a multitasking-based method to inject physical knowledge into a neural network aimed at detecting events of drillstring washout from real-time field measurements.

RHEINISCHE MASSIF

1,561,284

CLIMATIC VARIABILITY DURING THE LATE DEVONIAN KELLWASSER CRISIS ON ASTRONOMICAL AND MILLENNIAL TIMESCALES

N.Wichern, T.Nohl, P.Kaskes, L.Percival, R.T.Becker and D.De Vleeschouwer (Westfaelische Wilhelm Univ; GeoZentrum Nordbayern; Brussels Vrije Univ). *21ST INTERNATIONAL SEDIMENTOLOGICAL CONGRESS [ISC] (Beijing, China, 8/22-26/2022) ABSTRACT BOOK* p.167, 2022. (Available at <http://www.isc2022.org.cn> as of 9/22/2022; **Abstract only**)

The Late Devonian (ca. 379-359 Ma) was characterised by a series of widespread marine anoxic events, documented in the rock record by black shales and limestones. The greatest of these, the Kellwasser Crisis at the Frasnian-Famennian boundary, was associated with one of the "Big five" Phanerozoic mass extinctions. Despite decades of research, it remains controversial what triggered the Kellwasser Crisis and why the Late Devonian ocean was particularly sensitive to widespread anoxia. De Vleeschouwer et al. (2017) hypothesised that the exact timing of tipping the Devonian system into oceanic anoxia could have been related to a particular sequence of astronomical forcing configurations. First, a long-term eccentricity minimum (or "node") creates relatively stable climate conditions for several tens of thousands of years, during which thick continental regoliths are formed. Then, a rapid increase in eccentricity intensifies climate variability and triggers the release of nutrients from the continents into the oceans. To test this hypothesis, we have generated high-resolution elemental records of the Winsenberg roadcut (eastern Rhenish Massif, Germany), employing a number of different X-Ray Fluorescence (XRF) methods. The Winsenberg section is 12 m thick and reflects a deeper outer shelf environment just southeast of the Brilon Reef Complex. It features well-expressed Lower and Upper Kellwasser black shales/limestones (LKW and UKW) that are 150 and 80 cm thick, respectively. While rhythmically bedded carbonates crop out in between the two Kellwasser intervals, the 72-cm thick Usseln Limestone occurs directly below the LKW. This limestone bed contains strongly-expressed cm-scale rhythmical variations in carbonate content and can be traced through much of the Rhenish Massif (Gereke, 2007). Lithologic cyclicity is smaller in scale but also more evident in the Usseln Limestone, compared to the stratigraphic interval in between the two Kellwasser shales. This distinction dictates a difference in XRF analytical approach: while the interval between the LKW and UKW was analysed at a cm-scale using a portable XRF analyser, the Usseln Limestone was XRF-imaged at mm-scale resolution using μ XRF elemental mapping. These combined methods allow for a detailed investigation of Winsenberg's environmental response throughout the Kellwasser Crisis, on both astronomical and millennial timescales. On astronomical timescales, the stable 405-kyr eccentricity "metronome" cycle defines an astrochronological framework that is largely in line with other globally-distributed astrochronologies. The Winsenberg floating chronology will form the basis for testing the eccentricity minimum hypothesis, which is a work in progress. The μ XRF images of the Usseln Limestone are combined with petrographic thin-section analysis to show that diagenetic processes did not superimpose the primary rhythm of millennial-scale climate variability.

RIO DO PEIXE BASINS AREA

1,561,285

AN INTEGRATED STRUCTURAL AND MAGNETIC FABRIC STUDY TO CONSTRAIN THE PROGRESSIVE EXTENSIONAL TECTONICS OF THE RIO DO PEIXE BASIN, BRAZIL

M.A.Nicchio, F.Balsamo, F.Cifelli, F.C.C.Nogueira, L.Aldega, F.H.R.Bezerra, D.L.Vasconcelos and J.A.B.Souza (Parma Univ; Roma III Univ). *TECTONICS* v.41, no.10, Oct. 2022. (ISSN 0278-7407; ISSN 1944-9194; Article no.e2022TC007244)

We constrained the tectonic evolution of the intracratonic Cretaceous Rio do Peixe Basin (RPB) in NE Brazil, combining structural and Anisotropy of Magnetic Susceptibility (AMS) data. We analyzed the structural features of four sites along two major faults bordering the basin, the NE-striking Portalegre Fault and the E-W-striking Malta Fault. AMS data from 42 sites in the syn-

rift sandstone suggest two stretching directions driving the opening of the RPB. The early syn-rift phase I resulted from N-S to NNE-SSW stretching direction with vertical σ_1 , producing normal fault displacement along the E-W-striking Malta Fault and right-lateral transtension along the NE-striking Portalegre Fault, Sitio Sagui and Lagoa do Forno faults. The syn-rift phase II resulted from NW-SE stretching direction with vertical σ_1 , causing normal displacement on NE-striking major faults and left-lateral transtension on E-W-striking major faults. Additionally, the NW-SE extension was responsible for forming NE-striking extensional faults and deformation bands in sedimentary units. The RPB developed due to the intraplate deformation of the Borborema Province during the early stage of the Pangea Breakup and recorded two stretching directions that gradually shifted from NNE-SSW to NW-SE as a consequence of the South America clockwise rotation. The extensional stress orthogonal to the main E-W-striking and NE-striking Precambrian shear zones facilitated the opening and evolution of the RPB.

ROCKY MT AREA

1,561,286

EVIDENCE FOR THE CA 1.4 Ga PICURIS OROGENY IN THE CENTRAL COLORADO FRONT RANGE

A.A.Mahatma, Y.D.Kuiper and C.S.Holm-Denoma (Colorado Sch Mines; US Geological Survey). *PRECAMBRIAN RESEARCH* v.382, Nov. 2022. (ISSN 0301-9268; Article no.106878)

We present the first evidence for sedimentation and new evidence for penetrative deformation and metamorphism in the central Colorado Front Range associated with the ca. 1.48-1.35 Ga Picuris orogeny. This orogeny has recently been recognized in New Mexico, Arizona and southern Colorado and may be part of a larger active accretionary margin that includes the ca. 1.51-1.46 Ga Pinware and Baraboo events, in eastern Canada and central US respectively, that preceded the amalgamation of the Rodinian supercontinent. We demonstrate that in addition to ca. 1.4 Ga reactivation of northeast-trending Paleoproterozoic shear zones, regional folding occurred in an area south of Mt. Evans, away from these shear zones. Detrital zircon from one quartzite yielded U-Pb laser ablation inductively coupled mass spectrometry (LA-ICPMS) major age populations of ca. 1.81-1.61 Ga and ca. 1.49-1.38 Ga, and minor ones of ca. 1.90 Ga and ca. 1.56 Ga. The Paleoproterozoic and ca. 1.49-1.38 Ga populations have numerous local and regional sources. The ca. 1.56 Ga age population may represent a minor exotic population as recognized in Defiance, Arizona the Yankee Joe and Blackjack Formations in Arizona, the Four Peaks area in Arizona, and the Tusas and Picuris Mountains in New Mexico. Alternatively it may be a result of mixing between zircon age domains reflecting the older and younger populations, or Pb loss from 1.81 to 1.61 Ga zircon. In-situ LA-ICPMS U-Pb analysis on monazite from four biotite schist samples yielded ca. 1.74 Ga and ca. 1.42 Ga age populations, and separate populations that show ca. 1.68-1.47 Ga and ca. 1.39-1.33 Ga age spreads. The ca. 1.74 Ga and ca. 1.68-1.47 Ga populations may be detrital or metamorphic. Monazite ages between ca. 1.6 Ga and ca. 1.5 Ga may be due to the mixing of age domains or Pb loss, because metamorphism during that time has not been recognized in Laurentia. The ca. 1.42 Ga and ca. 1.39-1.33 Ga populations are most likely metamorphic and consistent with the age of the ca. 1.48-1.35 Ga Picuris orogeny. The evidence for ca. 1.4 Ga sedimentation, and especially regional folding and metamorphism in the central Colorado Front Range indicate that the impact and extent of the Picuris orogeny in the southwestern U.S. are larger than previously thought. (c2022 Elsevier B.V.)

RUSSIAN PLATFORM

1,561,287

STEPWISE INCREASING PALEOTEMPERATURES IN THE LATE JURASSIC-EARLY CRETACEOUS EPEIRIC BASIN OF THE EASTERN RUSSIAN PLATFORM

K.Nikashin and S.Zorina (Kazan Federal Univ). *21ST INTERNATIONAL SEDIMENTOLOGICAL CONGRESS [ISC] (Beijing, China, 8/22-26/2022) ABSTRACT BOOK* pp.192-193, 2022. (Available at <http://www.isc2022.org.cn> as of 9/22/2022; **Abstract only**)

Aside from the long-term periods of warm climate, several

hyperthermal events are identified in the Jurassic and Cretaceous (Foster et al., 2018), most of which are associated with oceanic anoxic events (OAEs) and black shale accumulation. In the Eastern Russian Platform (North-Eastern Peri-Tethys), several Mesozoic black shale formations are widely occurred, among those the Middle Volgian (Upper Jurassic) Promzino formation and the OAE 1a-related Lower Aptian (Lower Cretaceous) Ulyanovsk formation are known. To reconstruct paleotemperatures and the depositional environments, the stable oxygen and carbon isotopes of biogenic carbonates (more than 200 ammonite, bivalve, and benthic foraminifer shells and belemnite rostra) from the Upper Jurassic-Lower Cretaceous succession were analyzed. The lack of significant diagenetic alterations of carbonates as well as their mineralogy were preliminarily established using element geochemistry, Raman spectrometry, and electron microscopy data. Based on the first results of the $\delta 18O$ analysis, a paleotemperature curve was constructed using equations from (Grossman, Ku, 1986; Anderson, Arthur, 1983). This curve shows quite a warm climate in the Late Jurassic in study region, with water column temperatures ranging in 17-25°C. Noteworthy, temperatures calculated for benthic foraminifer shells are generally similar to those for ammonites suggesting a low temperature gradient in water column and hence a weak water stratification. Slight positive temperature excursion during the deposition of the Promzino black shales does not match the hyperthermal event (18-23°C) which is confirmed by temperatures curve constructed for the temperate belt of the Northern hemisphere (Veizer, Prokoph, 2015). Rather abrupt warming of almost 4°C is reported for the Russian Platform in the Later Jurassic (Price, Rogov, 2009), but the maximum temperature obtained (20°C) is much lower than that typical for hyperthermal event. Interestingly, our results show an unexpected cold snap (10°C) in the uppermost Promzino formation which could be probably caused by the strong phase of volcanic activity (Rentgarten, Kuznetsova, 1967). Nevertheless, warm climate reconstructed could maintain high productivity in the highly restricted basin in the Middle Volgian (Zorina et al., 2020) which is among major factors contributing to the enhanced preservation of the organic matter in the Eastern Russian Platform. Trend of temperature evolution during the Early Cretaceous is partly similar to the global one, but temperatures reconstructed for the study basin in the Later Hauterivian and Barremian generally exceed the global values by more than 5°C with occasional drop to 8°C detected in the Later Hauterivian. This discrepancy could be explained by the specificity of basin circulation and strong phases of volcanic activity (Zorina et al., 2020).

RUSSIAN REPUBLIC ASIA 1,561,288

IT'S A TRAP: ENVIRONMENT AND BIOGEOGRAPHY OF SIBERIA ACROSS THE FRASNIAN-FAMENNIAN

E.M.Dowling, T.H.Torsvik and M.Domeier (Oslo Univ). *65TH ANNUAL PALAEOLOGICAL ASSOCIATION MEETING (Manchester, UK, 12/18-20/2021) PROGRAMME AND ABSTRACTS* pp.22-23, 2021. (Available at <http://www.palass.org> as of 11/1/2022; **Abstract only**)

The Late Devonian was a period of biotic turbulence, prolonged climate instability, and oceanic anoxia on a global scale. It was also a critical period of biotic evolution, hosting diverse fish fauna and the earliest limbed tetrapods. Because it was geologically and biotically active, the Late Devonian consistently presents new insights into the conditions and patterns of ecosystem development. Here we report the results of palaeoenvironmental review and biogeographical assessment of Siberia in the Late Devonian. Late Devonian Siberia hosts terrestrial, marginal and marine settings, presenting a unique cross-section of the local environment. The Viluy Traps, a large igneous province (LIP), is considered to be a key feature of the Siberian landscape; its active pulses have been correlated to Late Devonian extinction across the region. Taxic distributional data were collected from museum collections and published literature and supplemented by the Paleobiology Database. Once cleaned and validated, the data were tested across time, area and geological regime. Using fossil occurrences, different types of survivorship were marked and ranked within a geological province. This was then tested against the temporal distribution of LIP events. The assessment of changing palaeoenvironmental and

biogeographic profiles across the Frasnian-Famennian events provides unique insight into the spatial structure of extinction and recovery.

SANDSTONE RESERVOIR 1,561,289

CONFIGURATION CHARACTERIZATION OF UNDERGROUND DEEP-SEA CHANNEL RESERVOIR DRIVEN BY GEOLOGICAL MODEL

X.Zhao and L.Fei (Southwest Petroleum Univ). *21ST INTERNATIONAL SEDIMENTOLOGICAL CONGRESS [ISC] (Beijing, China, 8/22-26/2022) ABSTRACT BOOK* p.1561, 2022. (Available at <http://www.isc2022.org.cn> as of 9/22/2022; **Abstract only**)

Deep sea channel is the migration channel of terrigenous debris to deep-sea plain. It is also one of the main oil and gas reservoir units in deep-sea sedimentary environment. It has important value and significance of oil and gas resources exploration and development. Studies have confirmed that although the deep-sea channel reservoir often has high porosity and permeability, its plane flow path and internal building structure are complex and changeable. Even in a very short lateral distance, the reservoir thickness and connectivity will change greatly, which greatly increases the drilling risk and reduces the design quality of development scheme. In addition, due to the limitation of marine sedimentary environment and operation cost, deep-sea oil and gas fields often have "few wells, large well spacing and thin well pattern". The traditional reservoir configuration characterization method suitable for onshore dense well pattern is difficult to adapt to deep-sea oil and gas fields. In addition, the complex superposition relationship of channel reservoir itself brings challenges to the high-precision prediction of underground deep-sea channel reservoir, which affects the efficient development of deep-sea channel reservoir. Therefore, this paper proposes a geological model driven characterization method of underground deep-sea channel reservoir configuration. The specific process is as follows: Construction of development scale channel configuration mode: on the development scale, the deep-sea channel is divided into four levels: channel system, complex channel set, complex channel and single channel. Then, based on the shallow high-frequency 3D seismic data, the vertical superposition mode and plane migration mode of four levels of deep-sea channel are established.

SANTOS BASIN 1,561,290

ELECTROFACIES DEFINITION AND ZONATION OF THE LOWER CRETACEOUS BARRA VELHA FORMATION CARBONATE RESERVOIR IN THE PRE-SALT SEQUENCE OF THE SANTOS BASIN, SE BRAZIL

M.M.Camargo, G.F.Chinelatto, M.Basso and A.C.Vidal (Campinas State Univ). *JOURNAL OF PETROLEUM GEOLOGY* v.45, no.4, pp.439-459, Oct. 2022. (ISSN 0141-6421; ISSN 1747-5457)

Lower Cretaceous carbonates in the pre-salt succession in the Santos Basin, eastern Brazil, are highly heterogeneous in terms of their reservoir characteristics as a result of depositional and diagenetic factors. Electrofacies have widely been used for reservoir zonation and, when allied with computer-based methods such as neural networks, may help with the study of such complex reservoir rocks and with the identification of high-quality reservoir zones. In this work, an unsupervised artificial neural network known as a self-organizing map (SOM) was used to carry out a zonation of the pre-salt carbonates in the Aptian Barra Velha Formation, the main reservoir unit in the Santos Basin. Available data included gamma-ray, neutron porosity, resistivity deep, sonic, density, photoelectric factor, total porosity and effective porosity profiles from 21 wells together with mineralogical models. Core descriptions and thin section images were used as additional data for the lithological characterization of the electrofacies and consequently for reservoir zonation. A total of four electrofacies were defined from the SOM application, and five reservoir zones were identified. The characterization of the reservoir zones also considered the structural locations of the wells based on the relative depth to top- Barra Velha Formation; well locations were classified as structurally high, intermediate or low. Based on the

reservoir zone characteristics, the results could be correlated with zonations in previous studies. A general tendency was noted for there to be an increase of finer-grained sediments in the formation in wells located in structural lows; packstone and mudstone facies were prevalent in these wells and were in general characterized as poor-quality reservoir rocks. By contrast, the shrubstones and grainstones which were more frequent in structurally high wells comprised higher quality reservoir rocks. The basal reservoir zone showed wide lithological variation compared to the overlying reservoir zones. Grainstone-dominated facies were identified in the middle of the formation, and the uppermost reservoir zones were characterized by an upward increase in shrubstones and reworked grainstones which in general pointed to better quality reservoirs.

SASKATCHEWAN**1,561,291****LORICIFERAN SCFs FROM THE CAMBRIAN OF CANADA: THE ORIGINS OF A MEIOFAUNAL PHYLUM**

T.H.P. Harvey and N.J. Butterfield (Leicester Univ; Cambridge Univ). *58TH ANNUAL PALAEOONTOLOGICAL ASSOCIATION MEETING (Leeds, UK, 12/16-19/2014) ABSTRACTS* p.29, 2014. (Available at <http://www.palass.org> as of 11/15/2022; **Abstract only**)

Miniature animals that inhabit interstitial spaces in sediments (the meiofauna) are scarcely represented in the fossil record, and are often under-sampled in molecular phylogenetic analyses. Therefore, there are few constraints on the timings or mechanisms of their evolution. Here, we report miniature scalidophoran worms, with particular characters from the phylum Loricifera, from the Middle/Upper Cambrian Deadwood Formation of Saskatchewan, Canada. The specimens (n = 72) occur as small carbonaceous fossils (SCFs) extracted using hydrofluoric acid from mudrock. Most specimens consist of an empty cuticular lorica, but a few contain remnants of the introvert appendages (scalids), and one specimen preserves an intact introvert with several hundred scalids. Despite the adult morphology of the introvert, the total body length does not exceed approximately 300 µm, suggesting a meiofaunal ecology, as in modern loriciferans. At the same time, the fossils share some characters with extant larval priapulids and extinct "macro-loricate" worms, consistent with loriciferans being miniaturized priapulids. We discuss the implications for ecdysozoan phylogeny and the evolution of the meiofauna.

SCOTLAND**1,561,292****CHONDRICHTHYAN DIVERSITY AND DISTRIBUTION IN THE EARLY CARBONIFEROUS: NEW EVIDENCE FROM THE TOURNAISIAN OF NORTHERN BRITAIN**

T.R. Smithson, K.R. Richards, R. Bennion and J.A. Clack (Cambridge Univ). *58TH ANNUAL PALAEOONTOLOGICAL ASSOCIATION MEETING (Leeds, UK, 12/16-19/2014) ABSTRACTS* pp.45-46, 2014. (Available at <http://www.palass.org> as of 11/15/2022; **Abstract only**)

The end-Devonian extinction event marked a profound change in the diversity of fishes. The dominant Devonian taxa--the acanthodians, placoderms and sarcopterygians--were suddenly replaced by minor components of the fauna, the actinopterygians and chondrichthyans. This replacement began in the Early Carboniferous, but the evidence for it is poor. Until recently, the earliest Carboniferous chondrichthyans were known mainly from teeth from localities in China, Russia and North America. In the UK, the entire Tournaisian chondrichthyan fauna was represented by two teeth. Collecting at two new sites in the Scottish Borders has uncovered an extraordinarily diverse fauna of chondrichthyans. Represented by well-preserved cladodont, xenacanth and bradyodont teeth, most of the taxa are new and undescribed. The bradyodont teeth have been found in large numbers, and they exhibit a broad range of shapes and sizes. This adds to growing evidence that, in the UK, immediately after the end-Devonian extinction, a durophagous feeding habit was common. The UK Tournaisian bradyodonts were much larger than their younger relatives from the later Carboniferous. In contrast, the cladodont and xenacanth sharks were relatively smaller. All known Tournaisian chondrichthyan sites are in tropical palaeolatitudes, suggesting that sharks may have had a restricted distribution following the extinction event.

SEYMOUR ISLAND**1,561,293****LIFE AND DEATH AT HIGH LATITUDES: A REASSESSMENT OF THE CRETACEOUS-PALEOGENE (K-Pg) MASS EXTINCTION EVENT IN ANTARCTICA**

J.D. Witts, P.B. Wignall, J.E. Francis, R.J. Newton, J.A. Crame, V.C. Bowman and R.J. Whittle (Leeds Univ; British Antarctic Survey). *58TH ANNUAL PALAEOONTOLOGICAL ASSOCIATION MEETING (Leeds, UK, 12/16-19/2014) ABSTRACTS* p.52, 2014. (Available at <http://www.palass.org> as of 11/15/2022; **Abstract only**)

The Cretaceous-Paleogene (K-Pg) extinction of 66 Ma is a key event in Earth history, with the extinction of many previously dominant terrestrial and marine groups providing a foundation for the subsequent evolution and expansion of the modern fauna during the Cenozoic. The highest southern latitude site for studying this interval is Seymour Island, Antarctica (65°S today, and during the Late Cretaceous). Here, a thick and abundantly fossiliferous Maastrichtian-Danian (ca. 70-65 Ma) section is preserved within a sedimentary sequence deposited in a back-arc basin to the East of the Antarctic Peninsula. We have produced stratigraphic range data for major macrofossil groups as well as stable isotope records (carbon and sulfur isotopes) based on new sedimentary sections and a taxonomic reassessment of the fauna from the approximately 1100-m-thick Lopez de Bertodano Formation exposed on Seymour Island. Our results show a stable Maastrichtian community, with fluctuations in the diversity of the fauna u-section probably being related to sea-level and other latest Cretaceous environmental changes even before a single pulse of extinction coincident with the K-Pg boundary. These new data do not support claims for a double extinction pulse in Antarctica, but they do allow us to examine the latitudinal and taxonomic selectivity of this major mass extinction event.

SHAHEJIE FM**1,561,294****DISTRIBUTION REGULARITY OF THE COUPLING RELATIONSHIP BETWEEN TIGHT SANDSTONE RESERVOIR DENSIFICATION AND OIL AND GAS FILLING IN THE THIRD MEMBER OF SHAHEJIE (ES3) FORMATION IN BOHAI BAY BASIN**

H. Hu, D. Li, K. Zhao and Z. Zheng (China Ministry Natural Rsc; CNOOC Research Inst Ltd). *21ST INTERNATIONAL SEDIMENTOLOGICAL CONGRESS [ISC] (Beijing, China, 8/22-26/2022) ABSTRACT BOOK* p.269, 2022. (Available at <http://www.isc2022.org.cn> as of 9/22/2022; **Abstract only**)

The tight sandstone in the Bohai Bay basin is rich in oil and gas resources, mainly distributed in the third member of Shahejie Formation (Es3). The differential tectonic evolution leads to obvious differences in diagenetic evolution history and oil and gas filling history in different regions of the basin. However, there is still a lack of research on the relationship between reservoir densification process and oil and gas filling. Based on the relationship between reservoir densification and oil and gas filling, tight sandstone oil and gas reservoirs can be divided into three types: "accumulation before tightness" type (type I); "accumulation synchronization with tightness" type (type II); and "accumulation after tightness" type (type III). Based on the time coupling relationship between reservoir densification and main hydrocarbon generation and expulsion period, the coupling relationship between diagenesis and accumulation of tight sandstone reservoir in the Es3 Formation is characterized by multi-layer ring distribution centered on Bozhong Depression. The outer ring area includes the north of Jizhong Depression and Changwei Depression. The sub outer ring area mainly includes Liaohu Depression, Lingqing Depression and the north of Liaodongwan Depression. The middle ring area mainly includes the south of Jizhong Depression, Jiyang Depression and Huanghua Depression. The inner ring area is mainly Bozhong Depression. Two periods of oil and gas charging occurred in the Es3 formation, respectively in the middle and late Paleogene and Neogene to Quaternary. From the periphery of the basin to the center, there is an evolution law of "early one-stage hydrocarbon charging"- "two-stage hydrocarbon charging, early mainly"- "two-stage hydrocarbon charging, late mainly"- "late one-stage charging". The evolution of reservoir porosity in the Es3 Formation presents

the characteristics of "compaction and cementation porosity reduction"- "dissolution porosity increase"- "cementation porosity reduction"- "weak dissolution porosity increase". The densification time of the reservoir from the outer ring to the center presents the evolution law of "middle Paleogene-middle to late Paleogene-late Paleogene to early Neogene-middle to Late Neogene". For the first stage of oil and gas filling in the middle and late Paleogene, from the outer ring to the middle ring, the coupling type presents the distribution law of "type III-type II or type III-type I or type II". For the second stage of oil and gas filling from Neogene to Quaternary, the whole basin is dominated by type III coupling relationship. The outer ring and sub outer ring are mainly tight oil and gas reservoirs with type III coupling relationship, which is likely to form relatively dispersed continuous tight oil and gas accumulation; In addition to type III oil and gas reservoirs, tight oil and gas reservoirs with type I and type II coupling relationship are also developed in the middle ring and inner ring, which is likely to form relatively concentrated trap tight oil and gas accumulation, and the exploration is relatively favorable.

SHAHEJIE FM

1,561,295

ENRICHMENT MECHANISM OF ORGANIC MATTER IN SALINE LACUSTRINE BASIN

C.Zhu and F.Jiang (China Univ Petroleum). *21ST INTERNATIONAL SEDIMENTOLOGICAL CONGRESS [ISC] (Beijing, China, 8/22-26/2022) ABSTRACT BOOK* p.274, 2022. (Available at <http://www.isc2022.org.cn> as of 9/22/2022; **Abstract only**)

The organic matter enrichment is the basis of oil and gas resources evaluation. The lacustrine shale oil and gas resources is rich from Mesozoic and Cenozoic in China. However, due to the small area of the lacustrine basin, the hydrological conditions of the lake is disturbed by the sedimentary environment and affect the balance of evaporation and precipitation resulting from the small area of lacustrine basin (Katz, 1995), which leading to the change of lake water properties and complex organic matter enrichment (Pedersen and Calvert, 1990). The Dongpu Depression is a typical continental faulted lacustrine basin in Bohai Bay Basin in China. During the sedimentary period of the lower sub-member of Es3 (Member 3 of the Shahejie Formation), the deposition environment of saline and fresh-water were developed in the north and south region, respectively. In the past 50 years of exploration and development, 93.7% of oil and 80% of natural gas have been found in salt water sedimentary environment (Zhang et al., 2017). The shale deposited in the north region develop salt rocks (mean value: 8.24%) and carbonate minerals (mean value: 34.79%) with an average TOC of 1.17%. The shale in the south region develop rare salt rocks with an average TOC of 0.44%. The carbonate minerals are relatively few (with an average of 20.5%). Combined with the data analysis of major and trace elements, it is considered that the climate was arid during the sedimentary period of the lower sub-member of Es3. The salinity of the ancient lake in the northern region is high, and halophilic algae such as dinoflagellate are developed, which increases the paleoproductivity in this period. In the southern region, the salinity of ancient lake is low, green algae are mainly developed, the degree of chemical weathering is medium, and the terrigenous input is high. According to the further analysis of the organic matter enrichment mechanism of the saline sedimentary environment in the north, it is found that the TOC shows an obvious positive correlation with the paleoproductivity, which increases first and then decreases with the paleosalinity, reaching the maximum when the paleosalinity is 11 per mill. Based on the palynological analysis, it is found that when the salinity of the northern region is 12 per mill ca. 13 per mill and the TOC content is as low as 0.2%, the sporopollen development mainly includes Ephedra and Podocarpites. It may be that the seasonal arid climate leads to the increasing terrigenous input, which is not conducive to the enrichment of organic matter. When the salinity is 10 per mill ca. 12 per mill, the TOC content exceeds 1.5%, the dinoflagellate and acritarcha algae are developed. In addition, the humid climate and stable ancient lake leads to the anoxic bottom water, which is conducive to the enrichment of organic matter.

SHAHEJIE FM

1,561,296

MINERALOGICAL AND GEOCHEMICAL CHARACTERIZATION OF CALCAREOUS SHALE IN THE LACUSTRINE BASIN: IMPLICATIONS FOR PALEOSALINITY, PALEOCLIMATE, AND PALEOREDOX CONDITIONS

D.Khan, L.Qiu, C.Liang and Y.Yang (China Univ Petroleum). *21ST INTERNATIONAL SEDIMENTOLOGICAL CONGRESS [ISC] (Beijing, China, 8/22-26/2022) ABSTRACT BOOK* p.280, 2022. (Available at <http://www.isc2022.org.cn> as of 9/22/2022; **Abstract only**)

Shale is an important self-sourced reservoir rock in many sedimentary basins worldwide. In this research work, a geochemical history of variations of sedimentary environment in the lacustrine basin is analyzed based on extensive shale samples collected from the lower 3rd member (Es3L) and upper 4th member (Es4U) of the Paleogene Shahejie Formation in the Boxing Sag (Dongying Depression, East Coast of China). The representative shale samples were analyzed for total organic carbon (TOC) contents, mineralogical composition, the concentration of different elements (major, minor, and trace), kerogen types and vitrinite reflectance (Ro), and different sedimentary structures to understand the evolution of the depositional settings and their effect on the distribution of shale lithofacies in this basin. The TOC content in this shale is ranging from 0.08% to 13.6% (average 2.45%). Ro values range from 0.55-1.19% (avg. 0.85%) with type-I to type-II kerogens. The studied shale is composed of calcite (average 37.83%), dolomite (avg. 10.47%), quartz (avg. 23.8%), plagioclase (avg. 3.91%), clay (20.84%), and pyrite (2.85%). Seven lithofacies have been determined including mixed shale, calcareous shale, laminated limestone, argillaceous shale, dolomitic shale, siliceous shale, and siliceous dolomite based on mineral composition, TOC contents, and sedimentary structures. Different geochemical proxies including Sr/Ba, Ca/Ca+Fe, C-values, CIA values, Ti/Al, Al/Al+Fe, Al/Ti, V/V+Ni, Ni/Co, and Fe/Ca+Mg were used to interpret salinity, paleoclimate, detrital influx, provenance, paleoredox and water depth of the depositional environment in the studied shale. The detailed interpretation of the sedimentary environment suggested that during the deposition of Es3L shale, the terrigenous influx was high in shallow to a deep open lacustrine system with higher primary biogenic productivity. Semi-humid climatic conditions with higher precipitation rates prevailed during the deposition of this shale. On the other, relatively limited terrigenous input with low bioproductivity prevailed during the deposition of Es4U shale in the study area. Semi-arid to humid climatic conditions with strong evaporation prevailed during the deposition of this shale. In this research work, a detailed depositional model of the Es3L-Es4U shale in Boxing Sag is established. The interpretations deduced from the current research work are likely to not only can expand the knowledge of shale lithofacies and genesis of lacustrine fine-grained sedimentary rocks, but can also offer a theoretical foundation for lacustrine shale oil exploration and development.

SHAHEJIE FM

1,561,297

LITHOFACIES AND SEQUENCE STUDIES OF LIME-RICH FINE-GRAINED SEDIMENTARY ROCKS IN THE LOWER ES3 AND UPPER ES4 BOXING SAG

S.Y.Li, L.Qiu and Y.Yang. *21ST INTERNATIONAL SEDIMENTOLOGICAL CONGRESS [ISC] (Beijing, China, 8/22-26/2022) ABSTRACT BOOK* p.283, 2022. (Available at <http://www.isc2022.org.cn> as of 9/22/2022; **Abstract only**)

It's the basis of shale oil theory research and exploration and development to accurately divide the sequence and summarize the lithofacies characteristics and evolution law of the high-TOC lime-rich fine-grained sedimentary rocks in Boxing Sag. The study shows that the fine-grained sedimentary rocks in the Boxing subsag have the following characteristics: (1) The fine-grained sedimentary rocks in the study area are characterized by rich gray matter. CO isotopes of different lithofacies micro-areas show that the $\delta^{13}C$ values (-6.257, -0.313) are consistent with the carbonate values of Ordovician system in North China. Therefore, it's speculated that the gray matter may be mainly derived from the surrounding

Ordovician uplift; (2) On the basis of mineral content, sedimentary structure and TOC content, fine-grained sedimentary rocks are divided into 11 lithofacies: organic-rich massive siliceous clastic type (carbonate type) mixed fine-grained sedimentary rocks, organic-bearing layers argillaceous dolomite, organic-rich lamellar (massive) (layered) carbonate-type mixed fine-grained sedimentary rock, organic-rich lamellar argillaceous limestone, organic-rich lamellar (layered) carbonate mixed fine-grained sedimentary rocks, organic-rich lamellar mudstone facies, and organic-rich layered siltstone facies; (3) Combined with seismic, logging, logging, geochemical parameters and other data, the sequence stratigraphic framework of the lower Es3-upper Es4 in Boxing subsag was established, and it was divided into two three parts, level sequence: Sequence one, the lake transgression domain and the highstand domain developed, which may be due to the erosion of the lowstand domain under the Es3; the highstand domain was divided into late highstand domain and early highstand domain by lithofacies assemblages and logging curves; sequence two, there are complete low-stand domain, lake transgression domain and high-stand domain. Then, the logging curve is processed by cyclog software, and the lower part of Es3 is further divided into 10 sublayers (C1-C10), and the upper Es4 is divided into 9 sublayers (C1-C9); (4) Lower Es3: A small amount of organic-rich massive clastic mixed fine-grained sedimentary rocks developed in the late high stand area, and a large amount of organic-rich massive (laminar) carbonate mixed fine-grained sedimentary rocks developed with the decrease of terrigenous input. When the content is higher, organic-rich layered carbonate-type mixed fine-grained sedimentary rocks develop; a large number of organic-rich layered carbonate-type mixed fine-grained sedimentary rocks develop in the early highstand, and a small amount of organic-rich layered carbonate-type mixed fine-grained sedimentary rocks develop when the water is shallow. The TOC content of the lake transgression area can reach up to 13.6%, and a large amount of organic-rich lamellar limestone and a small amount of organic-rich lamellar carbonate migmatite are developed.

.....
SHAHEZI FM **1,561,298**

**ENVIRONMENTAL MAGNETISM AND
 CYCLOSTRATIGRAPHIC ANALYSIS OF THE LACUSTRINE
 SUCCESSIONS OF THE LOWER KISH FORMATION IN THE
 EARLY CRETACEOUS SONGLIAO BASIN,
 NORTHEASTERN CHINA**

S.Zhang and H.Wu (China Univ Geosci, Beijing). *21ST INTERNATIONAL SEDIMENTOLOGICAL CONGRESS [ISC] (Beijing, China, 8/22-26/2022) ABSTRACT BOOK* p.272, 2022. (Available at <http://www.isc2022.org.cn> as of 9/22/2022; **Abstract only**)

Continuous cores of the lower Cretaceous in Songliao Basin, northeastern China, have been drilled out by the International Continental Drilling Project of SK-2 borehole, providing unprecedented geological materials for investigations of the early Cretaceous continental paleoenvironment and paleoclimate. In this study, we systematically studied the lacustrine successions of the lower Shahezi Formation (K1sh) in depth 4542-5694 m using the techniques of environmental magnetism, microscopic imaging, geochemical stratigraphy and cyclostratigraphy. Magnetic analysis reveals that there is an inverse correlation between magnetic susceptibility (MS) and lithology, where mudstones hold the largest values, and sandstones hold the smallest. The main magnetism carriers in the lower K1sh are pseudo-single-domain (PSD) and/or multi-domain (MD) ferromagnetic minerals, whilst the mainly dominant minerals of MS are paramagnetic and ferromagnetic minerals. To further explore the genesis of the environmental and climatic variations, MS was utilized as an alternative proxy to proceed with cyclostratigraphic analysis. Sedimentary cycles of 113.04 m, 34.11 m, 13.34 m and 6.00 m are significant in power spectrum, which are in ratio highly accordant with long eccentricity (405 kyr), short eccentricity (124 kyr), obliquity (47 kyr), and precession (21 kyr) cycles in Early Cretaceous, proving the considerable impact of astronomical cyclicity on sedimentary rhythmicity. Long eccentricity controlled sedimentary facies, short eccentricity and precession are regarded to have mutually shaped the lake level oscillations. It should be noted that semi-precession

periods identified from MS and the U sequence is most likely to directly drive the sand-mudstone alternations with the seasonal discrepancies of summer insolation. Finally, by tuning the inferred long and short eccentricity cycles to 405 kyr and 124 kyr orbital eccentricity theoretical curves, we established floating astronomical time scales (FATS) of 3356.99 kyr and 3248.80 kyr respectively, both of which fall into the range of the published U-Pb ages. Sedimentation rate was estimated ranging from 27.50 cm/kyr to 28.91 cm/kyr, confirming the rapid deposition characterized within the fault lacustrine basin. In summary, our study acquired experimentally detailed magnetic characteristics of the early Cretaceous terrestrial sediments, shed new light on the astronomically forced configurations of paleoclimate on these magnetic properties, and provided a preliminary geochronological constraint for further marine-terrestrial comparison towards coeval strata.

.....
SHANNON ESTUARY **1,561,299**

**FAVORABLE IMPRESSIONS: AMMONOID TAXONOMY AND
 BIOSTRATIGRAPHY IN THE CARBONIFEROUS SHANNON
 BASIN, WESTERN IRELAND**

A.Lacchia (Trinity Coll, Dublin). *58TH ANNUAL PALAEOONTOLOGICAL ASSOCIATION MEETING (Leeds, UK, 12/16-19/2014) ABSTRACTS* p.32, 2014. (Available at <http://www.palass.org> as of 11/15/2022; **Abstract only**)

In the Carboniferous Shannon Basin, Western Ireland, ammonoids are largely preserved as 2D moulds. Taxonomy of 2D ammonoids relies on knowledge of shell ornament which varies with ontogeny. A detailed study of ontogenetic changes, based on the systematic description of 3D shells, is needed in order to provide robust taxonomic identifications but is not yet available for many ammonoids in the basin, whose fill spans part of the Alportian and Kinderscoutian substages. Ammonoids are present throughout the succession, but are concentrated in thin dark shales, which are thought to represent intervals of sediment starvation and are referred to as condensed sections or "ammonoid bands". The make-up of the ammonoid assemblages in these bands shows that, while some bands are distinctive and useful in both intrabasinal and extrabasinal correlation, the faunas of others are far more diverse than previously thought. This puts into question the idea of a series of discrete, widespread ammonoid bands in the regional Namurian Stage, each with a diagnostic assemblage.

.....
SHANXI **1,561,300**

**MULTIPLE-POINT GEOSTATISTICAL SIMULATION OF
 OUTCROP BASED ON UAV OBLIQUE PHOTOGRAPHIC
 DATA: A CASE STUDY OF SHIHEZI FORMATION IN
 PINGTOU TOWNSHIP, LULIANG CITY, SHANXI**

S.Yin and G.Chen (Yangtze Univ). *21ST INTERNATIONAL SEDIMENTOLOGICAL CONGRESS [ISC] (Beijing, China, 8/22-26/2022) ABSTRACT BOOK* p.1554, 2022. (Available at <http://www.isc2022.org.cn> as of 9/22/2022; **Abstract only**)

Aiming at shortcomings in the traditional research methods of outcrops, using the agility, overall perspective and high-degree quantification of UAV oblique photography, the authors have completed the collection, processing and geological interpretation of delta outcrops, and established the three-dimensional digitized outcrop model and quantitative geological knowledge database of reservoirs. Through the fine analysis and comparative study of multiple outcrop sections, and the use of such methods as lithofacies combination, hierarchical interface, interaction of plane and section, sequential indicator stochastic simulation and multiple-point geostatistical simulation, this study establishes the three-dimensional multiple-point statistical model of the outcrop area. The study shows that: (1) The three-dimensional coordinate system of the oblique photographic data collected by UAV after processing is fully coupled with the information of high-precision images, realizing the three-dimensional digitalization, visualization and quantification of the geological information of outcrops. Under the setting of well points, in combination with the lithofacies constraints of well point, this paper carries out a comparison of outcrops with cross-well base-level cycles and the tracking of substrata, and establishes the spatial stratigraphic framework and

quantitative reservoir geological knowledge database of the outcrop area. (2) Combining the analysis of traditional outcrop sections and the quantitative reservoir geological knowledge database of modern UAV oblique photography is a complementary means of establishing the spatial distribution of geological attributes and geological models in the study area, which improves the rationality of research results. Three types of genetic sandbodies with great differences in architecture is developed from bottom to top in the outcrop area, i.e., crossed-superimposed distributary channels, distributary channels superimposed with sheet sand bars, and skeletal sandbodies such as thin sheet sandbody or isolated distributary channels. (3) UAV oblique photography model expands the study of two-dimensional irregular outcrop sections into three-dimensional space, and establishes a three-dimensional sequential indicator stochastic simulation model, which not only enhances the correlation between the sections, but also provides strong support for studying the plane sedimentary microfacies of outcrops, and finely describing the distribution of sandbody architecture by the interaction of plane and section.

SHAYAR UPLIFT

1,561,301

DENSIFICATION OF THE LOWER CRETACEOUS TIGHT SANDSTONES, SANDAOQIAO AREA, WESTERN TABELI UPLIFT IN THE TARIM BASIN: IMPLICATION FOR PALEO-UPLIFT EVOLUTION

S.Qin, R.Wang and Z.W.Shi (China Univ Geosci, Wuhan). *21ST INTERNATIONAL SEDIMENTOLOGICAL CONGRESS (ISC) (Beijing, China, 8/22-26/2022) ABSTRACT BOOK* p.1572, 2022. (Available at <http://www.isc2022.org.cn> as of 9/22/2022; **Abstract only**)

Previous practices proved that sandstone reservoir of Lower Cretaceous is partial tight in the Tabei uplift. And the petroleum accumulation is related to the paleo-uplift distribution. At the aid of seismic, core and drilling data, three stratigraphic sequences and sedimentary facies are identified. And using porosity and permeability, thin section, cathode luminescence and pore structure data describe the reservoir characteristics. Based results above to clarify the relation between reservoir densification and paleo-uplift evolution. The target layers are Lower Cretaceous Yageliemu Formation (K1y), Shushanhe Formation (K1s) and Baxigai Formation (K1b). The K1y and lower K1s are regarded as the first stratigraphic sequence of Lower Cretaceous (K1SQ1). And the upper K1s and K1b are considered to be K1SQ2 and K1SQ3, respectively. The K1SQ1 in the study area develops braided-river delta. Then rising sea level submerges the uplift and the study area develops bar. The provenance of K1SQ1 and K1SQ2 comes from the weathering products of northwest denuded zone. The K1SQ3 develops meandering river delta derived from southeast area. The results show the reservoir has an averaged porosity of 7.8% and an averaged permeability of 9.7 mD, indicating a low porosity and medium permeability reservoir. However, the physical properties of reservoirs in different sequences are different. The reservoir in K1SQ3 has the maximum averaged porosity (10.3%) and permeability (34.6mD), followed by K1SQ1 (7.2%, 2.1mD) and K1SQ2 (6.7%, 0.29mD). Meanwhile, the results of mercury injection indicates that the pore structure of K1SQ3 is more connected. Sedimentation and diagenesis are main factors that controlling the partial densification of reservoir, which is closely related to the uplift evolution. (1) When the uplift was submerged, it inherited to form a bar. The grain size of bar within K1SQ2 is smaller which makes the primary porosity is limited. (2) Cathode luminescence results show that the calcite cements within reservoir of K1SQ2 are much more developed than that of K1SQ1 and K1SQ3. The cements block the pores and throats which significantly decreases the physical properties of reservoir. These cements in bar are developed because the bar is far away from the Terrigenous clastic. The settings of shallow lacustrine makes it is favorable for calcite cements formation. In summary, uplift evolution makes the sedimentary facies and diagenesis environments change, then they will affect the reservoir quality.

SIBERIAN PLATFORM

1,561,302

NEOPROTEROZOIC EVOLUTION OF THE NORTHWESTERN MARGIN OF THE SIBERIAN PLATFORM

B.B.Kochnev, A.K.Khudoley, N.S.Priyatkina, S.Andrew Dufrane, B.G.Pokrovsky, A.B.Kuznetsov, O.K.Kaurova and V.V.Marusin (Trofimuk Inst; St Petersburg State Univ). *PRECAMBRIAN RESEARCH* v.382, Nov. 2022. (ISSN 0301-9268; Article no.106877)

New geochronological, geochemical and carbon isotope data from the Igarka Uplift constrain the age and reveal geodynamic evolution of the northwestern Siberian Platform in the latest Mesoproterozoic and Neoproterozoic. Dolostones of the Medvezhy Formation, the oldest part of the sedimentary succession, correspond to the latest Mesoproterozoic (ca. 1000 Ma) according to stable isotopic composition. Overlying volcano-sedimentary Ludy, Gubinskaya and Igarka formations are no older than 715 Ma according to detrital zircon ages and carbon isotope data. Chemical composition of the Igarka Formation and synchronous mafic intrusions of the Gubinskaya Formation suggest a single magma source developed in an intraplate rifting environment. The Ediacaran Chernaya Rechka and Izluchina formations unconformably cover both meso- and mid-Neoproterozoic sequences. The age of the Ediacaran units are confirmed by the Pb-Pb isochron age of 610 ± 50 Ma and large positive C-isotope anomaly in the Chernaya Rechka limestones. Abundant Neoproterozoic (950-800 Ma) detrital zircons in the studied Neoproterozoic sedimentary rock units points to the existence of a hypothetic large Neoproterozoic orogenic belt on the northeastern periphery of the Siberian Platform unexposed nowadays. The pre-Ediacaran rift trough of the Igarka Uplift and other similar structures, mark extensional environments along the present western margin of the Siberian platform in the mid-Neoproterozoic. These structures are coeval to a large igneous province (ca. 720 Ma) at the northern Laurentia associated with the Rodinia breakup. (c2022 Elsevier B.V.)

SICHUAN

1,561,303

BIOSTROMAL UNIT FROM THE MIDDLE DEVONIAN JINBAOSHI FORMATION, SICHUAN, SOUTHWEST CHINA: IMPLICATIONS FOR ECOLOGICAL STRUCTURE OF COEVAL REEF COMMUNITIES

J.Huang, Y.Li, S.Kershaw, W.Guo, K.Liang and W.Qie (Nanjing Inst Geol Palaeont; Brunel Univ). *PALAEOGEOGRAPHY, PALAEOCLIMATOLOGY, PALAEOECOLOGY* v.608, 12/15/2022. (ISSN 0031-0182; Article no.111272)

This study provides a comprehensive palaeontological and palaeoecological analysis of a middle Givetian (Middle Devonian) coral-stromatoporoid biostromal unit from the upper member of the Jinbaoshi Formation, northern Sichuan Province, Southwest China. The biostromal unit is 17.7 m of medium- to thick-bedded limestones, and lacks observable morphological relief in the field. Diverse shallow marine benthic fossils are common elements of the biostromal unit encompassing stromatoporoids (7 genera), tabulate corals (4 genera), brachiopods (2 genera), plus unidentified rugose corals, chaetetids, bryozoans, tubeworms, ostracods, gastropods, crinoids and calcimicrobes. In terms of the biotic composition and biostrome-building contributors, three ecological units are recognized: *Alveolites-Clathrocoelona* community (EU 1), *Salairrella-Pseudotrurpetostroma* community (EU 2) and *Scoliopora-Idiostroma* community (EU 3). High fragmentation of bioclasts partially with micritic envelopes in wackestone, packstone to grainstone matrix and the dominance of low-profile stromatoporoids indicate deposition in shallow water conditions with episodic high sedimentation rate and frequent turbulent periods. Muddy silt- to sandstone facies overlie the biostromal unit, and are interpreted to represent a shallowing-up sequence, together with terrigenous input, thus triggering termination of the biostromal unit. This biostromal unit is similar to the other early to middle Givetian reefs of South China, East Australia, West Europe, East Europe and North Africa in relation to their fossil composition and reef-building characteristics. The stability of the reef communities (i.e. no conspicuous extinction) and common occurrence of unusual reef structures (e.g. coverstone) are thus interpreted as significant biotic factors for the expansion of large-scale ecosystems during the Phanerozoic reef-building acme. (c2022 Elsevier B.V.)

SICHUAN

1,561,304

REINVESTIGATION ON THE CONODONTS FROM THE KUHFENG AND TOPMOST CHIHHSIA FORMATIONS AT THE ZHENGPANSHAN SECTION IN LONGTAN, NANJING

D.X.Yuan and S.Z.Shen (China Univ Mining Technol; Nanjing Univ). *5TH INTERNATIONAL CONODONT SYMPOSIUM [ICOS] (Wuhan, China and Online, 6/24-27/2022) PROGRAM AND ABSTRACTS* p.52, 2022. (Abstract only)

The base of the Guadalupian Series (Middle Permian) has been defined by the first appearance datum (FAD) of the conodont *Jinogondolella nankingensis* at the Stratotype Canyon section in the Guadalupe Mountains National Park in Texas, USA. However, both the holotype of the conodont *J. nankingensis* and the geochronologic age of the Cisuralian-Guadalupian boundary (CGB) in the official International Chronostratigraphic Chart were obtained from the base part of the Kuhfeng Formation at the Zhengpanshan section in Longtan of Nanjing, southeast China. Therefore, the Zhengpanshan section has actually become one of the international standard section for the correlation around the CGB. We here review previously reported data (e.g., Jin, 1960; Wang et al., 1987; Wang, 1995) and report our newly recovered conodont specimens from the Kuhfeng and topmost Chihhsia formations at the Zhengpanshan section. Jin (1960) named seven new species, including: *Neoprioniodus lanceolatus*, *N. nankingensis*, *Lonchodina lungtanensis*, *Ozarkdina lungtanensis*, *O. chengpanshanensis*, *Synprioniodina kufengensis* and *Gondolella nankingensis*, from the lower part of the Kuhfeng Formation at the section. However, only *G. nankingensis* (= *Jinogondolella nankingensis* in this study) was conodont P1 element, and all the others were ramiform elements which are difficult to be re-identified. Two more new species, *Sweetognathus subsymmetryricus* and *S. paraguizhouensis*, were illustrated from the base part of the Kuhfeng Formation at the same section by Wang et al., (1987), but these *S. paraguizhouensis* were referred to *S. subsymmetryricus* by Shen et al., (2013). Because the holotype of *Jinogondolella nankingensis* was lost, Wang (1995) suggested one neotype of it from *Zhengpanshan*, and also illustrated *Hindeodus minutus*, *Pseudohindeodus* sp., *Sweetognathus subsymmetricus* and *S. guizhouensis* from the base part of the Kuhfeng Formation. In view of the difference between these *S. guizhouensis* and the holotype, we here consider that they are not *S. guizhouensis*. In addition, eight species of five genera have been identified in this study from the topmost part of the Chihhsia Formation to the middle part of the Kuhfeng Formation at the section: *Hindeodus minutus*, *H. typicalis*, *H. sp.*, *Jinogondolella-aserrata*, *J. sp.*, *Pseudohindeodus ramovsi*, *Pseudosweetognathus costatus* and *Sweetognathus subsymmetricus*. Three conodont zones--the *S. subsymmetryricus*-*Pseudosweetognathus costatus* Zone in the topmost part of the Chihhsia Formation and the *Jinogondolella nankingensis* and *J. aserrata* zones in the lower-middle part of the Kuhfeng Formation--have been recognized at this section. The updated conodont biostratigraphy shows that the CGB should be located at the base of the Kuhfeng Formation at the Zhengpanshan section, and the lower part of the Kuhfeng Formation belongs to the Roadian Stage. The middle part of the Kuhfeng Formation has yielded the conodont *J. aserrata*, which probably indicates a Wordian age.

SICHUAN BASIN

1,561,305

GENETIC MECHANISM OF EYEBALL-SHAPED LIMESTONE IN FIRST MEMBER OF MIDDLE PERMIAN MAOKOU FORMATION IN SOUTHEAST SICHUAN BASIN

Y.Han, Y.Hao, W.Han, J.Lin, H.Zhao and S.Li (Sinopec; Zhongyuan Oilfield Co). *PETROLEUM GEOLOGY AND RECOVERY EFFICIENCY (YOUQI DIZHI YU CAISHOULU)* v.29, no.6, pp.12-21, Nov. 2022. (ISSN 1009-9603; In Chinese)

[Full article and English abstract available from P.A.]

SICHUAN BASIN

1,561,306

MICROMECHANICAL CHARACTERISTICS OF MARINE/CONTINENTAL SHALE BASED ON INDENTATION TEST

L.Chen, D.Zhang, S.Lue and S.Wang (State Key Laboratory China; China Univ Geosci, Wuhan). *PETROLEUM GEOLOGY AND RECOVERY EFFICIENCY (YOUQI DIZHI YU CAISHOULU)* v.29, no.6, pp.31-38, Nov. 2022. (ISSN 1009-9603; In Chinese)

[Full article and English abstract available from P.A.]

SICHUAN BASIN

1,561,307

PREDICTION OF ULTRA-TIGHT SANDSTONE RESERVOIR PERMEABILITY BY CAPILLARY PRESSURE CURVE BASED ON PARTIAL LEAST SQUARES REGRESSION METHOD

Y.Guo, L.Sima, L.Wang and Y.Guo (Southwest Petroleum Univ). *PETROLEUM GEOLOGY AND RECOVERY EFFICIENCY (YOUQI DIZHI YU CAISHOULU)* v.29, no.6, pp.67-76, Nov. 2022. (ISSN 1009-9603; In Chinese)

[Full article and English abstract available from P.A.]

SICHUAN BASIN

1,561,308

EVIDENCE OF Hg ENRICHMENT AT THE SPBE FROM LOWER JURASSIC CONTINENTAL SUCCESSION OF THE SICHUAN BASIN, CHINA

H.Jiang, M.Franceschi, X.Jin, E.Petranich, C.Landucci, E.Pavoni, N.Barago, S.Covelli, L.Bonini et al. (Trieste Univ). *21ST INTERNATIONAL SEDIMENTOLOGICAL CONGRESS [ISC] (Beijing, China, 8/22-26/2022) ABSTRACT BOOK* p.186, 2022. (Available at <http://www.isc2022.org.cn> as of 9/22/2022; Abstract only)

In the Early Jurassic, there is a globally recognized perturbation of the carbon cycle occurred at the Sinemurian-Pliensbachian transition, named "Sinemurian-Pliensbachian Boundary Event" (SPBE, ca 192.5 Ma). The SPBE is associated with environmental and climate perturbations such as increased runoff, changes in marine shallow water carbonate production, enhanced preservation of organic matter and dysoxic conditions in the oceans. Evidence mainly comes from the marine realm, while other sedimentary settings around the world has been less investigated. Recent works have highlighted the presence of a prominent negative perturbation of the $\delta^{13}\text{C}_{\text{org}}$ in Lower Jurassic lacustrine succession of the Sichuan Basin, which has been correlated to the SPBE (Franceschi et al., 2022). The causes of the SPBE are still unclear, but a potential link to late phases of volcanism of the Central Atlantic Magmatic Province has been hypothesized based on mercury (Hg) enrichments observed in Sinemurian-Pliensbachian marine successions of the Western Tethys (Shollhorn et al., 2020). Studies have put forward the hypothesis of a warming trend in the lower Pliensbachian that may have culminated in short-lived hyperthermals (e.g. Silva et al., 2015). In this contribution, we present Hg and TOC content data from the Lower Jurassic lacustrine succession of the Sichuan Basin (Eastern Tethys) in the Dacao section where a high resolution $\delta^{13}\text{C}_{\text{org}}$ record is already available (Franceschi et al., 2022). Results highlight Hg enrichments coincident with the negative $\delta^{13}\text{C}_{\text{org}}$ shift that is interpreted as the SPBE. The relative low correlation with TOC data, suggests that Hg could be volcanogenic. This, together with the fact that the Hg enrichment at the Sinemurian-Pliensbachian transition is documented in the continental realm, strengthen the hypothesis of a global-scale link between the SPBE and volcanic activity. Preliminary results of elemental analysis carried out with pXRF further reveals enrichment trends in elements such those of the group of clay minerals that may be compatible with variations in runoff intensity caused by climate change to more humid conditions at the SPBE. Our results provide clues as to how climate changes associated with the SPBE may have been linked to volcanic activity and have had global extent.

SICHUAN BASIN

1,561,309

CHARACTERIZATION OF PORE STRUCTURE OF DEEP SHALE BASED ON SHAPE COEFFICIENT

B.Zhu, R.Pan and J.Meng (Yangtze Univ). *21ST INTERNATIONAL SEDIMENTOLOGICAL CONGRESS [ISC]*

(Beijing, China, 8/22-26/2022) ABSTRACT BOOK p.1558, 2022. (Available at <http://www.isc2022.org.cn> as of 9/22/2022; **Abstract only**)

Deep shale gas is gradually becoming the key exploration and development object in Sichuan Basin, China. The corresponding nano pore characterization technology and method of deep shale gas also need to be further developed and innovated. Field emission scanning electron microscope was used to observe and extract the minimum ferite diameter of micropores, mesopores and macropores. The elliptical shape coefficient of organic pores was obtained through calculation. The pore structure of deep organic-rich siliceous shales of the Longmaxi Formation in the Luzhou area of the southern Sichuan Basin was characterised quantitatively by shape factors. According to the ideal (oval) organic pore shape coefficient, micropores (0.93) are the least affected by compaction, followed by mesopores (0.85), while macropores are the largest (0.61). Their shape gradually tends to be flat from circle. According to the true shape coefficient of organic pores, in the deep shale section with organic pores of about 4000 m, the shape of macropores was the worst preserved, common complex irregular ellipses are densely and disorderly distributed in organic matter, and the true shape coefficient was about 0.3-0.6; The mesoporous shape was well preserved, the common approximate regular ellipse is sparse and disorderly distributed in organic matter, and its true shape coefficient was about 0.6-0.9; The shape of micropores was the best preserved. They are usually approximately regular circles, which are densely and evenly distributed in organic matter, and their true shape coefficient was about 0.9-1.0. The preservation and distribution of full pore organic pores are characterized by shape coefficient, and the heterogeneity of pore structure decreases from macropores to micropores. Therefore, micropores and mesopores are the main enrichment sites of adsorbed gas and free gas.

SLOVENIA

1,561,310

HARDSHIPS OF CONODONT BIOSTRATIGRAPHY THROUGH THE LOWER/MIDDLE NORIAN BOUNDARY IN THE WESTERN TETHYS

V.Karadi (Eotvos Lorand Univ). 5TH INTERNATIONAL CONODONT SYMPOSIUM [ICOS] (Wuhan, China and Online, 6/24-27/2022) PROGRAM AND ABSTRACTS p.51, 2022. (**Abstract only**)

The application of conodonts for Norian biostratigraphy dates back to the late 1950s; however, its accuracy developed rather slowly, and the existing Norian conodont biozonation of the Western Tethys has still to be refined. The improvement of the zonal scheme faces several hardships, especially through the Lower/Middle Norian (Lacian/Alaunian) transition and in the Middle Norian (Alaunian). On the one hand, the problem originates in the over-simplified taxonomy of Norian conodonts, since thorough and detailed systematic studies have never accompanied biostratigraphic investigations. Stratigraphers often gather taxa under 3 to 6 species names, the majority of which were introduced in the second half of the 20th century. This act generated artificially long ranges for these commonly used species (e.g. *Epigondolella abneptis*, *E. multidentata*, *Mockina postera*). On the other hand, sections with useful conodont material are scarce, since the high rate of juvenile mortality is a widespread feature in the Alaunian. Even if adult specimens are available, stratigraphic evaluation is in most cases hampered by sedimentary (micro)breccias and/or neptunian dykes in the Lacian/Alaunian transition and slump structures through the Alaunian, which result in reworking and mixed conodont assemblages. Within the frames of a research project launched a couple of years ago for the refinement of the Norian conodont zonation of the Western Tethys, sampling campaigns were carried out to recover diverse Lacian and Alaunian conodont assemblages. The Dovsko succession in Eastern Slovenia yielded rich faunas through the Lacian/Alaunian transition, which shed light to the large morphological variety of Alaunian conodonts of the Tethys realm. The fauna included species well-known from western North America (e.g. *Epigondolella spiculata*, *E. tozeri*), but several new species were also found (e.g. *E. senovoensis*, *E. slovenica*, *E. ritae*). The typically Lacian ancyrogondolellids (e.g. *Ancyrogondolella rigoi*, *A. triangularis*) are present also in the inevitably Alaunian part of the section characterized by

Norigondolella steinbergensis and the high number of specimens with a forward shifted pit and a posteriorly prolonged keel. Microfacies analysis revealed the presence of neptunian dykes at the base of the Lacian/Alaunian transition and intraclasts in several levels of the section. These features raise uncertainties concerning the first occurrences of certain lower Alaunian species, as well as the range of the Lacian genus *Ancyrogondolella*, since several specimens might be reworked.

SLOVENIA

1,561,311

CONODONTS OF SLOVENIA

T.Kolar-Jurkovsek and B.Jurkovsek (Slovenia Geological Survey). 5TH INTERNATIONAL CONODONT SYMPOSIUM [ICOS] (Wuhan, China and Online, 6/24-27/2022) PROGRAM AND ABSTRACTS p.71, 2022. (**Abstract only**)

Conodonts are elements of a feeding apparatus of an extinct group of jawless vertebrates that can be found from Paleozoic to Triassic marine strata. They display worldwide distribution and rapid evolution, and due their mineralogical composition and resistance to rock diagenesis they are valuable tool in global biostratigraphy. The beginning of conodont research in the region dates back to the 1960s and it is one of the most important paleontologic methods used to determine relative geological age at the Geological Survey of Slovenia, especially by knowing that nearly a third of national area is covered by Triassic strata. The book *Conodonts of Slovenia* presents the result of systematic conodont research in Slovenia found in marine sedimentary rocks of the Eastern and Southern Alps, the External Dinarides and the transitional area between the External and Internal Dinarides. This work represents a fundamental scientific work in the field of paleontology and biostratigraphy in Slovenia. It is supported by original art reconstructions, numerous graphic illustrations, field photographs, and 44 plates with conodont elements. The selection of literature contains 364 reference sources, which provides more detailed insight into the conodont research of the studied area and in the world. Based on the studied conodonts in the Paleozoic strata of Slovenia, 18 Devonian, Carboniferous and Permian associations were distinguished. A conodont zonation scheme for the strata ranging through the entire Triassic was established; it identified 34 zones and two subzones. Among the study results, the determined Permian-Triassic boundary, defined for the first time in the territory of Dinarides according to international criteria, undoubtedly stands out.

SONGLIAO BASIN

1,561,312

SPATIO-TEMPORAL EVOLUTION AND DYNAMIC MECHANISM OF LOWER CRETACEOUS VOLCANIC-SEDIMENTARY STRATA IN SONGLIAO BASIN, NORTHEAST CHINA: IMPLICATIONS FOR REGIONAL TECTONIC EVOLUTION

C.Chen and Y.Gao (Jilin Normal Univ; Jilin Univ). 21ST INTERNATIONAL SEDIMENTOLOGICAL CONGRESS [ISC] (Beijing, China, 8/22-26/2022) ABSTRACT BOOK p.331, 2022. (Available at <http://www.isc2022.org.cn> as of 9/22/2022; **Abstract only**)

The Early Cretaceous tectonic evolution in Northeast China may be affected by the Mongolia Okhotsk and the ancient Pacific tectonic domain, but the mode of action, scope of influence and transform time of the two tectonic region have been controversial. Early Cretaceous magmatic rocks are widely distributed in Northeast China. Their spatial and temporal distribution and geochemical characteristics do not clearly reflect the dynamic mechanism. The Xujiaweizi fault depression SK-2 drilling area of the International Continental Scientific Drilling Program, located in the central part of Northeast China, is one of the large grabens in the Songliao Basin. It is mainly a set of thick volcanic-sedimentary strata formed in the Early Cretaceous (118-101 Ma). Its formation and evolution process may record the history of regional tectonic evolution in detail, and it is an important research area to solve the problem of regional tectonic evolution. In this study, the volcanic-sedimentary strata (114-101 Ma) of Yingcheng Formation of Lower Cretaceous in Xujiaweizi graben are divided and compared based on three-dimensional seismic profiles,

boreholes and logging data. According to the geological and geophysical characteristics of lithology and interface, the volcanic-sedimentary strata are divided into three members, i.e. volcanic member I, sedimentary member II and volcanic member III, and the two volcanic members can be further divided into three volcanic eruption stages respectively. Combined with the characteristics of the main faults in the Xujiaweizi graben, the plane distribution maps of each stratigraphic sequence-three volcanic/sedimentary members and six volcanic eruption stages are compiled. It is found from the plane maps that the volcanic-sedimentary strata of the Lower Cretaceous have the spatio-temporal evolution law of migration from southeast to northwest from early to late, accompanied by the NNW-SSE sinistral strike-slip deformation. According to the regional tectonic setting, the spatio-temporal evolution of the volcanic-sedimentary strata of the Lower Cretaceous should be related to the westward subduction of the paleo-Pacific. Therefore, during the period 114-101 Ma, the westward subduction of the paleo-Pacific plate had a significant influence on the tectonic evolution of Northeast China, and the scope of influence included at least the SB and its eastern region.

SONGLIAO BASIN

1,561,313

DISCOVERY OF THE LATE JURASSIC-EARLY CRETACEOUS LAMPROPHYRES IN WESTERN SONGLIAO BASIN OF NORTHEAST CHINA AND THEIR CONSTRAINT ON REGIONAL LITHOSPHERIC EVOLUTION

T.Yu, P.Wang, Y.Zhang and Y.Gao (Jilin Univ). *21ST INTERNATIONAL SEDIMENTOLOGICAL CONGRESS [ISC] (Beijing, China, 8/22-26/2022) ABSTRACT BOOK* p.341, 2022. (Available at <http://www.isc2022.org.cn> as of 9/22/2022; **Abstract only**)

Contradictory to common concept that the lithosphere in NE China was thinned from Late Jurassic through Early Cretaceous. We discovered, however, a thickening episode in the long-term thinning background. A series of lamprophyre dikes have been recently found in the Tuquan Basin of western Songliao Basin. They were subsequently dated at 156.0 ± 2.3 Ma, 132.9 ± 1.2 Ma, and 126.2 ± 2.5 Ma, respectively, using the zircon U-Pb technique. The lamprophyres are subdivided into Late Jurassic biotite orthoclase lamprophyre (BOL) and Early Cretaceous quartz magnetite lamprophyre (QML). The BOL and QMLs are shoshonite and calc-alkaline in series, characterized by high contents of FeOT, TiO₂, MgO, and Mg# values, and are enriched in LREEs and LILEs but depleted in HREEs and HFSEs. They have high ratios of (La/Yb)_N, La/Ta, La/Nb, Th/Y, Ba/Nb, Ba/Ta, and Ba/Th, and low ratios of Rb/Ba, La/Sm, and Nb/Zr. These features collectively point to the derivation of the dike magmas from the partial melting of enriched lithospheric mantle that had been previously metasomatized by subduction-related fluids. The BOL has high ratios of Rb/Sr (0.42) and K/Yb x 1000 (28.3), and low ratios of Ba/Rb (13.5) and Dy/Yb (2.35), suggesting a magma derivation from high degree partial melting of phlogopite-bearing lherzolite mantle in the spinel-garnet transition zone at a depth about 60 km, the QMLs have low ratios of Rb/Sr (0.020.06) and K/Yb x 1000 (8.1319.73), and high ratios of Ba/Rb (17.642.6) and Dy/Yb (3.484.09), indicating that the magmas were derived by low degree partial melting of lherzolite mantle in the garnet zone at a depth of ca. 85 km, the younger QML (126.2 ± 2.5 Ma) has lower Dy/Yb ratio (3.483.92) than that of the older QML (132.9 ± 1.2 Ma) with Dy/Yb ratio of 4.09, implying that the younger magma was produced at a shallower mantle depth (85 km) than that of the older one. These indicate that in the period of 156-132 Ma, the lithosphere thickened by approximately 25 km at a rate of approximately 1.0 km/Myr. A new geodynamic evolution model of three stages was thus proposed.

SONGLIAO BASIN

1,561,314

CHARACTERISTICS OF VOLCANO STRATIGRAPHIC ELEMENTS IN FAULTED DEPRESSION BASIN AND ITS GEOLOGIC SIGNIFICANCE: A CASE ANALYSIS OF FULL CORING WELL OF LOWER CRETACEOUS YINGCHENG FORMATION IN JIUTAI, JILIN PROVINCE

J.Hu and H.Tang (Jilin Univ). *21ST INTERNATIONAL SEDIMENTOLOGICAL CONGRESS [ISC] (Beijing, China,*

8/22-26/2022) ABSTRACT BOOK p.343, 2022. (Available at <http://www.isc2022.org.cn> as of 9/22/2022; **Abstract only**)

Volcano stratigraphy has special temporal and spatial attributes and geological record characteristics, but it has not attracted enough attention in the analysis of basin filling. In order to further clarify the geological attributes of volcano stratigraphy, the characteristics and geologic significance of volcano stratigraphic elements of Lower Cretaceous Yingcheng Formation in Songliao Basin were studied by taking the full coring shallow drilling wells (Y1D1 and Y3D1) as examples. The results are described as follows: 3 eruptive interval unconformity boundaries and 10 eruptive conformity / unconformity boundaries are identified in the volcano stratigraphy of the first member of Yingcheng Formation in well Y1D1. 2 eruptive interval unconformity boundaries and 8 eruptive conformity / unconformity boundaries are identified in the volcano stratigraphy of the third member of Yingcheng Formation in well Y3D1. According to the attributes of eruptive interval unconformity boundary, the volcano stratigraphy of well Y1D1 can be divided into 4 volcano edifices, and the volcano stratigraphy of well Y3D1 can be divided into 3 volcano edifices. Rare earth and trace elements have a good response to the volcano edifice. There are 6 types of deposit unit: simple lava flow, braided lava flow, dome, pyroclastic flow, base surge and lahar. The emission intensity of volcano gas during the eruption of lava units is weaker than that of pyroclastic units. Volcano stratigraphy has the time attributes of short construction time and long eruptive interruption time, and the construction rate of volcano stratigraphy cannot be calculated simply by using the stratigraphy thickness and the time difference between the top and bottom of the test.

SONGLIAO BASIN

1,561,315

A NEW HYBRID METHOD BASED ON SPARROW SEARCH ALGORITHM OPTIMIZED EXTREME LEARNING MACHINE FOR BRITTLENESS EVALUATION

F.Zhang, S.Deng, H.Zhao and X.Liu (China Univ Petroleum; Jilin Oilfield Res Inst). *JOURNAL OF APPLIED GEOPHYSICS* v.207, Dec. 2022. (ISSN 0926-9851; Article no.104845)

Shale brittleness is the key parameter to optimize reservoir fracturing modification and improve productivity. However, conventional methods based on rock mechanics and mineralogical parameters are limited by the lack of shear wave velocity and mineral composition data. Machine learning algorithms have been applied in the field of geophysical exploration, but the prediction accuracy of existing algorithms needs to be improved. In this study, a new hybrid model, an integration of the Sparrow Search Algorithm (SSA) and the Extreme Learning Machine (ELM), named SSA-ELM, is proposed for predicting the brittleness index. ELM is performed to create the original brittleness model, meanwhile, the SSA algorithm is utilized to automatically explore the hyperparameters of the model. Additionally, we also use 12 other favorite machine learning algorithms to validate the superiority of the proposed model combined with traditional logs and XRD-derived brittleness. 82 mineral brittleness databases from 5 exploration wells in the Songliao Basin, China were established. The simulation results of two Test wells indicate that the SSA-ELM model has the most accurate predictions and excellent generalization capability. The brittle profiles established based on the SSA-ELM model can effectively guide the fracturing exploration of shale oil reservoirs. (c2022 Elsevier B.V.)

SOURCE CODE

1,561,316

PYLEOCLIM: PALEOCLIMATE TIMESERIES ANALYSIS AND VISUALIZATION WITH PYTHON

D.Khider, J.Emile-Geay, F.Zhu, A.James, J.Landers, V.Ratnakar and Y.Gil (Southern California Univ). *PALEOCEANOGRAPHY AND PALEOCLIMATOLOGY* v.37, no.10, Oct. 2022. (ISSN 2572-4525; Article no.e2021PA004509)

We present a Python package geared toward the intuitive analysis and visualization of paleoclimate timeseries, Pyleoclim. The code is open-source, object-oriented, and built upon the standard scientific Python stack, allowing users to take advantage of a large collection of existing and emerging techniques. We describe the code's philosophy, structure, and base functionalities

and apply it to three paleoclimate problems: (a) orbital-scale climate variability in a deep-sea core, illustrating spectral, wavelet, and coherency analysis in the presence of age uncertainties; (b) correlating a high-resolution speleothem to a climate field, illustrating correlation analysis in the presence of various statistical pitfalls (including age uncertainties); (c) model-data confrontations in the frequency domain, illustrating the characterization of scaling behavior. We show how the package may be used for transparent and reproducible analysis of paleoclimate and paleoceanographic datasets, supporting Findable, Accessible, Interoperable, and Reusable software and an open science ethos. The package is supported by an extensive documentation and a growing library of tutorials shared publicly as videos and cloud-executable Jupyter notebooks, to encourage adoption by new users.

SOURCE ROCK 1,561,317

NANOSCALE PHYSICAL PARAMETERS OF SOURCE ROCKS IDENTIFIED BY ATOMIC FORCE MICROSCOPY: A REVIEW

Y.Liu, G.Zou, J.She, B.Deng and H.Yang (China Univ Mining Technol; Shanxi Geo-Environ Ctr). *GEOLOGICAL JOURNAL* v.57, no.10, pp.4345-4356, Oct. 2022. (ISSN 0072-1050; ISSN 1099-1034)

The refinement of nanoscale physical parameters of source rocks has benefitted from continuous innovations in technology and methods. Traditional methods for detecting reservoir physical properties are limited by the properties of the instruments. Atomic force microscopy (AFM) provides new methods and approaches for furthering our understanding and exploring the nanoscale world. Its wide range of applications and gradually developed multiscenario application modes make it an ideal tool for the characterization of nanoscale physical properties of source rocks (coal, shale, mudstone, sandstone, etc.). We highlight the advantages of AFM in regard to performing nondestructive 3D imaging and mechanical property measurements with nanoscale resolution in any desired environment (air, vacuum, liquid). The limitations of AFM applied to source rocks are also summarized. The process has great potential in micro/nanopore characterization, surface morphology characterization, in situ micromechanical property acquisition, wettability research, and so on. The gradual development and improvement of this new model will expand new methods, bring enlightenment to basic research on unconventional oil and gas resources, and provide a scientific basis for the exploration and development of unconventional oil and gas resources.

SOURCE TO SINK 1,561,318

A NOVEL APPROACH FOR STUDYING SOURCE-TO-SINK SYSTEM USING STRATIGRAPHIC FORWARD MODELLING

J.Gao, K.Liu and J.Liu (China Univ Petroleum). *21ST INTERNATIONAL SEDIMENTOLOGICAL CONGRESS [ISC] (Beijing, China, 8/22-26/2022) ABSTRACT BOOK* p.235, 2022. (Available at <http://www.isc2022.org.cn> as of 9/22/2022; **Abstract only**)

The study of source-to-sink (S2S) system has become an integral part of depositional system and basin analysis. Conventionally S2S analysis mostly invokes comparing heavy mineral assemblages, elemental compositions and geochronology of certain minerals (e.g., zircon) from sources and sinks. This approach, however, depends heavily on the availability of outcrop, core or cutting samples from both the provenance (source) and basin (sink) areas, and is not always applicable. This is especially true, when analyzing ancient S2S or in exploration frontier basins, where the provenance may have already been eroded away or buried, or few samples are available from limited subsurface drillings. The other challenging issue with the conventional approach is that the interpretation of the mineralogical, geochemical and geochronological data from individual provenances may not be unique or the data do not have the spatial-temporal resolution to differentiate sediment provenances. Here, we propose an alternative approach for S2S analysis using stratigraphic forward modeling (SFM), which allows us to study the sediment transport process of the S2S system quantitatively and reproduce the dynamic evolution of the sediment routing system. The

procedure involves the reconstruction of a 3D stratigraphic model for the basin (sink) to be investigated using a hydrodynamics-based sedimentary modelling program that mimics the depositional processes during the basin-fill process. Once the model is calibrated and validated with available seismic, well log or core data, it can then be used to generate lithological, sedimentary facies and chronological information at each grid cell. Such information can be extracted to quantitatively determine the contribution from individual sediment provenances, achieving a quantitative analysis of the S2S system. The animated SFM also allows the visualization of the S2S depositional process in 3D. The construction of a SFM requires four major input parameters including (1) initial topography, (2) tectonic movement, (3) base-level change and (4) sediment supply. These input data can be derived from our existing understanding of regional geology (e.g., conceptual model, published literatures), available seismic, well log and core data, and modern analogues. For S2S analysis, it is crucial to preset the sediment supply parameter comprising source locations, sediment compositions, discharge rates, etc. A novel method is designed to preset sediment supply from multiple sources in which the sediment at each source is being released alternately to chronologically differentiate the relative contributions from different sources at any given grid cells in the basin at a given time step (duration). A conceptual sedimentary basin model of 80 x 98 km in dimension with three sediment provenances was used to demonstrate the effectiveness of this novel approach for S2S analysis.

SOUTHEAST ASIA 1,561,319

CORRELATION AMONG THE AILAOSHAN-SONG MA-SONG CHAY OROGENIC BELTS AND IMPLICATIONS FOR THE EVOLUTION OF THE EASTERN PALEO-TETHYS OCEAN

Y.Wang, W.Lin, M.Faure, V.Van Nguyen, L.Meng, Y.Chu, W.Wei, H.L.T.Thu, C.Lepvrier et al. (Chinese Academy Sciences). *TECTONOPHYSICS* v.843, 11/20/2022. (ISSN 0040-1951; Article no.229618)

The timing and mechanism of the combination between the South China Block (SCB) and the Indochina Block (IB) are controversial. Three ophiolitic melange zones (Ailaoshan, Song Ma, and Song Chay) have been proposed as suture zones within this collisional orogen. However, the relationships among the three corresponding tectonic belts are unclear. In this study, we present detailed structural data for the three tectonic belts. The bulk architectures of the Ailaoshan, Song Ma, and Song Chay belts correlate well with one another. This similarity is also revealed by our new zircon U-Pb geochronological results from the Song Ma and Song Chay ophiolites. The regional deformation age is constrained to between 250 and 240 Ma by our new muscovite ⁴⁰Ar/³⁹Ar ages, and the medium-low temperature conditions are revealed by the quartz c-axis fabric. Considering the transformation effect of the Cenozoic large-scale sinistral strike-slip of the RRF and DBF, the Early Mesozoic Ailaoshan, Song Ma, and Song Chay suture zones should represent different segments of the same belt. Based on this hypothesis, we compiled the ages of the magmatism in this region, which allows us to propose an evolutionary model as follows: (i) ca 380–310 Ma continental rifting and subsequent Ailaoshan–Song Ma–Song Chay ocean spreading as a branch of the Paleo-Tethys, (ii) ca 310–250 Ma oceanic subduction coeval with continental-arc magmatism, (iii) ca 250–240 Ma continental collision, (iv) ca 240–220 Ma post-collisional extension. (c2022 Elsevier B.V.)

SOUTH GERMAN BASIN 1,561,320

SEDIMENTOLOGY AND SEQUENCE STRATIGRAPHY OF THE AALENIAN FROM SOUTHERN GERMANY

T.Mann, A.Bornemann and J.Erbacher (Fed Inst Geosci Nat Rscs). *21ST INTERNATIONAL SEDIMENTOLOGICAL CONGRESS [ISC] (Beijing, China, 8/22-26/2022) ABSTRACT BOOK* p.228, 2022. (Available at <http://www.isc2022.org.cn> as of 9/22/2022; **Abstract only**)

Middle Jurassic sedimentary deposits in southern Germany have accumulated in a shallow-marine shelf environment and are typically dominated by thick clayey lithologies with increasing

occurrences of sandstones in the upper parts. The sedimentary evolution and paleoclimatic significance of these often poorly exposed deposits remain largely unexplored. Here we present a suite of high-resolution x-ray fluorescence (XRF) core scanning data from southern Germany covering the entire Aalenian stage. The overall objective of this study is to identify Transgressive-Regressive cycles based on the analysis of three cores obtained during scientific drilling campaigns in 2019-2021. Cores have been analyzed with an Avaatech XRF Core Scanner at a 10 mm sampling interval, an energy of 10 keV and a current of 500 µA to measure element intensities ranging from aluminium through iron. Resulting trends in elemental ratios indicative for subtle grain-size variations such as Si/Al are used to reconstruct shoreline trajectories and establish a sequence stratigraphic framework. Particularly the thick and largely homogenous Opalinuston Formation appears suitable in that respect, likely resulting from extraordinarily high sedimentation rates during the lower Aalenian in southern Germany, thus providing a complete but unexplored archive of paleoclimatic signals. For the upper Aalenian, a fennoscandian sandstone provenance resulting from uplift of the North Sea dome has been suggested. Such an exotic source area has important implications regarding transport processes and, consequently, the underground architecture of upper Aalenian sandstones. Accordingly, this project will also investigate sediment provenance in order to provide a holistic view of the sedimentary evolution of the South German Basin during the Aalenian.

.....
SPAIN **1,561,321**

RESERVOIR CHARACTERIZATION OF MID-CRETACEOUS TAR SANDSTONES OUTCROPPING IN NORTHERN SPAIN

G.R.Valverde (Madrid Politecnica Univ). *83RD ANNUAL EAGE CONFERENCE (Online and Madrid, Spain, 6/6-9/2022) ABSTRACTS 2022.* (Abstract no.626; Available at <http://www.earthdoc.org> as of 7/7/2022; 5 pp; **Abstract only**)

The Utrillas Formation, widely present on vast area of Spain, now in production of gas and light condensate at Viura (Rioja). This formation presents outcrops around the producing field, Fuentetoba (Soria) and Torrelapaja (Zaragoza), along the Iberian Range and Huidobro and Basconillos del Tozo (both in Burgos province) at the southern edge of the Basque-Cantabrian Basin, that allow us to interpolate the properties of the sandstone reservoir present in Viura. The main objective will consist in evaluate the different samples taken at the different outcrops, impregnate them with blue epoxy to magnify the contrast between the pore and the grain. Then the samples are grounded to obtain thin sections to observe with a petrographic microscope, used to create a basic analysis. A point counting is made to ensure adequate accuracy. The hypothesis that explains the presence of hydrocarbons and the lack of lateral continuity might be the presence of thin layers of black shales that generated oil in the first place, and due to erosive processes, when exposed to the atmosphere the bacteria took place of the most volatile fractions leaving only the tar behind.

.....
SPAIN **1,561,322**

A DIVERSE LATE EDIACARAN SKELETAL FOSSIL ASSEMBLAGE FROM CENTRAL SPAIN

I.C.Sanchez, M.M.Mus, S.Jensen and T.Palacios (Extremadura Univ). *58TH ANNUAL PALAEOLOGICAL ASSOCIATION MEETING (Leeds, UK, 12/16-19/2014) ABSTRACTS p.25, 2014.* (Available at <http://www.palass.org> as of 11/15/2022; **Abstract only**)

Knowledge of late Ediacaran (ca. 551-541 Ma) skeletal fossils is critical to unravel the earliest evolution of animals, including the acquisition of biomineralized hard parts. However, fossils of this age are scarce and their diversity remains poorly known. Late Ediacaran platform carbonates from the Ibor Group in the area of Villarta de los Montes, central Spain, have recently yielded a diverse skeletal fossil assemblage. Fossils occur as moulds in siliciclastic levels and mineralized (preserving a carbonatic composition or secondarily pyritized or phosphatized) in carbonate beds. The assemblage is dominated by *Cloudina*, a millimetric tubular fossil consisting of stacked funnel-shaped elements. Two species, *C. hartmannae* and *C. carinata*, that differ both in funnel

morphology and imbrication pattern are present. Particularly well-preserved *C. carinata* have also been found in related olistostromic levels within the Valdelacasa anticline. The Villarta de los Montes assemblage also includes the first *Sinotubulites baimatuensis* specimens from north-west Gondwana. *Sinotubulites* is a millimetric fossil with a tube-in-tube construction and a folded, irregular ornamentation in the outermost layers. Small, winding tubular fossils and flask-shaped fossils similar to *Protolagena* have been also observed. Such relatively high diversity in a late Ediacaran assemblage has been previously described only from South China.

.....
SPITZBERGEN **1,561,323**

THE MIDDLE PERMIAN MASS EXTINCTION IN HIGH LATITUDES

P.B.Wignall and D.P.G.Bond (Leeds Univ; Hull Univ). *58TH ANNUAL PALAEOLOGICAL ASSOCIATION MEETING (Leeds, UK, 12/16-19/2014) ABSTRACTS p.51, 2014.* (Available at <http://www.palass.org> as of 11/15/2022; **Abstract only**)

The mass extinction at the end of the Permian is one of the best-known crises of the Phanerozoic. However, it was preceded by a little-known extinction around ten million years earlier. This Capitanian crisis was first identified 20 years ago; it affected taxa from shallow-water tropical sites such as fusulinids, rugose corals, and brachiopods. However, the impact of the crisis on higher latitude communities has not been addressed. The Kapp Starostin Formation is a mixed carbonate-spiculite ramp unit that accumulated at mid-high Boreal latitudes. It contains an abundant benthic fauna of brachiopods, bryozoans, corals, sponges and bivalves but mostly lacks stratigraphically useful fossils such as conodonts and ammonoids. Chemostratigraphic evidence (from strontium and carbon isotope variations) suggests that the Middle/Late Permian boundary is approximately 80 m from the top of the formation. Range charts in the Kapp Starostin reveal that there was a major abrupt extinction event in the latest Middle Permian. The Capitanian mass extinction thus developed in both the low and mid latitudes. The benthic communities in the Kapp Starostin Formation subsequently recovered and now consist of a diverse brachiopod/bivalve/bryozoan/sponge assemblage.

.....
STRATIGRAPHIC BOUNDARY **1,561,324**

THE REDEFINITION OF THE DEVONIAN-CARBONIFEROUS BOUNDARY: STATE OF THE ART

C.Corradini and M.Aretz (Trieste Univ; Paul Sabatier Univ). *5TH INTERNATIONAL CONODONT SYMPOSIUM [ICOS] (Wuhan, China and Online, 6/24-27/2022) PROGRAM AND ABSTRACTS pp.69-70, 2022.* (**Abstract only**)

The criterion for defining the base of the Carboniferous System is placed to coincide with the First Appearance Datum (FAD) of the conodont species *Siphonodella sulcata*; the GSSP (Global Stratotype Section and Point) is located in La Serre Trench E' section (Paproth et al., 1991). Problems in discrimination of *Si. sulcata* from the supposed ancestor *Si. praesulcata* were already known when the GSSP was established (e.g., Wang & Yin, 1984; Ji, 1987). Flajs & Feist (1988) published a biometric study of *S. praesulcata* and *S. sulcata* based on the material from La Serre, demonstrating that transitional forms are very common. Despite these taxonomical uncertainties, the FAD of *Si. sulcata* was chosen to define the base of the Tournaisian. Further studies on the stratotype section have revealed other problems, such as lack of other important stratigraphic guides and the existence of reworking (e.g., Ziegler & Sandberg, 1996; Casier et al., 2002). After the discovery of *Siphonodella sulcata* below the boundary just above a facies change in the GSSP section (Kaiser, 2009), the definition of the base of the Carboniferous has been back on the agendas of the Devonian and Carboniferous subcommissions. A joined SDS/ISCS Task group was established in 2009 to redefine the base of the Carboniferous and thus to regain stratigraphical stability in this critical interval of Earth history. Task group members have been active in various aspects related to the boundary definition and a wealth of new data has become available (e.g., Corradini et al., 2011, 2017; Kaiser et al., 2015; Prestianni et al., 2016; Marshall et al., 2020). Characteristic for many studies are

multi-disciplinary approaches, which combine palaeontological, sedimentological, geochemical and petrophysical methods and data (e.g., Babek et al., 2016; Kumpan et al., 2014; Matyja et al., 2015). The task group met several times at various international meetings (e.g., Strati, IPC, ICCP) and online. Also, a dedicated workshop with two days of discussions and a field trip to the classical sections in the Montagne Noire, where the present GSSP is located, was organized in Montpellier in September 2016. On that occasion it was decided to test a possible position of the Devonian-Carboniferous Boundary based on a point in time defined by "the base of the *Protognathodus kockeli* conodont Zone, the end of the Devonian mass extinction and beginning of the Carboniferous radiation, and the top of a major regression (the top of the Hangenberg Sandstone)". This point in time is based on different criteria, which should increase the potential of placing the boundary in different facies realms and provinces, and increase the practicability of global correlations.

STYRIA

1,561,325

PALEOVEGETATION AND PALEOCLIMATE INFERENCES OF THE EARLY LATE SARMATIAN PALYNOFLORA FROM THE GLEISDORF FM. AT GRATKORN, STYRIA, AUSTRIA

C.Geier, J.M.Bouchal, S.Ulrich, M.Gross, R.Zetter, T.Denk and F.Grimsson (Vienna Univ; Universalmuseum Joanneum; Swedish Museum). *REVIEW OF PALAEOBOTANY AND PALYNOLOGY* v.307, Dec. 2022. (ISSN 0034-6667; Article no.104767)

The Gleisdorf Formation (Fm.) deposits in the clay pit at Gratkorn, Styria, Austria, are dated to 12.2–12 Ma, and are of late Middle Miocene age (late Serravallian or Sarmatian). To reconstruct the paleovegetation and estimate the paleoclimate at this important vertebrate site, the palynoflora close to the boundary between the vertebrate-bearing layers of the Gratkorn Fm. and the overlying limnic clay deposits of the Gleisdorf Fm. was investigated. Using the single-grain method, 140 palynomorphs were identified. The palynoflora suggests that the paleovegetation was characterised by well-drained lowland and upland forests, riparian forest, and swamp forests. Depending on the dominating tree species, lowland and upland forests might have had closed or more open canopies. Open habitats included wet meadows and shrublands. In addition, conifers were present in the swampy lowlands and the forested uplands. The most prominent paleoclimatic signatures of the palynoflora indicate a fully humid warm temperate climate, with hot to warm summers and cool winters (*Cfa*-, *Cfb*-climate), and a seasonal climate with cool and drier winters and hot to warm and wetter summers (*Cwa*-, *Cwb*-climate). Our results align with existing studies bordering the Styrian Basin and support the presence of subtropical to warm-temperate vegetation around Gratkorn during the Sarmatian. (c2022 The Authors. Elsevier B.V.)

SUBEI BASIN

1,561,326

THE HETEROGENEITY OF LITHOFACIES TYPES, COMBINATION MODES, AND SEDIMENTARY MODEL OF LACUSTRINE SHALE RESTRICTED BY HIGH-FREQUENCY SEQUENCE

B.Sun, X.Liu, J.Liu, G.Wang, H.Shu, Y.Luo, T.Liu and Z.Hua (China Univ Petroleum; Sinopec Int Petrol Corp). *GEOLOGICAL JOURNAL* v.57, no.10, pp.4035-4051, Oct. 2022. (ISSN 0072-1050; ISSN 1099-1034)

The second Member of the Funing Formation in the Haian Sag of the Subei Basin is a set of organic-rich fine-grained sedimentary rocks, which is a key interval for shale oil exploration. Under the premise of establishing a high-frequency sequence framework, the fine description of the lithofacies change characteristics of the continental fine-grained sedimentary rocks is the basis for the prediction of shale oil favourable areas and the optimization of the production horizons. This study is established through wavelet transformation of the natural gamma curve of the high-frequency sequence framework of the second Member of the Funing Formation, using thin-section observation, total organic carbon analysis, and X-ray diffraction experiments to study the lithofacies types and characteristics of fine-grained sedimentary rocks, and discuss the combination of lithofacies under the high-frequency

sequence framework Mode and influencing factors. The results show that the second Member of Funing Formation is composed of three-level sequence of low-level system tract (LST), transgressive system tract (TST), and early high-level system tract (EHST), corresponding to 6 fourth-level sequences and 10 fifth-level sequences. According to the division scheme of "abundance of organic matter + mineral composition + sedimentary structure", it is found that 12 types of lithofacies were developed in the fine-grained sedimentary rocks of the second Member of Funing Formation. The lithofacies type is affected by the palaeoenvironment. The organic matter facies are mainly controlled by palaeo-water depth and palaeo-redox conditions, the components are mainly controlled by palaeo-water depth and palaeo-salinity, and the tectonic facies are mainly controlled by palaeo-redox and palaeo-salinity. The lithofacies are regularly superimposed in the high-frequency sequence framework, and three combination modes of A, B, and C are developed. Among them, the type A lithofacies are developed in the low-stand system tract, and the type B lithofacies are developed in the transgressive system. The C-type lithofacies assemblage developed near the largest flooding surface and the early highstand system tract, and combined with palaeoenvironment analysis to establish a lithofacies sedimentary model.

SUBEI BASIN

1,561,327

THE QUANTITATIVE EVALUATION OF FAULT SEALING DURING THE CENOZOIC IN GAOYOU DEPRESSION, SUBEI BASIN

W.Yu (Sinopec Research Inst). *GEOLOGICAL JOURNAL* v.57, no.10, pp.4099-4109, Oct. 2022. (ISSN 0072-1050; ISSN 1099-1034)

The quantitative evaluation of fault sealing is conducted based on comprehensive analysis of mechanism and type analysis of fault seal, fault seal evaluation, and case study analysis. The results indicate that the properties of fault sealing are the interaction of fault order, net-to-gross ratio, fault activity, mud distribution on fault walls, fault dip, and buried depth. In addition, there are three types of fault sealing, including juxtaposition seal, fault rock seal, and cementation seal. Furthermore, the opening and closing of faults play an essential role in controlling hydrocarbon migration and accumulation. Finally, the fault sealing plays a controlling role in reservoir preservation.

SURAT BASIN

1,561,328

PSEUDORETICULATE - SUBRETICULATE - RETICULATE NUMMULITES AND THEIR POSSIBLE EVOLUTION IN THE MIDDLE EOCENE - LOWER OLIGOCENE SUCCESSION OF SURAT-BHARUCH, GUJARAT, INDIA

S.K.Mukhopadhyay. *MICROPALAEONTOLOGY* v.68, no.6, pp.505-556, 2022. (ISSN 0026-2803; ISSN 1937-2795)

A biostratigraphically well constrained middle Eocene to lower Oligocene shelf succession (ca. 33 m) of the Amravati Formation in the Vagalkhod-Dinod area of Surat-Bharuch Districts, Gujarat, India contains Nummulites having varied septal filaments, among which complicated filaments show progressive changes in the succession. Complications by the intersection of filaments with spiral laminae/ridge, bifurcation of filaments at low angle and joining by transverse trabeculae, and bifurcation and re-joining of filaments at high and varied angles, and consecutive bifurcation and trifurcation of filaments allowed their categorization in different species. Successive appearances of pseudoreticulate filaments (*Nummulites acutus*, *Nummulites broachensis* and *Nummulites longilocula*), subreticulate filaments (*Nummulites hormoensis* and *Nummulites ptukhiani*) and reticulate filaments (*Nummulites fabianii*, *Nummulites retiatus* and *Nummulites fichteli*) reflect gradual complication with time, producing a bioseries that is also manifested by changes in canals and equatorial chambers. The eight species of *Nummulites* are differentiated and described within the pseudoreticulate-subreticulate-reticulate group and based on their stratigraphic distribution, seven zones in ascending order namely, the *Nummulites acutus* Assemblage Zone, *Nummulites broachensis* Range Zone, SRG Barren zone, *Nummulites hormoensis*-*Nummulites fabianii* Interval Zone, *Nummulites fabianii* Range

Zone, *Nummulites fabianii*-*Nummulites retiatus* Interval Zone and *Nummulites fichteli* Range Zone are recognized and described. The zones are tentatively correlated with the SB zones and their ages are assigned by planktonic foraminiferal zones. Complexity of septal filaments within the *Nummulites* of the succession began with the development of pseudoreticulation (by the intersection of radial filaments with spiral laminae) during the late Lutetian; afterward during the early Bartonian Stage bifurcation develops in a septal filament along with occasional joining by transverse trabeculae; subreticulation remained restricted to the late Bartonian, while reticulation appeared at the beginning of the Priabonian to flourish during the Priabonian to mid Rupelian.

SVALBARD

1,561,329

RE-EXPLORING THE EXCEPTIONALLY PRESERVED FOSSILS OF THE TONIAN SVANBERGFJELLET FORMATION OF SVALBARD TO UNDERSTAND THE RISE OF EUKARYOTES

S.Mughal, G.O.Wedlake, T.M.Gibson, A.E.G.Millikin, J.V.Strauss, A.D.Rooney, N.J.Tosca, K.D.Bergmann and R.P.Anderson (Oxford Univ). *65TH ANNUAL PALAEOLOGICAL ASSOCIATION MEETING (Manchester, UK, 12/18-20/2021) PROGRAMME AND ABSTRACTS* p.82, 2021. (Available at <http://www.palass.org> as of 11/1/2022; **Abstract only**)

The diversification of complex eukaryotic life during the Neoproterozoic Era is one of the greatest geobiological transitions in our planet's history. The Tonian (1,000-720 Ma) Svanbergfjellet Formation, Svalbard, provides an exceptional view into this nascent eukaryotic world with the preservation of entirely soft-bodied microfossils including examples of the oldest green algae. Despite their importance, Svanbergfjellet microfossils have not been studied in depth since the early 2000s. We present microfossil data from new samples taken in a high-resolution stratigraphic framework (sampling at approximately 5-10 cm intervals) at two localities in northeastern Spitsbergen: De Geerbukta, where the fossils were originally discovered, and Freken, a new site in southern Lomfjorden. Over 1,000 microfossils are documented from mudstone strata bracketed by stromatolitic bioherms of the informal algal dolomite member. New palaeoenvironmental data, including detailed mineralogy and a Re-Os age constraint, provide context for emerging eukaryote biodiversity. Diversity and preservation quality vary markedly between samples, but the newly documented microfossils are highlighted by an exceptionally preserved population of the possible chlorococcolan alga *Palaeastrum*.

TABAS NAYBAND AREA

1,561,330

CONODONT FAUNA OF UPPER CAMBRIAN-LOWER ORDOVICIAN BOUNDARY INTERVAL FROM SHIRGESHT FORMATION, NORTH OF TABAS, EAST-CENTRAL-IRAN

S.Mohaghegh, A.Ghaderi, A.R.Ashouri and H.Jahangir-Oghli (Ferdowsi Univ; Nanjing Inst Geol Palaeont). *5TH INTERNATIONAL CONODONT SYMPOSIUM [ICOS] (Wuhan, China and Online, 6/24-27/2022) PROGRAM AND ABSTRACTS* p.72, 2022. (**Abstract only**)

The Upper Cambrian-Ordovician strata exposed along Dahaneh-Kalut valley, about 65 km north of Tabas City in Central Iran, are called the Derenjal and Shirgesht formations (Ruttner et al., 1968). The Derenjal Formation is overlain by the Shirgesht Formation, which is informally subdivided into three members. In all, 116 samples of carbonate rocks have been collected from the Upper Derenjal Formation and the Shirgesht Formation's first member. A total of 32 species assigned to 18 genera were recovered from over 610 identifiable conodont specimens. Eight regional zones are established; listed in ascending order, they are: the *Furnishina-Prooneotodus* Ass. Zone, *Proconodontus*, *Eoconodontus*, *Cordylodus andresi*, *Cordylodus proavus*, and *Cordylodus lindstromi* from Furongian, and *Cordylodus angulatus* and *Rossodus manitouensis* from the Tremadocian. The fauna completely lacks shallow-water tropical taxa and most probably belongs to the cold domain of the Shallow Sea Realm. In the absence of determining taxa (*Iapetognatus*), the Cambrian-Ordovician boundary interval is located approximately in the *C. lindstromi* Zone. These new data

from faunas of this interval enable a new understanding of the age and stratigraphic position of the Lower part of the Shirgesht Formation in East-Central Iran. Based on the new conodont data, the lower part of the Shirgesht Formation dates to the upper part of Jiangshanian, stage 10 to Early Tremadocian, respectively. It makes it possible to correlate this area with the adjacent areas in Iran and other equivalents worldwide.

TAIWAN

1,561,331

HYDROCLIMATE DYNAMICS IN THE PLIO-PLEISTOCENE WESTERN PACIFIC

R.Vaucher, C.Zeeden, A.I.Hsieh, S.Kaboth-Bahr, A.T.Lin, C.S.Horng and S.E.Dashtgard (Lausanne Univ; Leibniz Inst Appl Geophys; Simon Fraser Univ). *21ST INTERNATIONAL SEDIMENTOLOGICAL CONGRESS [ISC] (Beijing, China, 8/22-26/2022) ABSTRACT BOOK* p.223, 2022. (Available at <http://www.isc2022.org.cn> as of 9/22/2022; **Abstract only**)

The Plio-Pleistocene stratigraphic record of shallow-marine environments from the Western Foreland Basin (WFB), Taiwan, is an excellent climate archive because of its high temporal completeness promoted through high rates of accommodation creation and sedimentation. To date, only a limited interval of early Pleistocene shallow-marine strata (approximately 220 kyrs) has been astrochronologically tuned, revealing traceable climate oscillations. Here, we astrochronologically tuned the Chinshui Shale and the lower part of the Cholan Formation of the WFB, extending the record of climate oscillations from 3.7 to 1.9 Ma. These strata are tuned to a tropical deep-sea stable oxygen isotope ($\delta^{18}O$) record with an established time scale. The Chinshui Shale is mudstone-dominated and was deposited mostly in offshore settings. The Cholan Formation comprises mainly heterolithic strata deposited in shallower marine settings (i.e., offshore transition and nearshore environment). In this study, we use two borehole gamma-ray profiles from the Chinshui Shale and the Cholan Formation. High gamma-ray values reflect clay-rich mudstone intervals and correlate to lower values of $\delta^{18}O$ in the reference record. Low gamma-ray values point to sandstone-dominated packages and correlate with higher values of $\delta^{18}O$. Our results show that alternating mudstone-dominated to sandstone-dominated successions during the late Pliocene to early Pleistocene are orbitally paced, and the stratigraphic record of WFB is effectively "complete" for the studied time frame between 3.7 to 1.9 Ma. The results also allow us to (i) tune the upper Pliocene-lower Pleistocene Chinshui Shale and lower part of the Cholan Formation, (ii) refine the magneto-biostratigraphic framework established for this time interval in the WFB of Taiwan, and (iii) lay the groundwork for connecting climatic changes in Taiwan during this time to global climate change impacts.

TALIMU BASIN

1,561,332

SEDIMENTARY EVOLUTION OF THE SOUTHWESTERN TARIM BASIN DURING THE CRETACEOUS IN RESPONSE TO BASIN-RANGE COUPLING: NEW INSIGHTS FROM BASIN AND LANDSCAPE DYNAMICS MODELLING

J.Chang, K.Liu and J.Liu (China Univ Petroleum). *21ST INTERNATIONAL SEDIMENTOLOGICAL CONGRESS [ISC] (Beijing, China, 8/22-26/2022) ABSTRACT BOOK* p.236, 2022. (Available at <http://www.isc2022.org.cn> as of 9/22/2022; **Abstract only**)

Sedimentary basin evolution can be reconstructed through modelling the landscape dynamics processes in response to basin-range coupling. In tectonically active regions, it is difficult to effectively restore the paleogeography and paleogeomorphology using conventional methods due to strong tectonic deformation after the initial sedimentary deposition. Several conceptual models have been proposed regarding the sedimentary evolution during the Cretaceous in the southwestern Tarim Basin, China. However, none of them can adequately account for all the research results of the stratigraphic architecture, paleogeography and sedimentary facies in a quantitative way. This study presents the first attempt to simulate the stratigraphic and sedimentary evolution of the southwestern Tarim Basin during the Cretaceous in three dimensions using a basin and landscape evolution modelling

approach. The Badlands software was used to simulate the landscape evolution and sedimentation in response to basin-range coupling. The program is able to generate a more refined landscape model by simulating the tectonic process, climatic changes, base level oscillation and sediment flux. A 3D stratigraphic model of the Early Cretaceous is built by using seismic profiles, structurally balanced cross-sections, well and outcrop data. Relevant parameters such as base-level change, tectonic movement, rainfall, sediment and erosion were assigned to the numerical model to simulate the coupling effect of the orogenic belt denudation and basin sedimentary fill. The simulation results show that: (1) the presence of paleo-uplift within the basin can better match the present-day observed sediment thickness and distribution. (2) sedimentary provenance was sourced primarily from the West Kunlun orogenic belt with the Makit Slope to the north and the paleo-uplift within the basin only providing limited amount of sediment volumetrically and (3) there were no lakes in the basin during the Early Cretaceous, and a major river system developed in the basin along the trend of the orogenic belt east-westward. The 3D stratigraphic model has offered some new insights on the spatial distribution of the Cretaceous reservoir beds in the southwest Tarim Basin for further petroleum exploration.

TALIMU BASIN**1,561,333****JURASSIC BASIN TYPES AND PALEO GEOGRAPHIC PATTERN IN SOUTHWEST DEPRESSION OF TARIM BASIN**

J.Li, L.Zhang, Z.Wang, Y.Yan and C.Sun (China Univ Petroleum; Res Inst Petrol Explor Dev). *21ST INTERNATIONAL SEDIMENTOLOGICAL CONGRESS [ISC] (Beijing, China, 8/22-26/2022) ABSTRACT BOOK* p.237, 2022. (Available at <http://www.isc2022.org.cn> as of 9/22/2022; **Abstract only**)

The Tarim Basin belongs to the rejuvenated foreland basin, which is characterized by multi-stage superimposition. The southwest depression is affected by the Pamir salient and the tectonic compression deformation is intense. Therefore, it is of great significance to accurately recover the prototype basin of southwest depression for exploration. In this paper, the UAV is used for the first time to build a macroscopic 3-D geological model in the region, and the distribution and filling characteristics of the southwest depression basin are studied on the basis of 1-D drilling, 2-D outcrop and 3-D seismic data. It is pointed out that there is no "Jurassic pan-lake basin" in the Jurassic which connects the vast area in front of West Kunlun mountain, and based on this, the differential distribution model of Jurassic basin in Southwest Depression is established. Research suggests that large scale intracontinental orogeny developed in southwest Depression of Triassic, and large scale thrust fold belt developed along piedmont under compression environment. The thermochronology data show that the tectonic activity in the west was earlier than that in the east, and the different tectonic activity caused the folding belt to disappear gradually in an arc eastward. During the Jurassic sedimentary period, the southwest depression was dominated by extensional environment, and the orogenic belt root collapsed, resulting in the development of faulted basins between fold belt and orogenic belt. The fold belt became a high palaeogeomorphic position, which separated Jurassic deposits and provided sediments for foreland depressions. The paleogeographic pattern of "fault lake basin in the west and depression in the east" was formed by the fold belt as the boundary. The lake basin types mainly include fault lake basin, small intermontane lake basin within the fold belt and discontinuous depression lake basin.

TALIMU PLATFORM**1,561,334****EARLY PALEOZOIC COLLISION-RELATED STRUCTURES IN THE TARIM CRATON, NW CHINA: IMPLICATIONS FOR THE PROTO-TETHYS EVOLUTION**

Y.Li, Y.Gao, H.Zhou, G.Zhang, L.Wen, Y.Zhao, C.Li, D.Zheng, Y.Liu et al. (Beijing Inst Geol Geophys). *JOURNAL OF ASIAN EARTH SCIENCES* v.241, Jan. 2023. (ISSN 1367-9120; Article no.105458)

The Tarim-Qaidam collision occurred along the southeastern margin of the Tarim Craton in the Early Paleozoic. This collision resulted in the formation of the Altun Suture, a Proto-Tethyan

suture. It is one of the northernmost suture zones in the Tethysides. This Proto-Tethyan suture was not re-opened during the period of Paleo- and NeoTethyan history, and, of course, no Paleo- or NeoTethyan suture was superimposed on it. The collision-related structures in response to this collision are well-preserved in the Tarim Basin. They were discovered during our careful seismic interpretation. The syn-collision structures mainly include a foreland fold-thrust belt (the Tangguzibas foreland fold-thrust belt) and three large basement-involved anticlines (the Lunnan, Tadong and Tazhong anticlines). While the post-collision structures are a series of normal faults and their combinations of an echelon fault zones. From the deformation characteristics of these syn-collision structures, it was inferred that their related collision occurred in the southeastern margin of the Tarim Craton. It is the Tarim-Qaidam collision which resulted in the formation of the Early Paleozoic Altun Suture. Analyzing the growth strata, unconformities, fault growth index and the strata involved in the collision-related deformation, the syn-collision structures were formed in the Late Ordovician to Early Silurian, and the post-collision structures in the Middle Silurian to Middle Devonian. It can be fairly deduced that the Tarim-Qaidam collision initiated in the Late Ordovician, lasted to the Early Silurian, and then evolved into the post-collision extensional stage of the Middle Silurian-Middle Devonian. (c2022 Elsevier Ltd.)

TANCHENG LUJIANG FAULT ZN**1,561,335****A NEW MODEL FOR THE SEGMENTATION, PROPAGATION AND LINKAGE OF THE TAN-LU FAULT ZONE, EAST ASIA**

C.Li, C.Zhang and T.D.Cope (China Univ Geosci, Beijing; DePauw Univ). *JOURNAL OF ASIAN EARTH SCIENCES* v.241, Jan. 2023. (ISSN 1367-9120; Article no.105466)

The Tan-Lu fault zone (TLF) is a major strike-slip fault with a long and complex history in East Asia, whose evolution provides a new perspective on the formation of large-scale faults (>1000 km long). Fault displacement analysis, geological mapping and U-Pb LA-ICP-MS dating have been performed to understand the evolution of the TLF. Along-strike displacement variation reveals that the TLF consists of two kinematically independent segments, the northern and southern TLF, with opposite long-term propagation directions. Structural and geochronological studies in the eastern Yanshan belt, located around the linkage area of the southern and northern TLF, indicate that NNE-trending sinistral strike-slip faults initiated at 167-164 Ma and were reactivated at 124-121 Ma. Structural analysis suggests that these early NNE-trending strike-slip faults transferred sinistral motion along the northern TLF into southward thrusting along the Yanshan belt, representing the Middle Jurassic southern termination of the northern TLF. Our studies suggest that the through-going TLF formed when the younger southward-propagating northern TLF merged with the older northward-propagating southern TLF in the Late Jurassic. A new model is thus proposed for the Mesozoic evolution of the TLF. The initiation and southward propagation of the northern TLF is interpreted to have resulted from the southward indentation of the Siberian craton into the amalgamated Central Asian Orogenic Belt and North China block. The divergent mega-splays of the northern TLF likely resulted from westward-younging formation during the clockwise rotation of northeast Asia. Coalescence of two genetically unrelated faults could be an alternative mode for large-scale fault formation. (c2022 Elsevier Ltd.)

TAOUDENNI BASIN**1,561,336****POST-DEPOSITIONAL TRANSFORMATIONS IN SEDIMENTARY ROCKS AND IMPLICATIONS FOR PALEOENVIRONMENTAL STUDIES: EVIDENCE FROM THE MESOPROTEROZOIC (CA. 1.1 GA) OF THE TAOUDENI BASIN, MAURITANIA**

M.Ghnahalla, A.El-Albani, A.A.Elmlola, O.M.Bankole, C.Fontaine, M.S.Sabar, A.Trentesaux, C.Laforest, A.Meunier et al. (Poitiers Univ). *AMERICAN JOURNAL OF SCIENCE* v.322, no.7, pp.898-937, Sept. 2022. (ISSN 0002-9599; ISSN 1945-452X)

Understanding paleoenvironmental dynamics linked to

biological evolution in Earth history is a major goal within the geological community. The difficulty of achieving this goal, at least in part, lies with the secondary transformations experienced by a majority of ancient rocks, especially through metamorphism and hydrothermal activity. The Mesoproterozoic (ca. 1.1 Ga) shallow-marine deposits from the Taoudeni Basin, Mauritania, have suffered a complex, multiphase tectonic, and thermal evolutionary history. Representative samples from two drill cores (a background site [S2] and a dolerite intrusion-bearing drill core [S1]) from the El Mreiti Group were evaluated for transformations and overprints of original mineralogies and geochemical compositions. Our results show that the drill core hosting the dolerite intrusion (S1) is characterized by a suite of minerals (that is, pyroxene, graphite, pyrrhotite, garnet, zeolite, and authigenic clay minerals) resulting from contact metamorphism and associated hydrothermal activity. However, compared to the S1, the S2 core shows no evidence of post-depositional transformation. The geochemical data obtained from S1 reveal a striking elevation of iron contents likely delivered from the hydrothermal fluids. Moreover, concentrations of redox-sensitive trace elements (molybdenum, uranium, and vanadium) increased dramatically during hydrothermal and metamorphic activity. This study demonstrates that need for caution when assessing paleoenvironmental conditions in ancient sedimentary rocks, particularly for iron and trace metal approaches commonly used in reconstructions of paleo-redox.

TARANAKI

1,561,337

NEW U-Pb ZIRCON AGES AND A REVISED INTEGRATED AGE MODEL FOR THE LATE MIOCENE NORTHERN TARANAKI COASTAL SECTION, NEW ZEALAND

M.W.Sagar, G.H.Browne, M.J.Arnott, D.Seward and D.P.Strogen (GNS Science; Victoria Univ, Wellington). *NEW ZEALAND JOURNAL OF GEOLOGY AND GEOPHYSICS* v.62, no.3, pp.357-370, 2019. (ISSN 0028-8306; ISSN 1175-8791)

New LA-ICP-MS U-Pb zircon ages of tuffs, from the northern Taranaki coastal section constrain depositional ages of the Mount Messenger Formation to 9.69 ± 0.12 and 9.43 ± 0.17 Ma at the Mohakaito and Tongaporutu rivers, respectively, and the Urenui Formation near Waiiau Stream to 8.45 ± 0.10 Ma. Our preferred new radiometric-biostratigraphic age model comprises lower and upper intervals characterised by relatively low and high undecomposed sedimentation rates of 102 ± 96 m/Ma (MSWD = 6.0) and 1358 ± 144 m/Ma (MSWD = 1.32), respectively. The poor linear fit to the lower interval could indicate either variable sedimentation rates, or an unconformity (0.7 ± 0.2 Ma) in the upper Mohakaito Formation or at the base of the Mount Messenger Formation. The 1569 m-thick upper interval between Mohakaito River and Waiiau Stream was deposited in 1.16 ± 0.01 Ma between $9.67 + 0.07/-0.05$ and $8.52 + 0.06/-0.07$ Ma. Predicted ages for intra-Tongaporutuan bioevents (e.g. base Tukemokihi Coiling Zone) do not overlap their assigned ages, highlighting the importance of propagating uncertainties into bioevent absolute ages and opportunities for future improvements to the age model, namely using high-precision geochronology to acquire ages for additional tuffs and improve precision of existing ages.

TAURUS MT

1,561,338

CRETACEOUS OCEANIC ANOXIC EVENTS IN TURKEY: COLLABORATION OF OCEANIC, CLIMATIC AND TECTONIC CHANGES

I.Omer Yilmaz (Middle East Technical Univ). *21ST INTERNATIONAL SEDIMENTOLOGICAL CONGRESS [ISC] (Beijing, China, 8/22-26/2022) ABSTRACT BOOK* p.178, 2022. (Available at <http://www.isc2022.org.cn> as of 9/22/2022; **Abstract only**)

Occurrences of black shale deposits in Mid-Barremian, Aptian, Cenomanian/Turonian stages in different basins in Turkey are recorded as Cretaceous oceanic anoxic events. The Mid-Barremian black shales (MBE) have been recorded within turbidite succession in deep marine setting in central Sakarya zone of Pontides (Yilmaz et al., 2012). The 2‰ shifts in carbon isotope curve is recorded in parallel with European basins, but with low TOC value. The Aptian black shales (OAE1a) are recorded in pelagic carbonate slope

environments in central Sakarya zone of Pontides and represented by a negative carbon isotope shift with 2‰, and TOC around 2% (Yilmaz et al, 2004; Hu et al, 2012). In Sakarya zone of Pontides, OAE2 is recorded in pelagic slope carbonates (Yilmaz et al, 2010) with carbon isotope curve more than 1‰ positive shift and > 2% TOC. Another OAE2 was recorded in Antalya Nappes of Taurides without carbon isotope curve but TOC > 20% (Yurtsever et al. 2003, Bozcu et al. 2011). Platform equivalents of OAE2 have been recorded on the Arabian Platform carbonates in SE Turkey (Mulayim et al., 2019; 2020). In the north of Arabian Platform, there is a sudden change from upper Cenomanian shallow water platform carbonates to lower Turonian hemipelagic shales/clayey limestones with high organic carbon content. Stable isotope content of the transition is well recorded with change around +1.9‰, and the temperature difference is calculated around 2.2°C (Yilmaz et al, 2020). Interesting point of the OAE2 on Arabian Platform is to follow a drowning phase and covered by black shales in lower Turonian. The OAE1a and OAE2 levels recorded in Turkey can easily be correlated with European examples and mainly controlled by sea level and tectonics in large-scale and climate and oceanographic changes in small-scale. The most extensive distribution of the OAE records in Turkey belong to OAE1a and OAE2, and display potential for source rocks for hydrocarbon exploration.

TIEN SHAN

1,561,339

COUPLING MECHANISM OF BASIN AND OROGEN IN THE TIANSHAN OROGENIC BELT SINCE LATE MESOZOIC: INFLUENCE ON THE SOURCE-SINK PROCESS OF SANDSTONE-TYPE URANIUM MINERALIZATION

F.Y.Zhao, S.H.Jiang, S.Z.Li, M.X.Dai, G.Wang, D.C.Nobes and Y.X.Zhu (East China Univ Technology; China Ocean Univ; China Univ Sci & Technol). *GEOLOGICAL JOURNAL* v.57, no.10, pp.4011-4034, Oct. 2022. (ISSN 0072-1050; ISSN 1099-1034)

The coupling mechanism of the Tianshan Orogenic Belt (TOB) and the basins on its sides (Junggar, Turpan-Hami, Tarim, Yili, etc.) since the Late Mesozoic was complex and multi-levelled. Based on gravity, magnetism, Moho discontinuity, and lithospheric velocity structure of the TOB, together with the structural and sedimentary data of the basins, a model is proposed to reflect the influence of the basin-orogen coupling on the regional source-sink processes of sandstone-type uranium mineralization since the Late Mesozoic. Generally, there are four main stages of tectonic movements that have changed the coupling mechanism of basin and orogeny: including the Early Yanshanian Movement, the Late Yanshanian Movement, the Middle Himalayan Movement, and the Late Himalayan Movement. These four movements together controlled the mineralization of the sandstone-type uranium deposits in the TOB together. The mineralization of sandstone-type uranium deposits in the TOB can be divided into three metallogenic stages: the ore-bearing formation stage (T-J2), the tectonic reversal-related metallogenic stage (J3-N1), and the epigenetic regenerating ore-preserving stage (N2-Q). The tectonic reversal-related metallogenic stage can be subsequently divided into three sub-stages: the pre-metallogenic stage (J3), the sub-metallogenic stage (K), and the main metallogenic stage (E-N1). The associated uplift led to the deformation of the mineralized strata in the basins, while the reducing agent migration along faults enhanced the reduction environment within the strata, which affected the enrichment and distribution of the uranium mineralization in the strata. Meanwhile, the recharge and the change of flow state of groundwater also contributed to the later transformation and mineralization. The intra-continental subduction caused deep lithospheric buckling and depression in the TOB, accompanied by local-scale mantle convection, which accounts for both tectonic and geodynamic settings for the regional basin-orogen coupling mechanism. In addition, the far-field effect of the India-Eurasian collision also provided the driving force for the sandstone-type uranium mineralization in the TOB.

TRENT FIELD

1,561,340

QUARTZITIC SANDSTONES IN THE NAMURIAN AND LOWER WESTPHALIAN SUCCESSION OF THE SOUTHERN NORTH SEA: A NEW HIGH-PERMEABILITY CARBONIFEROUS RESERVOIR TYPE

G.A.Blackbourn and J.D.Collinson (Blackbourn Geoconsulting). *JOURNAL OF PETROLEUM GEOLOGY* v.45, no.4, pp.363-393, Oct. 2022. (ISSN 0141-6421; ISSN 1747-5457)

Most of the potential sandstone reservoirs within the Namurian and lower Westphalian succession of the Southern North Sea Basin are originally feldspathic sands in which the feldspar has mainly been altered to microporous kaolinite clays. The sandstones provide a moderate porosity (typically 8-15%, depending mainly on grain size), but permeability is severely limited owing to the microporous nature of much of the porosity. Permeability is typically 1 mD or less, rising to a few tens of millidarcies in occasional coarse- and very coarse-grained sands. Predicting the presence of higher-permeability reservoir zones is therefore a critical exploration problem in these successions. Quartzitic sands have been discovered in places, especially for example in the Trent field (block 43/24), where physical reworking of sands during the transgressions that preceded the deposition of marine bands removed much of the feldspar, so that less clay was formed during burial diagenesis. Although these sandstones display moderately elevated permeabilities, commonly several to several tens of millidarcies, they are usually fine-grained, which limits their reservoir potential. A particular type of quartzitic sandstone reservoir has been identified quite widely within the Namurian and lower Westphalian succession of the Southern North Sea. This type is indistinguishable in terms of sedimentology and inferred detrital composition from the originally feldspathic facies which now form the widespread kaolinite-rich, low-permeability sandstones. However, it has a very low kaolinite content (commonly 1-2%, compared with a more usual 5-20%) so that these sandstones display permeabilities of the order of several hundred millidarcies. Wireline log data from nineteen wells within UK Quadrants 43 and 44 have been examined, and all relevant core logged in order to compare the depositional settings of the quartzitic and non-quartzitic sandstones. Existing data from over 500 petrographic thin sections from the area have been reviewed and 78 new thin sections analysed to determine the petrographic controls on reservoir quality in both sandstone types. The diagenetic histories of each type have been interpreted. The dissolution of feldspars during diagenesis of the quartzitic sandstones, without a substantial residue of kaolinite or other aluminium-rich mineral, is attributed to the mobilisation of aluminium within organic complexes. This is thought to require the presence of certain organic acids.

TURBIDITE

1,561,341

ARCHITECTURE OF DEEP MARINE AND DEEP LACUSTRINE TURBIDITE LOBE DEPOSITS

L.Zhang, W.Zhang, J.Xu, Y.Deng, D.Liu and Y.Wang (PetroChina Research Inst). *21ST INTERNATIONAL SEDIMENTOLOGICAL CONGRESS [ISC] (Beijing, China, 8/22-26/2022) ABSTRACT BOOK* p.1568, 2022. (Available at <http://www.isc2022.org.cn> as of 9/22/2022; **Abstract only**)

Deepwater (deep-marine and deep-lacustrine) turbidites are sedimentary sand-bodies with good physical properties, and their complex internal structures and heterogeneities directly control the distribution of residual oil. In recent years, significant progress has been made in the exploration and development of deep-marine turbidities, and a series of giant oil and gas fields have been discovered, making deepwater domain an important strategic replacement area for future global oil and gas resources. Architectural characteristics of deepwater turbidite channels have been extensively studied, whereas works on the architecture hierarchy and anatomy of the turbidite lobes are less. In this study, three turbidite lobe analogues are investigated and correlated: the deep-marine Carboniferous Ross Sandstone Formation outcrops in western Ireland, the deep-marine Silurian Longmaxi Formation cores in the Sichuan Basin, and the deep-lacustrine Triassic Yanchang Formation outcrops in southeast Ordos Basin. Based on

detailed anatomy, deep-marine and deep-lacustrine turbidite lobes can be comparable in many aspects: (1) three genetic units are recognized: turbidite lobe, turbidite channel, and slump-slide; (2) turbidite lobes can be classified into a similar four-fold hierarchy from bed, lobe element, lobe, to lobe complex. The architecture units at each hierarchical level and the corresponding architecture interfaces have completely different characteristics, among which the lobes show characteristics of evident compensational stacking, and the lobe elements display a thickening-upward pattern; (3) typical thickening-upward cycles consist of, from bottom to top: laminated shales/shales with interbedded siltstone beds; interbedded sandstones/siltstones and mudstones; structureless massive sandstones with a strong degree of amalgamation and load structures at bases. In general, the turbidite lobe deposits appear as tabular, parallel/sub-parallel sandstone with mudstone interbeds. Turbidite lobe deposits transit from thick, massive sandstones with high net-to-gross ratio and high degree of amalgamation at the proximal region into thin sandstones interbedded with mudstones with low net-to-gross ratio and degree of amalgamation towards distal fringes both laterally and longitudinally. By detailed anatomy of hierarchy and lateral tracing of architectural units, this study suggests that, despite less extent and shallower water depth, deep-lacustrine turbidite lobes have similar features with deep-marine turbidite lobes, in terms of depositional mechanism, genetic units, architecture hierarchy, and lateral distribution of facies associations. This could benefit future exploration and development of deepwater turbidite lobe reservoirs.

TWEED BASIN

1,561,342

REPEAT COLONIZATION OF TEMPORARY WATER BODIES BY EARLY CARBONIFEROUS INVERTEBRATES

C.Bennett, P.Brand, S.Davies, T.Kearsey, D.Millward, T.Smithson and M.Williams (Leicester Univ; British Geological Survey; Cambridge Univ Museum). *58TH ANNUAL PALAEOLOGICAL ASSOCIATION MEETING (Leeds, UK, 12/16-19/2014) ABSTRACTS* p.21, 2014. (Available at <http://www.palass.org> as of 11/15/2022; **Abstract only**)

The Tweed Project investigates the rebuilding of Carboniferous ecosystems following the end Devonian mass extinction. New fossils populate "Romer's Gap" with a diversity of tetrapods, fish (gyracanthids, lungfish, rhizodonts, actinopterygians and chondrichthyans), invertebrates (malacostracans, eurypterids, scorpions and myriapods) and plants. The fossil-bearing Ballagan Formation was deposited on an extensive low relief, coastal-alluvial, vegetated floodplain, with temporary pools and shallow lakes. Bivalves and ostracods are the most numerous invertebrates in the formation and are here described from the 502 m thick Norham West Mains Core. Present in over 150 horizons, euryhaline/non-marine *Modiolus* bivalves and *Leiocopida* and *Podocopida* ostracods dominate, with an associated fauna of fish (actinopterygians, chondrichthyans and dipnoans, which likely predated the ostracods and bivalves), and rarer eurypterids, Spinicaudata, gastropods and *Spirorbis*. The majority of these fossils occur in sedimentary deposits that overlie palaeosols or desiccation horizons, indicating the repeated occupation of temporary pools and lakes after periods of desiccation. Most of the bivalve specimens are juveniles suggesting short-lived aquatic environments. Living freshwater Unionidae bivalves attach to the gills of fish in a phoretic parasitic larval stage, as a mechanism for dispersal. We explore the links between Early Carboniferous fish, bivalves and ostracods in their radiation into these temporary environments.

UKRAINE

1,561,343

THE CONIFORM CONUNDRUM: INSIGHTS INTO THE FORM AND FUNCTION OF THE PANDERODUS APPARATUS

I.Leonhard, B.Shirley, D.Murdock and E.Jarochowska (Vienna Univ; Friedrich Alexander Univ; Oxford Univ; Utrecht Univ). *5TH INTERNATIONAL CONODONT SYMPOSIUM [ICOS] (Wuhan, China and Online, 6/24-27/2022) PROGRAM AND ABSTRACTS* pp.57-58, 2022. (**Abstract only**)

Conodonts are regarded as the earliest vertebrates bearing

tooth-like structures and provide insight into the functional evolution of vertebrate feeding systems. They bear tooth-like, microscopic phosphatic structures, known as elements, which lay within the animals' oropharyngeal cavity. Information about their relative positions is key to identify positional homologies between different conodont apparatuses. This knowledge will not only help to resolve the phylogeny of conodonts but also will help to reconstruct early vertebrate evolution. The scarcity of information on the 3D positioning of these elements hinders reconstructions of early vertebrate evolution and limits the understanding of functional morphology. Architectural reconstructions of conodont apparatuses can be obtained from rare forms of preserved diagenetically fused clusters and natural bedding assemblages. Simple con-shaped coniform conodonts correspond to the least derived conodonts and are particularly enigmatic, as most studies focus on function and biomechanics of more derived, "complex" conodonts. We employ non-destructive Synchrotron Radiation X-Ray Tomographic Microscopy (SRXTM) to produce virtual 3D models of the apparatus of the coniform conodont *Panderodus unicostatus* using a thirteen-element fused cluster from the Llandovery Teremtsy Beds of Podolia (Silurian), Ukraine. We set out to: (1) reconstruct the *Panderodus apparatus* based on a thirteen-element cluster; and (2) compare the element arrangement to occlusion mechanisms in the apparatuses of recent cyclostomes and chaetognaths (arrow worms).

VANCOUVER ISLAND AREA 1,561,344

EOCENE TERRANE ACCRETION IN NORTHERN CASCADIA RECORDED BY BRITTLE LEFT-LATERAL SLIP ON THE SAN JUAN FAULT

N.Harrichhausen, K.D.Morell, C.Ragalla, E.M.Lynch and L.J.Leonard (Calif Univ, Santa Barbara; Northern Arizona Univ; Victoria Univ, BC). *TECTONICS* v.41, no.10, Oct. 2022. (ISSN 0278-7407; ISSN 1944-9194; Article no.e2022TC007317)

The San Juan fault (SJF), on southern Vancouver Island, Canada, juxtaposes the oceanic Wrangellia and Pacific Rim terranes in the northern Cascadia forearc, and has been suggested to play a role in multiple Mesozoic-Cenozoic terrane accretion events. However, direct observations of the SJF's kinematics have not been documented and its exact role in accommodating strain arising from terrane accretion is unknown. To test if, how, and when the SJF accommodated accretion-related strain, we use geologic mapping, kinematic inversion of fault-plane slickenlines, and dating of marine sediments to constrain the timing and direction of brittle slip of the SJF. P- and T-axes from kinematic inversions indicate predominantly left-lateral slip. Left-lateral brittle faulting cross-cuts ca. 51 Ma magmatic intrusions and foliation, providing a maximum age of brittle deformation. The fault zone is non-conformably overlain by a >300 m-thick sequence of clastic marine shelf and slope sediments that are not left-laterally offset. A strontium isotope age of foraminifers helps constrain the depositional age of the sediments to late Eocene-early Oligocene, bracketing left-lateral slip to the Eocene. Eocene left-lateral slip is temporally and kinematically consistent with regional southwest-northeast compression during accretion of the Siletzia ocean island plateau, suggesting brittle slip on the SJF accommodated strain resulting from the accretion of this terrane. This result does not support hypotheses that brittle slip along the SJF directly accommodated earlier accretion of the Pacific Rim terrane to Wrangellia, instead it offsets the older accretionary boundary between these two terranes.

VIETNAM 1,561,345

SILURIAN OSTRACODS WERE PIONEER COLONISTS OF ESTUARIES

A.McGairy, T.Komatsu, M.Williams, T.H.P.Harvey, C.G.Miller, P.D.Nguyen, J.Legrand, T.Yamada, D.J.Siveter et al. (Leicester Univ). *65TH ANNUAL PALAEOONTOLOGICAL ASSOCIATION MEETING (Manchester, UK, 12/18-20/2021) PROGRAMME AND ABSTRACTS* pp.79-80, 2021. (Available at <http://www.palass.org> as of 11/1/2022; **Abstract only**)

Ostracod crustaceans occupy an exceptional range of modern aquatic environments and are invaluable palaeoenvironmental

indicators in the fossil record. However, pre-Carboniferous records of supposed marginal marine and non-marine ostracods are poorly documented and the timing of their marine to non-marine transition has proven to be elusive. Here, we reassess the early environmental history of ostracods from new late Silurian finds in northern Vietnam. Two low-diversity but distinct ostracod assemblages are associated with estuarine deposits of the Si Ka Formation. This occurrence is consistent with previous incidental reports of ostracods occupying marginal and brackish settings through the late Silurian and Devonian. We show that ostracods were pioneering the occupation of marginal marine and estuarine settings 60 million years before the Carboniferous and that ostracods were a component of the early phase of transition from marine to non-marine environments.

WALES 1,561,346

REDUCED PLATE MOTION CONTROLLED TIMING OF EARLY JURASSIC KAROO-FERRAR LARGE IGNEOUS PROVINCE VOLCANISM

M.Ruhl, S.P.Hesselbo, H.C.Jenkyns, W.Xu, R.L.Silva, K.J.Matthews, T.A.Mather, C.M.Niocaill and J.B.Riding (Trinity Coll, Dublin). *21ST INTERNATIONAL SEDIMENTOLOGICAL CONGRESS [ISC] (Beijing, China, 8/22-26/2022) ABSTRACT BOOK* p.190, 2022. (Available at <http://www.isc2022.org.cn> as of 9/22/2022; **Abstract only**)

Large igneous province (LIP) emplacement is commonly associated with mantle plume upwelling, leading to surficial magmatism, proposed to have driven past global change events by volcanic carbon emission. One of Earth's largest past environmental perturbations, the Early Jurassic Toarcian oceanic anoxic event (T-OAE; ca 183 Ma), has been linked to emplacement of the Karoo-Ferrar LIP. However, the role of mantle plumes in controlling the onset and timing of LIP magmatism is poorly understood. Here, utilizing global plate reconstruction models, and Lower Toarcian sedimentary mercury (Hg) concentrations from the Mochras borehole (Wales, UK), we demonstrate (1) that the Early Toarcian OAE occurred coevally with Karoo-Ferrar LIP emplacement, and (2) suggest that the timing and duration of LIP-emplacement was governed by a reduction in local Pangean plate motion associated with a reversal in plate movement direction. With this, we present a new model that mechanistically links Earth's interior and surficial processes, and we show that this mechanism is consistent with the timing of several of the largest LIP volcanic events throughout Earth history and thus, by inference, the timing of many of Earth's past global climate change and mass extinction events.

WALES 1,561,347

A SURFEIT OF SPONGES: UNEXPECTED ORDOVICIAN DIVERSITY IN CENTRAL WALES, UK

J.P.Botting and L.A.Muir. *58TH ANNUAL PALAEOONTOLOGICAL ASSOCIATION MEETING (Leeds, UK, 12/16-19/2014) ABSTRACTS* p.22, 2014. (Available at <http://www.palass.org> as of 11/15/2022; **Abstract only**)

Sponges are generally considered to be minor components of Ordovician communities in siliciclastic settings, but this may be an underestimate due to their low preservation potential. The Builth Inlier (Middle and Late Ordovician) yields abundant articulated sponges, providing a unique opportunity to assess the ecological distribution of different sponge groups and to estimate their true palaeobiodiversity. Long-term fieldwork has yielded more than 100 new sponge species from a range of sites. Clear patterns are evident in the distribution of particular groups, with more derived taxa occupying shallow water, and the more primitive reticulosans dominating offshore communities. One new fauna from intermediate depth contains a diverse protomonaxonid-dominated sponge assemblage resembling that of the Burgess Shale. Most articulated faunas in the inlier are diverse, with little taxonomic overlap between different assemblages. This indicates higher α - and β -diversity than any other co-occurring group, and/or very low sampling saturation. These factors imply that, despite being the most diverse group known in these deposits, all aspects of their diversity are underestimated. If the Builth Inlier is typical of

Ordovician ecosystems in general, then palaeontologists are missing an unexpectedly large component of biodiversity during the Great Ordovician Biodiversification Event.

WEATHERING 1,561,348

A ROBUST CHEMICAL WEATHERING INDEX FOR SEDIMENTS CONTAINING AUTHIGENIC AND BIOGENIC MATERIALS

T.Cho and T.Ohta (Waseda Univ). *PALAEOGEOGRAPHY, PALAEOCLIMATOLOGY, PALAEOECOLOGY* v.608, 12/15/2022. (ISSN 0031-0182; Article no.111288)

Chemical weathering is an important process at Earth's surface. Given that the chemical composition of sediments reflects the weathering environment in which they were generated, this can provide insights into the intensity and style of weathering during the past. Weathering indices calculated from the whole-rock geochemical compositions of sedimentary rocks are widely used. However, these indices have limitations, such as contamination by non-silicate minerals. To develop a weathering index widely applicable to sedimentary rocks formed under various conditions, we used compositional data and multivariate statistics to analyse a dataset for igneous rocks and their weathering profiles. The chemical variations of the igneous rocks and weathering trends were independently extracted from the dataset, and a new weathering index (the robust weathering (RW) index) is proposed. The applicability of the RW index was assessed using saprolite profiles and zonal soils. We further applied the RW index to a carbonate-rich paleosol to test its use in studies of paleoclimate. The RW index is robust even for sediments containing a large amount of non-silicate materials, and thus enables comparison of the weathering intensity of a wide range of sedimentary rocks. Spatial-temporal reconstructions of paleo-weathering conditions will be improved by applying the RW index to terrestrial and marine sediments. (c2022 Elsevier B.V.)

WEST ATLANTIC OCEAN 1,561,349

THE CAUSE OF LATE CENOZOIC MASS EXTINCTION IN THE WESTERN ATLANTIC: INSIGHTS FROM SCLEROCRONOLOGY

A.L.A.Johnson, A.Valentine, M.J.Leng, D.Surge and M.Williams (Derby Univ; NERC Isotope Geosci Lab; No Car Univ, Chapel Hill; Leicester Univ). *58TH ANNUAL PALAEOONTOLOGICAL ASSOCIATION MEETING (Leeds, UK, 12/16-19/2014) ABSTRACTS* p.31, 2014. (Available at <http://www.palass.org> as of 11/15/2022; **Abstract only**)

Heavy late Cenozoic extinction amongst marine molluscs in the western Atlantic has traditionally been interpreted as a consequence of climatic deterioration. However, the pattern of extinction was not the same in the eastern Atlantic, where conditions also became colder. A fall in primary productivity, suggested by a decline in phosphate deposition, may be the real explanation for western Atlantic extinctions. Evidence in support comes from isotopic- and increment-based (sclerochronological) indications of growth rate in Pliocene scallops. A western Atlantic genus that has survived to the present (*Placopecten*) had the same moderate growth rate in the Pliocene as now, while two genera that became extinct (*Carolinapecten* and *Chesapeakepecten*) had growth rates as fast as any known amongst living scallops. Such rapid growth implies abundant food. Selective extinction of a fast-growing species has also been documented amongst Pliocene oysters in the Caribbean region and attributed to a decline in primary productivity. The likely cause of this is the development of the Central American Isthmus and the consequent reorganization of oceanic circulation in the Gulf of Mexico and wider North Atlantic.

WESTERN CANADA 1,561,350

THE CURIOUS CASE OF CHAETAE IN BRACHIOPODS FROM THE MIDDLE CAMBRIAN BURGESS SHALE

T.P.Topper, L.E.Holmer, L.Strotz, N.Tait, Z.Zhang and J.B.Caron (Uppsala Univ; Macquarie Univ; Northwest Univ, China; Royal Ontario Museum). *58TH ANNUAL PALAEOONTOLOGICAL*

ASSOCIATION MEETING (Leeds, UK, 12/16-19/2014) ABSTRACTS p.49, 2014. (Available at <http://www.palass.org> as of 11/15/2022; **Abstract only**)

Over the years, the Burgess Shale Lagerstaette has given us a range of extraordinary creatures that are exquisitely preserved in the dark shales of the Canadian Rockies. In a community dominated by arthropods, brachiopods are the forgotten phylum in the Lagerstaette deposit, yet as the second most abundant benthic filter feeder, brachiopods were undoubtedly an essential component of the Burgess Shale community. One of the more remarkably preserved brachiopods from the Cambrian Stage 5 Burgess Shale is *Micromitra burgessensis*. *Micromitra* is exceptionally preserved, exhibiting elongate chaetae that fringe the mantle and extend far beyond the margin of the biomineralized shell. Chaetae of extant brachiopods have been interpreted as potentially performing a range of defensive and sensory functions in addition to assisting in feeding, burrowing and actively warding off encroaching organisms. The shape, size and frequency of the chaetae possessed by *M. burgessensis* are unique amongst Recent and fossil brachiopod taxa. Here we explore the potential functions of these distinctive chaetae. Chaetae have now been documented from a variety of extant and fossil brachiopod groups and the wide morphological variation observed across families indicates that chaetae may be a potentially significant tool for taxonomic, phylogenetic and palaeoecological studies of the phylum.

WHITEHORSE BASIN 1,561,351

PALEOENVIRONMENTAL INTERPRETATION OF THE LATE TRIASSIC NORIAN - RHAETIAN BOUNDARY INTERVAL IN THE WHITEHORSE TROUGH (STIKINE TERRANE, NORTHERN CANADIAN CORDILLERA)

J.Z.X.Lei, M.L.Golding and J.M.Husson (Victoria Univ; Canada Geological Survey). *PALAEOGEOGRAPHY, PALAEOCLIMATOLOGY, PALAEOECOLOGY* v.608, 12/15/2022. (ISSN 0031-0182; Article no.111306)

The Norian - Rhaetian boundary (NRB) is associated with significant faunal turnover in a wide variety of groups. Following the relative stability of the Norian Stage, this boundary potentially marks the beginning of a protracted and continuous episode of elevated extinction rates, which culminated with the end-Triassic mass extinction. Despite the importance of the NRB to paleontological trends in the Late Triassic, much about this event remains enigmatic, including potential causal mechanisms as well as the characteristics of the resulting paleoenvironmental changes. Fossiliferous limestone of the Sinwa Formation occurs in extensive outcrops throughout northwestern British Columbia and provides an exceptional record of Upper Triassic stratigraphy that represents a paleogeographic region largely uninvestigated prior. The present study integrates lithostratigraphic, paleontological, and geochemical data to reconstruct the shallow marine paleoenvironments recorded by the Sinwa Formation in two sections on Mount Sinwa, south of Atlin, within the Stikine Terrane. The progression of lithological facies observed in these sections suggests a gradual base level rise throughout the late Norian. Following this steady facies progression is a prominent shift from coral reef boundstone to shale near the top of both sections. This facies change approximately coincides with the NRB interval as evidenced by the first occurrence of the latest Norian - Rhaetian conodont species *Mockina mosheri* morphotype B, as well as by Re - Os isochron ages of organic-rich limestone. Although the base level rise observed at the NRB interval could be due to regional tectonics, it could also potentially be recording eustatic sea level rise given the lack of consensus around sea level change at the NRB. Measurements of late Norian 87Sr/86Sr ratios on Mount Sinwa are consistent with those recorded in Tethyan studies, but the Panthalassan record overall does not replicate the same drop across the NRB observed in the Tethys. The lithological facies shift is also immediately preceded by a negative excursion in the $\delta^{13}C$ values of carbonate, indicating that the NRB interval on Mount Sinwa is associated with coral reef collapse as well as the globally observed disruption of carbon cycling. (c2022 Elsevier B.V.)

WHITE RIVER GR

1,561,352

SEDIMENT PROVENANCE AND STRATIGRAPHIC CORRELATIONS OF THE PALEOGENE WHITE RIVER GROUP IN THE BIGHORN MOUNTAINS, WYOMING

J.R.Malone, D.H.Malone and J.P.Craddock (Texas Univ, Austin; Illinois State Univ; Macalester Coll). *THE MOUNTAIN GEOLOGIST* v.59, no.4, pp.273-293, Oct. 2022. (ISSN 2327-2945)

Detrital zircon ages for tuffaceous sandstones and conglomerates of the White River Group provide insights on Paleogene basin evolution, magmatic activity, and paleodrainage throughout the Laramide broken foreland basin system of the northern Rocky Mountains in the western United States. Nonmarine deposits of the upper Eocene-Oligocene White River Group are preserved irregularly across northern Wyoming and western South Dakota. Residual Laramide uplifts and active magmatic centers supplied clastic and volcanoclastic sediment to broad, low-relief valleys beginning around 40 Ma. Subhorizontal strata of the White River Group are exposed in the elevated Bighorn Mountains (ca. 2300 to 2800 m), where sections ca. 10-50 m thick rest unconformably on Precambrian-Paleozoic rocks along a surface of moderate to low relief (up to 150 m). U-Pb ages were obtained for detrital and igneous (ash-fall) zircons from seven samples (3 tuffaceous sandstones, 2 conglomerates, 2 sandstones) spanning three localities in the Bighorn Mountains (Darton's Bluff, Hazelton Road, Freeze Out Point). Each locality contains conglomeratic layers, with clasts of local crystalline basement, and interbedded tuffaceous sandstones. Detrital zircon age spectra for four samples reveal peak ages around 2.9 Ga, matching the age of Archean crystalline basement within Bighorn Mountains, and maximum depositional ages (MDAs) of 27 Ma (sample 20BH15; Oligocene) and 35 Ma (sample F'O-2; late Eocene). During the Paleogene, the Bighorn Mountains region received sediment from local crystalline basement and long-distance river transport from igneous and sedimentary sources to the west. The Bighorn Mountains were exhumed and stripped of Phanerozoic cover strata by early Eocene time, suggesting that post-Laramide input from Paleozoic-Mesozoic strata was likely from relict highlands of the Cordilleran (Sevier) fold-thrust belt rather than local Laramide block uplifts. In addition, Cenozoic magmatic provinces in the San Juan Mountains and Great Basin are inferred to have contributed volcanoclastic sediment through both eruptive ash clouds and north- to northeast-flowing fluvial systems that reached northeastern Wyoming. The White River Group preserved in the Bighorn Mountains represents localized late Eocene-Oligocene sediment accumulation atop a Laramide basement high coeval with regional deposition across the adjacent Great Plains. Both regions were supplied sediment from alluvial fans and fluvial drainage networks that tapped Laramide basement uplifts, Cordilleran thrust-belt, and foreland sources, along with Cenozoic igneous centers of the western U.S. interior.

XIHU DEPRESSION

1,561,353

MICRO SLOPE BREAK AND ITS CONTROL ON SEQUENCE, SEDIMENTATION AND HYDROCARBON ACCUMULATION OF PINGHU FORMATION IN K AREA, XIHU SAG

L.Li (China Nat Offshor Oil Corp). *21ST INTERNATIONAL SEDIMENTOLOGICAL CONGRESS [ISC] (Beijing, China, 8/22-26/2022) ABSTRACT BOOK* p.322, 2022. (Available at <http://www.isc2022.org.cn> as of 9/22/2022; **Abstract only**)

Based on the analysis of the pre-existing structures and palaeogeomorphology, the typical and characteristic micro-slope break zones are identified in the study area, and their genetic type is flexural slope break. The NW-trending pre-existing structure formed during the Indo-Chinese Movement was reactivated during the Pinghu Movement, forming the structure "down-fault and up-torsion", which was a flexural slope break during the Pinghu Formation. The controlling effects of micro-slope break zone on sequence development pattern, sedimentary system distribution characteristics and dominant reservoir distribution are established. Based on the hydrocarbon source conditions, reservoir conditions, migration conditions, trap conditions and preservation conditions, the hydrocarbon accumulation model of "hydrocarbon generation in

low slope belt-separation trough controlling migration and accumulation-micro slope break controlling trap and reservoir" is proposed, which effectively guides the evaluation of the K Area. According to the comprehensive analysis of the control of micro-slope break on sequence, deposition and hydrocarbon accumulation of Pinghu Formation in the K area of Xihu Sag, the scale of slope break zone research is extended, and the slope break zone theory is enriched.

XINJIANG

1,561,354

A SYNTHESIS OF CARBONIFEROUS STRATIGRAPHY IN XINJIANG, NORTHWEST CHINA WITH EMPHASIS ON REGIONAL AND GLOBAL CORRELATIONS

Y.Tang, X.Ye, X.Wang, X.Huang, Z.Hou, K.Hu, S.Yang, Y.Li, F.Zhang et al. (Xinjiang Oilfield Res Inst). *JOURNAL OF ASIAN EARTH SCIENCES* v.241, Jan. 2023. (ISSN 1367-9120; Article no.105476)

The Carboniferous is the most widely distributed system in the pre-Mesozoic strata of Xinjiang, Northwest China, and they are exposed in structurally independent units within various tectonic settings across the southwest Central Asian Orogenic Belt and Tarim Craton in Northwest China. According to the lithofacies associations and biotic assemblages, the Carboniferous successions of Xinjiang can be divided into 18 stratal regions, and each of these stratal regions may be further separated into several subregions in terms of lithology, biota, and geochronologic data. The depositional succession of each region is described on the basis of the key section. The marine fossils such as foraminifers (fusulinids), brachiopods, corals, and conodonts, as well as nonmarine fossils such as plants and pollens are reviewed in this study. Combined with the geochronologic data from the volcanic rocks and ash layers, a refined scheme of the Carboniferous successions in different regions across Xinjiang, Northwest China is obtained. The detailed and newly established stratigraphic framework of the Carboniferous strata could be very helpful for the regional and global stratigraphic correlations. It can also offer a new and reliable chronostratigraphic foundation for the comprehensive understanding of the tectonic evolution and petroleum exploration in Central Asia. (c2022 Elsevier Ltd.)

YANCHANG FM

1,561,355

IDENTIFICATION AND QUANTITATIVE CHARACTERIZATION OF SILTY LAMINAE AND BEDS IN LACUSTRINE ORGANIC-RICH SHALES

J.Liu, G.Wang and Y.Fan (PetroChina Research Inst; China Univ Petroleum). *21ST INTERNATIONAL SEDIMENTOLOGICAL CONGRESS [ISC] (Beijing, China, 8/22-26/2022) ABSTRACT BOOK* pp.265-266, 2022. (Available at <http://www.isc2022.org.cn> as of 9/22/2022; **Abstract only**)

Influenced by sedimentary environments such as sediment provenance, paleoclimate, the geochemistry of the water body and paleoproductivity, various laminae and beds are developed in the lacustrine organic-rich shales. Silty laminae and beds developed in the shale formation in the freshwater lake basin are important reservoir spaces and efficient channels for oil and gas migration. In addition, the identification and characterization of silty laminae and beds are critical to the sedimentary environment analysis, formation evaluation and sweet spot optimization. Researchers carried out a lot of studies on the drilled rock samples which contain silty laminae and beds, including core description, mineral composition analysis, scanning electron microscope, particle size, nitrogen adsorption and other experimental methods. Mathematic methods such as unsupervised clustering, fractals and joint characterization are used in the quantitative characterization of silty laminae and beds. However, drilled rock samples are limited and expensive, it is challenging to realize the fine evaluation of heterogeneous organic-rich shale formations. Chang 7 member organic-rich shale formation in the Ordos basin is studied in this research. We used conventional logging and electric imaging logging to realize the identification and quantitative characterization of silty laminae and beds in lacustrine organic-rich shales. It mainly includes the following three steps: (1) Lithology identification: the logging response characteristics of pure shale,

silty laminae and beds, pyrite enriched layers and tuff layers in the organic-rich shale formation are analyzed. The criterion of lithology identification is established, and it can be clear that the silty laminae and beds with thickness greater than 1 cm can be identified by the electric imaging logging; (2) Identification of silty beds: the essence of silty beds identification based on the electric imaging logging is edge detection. A new method based on image processing and morphology is established, including the comprehensive process of electrical imaging logging, edge detection based on Sobel horizontal operator, and open operation. The silty laminae and beds with thickness greater than 1 cm can be identified by this new method; (3) Quantitative characterization of silty laminae and beds: based on the identification of organic-rich shales and silty beds, the thicknesses of silty beds are counted. It is clear that the distribution of the thickness of silty beds can be characterized by fractals. Therefore, the total thickness calculation model of silty laminae and beds can be established by the comprehensive analysis of electric imaging logging and drilled rock samples. This research indicates that the silty laminae and beds identified by electrical imaging logging and core observation have a good consistency. This new method can be used in the uncored wells to realize the identification and quantitative characterization of silty laminae and beds. Moreover, the results are critical in the sedimentary environment analysis, formation evaluation and sweet spot optimization.

.....
YANCHANG FM **1,561,356**

ESTABLISHMENT OF AN AGE-CALIBRATED ASTRONOMICAL TIME SCALE FOR THE CHANG 7 MEMBER OF THE TRIASSIC YANCHANG FORMATION WITHIN THE ORDOS BASIN, CENTRAL CHINA

Y.Li and R.Yang (Shandong Univ Sci Technol). *21ST INTERNATIONAL SEDIMENTOLOGICAL CONGRESS [ISC] (Beijing, China, 8/22-26/2022) ABSTRACT BOOK* p.273, 2022. (Available at <http://www.isc2022.org.cn> as of 9/22/2022; **Abstract only**)

Astrochronology provides a method for developing highly detailed internal time scales for understanding Earth's history and rates of processes. During the Triassic, large continental lakes formed in the Ordos Basin of Central China. The lacustrine facies of the 7th Oil Member (Chang 7 Member) of the Yanchang Formation in the southern Ordos Basin displays cyclic changes in clay content, color and other properties. U-Pb geochronology of zircons from a basal tuff (ca. 239 Ma) and of detrital zircons from two sandstone beds within the reference Well N36 were used to constrain the stratigraphic ages and to identify possible provenance of the siliciclastics. Detailed time-series analysis was performed on the natural gamma (GR) logs and on the elemental concentrations of Fe and of Al. The resulting astronomical time scale for the Chang 7 Member, as constrained by the U-Pb dating, spans the interval from ca. 239 Ma through ca. 229 Ma; therefore, it was deposited during the Ladinian and Carnian (late Middle through earliest Late Triassic). The distribution of detrital zircon dates show that the Chang 7 Member in the southern Ordos Basin has multiple provenance characteristics. The southern Ordos Basin is far from this provenance area, which is reflected in the low sediment accumulation rate (0.5-2 cm/kyr). In contrast to underlying members, the lacustrine sediments of the Chang 7 Member hosts a large number of tuffs and seismites. This change is interpreted as a product of the initiation of collisional tectonics that formed the North Qinling orogenic belt on the southern margin of the Ordos Basin.

.....
YANCHANG FM **1,561,357**

STUDY ON CHANG 8 SEDIMENTARY SYSTEM AND SAND BODY DISTRIBUTION LAW IN HUANXIAN-HEQI AREA

(Southwest Petroleum Univ). *21ST INTERNATIONAL SEDIMENTOLOGICAL CONGRESS [ISC] (Beijing, China, 8/22-26/2022) ABSTRACT BOOK* p.277, 2022. (Available at <http://www.isc2022.org.cn> as of 9/22/2022; **Abstract only**)

Ordos Basin is the most important oil and gas resource exploration and development base in China at present. Recently, a major breakthrough has been made in the exploration of Chang-8

oil reservoir group in Huanxian-Heqi area, and oil-rich sand belt has been found. Although the lithology, sedimentary structure, structure and fossil characteristics of cores in the early stage determined that Chang-8 oil reservoir group has shallow water sedimentary characteristics. However, the unclear understanding of the provenance, sedimentary system types and sand body distribution characteristics of Yanchang 8 reservoir group restricts the further exploration. Based on the analysis of lithology, sedimentary structure, structure and fossil characteristics in Huanxian-Heqi area, this study systematically carried out the work of provenance, sedimentary system, sand body distribution law and so on. The sedimentary center of Ordos Basin is distributed in NW-SE direction, and Huanxian-Heqi area is located in the southwest of the sedimentary center, which is mainly influenced by the western and southwest provenances from the regional background analysis. During the long sedimentary period, the ancient water depth of the lake basin was high in the central and western parts and low in the eastern part. Compared with the Chang 82 period, the Chang 81 lake basin has expanded in scope and the water body has gradually deepened. Expansion to the south is obvious. The bottom shape of the lake is higher in the west and southwest, and lower in the middle and east. During the 82 period, the delta plain was mainly located in the west and south of Huanxian-Heqi area, with braided channel and flood plain deposits, which were distributed from southwest to northeast. Delta front deposits are located in the northeast direction of the plain, and underwater distributary channels are mainly developed. The water depth extending to Huanxian-Heqi-Wujiao-Baima-Haojiajian area gradually increased, and developed into estuary dam, far sand dam and sheet sand deposit. The water depth of Chang 81 period is higher than that of Chang 82, and the delta plain is mainly located in the west of Huanxian-Heqi area. Delta front deposits are located in the central and eastern part of the study area, and underwater distributary channels are mainly developed. The Zhonghuan County-Hedao-Heqi-Wujiao-Haojiajian area is distributed on the outside of the delta front, with deep water body, with far sand bar and sheet sand. The favorable reservoir sand bodies in Chang 82 section are mainly the superimposed sand bodies of underwater distributary channel, mouth bar and far bar in delta front; The water depth of Chang 81 section in Huan-Heqi area is longer than that of 82 section, and the favorable area moves southward. The reservoir sand bodies are mainly the superimposed sand bodies of underwater distributary channel, estuary bar and far sand bar in delta front.

.....
YANGTZE PLATFORM **1,561,358**

ORIGIN OF THE CRYOGENIAN IRON FORMATIONS: CLIMATIC FLUCTUATION COUPLING WITH LOCAL HYDROTHERMAL IRON INPUT

B.Yan, X.Zhu, Z.Li and J.Li (Beijing Inst Geology). *PRECAMBRIAN RESEARCH* v.382, Nov. 2022. (ISSN 0301-9268; Article no.106885)

The brief resurgence of iron formation deposition during the Neoproterozoic Era appears to have been closely associated with the glaciation deposits. However, the genesis of these Cryogenian iron formations (CIFs) remains unclear. Here, we present Fe isotopic compositions and rare earth element (REE) contents for four Fulu iron formation (IF) lithostratigraphic sequences in the Sanjiang area, South China. The Fulu IF strata are in conformable contact with the underlying Chang'an glacial succession. However, owing to lack of glacial deposits evidence, they are interpreted to have formed in non-glacial conditions, probably during a warm period Sturtian glaciation. Because of the shrinking ice cover over the ocean surface, more oxidants have been transferred from the atmosphere to the ocean during this Sturtian warm period, leading to reconstruction of a redox-stratified ocean. Local hydrothermal vent systems provided dissolved Fe(II) to form the IFs, as inferred from the $\delta^{56}\text{Fe}$ values and Eu anomalies of the Fulu IFs. Our results allow us to propose a new genetic model for the origin of CIFs; whereby partial Fe(II) oxidation caused the precipitation of Fe(III) oxide and enabled the deposition of CIFs. This occurred under redox-stratified conditions over an extended warm climatic period in combination with iron sourced from local hydrothermal activities during Cryogenian glaciations. (c2022 Elsevier B.V.)

YANGTZE PLATFORM

1,561,359

THE RECORD OF EARLY SILURIAN CLIMATE CHANGES FROM SOUTH CHINA AND BALTICA BASED ON INTEGRATED CONODONT BIOSTRATIGRAPHY AND ISOTOPE CHEMOSTRATIGRAPHY

G.Yan, O.Lehnert, P.Mannik, M.Calner, X.Luan, F.Gong, L.Li, X.Wei, G.Wang et al. (Chinese Academy Sciences). *5TH INTERNATIONAL CONODONT SYMPOSIUM [ICOS] (Wuhan, China and Online, 6/24-27/2022) PROGRAM AND ABSTRACTS* p.75, 2022. (Abstract only)

The Baizitian section is a classical Silurian section in China located on the Yangtze Block, South China Palaeoplate. The exposed Silurian strata include the Lungmachi (Rhuddanian-Telychian), the Xiabaizitian (Telychian-lower Sheinwoodian), the Shangbaizitian (Sheinwoodian-Homerian), and the Goukou (Homerian-Ludfordian) formations. The Telychian to Sheinwoodian strata at this section were sampled and studied for carbon isotope stratigraphy and conodont biostratigraphy. The paired $\delta^{13}\text{C}_{\text{carb}}$ and $\delta^{13}\text{C}_{\text{org}}$ data reveal a pronounced positive excursion, the Manitowoc carbon isotope excursion (Manitowoc CIE, Manitowoc Excursion) in the upper *Pterospirifer eopennatus* Zone and the lower *Pterospirifer amorphognathoides amorphognathoides* Superzone, with an increase of approximately 2 per mill in $\delta^{13}\text{C}_{\text{carb}}$ and approximately 5 per mill in $\delta^{13}\text{C}_{\text{org}}$. Well-constrained by conodont biostratigraphy, the Manitowoc CIE is an essential tie-point for correlation between the Baizitian succession and the Telychian strata of Baltica and Laurentia. Our new $\delta^{13}\text{C}_{\text{carb}}$ and $\delta^{13}\text{C}_{\text{org}}$ data imply that the carbon isotope excursion previously recognised as the Ireviken Excursion (Early Sheinwoodian CIE) at this section should be revised as the Manitowoc CIE. The $\Delta^{13}\text{C}$ data in this study suggest a slight drop of atmospheric CO_2 and thus add evidence for a perturbation of the global carbon cycle during the middle Telychian. We suggest a detailed re-evaluation of the early Silurian climate changes inferred from the Viki core from Estonia together with stable isotope data published from other sections of Baltica (Latvia, Sweden). Based on the combined information from the conodont apatite oxygen isotope records from Estonia and the significant stratigraphic gaps recognized at the Baizitian section, we propose that the stratigraphic gaps in Sichuan should correlate with the Telychian Valgu and the early Sheinwoodian glaciation.

YANGTZE PLATFORM

1,561,360

CONODONTS FROM THE OLENEKIAN-ANISIAN BOUNDARY INTERVAL, YOUPING, SOUTH CHINA, WITH DISCUSSION ON THE PRIMARY INDEX IN THE REORGANIZATION OF THE BASE OF MIDDLE TRIASSIC

Y.Chen, Y.Zhang, H.Jiang, J.G.Ogg and Y.Gong (China Univ Geosci, Wuhan; Purdue Univ; Henan Aero Geophys Survey). *5TH INTERNATIONAL CONODONT SYMPOSIUM [ICOS] (Wuhan, China and Online, 6/24-27/2022) PROGRAM AND ABSTRACTS* p.47, 2022. (Abstract only)

The Early-Middle Triassic/Olenekian-Anisian boundary interval was the last phase of the prolonged recovery after the end-Permian mass extinction. Despite this, there is not yet a globally accepted definition (global stratotype section of point, GSSP) for the base of the Anisian. The first appearance of the conodont *Chiosella timorensis* (Norgmi, 1968) has been long considered the proxy index for the OAB. However, this species has been obtained along with the traditionally late Spathian ammonoids of the *Haugi* zone (Goudemand et al., 2012), which generated doubts about its suitability. Subsequently, a number of possible alternative conodont indexes for the base of Anisian have been proposed, including: *Gladignathodus tethydis*, *Magnigondolella alexanderi*, *Neogondolella curva*, etc., since their first occurrences in the proposed section are stratigraphic higher than the FO of the *Chiosella timorensis*. However, the global synchronous feature, taxonomy, and relationship of these possible earliest Anisian conodonts remain understudied. In the Youping section, South China, eastern Tethys, the latest Spathian-earliest Anisian conodont assemblage—including: *Triaspathodus ex. gr. homeri*, *Chiosella timorensis sensu stricto*, *Ch. timorensis sensu lato*, *Gl. tethydis*, *Mg. alexanderi*, *N. g. curva*, etc.—has been recognized.

Associated potential markers that have been proposed to aid recognition of OAB include the peak of $\delta^{13}\text{C}$ excursion (Early Anisian Event, Cramer and Jarvis 2020), and the shift from reversed polarity zones to normal-polarity magnetozones (Base of MT1n; Hounslow et al., 2007). We have evaluated the global synchronously of the possible conodont indexes for base Anisian, via the geomagnetic polarity magnetozones between the Western Tethys nominated Desli Caira and Kcira-A section and Eastern Tethys candidate Wantou, Guandao, and Youping sections in this study. It suggests that the FO of *Gl. tethydis* situated below the MT1n (Middle Triassic first normal magnetozones, designation followed from Hounslow and Muttoni, 2010) or within the MT3n; the FO *Ch. timorensis s.l.* situated below the MT1n or above the MT1n. The *Ng. curva* occurs slightly above the *Ch. timorensis* in both sections, but the FO of *Ng. curva* is below the MT3n or near the base of MT3n. On the controversy, the *Ch. timorensis sensu stricto* is still situated in the MT1-2 magnetozones among the sections, which indicated that the FO of the *Ch. timorensis sensu stricto* has advanced in the global synchronous correlation compared to other proposed alternative index species for the OAB. As we have stated previously, a multi-proxy approach to identify the OAB will yield a more accurate and reliable cross-region correlation and lead to the recognition of the primary index with a global synchronous feature.

YANGTZE PLATFORM

1,561,361

THE DOUSHANTUO FORMATION, THE ONSET OF THE EDIACARAN RIFTS IN SOUTH CHINA

K.Chen (China Geological Survey). *21ST INTERNATIONAL SEDIMENTOLOGICAL CONGRESS [ISC] (Beijing, China, 8/22-26/2022) ABSTRACT BOOK* p.323, 2022. (Available at <http://www.isc2022.org.cn> as of 9/22/2022; Abstract only)

The Ediacaran Doushantuo Formation (ca. 635-551 Ma) in South China is one of the most intensively investigated units in the world, as it contains exceptionally well-preserved fossils of multicellular eukaryotes including early animals. The majority of the Doushantuo Formation was deposited on a rimmed carbonate shelf of the Yangtze platform, with a shelf margin shoal that restricted the shelf lagoon from the open ocean. However, the previous studied were mostly based on the outcrops without detailed analysis of the interior of the platform. We analysis the drilled data in the interior of the Yangtze platform, indicating that there existed two rifts, one is the Deyang-Anyue rift in the West and the EXi rift in the East. This study established a stratigraphic framework of the Doushantuo formation by litho-, chemo-, bio-, and sequence stratigraphy. Regional correlation across South China relies on two distinctive marker beds, the cap carbonate at the base and the organic-rich black shale at the top of the Doushantuo Formation. During Ediacaran and Lower Cambrian, the Doushantuo Formation, the Dengying Formation, and the Niutitang Formation represent different stages of the rifts at the Yangtze platform from bottom to up. Firstly, the Doushantuo Formation indicates the beginning of the rifts in South China. Secondly, carbonatite of the Dengying formation was controlled by syn-sedimentary faults, which forming the "graben-horst" structural model, with Deyang-Anyue and EXi rifts. Finally, a set of organic-rich shale filled up the rifts by Niutitang Formation during the Early Cambrian. The rifts provided the geological background of location for the conventional and unconventional nature gas exploration.

YANGTZE PLATFORM

1,561,362

COEVAL CHANGES OF CARBONATE PLATFORM ENVIRONMENT AND CARBON ISOTOPE AT PERMIAN-TRIASSIC BOUNDARIES IN SOUTH CHINA AND LHASA BLOCK

J.He, X.Hu and Z.Han (Chengdu Univ Technology; Nanjing Univ). *21ST INTERNATIONAL SEDIMENTOLOGICAL CONGRESS [ISC] (Beijing, China, 8/22-26/2022) ABSTRACT BOOK* p.188, 2022. (Available at <http://www.isc2022.org.cn> as of 9/22/2022; Abstract only)

The Permian-Triassic boundary (PTB) has experienced the largest biological extinction in the geological history, and there has

been a significant global carbon isotope excursion, accompanied by the development of unconformity, anachronistic facies and Occurrence of hyperthermal event. However, there are absence of detailed studies in carbonate platform environment in response to the carbon isotopic excursion around the PTB. This study measured three carbonate platform sections throughout the PTB located on the South China (Liangfengya section near Chongqing, Taiping section in Guangxi) and Lhasa block (Wenbudangsang section near Gaize). High-precision carbonate microfacies and carbon apposition stratigraphic analysis were carried out, and 14 types of carbonate microfacies were recognized. Carbonate microfacies show that during the latest Permian, the Liangfengya section and the Taiping section are in the inner ramp environment as a whole, and the Wenbudangsang section is in the outer ramp environment. The carbonate carbon isotopes during PTB can be divided into four stages: NC1 (before carbon isotope excursion event), NC2 (carbon isotope excursion event initiation stage), NC3 (carbon isotope excursion event continuous stage) and NC4 (after carbon isotope excursion event). Comprehensive studies on sedimentary microfacies, carbon isotope changes and fossil records show that there is an evolutionary sequence of NC2 with unconformity development and anachronistic facies development followed by the NC3 stage. Taking the duration of NC2 stage in the Meishan section as the standard (approximately 58 kyr), the occurrence time of sedimentary events in different sedimentary sections is restored by stratigraphic thickness interpolation. The hard ground structure first appeared in the Liangfengya section at approximately 9 kyr later the start of NC2 stage, and the last appeared in the Wenbudangsang section at approximately 46 kyr later the start of NC2 stage. Stratigraphic loss occurs at approximately 6 kyr later the start of NC2 stage in areas where microbialites are not developed, and at approximately 37 kyr later the start of carbon isotope negative bias in areas where microbialites are developed. At the same time, the emergence of hard ground structure or stratum loss is often accompanied by the development of anachronistic facies, in which the main development of microbialites and oolitic limestone is concentrated in NC2 stage, and the main development of dolomite is in NC3 stage. Compared with the PTB, with the intensification of the earth's temperature increase, the carbonate platform in the shallow sea environment will take the lead in the sudden change of the marine environment, spread to the deep-water environment approximately 37 kyr later, and accompanied by the emergence of microbialites and oolitic limestone.

YANGTZE PLATFORM

1,561,363

THE DISTURBANCE OF TERRESTRIAL ECOSYSTEMS DURING THE PERMIAN-TRIASSIC TRANSITION IN SOUTH AND NORTH CHINA

D.Chu (China Univ Geosci, Wuhan). *21ST INTERNATIONAL SEDIMENTOLOGICAL CONGRESS [ISC] (Beijing, China, 8/22-26/2022) ABSTRACT BOOK* p.202, 2022. (Available at <http://www.isc2022.org.cn> as of 9/22/2022; **Abstract only**)

The Permian-Triassic mass extinction (PTME) had a catastrophic impact on both marine and terrestrial ecosystems and was the most severe crisis of the Phanerozoic. It is widely attributed to the global environmental changes caused by the contemporaneous volcanism. The timing and nature of the terrestrial crisis is unclear. The terrestrial sediments in South China record increased abundance of fossil charcoal coincident with the onset of a negative carbon isotope excursion (CIE) and the loss of tropical rainforest vegetation, both of which occurred immediately before the peak of Hg concentrations. We find a significant peak of spore tetrads of lycopsid plants coeval with increases in metal concentrations above the main terrestrial extinction interval in South China, which suggests that survivor lycophyte plants were under huge stress after the loss of the Permian forests. However, the crisis of conifer and the dramatic decrease of total organic carbon content in North China occurred before the negative CIE and significantly preceded the increase of Hg content. These evidences probably suggest that the crisis of different terrestrial ecosystems is asynchronous. To obtain a more complete understanding of the specific processes and driving mechanisms of terrestrial PTME, high-resolution and in-depth studies are urgently needed to reveal the biological and environmental evolution in the terrestrial record.

YANGTZE PLATFORM

1,561,364

A MIDDLE WUCHIAPINGIAN HYDROCLIMATE INDUCED ACCELERATION IN BASALTIC LANDSCAPE EROSION IN PALEOTROPICAL SOUTH CHINA

J.Yang, P.A.Cawood, Y.Du, W.Weil and J.Ren (China Univ Geosci, Wuhan; Monash Univ). *21ST INTERNATIONAL SEDIMENTOLOGICAL CONGRESS [ISC] (Beijing, China, 8/22-26/2022) ABSTRACT BOOK* p.208, 2022. (Available at <http://www.isc2022.org.cn> as of 9/22/2022; **Abstract only**)

Chemical weathering and physical erosion are major factors affecting landscape evolution and shaping Earth's surface. Modern observations and measurements along with modelling suggest significant effects of hydroclimate on catchment erosion and weathering. But to reveal the hydroclimate influences on catchment-averaged erosion and weathering from geological records is challenging. Here we present proxy data on the provenance, source weathering and paleowater salinity from the early Late Permian sedimentary successions in western South China. The analyzed successions are dominated by basaltic mudrocks and sandstones derived from the Emeishan large igneous province. A negative organic carbon isotope excursion (CIE) was observed from all the studied three successions. Based on this CIE, these studied estuary-deltaic successions can be correlated with deep-water and shallow marine successions in South China and with terrestrial successions in eastern Australia where the last Permian glacial-deglacial cycle was recorded. Reported high-precision tuffaceous zircon U-Pb ages support these stratigraphic correlations and constrain this early Late Permian CIE at around 258-257 Ma, corresponding to the middle Wuchiapingian deglaciation. Through this strata interval with CIE, mudrock chemical and mineral compositions consistently demonstrate a decrease in source chemical weathering intensity and detrital zircon data suggest a prominent unroofing of the Emeishan volcanic provenance. Using proposed relationships of chemical weathering rate with land surface temperature and with denudation (total erosion) rate for present-day basaltic landscapes, the denudation rates of the Emeishan basaltic landscape were calculated based on the published seawater temperatures from South China and show high values (approximately 300 t/km²/yr) in the interval with CIE than in the underlying and overlying intervals (both are approximately 200t/km²/yr). During the acceleration interval, denudation rate is negatively correlated ($r^2 = 0.56$) with mudrock B/Ga ratio which shows a distinct decrease from > 6 to < 3 . This decrease in mudrock B/Ga ratio reflected a marine to freshwater facies change and suggest an enlargement in freshwater influx for these middle Wuchiapingian estuary-deltaic environments in South China. Such water salinity changes along with the co-increased sandstone proportion in studied successions and occurrences of terrigenous clastic depositions in deep-water and shallow marine successions support an enhancement in fluvial sediment and freshwater supply, which were possibly related to strengthened rainfalls. It follows that the erosion acceleration of basaltic landscapes was likely associated with hydroclimate change in South China during the middle Wuchiapingian warming. Landscape evolution modelling supports this hypothesized causal linkage and further indicates an increase of precipitation by approximately 2-3 times for the observed acceleration in landscape erosion.

YANGTZE PLATFORM

1,561,365

RAPID CLIMATIC FLUCTUATION DURING THE GUADALUPIAN-LOPINGIAN TRANSITION: RECORDED BY WEATHERING INDEX OF GEOCHEMICAL ACID-INSOLUBLE RESIDUA OF CARBONATE ROCK, SOUTH CHINA

S.Sun and A.Chen (Chengdu Univ Technology). *21ST INTERNATIONAL SEDIMENTOLOGICAL CONGRESS [ISC] (Beijing, China, 8/22-26/2022) ABSTRACT BOOK* pp.210-211, 2022. (Available at <http://www.isc2022.org.cn> as of 9/22/2022; **Abstract only**)

The Guadalupian-Lopingian boundary (GLB) transition was regarded as a gradual warming period with the termination of the Late Paleozoic Ice Age (LPIA). However, the glacial-nonglacial cycles from Eastern Australia imply that the period was also

influenced by climatic fluctuations. We here report on a GLB section of the South China Block confined by the conodont biostratigraphy to constrain weathering intensity and the associated climatic fluctuation during this critical interval. The chemical weathering indices were estimated by analyses of acid-insolubles residua extracted from carbonate rocks. Two weak weathering units, Unit 1 and 3, Early Capitanian and Early Wuchiapingian and two strong weathering units, Unit 2 and 4, Late Capitanian and Middle Wuchiapingian are identified. $\delta^{13}\text{C}_{\text{carb}}$ generally follow well the variation tracks of weathering indices. Two weak weathering units (Unit 1 and 3) correspond to the P3 glacial and the P4 glacial in high-latitude region of Australia. The strong weathering unit (Unit 2) is closely related to the eruption of the Emeishan Large Igneous Province (ELIP). These climatic fluctuations of the GLB transition also influenced the biodiversity. The CIA-converted land surface temperature and reported seawater temperature reflect the synchronous response of continental climate and marine conditions. The high temperature associated with the peak of the ELIP may be responsible for the GLB extinction.

YANSHAN RANGE 1,561,366

EVIDENCE OF TRANSIENT OXYGENATION IN THE MESOPROTEROZOIC OCEAN FROM THE YANSHAN BASIN, NORTH CHINA

X.Chen, M.Li, K.Zong, Y.Liu, T.Zhang and Y.Shen (Hefei Univ Technology; China Univ Geosci, Wuhan; China Univ Petroleum). *PRECAMBRIAN RESEARCH* v.382, Nov. 2022. (ISSN 0301-9268; Article no.106880)

Predominantly anoxic conditions with a heterogeneous stratified water column are widely accepted for the Mesoproterozoic ocean. However, transient and episodic oxygenation during the Mesoproterozoic has been recently hypothesized, which may have been an important trigger for eukaryote evolution. In this study, we analyzed the Ce anomalies of the Gaoyuzhuang and Hongshuizhuang formations in North China, to investigate the Earth's surface environment during the Mesoproterozoic. Our data of negative Ce anomalies in the Gaoyuzhuang and Hongshuizhuang formations, reaching 0.73 and 0.84, respectively, suggest transient oxygenations of the surface environment. We applied a CeN/CeN* depth model to quantify these transient oxygenations and the results suggest that the atmospheric oxygen level would have increased by 0.01-0.03% present atmospheric level (PAL), 0.02-0.05% PAL, and 0.1-0.4% PAL, with the respective initial levels of 0.05% PAL, 0.1% PAL, and 1% PAL, in the Gaoyuzhuang and Hongshuizhuang formations. Our results suggest that although oxygen levels in the Mesoproterozoic were low, transient oxygenation may have occurred in the surface ocean, which would have provided vital niches for the evolution of eukaryotes. (c2022 Elsevier B.V.)

YELLOW RIVER DELTA 1,561,367

SOIL CLASSIFICATION AND SITE VARIABILITY ANALYSIS BASED ON CPT - A CASE STUDY IN THE YELLOW RIVER SUBAQUATIC DELTA, CHINA

Z.Yang, X.Liu, L.Guo, Y.Cui, X.Su and X.Ling (Qingdao Univ Technology; Shandong Univ; China Ocean Univ). *JOURNAL OF MARINE SCIENCE AND ENGINEERING* v.9, no.4, April 2021. (ISSN 2077-1312; Article no.431)

The Yellow River Delta is located at the junction of the Yellow River and Bohai. The impact function from the river and the dynamics of the ocean tides make the soil composition and distribution in this area substantially complicated. In order to test the distribution and variation of the soil layers in the Yellow River Delta, the soil layers in the test area were classified and the variation was calculated using the cone penetration test (CPT). The following conclusions were drawn: (1) the soil in the measured area is mainly composed of sensitive fine-grained soil, accounting for about 70% of all soil types, and the content of sensitive fine-grained soil in the far-sea position is higher than that in the offshore position in the direction perpendicular to the coastline. (2) It has a high vertical variability index (VVI) at the near-shore location, above 45%, and a low vertical variability at the far coast, generally

below 20%. (3) The horizontal variability index (HVI) changes significantly near the coast, and it remains below 45% in the test area.

YILGARN CRATON 1,561,368

SEISMIC REFLECTION AND POTENTIAL FIELD CONSTRAINTS ON IMBRICATION AND EXHUMATION OF THE PALEOARCHEAN NARRYER TERRANE, YILGARN CRATON

S.E.Sellars, A.J.Calvert and M.P.Doublier (Simon Fraser Univ; Geoscience Australia). *TECTONICS* v.41, no.10, Oct. 2022. (ISSN 0278-7407; ISSN 1944-9194; Article no.e2022TC007343)

The Narryer Terrane, which is located on the northwest margin of the Yilgarn Craton, is one of the oldest preserved blocks of continental crust on Earth with rocks as old as 3.73 Ga and detrital zircons up to 4.4 Ga. In 2010-11, three deep seismic reflection profiles were acquired over the terrane, and interpreted to show that during the Neoproterozoic the Narryer Terrane was thrust over the northwest edge of the Youanmi Terrane, which represents the core of the Yilgarn Craton, and in turn underthrust from the north by the Glenburgh Terrane during the Paleoproterozoic. We have reprocessed the seismic data to improve the imaging, extract 3D reflector orientations, and determine near-surface velocity models. We locate the shear zone along which the Narryer Terrane was exhumed and correlate upper crustal faults interpreted in the seismic data with near-surface faults and shear zones identified in a regional map of the first vertical derivative of the total magnetic field. One >150 km and two ca. 50 km-long shear zones divide the exposed Narryer Terrane into distinct structural domains that were probably juxtaposed relatively late in the thrusting of the Narryer Terrane over the Youanmi Terrane in the Paleoproterozoic. While most supracrustal rocks occur in the Northern and Southern domains, the Western Domain where magmatic ages are <3.0 Ga, high mass density, consistent with exhumation from the middle-lower crust, and is made up of four blocks that exhibit differing patterns of seismic reflectivity, indicating they were likely combined prior to their exhumation.

YINCHUPU FM 1,561,369

ORIGINATION OF THE RAMIFORM-PECTINIFORM APPARATUSES IN CONODONTS - NEW EVIDENCE FROM THE LOWER ORDOVICIAN OF SOUTH CHINA AND AUSTRALIA

Y.Y.Zhen, Y.D.Zhang, Z.Y.Chen and L.W.Wang (New South Wales Geol Surv; Nanjing Inst Geol Palaeont; Res Inst Geol Mineral Rscs). *5TH INTERNATIONAL CONODONT SYMPOSIUM [ICOS] (Wuhan, China and Online, 6/24-27/2022) PROGRAM AND ABSTRACTS* p.73, 2022. (Abstract only)

The morphological diversity of conodonts experienced a major origination and radiation event during the late Tremadocian to early Floian, when the coniform dominated late Cambrian and earliest Ordovician communities transformed into the much-diversified Ordovician communities characterized by the appearance and subsequent dominance of many major clades with a ramiform-pectiniform apparatus. The origination and early evolution of *Prioniodus* in the late Tremadocian is one of the best examples of this most significant diversification event in the evolutionary history of conodonts. A conodont fauna of the late Tremadocian to early Floian age (Early Ordovician) is documented from the Yinchufu Formation of Zhejiang Province, South China. It is characterized by the occurrence of two species of *Prioniodontidae*, a new species of *Prioniodus* and *Acodustriangularis*. The new species may represent the most primitive species of this genus, which was erected by Pander more than 160 years ago. In the next 100 years nearly 200 species (mostly form species) from the Ordovician to Permian were named and assigned to *Prioniodus*, making it a name embedded in a vast number of conodont literature. More recent studies in the 1950s and 1960s concluded that most of these species were not morphologically related to its type species of the Early Ordovician and reassigned to various genera belonging to different families and even orders. Based on a literature review of all the species that were assigned to *Prioniodus*, only six multi-element species are confirmed to belong

to this genus. Our morphometrics analysis of these six species shows that they form a monophyletic group directly evolved from an adentate species of *Acodus*, likely *Acodus triangularis*. This study is further supported by a cladistic analysis to better elucidate the evolution of the *Prioniodus* lineage through late Tremadocian to Floian of the Early Ordovician and its phylogenetic relationships with other related taxa. The new evidence supporting the origination and evolution of the *Prioniodus* species discussed in this study underpins their biostratigraphic applications as biozonal index species. The origination of ramiform-pectiniform apparatuses as represented by the appearances of *Prioniodus* and other taxa in the late Tremadocian and Floian might be a major response of the conodont animals to occupy and adapt to increasingly diversified environments in the shelf and slope settings. The biofacies distribution of the six *Prioniodus* species indicates that *Prioniodus* might have originated in deep water slope settings and progressively spread into distal and then interior shelves in the late Tremadocian and diversified in the Floian, with *Prioniodus amadeus* possibly representing a relict species survived well into the Middle Ordovician (Dapingian) and restricted to shallow water environments in the Amadeus Basin of central Australia.

YINGGEHAI BASIN

1,561,370

THE HOANH BO TROUGH-A LANDWARD KEYHOLE TO THE SYN-RIFT LATE EOCENE-EARLY OLIGOCENE TERRESTRIAL SUCCESSION OF THE NORTHERN SONG HONG BASIN (ONSHORE NORTH-EAST VIETNAM)

A.Wysocka, H.van Tha, U.Czarniecka, E.Durska, A.Filipek, P.D.Pha, N.Q.Cuong, D.Zaszeowski, D.M.Tuan et al. (Warsaw Univ). *GEOLOGICAL JOURNAL* v.57, no.10, pp.4216-4241, Oct. 2022. (ISSN 0072-1050; ISSN 1099-1034)

Located on the northern Vietnam onshore/offshore transition, the Hoanh Bo Trough is an excellently exposed terrestrial Palaeogene sedimentary sequence that may be treated as an analogue for regional interpretations of the sedimentary and structural evolution of the northern Song Hong Basin. The Hoanh Bo Trough lies to the north of the northern Song Hong Basin and to the west of the Beibuwan Basin, the origin and evolution of which are linked with Palaeogene South China Sea rifting. Field and archival well sedimentological observations were made throughout the Palaeogene succession of the Hoanh Bo Trough, and samples were collected for palynological, petrographical, and geochemical analysis. Based on the coexistence of particular lithofacies, proximal alluvial fan, distal alluvial fan, fluvial alluvial plain with channels, alluvial plain and/or lake margin, and lacustrine facies associations were distinguished. Palynological analyses suggest the sedimentary infill of the Hoanh Bo Trough is of the Late Eocene–Early Oligocene age and was deposited in a very warm tropical/subtropical climate. In turn, geochemical results demonstrate that the deposits have intermediate chemical maturity and were probably reworked from older sedimentary rock sources. Moreover, it is suggested to combine the Dong Ho and Tieu Giao formations and synonymize them as the Dong Ho Formation. The sedimentary pattern, age, climatic conditions, and structural evolution of the Hoanh Bo Trough align well with the rift initiation, rift development, and rift termination tectonic system tracts. Moreover, the Hoanh Bo Trough could be treated as a landward keyhole for the offshore basins: for instance, the Kien An Basin in the northern Song Hong Basin.

YINGGEHAI BASIN

1,561,371

FLOW MECHANISM AND PORE STRUCTURES OF TIGHT SANDSTONE BASED ON DIGITAL CORE ANALYSIS

X.Wang, J.Huan, X.Peng, C.Zhang, W.Yuan and Y.Wang (CNOOC Ltd; Colchis Petro Consult Ltd). *PETROLEUM GEOLOGY AND RECOVERY EFFICIENCY (YOUQI DIZHI YU CAISHOULU)* v.29, no.6, pp.22-30, Nov. 2022. (ISSN 1009-9603; In Chinese)

[Full article and English abstract available from P.A.]

YORKSHIRE AREA

1,561,372

A QUANTITATIVE COMPARISON OF DISPERSED SPORES/POLLEN AND PLANT MEGAFOSSIL ASSEMBLAGES FROM A MIDDLE JURASSIC PLANT BED FROM YORKSHIRE, UK

S.M.Slater and C.H.Welman (Sheffield Univ). *58TH ANNUAL PALAEOBOTANICAL ASSOCIATION MEETING (Leeds, UK, 12/16-19/2014) ABSTRACTS* pp.44-45, 2014. (Available at <http://www.palass.org> as of 11/15/2022; **Abstract only**)

Detailed quantitative data have previously been collected from palaeobotanical plant megafossil assemblages from a Middle Jurassic (Aalenian) plant bed from Hasty Bank, North Yorkshire, UK. We conducted a similar analysis of palynological dispersed sporomorph (spores and pollen) assemblages collected from the same section using the same sampling regime. Both dispersed sporomorph and plant megafossil assemblages display consistent changes in composition, diversity and abundance through time. However, the dispersed sporomorph and plant megafossil datasets provide conflicting evidence for the nature of the parent vegetation. Multivariate analysis of sporomorph occurrence/abundance and palynofacies data suggests that temporal variation in sporomorph/plant megafossil assemblages is the result of depositional change between claystone, siltstone and grey clay lithologies, which reflect discrete depositional environments and different vegetation types. The reproductive strategies of parent plants are considered to be a principal factor in shaping many of the major abundance and diversity irregularities between dispersed sporomorph and plant megafossil data sets that seemingly reflects different parent vegetation. Preferential occurrence/preservation of sporomorphs and equivalent parent plants is a consequence of a complex array of biological, ecological, geographical, taphonomic and depositional factors that act inconsistently between and within fossil assemblages, which results in significant discrepancies between data sets.

YUNNAN

1,561,373

A NEW LIBERATION LAGERSTAETTE FROM SOUTHWEST CHINA DURING CARNIAN PLUVIAL EPISODE

Z.Ma, T.Zhang, J.Chen, J.Zeng, X.Zhang, S.Li and H.Li (Southwest Petroleum Univ; Fuzhou Univ). *21ST INTERNATIONAL SEDIMENTOLOGICAL CONGRESS [ISC] (Beijing, China, 8/22-26/2022) ABSTRACT BOOK* pp.205-206, 2022. (Available at <http://www.isc2022.org.cn> as of 9/22/2022; **Abstract only**)

We report the Luxi biota, a new Liberation Lagerstaette from the Triassic Carnian Xiaowa Formations in Yunnan, South China, with close faunal links to the biota of Cassian Formation in Italy. The biota described from the marls of the Julian 2 siltstone were deposited during a major, Tethyan-wide climate crisis--the so-called Carnian Pluvial Episode (CPE)--characterized by an amount of terrigenous clastics input the marine and a demise of carbonate platforms. The biodiversity of the Luxi biota includes Cephalopoda (Ammonitida, Phragmoteuthida, Orthocerida, Nautilida and Belemnitida), Gastropoda, Bivalvia, Brachiopoda, Crinoidea and plant fossils. The fossil community from three different lithological parts of the Xiaowa Formation exhibits different preservation forms and combinations in each part. In the lower part, abundant compressed *Trachyceras multituberculatum* and *Halobia yunnanensis* were found in black mud-limestone; The middle part is dominated by the lime-siltstone. At the base of the middle part contains three-dimensional preserved *Sinobelemnitidae* and *Michelinoceras* with a few pyritized ammonoids (*Austrotrachyceras*, *Sirenites*). However, *Sinobelemnitidae* rapidly disappeared and replaced by some gastropods such as *Anulifera*, *Zygopleura*, *Neritaria* etc.. Based on electronic microscope scanning, some gastropods preserve the protoconch and all protoconches indicate these gastropods were a nonplanktotrophic lifestyle during the larval stage. Besides the gastropods, a few phragmoteuthids (*Phragmoteuthis*), bivalves (*Halobia*, *Monotis*) and brachiopods (*Norella*, *Neoretzia*) with low fossilized are also found in this part. The upper part is black shell. It contains a large amount of three-dimensional preserved ammonoids (*Austrotrachyceras*, *Neoprotrachyceras*, *Sirenites*, *Yakutosirenites*, *Anasirenites*),

brachiopods and crinoid stems. This important discovery indicate (1) bio-community change accompany by the environmental fluctuation during CPE. To be more specific, the three parts of Luxi biota represent a planktotrophic biotic combination transferred to a benthic biotic combination during terrigenous clastics inputting. The benthic biotic combination returned to planktotrophic biotic combination after terrigenous clastics inputting. (2) Due to fossilization has been affected by the carbonate production crisis and an amount of terrigenous clastics inputting, some vulnerable and delicate parts of fossils can be preserved. It provides favorable conditions for the formation of Liberation Lagerstaette.

ZHONGGUAI UPLIFT

1,561,374

GEOCHRONOLOGY, GEOCHEMISTRY, AND TECTONIC SIGNIFICANCE OF CARBONIFEROUS ANDESITES OF ZHONGGUAI UPLIFT IN NORTHWESTERN MARGIN OF JUNGGAR BASIN

L.Shao and F.Yu (China Univ Petroleum). *21ST INTERNATIONAL SEDIMENTOLOGICAL CONGRESS [ISC] (Beijing, China, 8/22-26/2022) ABSTRACT BOOK* p.338, 2022. (Available at <http://www.isc2022.org.cn> as of 9/22/2022; **Abstract only**)

In order to deepen the understanding of the Carboniferous tectonic background in the western part of the Central Asian orogenic belt, the core and samples of andesites in JinLong 10 well area of Zhongguai uplift in the northwest margin of Junggar basin have been studied in petrography, chronology and geochemistry. The results show that brown gray, grayish green and dark gray andesites are mostly developed in the study area andesites in the study and they are belong to low potassium to medium potassium calc alkaline rock series, and its REE diagram is slightly inclined to the right, with weak Eu negative anomaly. In the standardized spider diagram of the original mantle, The Pb and LILE (Rb, Ba) enrichments and HFSE (Nb, Ta, Zr) depletions resemble those of typical subduction-related arc volcanic rocks. The Th/La, Th/Ce and Lu/Yb ratios of andesites are below those of average continental crust, but similar to those of typical mantle-derived magmas. The andesites in the study area belong to the normal island arc volcanic rocks and atypical adakite, which are derived from the water rich mantle wedge and are formed by the partial melting of the fluid metasomatic mantle wedge produced by the dehydration of the subduction plate. The zircon U-Pb dating of andesites LA-ICP-MS shows that the crystallization age is 322.4 ± 1.1 Ma, which is in the Middle Carboniferous, in line with the time range of the first tectonic magmatic event of the extinction of the western Junggar residual ocean basin (329 ca. 320 Ma). Combined with regional geological background and comparison with magmatite in similar period, it is considered that the andesites in the study area was formed in the continental arc environment, and was the product of subduction of the residual oceanic basin in West Junggar, and the remnant ocean basin was not completely closed at 322.4 ± 1.1 Ma.

ZHUJIANGKOU BASIN

1,561,375

CONNECTIVITY AND PERMEABILITY OF ZHUHAI TIGHT SANDSTONE HETEROGENEOUS RESERVOIRS FROM WESTERN PEARL RIVER MOUTH BASIN (CHINA) BY NUCLEAR MAGNETIC RESONANCE

S.Zhou, Y.Deng, H.Wang, Z.Pan and D.Yan (China Univ Geosci, Wuhan; CNOOC (China) Co Ltd; Northeast Petroleum Univ). *APPLIED GEOCHEMISTRY* v.143, Aug. 2022. (ISSN 0883-2927; Article no.105381)

Resolving pore attributes and connectivity of oil-bearing sandstone formations is key to the precise estimation of the oil storage and flowing capacity of the reservoirs. However, very few studies have quantitatively characterized the individual porosities of interconnected pores and inaccessible pores. This study addresses these research gaps by studying Zhuhai sandstone from the western Pearl River Mouth Basin, China, with very low to medium permeability (0.055-346 mD). Nuclear magnetic resonance (NMR) centrifugation distinguished the interconnected and inaccessible pores. NMR T2 parameters (T2 cutoff and T2g) had a distinct impact on the connectivity index and irreducible water saturation. This study successfully developed an adaptable model

that can efficiently estimate permeability in heterogeneous porous media, where no samples are taken, using NMR log. The permeabilities calculated by Schlumberger Doll Research, Coates-cutoff, Coates-BVI, and SDR-reg models were compared with those measured using a gas permeameter. Permeabilities were best calculated using flow-accessible porosity (i.e., Coates-BVI model, 95% matching) rather than other models. The connectivity (0.13-0.84) and movable fluid porosity (1.46-19.32%) were the primary factors that control permeability, and the fracture/crack attributes determined dual porosity. The study revealed that illite in clay minerals exerts a positive control on permeability by sheltering the interconnected primary porosity. (c2022 Elsevier Ltd.)

ZHUJIANGKOU BASIN

1,561,376

STRUCTURAL EVOLUTION AND MECHANISM OF PANYU 4 SAG, PEARL RIVER MOUTH BASIN, SOUTH CHINA SEA

B.Guo, F.Yu and H.Li (China Univ Petroleum). *21ST INTERNATIONAL SEDIMENTOLOGICAL CONGRESS [ISC] (Beijing, China, 8/22-26/2022) ABSTRACT BOOK* p.330, 2022. (Available at <http://www.isc2022.org.cn> as of 9/22/2022; **Abstract only**)

The Panyu 4 Sag is a relatively independent hydrocarbon-rich sub-unit that is located on the western side of the southeastern margin of the Zhuoyi Depression, Pearl River Mouth Basin, South China Sea. In order to further understand the evolution of the Panyu 4 Sag, we present the results of seismic interpretation and analogue modeling to discuss the origin of the Panyu 4 Sag in this paper. Firstly, we describe the geological settings of the studied area based on literature. Secondly, we study the distribution and evolution of fault and sedimentation according to seismic interpretation and structural-sedimentary features of different members of the Wenchang Formation. Thirdly, for understanding the evolution of internal sub-structural units, we carried out analogue modeling to illustrate the formation in different periods to better constrain the evolution of the Panyu 4 Sag. Finally, a model for the formation of the Panyu 4 Sag was proposed. The Panyu 4 Sag can be divided into five parts (Northern, Central, Southern, Western, and Northwestern Sub-sags). The faults of the Panyu 4 Sag can be broadly divided into three fault assemblages that are oriented NE, NEE, and NWW. The NE-trending faults were mainly active during the deposition of members 6 to 2 of the Wenchang Formation, these faults had a significant controlling effect during the early deposition of sag. The NEE-trending faults are accommodation faults related to the NE-trending faults; they are short in extension and did not control deposition. The NWW-trending faults are primarily late-stage faults that were mainly active during the deposition of member 1 of the Wenchang Formation to Enping Formation; they controlled the distribution of late deposition. The Panyu 4 Sag has undergone three cycles of structural evolutionan early rift period (Wenchang Formation), a late rift period (Enping Formation), and a thermal subsidence period (Zhuhai Formation to Quaternary). Seismic interpretation and sandbox modeling results show that Panyu 4 Sag suffer two phases extension resulting in the superposition of structures of different generations during the Cenozoic. Influenced by the evolution of regional geological stresses, the stress field mainly exhibited a shift from NW-SE-trending tension to S-N-trending tension; the shift occurs in the upper Wenchang Formation. A combination of the above and the pre-existing basement fault systems controlled the transformation and superposition of the sedimentary features of the Panyu 4 Sag, resulting in the complex tectonic geomorphology of the present sag.

ZHUJIANGKOU BASIN

1,561,377

INFLUENCE OF TECTONISM AND VOLCANISM ON DEPOSITIONAL SYSTEM IN SOUTH SLOPE AREA OF LUFENG SAG, PEARL RIVER MOUTH BASIN, SOUTH CHINA SEA

X.Tang, Y.Yu and Y.Li (China Univ Petroleum). *21ST INTERNATIONAL SEDIMENTOLOGICAL CONGRESS [ISC] (Beijing, China, 8/22-26/2022) ABSTRACT BOOK* p.334, 2022. (Available at <http://www.isc2022.org.cn> as of 9/22/2022; **Abstract**)

only)

Lufeng Sag, located in the Pearl River Mouth Basin on the northern continental margin of the South China Sea, is one of the important sag with abundant oil and gas. The Paleogene Wenchang Formation was a continental sedimentary system with a large number of braided river deltas developed in the slope area. In this study, we adopted palaeogeomorphic map, seismic data, well data and the casting thin sections to clarify the impact of basement geomorphology, faulting and volcanism on sedimentary system in slope area. Huilu low uplift in the south of Lufeng Sag was a continuous source in the Paleogene. Through the geomorphic highs and slope changes of the basement paleogeomorphic map, 13 ancient gullies supplying sources to the south of Lufeng sag were identified, including U-type, W-type and composite type. The U-type ancient gullies are formed in channel maturity, with strong sand transport capacity and long sediment transport distance. The seismic facies have a strong amplitude, a high frequency, a high continuity and a low angle progradation reflection, resulting in braided river delta deposits with large plane range, long extension and large vertical thickness. The W-type ancient gullies are formed in the late bifurcation of the channel, during which hydrodynamic force is weakened and sand transport capacity of the gully is weak. The seismic facies are medium amplitude, medium frequency and medium continuous forward reflection, forming the same type of the delta but with small plane range, short extension and small vertical thickness. The composite ancient gullies are formed by the superposition of U-type and W-type ancient gullies, with medium sand transport capacity. In addition, the Paleogene rifting was accompanied by numerous faults and local volcanic eruptions in the slope area. Volcanic eruption forms volcanic debris, crystal debris and volcanic ash, which do not affect the shape and size of the sand body, but alter the reservoir's physical properties of it, especially the tuffaceous filling will significantly reduce the reservoir permeability. Faults have an obvious influence on the size of the delta, some of which strike in the same direction as source injection, forming fault trough source channels. The fault trough controlled by a single fault has the characteristics of dustpan structure and wedge filling seismic phase in the vertical provenance direction seismic profile, whereas the fault trough controlled by two dip-faults has the characteristics of symmetrical structure and parallel-subparallel seismic phase in the vertical provenance direction seismic profile. When the fault activity is stronger, the sand transport capacity of the fault trough is stronger, and the scale of the delta is larger. When the catchment area, width-depth ratio, and cross-sectional area of the ancient gully and fault trough are quantitatively analyzed and compared to the corresponding area of the delta, it can be seen that the catchment area and the multiplication of width depth ratio and cross-sectional area are both positively correlated with the area of the sedimentary sand body.

ZHUJIANGKOU BASIN

1,561,378

EOCENE MAGMATIC ACTIVITY AND ITS INFLUENCE ON THE FORMATION OF LACUSTRINE HIGH-QUALITY SOURCE ROCKS IN THE WESTERN ZHU I DEPRESSION, PEARL RIVER MOUTH BASIN

X.Shan, C.Xu, G.Hao, J.Yi, M.Shen, Y.Rexiti and K.Li (Jilin Univ). *21ST INTERNATIONAL SEDIMENTOLOGICAL CONGRESS [ISC] (Beijing, China, 8/22-26/2022) ABSTRACT BOOK* pp.339-340, 2022. (Available at <http://www.isc2022.org.cn> as of 9/22/2022; **Abstract only**)

Following the collapse of the Yanshanian orogenic belt, mantle magma uplift, crustal stretching and thinning, and multiperiod strong magmatic activities widely developed during the Eocene in South China, especially in the western Zhu I depression, Pearl River Mouth Basin (PRMB). Moreover, the Eocene lacustrine mudstone of the Wenchang Formation has high OM abundance (total organic carbon (TOC): maximum of 3.20 wt%) and is an important source rock in the PRMB and in South China. Thus, the sedimentary records of the Eocene Wenchang Formation in the western Zhu I depression provide an interesting perspective for understanding the influence of magmatic activity on the formation of lacustrine high-quality source rocks. Based on detailed analysis of new three-dimensional seismic and drilling data and recent

research results, using geophysical, basin analysis and geochemical means, this paper systematically analyzes the magmatic activity of Paleogene in Zhu I depression and its influence on the reconstruction of basin structure and the development of source rocks. The results suggested that extensive magmatic underplating (mainly distributed in the depression) in the sedimentary period of Wenchang Formation of Zhu I depression, and the multi-stage magmatic underplating may be controlled by the rift of Zhuqiong movement and the tectonic transformation of Huilu movement. Under the joint influence of pre-existing faults and magmatic emplacement, Zhu I depression presents the complexity and diversity of structure. The pre-existing detachment system controls the extension of the basin and forms many elliptical depressions with small aspect ratio. The synsedimentary magmatism promotes the tilt and rotation of the hanging wall of the detachment fault, resulting in the weakening of axial provenance, and the enhancement of gentle slope provenance and the development of large delta deposits. Meanwhile, the subsidence area in the fault depression forms an uncompensated deep lake environment, which provides excellent conditions for the formation of high-quality source rocks. In addition, the detailed geochemical analysis of source rocks in the study area reveal that multiple hydrothermal activities occurred during Wenchang deposition, which is considered to be related to magmatic underplating in the same sedimentary period. During the hydrothermal activity period, regional tectonic activity caused the hydrothermal fluid to jet upward along the tensile fractures in the lake basin basement, thereby inputting abundant nutrients (Fe, Cu, Ni, P, Zn, etc.) and the common prosperity of lake microalgae and terrestrial plants greatly improved lake primary productivity. High lake level led to a reducing bottom water environment, and abundant reducing gases (H₂S, SO₂, and CH₄) were released into the lake along the hydrothermal overflow channel, which further influenced the anaerobic conditions of the bottom water. Therefore, the eugenic environment formed by magmatic hydrothermal activity (high biological productivity and reduction conditions) further promoted the development of high-quality source rocks of Wenchang Formation.

ZHUNGAER BASIN

1,561,379

CHARACTERISTICS AND ORIGIN OF CONGLOMERATE DIAGENETIC TRAPS IN THE JUNGGAR BASIN

W.G.Dong, P.J.Guo, Q.Y.Qiang and Q.Wen (Res Inst Petrol Explor Dev). *21ST INTERNATIONAL SEDIMENTOLOGICAL CONGRESS [ISC] (Beijing, China, 8/22-26/2022) ABSTRACT BOOK* p.1556, 2022. (Available at <http://www.isc2022.org.cn> as of 9/22/2022; **Abstract only**)

The reservoir lithology of Trassic Baikouquan Formation is primarily fan delta conglomerate with low porosity, permeability, and compositional and structural maturity. The properties of the distributary channel conglomerate of the fan delta front are better than those of the distributary channel of the fan delta plain, and reservoirs in delta front have strong heterogeneity. So far, there is still controversy over the types of hydrocarbon trap in the fan delta front, which has led to the different understanding of hydrocarbon accumulation [Lei et al., 2015; Zhi, 2017]. In this study, 225 samples were collected from 31 wells for reservoir characteristics and diagenetic research. Based on reservoir characteristics and diagenesis of reservoirs and dense layers at different burial depths, the relationship between every single factor and secondary pore development was analyzed according to differences in sedimentary facies, detrital feldspar content, formation temperature, and formation water characteristics. These parameters define the formation mechanism of the traps. The reservoirs underwent a series of diagenetic events during the burial process, accompanied by changes in reservoir structures and properties. Influencing factors, including rock composition, structure, and diagenetic environment, i.e., temperature, pressure, fluid, and tectonics, created strong heterogeneities during the processes changing reservoir quality. Microscopic observations of the Baikouquan Formation reservoirs in the Mahu sag show that the reservoir qualities are mainly related to diagenesis. Diagenetic differences are primarily due to rock composition, paleogeothermal environment, and formation fluids during burial. Reservoir

qualities of the Baikouquan Formation were improved during deep burial due to the formation of secondary pores from feldspar dissolution. The detrital feldspar in the front reservoirs dissolved and secondary pores formed when the formation temperature was in the correct range for a weakly acidic fluid environment. Feldspar dissolution mainly depends on feldspar concentrations, weak acid formation, and paleo-temperatures. When all three conditions are not satisfied, i.e., low feldspar concentrations, non-acidic water, or inappropriate paleo-temperatures, the reservoir quality cannot be effectively improved and instead becomes a diagenetic dense layer that acts as a barrier to oil and gas.

ZHUNGAER BASIN

1,561,380

MAIN CONTROLLING FACTORS TO ORGANIC MATTER ENRICHMENT IN THE SHALES OF PERMIAN LUCAOGOU FORMATION, JIMSAR SAG

Z.Zhang, K.Xi, M.Lin and K.Li (China Univ Petroleum). *21ST INTERNATIONAL SEDIMENTOLOGICAL CONGRESS [ISC] (Beijing, China, 8/22-26/2022) ABSTRACT BOOK* p.233, 2022. (Available at <http://www.isc2022.org.cn> as of 9/22/2022; **Abstract only**)

The organic matters distribution characteristics and the enrichment controlling factors in the shales of Permian Lucaogou Formation were studied by integration using cores observation, thin sections identification, x-ray diffraction, rock pyrolysis analysis and element geochemistry analysis. The results showed that the rock types mainly consist of silty dolomite, micrite dolomite, tuffaceous dolomite, dolomitic siltstone, silty tuff and tuffaceous siltstone. There are three major laminae types in the research area, the tuff laminae, terrestrial debris laminae and carbonated texture laminae. The main types of laminae combinations are the "tuff texture + carbonate" binary laminae combination, "tuff texture + terrestrial debris" binary laminae combination, and "carbonated texture + terrestrial debris" binary laminae combination. In general, the rocks mixed with pyroclastic and chemical sediments are the most conducive to organic matter enrichment, and the higher the content of pyroclastic components, the more organic matter accumulation. Microscopically, organic matter is mainly concentrated in the tuff laminae. The content in the carbonate laminae is low, and almost no organic matter is visible in terrestrial detrital laminae. The organic-rich lithofacies are mainly laminar tuffaceous siltstone and tuffaceous dolomite, the organic matter distribution continuously in strip-shapes. The laminated dolomitic siltstone and silty dolomite mainly contain the scattered organic matter, and they show relatively low organic matter content. The massive micrite dolomite and siltstone are characterized by organic-poor features. The main controlling factors to organic matter enrichment in different lithofacies are significantly different. Productivity is the main controlling factor to organic enrichment of silty dolomite and micrite dolomite, while the organic matter in silty and tuffaceous dolomite is mainly controlled by redox environment. The higher specific surface area of clay minerals can easily absorb organic matter to form stable organoclay complex, which allows the organic matter to be effectively preserved in dolomitic siltstone and tuffaceous siltstone.

ZHUNGAER BASIN

1,561,381

CHARACTERISTICS AND CONTROLLING FACTORS OF GLUTENITE RESERVOIR ROCK QUALITY OF RETROGRADATIONAL FAN DELTA: A CASE STUDY OF THE UPPER WUERHE FORMATION OF THE MAHU SAG, THE JUNGGAR BASIN

Y.Ma, G.Wang, S.Pan, Y.Qu, J.Guo and L.Huang (Res Inst Petrol Explor Dev). *21ST INTERNATIONAL SEDIMENTOLOGICAL CONGRESS [ISC] (Beijing, China, 8/22-26/2022) ABSTRACT BOOK* p.234, 2022. (Available at <http://www.isc2022.org.cn> as of 9/22/2022; **Abstract only**)

The glutenite reservoir rock of the fan delta facies is associated with a complex sedimentary environment and high heterogeneity, and by far the characteristics and controlling factors of the reservoir rock quality have not been well understood. By comprehensively investigating the lithofacies, petrology, physical properties and diagenesis of the Upper Wuerhe Formation of the

Mahu Sag, the Junggar Basin, it is concluded that the Upper Wuerhe Formation develops three major groups of lithofacies, totally consisting of 11 sub-types, and reservoir rock properties of different lithofacies are greatly varied. This research shows that the lithofacies attributed to the tractive current and density current have well-sorted rock particles, low mud content, well-developed secondary dissolved pores, and thus high overall reservoir rock quality. On the contrary, the lithofacies based on debris flow and sheet flow, are observed with high mud content, suppressed development of intergranular and dissolved pores, and thus poor reservoir rock quality. The system tract controls the macro variation of the reservoir rock quality. The best quality is found in the highstand system tract, followed by those of the lake transgression and at last lowstand system tracts. The micro variation of the reservoir rock quality is determined by the mud content, rock particle size and dissolution. The muddy matrix mainly damages the pore connectivity, and presents the strongest correlation with permeability. The reservoir rock with concentrated particle sizes and well-sorted particles has quality better than those of reservoir rocks composed of excessively large or small particles. Dissolution effectively improves the storage capability of the reservoir rock, resulting in an average porosity increment by 4.2%.

GEOCHEMISTRY

BIOGENIC SEDIMENTARY STRUCTURE

1,561,382

SOLVING DARWIN'S DILEMMA? DIFFERENTIAL TAPHONOMY REVEALS TISSUE BIOCHEMISTRY DEPENDENCE OF MOULD/CAST EXCEPTIONAL FOSSIL PRESERVATION

B.A.MacGabhann, J.D.Schiffbauer, J.W.Hagadorn, P.Van Roy, E.P.Lynch, L.Morrison and J.Murray (Edge Hill Univ; Missouri Univ; Denver Museum). *58TH ANNUAL PALAEOONTOLOGICAL ASSOCIATION MEETING (Leeds, UK, 12/16-19/2014) ABSTRACTS* p.35, 2014. (Available at <http://www.palass.org> as of 11/15/2022; **Abstract only**)

Molecular palaeontology suggests that animals emerged nearly 800 million years ago perplexingly, over 200 million years before the oldest known megascopic fossils. The enigmatic cast-and-mould siliciclastic preservation of these first fossils is widespread in Neoproterozoic deposits, suggesting a predominance of taphonomic conditions unlike those on the present-day Earth. However, by examining and comparing fossil eldondites preserved as moulds and casts in the Ordovician Tafalalt Lagerstaette in Morocco and as compressions in the Burgess Shale, we have shown the former taphonomic mode to depend on the formation of aluminosilicate and/or iron sulphide moulds on specific organic surfaces. This occurs via adsorption of reduced iron ions onto tissues composed primarily of high molecular weight biopolymers which require enzymatic degradation prior to decay, and nucleation of sulphides or aluminosilicates around adsorbed ions. Animals lacking tissues primarily composed of such high molecular weight biopolymers, which must have included the first animals to evolve, thus could not have been fossilized in this style. Understanding the origin and earliest evolution of metazoans will therefore require a focus on alternative modes of fossilization.

BIOMINERALIZATION

1,561,383

ARAGONITE/CALCITE SEAS AND THE EVOLUTION OF BIOMINERALIZATION

U.B.Balthasar (Plymouth Univ). *58TH ANNUAL PALAEOONTOLOGICAL ASSOCIATION MEETING (Leeds, UK, 12/16-19/2014) ABSTRACTS* p.19, 2014. (Available at <http://www.palass.org> as of 11/15/2022; **Abstract only**)

The vast majority of marine invertebrate skeletons are composed of the CaCO₃ polymorphs aragonite and calcite, yet the influence of seawater composition on the evolution of calcareous skeletal composition is poorly understood. Conventional thinking is that a threshold in the marine Mg:Ca ratio determines CaCO₃

polymorph formation with Phanerozoic Mg:Ca oscillations resulting in periods of "aragonite seas" or "calcite seas": the principal environmental context in which the evolution of biogenic CaCO₃ is assessed. I present data from CaCO₃ precipitation experiments to show that the concept of a distinct threshold is misleading because Mg:Ca ratio and temperature combined result in a Phanerozoic continuum of co-existing aragonite-calcite seas with aragonite-facilitating conditions existing throughout the Phanerozoic in shallow warm-water (> 20°C) environments. The comparison between Phanerozoic models of Mg:Ca (expressed as percent of non-biogenic aragonite) and the Phanerozoic occurrence of skeletal aragonite shows that the skeletal composition of reefs tracks the marine Mg:Ca ratio with a lag of tens of millions of years. This pattern cannot be explained by mass extinctions or changing skeletal mineralogy and thus points to a more complex influence of seawater composition on biocalcification than previously appreciated.

CALCIUM CARBONATE

1,561,384

CARBON ISOTOPE FRACTIONATION AND ITS TRACER SIGNIFICANCE TO CARBON SOURCE DURING PRECIPITATION OF CALCIUM CARBONATE IN THE PRESENCE OF *BACILLUS CEREUS* LV-1

L.Huang, F.Li, C.Ji, Y.Wang and G.Yang (Nanjing Agricultural Univ). *CHEMICAL GEOLOGY* v.609, 10/20/2022. (ISSN 0009-2541; Article no.121029)

Microbial-induced carbonate precipitation (MICP) has the potential to immobilize carbon durably. The carbon source of carbonate minerals is the crucial issue for understanding the fixation mechanism of CO₂ by MICP. However, the carbon source and its temporal changes in microbial-induced carbonate minerals remain little explored. In this study, calcium carbonate (CaCO₃) biomineralization experiments have been carried out using *Bacillus cereus* in the medium without additional dissolved inorganic carbon (DIC). X-ray diffraction (XRD), attenuated total reflection-infrared spectroscopy (ATR-IR) and scanning electron microscopy (SEM) indicated that the precipitate produced mainly consisted of rhombohedral and irregular calcite. The $\delta^{13}\text{C}$ values of DIC, dissolved organic carbon (DOC), and calcite were the main parameters studied. Carbon isotope fractionation was characterized by carbon isotope offset ($\Delta^{13}\text{C}_{\text{calcite-DIC}}$ or $\Delta^{13}\text{C}_{\text{calcite-fluid}}$). The $\Delta^{13}\text{C}_{\text{calcite-DIC}}$ values ranged from +8.2 per mill to +21.5 per mill, indicating that strain LV-1 induced the accumulation of ^{13}C in calcite. The $\Delta^{13}\text{C}_{\text{calcite-fluid}}$ values indicated that the calcite was up to +15.0 per mill (on average) ^{13}C -enriched relative to the fluid. Calculated chemical mass balance data showed that the proportion of CO₂(g) derived from DOC on days 16 and 20 was negative, but it became positive after day 20. Meanwhile, the $\delta^{13}\text{C}_{\text{CO}_2(\text{g})}$ value calculated by isotope mass balance was -8.5 per mill, near to $\delta^{13}\text{C}$ for air (-8.0 per mill) on day 16, and then shifted to -16.4 per mill, similar to $\delta^{13}\text{C}$ for tryptone (-17.2 per mill) after day 20. These results suggested that the amount of CO₂ arising from organic matter through bacterial respiration and the action of enzymes might determine whether the carbon in calcite was derived from organic carbon or atmospheric CO₂. Our findings corroborate the potential utility of MICP for immobilization of CO₂ to reduce net soil CO₂ emissions and to mitigate the greenhouse effect. Microbial-driven carbon isotope fractionation can also cause great carbon isotope shifts in calcite. Thus, carbon isotope value might be used as a marker to identify whether carbonate minerals/rocks are of microbial origin. (c2022 Elsevier B.V.)

CAUVERY BASIN

1,561,385

MAJOR, TRACE AND RARE EARTH ELEMENTAL GEOCHEMISTRY OF SANTONIAN-CAMPANIAN ONLAND-OFFSHORE TRANSITION IN A GILBERT-TYPE DELTAIC SETTING, CAUVERY BASIN, SOUTHERN INDIA

M.Ramkumar, A.Fathima, R.Nagarajan, M.Santosh and D.Menier (Periyar Univ; Curtin Univ; China Univ Geosci, Beijing; Bretagne Univ). *GEOLOGICAL JOURNAL* v.57, no.10, pp.3988-4010, Oct. 2022. (ISSN 0072-1050; ISSN 1099-1034)

The spatially widely distributed and temporally protracted Santonian–Campanian stratigraphic records of the Sillakkudi

Formation of the Ariyalur Group, Cauvery Basin, southern India represent an onland exposure of a Gilbert-type delta. Here, we present geochemical, mineralogical, and petrographic analyses of two composite stratigraphic sections, and evaluate the climatic, tectonic, and other factors that contributed to the spatio-temporal uniqueness of this formation. A range of low to intensive weathering, simultaneous exhumation/erosion, physical transport, and chemical weathering, prevalent at different parts of the source region and or the existence of multiple channels that drained varied source regions and hence varied lithologies at exhumation surfaces which in turn experienced seasonally varied flow conditions were interpreted. The prevalence of physical erosion during the initial stages of the deposition of the Sillakkudi Formation that progressed towards higher intensities of chemical weathering, in tune with the increase in atmospheric temperature and sea-level rise during the later stages of the formation, is evidenced. Occurrences of positive and negative Eu anomalies and a progression from active to passive tectonic setting of samples, concomitant with change from tectonic control to relative sea-level and the sediment influx controlled nature of deposition from Santonian–Campanian is recorded. Together, three sets of related factors namely, tectonics, increase of atmospheric temperature and sea-level rise operated independently, and the enforced transience of transformation of the source terrain from active to passive margin, the transformation of depositional setting from fluvial to estuarine/intertidal to open marine, and shifting of principal loci of deposition from onland to offshore, are documented. The causal link between the progressive increase of sea-level control over the depositional system during the Santonian–Campanian as recorded by this study could be due to the rise in atmospheric temperature that in turn might have been influenced by the movement of the Indian Plate from low latitudes towards the equatorial region. The second implication of the results is that the studies attempting to document tectonic setting, provenance, and weathering, with the help of geochemical discriminant diagrams, should also consider the spatial and temporal changes in the source area as well as depositional setting.

CHADAMU BASIN

1,561,386

COMPARING THE ADSORPTION OF CARBON DIOXIDE AND METHANE IN CARBONIFEROUS SHALE FROM THE QAIMAN BASIN, CHINA

B.Cao and Q.Yu (China Univ Geosci, Beijing). *APPLIED GEOCHEMISTRY* v.143, Aug. 2022. (ISSN 0883-2927; Article no.105368)

The differences in the adsorptions of methane and carbon dioxide are closely related to the geochemical properties and pore structure of shale, and this variability is of great significance for energy exploitation and environmental issues. In this study, the geochemical composition and nanopore distribution of four Carboniferous shale samples collected from different depths in the eastern Qaidam Basin, China, were analyzed. Isothermal adsorption experiments with CO₂ and CH₄ were carried out within a pressure range of 0-9 MPa at a temperature of 313.15 K. For the four samples, the amount of adsorbed CO₂ was 2-7 times higher than that of CH₄, indicating that CO₂ injection is promising for shale gas extraction in the Qaidam Basin. Based on the Langmuir model, a new parameter was introduced to represent the adsorption affinity of CO₂ relative to CH₄ of shale. This parameter is related to the Langmuir constant for shales. Its relationships with the organic matter content, mineral composition and pore structure are analyzed. The relative affinity parameter is useful for optimizing the pressure of CO₂ injection to enhance the extraction efficiency. (c2022 Elsevier Ltd.)

CLIPPERTON FRACTURE ZONAR

1,561,387

STUDY ON THE MECHANICAL PROPERTIES OF SILTY CLAY SEDIMENTS WITH NODULAR HYDRATE OCCURRENCE

C.Lu, P.Xie, H.Li, X.Zhang, X.Lu, B.Zhang, Z.Zhang, X.Qin, S.Zhang et al. (China Geological Survey). *JOURNAL OF MARINE SCIENCE AND ENGINEERING* v.10, no.8, Aug. 2022. (ISSN 2077-1312; Article no.1059)

Natural gas hydrates are a strategic energy resource in China. The China Geological Survey has discovered segregated hydrate mass formations under the seepage mechanism in the South China Sea through exploration, and gas hydrates occur in nodular, massive, and vein formations in silty clay sediment. Previous work has focused on the analysis of sediment mechanical properties with respect to the uniform distribution of natural gas hydrates in pore spaces, but the mechanical properties of hydrate-bearing sediments containing segregated hydrate masses are not well understood. Spherical hydrates are used to characterize nodular hydrates, a method is proposed for the preparation of sediment samples containing segregated hydrates masses, and a series of triaxial compression tests are carried out on the samples containing spherical hydrates with two kinds of particle sizes at a certain volume fraction. The paper presents triaxial stress-strain curves for the samples containing spherical hydrates. A model for predicting elastic modulus is established. The results present two distinct stages in the triaxial compression tests of silty clay sediments containing spherical hydrates; they also show that the elastic moduli predicted by the model are in good agreement with the experimental results when the model parameters are set at $\alpha = 0.5$ and $\beta = -0.21$. These results provide fundamental mechanical parameters for the safety evaluation of strata containing segregated gas hydrates.

CRETE

1,561,388

ORGANIC GEOCHEMICAL SIGNATURES OF THE UPPER MIOCENE (TORTONIAN-MESSINIAN) SEDIMENTARY SUCCESION ONSHORE CRETE ISLAND, GREECE: IMPLICATIONS FOR HYDROCARBON PROSPECTIVITY

A.G.Maravelis, G.Kontakiotis, S.Bellas, A.Antonarakou, C.Botziolis, H.T.Janjuhah, P.Makri, P.Moissette, J.J.Cornee et al. (Aristotle Univ). *JOURNAL OF MARINE SCIENCE AND ENGINEERING* v.10, no.9, Sept. 2022. (ISSN 2077-1312; Article no.1323)

The definition of pre-Messinian source rocks in the eastern Mediterranean is of paramount importance for hydrocarbon exploration because of the ability of salt to act as a high-quality seal rock. This research evaluates the organic geochemical features of the Upper Miocene (Tortonian-Messinian) sedimentary succession onshore Crete Island, Greece. The study employs original (Messinian, Agios Myron Fm) and published (Tortonian, Viannos Fm, Skinias Fm, Moulia Fm, and Messinian Ploutis section) results from organic geochemical analyses of mudstone samples. One hundred and one samples were examined using standard organic geochemistry methodology (Rock-Eval II and VI-TOC) to define the origin, type, and degree of organic matter maturity. The data indicate that the studied samples have poor to fair gas-prone source rock potential. These possible source rock units have not experienced great temperatures during burial, and, thus, their organic matter is thermally immature. The sub-salt (Tortonian-Messinian) source rock units are likely to be of higher thermal maturity in the western and eastern south Cretan trenches because of tectonic subsidence and a thicker sedimentary overburden. Several traps can grow in these regions, associated with normal faults, rotated blocks and unconformities (both below and above the unconformities). This research provides a basis for the further evaluation of the hydrocarbon potential in Crete Island. It is an area that shares geological similarities with the surrounding regions that contain proven reserves and is of crucial economic and strategic importance.

EUROPE

1,561,389

MIDDLE MIOCENE CLIMATE AND STABLE OXYGEN ISOTOPES IN EUROPE BASED ON NUMERICAL MODELING

S.Botsyun, T.A.Ehlers, A.Koptev, M.Boehme, K.Methner, C.Risi, C.Stepanek, S.G.Mutz, M.Werner et al. (Tuebingen Univ). *PALEOCEANOGRAPHY AND PALEOCLIMATOLOGY* v.37, no.10, Oct. 2022. (ISSN 2572-4525; Article no.e2021PA004442)

The Middle Miocene (15.99–11.65 Ma) of Europe witnessed major climatic, environmental, and vegetational change, yet we are lacking detailed reconstructions of Middle Miocene temperature

and precipitation patterns over Europe. Here, we use a high-resolution (ca 0.75°) isotope-enabled general circulation model (ECHAM5-wiso) with time-specific boundary conditions to investigate changes in temperature, precipitation, and $\delta^{18}O$ in precipitation ($\delta^{18}Op$). Experiments were designed with variable elevation configurations of the European Alps and different atmospheric CO₂ levels to examine the influence of Alpine elevation and global climate forcing on regional climate and $\delta^{18}Op$ patterns. Modeling results are in agreement with available paleobotanical temperature data and with low-resolution Middle Miocene experiments of the Miocene Model Intercomparison Project (MioMIP1). However, simulated precipitation rates are 300–500 mm/yr lower in the Middle Miocene than for pre-industrial times for central Europe. This result is consistent with precipitation estimates from herpetological fossil assemblages, but contradicts precipitation estimates from paleobotanical data. We attribute the Middle Miocene precipitation change in Europe to shifts in large-scale pressure patterns in the North Atlantic and over Europe and associated changes in wind direction and humidity. We suggest that global climate forcing contributed to a maximum $\delta^{18}Op$ change of ca 2‰ over high elevation (Alps) and ca 1‰ over low elevation regions. In contrast, we observe a maximum modeled $\delta^{18}Op$ decrease of 8‰ across the Alpine orogen due to Alpine topography. However, the elevation- $\delta^{18}Op$ lapse rate shallows in the Middle Miocene, leading to a possible underestimation of paleotopography when using present-day $\delta^{18}Op$ -elevation relationships data for stable isotope paleoaltimetry studies.

FUKUI PREFECTURE

1,561,390

MERCURY EVIDENCE FOR COMBUSTION OF ORGANIC-RICH SEDIMENTS DURING THE END-TRIASSIC CRISIS

J.Shen (China Univ Geosci, Wuhan). *21ST INTERNATIONAL SEDIMENTOLOGICAL CONGRESS [ISC] (Beijing, China, 8/22-26/2022) ABSTRACT BOOK* p.180, 2022. (Available at <http://www.isc2022.org.cn> as of 9/22/2022; **Abstract only**)

The sources of isotopically light carbon released during the end-Triassic mass extinction remain in debate. Here, we use mercury (Hg) concentrations and isotopes from a pelagic Triassic-Jurassic boundary section (Katsuyama, Japan) to track changes in Hg cycling. Because of its location in the central Panthalassa, far from terrigenous runoff, Hg enrichments at Katsuyama record atmospheric Hg deposition. These enrichments are characterized by negative mass independent fractionation (MIF) of odd Hg isotopes, providing evidence of their derivation from terrestrial organic-rich sediments ($\Delta^{199}Hg < 0‰$) rather than from deep-Earth volcanic gases ($\Delta^{199}Hg$ approximately 0‰). Our data thus provide evidence that combustion of sedimentary organic matter by igneous intrusions and/or wildfires played a significant role in the environmental perturbations accompanying the event. This process has a modern analog in anthropogenic combustion of fossil fuels from crustal reservoirs.

GAFSA BASIN

1,561,391

GEOCHEMICAL ANALYSES OF SEEP OILS IN THE SOUTHERN GAFSA BASIN, SW TUNISIA: REASSESSMENT OF REGIONAL HYDROCARBON POTENTIAL

K.Dadi, R.Ahmadi, A.B.Mohamed, C.Khalfi, N.Mbarki and J.A.Ouali (Sfax Nat Sch Engineering; Tunisian National Oil Co). *JOURNAL OF PETROLEUM GEOLOGY* v.45, no.4, pp.417-437, Oct. 2022. (ISSN 0141-6421; ISSN 1747-5457)

The recent discovery of surface oil seeps in the Tamerza area in the west-central Gafsa Basin (southern Tunisia) has prompted a re-evaluation of the hydrocarbon potential of the region. In this paper, we report the results of analyses of seep oils by Rock-Eval pyrolysis (n = 6) and gas chromatography – mass spectrometry (n = 4). The goals of the study were to assess the composition of the seep oils, to investigate the relationship between the seep oils and potential source rocks, and to highlight the significance of the seep oils for oil exploration in the region. In the Tamerza area, surface oil seeps have been recorded in numerous formations ranging between the Upper Cretaceous Abiod Limestone Formation and the lower Miocene Sehib Siltstone Formation. The results of this study showed that all the seep oil samples analysed in general had a

similar geochemical fingerprint: for example, Pr/Ph values are lower than 1; a plot of Pr/n-C17 (0.27- 0.36) versus Ph/n-C18 (0.3-0.8) indicates a marine source rock deposited under reducing anoxic conditions; and Ts/(Ts+Tm) ratios indicate that the source rock was thermally mature. Correlation studies suggest that the oils originated from Cenomanian-Turonian shales corresponding to the informally-named Bahloul equivalent formation. Oil expulsion from this source rock at the seep locations is inferred to have ended by middle Miocene time. However the main phase of folding occurred here in the Pliocene – early Quaternary, and the resulting anticlinal folds are not therefore prospective structural traps for hydrocarbons because they developed after migration had already ceased. Stratigraphic traps and salt structures in the region may be of greater exploration interest. A surface oil seep sample was also recovered from the Quaternary upper Segui Formation at Jebel Orbata in the east of the Gafsa Basin. Analysis of this oil sample showed that it has similar geochemical characteristics to the seep oils from the Tamerza area, but that it appears to have had a much more recent migration history. In the eastern Gafsa Basin, Pliocene – early Quaternary anticlinal structures could therefore constitute effective structural traps charged by the same Bahloul equivalent formation source rock.

.....
GUIZHOU **1,561,392**

ENVIRONMENTAL CO-EVOLUTION IN SOUTH CHINA DURING THE CRYOGENIC INTERGLACIAL: EVIDENCE FROM TRACE ELEMENT GEOCHEMISTRY

Y.Chuang and R.Yin (Chinese Academy Sciences). *21ST INTERNATIONAL SEDIMENTOLOGICAL CONGRESS [ISC] (Beijing, China, 8/22-26/2022) ABSTRACT BOOK* pp.216-217, 2022. (Available at <http://www.isc2022.org.cn> as of 9/22/2022; **Abstract only**)

Earth witnessed two global glaciation events (named Sturtian and Marinoan) during the Neoproterozoic Cryogenian. The Cryogenian interglaciation, occurring between these two glacial events, was a key period for the formation of manganese resources and polymetallic black shales in the world. However, the formation mechanism and environmental changes of this interglacial period remain poorly understood. This study investigates the elemental geochemistry of the Cryogenic glacial-interglacial sequence (Tieshiao and Datangpo Formations) in the Wuhe Section, Guizhou, SW China, and demonstrates that: (1) the Cryogenic interglaciation was driven by large volcanism, which not only directly released large amounts of volcanic components (e.g., Hg, V and Tl) into the ocean, but also triggered global warming, leading to enhanced continental chemical weathering and the input of terrigenous substances (e.g., Y, Nb, Ta, Zr and Hf) into the ocean. Volcanism and terrigenous weathering introduced abundant nutrients into the ocean, enhancing marine productivity and the oxygenation of surface seawater, leading to precipitation of Mn from seawater to cause large-scale manganese ore formation in this period; (2) Elements (e.g., In, Sn, Ag, Cu, Zn, Pb and Bi) enriched in submarine hydrothermal fluids show low anomalies during the Cryogenic interglaciation, suggesting that the Cryogenic interglaciation was not driven by submarine volcanism, but more likely by large-scale terrestrial volcanism. Results of this study reveal a close coupling of the evolution of the "ocean-atmosphere-land" system during the Cryogenic interglaciation.

.....
GULF COAST **1,561,393**

CLUMPED ISOTOPE ANALYSIS REVEALS AMMONITE PALAEOECOLOGY AND LATEST CRETACEOUS CLIMATE VARIABILITY IN THE US GULF COASTAL PLAIN

J.D.Witts, C.E.Myers, S.V.Petersen, J.Hoffmann, J.Naujokaityte, R.Rovelli, M.P.Garb, G.Phillips and N.H.Landman (Bristol Univ). *65TH ANNUAL PALAEOONTOLOGICAL ASSOCIATION MEETING (Manchester, UK, 12/18-20/2021) PROGRAMME AND ABSTRACTS* pp.99-100, 2021. (Available at <http://www.palass.org> as of 11/1/2022; **Abstract only**)

Geochemical records from well-preserved shell carbonates are used to reconstruct the palaeoecology and habitat of ammonoid cephalopods (ammonites) and the evolution of ancient marine ecosystems and climate. Carbonate clumped isotope ($\Delta 47$) analysis

is a promising tool that does not rely on assumptions of ancient seawater composition, which hamper "traditional" stable isotope studies. We present a multi-taxon dataset from the Maastrichtian Owl Creek Formation, Tippah County, Mississippi. This site contains an exceptionally preserved molluscan fauna constrained by macro- and microfossil biostratigraphy to the final approximately 300 kyr of the Cretaceous. Fossils of three ammonite genera, infaunal bivalves and rare nautilids were systematically collected and sampled throughout a nine-meter-thick section. Preservation was assessed using the SEM preservation index (PI). Clumped isotope palaeotemperatures and $\delta 18O$ seawater values reveal overlap in values and close agreement between all taxa. Ammonites and benthic bivalves thus secreted their shells in isotopic equilibrium with seawater of the same composition and probably lived in similar environments. We see no evidence that ammonites exhibit "vital effects" with respect to their clumped isotope composition. These data provide new constraints on the palaeoecology of extinct cephalopod taxa and marine climate evolution in the Gulf Coastal Plain immediately prior to the end-Cretaceous mass extinction.

.....
INDIA **1,561,394**

GLAUCONITE AUTHIGENESIS DURING THE WARM CLIMATIC EVENTS OF PALEOGENE: CASE STUDIES FROM SHALLOW MARINE SECTIONS OF WESTERN INDIA

T.Roy Choudhury and S.Banerjee (IIT Bombay). *21ST INTERNATIONAL SEDIMENTOLOGICAL CONGRESS [ISC] (Beijing, China, 8/22-26/2022) ABSTRACT BOOK* pp.175-176, 2022. (Available at <http://www.isc2022.org.cn> as of 9/22/2022; **Abstract only**)

This study explores authigenic mineralization associated with Paleogene warm climatic intervals within passive continental margin sediments in western India, represented by continental to marginal marine to shallow open marine sedimentary packages. These sedimentary packages are punctuated by -cm to -m thick glauconitic shale units, ubiquitous in transgressive shallow marine deposits of Cambay, Kutch, Jaisalmer, and Barmer basins. The Paleogene sediments, having extremely precise biostratigraphic age constraints, represents one of the warmest periods in the Cenozoic era. High-resolution biostratigraphic data, integrated with carbon isotope signatures, demarcate the Paleogene hyperthermal events and reveal an exceptionally high abundance of glauconite corresponding to the warming events. Although most of these glauconites are confined within the upper Paleocene-lower Eocene sediments, glauconite deposits also occur within the middle Eocene and upper Oligocene sediments. In all of these basins, glauconitic shales alternate with limestone/marl and/or grey shale unit representing an open shallow marine depositional setting. Green shale shows fine silt to fine sand-sized glauconite pellets, associated with glauconite infillings within the pores of bioclasts, randomly dispersed in a clayey matrix. The geochemical composition of glauconite varies widely, encompassing the entire maturity spectrum of glauconite minerals. The K₂O content of the glauconite pellets varies from 4 to 8 wt%, while the infillings variety is invariably poorer in K₂O. The glauconites within the upper Paleocene-lower Eocene sediments manifest high Al₂O₃ content (> 10 wt%) while the glauconites within the middle Eocene and lower Oligocene show considerably low Al₂O₃ (< 8 wt%). Despite the highly variable maturity and the Al₂O₃ content, these glauconites are rich in Fe₂O₃ (total), exceeding 20 wt% in most of the cases. The glauconitic shales show minor bioturbation and are rich in rectilinear benthic foraminifera, indicative of the oxygen-depleted bottom-water conditions. The unusual composition of upper Paleocene-lower Eocene glauconites relates to their formation within kaolinite substrates during the extremely warm climatic interval. Contrary to this, during the middle Eocene and Late Oligocene, the waning phase of Paleogene warm climatic conditions, glauconite formed by the initial authigenic precipitation of Fe-smectite/Fe-Al-smectite and its subsequent maturation. The warm climatic condition enhanced the precipitation and runoff, which supplied enhanced nutrients including K, Fe, Al, Si, and Mg into the shallow marine environment, facilitating prolific organic growth and enriching the seawater with cations. The decomposition of organic matter might have resulted in an oxygen-depleted

bottom water condition, which was suitable for the mobility and fixation of iron into the glauconite structure.

JIYANG DEPRESSION 1,561,395

PREDICTION METHOD OF TOTAL ORGANIC CARBON IN SHALE OIL RESERVOIR BASED ON PCA-CNN MODEL

Q.Guan (Shengli Oilfield Res Inst). *PETROLEUM GEOLOGY AND RECOVERY EFFICIENCY (YOUQI DIZHI YU CAISHOULU)* v.29, no.6, pp.49-57, Nov. 2022. (ISSN 1009-9603; In Chinese)
[Full article and English abstract available from P.A.]

KARNATAKA 1,561,396

BIO-GEOCHEMICAL AND DEPOSITIONAL FRAMEWORK OF SILICICLASTIC SEDIMENTS FROM AN OXYGENATED NEOPROTEROZOIC EPEIRIC SHELF UNDER WARM AND HUMID CLIMATE IN THE BACKDROP OF NEOPROTEROZOIC OXYGENATION EVENT (NOE)

A.Sen, S.Mukhopadhyay, P.Samanta, S.Ghosh and S.Bose (Jadavpur Univ; North Bengal Univ). *21ST INTERNATIONAL SEDIMENTOLOGICAL CONGRESS [ISC] (Beijing, China, 8/22-26/2022) ABSTRACT BOOK* pp.226-227, 2022. (Available at <http://www.isc2022.org.cn> as of 9/22/2022; **Abstract only**)

Major, trace and stable isotopic investigations have been carried out on siliciclastic fine-grained sediments of Cave-temple Arenite Member of Neoproterozoic Badami Group of Karnataka, southern India. U-Th-Pb isotopic constraints of overlying limestone units of Konkankoppa Member provided an apparent age of this Basin as 960 Ma (Joy et al., 2019). Age of mafic intrusive from underlying Mesoproterozoic sequence (Pillai et al., 2018) and recent works on tectono-sedimentological and paleogeographic models (Samanta et al., 2021) also suggest an age of 900-800 Ma for initial Badami sediments and correlate it to break-up of Rodinia Supercontinent. The whole succession of the studied Member is composed of three sedimentary cycles, where the middle cycle is a fluvio-marine one. State-of-the-art facies study and sequence stratigraphic analyses have been used to reconstruct the palaeogeographies of the studied marine succession. The sequence model reveals a marine siliciclastic deposition related to a shallow epeiric platform or seaway, where the marine inundation took place from the western margin of the Basin. Depositional environment varies from sand-dominated, shallow waters of upper-shore regimes to comparatively deeper waters of outer shelf, where sediments are muddy and rich in authigenic clays, like ferric-illite and glauconites. Major oxide composition of shales, siltstones and clay rich sandstones have been utilized to infer Chemical Index of Alteration (CIA) and probable climatic condition during marine transgression and regression. Where, the underlying fluvio-alluvial cycle was deposited in a semi-arid to semi-humid condition (Samanta et al., 2021), the studied marine sediments were deposited in a warm and humid climate that preferred pronounce chemical weathering. Biogenically induced trace metals and stable carbon isotopic values have been used to infer the palaeo-productivity of the marine water column. Bi-metal ratios and REE pattern reveal a redox stratification within the water column. Where, shallow marine sediments of inner shelf deposited in an oxic water column, deeper muddy sediments from offshore-transition and outer shelf deposited within suboxic to anoxic-euxinic waters. Shallow marine sandstones bear ample evidences of microbial proliferation, as MRS (Microbially Related Structures), within photic zone. $\delta^{13}\text{C}_{\text{org}}$ (VPDB) values also infer that shallow water was dominated with photo-autotrophs ($\delta^{13}\text{C}_{\text{org}}$ values between -22‰ to -25‰), where deeper water might have been a niche for anaerobic and sulphur reducing chemoautotrophs ($\delta^{13}\text{C}_{\text{org}}$ values < -25‰) (Kodina et al., 1996; Hayes et al., 1999). Presence of clustered framboidal pyrites within deeper most black shales from the outer shelf also supports this contention.

KOM OMBO BASIN 1,561,397

CHARACTERIZATION OF LOWER CRETACEOUS ORGANIC-RICH SHALES FROM THE KOM OMBO BASIN, EGYPT: IMPLICATIONS FOR CONVENTIONAL OIL

GENERATION

M.Hail Hakimi, N.M.Lotfy, M.M.El-Nady, W.A.Makled, F.S.Ramadan, A.Rahim, S.M.Talha Qadri, A.Lashin, A.E.Radwan et al. (Taiz Univ). *JOURNAL OF ASIAN EARTH SCIENCES* v.241, Jan. 2023. (ISSN 1367-9120; Article no.105459)

This study uses organic geochemical and petrographic analyses to characterise the organic-rich shales from the Lower Cretaceous Kom Ombo Formation in the Kom Ombo Basin. The overall results show that the Kom Ombo shales are considered to have good petroleum source rock potential with total organic carbon (TOC) content > 1 wt% and hydrocarbon yields of up to 27.62 mg hydrocarbons/g rock. Based on lipid biomarker ratios and carbon isotopes, the Kom Ombo shale contains a blend of organic matter derived primarily from algal marine and other aquatic organic matter, with some terrigenous land plants, deposited under anoxic conditions. These findings of organic matter (OM) input and depositional conditions are consistent with the high TOC content of up to 6.61 wt% and mainly Types II and II/III kerogen, with small amounts of Type III kerogen, thus yielding both oil and gas, with oils of high to low wax contents. Geochemically, the dominance of oil generation potential is in agreement with the presence of considerable concentration of fluorescent liptinite macerals. The chemical and optical maturity results show that the majority of the examined Kom Ombo shale samples have entered the main stage of oil generation, exhibiting a range of early-mature to late-mature. Therefore, as highlighted in this study, the oil generation potential of the Kom Ombo shales may represent a good opportunity for future conventional petroleum exploration. (c2022 Elsevier Ltd.)

MADISON GR 1,561,398

PRELIMINARY IDENTIFICATION AND EVALUATION OF PETROLEUM SOURCE BEDS WITHIN THE MISSISSIPPIAN MADISON GROUP: A STEP TOWARD REDEFINING THE MADISON PETROLEUM SYSTEM OF THE WILLISTON BASIN

T.O.Nesheim and C.J.Onwumelu (North Dakota Geol Survey; North Dakota Univ). *THE MOUNTAIN GEOLOGIST* v.59, no.4, pp.315-340, Oct. 2022. (ISSN 2327-2945)

The Mississippian Madison Group has been the most productive conventional oil play interval in the Williston Basin with more than 32,000 productive wells and 4.6 billion BOE of cumulative production to date. After 70+ years of exploration and development in the unit, the Madison could be considered a relatively "mature" hydrocarbon play interval. Initial geochemical fingerprinting studies beginning in the 1970s linked Madison reservoir oils to the underlying Bakken shale source beds. However, numerous ensuing geochemical fingerprinting studies with improved technology and techniques have concluded that most Madison reservoir oils are distinct from Bakken oils and therefore were internally sourced by undefined Madison source rock(s). Previously undocumented carbonate source rock intervals are observed in core and wireline logs within the upper Lodgepole-lower Tilston and lower Bluell stratigraphic section of the Madison Group. Both source rock intervals contain present day TOC values of 1% to ≥ 5%, plot along Type I/II (oil prone) kerogen signatures using hydrogen versus oxygen index values, reach 40+ feet (12+ m) gross thickness, extend laterally in the subsurface for at least tens of miles (1-2 million acres), and appear to be within the peak oil generation window (436-456° Tmax). Understanding the stratigraphic positions, lateral extents, and hydrocarbon generation significance of petroleum source beds may be the key to unlocking one or more unconventional Madison resource plays within the Williston Basin.

MASS MORTALITY 1,561,399

"DEATH METAL" IN THE EARLY PALAEOZOIC

T.R.A.Vandenbroucke, P.Emsbo and A.Munnecke (UMR-CNRS; US Geological Survey; Erlangen Nuernberg Univ). *58TH ANNUAL PALAEOONTOLOGICAL ASSOCIATION MEETING (Leeds, UK, 12/16-19/2014) ABSTRACTS* p.50, 2014. (Available at <http://www.palass.org> as of 11/15/2022; **Abstract only**)

Some, if not most, of the major Ordovician-Silurian extinction events coincided with glacial episodes. However, it has become

increasingly clear that cooling, itself, is not a viable kill-mechanism to explain these extinctions. Interestingly, these events are announced by the appearance of malformed organic-walled fossil zoo- and phytoplankton. New geochemical analyses (using ToF-SIMS and LA-ICP-MS) of these teratological microfossils and their host rocks, through a mid-Pridoli event, show a correlation between teratology and a dramatic increase in redox-sensitive metals. By analogy with metal-induced teratology in modern marine environments, our results suggest that these *in vivo* teratological reactions result from the pollution of the Silurian marine environment by toxic metals. These new data appear to link the initiation of the mass extinctions with the cycling of harmful redox-sensitive metals that are likely related to Ocean Anoxic Events (OAEs), rather than with climate change. Our work introduces metal-induced teratology as a potential independent proxy for monitoring palaeo-ocean geochemistry in deep time.

.....
MIOCENE **1,561,400**

THE LATE MIOCENE CARBON ISOTOPE SHIFT DRIVEN BY SYNERGETIC TERRESTRIAL PROCESSES: A BOX-MODEL STUDY

J.Du, J.Tian and W.Ma (Tongji Univ; Second Inst Oceanography). *21ST INTERNATIONAL SEDIMENTOLOGICAL CONGRESS [ISC] (Beijing, China, 8/22-26/2022) ABSTRACT BOOK* p.209, 2022. (Available at <http://www.isc2022.org.cn> as of 9/22/2022; **Abstract only**)

As the most significant carbon isotope excursion in the past 10 Ma, the Late Miocene Carbon Isotope Shift (LMCIS, 7.65 to 6.5 Ma) offers a great opportunity to investigate the carbon-climate dynamics in a warmer-than-today world. However, the driving mechanisms of the LMCIS remain controversial. In this study, we used a 7-box biogeochemical model to simulate the long-term seawater $\delta^{13}\text{C}$ and atmospheric CO_2 changes during the late Miocene. Based on the quantitative parameterization of two terrestrial processes (C4-grasses expansion and enhanced weathering input) during the late Miocene, our results show that the synergy between the two terrestrial processes may ultimately result in the LMCIS via the perturbation of the land-sea carbon fluxes. Moreover, our results reveal that the re-partitioning of alkalinity and nutrients between the land and the ocean may have influenced the long-term atmospheric CO_2 change during the late Miocene.

.....
NORTH ATLANTIC OCEAN **1,561,401**

LIP VOLCANISM (NOT ANOXIA) TRACKED BY Cr ISOTOPES DURING OCEAN ANOXIC EVENT 2 IN THE PROTO-NORTH ATLANTIC REGION

L.N.Yobo, C.Holmden, A.D.Brandon, K.V.Lau, J.S.Eldrett and S.Bergman (Texas A&M Univ; Saskatchewan Univ; Houston Univ; Pennsylvania State Univ). *GEOCHIMICA ET COSMOCHIMICA ACTA* v.332, pp.138-155, 9/1/2022. (ISSN 0016-7037)

Chromium is a redox sensitive element that exhibits a large range of isotopic compositions in Earth's surface environments because of Cr(VI)-Cr(III) transformations. This property of Cr has been exploited as a tracer of Earth's oxygenation history using marine sediments. However, paleoredox applications using Cr are difficult to implement due to its complicated cycling, which creates spatial variability in seawater $\delta^3\text{Cr}$ values. Applications are further hindered by the potential for variability in the major inputs of Cr, such as submarine volcanism, to mask redox processes. Two previous reports of negative excursions in sedimentary $\delta^3\text{Cr}$ values during the middle Cretaceous Ocean Anoxic Event 2 (OAE 2) demonstrate these complications. Observed negative shifts in marine sediments conflict with the positive shifts expected in response to the increased drawdown of isotopically light Cr(III) prompted by the expansion of anoxic depositional sinks. In this study, a marine carbonate succession cored from the Eagle Ford Formation in Texas, USA, in the southern part of the Western Interior Seaway, depicts the negative 1.5‰ $\delta^3\text{Cr}$ excursion occurring in two steps, with the second step reaching peak minimum values indistinguishable from isotopically unfractionated igneous sources. In contrast to published $\delta^3\text{Cr}$ records, each step stratigraphically matches proxy evidence for increased eruption

frequency and/or intensity of volcanic activity using combined $^{187}\text{Os}/^{188}\text{Os}$, $^{87}\text{Sr}/^{86}\text{Sr}$ and Os concentration proxies previously measured from the same core, supporting higher inputs of volcanically sourced Cr to the oceans as the driver for the negative Cr isotope excursion. (c2022 Elsevier Ltd.)

.....
NORTH CHINA PLATFORM **1,561,402**

COUPLED CONODONT (Δ) $^{18}\text{OPO}_4$ AND $^{87}\text{Sr}/^{86}\text{Sr}$ RECORDS INDICATE HYDROCLIMATE CHANGES IN NORTH CHINA AT THE PERMO-CARBONIFEROUS TRANSITION

Y.Wang and J.Yang (China Univ Geosci, Wuhan). *21ST INTERNATIONAL SEDIMENTOLOGICAL CONGRESS [ISC] (Beijing, China, 8/22-26/2022) ABSTRACT BOOK* p.214, 2022. (Available at <http://www.isc2022.org.cn> as of 9/22/2022; **Abstract only**)

The significance of chemical proxies from semi-restricted marine depositions are debated. Recent studies have shown decoupling of epicontinental isotopic records from open-marine ones and suggested superposition of regional hydro-climate factors, such as freshening, coastal upwelling, temperature, and salinity. We analyzed oxygen and strontium isotopes of conodont apatite (genera *Streptognathodus*) from Permo-Carboniferous epicontinental successions in southern North China and tested how the connection of epicontinental isotope variability in the sea to large-scale ocean-atmosphere processes. Average $\delta^{18}\text{O}$ values are around 16.7 per mill and decrease from 18.0 per mill to 16.2 per mill from the early Gzhelian to Asselian. These $\delta^{18}\text{OPO}_4$ values are consistently lower than that of contemporary open-marine successions. The strontium isotope ratios are between 0.70825 and 0.70948, with an average value of approximately 0.70858. The $^{87}\text{Sr}/^{86}\text{Sr}$ values are consistently higher than the corresponding open-marine records. Optical observations and trace element characters suggest no significant diagenetic influences on the analyzed conodont domains. It is therefore that the obtained $\delta^{18}\text{O}$ and $^{87}\text{Sr}/^{86}\text{Sr}$ values could reflect the oxygen and strontium isotopic features of the seawater from which these conodont apatites were precipitated. We hypothesized an extensive effects on the epicontinental sea waters from fluvial discharges which supply freshwater with low $\delta^{18}\text{O}$ and high $^{87}\text{Sr}/^{86}\text{Sr}$ due to the drainages in Proterozoic basements of North China. This study emphasized the linkage of hydroclimate conditions to the biogeochemical evolutions in epicontinental seas and highlighted the cautions to interpret chemical proxies from shallow marine records.

.....
ORDOS BASIN **1,561,403**

NITROGEN CYCLE PERTURBATIONS LINKED TO CHEMOCLINE COLLAPSE DURING THE JENKYN'S EVENT (EARLY TOARCIAN OAE)

B.Li, X.Jin, P.Qiao, Z.Shi and D.B.Kemp (Chengdu Univ Technology; Tongji Univ; China Univ Geosci, Wuhan). *21ST INTERNATIONAL SEDIMENTOLOGICAL CONGRESS [ISC] (Beijing, China, 8/22-26/2022) ABSTRACT BOOK* p.172, 2022. (Available at <http://www.isc2022.org.cn> as of 9/22/2022; **Abstract only**)

Marine nitrogen cycle perturbations during the Jenkyn's Event (Toarcian Oceanic Anoxic Event, ca 183 Ma) have been documented by nitrogen isotope ($\delta^{15}\text{N}$) signals. These signals emphasize the impact of seawater redox changes on the biogeochemical nitrogen cycle. However, to date there have been no studies on the lacustrine nitrogen cycle during the Jenkyn's Event. In this study, we report the first $\delta^{15}\text{N}_{\text{bulk}}$ data from the Anya section of the Ordos Basin, North China and establish a model of the lacustrine nitrogen cycle through the Jenkyn's Event. Based on the co-variation of $\delta^{15}\text{N}_{\text{bulk}}$ values with independent proxies for redox change (Corg/P ratios and $\delta^{34}\text{S}_{\text{py}}$) from this study and previous work, three phases of Anya deposition are identified: (1) Prior to, and during the early part of the Jenkyn's Event, a positive excursion in $\delta^{15}\text{N}_{\text{bulk}}$ values (approximately + 3.9 to + 7.4‰) across a black shale interval occurred. This positive excursion indicates that nitrogen loss (via partial denitrification and/or anammox) was dominant. (2) A negative excursion in $\delta^{15}\text{N}_{\text{bulk}}$ (approximately + 7.4 to + 2.5‰) correlates with a negative $\delta^{13}\text{C}_{\text{org}}$ excursion that demarcates the

main phase of the Jenkyns Event. This negative excursion can be attributed to the predominance of nitrogen fixation (nitrification and nitrate assimilation) within oxygen-rich water, where chemocline collapse promoted upwelling of ¹⁵N-enriched ammonium. However, ¹⁵N-enriched ammonium is more likely to be oxidized in oxygen-rich water and then incorporated into the pool of dissolved inorganic nitrogen (DIN). Additionally, an increased input of land plants (Type III kerogen) and a change in the hypolimnion's redox conditions (anoxic to dysoxic-oxic) suggest that chemocline collapse was most likely related to an enhanced hydrological cycle during the Jenkyns Event. (3) Following the chemocline collapse, a positive excursion in $\delta^{15}\text{N}_{\text{bulk}}$ (approximately + 2.5 to + 6.4‰) occurs in the later Jenkyns Event and its recovery phase, implying that nitrogen loss was once again prevalent. However, a dysoxic-oxic hypolimnion may have been formed as a result of lake level falls during lake regression, which may explain the subsequent stabilization of $\delta^{15}\text{N}_{\text{bulk}}$. This study suggests that chemocline collapse may play a significant role in the biogeochemical nitrogen cycle in lacustrine systems, and contributes to our understanding of the terrestrial response to the Jenkyns Event.

PALEOCENE 1,561,404

TOWARDS A CONSISTENT EXTRATERRESTRIAL 3He CHRONOLOGY OF THE PALEOCENE-EOCENE THERMAL MAXIMUM

G.Suan, N.Pige, P.H.Blard, K.A.Farley and E.Mattioli (Lyon I Univ; Lorraine Univ; California Inst Technol). *21ST INTERNATIONAL SEDIMENTOLOGICAL CONGRESS [ISC] (Beijing, China, 8/22-26/2022) ABSTRACT BOOK* p.191, 2022. (Available at <http://www.isc2022.org.cn> as of 9/22/2022; **Abstract only**)

The Paleocene-Eocene Thermal Maximum (PETM) was one of the most severe episodes of rapid greenhouse warming of the geological past. Identifying the key drivers of the carbon cycle across the PETM requires an accurate, highly resolved chronology of the event and its characteristic phases. The duration of these various phases estimated by cyclostratigraphic and extraterrestrial extraterrestrial ³He (³HeET) methods, however, vary greatly, hindering a detailed understanding of the impact of rapid warming on Earth System dynamics. To reconstruct sedimentation rates across the PETM, we present new high-resolution ³HeET contents measured at CRPG and Caltech of nanofossil ooze spanning the Paleocene-Eocene boundary at ODP Site 1209 (North Pacific). The measured ³He/⁴He ratios approach those measured in modern interplanetary dust particles and show that > 99.9% of sedimentary ³He is of extraterrestrial source. Cycle-based age models imply ³HeET fluxes of 0.31 ± 0.02 pcc/cm²/ka before and after the PETM, supporting the hypothesis of a constant flux across the event. Assuming this flux remained constant through the PETM, our ³HeET-based sedimentation rates reveal an episode of extreme condensation across the PETM onset and indicate that the interval of anomalously ¹³C-depleted values (body/core) lasted approximately 185 ka. The termination of the PETM core coincided with a surprisingly fast (< 30 ka) increase of carbonate fluxes, which remained elevated for approximately 80 ka, in line with other oceanic records. Based on these results and a comprehensive reassessment of previous ³HeET and cyclostratigraphic records, we construct an integrated and globally consistent age model for the PETM in continental, shallow marine, and deep-sea settings. The implications of the new chronology for the causes and consequences of the PETM will be discussed.

POLAND 1,561,405

A BIOTIC CRISIS DRIVEN BY AN ABRUPT SHIFT TO WELL OXYGENATED OLIGOTROPHIC CONDITIONS AND A COLLAPSE OF PRIMARY PRODUCTIVITY IN THE EPICONTINENTAL SEA ECOSYSTEMS DURING THE CTBE

M.Bojanowski, Z.Dubicka, D.Peryt and M.Barski (Polish Academy Sciences; Warsaw Univ). *21ST INTERNATIONAL SEDIMENTOLOGICAL CONGRESS [ISC] (Beijing, China, 8/22-26/2022) ABSTRACT BOOK* p.198, 2022. (Available at <http://www.isc2022.org.cn> as of 9/22/2022; **Abstract only**)

The Cenomanian-Turonian Boundary Event (CTBE), also

referred to as the Oceanic Anoxic Event 2 (OAE-2), was investigated in a section representing the shallow epicontinental sea of the Central European Basin in Poland. This event was one of the strongest biotic crises of the Mesozoic, which impoverished marine biota, benthic foraminifera in particular. The crisis is expressed in the section examined by significant changes in foraminiferal and organic dinoflagellate assemblages, which indicate a switch to highly oligotrophic conditions associated with a collapse of primary production concomitant with the onset of the OAE-2. This switch correlated with a significant shift in N isotope signature in bulk organic matter, which we analyzed in detail. Yet, despite these biotic and isotopic changes, lithology and depositional conditions remained unchanged throughout the event, which suggests an environmental control on these variations. Expansion of anoxic conditions in the basinal settings is accompanied by a sudden decrease of $\delta^{15}\text{N}_{\text{org}}$ values (< -2‰) and high organic primary productivity during the OAE-2. These depleted $\delta^{15}\text{N}_{\text{org}}$ values are thought to be chiefly driven by the assimilation of recycled ammonium, not nitrate, by primary producers, which was delivered to the photic zone from anoxic bottom waters. High production rate of this ¹⁵N-depleted biomass boosted by denitrification and anammox in such "ammonium ocean" caused the residual ¹⁵N enrichment in the remaining fixed N pool in the surface layer. Unlike the basinal settings, we observe a drastic increase of $\delta^{15}\text{N}_{\text{org}}$ values to > +5‰ in the epicontinental setting examined during the OAE-2, which indicates that productivity was dominated by nitrate (and nitrite) and that the ammonium from the ocean did not reach the epicontinental setting. Instead, we propose that the shallow oceanic waters, with strongly ¹⁵N-enriched nitrate spread laterally onto epicontinental settings. Yet, our micropaleontological data show that fully oxic and low-productivity conditions occurred at that time in the area, so at such low level of bioavailable N, the additional delivery of strongly ¹⁵N-enriched nitrate was able to increase the overall $\delta^{15}\text{N}$ of organic matter deposited in the epicontinental basin. Our integrated foraminiferal and dinoflagellate cyst study, supplied with N isotopic data, indicate that the biota were impacted by an abrupt shift to well oxygenated oligotrophic conditions and a collapse of primary productivity in the epicontinental Central European Basin. Because the event was concurrent with the development of extensive and extreme oceanic bottom water anoxia that reached the photic zone in oceanic settings, we infer that the biotic crisis in the shelf seas during the OAE-2, and possibly during other OAEs, was triggered by this anomalous nutrient cycling in Earth's oceans.

SARDINIA 1,561,406

MAPPING MINERALOGICAL HETEROGENEITIES AT THE NM-SCALE BY SCANNING ELECTRON MICROSCOPY IN MODERN SARDINIAN STROMATOLITES: DECIPHERING THE ORIGIN OF THEIR LAMINATIONS

J.Debrie, D.Pret, N.Menguy, I.Esteve, P.Sans-Jofre, J.P.Saint Martin and K.Benzerara (Paris-Sorbonne Univ; Poitiers Univ). *CHEMICAL GEOLOGY* v.609, 10/20/2022. (ISSN 0009-2541; Article no.121059)

Stromatolites are found throughout the geological record and have received strong attention because they provide precious information about paleoenvironments and microbial paleobiodiversity. However, while this information is interpreted based on our knowledge about modern analogs, the latter remains incomplete. Here, we investigated the environmental and biological information recorded by modern stromatolites in Mari Ermi, a coastal pond in Western Sardinia that experiences severe seasonal evaporation and large salinity variations. For this purpose, we combined a variety of analytical tools, allowing to characterize the mineralogical composition of these stromatolites from the bulk, centimeter-scale to the nanometer-scale and assess the spatial distribution of the mineral phases. In particular, we used quantified x-ray elemental maps provided by energy dispersive x-ray spectrometry analyses coupled with scanning electron microscopy (SEM-EDXS). These maps were processed using an innovative data treatment allowing (i) mineral phase recognition, (ii) assessment of the mineral formula of each phase and (iii) mapping of their spatial distribution with a spatial resolution down to a hundred nanometers. Overall, this proved as an efficient approach to

unravel mineralogical heterogeneities and detect informative mineral phases overlooked by bulk analyses. Mari Ermi stromatolites were mostly composed of magnesian calcite with an average Mg/Ca of 0.1-0.2 as indicated by bulk analyses. However, microscopy observations revealed variable Mg-contents of calcite with a specific distribution, the most Mg-enriched calcites (Mg/Ca up to 0.5) being systematically distributed around microbial remnants. Moreover, Mari Ermi stromatolites comprised an alternation of Mg-richer and Mg-poorer laminae, which paralleled the varying enrichment in microbial remnants of alternating laminae. The combination of SEM-EDXS, focused ion beam milling and transmission electron microscopy allowed to detect several minor phases, hardly or not detected at all by bulk analyses, such as aragonite, a variety of clay minerals as well as a gypsum-like phase. An additional calcium sulfate phase, best interpreted as S-apatite (cesanite), was detected by SEM-EDXS. Overall, this mineral assemblage and its definite spatial distribution record only discrete stages of the evaporation of Mari Ermi lagoon. Moreover, microorganisms seem to have a major control on Mg substitution in calcite. As a result, the dynamics of microbial populations, influenced by the salinity variations induced by evaporation in the lagoons, generates the formation of laminae in Mari Ermi stromatolites. (c2022 Elsevier B.V.)

SHANDONG

1,561,407

GEOCHEMICAL ANALYSIS OF SEDIMENTARY ENVIRONMENT OF LAIYANG GROUP IN TAOLIN AREA, RIQINGWEI BASIN

B.Bai, Y.Zhou and H.Xu (China Univ Petroleum; Kunming Prosp Design Inst). 21ST INTERNATIONAL SEDIMENTOLOGICAL CONGRESS [ISC] (Beijing, China, 8/22-26/2022) ABSTRACT BOOK p.225, 2022. (Available at <http://www.isc2022.org.cn> as of 9/22/2022; Abstract only)

The Early Cretaceous marine sedimentary strata in the coastal area of eastern Shandong Province are scattered among rift continental basins. The study shows that a large-scale NE-trending rift basin, named the Riqingwei Basin, was during the Late Mesozoic. However, the sedimentary environment of the basin is still controversial. In this study, 14 siliceous sandstone samples from the Early Cretaceous Laiyang Group in the Taolin section of the Riqingwei Basin were taken as the research objects, and the evolution of sedimentary paleoenvironment was studied by petrology and elemental geochemistry. The geochemical indicators of the samples constrain the paleoenvironmental characteristics. (1) The CIA value of 70% of the samples CIA = 50-60, reflecting the weak chemical weathering conditions and stable tectonic background in the source area. The PIA value of the sample PIA = 36-74, which was lower than that of PAAS, indicating that the weathering degree of the source area was low. The SiO₂/Al₂O₃ ratio in the study sample fluctuated between 2.84 and 4.11, indicating that the source composition was immature. (2) According to (Fe + Mn)/Ti and MnO/TiO₂ values, The Laiyang period in the study area was formed in the marginal sea environment and some strata were affected by hot water. (3) The Sr/Cu values of the studied samples were greater than 5 and the C values of 70% of the samples were approximately 0.3-0.6; at the same time, the ancient water temperature calculation shows that the max sedimentary temperature of Laiyang period is 28.4°C, which generally reflects the climatic conditions of hot and drought. (4) The V/(V + Ni) values of the studied samples were greater than 0.46, and the Ceanom values (Ceanom = approximately -0.032-0.056), indicating that the sedimentary environment was in anoxic condition. (5) The 100MgO/Al₂O₃ values of the studied samples are greater than 10, CaO/(Fe + CaO) values are 0.10 to approximately 0.54, Sr/Ba values are 0.14 to approximately 0.67, indicating that the sedimentary environment is a marine environment with low to medium salinity. (6) The MnO/Fe value of the samples in the study area are 0.005 to approximately 0.015, indicating the acidic or weak acidic sedimentary water conditions. The ΣREE of the samples is high, the REE distribution curve is gentle weak right-leaning type, the difference of light and heavy rare earth elements is not obvious, and there are Eu positive anomalies and Ce weak positive anomalies. The value of LREE/HREE (10.2-11.97), and the La/Ce ratio of some samples is less than 1.

SULFUR ISOTOPE RATIO

1,561,408

SULFUR MASS-INDEPENDENT FRACTIONATION DURING SO₂ PHOTOLYSIS IN LOW-TEMPERATURE/PRESSURE ATMOSPHERES

Y.Endo, Y.Sekine and Y.Ueno (Tokyo Inst Technol). *CHEMICAL GEOLOGY* v.609, 10/20/2022. (ISSN 0009-2541; Article no.121064)

Mass-independent fractionation of sulfur isotopes (MIF-S) has been observed in Archean sedimentary rocks and modern stratospheric sulfate aerosol (SSA). Photolysis of SO₂ is known to cause significant MIF-S and could be related to the observed MIF-S. However, previous experiments with SO₂ photolysis at room temperature, or at low temperatures and atmospheric pressure, did not quantitatively explain quadruple sulfur isotopic compositions ($\delta^{34}\text{S}$, $\Delta^{33}\text{S}$, and $\Delta^{36}\text{S}$ values) of the Archean sedimentary rocks and the modern SSA. Here we describe sulfur isotopic fractionation during SO₂ photolysis including isotopic self-shielding at low temperatures (down to 228 K) and low pressures (from 5.9 to 9.8 kPa) where pressure broadening of SO₂ becomes negligible. Results indicate that magnitudes of sulfur isotopic fractionation factors (34ϵ , 33ϵ , and 36ϵ values, where $33\epsilon = 33\epsilon - 1000 \times [(1 + 34\epsilon/1000)0.515 - 1]$ and $36\epsilon = 36\epsilon - 1000 \times [(1 + 36\epsilon/1000)1.90 - 1]$) increase with decreasing temperature, with values at 228 K being about four times those at 296 K (34ϵ of up to +344 0/00). Meanwhile, $33\epsilon/34\epsilon$ and $36\epsilon/33\epsilon$ ratios are roughly independent of temperature over the temperature range (by approximately +0.1 and - 3.1, respectively), although the $33\epsilon/34\epsilon$ ratios slightly increase with decreasing temperature, ranging from + 0.08 to + 0.13. A two-component mixing model involving SO₂ oxidation by OH and SO₂ photolysis in the stratosphere reproduces $\delta^{34}\text{S}$ and $\Delta^{33}\text{S}$ values of modern SSA when the contribution ratio of SO₂ photolysis to SO₃ production is 20%. The contribution ratio of 20% is consistent with a previous estimation by Whitehill et al. (2015). However, $\Delta^{33}\text{S}/\delta^{34}\text{S}$ ratios at low temperatures are far from those of Archean sedimentary rocks, calling for an additional mechanism (or mechanisms) to explain Archean MIF-S. (c2022 Elsevier B.V.)

TALIMU BASIN

1,561,409

UPPER EDIACARAN FIBROUS DOLOMITE VERSUS ORDOVICIAN FIBROUS CALCITE CEMENT: ORIGIN AND SIGNIFICANCE AS A PALEOENVIRONMENTAL ARCHIVE

Y.Hu, C.Cai, Y.Li, R.Zhou, F.Lu, J.Hu, C.Ren, L.Jia, Y.Zhou and K.Lippert. *CHEMICAL GEOLOGY* v.609, 10/20/2022. (ISSN 0009-2541; Article no.121065)

Fibrous carbonate cement is a common phase in marine phreatic environments - but its origin and diagenetic history are underexplored. This paper compares two fibrous fabrics that are different in terms of their peculiarities but share important similarities regarding their essentials: upper Ediacaran fibrous dolomite cement and Upper Ordovician fibrous calcite cement, both from the Tarim Basin, China. The focus is on the significance of these fabrics as archives of their marine paleoenvironment. Upper Ediacaran fibrous dolomite cement is present as (i) a fascicular-optic and (ii) a radial-fibrous phase. Judging from the optical length-slow character and luminescent zones, radial-fibrous dolomite cement precipitated directly from early diagenetic marine porewater. Fascicular-optic dolomite cement has a length fast optical character and hence likely formed as a high-Mg calcite precursor penecontemporaneously in a reefal, shallow-marine diagenetic environment. Similarly, two types of Upper Ordovician fibrous cement are present: (i) radiaxial-fibrous and (ii) fascicular-optic calcite cement. Fascicular-optic calcite precipitated in a marine phreatic platform environment, whereas radiaxial-fibrous calcite cement formed in an early marine diagenetic porewater environment. Both fabrics arguably replace a magnesium calcite precursor. For the case of the Tarim Basin, cathodoluminescence and redox-sensitive elements indicate predominantly anoxic, upper Ediacaran marine waters (Ce anomaly = 0.8 ± 0.2), and suboxic, Upper Ordovician shallow-marine seawater (0.7 ± 0.2). Based on PHREEQC modeling, the shallow burial, upper Ediacaran porewater (5.1) yields a higher dolomite saturation index than upper Ediacaran (4.8) and Upper Ordovician seawater (3.7). The direct precipitation of radial-fibrous dolomite from Ediacaran porewaters was likely induced due to organic matter decomposition

and related seawater oxygen depletion, elevated Mg²⁺/Ca²⁺ ratios, and high alkalinity values. Modeling and proxy data show significant hydrogeochemical differences between seawater and porewater in the upper meters of the sediment column. The upper Ediacaran seawater apparently favored fibrous cement formation with magnesium calcite precursors. In contrast, fibrous dolomite cement was directly precipitated in an early-diagenetic marine porewater regime. The comparability of proxy data reflecting seawater and such recording early diagenetic marine porewater is critically discussed. (c2022 Elsevier B.V.)

TALIMU BASIN 1,561,410

BIOGEOCHEMICAL RESPONSES TO GLOBAL WARMING DURING THE PALEOCENE-EOCENE THERMAL MAXIMUM IN THE EASTERN TETHYS

Q.Wu and Y.Cui (Montclair State Univ). *21ST INTERNATIONAL SEDIMENTOLOGICAL CONGRESS [ISC] (Beijing, China, 8/22-26/2022) ABSTRACT BOOK* p.183, 2022. (Available at <http://www.isc2022.org.cn> as of 9/22/2022; **Abstract only**)

The Paleocene-Eocene Thermal Maximum (PETM; 56 Ma) represents a rapid and sustained climate perturbation event that coincides with the emplacement of the North Atlantic Igneous Province (NAIP). Although proxies for chemical weathering, biological productivity, and oceanic deoxygenation are commonly used in the deep oceans, the role of the eastern Tethys, a subtropical shallow marine environment, in regulating the carbon cycle dynamics and climate feedbacks is poorly understood. Here we present geochemical data from the Tarim Basin, northwestern China to assess the environmental responses of the eastern Tethys to the PETM. An increase in chemical weathering proxies (chemical index of alteration, chemical index of weathering, modified chemical index of alteration, and plagioclase index of alteration) indicates enhanced terrestrial input shortly after the PETM onset, possibly due to an intensified chemical and physical weathering. The PETM onset is also characterized by an increase in Mo and V concentrations, indicating an expansion of oceanic anoxia. At the same time, primary productivity appears to increase abruptly, presumably due to an increased riverine flux of nutrients (N, Fe, and P) that stimulated marine productivity. The ecosystem stress imposed by elevated nutrient fluxes and anoxia expansion is likely amplified by simultaneously intensified chemical and physical weathering, highlighting the importance of integrating geochemical proxies in tracking the environmental responses to climate changes.

UNCONVENTIONAL GAS RECOVERY 1,561,411

PERFORMANCE AND MECHANISM OF THE PYRITE-KEROGEN COMPLEXES OXIDATION WITH H₂O₂ AT LOW TEMPERATURE DURING SHALE STIMULATION: AN EXPERIMENTAL AND MODELING STUDY

D.Liu, M.Yi, S.Yang, F.Liu and Y.Li (China Univ Geosci, Wuhan). *APPLIED GEOCHEMISTRY* v.143, Aug. 2022. (ISSN 0883-2927; Article no.105382)

Pyrite and organic matter (OM) play important role during rock chemical weathering and shale gas exploitation, the oxidation of which by O₂ is widely recognized. But the performance and mechanism of pyrite and kerogen oxidizing with H₂O₂ during shale gas production are not well understood, and the impact of carbonates and clays on the oxidation process is still not known. In this study, the performance of the gas bearing carbonate-rich shale oxidation with 15 wt% H₂O₂ at low temperature was firstly explored. The total oxidation-dissolution capacity of the studied shale with H₂O₂ at room temperature was less than 5%, which is significantly poorer than shale richness in silicates. To unravel the underlying mechanisms leading to the divergent oxidation dissolution of shale with different compositions, pyrite-kerogen complexes were isolated from shale and batch experiments between individual key components including pyrite/kerogen/carbonates/clays and H₂O₂ were performed. On the basis of mechanistic understanding, kinetic models of the pure components reaction with H₂O₂ were also developed. Results show that pyrite is preferentially oxidized by H₂O₂ when compared to

kerogen, and possesses a reaction rate 1-3 orders of magnitude larger than kerogen at different pyrite/kerogen mass ratio. Pyrite can induce the Fenton-like reactions to promote kerogen oxidation. The contribution of hydroxyl radicals on the oxidation of kerogen was about 22% for pyrite-kerogen complex with a pyrite/kerogen mass ratio of 1.65. Existence of calcite can buffer the solution pH to a circumneutral condition and induce the precipitation of Fe(III)-(oxy)hydroxides and anhydrite on the surface of the pyrite-kerogen complexes, thus to limit the generation of hydroxyl radicals and encapsulate the pyrite-kerogen complex, so as to inhibit the oxidation of these reduced components. This finding presents new insight into the mechanisms of H₂O₂-based oxidation stimulation of shale and provides guidance for the optimization of fracturing recipe. (c2022 Elsevier Ltd.)

YANGTZE PLATFORM 1,561,412

ISOTOPIC AND ELEMENTAL CHARACTERISTICS OF THE EDIACARAN DOUSHANTUO FORMATION, SOUTH CHINA: NEW INSIGHTS FOR GREAT OXYGENATION EVENTS

Y.Li, T.Zhang and T.Fan (China Univ Geosci, Beijing). *21ST INTERNATIONAL SEDIMENTOLOGICAL CONGRESS [ISC] (Beijing, China, 8/22-26/2022) ABSTRACT BOOK* p.213, 2022. (Available at <http://www.isc2022.org.cn> as of 9/22/2022; **Abstract only**)

The Ediacaran Period (635-542 Ma), a critical period throughout Earth history, witnessed major marine carbon cycle perturbations, great oxygenation events, biological systems innovations, and regional Ediacaran glaciation events. However, the origin of these negative carbon isotope anomalies and great oxygenation events remain highly debated. Here, we present high-resolution carbon and strontium isotope, and elemental records of drill core samples from the Ediacaran Doushantuo Formation, Yichang City, Hubei Province, South China. The $\delta^{13}C$ profiles display five negative carbon isotope excursions (EN1, EN1-1, EN1-2, EN2 and EN3), which consist of three major negative excursions (EN1, EN2 and EN3) and two minor, local negative excursions (EN1-1 and EN1-2). Both EN2 and EN3 excursions display highly basin-scale spatial heterogeneity along the shelf-to-basin transect across the Yangtze Platform. Overall, Doushantuo Formation $\delta^{13}C_{carb}$ values in deeper intrashelf basin sections are ca. 3-5‰ lower than those in the shallower intrashelf basin, shelf margin and upper slope sections, and are ca. 5-10‰ lower than those in the inner shelf sections, respectively. High spatial heterogeneity in the magnitude and timing of EN2 and EN3 excursion across the proximal to distal transect reflects dynamic oxidation in the surface ocean between elevated oxidant availability with limited spatiotemporal distribution and reduced carbon from the subsurface dissolved organic carbon (DOC) pool. Elevated oxidant availability during the EN2 and EN3 is primarily associated with the long-term late Neoproterozoic oxidation event combined with enhanced continental weathering. Doushantuo Formation 87Sr/86Sr records exhibit two significantly positive 87Sr/86Sr excursions (P1 and P2), roughly coinciding with the EN2 and EN3 excursions. Elevated 87Sr/86Sr ratios during the P1 and P2 events are likely linked to the overall rise in continental weathering rates during the assembly of Gondwana at ca. 0.6-0.5 Ga. Additionally, redox-sensitive trace elements (Mo, U and V) also display significantly enrichments within EN2 and EN3 excursions, which indicates oceanic oxygenation events. A compilation of $\delta^{13}C$, 87Sr/86Sr, and redox-sensitive trace elements record during the Ediacaran suggests that increasing continental weathering provokes oceanic oxygenation that leading to negative carbon isotope anomalies.

YANGTZE PLATFORM 1,561,413

GEOCHEMICAL CHARACTERISTICS OF EARLY CAMBRIAN ELEMENTS AND THEIR PALEOENVIRONMENTAL SIGNIFICANCE IN THE WESTERN MARGIN OF THE UPPER YANGTZE RIVER

W.Chen and J.Tian (Chengdu Univ Technology). *21ST INTERNATIONAL SEDIMENTOLOGICAL CONGRESS [ISC] (Beijing, China, 8/22-26/2022) ABSTRACT BOOK* p.224, 2022. (Available at <http://www.isc2022.org.cn> as of 9/22/2022; **Abstract**)

only)

The petrology and element geochemistry of well JS1 in the Early Cambrian Maidiping-Qiongzhusi Formation in the western margin of the upper Yangtze are studied, and the characteristics of elemental geochemistry and sedimentary environment of Maidiping-Qiongzhusi Formation were discussed, so as to provide a theoretical basis for determining the paleoenvironmental evolution of Maidiping-Qiongzhusi Formation and shale gas exploration evaluation. The comprehensive analysis of geochemical characteristic parameters such as organic carbon, whole rock host, trace and rare earth elements shows that the characteristic parameters such as $Al_2O_3/(Al_2O_3 + Fe_2O_3)$, MnO/TiO_2 , Zn-Ni-Co, U-Th and Y/Ho of Maidiping-Qiongzhusi Formation in JS1 well area indicate that it belongs to the continental margin sedimentary environment affected by terrigenous debris, and the parent source mainly comes from the mixing of sedimentary rocks and granite. The results show that light rare earth elements (LREE) is enriched relative to heavy rare earth elements (HREE) in Maidiping Formation (La:Yb) $N = 6.05$, slightly to the right, and the average δEu is slightly less than 1, indicating normal seawater deposition, shallow water, and not significantly affected by hydrothermal action. The Qiongzhusi Formation has obvious light rare earth elements differentiation (La:Yb) $N = 7.69$, LREE enrichment, HREE depletion, and obvious right dip, with weak negative δCe and δEu anomalies, and transient or intermittent hydrothermal activity disturbance. The comparison of δCe anomaly characteristics ($\delta Ce = 0.36$) and regional geochemical parameters shows that the water body of Maidiping Formation is dominated by oxidation conditions, and the sedimentary evolution process is tidal flat facies and shelf facies regionally, while the sedimentary environment of Qiongzhusi Formation is shallow water and deep water shelf facies of reduction-weak oxidation-weak reduction environment.

YINGGEHAI BASIN**1,561,414****PALAEOVEGETATION AND PALAEOCLIMATE EVOLUTION IN THE LATE OLIGOCENE-EARLY PLIOCENE SHALES IN THE YING-QIONG BASIN, SOUTH CHINA SEA**

W.Ding, Y.Gao, D.Hou and S.C.George (CNOOC Research Inst; China Univ Geosci, Beijing; Macquarie Univ). *21ST INTERNATIONAL SEDIMENTOLOGICAL CONGRESS [ISC] (Beijing, China, 8/22-26/2022) ABSTRACT BOOK* pp.219-220, 2022. (Available at <http://www.isc2022.org.cn> as of 9/22/2022; **Abstract only**)

The sedimentary rocks of the Yinggehai-Qiongdongnan Basin in the northern South China Sea preserve important records of the complicated interactions between terrigenous sediments and the East Asian monsoon climate. It remains obscure how higher plant-derived biomarkers and the inferred floral changes respond to the East Asian monsoon climate in the South China Sea. The late Oligocene-early Pliocene palaeovegetation and palaeoclimate in the Ying-Qiong Basin, South China Sea were comprehensively reconstructed using higher plant-derived biomarkers, palynological records, kerogen maceral compositions, and trace elements of shales. During the period from about 24.9-18.3 Ma, there are trends of higher relative abundances of plant-derived biomarkers including oleanane, des-A-oleanane, rearranged oleananes, taraxastane, bicadinanes, high molecular weight n-alkanes ($C_n \geq 27$), C19 tricyclic terpane, and C29 $\alpha\alpha\alpha$ 20R sterane in the younger sediments. Similarly, over this period, there are records of increasing amounts of tropical/subtropical angiosperms and pteridophytes in the younger sediments, and lesser amounts of temperate *Pinus* and *Alnus* species. The bloom of the dominant tropical-subtropical higher plants and the large influx of terrigenous organic matter during this period were likely associated with extra precipitation under a warming climate. This warming and more humid climate is related to the establishment of the East Asian monsoon in the South China Sea at about 24.9 Ma in the late Oligocene, which was likely caused by uplift of the northern Himalaya-Tibetan Plateau. During the period from about 8.2-2.7 Ma (corresponding to the deposition of the upper Huangliu Formation to the lower Yinggehai Formation), there was a remarkable decline of inferred higher plant inputs and vitrinite

proportion in the kerogen. The temperate species *Pinus* and *Alnus* became more dominant, and ferns became less abundant in the lower Yinggehai Formation compared to the underlying late Miocene sediments. Various higher plant-derived aromatic hydrocarbons including cadalene, retene, 1,2,7-trimethylnaphthalene, 1-methylphenanthrene (1-MP), 1,7-dimethylphenanthrene (1,7-DMP), 6-isopropyl-1-isoheptyl-2-methylnaphthalene (ip-iHMN) and other polycyclic aromatic hydrocarbons (PAHs) were identified. Higher plant parameters suggest that the relative abundance of total terrigenous organic matter in the early Pliocene was lower than in the angiosperm-dominated organic matter in the late Miocene Huangliu Formation. Various gymnosperm/angiosperm indices including retene/(retene + cadalene), 1-MP/9-MP, and 1,7-DMP/(1,3- + 3,9- + 2,10 + 3,10-DMP), and the higher plant index, indicate that gymnosperms made a larger contribution to the organic matter when the lower Yinggehai Formation was deposited during the early Pliocene.

GEOPHYSICS**ADRIATIC SEA****1,561,415****CHANGING DIRECTIONS OF THE TECTONIC STRUCTURES, CONSISTENT PALEOMAGNETIC DIRECTIONS AT THE NE IMBRICATED MARGIN OF STABLE ADRIA**

E.Marton, V.Cosovic, G.Imre and M.Velki (Szabalyozott Tevekenysegek; Zagreb Univ). *TECTONOPHYSICS* v.843, 11/20/2022. (ISSN 0040-1951; Article no.229594)

The imbricated margin of stable Adria, which belongs to the External Dinarides, comprises a chain of islands, which follow the dominant NW-SE Dinaric trend in the northern segment, while the dominant tectonic orientation changes to WNW-ESE in the central Adriatic area, near Split. The new paleomagnetic results documented in this paper are from the islands of the latter and can be interpreted in terms of tectonics together with already published robust data sets from the Northern Adriatic Islands and stable Adria, respectively. The problems addressed are the proposed extra CCW rotation in the central Adriatic area relative to the rest of the Dinarides, the differences in the tectonostratigraphic models of the offshore External Dinarides, the relationship to Stable Adria and the reason for the arcuated shape of the thrust front between stable and imbricated Adria. From the five largest Central and Southern Adriatic Islands over 1000 independently oriented cores, representing 98 Upper Tithonian – Paleocene carbonate localities, were subjected to standard laboratory processing of the natural remanent magnetization, component analysis, and statistical evaluation on locality and between locality levels. The results lead to the conclusion that these islands moved in close co-ordination with both, the Northern Adriatic Islands and stable Adria, at least from the Albian on. The different tectonic trends characterizing the islands and reflected also in the arcuated shape of the thrust front between Stable and Imbricated Adria is explained by the dominance of one of the Late Cretaceous and younger compressional strain fields. The structures due to the Late Cretaceous strain field are dominant in Cres island (N-S trend), the ones formed during the Late Eocene-Early Oligocene prevail in the Northern Adriatic islands (NW-SE trend), SE of Cres. The WSW-ENE general orientation of the structures in the Central Adriatic area is due to the strong neotectonic deformation. (c2022 Elsevier B.V.)

AMPLITUDE VERSUS OFFSET**1,561,416****A NEW APPROXIMATION TO THE REFLECTION COEFFICIENT BASED ON THE DIFFUSIVE-VISCOUS WAVE EQUATION**

Z.Wang, J.Gao, L.Zhao and C.Meng (Xi'an Jiaotong Univ). *83RD ANNUAL EAGE CONFERENCE (Online and Madrid, Spain, 6/6-9/2022) ABSTRACTS* 2022. (Abstract no.610; Available at <http://www.earthdoc.org> as of 7/7/2022; 5 pp; **Abstract only**)

The frequency-dependent seismic anomalies related to the hydrocarbon reservoirs have lately attracted wide attentions, and the diffusive-viscous wave equation was built to explain these anomalies. Frequency-dependent amplitude versus angles of incidence (FAVA) inversion is a commonly used and effective reservoir prediction technique. The existing frequency-dependent reflection coefficient formula based on the diffusive-viscous wave equation is complex and highly nonlinear, containing eight model parameters, then it is difficult to apply for FAVA inversion. In this abstract, we derive a simplified reflection coefficient formula for the diffusive-viscous wave equation. The new formula contains half of the model parameters of the exact formula, which greatly shrinks the search space of the global optimization algorithm and improves computational efficiency in FAVA inversion. The accuracy of the approximate formula is analyzed by the forward modeling. The test results show that the proposed formula is applicable within incident angle of 35 degrees and the frequency band range of seismic exploration, which supplies a theoretical foundation for the practical application of the FAVA inversion based on the diffusive-viscous wave equation.

AMPLITUDE VERSUS OFFSET 1,561,417

POST-CRITICAL AND NEAR-CRITICAL REFLECTIONS IN SEISMIC AVO INVERSION

A.Gisolf and P.Haffinger (Delft Inversion). *83RD ANNUAL EAGE CONFERENCE (Online and Madrid, Spain, 6/6-9/2022) ABSTRACTS 2022*. (Abstract no.617; Available at <http://www.earthdoc.org> as of 7/7/2022; 5 pp; **Abstract only**)

In this paper, the role of near-critical and post-critical angles in AVO inversion is investigated. Three different methods for forward modelling of near/post critical angle AVO data are presented: the Kennett method, the differential elastic wave-equation and the integral representation of the elastic wave-equation. For inversion of near and post critical data only the integral representation of the elastic wave-equation is used. A comparison is made, first between conventional AVO inversion and wave-equation based inversion for angles well below critical angle, and subsequently between wave-equation based inversion for the low angle range, and for a high angle range where for some layers critical angle is exceeded. It turns out that the biggest improvement is between conventional inversion and wave-equation based inversion for the low angle data. There is little improvement between the results of wave-equation based inversion for the relatively low angle data, and the results of wave-equation based inversion for the high angle data for which in places critical angle is exceeded. This is explained by qualitative analysis of the information content of high angle illumination data.

AMPLITUDE VERSUS OFFSET 1,561,418

THREE-TERM AVO INVERSION USING GROUP TOTAL VARIATION REGULARIZATION

C.Li and X.Liu (China Univ Geosci, Beijing). *JOURNAL OF APPLIED GEOPHYSICS* v.207, Dec. 2022. (ISSN 0926-9851; Article no.104854)

The seismic amplitude-versus-offset (AVO) inversion based on the total variation (TV) regularization is used to estimate blocky solutions for elastic parameters. It is achieved by minimizing the l1-norm of the first-order difference for model parameters. As the parameters in the subsurface are highly correlated with each other, a group optimization strategy was applied to the TV regularized AVO inversion. A group TV-norm that is a composition of the TV-norm and the l2-norm was designed. In this way, the TV regularization is performed among groups to promote sparsity of the gradients for the model parameters. By contrast, l2 regularization is performed within each group to constrain uniformity. The new three-term AVO inversion algorithm based on group TV regularization helps estimate the elastic parameters with desired blocky structure. Also, this algorithm ensures correlated resulting solutions even when no covariance matrix is used. It has proved to obtain good results in numerical and field examples. (©2022 Elsevier B.V.)

BAHIA SUL ESPIRITO SANTO B 1,561,419

BUILDING HIGH-RESOLUTION MODELS AND SYNTHETIC SEISMIC DATA TO EVALUATE INTERPRETATION SCENARIOS

T.S.Cabral, R.L.Fernandes, D.P.Bendoraitis, J.E.Goncalves and L.A.Santos (Petroleo Brasileiro SA). *2ND ANNUAL SEG/AAPG APPLIED GEOSCIENCE AND ENERGY INTERNATIONAL MEETING [IMAGE] (Houston, TX, 8/28/2022-9/1/2022) ABSTRACTS* pp.2522-2526, 2022. (ISSN 1949-4645; Available at <http://library.seg.org> as of 10/3/2022; **Expanded abstract**)

Building suitable velocity models is often a challenging task in projects that involve seismic modeling. We present a simple workflow inspired by poststack inversion to build high-resolution models that, combined with finite-difference modeling, can be used to evaluate interpretation scenarios in challenging areas. In this workflow, a low-frequency impedance derived from migration velocity is combined with a medium- to high-frequency pseudo-impedance volume derived from seismic. We apply the workflow on data from the Espirito Santos Basin, offshore Brazil, to evaluate two interpretation scenarios proposed for the base of salt. Analysis of the synthetic data obtained from this workflow allowed us to draw conclusions about the model and to determine which interpretation is more likely to be closer to the truth.

BOHAI BAY 1,561,420

APPLICATION OF LEAST SQUARES ONE-WAY WAVE MIGRATION IN IRREGULAR SAMPLING DATA OF BOHAI BAY BASIN

Y.Lu, D.Li, Y.Wang, J.Meng, X.Feng, D.Hu, X.Wu and Z.Kong (BGP CNPC). *2ND ANNUAL SEG/AAPG APPLIED GEOSCIENCE AND ENERGY INTERNATIONAL MEETING [IMAGE] (Houston, TX, 8/28/2022-9/1/2022) ABSTRACTS* pp.2749-2753, 2022. (ISSN 1949-4645; Available at <http://library.seg.org> as of 10/3/2022; **Expanded abstract**)

The conventional migration imaging technology is not the inverse of Born forward modeling, but its conjugate. Because the field acquisition and imaging processing are affected by the complexity of surface obstacles and subsurface medium, it is difficult to eliminate the influence of seismic wavelet. The obtained imaging is the fuzzy result of the real reflection coefficient filtered by Hessian matrix. It can not provide reliable results reflecting the dynamics characteristics of seismic wave field with high amplitude fidelity. The least squares migration technology based on inversion theory regards the imaging problem as an inverse problem, determines the rationality of imaging by comparing the correlation between the synthetic data generated by the migration image and the field data, and improves the correlation through iterative correction imaging, so as to obtain the imaging results with higher resolution and better amplitude fidelity. In this paper, the least squares one-way wave migration is applied on both the forward simulation data and the irregular spatial sampling data of Bohai Bay Basin, which effectively improves the resolution and fidelity of seismic data and the imaging of uneven illumination area of the geometry.

BOHAI BAY 1,561,421

APPLICATION OF 3D CONVERTED WAVE PROCESSING TECHNOLOGY IN IMAGING OF GAS CLOUD AREA

M.Xue, Z.Zhang, J.Zhang and Z.Ma (CNOOC (China) Ltd). *2ND ANNUAL SEG/AAPG APPLIED GEOSCIENCE AND ENERGY INTERNATIONAL MEETING [IMAGE] (Houston, TX, 8/28/2022-9/1/2022) ABSTRACTS* pp.2769-2773, 2022. (ISSN 1949-4645; Available at <http://library.seg.org> as of 10/3/2022; **Expanded abstract**)

The gas cloud in the Bohai Sea is relatively developed, and the quality of the P wave data in this area is poor, which is difficult to meet the needs of structure research. Based on the multi-component seismic data collected in the large gas cloud area of the Bohai Sea, this paper carried out research on the processing of PS converted wave data, and formed a number of key technologies, including component rotation, anisotropy correction, multiple suppression, prestack migration, etc. The final processing results

show that the imaging quality of the converted wave in the gas cloud area is obviously better than that of the P wave, which supports the structure research in the gas cloud area.

BOULDIN CREEK AREA 1,561,422

INSIGHTS INTO THE PRESENCE, DISTRIBUTION, THICKNESS, AND DURATION OF THE CTBE, DUE TO EROSION BY AN EARLY TURONIAN SEQUENCE BOUNDARY ACROSS TEXAS

A.D.Donovan, B.V.Miller, M.C.Pope and A.Pramudito (Texas A&M Univ). *2ND ANNUAL SEG/AAPG APPLIED GEOSCIENCE AND ENERGY INTERNATIONAL MEETING [IMAGE] (Houston, TX, 8/28/2022-9/1/2022) ABSTRACTS* pp.2495-2497, 2022. (ISSN 1949-4645; Available at <http://library.seg.org> as of 10/3/2022; **Expanded abstract**)

At the Bouldin Creek outcrop locality near Austin, Texas, an Early Turonian unconformity was defined, and its associated 2 million year hiatus documented using ID-TIMS U-PB dating of zircons. The hiatus explains why the positive carbon isotope ($\delta^{13}C$) excursion, typically associated with the Cenomanian/Turonian Boundary Event (CTBE), is absent at this locality.

BRAZIL 1,561,423

FAST ANISOTROPIC VISCOELASTIC MODELING AND APPLICATION IN QUANTITATIVE SEISMIC RESERVOIR CHARACTERIZATION

S.Tan, S.Lee, J.E.Anderson, H.Wang, O.Burtz, P.Routh, R.Lu and Y.Yu (ExxonMobil Integr Solut Co; ExxonMobil Upstream Res Co). *2ND ANNUAL SEG/AAPG APPLIED GEOSCIENCE AND ENERGY INTERNATIONAL MEETING [IMAGE] (Houston, TX, 8/28/2022-9/1/2022) ABSTRACTS* pp.2502-2506, 2022. (ISSN 1949-4645; Available at <http://library.seg.org> as of 10/3/2022; **Expanded abstract**)

Understanding and compensating for attenuation effect is crucial to obtain a high-resolution seismic volume with high-fidelity amplitude for quantitative seismic reservoir characterization. The conventional anisotropic viscoelastic wave equation is computationally expensive because of the large number of memory variables. We have developed a new anisotropic viscoelastic formulation to significantly reduce the number of memory variables and thus the computation cost. We demonstrate that viscoelastic modeling is necessary to match the field data in a Brazil pre-salt field.

BRAZIL 1,561,424

VELOCITY MODEL BUILDING AND IMAGING DRIVEN BY FWI WITH DUAL-AZIMUTH DATA IN A COMPLEX SALT ENVIRONMENT: BRAZIL CASE STUDY

X.Li, C.Gans, Y.H.Cha, D.Snyder, G.Palacharla, V.Gottumukkula, Y.He, H.Sun, T.Vdovina et al. (ExxonMobil). *2ND ANNUAL SEG/AAPG APPLIED GEOSCIENCE AND ENERGY INTERNATIONAL MEETING [IMAGE] (Houston, TX, 8/28/2022-9/1/2022) ABSTRACTS* pp.2596-2600, 2022. (ISSN 1949-4645; Available at <http://library.seg.org> as of 10/3/2022; **Expanded abstract**)

Using CGG recently acquired seismic data, ExxonMobil carried out a dual-azimuth (DAZ) velocity model building (VMB) and imaging project in Brazil's Santos basin. Major factors that contributed to velocity and image uplifts are briefly reviewed: Voronoi normalization, dual azimuthal well log constrained tomography, iterative full waveform inversion (FWI) leveraging 3D mesh interpretation and wave-equation-based map migration, pre-stack shot illumination compensation for RTM, and multi-azimuth smart merge. These key factors combined to produce significant velocity model and image improvements.

BRAZIL 1,561,425

A RECIPE FOR PRACTICAL ITERATIVE LSRTM WITH SYNTHETIC AND REAL DATA EXAMPLES FROM BRAZIL

V.Brytik, G.Palacharla, R.Bansal, D.Snyder, X.Li, Y.H.Cha,

P.Routh, I.Dura-Gomez, D.Pavlov et al. (ExxonMobil). *2ND ANNUAL SEG/AAPG APPLIED GEOSCIENCE AND ENERGY INTERNATIONAL MEETING [IMAGE] (Houston, TX, 8/28/2022-9/1/2022) ABSTRACTS* pp.2689-2693, 2022. (ISSN 1949-4645; Available at <http://library.seg.org> as of 10/3/2022; **Expanded abstract**)

Inversion-based imaging approaches such as LSRTM (Tarantola, 1987; Claerbout, 1992; Nemeth et al., 1999; Schuster, 2017) have become an important part of seismic processing, especially in complex geologic regions where both high fidelity structural imaging and amplitudes are required. However, owing to the high computational cost of the forward modeling and gradient estimation steps, and the iterative nature of the approach, application of LSRTM can be expensive. In this abstract we discuss several improvements to a standard iterative LSRTM workflow, which can speed-up convergence, aid in the recovery of physically meaningful properties such as impedance, and overall reduce the cost of application. The improvements include wavelet selection, smart preconditioning via NMF (non-stationary matching filter), inversion parameter selection, multi-domain analytic line search, use of an alternate migration operator and shot selection. These workflow improvements have allowed us to significantly reduce the cost of applying LSRTM, while still generating high fidelity and physically meaningful results.

BRAZIL 1,561,426

AMPLITUDE INVERSION OF OBS DIRECT ARRIVALS FOR SEABED ELASTIC PROPERTIES

J.Gaiser, M.de Souza Bazerra and J.Simmons (Gaiser Geophysical Consult; Colorado Sch Mines). *2ND ANNUAL SEG/AAPG APPLIED GEOSCIENCE AND ENERGY INTERNATIONAL MEETING [IMAGE] (Houston, TX, 8/28/2022-9/1/2022) ABSTRACTS* pp.2797-2801, 2022. (ISSN 1949-4645; Available at <http://library.seg.org> as of 10/3/2022; **Expanded abstract**)

As interest in shear waves (S-waves) grows for prestack depth migration of ocean-bottom node (OBN) data, it is imperative to obtain a good initial elastic model of the shallow seabed, for optimal wavefield separation and imaging. Compressional wave (P-wave) methods that use mirror migration, velocity analyses and tomography are not available for shallow converted P- to S-wave (PS-wave) data because of sparse node acquisition and low S-wave velocities. Conventional techniques use reflections from just below the seabed to invert for the elastic properties $V(P)$, $V(S)$ and density ρ . We estimate these properties by inverting the amplitude variations with ray parameter (horizontal slowness) of the direct arrival. Synthetic data shows exact results compared with analytic expressions for reflection and transmission coefficients of the seabed interface. Inverting field data from the deep-water Jubarte ocean-bottom cable (OBC) survey offshore Brazil also shows good results. However, some challenges remain related to calibrating particle velocity data with the pressure data for acoustic wavefield separation.

CAMEROON 1,561,427

DELINEATING STRUCTURAL FEATURES OF NORTH CAMEROON USING THE EIGEN6C4 HIGH-RESOLUTION GLOBAL GRAVITATIONAL MODEL

F.Eitel Kemgang Ghoms, L.T.Pham, R.Steffen, N.Ribeiro-Filho and R.Tenzer (Yaounde Univ; Vietnam National Univ; Lantmateriet; Para Federal Univ). *GEOLOGICAL JOURNAL* v.57, no.10, pp.4285-4299, Oct. 2022. (ISSN 0072-1050; ISSN 1099-1034)

The Cretaceous basins of the West and Central African Rift System (WCARS) are characterized by sinistral strike-slip movements observed between the Benue and Arabian-Nubian microplates. These basins share a similar basin-filling structure, history, and tectonic processes. They have attracted a significant interest in the study of their geodynamics and subsurface structure through geophysical exploration methods. Nevertheless, North Cameroon located in this microplate confluence has not yet been investigated in terms of identifying geological structures, such as lineaments and faults. To contribute to a better understanding of the northern Cameroon structural framework and its tectonic

context, we investigate the lineaments in northern Cameroon by using the EIGEN-6C4 gravitational model and a variety of recent processing techniques (Tilt derivative [TDR], Theta Map [TM], Horizontal tilt angle [TDX], and Edge Detector [ED]). Our results show that the lineaments are trending in ENE–WSW, NW–SE, NE–SW, and WNW–ESE directions. These directions are consistent with the Cretaceous Garoua Rift and granitoids of the Cameroon-Chad line. The presented result clearly delineates continuous architectonic features of the structural edges of the Saharan Metacraton, the Cretaceous Garoua Rift, the Bibemi-Lere granitoids, and the Adamawa faults.

CAMPECHE GULF 1,561,428

USING PREDICTED DYNAMIC PROPERTIES TO PERFORM SEISMIC SITE RESPONSE ANALYSES ON A BAY OF CAMPECHE CALCAREOUS SOIL DEPOSIT

V.M.Taboada, S.C.Cao, D.Cruz Roque, P.Barrera Nabor and F.A.Flores Lopez (Fugro; Changzhou Univ; Inst Mexicano Petroleo; Ingenieros Geo Mexicanos). *OFFSHORE TECHNOLOGY CONFERENCE [OTC] (Houston, TX, 5/2-5/2022) PROCEEDINGS 2022*. (ISBN 978-1-61399-852-6; OTC-31809; Available at <http://www.onepetro.org> as of 6/23/2022; 23 pp)

This study presents the influence of using predicted (calculated) normalized shear modulus (G/Gmax) and material damping ratio (D) curves on the design acceleration spectrum at the depth of maximum soil-pile interaction of a calcareous soil deposit in the Bay of Campeche. When comparing the predicted curves to the laboratory curves, it is concluded that due to limitations in the predicting models, the minimum confining pressure (σ'_m) that must be used to obtain a good match with the laboratory curves is 150 kPa. After performing site response analyses for three shear wave velocity profiles and eight recorded acceleration time histories, the design acceleration spectrum was developed based on the envelope of the 24 calculated acceleration spectra. The acceleration amplitudes of the design spectrum in the short period range are slightly larger using the calculated curves than the laboratory curves. For periods longer than 0.27 seconds, the acceleration amplitudes of the design acceleration spectra are identical for practical purposes when both calculated and laboratory curves are used. Therefore, it is recommended to use the equations presented herein to calculate the curves of G/Gmax and D for calcareous soils in practice for preliminary and final seismic site response analyses. They can be especially useful in final evaluations of large or critical projects to calculate the curves when time and cost constraints make it impractical to perform direct experimental determinations of G/Gmax and D curves for each soil layer encountered in the soil deposit. (Copyright 2022 OTC)

CAMPOS BASIN 1,561,429

IMPROVED SUBSALT IMAGING IN BRAZIL CAMPOS BASIN - CASCADED APPLICATION OF HYBRID INTERBED DEMULTIPLE, P- AND S-SALT VELOCITY JOINT MIGRATION, AND SUBSALT CONVERTED WAVE SUPPRESSION

R.Alai, F.Liu, D.Armentrout, D.Brookes, T.Johnson, M.Cvetkovic, G.Coskun, S.Sulaiman, K.K.Lee et al. (Petronas Carigali Sdn Bhd). *2ND ANNUAL SEG/AAPG APPLIED GEOSCIENCE AND ENERGY INTERNATIONAL MEETING [IMAGE] (Houston, TX, 8/28/2022-9/1/2022) ABSTRACTS* pp.2680-2684, 2022. (ISSN 1949-4645; Available at <http://library.seg.org> as of 10/3/2022; **Expanded abstract**)

The pre-salt play of Brazil Santos and Campos Basins has been the hot-spot for oil and gas companies since 2006 due to significant discoveries made and large volume of Yet-to-Find to chase. Seismic imaging plays a critical role in the success of companies from exploration to development of this major play. The pre-salt play is capped by thick salt with highly variable geometries and stratigraphy that leads to significant imaging and illumination challenges. It requires seismic data acquisition and processing programs specially tailored based on those challenges and learnings from the pre-salt imaging. In this abstract, we present the cascaded application of three critical technologies to improve the subsalt imaging in Brazil Campos basin data: hybrid interbed demultiple,

P- and S-salt velocity joint migration, and subsalt converted wave suppression. We will showcase in detail through examples the significant benefits of these cascaded applications to ensure subsalt images are more accurate and the true geology can be revealed, rather than being distorted through interbed multiples and converted waves related, particularly, to the stratified salt and carbonate layers.

CAMPOS BASIN 1,561,430

INTEGRATING LEGACY DATA WITH NEW TOWED-STREAMER ACQUISITION TUNED FOR IMAGING OBJECTIVES: A CAMPOS BASIN CASE STUDY

J.Burren and D.Unger (PGS). *2ND ANNUAL SEG/AAPG APPLIED GEOSCIENCE AND ENERGY INTERNATIONAL MEETING [IMAGE] (Houston, TX, 8/28/2022-9/1/2022) ABSTRACTS* pp.2685-2688, 2022. (ISSN 1949-4645; Available at <http://library.seg.org> as of 10/3/2022; **Expanded abstract**)

Results are presented from the processing of new acquisition in combination with complementary reprocessing of legacy data over 8200 square kilometers in the deep waters of the Campos Basin, offshore Brazil. The acquisition configuration was a result of extensive survey design and modeling studies, designed to meet both the technical needs of the area and the regulatory requirements of Brazil. Survey planning considered characteristics of the existing legacy data, specific geological targets, imaging challenges in resolving the pre-salt syn-rift section, and sampling requirements of high-end imaging methods. We show that the combination of a legacy survey with an appropriately designed new survey provides the basis for robust velocity building and notable improvements in image quality, which will bring greater confidence in interpretation and reservoir characterization work.

CHUXIONG BASIN 1,561,431

SHALLOW SHEAR WAVE VELOCITY STRUCTURE OF THE DONGSHAN SAG AREA USING SURFACE WAVE DATA IN A DEEP REFLECTION PROFILE OF THE YUANMOU AREA OF YUNNAN PROVINCE, CHINA

S.Chen, R.Gao, Z.Lu, X.Zhang, W.Li, Y.Liang, Y.Cheng and G.Wang (Chinese Academy Geol Sci). *TECTONOPHYSICS* v.843, 11/20/2022. (ISSN 0040-1951; Article no.229606)

Deep reflection seismic data contain abundant surface wave information for which the velocity structure in the near-surface shallow underground can be obtained using multichannel analysis of surface waves (MASW). This paper uses the MASW method to process deep reflection data in the Yuanmou area in Yunnan province, China. The MASW method uses the phase velocity spectral transformation of Rayleigh waves to obtain its dispersion curve. The initial model for different lithology classifications is established to invert the underground velocity structure. This study obtains a two-dimensional shear wave velocity structure profile to investigate the shear wave velocity structure. Generally, the study results have shown that the shear wave velocity structure obtained by the MASW method corresponds well with the surface conditions and accurately reflects faults' changes, folds, and lithology. Moreover, the formation sand content calculation shows a large difference in Dongshan sag's formation sand content. The sand contents of Cretaceous and Middle Jurassic strata are over 30% similar, and the sandstone content of underlying Early Jurassic strata is mostly 30% lower. The stratum buried depth of Early Jurassic strata is between 0-800 m. The dip angle of LZJF at this location is 90°. The west side of the LZJF is based on Proterozoic uplift, and the Quaternary sedimentary thickness exceeds 300 m above the uplift stratum. Whereas on the east side of the LZJF, the stratum of the Dongshan sag section is mainly a synclinal structure. (c2022 The Authors. Elsevier B.V.)

COMPRESSIVE SENSING 1,561,432

COMPRESSIVE SENSING FRAMEWORK USING THE LINEAR RADON TRANSFORM FOR 3D ULTRASONIC DATA RECONSTRUCTION IN A PINCH-OUT RESERVOIR MODEL

P.C.Assis, R.B.Silva, I.A.Lima Neto, A.C.Galante, A.L.Campi,

A.R.Oliveira, R.M.Missagia and M.A.R.Ceia. *2ND ANNUAL SEG/AAPG APPLIED GEOSCIENCE AND ENERGY INTERNATIONAL MEETING [IMAGE] (Houston, TX, 8/28/2022-9/1/2022) ABSTRACTS* pp.2621-2625, 2022. (ISSN 1949-4645; Available at <http://library.seg.org> as of 10/3/2022; **Expanded abstract**)

In this work, the key ideas of the compressive sensing (CS) theory help us present a framework for seismic data reconstruction. The program was applied on ultrasonic 3D data that mimics a marine seismic acquisition over a pinch-out reservoir model. First, we modeled a CS-based seismic survey by removing 40% of the shot families and applied a sparsity-promoting program to recover the data in the original grid. We also exploited the linear Radon transform by imposing wavefront constraints aiming to obtain a sparser representation of the wavefield. The results showed improved signal quality in pre- and post-stack data, demonstrating that CS ideas can be successfully applied to recover missing data.

CSEM METHOD 1,561,433

THE FEASIBILITY OF CSEM MONITORING IN GAS HYDRATE PRODUCTION OF THE RANGE OF POROSITY AND SATURATION

Y.Li, H.Lu, L.Wang, M.Eltayieb and E.Slob (Beijing Inform Technl Univ; Beijing Univ; Beihang Univ; Delft Univ Technol). *83RD ANNUAL EAGE CONFERENCE (Online and Madrid, Spain, 6/6-9/2022) ABSTRACTS* 2022. (Abstract no.625; Available at <http://www.earthdoc.org> as of 7/7/2022; 5 pp; **Abstract only**)

Natural gas hydrates production tests over the last two decades has shown that production is not without risks. Indirect effects in the sedimentary rocks of phase changes are changes in porosity, permeability, and saturation. From a field production test site, porosity changes in the range of 15% to 19% and saturation from 5% to 60% were reported. Monitoring is in principle possible using an electromagnetic survey with a downhole vertical electric source and a horizontal electric field receiver on the seafloor. Computed model responses over a wide frequency range and for many depth locations of an electric current source show that both changes can be detected. Best detectability occurs when the current source is below the reservoir layer in case of changes differences can be detected above, inside and below the reservoir layer at frequencies below 10 Hz. At a source operating frequency of 0.1 Hz maximum response difference between the two values in saturation occur when the source is 20 m above the top of the reservoir layer until 100 m below the bottom. Only below the top of the reservoir there is almost no difference in the electric field amplitude between the two saturation levels below 10 Hz.

CSEM METHOD 1,561,434

3D MCSEM MODELING BASED ON DOMAIN-DECOMPOSITION FINITE-ELEMENT METHOD

Z.Hui, C.Yin, W.Zhang, Y.Liu and B.Xiong (Chengdu Univ Technology; Jilin Univ; Guilin Univ Technology). *JOURNAL OF APPLIED GEOPHYSICS* v.207, Dec. 2022. (ISSN 0926-9851; Article no.104847)

Domain decomposition approach is effective in converting large modeling problems into many small ones, so that the parallel computation can be easily facilitated and the memory consumption can be largely reduced. In this paper, we developed a domain-decomposition method for 3D time-domain marine controlled-source (MCSEM) modeling based on Dual-Primal Finite-Element Tearing and Interconnecting technique (FETI-DP). We use tetrahedral grids to do the spatial discretization first and then partition the mesh into subdomains. In each subdomain, the finite-element equations are independently constructed using the first-order vector shape functions and boundary conditions. To build the interconnections among these subdomains, we establish the interface equation for the Lagrange multipliers that are used as the boundary conditions for the subdomains. After solving the equations, the electric field for all subdomains can be obtained from the Lagrange multipliers. For the time discretization, we use unconditionally stable backward Euler scheme. We validate our algorithm by comparing with a semi-analytical solutions for a uniform half-space model under the ocean. Numerical experiments show that compared to the

conventional finite-element method, our domain-decomposed method can save large amount of memory, render it possible to run 3D MCSEM modeling in small computational equipment. (c2022 Elsevier B.V.)

DAS SYSTEM 1,561,435

DAS WEAK SIGNALS RECOVERY UNDER CONDITION OF MULTIPLE COMPLICATED NOISE USING CA-MSRNet

Y.Li, Z.Zhao, Y.Tian and N.Wu (Jilin Univ). *JOURNAL OF APPLIED GEOPHYSICS* v.207, Dec. 2022. (ISSN 0926-9851; Article no.104844)

Over the years, distributed fiber-optical acoustic sensing (DAS) has been widely used in seismic exploration benefited from its numerous advantages over traditional geophones. However, the effective signals in real DAS records are contaminated by numerous complicated noise other than traditional geophones noise causing some artifacts in the following stratigraphic analysis imaging. Especially, the energy of the direct wave in DAS data is tremendously strong making the reflected signals weaker. Most of the conventional denoising approaches cannot achieve a satisfactory effect. Forced by these problems, we proposed a new denoising network model called channel attention-guided multiscale residual module neural network (CA-MSRNet). The proposed network framework has three main advantages: firstly, some interleaving dilated convolution operations are utilized to increase the receptive field effectively. Secondly, the channel attention technology plays a role in redistributing the weight coefficients of feature maps in channel. Thirdly, the multiscale convolution operation contributes to integrate multiscale spatial information. The above three technologies help CA-MSRNet capture features more easily and completely. Comprehensive experiments on both synthetic records and field data illustrate the superior performance of the proposed CA-MSRNet in two tasks of noise suppression and weak signal recovery compared with band-pass filter, F-X deconvolution and feed-forward denoising convolution neural network (DnCNN). (c2022 Elsevier B.V.)

DATA MANAGEMENT 1,561,436

DATA MANAGEMENT AND TEAMWORK

A.Dobrovolskiy (SPH Engineering). *FIRST BREAK* v.40, no.12, pp.85-93, Dec. 2022. (ISSN 0263-5046; ISSN 1365-2397)

As there is market demand for geophysical data management, sharing, and teamwork support systems, it is obvious that existing systems will evolve in terms of functionality, scalability, and access control/security features. At this time, the state-of-the-art is far behind what is available, for example, in the software development industry, and even in "office" document-management systems. Despite this, there are options for organizing data management and teamwork using available solutions, starting with basic file-sharing public platforms and going through more specialized solutions.

EGYPT 1,561,437

APPLICATIONS OF NEAR-FIELD HYDROPHONE DATA IMAGING IN A SHALLOW WATER ENVIRONMENT: A CASE STUDY FROM OFFSHORE EGYPT

M.El-Attar, O.Hossam, A.Kireev, A.Kanrar, U.F.A.Kader, K.Zhang, J.Deeds and J.Hassler (Schlumberger; Chevron Technical Ctr). *2ND ANNUAL SEG/AAPG APPLIED GEOSCIENCE AND ENERGY INTERNATIONAL MEETING [IMAGE] (Houston, TX, 8/28/2022-9/1/2022) ABSTRACTS* pp.2670-2674, 2022. (ISSN 1949-4645; Available at <http://library.seg.org> as of 10/3/2022; **Expanded abstract**)

Near-field hydrophone (NFH) data have gained significant attention recently, due to their unique properties and applications. The application of the NFH is no longer limited only to the determination of the source signature or performing shot-by-shot designation; it is extended to image near-seafloor geology in a shallow water environment, where traditional streamer primary imaging does not provide a clear or precise shallow image due to missing small angle reflections, near trace stretch, or interference, of the refracted arrivals. Additionally, the retrieved sub-surface

reflectivity information from NFH data can be incorporated in the demultiple process on the principle dataset acquired by the towed-streamer or ocean-bottom-node system.

ESPIRITO SANTO 1,561,438

PSEUDO S-WAVE SPLITTING EFFECTS ASSOCIATED WITH POOR RECEIVER COUPLING ON OCEAN BOTTOM MULTI COMPONENT DATA

M.de Souza Bezerra, J.Simmons and J.Gaiser (Colorado Sch Mines; Gaiser Geophysical Consult). *2ND ANNUAL SEG/AAPG APPLIED GEOSCIENCE AND ENERGY INTERNATIONAL MEETING [IMAGE] (Houston, TX, 8/28/2022-9/1/2022) ABSTRACTS* pp.2802-2806, 2022. (ISSN 1949-4645; Available at <http://library.seg.org> as of 10/3/2022; **Expanded abstract**)

Shear wave splitting analysis can provide knowledge about, among other properties, principal stress directions and fracture orientation. It is an essential step in multi-component, converted wave processing, with several successful examples in the literature. Caution must be taken, however, when performing such analysis on ocean bottom cable seismic data, which is highly susceptible to poor coupling effects between cables and the seafloor. We show how these coupling effects can simulate conventional splitting behavior that, once corrected, may reveal true splitting effects to be addressed.

EUROPE 1,561,439

SUB-BASALT IMAGING IN THE NW EUROPE ATLANTIC MARGIN - LATEST RESULTS

S.Baldock, M.Hart, S.Stokes, A.Macdonald, D.Mondal and J.Twigg (TGS). *83RD ANNUAL EAGE CONFERENCE (Online and Madrid, Spain, 6/6-9/2022) ABSTRACTS* 2022. (Abstract no.620; Available at <http://www.earthdoc.org> as of 7/7/2022; 5 pp; **Abstract only**)

Imaging beneath and within volcanic rocks is a longstanding challenge within seismic imaging. This problem is particularly acute in NW Europe, where volcanics affect a significant area of potentially hydrocarbon bearing formations. Using workflows developed over the course of several years and based on the results of synthetic and real data experiments a demonstrable uplift in seismic imaging quality is achieved. The results demonstrate the benefit of detailed velocity models built using dynamic matching FWI (DMFWI) and common offset RTM (COR) tomography together with more traditional ray-based methods. These velocity models provide interpretational insights as well as imaging uplift. A selection of results from real and synthetic datasets are used to demonstrate the results.

FULL WAVEFORM 1,561,440

FAST GAUSS-NEWTON FULL-WAVEFIELD MIGRATION

S.Abolhassani and E.Verschuur (Delft Univ Technol). *2ND ANNUAL SEG/AAPG APPLIED GEOSCIENCE AND ENERGY INTERNATIONAL MEETING [IMAGE] (Houston, TX, 8/28/2022-9/1/2022) ABSTRACTS* pp.2709-2713, 2022. (ISSN 1949-4645; Available at <http://library.seg.org> as of 10/3/2022; **Expanded abstract**)

Since the appearance of wave-equation migration, many have tried to push this technology to the limits of its capacity. Least-squares wave-equation migration is one of those attempts that tries to fill the gap between the migration assumptions and reality in an iterative manner. However, these iterations do not come cheap. A proven solution to limit the number of iterations is to correct the update direction in every iteration via a proper but cheap preconditioner that approximates the second-order partial derivatives, known as Hessian, of the data-error functional employed in the least-squares formulation. In this study, we will address this issue, namely the cheap computation of the Hessian inverse in the context of our one-way wave-equation-based migration method, cited as full wavefield migration. To do so, we will build and apply the Hessian inverse matrix depth by depth, reducing the Hessian matrix size considerably each time it is calculated. We prove the validity of our proposed method by two numerical examples.

FULL WAVEFORM 1,561,441

APPROXIMATE DATA-DOMAIN HESSIAN IN EXTENDED-SOURCE TIME-DOMAIN FULL WAVEFORM INVERSION USING MATCHING FILTER AND CONJUGATE GRADIENT METHOD

G.Guo, O.Stephane, G.Ali and S.A.Hosseini (Cote d'Azur Univ; Tehran Univ). *83RD ANNUAL EAGE CONFERENCE (Online and Madrid, Spain, 6/6-9/2022) ABSTRACTS* 2022. (Abstract no.622; Available at <http://www.earthdoc.org> as of 7/7/2022; 5 pp; **Abstract only**)

Wavefield reconstruction inversion (WRI) avoids cycle-skipping in full-waveform inversion (FWI) by computing wavefields with wave-equation errors (i.e., source extensions) such that simulated data closely match observed data with inaccurate velocity models. However, the implementation of time-domain WRI faces a practical challenge because the source extension in the right-hand side of the wave equation depends on the unknown data residuals. Recent studies show that source extensions are the least-squares solutions of the scattered-data (i.e., FWI data residuals) fitting problem for contrast-source estimation. As a result, source extensions are computed by propagating backward in time the deblurred FWI data residuals, where the deblurring operator is the inverse of the damped data-domain Hessian of the contrast-source estimation problem. We first estimate an approximate deblurring operator with matching filter, which can be used as a preconditioner for iterative refinement of the source extensions with a conjugate gradient method. Numerical tests validate the proposed scheme for accurate reconstruction of contrasted media from crude initial model.

FULL WAVEFORM 1,561,442

GPU-ACCELERATED MODELING AND SIMULATION OF ACOUSTIC WAVES FOR SEISMIC APPLICATIONS

J.Souza, J.Moreira, A.Oliveira, K.Roberts, E.Gomi, E.Silva and H.Senger (Sao Carlos Federal Univ; Sao Paulo Univ). *3RD EAGE HPC IN AMERICAS WORKSHOP (Online, 5/17-18/2022) ABSTRACTS* 2022. (Abstract no.WED09; Available at <http://www.earthdoc.org> as of 10/26/2022; 5 pp; **Abstract only**)

In this work, we evaluate the performance of an OCCA back-end implemented in the simwave stack. Simwave (de Souza et al., 2022) is an open-source Python package for simulating the propagation of acoustic waves in 2D or 3D domains. Simwave solves the constant and variable density acoustic wave equation with the finite-difference method and supports domain truncation techniques, several boundary conditions, and modeling sources and receivers with a user-defined acquisition geometry. This performance evaluation is important for improving simwave's graphic processing unit (GPU) support. The performance of the new back-end is compared with two native simwave back-ends for GPU offloading-OpenMP and OpenACC. Preliminary results show that the OCCA back-end outperforms the native back-ends in scenarios with better GPUs. Experiments involving more scenarios and investigations of OCCA as a full-performance portability solution for simwave will be addressed in future work.

GAS HYDRATE 1,561,443

ROCK PHYSICS MODELING OF ACOUSTIC PROPERTIES IN GAS HYDRATE-BEARING SEDIMENT

L.Zhan, B.Liu, Y.Zhang and H.Lu (Peking Univ; Chinese Academy Geol Sci). *JOURNAL OF MARINE SCIENCE AND ENGINEERING* v.10, no.8, Aug. 2022. (ISSN 2077-1312; Article no.1076)

Gas hydrates (GH) are well known to have an influential effect on the velocity and attenuation of gas hydrate-bearing sediments (GHBS). Based on rock physics modeling, sediment velocity has been extensively used to characterize the distribution of gas hydrate. However, the results obtained from different models show a significant variation. In this study, we firstly review and compare the existing rock physics modeling for velocity and attenuation. The assumption, characteristics, theoretical basis, and workflow of the modeling are briefly introduced. The feasibility and limitations of the published models are then discussed and compared. This study

provides insight into how to select a suitable rock physics model and how to conduct modeling in the application of the rock physics model to field data. Then, we introduce how to predict hydrate saturation, hydrate morphology, the dip angle of fracture, sediment permeability, and attenuation mechanisms from the comparison between the modeled and measured acoustic properties. The most important application of rock physics modeling is predicting the hydrate saturation and we discuss the uncertainties of the predicted saturation caused by the errors related to the velocity measurements or rock physics modeling. Finally, we discuss the current challenges in rock physics modeling related to optimizing the input parameters, choice of a suitable model, and upscaling problems from ultrasonic to seismic and well log frequencies.

GAS HYDRATE

1,561,444

EFFECT OF HYDRATE MICROSCOPIC DISTRIBUTION ON ACOUSTIC CHARACTERISTICS DURING HYDRATE DISSOCIATION: AN INSIGHT FROM COMBINED ACOUSTIC-CT DETECTION STUDY

Q.Bu, T.Xing, C.Li, J.Zhao, C.Liu, Z.Wang, W.Zhao, J.Kang, Q.Meng et al. (Qingdao Inst Marine Geol). *JOURNAL OF MARINE SCIENCE AND ENGINEERING* v.10, no.8, Aug. 2022. (ISSN 2077-1312; Article no.1089)

Geophysical detection techniques are important methods in marine gas hydrate exploration and monitoring, because the small-scale distribution of hydrates has a large impact on the wave velocity. The acoustic response characteristics of hydrate micro-distributions have strong significance for monitoring the hydrate dissociation process. In this paper, experiments simulating the hydrate dissociation process were carried out in a self-developed experimental device combining X-ray computed tomography (X-CT) scanning and ultrasonic detection, which allowed the acoustic wave characteristics and X-CT scanning results to be simultaneously obtained during the hydrate dissociation process. This study found that the hydrate dissociation stage is divided into three stages. The hydrate begins to dissociate at spots where it comes into touch with sand particles early in the dissociation process. The main factor affecting the acoustic wave velocity of hydrates in this stage is changes in the microscopic distribution of hydrate. In the middle stage, a large amount of hydrate decomposes, and the main factor affecting the acoustic wave velocity of hydrate in this stage is the change in hydrate content. In the later stage of hydrate dissociation, the hydrate distribution pattern consists mainly of the pore-filling type, and the hydrate micro-distribution at this stage is the main factor affecting the acoustic wave velocity. This study will be of great significance for understanding the microscopic control mechanism of hydrate reservoir geophysical exploration.

GREEN CANYON AREA

1,561,445

OVERCOMING SIGNAL PROCESSING CHALLENGES ON A DEEP-WATER SPARSE OBN SURVEY: A CASE STUDY FROM THE GULF OF MEXICO

M.Salgadoe, N.Seymour, H.Li and D.Chen (Schlumberger). *2ND ANNUAL SEG/AAPG APPLIED GEOSCIENCE AND ENERGY INTERNATIONAL MEETING [IMAGE]* (Houston, TX, 8/28/2022-9/1/2022) *ABSTRACTS* pp.2812-2816, 2022. (ISSN 1949-4645; Available at <http://library.seg.org> as of 10/3/2022; **Expanded abstract**)

We present the results of processing a large ocean-bottom node survey in the Gulf of Mexico. An ocean-bottom node survey was acquired in an area with extensive imaging challenges that remain unresolved using legacy towed-streamer data with the goal of aiding subsalt imaging and exploration. Challenges associated with simultaneous-source shooting, acquisition perturbations, and shear-on-vertical noise are addressed using a sparsity-promoting deblending scheme, a novel linearized travel time inversion, and a curvelet-domain shear-noise suppression flow, respectively. When these data are imaged with a revised earth model from full-waveform inversion the resulting image shows improvements in the subsalt section including clearer definition of the basement and subsalt targets.

GRONINGEN GAS FIELD

1,561,446

UNSUPERVISED AI WORKFLOW TO EVALUATE CO2 STORAGE AND GEOTHERMAL POTENTIAL OVER A GIANT MATURE GAS FIELD

B.Laugier and A.Aming (Seisnetics). *3RD EAGE HPC IN AMERICAS WORKSHOP* (Online, 5/17-18/2022) *ABSTRACTS* 2022. (Abstract no.WED06; Available at <http://www.earthdoc.org> as of 10/26/2022; 5 pp; **Abstract only**)

Seismic data remain a pillar of subsurface modeling and for our understanding of the potential for transitioning from oil and gas production to applications such as CO2 storage and geothermal projects. However, interpretation is a biased and time-consuming process that forces geoscientists to spend more energy picking horizons and building models than on interpreting the significance of the results and their implications for ultimate field development, CO2 storage, and evaluating geothermal projects. In this paper, we detail the use of a new unsupervised artificial intelligence method based on a genetic algorithm to automatically process the seismic data in an unbiased way and in record time.

HOKKAIDO ISLAND

1,561,447

HELIFALCON(R) AIRBORNE GRAVITY GRADIOMETRY AND HELITEM(R) AIRBORNE ELECTROMAGNETICS FOR GEOTHERMAL EXPLORATION, MUSADAKE-TESHIKAGA, JAPAN

J.Fejith, A.Ninomiya, H.Ishikawa, A.Shirota, T.Mouri, G.Nakamoto and A.Mantilla-Pimiento (Xcalibur Multiphysics; Sumiko Rscs Explor & Dev; Sumitomo Metal Co Ltd). *83RD ANNUAL EAGE CONFERENCE* (Online and Madrid, Spain, 6/6-9/2022) *ABSTRACTS* 2022. (Abstract no.630; Available at <http://www.earthdoc.org> as of 7/7/2022; 5 pp; **Abstract only**)

An integrated interpretation of geological and geophysical data for Japan Oil, Gas and Metals National Corporation (JOGMEC) in the Musadake-Teshikaga area, Hokkaido, Japan. HeliFalcon(R) airborne gravity gradiometer (AGG) and Helitem(R) airborne electromagnetic (AEM) and magnetic data were acquired to facilitate the identification of prospective areas for geothermal energy generation. The interpretation workflow included: (1) Investigation of the regional geologic setting, using public domain data. (2) Individual Interpretation of the acquired airborne datasets. (3) Integration of the airborne geophysical data interpretations. (4) Identification and prioritisation of the prospective geothermal zones. Tectonic and volcanic features are mapped using the AGG, magnetic and AEM data. The AEM data was also used to identify low resistivity zones that potentially correspond with hydrothermal alteration zones. Low resistivity zones were mapped from the AEM data and appear to correlate with areas that have relatively low magnetic amplitudes. This suggests possible magnetite destruction and demagnetization related to thermal or hydrothermal activity. Low resistivity zones are more pronounced and common in the eastern Musadake area and therefore the geothermal exploration will be focused on this area.

IMAGING

1,561,448

IMAGING THE SUBSURFACE USING ACOUSTIC SIGNALS GENERATED BY A VESSEL

S.Hegna (PGS). *FIRST BREAK* v.40, no.11, pp.47-53, Nov. 2022. (ISSN 0263-5046; ISSN 1365-2397)

The acoustic wavefield originating from a vessel has historically not been considered as a source of signal in the imaging of marine seismic data and is therefore treated as a source of noise. In this work, the feasibility of acquiring seismic data without an active source and instead using the acoustic wavefield generated by a vessel for imaging the subsurface has been investigated. There are areas around the world where the use of active marine seismic sources is not permitted throughout the year, or only permitted during short time periods. In such areas, acquiring seismic data using the acoustic signals generated by a vessel as a source may be an alternative. Using a vessel as a seismic source may also offer a low cost and low impact 4D monitoring solution with an opportunity for much more frequent acquisition of time lapse data

especially over permanent receiver installations. This work demonstrates that it is possible to obtain very high-resolution seismic images of the shallow subsurface by using acoustic signals generated by a vessel. This outcome is due to the broadband signals that the vessel generates combined with the fact that these signals are generated continuously while the vessel is moving, allowing for extremely dense source-side sampling along the vessel path.

IMAGING 1,561,449

ULTRA-HIGH RESOLUTION SEISMIC: APPLICATIONS OF P-CABLE IN THE ENERGY TRANSITION

L.MacGregor, L.Scott, R.Cooper and J.Nicholls (Ocean Floor Geophysics Inc). *FIRST BREAK* v.40, no.11, pp.67-70, Nov. 2022. (ISSN 0263-5046; ISSN 1365-2397)

The energy transition brings both challenges and opportunities for geophysicists. As the world transitions away from oil and gas as the primary source of energy, focus is shifting from traditional geophysical applications in hydrocarbon exploration, appraisal and monitoring, to applications in wind farm development, carbon capture and storage (CCS) and marine mineral prospecting. Although very different in some ways, these applications all share the requirement to provide high-resolution images of the shallow sub-seafloor. This requirement is driving the development of ultra-high resolution (UHR) seismic systems capable of characterising the shallow seafloor at metre or sub-metre resolution. The P-cable UHR 3D seismic system is one such approach. Developed by Sverre Planke and Christian Berndt (Planke & Berndt 2003), and commercialised in 2008, P-cable has been applied to the characterisation of hazards (e.g. Brookshire et al, 2015; Kassarie et al., 2017), characterising seep features (Brookshire et al, 2016), marine gas hydrates (for example Hornbach et al, 2012; Rajan et al., 2013), resolution of complex geology and faulting (for example Bellwald et al., 2019; Kasserie et al., 2017) and exploration, appraisal and 4D monitoring of hydrocarbon reservoirs (Hatchell et al., 2019; Smith & Mattox, 2020). With its ultra-high-resolution capabilities, the system is now finding application in both offshore wind farm and CCS settings.

KUWAIT 1,561,450

SEEING THROUGH THE SHEAR ZONE FOR THE FIRST TIME: THE IMPACT OF SEISMIC TECHNOLOGIES ON THE CLARITY OF SEISMIC IMAGE OVER BAHRAH FIELD

A.Mohamed, A.El-Emam, N.Brika, H.Bayri, A.Issa and K.Adeel (Schlumberger; Kuwait Oil Co). *2ND ANNUAL SEG/AAPG APPLIED GEOSCIENCE AND ENERGY INTERNATIONAL MEETING [IMAGE]* (Houston, TX, 8/28/2022-9/1/2022) *ABSTRACTS* pp.2675-2679, 2022. (ISSN 1949-4645; Available at <http://library.seg.org> as of 10/3/2022; **Expanded abstract**)

The Bahrah field in Kuwait, has a complex stratigraphic and structural setting and large heterogeneity of the reservoir quality which are factors controlling the oil accumulation and its production behavior. Seismic data in the study area is heavily contaminated with short- and long-period multiples. These challenges significantly deteriorate the seismic image particularly at the reservoir levels and impact both the structural and stratigraphic interpretation of the Cretaceous and Jurassic targets. The Bahrah field is located at the overlap area between two 3D seismic surveys with distinct acquisition geometries and parameters. These challenges have been addressed by successfully implementing a well-defined seismic processing workflow including technologies such as 5D regularization, 3D surface and internal multiples prediction, tilted transverse isotropic (TTI) depth velocity model building and 3D Kirchhoff depth migration (KDM). This study demonstrates the effectiveness of the applied processing workflows in providing seamless pre-migration merged data of both surveys free of short- and long-period multiples contamination. It also presents the comprehensive TTI depth velocity model building work which successfully integrates borehole geophysical measurements and surface seismic refraction and reflection energies to produce a unified and detailed TTI depth velocity model with accurate time to depth relationship which is an essential requirement for well placement. These workflows also provided a seamless 3D-high resolution KDM image across the original two

seismic surveys with clear definition of major and minor faults and well-preserved amplitude and azimuth information for improved reservoir characterization, leading to more accurate and detailed delineations of Bahrah reserves and better estimation of the reservoirs' properties.

LOGGING WHILE DRILLING 1,561,451

A NEAR-OPTIMAL QUADRATURE FOR 2.5D EM LOGGING-WHILE-DRILLING TOOL MODELING

H.Li, Z.Wu and X.Yue (Maxwell Dynamics Inc; Southwest Petroleum Univ; China Oilfield Svcs Ltd). *JOURNAL OF APPLIED GEOPHYSICS* v.207, Dec. 2022. (ISSN 0926-9851; Article no.104841)

In this paper, we present a novel near-optimal quadrature (NOQ) for 2.5-dimensional (2.5D) electromagnetic (EM) logging-while-drilling (LWD) tool modeling. We first briefly introduce the 2.5D finite difference scheme in anisotropic media. This leads to the inverse Fourier transform (IFT), i.e., integral along the ky plane, to derive the electric components. Then, we propose the near-optimal quadrature derived from an optimized integration path in the complex plane to implement the IFT procedure. We have proved that the selection of the integration nodes and weights is equivalent to finding the rational approximation of 1/ square of s, which is defined from i/ky. Both analytic and 3D solutions have verified the effectiveness and efficiency of the proposed algorithm. Specifically, we show that the number of quadrature points is significantly reduced using the proposed method. Compared to the Gauss-Hermite quadrature, the NOQ can save 75% of the computation time. Therefore, the efficiency of the 2.5D modeling is significantly improved. (c2022 Elsevier B.V.)

LONGMEN FIELD 1,561,452

RTM METHOD OF PRISMATIC-WAVES UNDER THE UNDULATING SURFACE: A CASE STUDY OF THE LONGMEN PIEDMONT

B.Ma, Y.Qu, Z.Li, J.Zhu and C.Liu (China Univ Petroleum). *2ND ANNUAL SEG/AAPG APPLIED GEOSCIENCE AND ENERGY INTERNATIONAL MEETING [IMAGE]* (Houston, TX, 8/28/2022-9/1/2022) *ABSTRACTS* pp.2774-2777, 2022. (ISSN 1949-4645; Available at <http://library.seg.org> as of 10/3/2022; **Expanded abstract**)

The imaging of complex high-steep structural areas in the Piedmont has always been a research hotspot. The ground in the Piedmont area has severe ups and downs, and the lateral speed change is obvious. In order to directly image the complex Piedmont, the reverse time migration technology based on coordinate transformation body meshing has been developed rapidly. Exploration in western China is mostly of various steep geological features, and imaging usually has the problem of insufficient illumination, which cannot capture accurate geological features. Reverse time migration technology is an advantageous imaging method for complex structures, but reverse time migration has certain defects in imaging complex high-steep structures, and the imaging results cannot meet the requirements of geological interpretation. This paper discusses a reverse time migration technique for dealing with prismatic waves on undulating surfaces, which have been found to increase the illumination of steep geological features, where primary waves are not visible. In order to increase the feasibility of this theory, I present the imaging results of field data in the Longmen Piedmont in northwestern Sichuan, China to verify the accuracy of this method for imaging high-steep structures.

LOPPA HIGH 1,561,453

MACHINE LEARNING ASSISTED SEISMIC INTERPRETATION: A CASE STUDY OF THE LOPPA HIGH AREA, BARENTS SEA

L.Dyer and S.Manral (Schlumberger). *FIRST BREAK* v.40, no.11, pp.33-39, Nov. 2022. (ISSN 0263-5046; ISSN 1365-2397)

The interpretation of faults and horizons from seismic data forms a critical part of the geoscience workflow, enhancing our

understanding of the subsurface and ultimately the chance of success in extracting hydrocarbons. The depiction of these vital seismic interpretations has long been restricted to conventional manual and semi-automatic techniques, which require geoscientists to work line by line over ever-expanding volumes of seismic data. The advent of machine learning (ML) and cloud computing technology has revolutionized tasks across multiple industries, enabling the identification of patterns in large multi-factor datasets. In this case study, we predict fault locations using 2D U-Net architecture convolutional neural network (CNNs) and predict horizons by employing radial basis functions (RBFs) and neural networks (NNs). We aim to demonstrate the gains in efficiency and geological insight found using ML technology as the bedrock of the seismic interpretation workflow, through the interpretation of a broadband seismic dataset from the Loppa High area, Barents Sea.

.....
MAGNETIC RESONANCE **1,561,454**

HARMONIC NOISE CANCELLATION OF MAGNETIC RESONANCE SOUNDING SIGNAL BASED ON WAVELET MODULUS MAXIMUM

T.Lin, S.Yu, H.Zhao, Y.Zhang and H.Sun (Jilin Univ). *JOURNAL OF APPLIED GEOPHYSICS* v.207, Dec. 2022. (ISSN 0926-9851; Article no.104839)

Magnetic resonance sounding (MRS) signals are often severely distorted by noise, primarily the power-line harmonics which originates from anthropogenic interferences. Noise cancellation is a particularly important issue for the application of the MRS method. In order to reduce the harmonic peaks as well as the noise floor between the 50 Hz harmonics effectively, a method based on the wavelet modulus maximum is proposed. The method is based on marking the local modulus maximum points in the wavelet transform coefficients and removed the modulus maximum contributed by noise for MRS signal reconstruction. The optimum wavelet basis for noise cancelling is determined through simulations with synthetic signals. The accuracy and stability of the proposed method are investigated using synthetic signals embedded in both artificial and field-recorded noise. In addition, the results of the test on field data show the proposed method can effectively improve the fitting accuracy of the signal parameters and obtain stable inversion results. (c2022 Elsevier B.V.)

.....
MEXICO GULF **1,561,455**

A CASE STUDY OF GENERATING SYNTHETIC SEISMIC FROM SIMULATION TO VALIDATE RESERVOIR MODELS

D.Kumar, J.Zhang, R.Chrisman, N.Islam and M.Le Good (BP). *2ND ANNUAL SEG/AAPG APPLIED GEOSCIENCE AND ENERGY INTERNATIONAL MEETING [IMAGE] (Houston, TX, 8/28/2022-9/1/2022) ABSTRACTS* pp.2512-2516, 2022. (ISSN 1949-4645; Available at <http://library.seg.org> as of 10/3/2022; **Expanded abstract**)

Reservoir models are used to effectively predict and manage the reservoir performance throughout its lifespan. If the models are not calibrated appropriately to all data sources including production, geology and seismic, it can result in misleading interpretation and erroneous production forecasts. Owing to uncertainties related to the subsurface and the limitations of data accessibility, one "best" model is not ideal. An ensemble of models, which considers a range of scenarios based on assumptions of the input reservoir uncertainties is better. In this study from a field in the Gulf of Mexico, seismic amplitudes are known to be less sensitive to the range of reservoir properties but are more sensitive to structural position and fluid contacts. We made use of synthetic seismograms from simulation models (Sim2Seis) to identify the reservoir models that best match the seismic data. The Sim2Seis workflow helped in understanding the uncertainty space of key static variables (structure, fluid contact, and net-to-gross), and guided the selection of more appropriate reservoir models to carry into simulation.

.....
MEXICO GULF **1,561,456**

SUCCESSFUL MODELLING AND SEA TRIAL OF NEW LOW-FREQUENCY SOURCES USING STANDARD ONBOARD AIR

SUPPLY

J.Aznar, B.Kuvshinov, G.Baeten, H.Macintyre, J.Large and S.Ronen (Sercel; Shell Global Solut Int BV; Shell Explor & Prod Co). *FIRST BREAK* v.40, no.11, pp.77-81, Nov. 2022. (ISSN 0263-5046; ISSN 1365-2397)

Typical source vessels used in marine seismic acquisition support the use of multiple large airgun arrays shooting at dense spatial sampling. For example, triple-source surveys using 5000 cui air-gun arrays shooting at 50 m inline shot intervals (16.66 m interval between individual shots) can be acquired by many source vessels currently available on the market. The pneumatic system on the vessel that is required to achieve such a shooting pattern has been well established, containing umbilicals, accumulators and compressors with sufficient capacity. The individual sources in the array are filled with compressed air supplied by the compressors. Air is transported to the sources via several umbilicals. Each airgun array consists of several sub-arrays which are fed by separate umbilicals. The air filling rate, and hence the minimum time interval between consecutive shots and associated inline shot density, is limited by the total capacity of the pneumatic circuit. Over the years, the pneumatic hardware installed on the vessel has been designed to accommodate a large variety of conventional shooting scenarios. However, pneumatic requirements are changing dramatically with the recent advance of dedicated low-frequency sources. In essence, these sources produce low frequencies by injecting a large volume of air into the water. An example of such a low-frequency source is the Tuned Pulse Source (TPS) (Ronen and Chelminski, 2017; Baeten et al., 2019). The air volume emitted by a single TPS source is 28,000 cui (459 litres), which is roughly six times the total volume injected by large conventional airgun arrays. Its environmental impact is, however, much lower than any conventional airgun array (Large et al., 2022). The large volume of injected air produces significantly more low-frequency energy than a conventional airgun array, generating bubbles with a resonance frequency (inversely proportional to the cube root of the injected volume) that is reduced from 8-10 Hz for a typical air gun array down to 2.5-3 Hz. This increase in low-frequency energy is limited in practice by the characteristics of the pneumatic system. Apart from the available compressor capacity, which in many practical cases is difficult (if not impossible) to alter, the properties of the umbilicals and orifices become critical determinants for the shot intervals--and hence the signal-to-noise ratio--that can be achieved. Owing to air friction inside the umbilical the required amount of air cannot be transported fast enough, even if the compressors can supply the necessary volume. In this paper the process of filling the air chamber of the low-frequency source is modelled, and the dependency of the filling time on the length and diameter of the umbilical is analysed. The model results are verified by field data. Also discussed is a new shot controller technology where shots are fired when the pressure in the firing chamber reaches a prescribed threshold--herein referred to as "shooting on pressure".

.....
MEXICO GULF **1,561,457**

APPLICATION OF POSTSTACK IMAGE ENHANCEMENT WITH DIP-GUIDED SELECTIVE STACKING IN SOUTHERN GULF OF MEXICO

J.Ravelo-Cervantes, R.F.Castrejon-Martinez, J.C.Hernandez-Villalobos, R.Ysaccis, S.Hernandez-Jaramillo and D.Saavedra-Castaneda (Schlumberger; Petroleos Mexicanos). *2ND ANNUAL SEG/AAPG APPLIED GEOSCIENCE AND ENERGY INTERNATIONAL MEETING [IMAGE] (Houston, TX, 8/28/2022-9/1/2022) ABSTRACTS* pp.2661-2664, 2022. (ISSN 1949-4645; Available at <http://library.seg.org> as of 10/3/2022; **Expanded abstract**)

We present the results of a model-based post-stack image enhancement methodology using the dip-guided selective stacking method (DGSS) based on Nichols et al., (2017) and applied to a Kirchhoff pre-stack depth migrated image in the southern Gulf of Mexico. For this purpose, we are using the methodology described and followed by Zdraveva et al., (2019). As presented in their work, this methodology offers the benefit of being applicable to virtually any image independently of the migration algorithm used and any post-migration conditioning processes. This makes it a suitable approach for image enhancement to improve interpretability, and

for subsequent processes such as AVO and inversion that are intended for the case study area (Gu et al., 2018).

MEXICO GULF 1,561,458

GEOMETRIC MODE DECOMPOSITION METHOD FOR DIFFRACTION SEPARATION

P.Lin, S.Peng, Y.Xiang, C.Li and X.Cui (China Univ Mining Technol). *2ND ANNUAL SEG/AAPG APPLIED GEOSCIENCE AND ENERGY INTERNATIONAL MEETING [IMAGE] (Houston, TX, 8/28/2022-9/1/2022) ABSTRACTS* pp.2837-2841, 2022. (ISSN 1949-4645; Available at <http://library.seg.org> as of 10/3/2022; **Expanded abstract**)

We propose a new diffraction-separation method that uses a geometry mode decomposition (GMD) algorithm to remove reflections and separate diffractions in the common-offset or poststack domain. The key idea of this method is based on the fact that, in the frequency-wavenumber (f-k) domain, strong reflections concentrate linearly along a certain dip direction whereas weak diffractions are distributed over a wide range of wavenumbers owing to their variable dips in the time-space domain. The Fourier-based GMD algorithm can effectively represent reflections with directional and linear geometric features by adaptively decomposing seismic data as a combination of the band-limited modes consisting of linear characteristics in the f-k domain. Synthetic and field examples demonstrate the good performance of the proposed method in removing strong reflections and separating weak diffractions, providing interpreters with detailed structural and stratigraphic information.

MICROSEISM 1,561,459

AUTOMATIC MICROSEISMIC EVENT LOCATION USING DEEP NEURAL NETWORKS IN ANISOTROPIC MEDIA

Y.Yang, H.Wang, Y.Li, C.E.Birnie and T.Alkhalifah (King Abdullah Univ). *83RD ANNUAL EAGE CONFERENCE (Online and Madrid, Spain, 6/6-9/2022) ABSTRACTS* 2022. (Abstract no.621; Available at <http://www.earthdoc.org> as of 7/7/2022; 5 pp; **Abstract only**)

Accurate microseismic event location offers invaluable insights into the subsurface conditions not only for oil and gas production but also for seismic hazard assessment. Conventional microseismic event location methods face considerable drawbacks like requiring manual traveltimes picking or large computational cost for simulating the wavefields. In fact, the need to locate microseismic events in real time leaves a gap for an automatic and efficient approach. Building on a previously developed method which is based on a deep convolutional neural network for microseismic event location, we propose an extension of such an approach to include the anisotropic nature of the Earth and irregular receiver sampling. Example application on a 2D SEAM time-lapse model illustrates both the accuracy and efficiency of this method. Moreover, we validate the practicability of this approach for both isotropic and anisotropic media considering that the Earth is predominantly anisotropic. Equally important, we demonstrate that this approach is not only feasible for the cases with a uniform receiver distribution, but also applicable to cases where the passive seismic data are acquired with irregularly spaced receivers.

MISSISSIPPI CANYON AREA 1,561,460

SIMULATING LARGE-SCALE STREAMER AND OBN ACQUISITION OVER SUBSALT TARGETS - AN EXAMPLE OF SUCCESSFUL REMOTE COLLABORATION BETWEEN SURVEY DESIGN AND SURVEY EVALUATION

D.Ridyard, D.Monk, D.Hite, L.Zuhlsdorff and T.Haugland (ACTeQ; NORSAR). *FIRST BREAK* v.40, no.11, pp.71-76, Nov. 2022. (ISSN 0263-5046; ISSN 1365-2397)

In this article we look at how ray-based wavefront modelling can be used to evaluate competing acquisition techniques with significantly different illumination properties and associated acquisition cost. We compare subsurface illumination of complex sub-salt reservoirs typical of those found in the Gulf of Mexico for a variety of towed-streamer and full azimuth long offset ocean bottom

node surveys. Single, dual and triple azimuth towed-streamer surveys are considered. This project was accomplished using a new connector between ACTeQ's survey design and optimization software and Norsar's 3D modelling software. This project is an excellent example of competitors collaborating to better achieve a customer's needs. The project was also accomplished in a fully remote environment, and none of the authors were in the same city at any time during the project. Remote collaboration is becoming an increasingly effective low-carbon approach to complex challenges.

MISSISSIPPI CANYON AREA 1,561,461

REGULARIZATION BY ROBUST DENOISING FOR ITERATIVE SIMULTANEOUS SOURCE SEPARATION

B.Bahia and M.D.Sacchi (Alberta Univ). *2ND ANNUAL SEG/AAPG APPLIED GEOSCIENCE AND ENERGY INTERNATIONAL MEETING [IMAGE] (Houston, TX, 8/28/2022-9/1/2022) ABSTRACTS* pp.2626-2630, 2022. (ISSN 1949-4645; Available at <http://library.seg.org> as of 10/3/2022; **Expanded abstract**)

Denoisers can improve the solution of general inverse problems via the regularization by denoising (RED) framework. Since many simultaneous source separation workflows are combinations of inversion and denoising methods, deblending stands out as an application of interest for RED. However, a critical point for iterative deblending is that little to no blending interference should leak into the signal space at the end of each iteration of the inversion. The non-Gaussian character of the blending noise points to denoisers that have strong noise reduction capabilities associated with robust statistics. This paper shows how robust denoisers can improve RED's performance in simultaneous sources separation by comparing the classic and robust versions of the Fourier thresholding in numerically blended examples.

MORRIS JESSUP RISE 1,561,462

GEOPHYSICAL INSIGHTS ON THE CRUSTAL STRUCTURE OF GREENLAND'S NORTHERN CONTINENTAL MARGIN TOWARDS THE MORRIS JESUP SPUR

A.Brotzer, T.Funck, W.H.Geissler, K.Piepjoh, I.Heyde and K.Berglar (Alfred Wegener Inst; Denmark Greenland Geol Sur; Fed Inst Geosci Nat Rscs). *TECTONOPHYSICS* v.843, 11/20/2022. (ISSN 0040-1951; Article no.229588)

During expedition PS115/1, the German research vessel Polarstern acquired seismic refraction data along a 102-km-long profile crossing Greenland's northern continental margin and extending up to the southwestern limit of the Morris Jesup Spur. A P-wave velocity model is obtained and validated by gravity modelling. A nearby seismic reflection line provides insights on the structures within the sedimentary cover. Beneath a 2-km-thick sedimentary cover with velocities of 1.8 km/s to 3.4 km/s, an up to 1.5-km-thick layer is characterized by velocities of 4.2 km/s and is interpreted to consist of volcanic rocks. This is consistent with proposed volcanic activity on the Morris Jesup Spur and exposed volcano-sedimentary rocks of the nearby Kap Washington Group. Below the volcanic rocks, an up to 7 km-thick unit with velocities of 4.4 to 5.8 km/s is interpreted to consist of metasedimentary rocks still belonging to the deformed units of the Franklinian Basin. The seismic reflection data image a tectonic overprint of the acoustic basement and the lowermost sedimentary layers. Tectonic faults indicating the tectonic overprint do not reach to the uppermost sedimentary layers. This hints at an older fracture zone that is also observed in the velocity model and aligns well with observed anomalies in the regional gravity and magnetic fields. The seismic velocity model reveals a highly extended continental crust that shows a magmatic overprint at all crustal levels. The upper crust is 5 km thick with a velocity of 6.0 km/s. However, in three distinct zones its thickness is up to 8 km and the velocity increases to 6.3 km/s. These zones are interpreted as magmatic intrusions into the upper crust. The lower crust represents a 9-km-thick high-velocity layer (7.2 km/s) that is interpreted as magmatic underplating or lower crustal sill intrusions. Such a high-velocity lower crust is not present in models of adjacent Arctic margins. (c2022 The Authors. Elsevier B.V.)

MULTIPLE REFLECTION**1,561,463****RESEARCH ON JOINT IMAGING OF PRIMARIES AND INTERNAL MULTIPLES BASED ON RTM**

Z.Li, S.Peng, Y.Ding, N.Qin, Z.Li, G.Tan, X.Chen and W.Wang (China Univ Petroleum; Sinopec Shengli Oil Co). *83RD ANNUAL EAGE CONFERENCE (Online and Madrid, Spain, 6/6-9/2022) ABSTRACTS* 2022. (Abstract no.627; Available at <http://www.earthdoc.org> as of 7/7/2022; 5 pp; **Abstract only**)

The existence of internal multiples has brought great influence to seismic data imaging. They are regarded as noise in conventional data processing, which need to be suppressed before imaging. However, the current suppression methods are usually of low accuracy with high costs. Considering that the internal multiples are also real reflections from the interfaces which contain abundant structural information, RTM can handle their imaging but with image artifacts introduced. Therefore, to avoid the high costs in internal multiple suppression and to eliminate the influence of internal multiples in imaging, deep research on the joint imaging of primaries and multiples based on RTM has been done in our manuscript. Firstly, the cause of the image artifacts in joint imaging is analysed. Then, strategies are proposed to solve the image artifacts in joint imaging of primaries and internal multiples. Finally, the feasibility and effectiveness of the proposed method are verified by numerical examples. The proposed method can realize the elimination of image artifacts in the image domain instead of the high-cost suppression of internal multiples in the pre-stack data domain, which has very important practical meaning, the migration of internal multiples may bring potential advantages to the imaging in complex cases.

MULTIPLE REFLECTION**1,561,464****GENERALIZED INTERNAL MULTIPLE ELIMINATION**

D.Zhang, C.Tsingas and M.S.Almubarak (Saudi Aramco). *2ND ANNUAL SEG/AAPG APPLIED GEOSCIENCE AND ENERGY INTERNATIONAL MEETING [IMAGE] (Houston, TX, 8/28/2022-9/1/2022) ABSTRACTS* pp.2817-2821, 2022. (ISSN 1949-4645; Available at <http://library.seg.org> as of 10/3/2022; **Expanded abstract**)

Correlation and convolution based internal multiple prediction is one of the most common methods to predict and subsequently attenuate internal multiples. Such technique is limited to the raypath of internal multiple that satisfy the "low-high-low" concept setting. In order to fulfill this condition, one straightforward way is to split (mute) the data into shallow and deep parts according to a phantom horizon. Internal multiples whose ray paths pass through the phantom horizon four times are predicted; and only one horizon can be set for each prediction trial. To overcome this drawback, we propose a generalized internal multiple prediction (GIMP) algorithm based on correlation and convolution by setting lower and upper limits of integration. GIMP does not require explicit horizon picks in order to separate the input data into different portions. It is a generalized process and it can predict all possible internal multiples at once.

MULTIPLE REFLECTION**1,561,465****TOWARDS UNDERSTANDING THE IMPACT OF THE EVANESCENT ELASTODYNAMIC MODE COUPLING IN MARCHENKO EQUATION-BASED DEMULTIPLE METHODS**

M.Dukalski, C.Reinicke and K.Wapenaar (Aramco Research Center; Delft Univ Technol). *2ND ANNUAL SEG/AAPG APPLIED GEOSCIENCE AND ENERGY INTERNATIONAL MEETING [IMAGE] (Houston, TX, 8/28/2022-9/1/2022) ABSTRACTS* pp.2827-2831, 2022. (ISSN 1949-4645; Available at <http://library.seg.org> as of 10/3/2022; **Expanded abstract**)

Marchenko equation-based methods promise data-driven, true-amplitude internal multiple elimination. The method is exact in 1-D acoustic media; however, it needs to be expanded to account for the presence of 2-D and 3-D elastodynamic wavefield phenomena, such as compressional (P) to shear (S) mode conversions, total reflections or evanescent waves. Mastering high waveform-fidelity methods such as this could further advance amplitude vs. offset

analysis and lead to improved reservoir characterization. This method expansion may comprise of re-evaluating the underlying assumptions and/or appending the scheme with additional constraints (e.g., minimum phase). To do that, we may need to better understand the construction of the Marchenko equation solutions, the so-called focusing functions, in a mathematically simple and numerically stable fashion. The latter could be a challenge at large angles of incidence where the elastodynamic effects and evanescent waves start playing a dominant role. We demonstrate that the elastodynamic focusing functions are the bridge between the Marchenko equation theory and the transfer matrix formalism. Using the latter, we show how we can try to gain further insights into how time-reversal (correlations) behaves when either of the elastic modes becomes evanescent. We also show how this construction allows us to shed light on into the mathematical properties of elastodynamic inverse transmissions, which takes us a step closer towards understanding the reconstruction of the elastodynamic minimum phase.

MULTIPLE REFLECTION**1,561,466****INTERNAL MULTIPLE ELIMINATION WITH AN INVERSE-SCATTERING THEORY GUIDED DEEP NEURAL NETWORK**

Z.Gu, L.Tao, H.Ren, R.S.Wu and J.Geng (Tongji Univ; Zhejiang Univ; Calif Univ, Santa Cruz). *2ND ANNUAL SEG/AAPG APPLIED GEOSCIENCE AND ENERGY INTERNATIONAL MEETING [IMAGE] (Houston, TX, 8/28/2022-9/1/2022) ABSTRACTS* pp.2832-2836, 2022. (ISSN 1949-4645; Available at <http://library.seg.org> as of 10/3/2022; **Expanded abstract**)

Deep neural networks can automatically mine specific features from seismic data, which can be used in the process of multiple elimination. Surface-related multiple elimination (SRME) can provide good labels for the neural network based multiple elimination. Different from SRME, it is difficult to distinguish internal multiples from primary reflections when the subsurface is complex. An extended single-sided autofocusing guided by inverse-scattering theory is introduced to remove internal multiples in a data-driven manner. In this study, we explore the potential of neural networks in identifying the internal multiples with the guidance of inverse-scattering theory. We feed the neural network with training data, consisting of the shot records with internal multiples, and the primary-only datasets as labels, which are generated by an extended single-sided autofocusing method. The primary-only labels can be beneficial to the U-net framework. The test results show that internal multiple elimination via the neural network takes the advantage of the extended single-sided autofocusing method and is cheaper when the neural network is well-trained. The corresponding reverse time migration (RTM) results show the validity of our work.

NETHERLANDS**1,561,467****ASSESSING PROPERTIES OF INTERNAL MULTIPLES FOR DIFFERENT GEOLOGIES**

P.Ras, M.Davydenko and E.Verschuur. *2ND ANNUAL SEG/AAPG APPLIED GEOSCIENCE AND ENERGY INTERNATIONAL MEETING [IMAGE] (Houston, TX, 8/28/2022-9/1/2022) ABSTRACTS* pp.2882-2886, 2022. (ISSN 1949-4645; Available at <http://library.seg.org> as of 10/3/2022; **Expanded abstract**)

Before processing and imaging seismic data, a proper understanding of the expected multiple reflection behavior can be crucial for a successful project. We combine 1D acoustic zero offset modeling, based on travel-time and amplitude analysis, with 1D acoustic full wavefield modeling to analyze internal multiples in terms of generators, velocities, relative strength and complexity of the interference pattern. This combined modeling methodology is tested on three earth models from different geologies and should be helpful when assessing potential effective multiple attenuation methods.

NOISE REDUCTION 1,561,468

AIDING SELF-SUPERVISED COHERENT NOISE SUPPRESSION BY THE INTRODUCTION OF SIGNAL SEGMENTATION USING BLIND-SPOT NETWORKS

S.Liu, C.Birnie, T.Alkhalifah and A.Bakulin (King Abdullah Univ; Saudi Aramco). *2ND ANNUAL SEG/AAPG APPLIED GEOSCIENCE AND ENERGY INTERNATIONAL MEETING [IMAGE]* (Houston, TX, 8/28/2022-9/1/2022) ABSTRACTS pp.2857-2861, 2022. (ISSN 1949-4645; Available at <http://library.seg.org> as of 10/3/2022; **Expanded abstract**)

Blind-spot networks have been shown to be natural noise suppressors under the assumption that noise is unpredictable based on the information fed into the network during training. Trained in a self-supervised manner, such approaches only utilize the original raw data to determine to remove the noise. In this work, we propose two novel elements for enhancing blind-spot denoising: (1) the introduction of a 2-class segmentation task to aid the network in identification of interest areas of signals that require particular attention during denoising; and (2) the introduction of a trace-wise noise mask designed to obscure the coherency of noise from being observed by the network. The joint scheme is achieved by introducing a joint loss function to balance between the two deep learning tasks. As such, the final joint scheme is the combination of a self-supervised, blind-spot denoising procedure and a supervised segmentation procedure. We illustrate how the joint scheme can improve the denoising performance of the network, hypothesizing that this is due to the introduction of prior information guiding the denoising procedure to areas of focus. Preliminary results from synthetic data contaminated by trace-wise noise, show an increase in the structural similarity index from 0.989 to 0.995, when comparing the optimal joint-scheme versus the pure denoising procedure. Future work will extend the procedure to field data where rule-based approaches will be used to generate the segmentation labels.

NORTH SEA 1,561,469

CAN SHALLOW SANDS BE RECOGNIZED BY SEISMIC INVERSION?

C.F.Gyllenhammar. *FIRST BREAK* v.40, no.12, pp.47-50, Dec. 2022. (ISSN 0263-5046; ISSN 1365-2397)

Seismic reflection and inversion are based on a wave being reflected from an interface where there is velocity and density contrast to give the acoustic impedance and the corresponding reflection coefficient. The acoustic impedance is the sum of the velocity and density. It has been shown that of the two parameters, the velocity difference is by far the most important for the reflection coefficient (Gardner, 1974). With respect to seismic inversion, it is not the acoustic impedance contrast that is important, but rather the sonic-density ($\Delta t, \rho_{ob}$) pair. The sand-shale contrast in a siliciclastic environment is governed by where the sonic-density pair is placed in the sonic-density cross-plot. Regardless of the acoustic impedance and the corresponding reflection coefficient, a sand will become a shale in the inversion process unless the sonic-density pair is plotted along the clean sand line. In this paper, I demonstrate that in North Sea sands shallower than 1500 m, the corresponding sonic-density pair seldom plots on the clean sand line, rather suggesting that it is a mudstone.

NORTH SEA 1,561,470

DECONVOLUTION OF UPGOING AND DOWNGOING WAVEFIELDS: A DATA EXAMPLE FROM THE NOAKA OBN EXPERIMENT

T.Seher, H.Masoomzadeh, Y.Ren, S.Baldock and B.Wang (TGS). *2ND ANNUAL SEG/AAPG APPLIED GEOSCIENCE AND ENERGY INTERNATIONAL MEETING [IMAGE]* (Houston, TX, 8/28/2022-9/1/2022) ABSTRACTS pp.2807-2811, 2022. (ISSN 1949-4645; Available at <http://library.seg.org> as of 10/3/2022; **Expanded abstract**)

Ocean bottom node surveys are popular tools for both seismic exploration and monitoring due to the possibility for superior imaging and velocity model building compared to towed streamer surveys. In addition, the size of ocean bottom experiments has been

increasing. This increase in frequency and survey size requires efficient processing solutions for attenuating free surface effects such as ghosts and multiples both in terms of usability and computing requirements. Traditionally, these processing steps were implemented by up-down wavefield separation to target the receiver-side effects, followed by separate source-side deghosting and demultiple. We have recently adopted the combination of up-down wavefield separation with up/down deconvolution or downgoing wavefield deconvolution as an alternative due to the simplicity of the process and the high quality of the results. In this paper, we review up/down deconvolution as a demultiple and deghosting method for the upgoing wavefield and describe downgoing wavefield deconvolution as a similar process for the downgoing wavefield. Moreover, we perform both up/down deconvolution and downgoing wavefield deconvolution in a single processing flow. This combination simplifies the processing sequence, decreases the human effort, and reduces processing turnaround compared to our legacy solution. While being more user-friendly, our new solution has conserved the advantages of the legacy solution and delivers complimentary images using the up- and downgoing wavefields. Crucially for regions with a shallow seafloor, the downgoing wavefield permits superior imaging of the shallow subsurface.

NORTH SEA 1,561,471

VZ DENOISE AND P/Z MATCHING IN 3D CURVELET DOMAIN

Y.Ren, C.Yang, T.Seher, M.Hawke and E.Cho (TGS). *2ND ANNUAL SEG/AAPG APPLIED GEOSCIENCE AND ENERGY INTERNATIONAL MEETING [IMAGE]* (Houston, TX, 8/28/2022-9/1/2022) ABSTRACTS pp.2862-2866, 2022. (ISSN 1949-4645; Available at <http://library.seg.org> as of 10/3/2022; **Expanded abstract**)

Ocean bottom node (OBN) seismic data processing commonly uses the combination of hydrophone (P) and vertical geophone (Z) components to separate upgoing and downgoing wavefields while attenuating ghosts and multiples. Because the vertical components are often contaminated by strong converted shear waves due to the scattering in the shallow subsurface, a good Vz noise removal is crucial for better P/Z calibration, wavefield separation and deconvolution. Most importantly, a better wavefield separation will in turn improve the quality of the seismic images. This paper will present a novel method of simultaneous Vz noise attenuation and P/Z calibration in the 3D curvelet domain. Furthermore, we will demonstrate that our new 3D method outperforms a 2-pass 2D curvelet approach. We will also assess the effect and necessity of Vz attenuation prior to shot carpet regularization. Both investigations are supported by field data examples from the Utsira OBN project.

NORWEGIAN SEA 1,561,472

A NOVEL APPROACH TO TRAIN SELF-SUPERVISED SEISMIC DENOISING DNN ARCHITECTURES

J.Romero, D.Oikonomou and O.Ibrahim (Earth Science Analytics). *FIRST BREAK* v.40, no.12, pp.71-77, Dec. 2022. (ISSN 0263-5046; ISSN 1365-2397)

Removing noise from seismic data is of prime importance for seismic processing workflows and is a matter of continuous research in the academic community. The challenging part of suppressing seismic noise is the diverse nature of seismic noise: it is found as a combination of random and coloured noise, which can be both structured and unstructured. Algorithms based on signal decomposition, domain transformation, and filtering, among others, have been successful for specific imaging targets, and hence they mostly identify a specific seismic noise component. Recently, convolutional neural network (CNN)-based denoisers have greatly outperformed standard denoising techniques mostly in natural and medical imaging applications. Furthermore, self-supervised frameworks have been proposed as a clever alternative to denoising when no ground truth exists. This work leverages four state-of-the-art U-Net-type architectures in a novel self-supervised fashion to remove seismic noise. The training seismic data corresponds to a generous number of real seismic surveys. For labelling, trace-wise corruption is applied to patches of the input data, so the CNN

learns to predict the corrupted tracts based on the receptive field. Our findings indicate that self-supervised learning using U-Net-type architecture trained on real data is able to considerably remove both structured and unstructured seismic noise.

NUMERICAL INVERSION 1,561,473

MULTIMODAL INVERSION OF RAYLEIGH WAVE DISPERSION CURVES BASED ON A GENERALIZED MISFIT FUNCTION

D.Zhang, B.Yang, Z.Yang, M.Zhang, Z.Xiong, D.Zhu and X.Zhang (Central South Univ (China); Southern Univ Sci Technol; HYDROCHINA Xibei Eng Corp). *JOURNAL OF APPLIED GEOPHYSICS* v.207, Dec. 2022. (ISSN 0926-9851; Article no.104849)

Fundamental mode dispersions, particularly higher ones obtained from weak and hard interlayers, are usually used for inversion to obtain the S-wave velocity profile. Higher mode dispersions are more informative for surface-wave inversion, thus benefiting both inversion stability and model resolution. In the multimodal inversion of the Rayleigh wave dispersion curves, the conventional root-mean-square based misfit function (RMF) is often deviated when the dispersion modes are misidentified. Alternatively, the inversion based on the determinant misfit function (DMF) may avoid misidentifications, but will still be limited to its inherent local minima. In order to reduce this complexity, the paper presents a generalized misfit function (GMF) for estimating the S-wave velocity profile. The generalized function allows for the inversion of both fundamental and higher modes dispersion, without mode-numbering. Before the inversion, the dispersion points are divided into the recognizable fundamental mode dispersion points and others. The RMF is then calculated using data from distinct fundamental mode dispersion, while the DMF was calculated using data from other points. Lastly, the RMF and the DMF were combined to form the GMF by normalizing. The results are based on both theoretical and real data sets and confirm the advantages of GMF in mode identification and inversion accuracy compared to both RMF and DMF. (c2022 Elsevier B.V.)

NUMERICAL INVERSION 1,561,474

ONE-WAY WAVEFORM INVERSION (OWI)

A.Ben Hassine, V.Duprat, R.Baina and D.Brito (OPERA; Pau Univ). *83RD ANNUAL EAGE CONFERENCE (Online and Madrid, Spain, 6/6-9/2022) ABSTRACTS 2022*. (Abstract no.632; Available at <http://www.earthdoc.org> as of 7/7/2022; 5 pp; **Abstract only**)

Reflection waveform inversion (RWI) has become an efficient method to generate low-wavenumber velocity models. It has shown a better performance for updating the deep model structures compared to the standard full waveform inversion (FWI). However, RWI is well known to suffer from the slow convergence problem making it high computational demanding. Time consistent wave equation inversion (TWIN) has recently been proposed to mitigate this problem by considering the consistency between velocity-depth positioning. Nevertheless, both RWI/TWIN rely on the assumption of the scale separation which requires a sufficiently smooth background velocity model. In case of lack of smoothness, the background velocity model will generate reflections that cannot be matched to the observed data. This issue may lead to a noisy sensitivity kernel that adds more non-linearity to the inversion scheme. In addition, the forward modeling which is an essential component of RWI/TWIN still represents an overburden step because solving the wave equation using the two-way propagator is highly expensive. In this proposal, we introduce an alternative to the two-way wave equation by using a one-way approach for the reflection waveform inversion. After a brief theoretical description of the one-way waveform inversion (OWI), we validate its accuracy on Chevron SEG 2014 benchmark.

OCEAN BOTTOM SEISMIC 1,561,475

THE MAKING OF A NODE

E.Hager, L.Combee, V.Jaavold and V.Husom (Shearwater

GeoServices). *FIRST BREAK* v.40, no.11, pp.55-60, Nov. 2022. (ISSN 0263-5046; ISSN 1365-2397)

Using wireless technology and super-efficient power management with intelligent charging and data harvesting, the node has been made as robust as possible with a very long operational life. A simple form factor lends itself to configuration for operational and environmental conditions. High-quality measurements are achieved through state-of-the-art sensors. It all adds up to an OBN (ocean bottom node) solution that satisfies all users: geophysical, commercial, and operational.

OCEAN BOTTOM SEISMIC 1,561,476

SUB-L(1) NORM REGULARIZED INVERSION DEBLENDING IN LOCAL 3D FK DOMAIN FOR OCEAN-BOTTOM NODE DATA

J.Sun, Z.Liu, M.Guo, G.Stock and B.Wang (TGS). *2ND ANNUAL SEG/AAPG APPLIED GEOSCIENCE AND ENERGY INTERNATIONAL MEETING [IMAGE] (Houston, TX, 8/28/2022-9/1/2022) ABSTRACTS* pp.2616-2620, 2022. (ISSN 1949-4645; Available at <http://library.seg.org> as of 10/3/2022; **Expanded abstract**)

Inversion deblending in a sparse transformed domain is an important approach to obtain high quality deblended data for simultaneous source acquisition. For ocean bottom node data, more than one vessel with multiple sources are used to reduce acquisition duration and increase shot density, but the increased blending fold tends to make the inversion solution unstable and less accurate. We present a new method and some tips to improve the stability and accuracy of inversion deblending for node data and demonstrate application on two different surveys. This new method uses sub-L(1) norm for regularization in the objective function, the Iterative Shrinkage-Thresholding Algorithm (ISTA) to solve for the deblended model, and time-variant local 3D FK transform to promote sparsity. Some pointers for improving deblending performance on field data are provided as well.

ORPHAN BASIN 1,561,477

ESTIMATING RELIABLE EARTH PROPERTIES FROM SIMULTANEOUS VELOCITY AND REFLECTIVITY INVERSION

Y.Yang, S.Arasanipalai, N.Chemingui and N.Montevicchi (PGS; Newfoundland Oil Gas Corp). *FIRST BREAK* v.40, no.12, pp.65-70, Dec. 2022. (ISSN 0263-5046; ISSN 1365-2397)

Seismic attributes are widely used in hydrocarbon exploration and play a key role in identifying prospects. Seismic inversion, particularly velocity and reflectivity, has typically been the solution for deriving earth models, which are then used to calculate these attributes. Traditionally, a workflow using full waveform inversion (FWI) followed by least-squares reverse time migration (LS-RTM) has been employed to invert for subsurface velocity and reflectivity models. Recently, Yang et al. (2021) introduced a new scheme that combines both inversions into a single process. A key aspect of the new solution is the separation of the low- and high-wavenumber components of the earth model, which enable the inversion to simultaneously update the velocity and reflectivity with minimal crosstalk. This approach is equivalent to performing FWI and LS-RTM simultaneously, where both velocity and reflectivity are continuously updated at each iteration. The iterative inversion compensates for incomplete acquisitions and varying illumination in the subsurface to provide true-amplitude earth reflectivity. The high-fidelity velocity and reflectivity models are then readily available for quantitative interpretation (QI). Moreover, they are employed to derive additional earth attributes--mainly relative impedance and density--to assess prospectivity. In this study, we demonstrate how simultaneous inversion can deliver reliable velocity and reflectivity models for interpretation using 3D seismic data from the Orphan and Salar Basins, offshore Newfoundland and Labrador, Canada. Also, we show how additional properties such as relative impedance and relative density can be estimated directly from the inverted models. With more reliable attributes, more insights into prospectivity can be obtained beyond the capabilities of conventional processing.

PELOTAS BASIN 1,561,478

CORRELATION BETWEEN HOMOLOGOUS BASINS IN THE SOUTHERN ATLANTIC INDICATES GREAT POTENTIAL FOR THE SOUTHERN PELOTAS BASIN IN BRAZIL

P.V.Zalan, R.Etherington and M.Cvetovic (ZAG Consulting; TGS). *FIRST BREAK* v.40, no.11, pp.61-66, Nov. 2022. (ISSN 0263-5046; ISSN 1365-2397)

The dense grid of 2D seismic data in the Southern Pelotas Basin enabled the identification and mapping of several potential prospects of mostly Late Cretaceous age. The most important ones are those interlayered with the source rocks, as demonstrated by the Brulpadda, Luiperd, and Venus discoveries. All of them were first identified by their turbidite-like geometries with associated bright spots. The confirmation of the anomalously low-velocity character of the bright spots was obtained by the sweetness attribute. DHIs were then obtained by the (F-N)*F attribute, unfolding Types III and IV AVOs. The correlation with the Orange Basin in Namibia and the occurrence of so many stratigraphic prospects of great dimensions indicate that the Southern Pelotas Basin is a potential petroleum-rich frontier that deserves the immediate attention of the petroleum industry and the drilling of deep wells in its deep and ultra-deep waters.

PENGLAI FIELD 1,561,479

PREDICTION AND REMOVAL OF INTERNAL MULTIPLES USING AN IMPROVED CFP APPROACH

Z.Jiang, Y.Yao and P.Zhang (Bohai Oilfield Res Inst). *2ND ANNUAL SEG/AAPG APPLIED GEOSCIENCE AND ENERGY INTERNATIONAL MEETING [IMAGE]* (Houston, TX, 8/28/2022-9/1/2022) ABSTRACTS pp.2877-2881, 2022. (ISSN 1949-4645; Available at <http://library.seg.org> as of 10/3/2022; **Expanded abstract**)

Prediction and removal of multiples play an important role in the geophysical exploration. Currently, study on multiples mainly lies on the surface multiples. We focus on extending the shot and receiver to the interface to generate internal multiples or to the nearby interface to realize the reconstruction of the base level. The reconstructed base level is considered as a new free surface. Using Surface-Related Multiple Suppression (SRME) method, we first forecast the internal multiples on each layer, and then we remove the multiples using matching and subtracting methods. We apply the proposed approach and workflow to synthetic and real data, which illustrates the internal multiples are predicted and removed well using the proposed approach.

PERSIAN GULF 1,561,480

SUPERVISED LEARNING APPROACH FOR MULTI-COMPONENT DEGHOSTING WITH A FOCUS ON SHALLOW WATER DATA

R.H.Baardman, J.Yoo and R.F.Hegge (Aramco Overseas Co BV). *FIRST BREAK* v.40, no.12, pp.51-57, Dec. 2022. (ISSN 0263-5046; ISSN 1365-2397)

In recent years, the use of machine learning (ML) has shown more and more successful applications, initially mainly in seismic interpretation (classification) but recently also in seismic processing challenges (regression) like denoising, interpolation and demultiple. In this paper, a supervised ML algorithm is proposed for receiver deghosting on multi-component data. A neural network is trained to map input pairs of hydrophone and geophone data into the deghosted up-going wavefield. This data-driven approach could offer a user-friendly alternative to existing deghosting methods, such as the PZ-summation approach, which is commonly used for multi-component streamer and ocean-bottom acquisitions. Although the PZ-summation approach offers an analytical solution to the deghosting problem, it requires some pre-processing steps that make it more time-consuming and user-intensive to run and to perform quality control on. The advantage of the proposed ML approach is that it can be directly applied to multi-component data without any parameterization. However, the success of the supervised method strongly depends on whether a neural network can be trained easily with minimal user-interaction and can be applied to various types of (field) data without adapting the

network for each individual case. To investigate if this is possible for the supervised multi-component receiver deghosting method, the selected neural network is trained on easy-to-model 1.5D data examples and applied to test data with increasing complexity. Results are very encouraging and evaluated to be at least on par with the existing PZ-summation deghosting method.

PETROPHYSICS 1,561,481

DEVELOPMENT OF MULTI-MODAL/MULTI-DIMENSIONAL IMAGE REGISTRATION TOOLS

M.Sarhan, L.A.Hathon, M.Myers and A.Arad (Houston Univ; Automated Analytics LLC). *2ND ANNUAL SEG/AAPG APPLIED GEOSCIENCE AND ENERGY INTERNATIONAL MEETING [IMAGE]* (Houston, TX, 8/28/2022-9/1/2022) ABSTRACTS pp.2498-2501, 2022. (ISSN 1949-4645; Available at <http://library.seg.org> as of 10/3/2022; **Expanded abstract**)

Understanding petrophysical properties is crucial in assessing subsurface reservoirs and exploiting hydrocarbon reserves. Modeling these properties using imaging and image analysis techniques when measurements cannot be made is becoming more common in industry as numerous imaging techniques that span a range of scales have become more widely available. Coupling information at different scales will lead to not only upscaling results from the pore to core and log scale but also to better understanding of the pore and grain structure of the formation, and thereby, its petrophysical properties. Accordingly, a range of registration techniques have been developed to integrate data from various imaging modalities. However, some challenges remain in rigorous registration due to artifacts arising from experimental procedures. Thus, this study aims to develop an image registration workflow linking the various imaging modalities by employing a proper mathematical optimization process to minimize spatial errors to acceptable limits.

QIANGTANG BASIN 1,561,482

PLACING ANOTHER PIECE OF THE TETHYAN PUZZLE: THE FIRST PALEOZOIC PALEOMAGNETIC DATA FROM THE SOUTH QIANGTANG BLOCK AND ITS PALEO GEOGRAPHIC IMPLICATIONS

B.Wei, X.Cheng, M.Domeier, N.Jiang, Y.Wu, W.Zhang, K.Wu, B.Wang, P.Xu et al. (Northwest Univ, China). *TECTONICS* v.41, no.10, Oct. 2022. (ISSN 0278-7407; ISSN 1944-9194; Article no.e2022TC007355)

The origin and drift history of the South Qiangtang block (SQB) is critical to understanding the internal dimensions and kinematics of the late Paleozoic to early Mesozoic Tethyan realm and the subsequent evolution of the Qinghai-Tibet Plateau, but so far no paleomagnetic data constrain the SQB in Paleozoic time. Here we present a paleomagnetic study of the middle Permian volcanic and sedimentary rocks from the SQB. Well-defined high-temperature components of magnetization were isolated from 6 sites of tuffaceous sandstone and 9 sites of basalt, but their directional populations are distinct. On the basis of a conglomerate test and comparisons with younger paleomagnetic data, we argue the basalts preserve a primary magnetization, whereas the sandstones may have been remagnetized during the Triassic. The magnetic directions from the basalt indicate that the SQB was located at a latitude of $22.3 \pm 5.8^\circ\text{S}$ during the middle Permian. Together with existing paleomagnetic data from other Tethyan continental blocks, this new constraint reveals that during the middle Permian the Neo-Tethys Ocean spanned ca. $10\text{-}20^\circ$ of latitude and the Paleo-Tethys Ocean spanned ca. 50° , but also that the latter was a composite ocean system which included at least two important branches. In further considering the geological records of the SQB, we propose the block rifted from the northern margin of Gondwana during opening of the Neo-Tethys in early Permian time, and then drifted rapidly northward until ultimately colliding with the North Qiangtang block and the southern margin of Laurasia during final closure of the Paleo-Tethys in the Triassic.

Q MEASURING

1,561,483

Q-COMPENSATED LEAST-SQUARES REVERSE TIME MIGRATION BY CONSIDERING VELOCITY AND Q PERTURBATIONS

J.Li, Y.Qu, C.Huang and Z.Li (China Univ Petroleum). *2ND ANNUAL SEG/AAPG APPLIED GEOSCIENCE AND ENERGY INTERNATIONAL MEETING [IMAGE] (Houston, TX, 8/28/2022-9/1/2022) ABSTRACTS* pp.2754-2758, 2022. (ISSN 1949-4645; Available at <http://library.seg.org> as of 10/3/2022; **Expanded abstract**)

The subsurface medium has severe viscoelasticity, leading to a strong absorption and attenuation effect on seismic waves. Q attenuation leads to weak amplitude and misplacement of reflectors in images. Numerous acoustic LSRTM methods have been proposed by only considering the perturbation of the Q parameter. In this paper, we propose a viscoacoustic least-squares reverse time migration with velocity and Q perturbations to produce the velocity and Q images simultaneously. In this method, a second-order weak viscoacoustic quasi-differential equation, which can be easily transformed between Q-compensation and Q-attenuation versions, is applied to derive the Q-attenuated linear Born operator, the Q-compensated adjoint operator, and the Q-compensated gradient equation. Numerical examples on two synthetic data sets demonstrate that with the iterations, the proposed viscoacoustic least-squares reverse time migration with velocity and Q perturbations produces better images of velocity and Q with high resolution, high SNR, balanced imaging amplitude, and few acquisition footprints.

Q MEASURING

1,561,484

INTERVAL Q FACTOR ESTIMATION BASED ON AN IMPROVED FREQUENCY SHIFT METHOD

J.Zhang, J.Li, S.Wang, W.Cheng, W.Geng, F.Wu and W.Tang (China Univ Petroleum). *JOURNAL OF APPLIED GEOPHYSICS* v.207, Dec. 2022. (ISSN 0926-9851; Article no.104853)

To characterize seismic attenuation information quantitatively, the quality factor Q is routinely used in seismic exploration. To obtain a more reliable Q value than the peak frequency shift (PFS) method, the improved frequency shift (IFS) method computes the peak frequency by the centroid frequency (CF) to improve the noise immunity. However, the IFS method assumes all wavelets are the standard Ricker shape and ignores the effect of attenuation on the wavelet, which greatly affects the accuracy of estimated Q values, especially in interlayer computations. Some analytical methods try to replace the original hypothesis with attenuated Ricker wavelets, but there are too many mathematical approximations, resulting in inaccurate analytical results. Here, a new formula is derived by matching the spectrums with the attenuated Ricker wavelets. The peak frequencies (PFs) of the reference and attenuated wavelet are calculated by the Gauss-Newton iteration method. Combined with fitted PFs, we derive another new formula to calculate the interval-Q value directly. With these modifications, the PFS improved (PFSI) method not only improves the accuracy of the Q factor but also has noise robustness. The synthetic data tests and field data application demonstrate the feasibility and effectiveness of the proposed method. (c2022 Elsevier B.V.)

Q MEASURING

1,561,485

Q-COMPENSATED LEAST-SQUARES REVERSE TIME MIGRATION WITH VELOCITY-ANISOTROPY CORRECTION BASED ON THE FIRST-ORDER VELOCITY-PRESSURE EQUATIONS

J.Zhu and Y.Qu (China Univ Petroleum). *83RD ANNUAL EAGE CONFERENCE (Online and Madrid, Spain, 6/6-9/2022) ABSTRACTS* 2022. (Abstract no.629; Available at <http://www.earthdoc.org> as of 7/7/2022; 5 pp; **Abstract only**)

Anisotropy and Q attenuation widely exist in the subsurface media and seriously affect the effect of seismic wave migration. In the conventional migration methods, anisotropy results in structural disorder, and Q attenuation leads to weak amplitude. In order to simultaneously correct for velocity-anisotropy and Q-attenuation during the migration, we propose a Q-compensated

least-squares reverse time migration with velocity-anisotropy correction (QLSRTM-VA) by constructing velocity-anisotropic Q-compensated forward modeling, Q-compensated adjoint and Q-attenuated demigration operators. These operators are developed by using the newly derived first-order velocity-anisotropic viscoacoustic quasi-differential wave equations with variable density, which are stable, can conveniently handle the variable density media and can be easily transformed between velocity-anisotropic Q-compensation and Q-attenuation versions. Numerical example shows that the proposed QLSRTM-VA method improves imaging resolution, signal-to-noise ratio, depth energy, and migration results through iterations.

RESERVOIR CHARACTERIZATION

1,561,486

INTELLIGENT CLUSTERING AND MODELING BASED ON GEOSCIENCE HETEROGENEOUS DATA

Z.Yanfang, S.Jianguo, L.Zhe, W.Guangyu and S.Yufei (China Univ Petroleum). *3RD EAGE HPC IN AMERICAS WORKSHOP (Online, 5/17-18/2022) ABSTRACTS* 2022. (Abstract no.WED05; Available at <http://www.earthdoc.org> as of 10/26/2022; 5 pp; **Abstract only**)

With the downward movement of exploration strata, the exploration objects are increasingly complex. Due to the poor quality of deep seismic data, the low main frequency, and the low resolution of sand bodies, it is difficult for conventional seismic interpretation methods to effectively solve the problem. Therefore, an effective comprehensive analysis method for seismic geology is needed. At present, the deep integration of artificial intelligence, big data, and geological exploration can more efficiently delineate the most potential target areas, reservoirs, and well positions; can obtain more accurate underground information; and can be applied to automatically interpret geological structures and predicting reservoir parameters, etc. Therefore, through research on the intelligent reservoir clustering method based on geoscience big data, we construct a reservoir parameter prediction model and a three-dimensional intelligent interpolation model that conform to the geological science knowledge base. Furthermore, the quantitative description of the reservoir parameters is finally realized.

REVERSE TIME MIGRATION

1,561,487

ELASTIC REVERSE-TIME MIGRATION WITHOUT WAVEFIELD DECOMPOSITION

D.Li and S.Chen (Zhejiang Univ). *2ND ANNUAL SEG/AAPG APPLIED GEOSCIENCE AND ENERGY INTERNATIONAL MEETING [IMAGE] (Houston, TX, 8/28/2022-9/1/2022) ABSTRACTS* pp.2778-2781, 2022. (ISSN 1949-4645; Available at <http://library.seg.org> as of 10/3/2022; **Expanded abstract**)

Elastic reverse time migration is a linear inversion of the reflectivity of the subsurface elastic interface using primarily reflected waves and primarily converted waves given a smooth migration model with accurate elastic wave kinematics. Combining this with the non-curl characteristic of P-waves and non-divergence characteristics of S-waves, we propose an innovative elastic reverse-time migration approach without wavefield decomposition applied to heterogeneous isotropic media. In this paper, pure propagators of P- and S-wave independent of each other are derived. We obtain ideal imaging results when we apply the proposed method to elastic synthetic seismic data generated by pure P- or S-wave source, demonstrating the validity of our method. Because the innovative migration method does not include wavefield decomposition which requires a large number of complex calculations, it has a great significant computational cost advantage over the migration method based on vector decomposition. Meanwhile, when compared to the Helmholtz separation migration method, it can avoid the loss of important geological information due to phase shift and amplitude distortion.

REVERSE TIME MIGRATION

1,561,488

2D ISOTROPIC AND VERTICAL TRANSVERSELY ISOTROPIC RTM USING SEG HESS VTI MODEL

R.Rastogi, A.Srivastava, M.Gawade, N.Mangalath, L.Bathula, B.Mahajan and S.Phadke (C-DAC). *2ND ANNUAL SEG/AAPG APPLIED GEOSCIENCE AND ENERGY INTERNATIONAL MEETING [IMAGE] (Houston, TX, 8/28/2022-9/1/2022) ABSTRACTS* pp.2782-2786, 2022. (ISSN 1949-4645; Available at <http://library.seg.org> as of 10/3/2022; **Expanded abstract**)

Reverse time migration (RTM) is an advanced imaging technique which uses two-way wave equation for wavefield extrapolation and avoids the approximation of wave equation. RTM algorithm is computationally very expensive. Higher order Finite Difference (FD) scheme is used to discretize the two-way scalar wave equation in Isotropic (ISO) and Vertical Transversely Isotropic (VTI) media. The recent advances in memory/storage capacity and improvements in computational capabilities of parallel servers have increased the feasibility of running RTM. The presented research work discusses implementation of in-house developed 2D ISO and VTI parallel RTM applications and their results. The implementation uses sliding velocity model approach to reduce memory/storage requirement of Conventional Saving approach of wavefield for RTM (CSRTM). The results of the applications are demonstrated using SEG Hess VTI model.

REVERSE TIME MIGRATION 1,561,489

A STABLE Q REVERSE TIME MIGRATION METHOD WITH REGULARIZATION

Y.Zhao (Yangtze Univ). *JOURNAL OF APPLIED GEOPHYSICS* v.207, Dec. 2022. (ISSN 0926-9851; Article no.104850)

Q reverse time migration (Q-RTM) is an effective method to compensate the deep amplitude energy of seismic records and improve the resolution. However, an important problem of the Q-RTM method is that the wavefield extrapolation process will generate high-frequency noise, resulting in unstable imaging results. On the basis of the decoupled viscoacoustic wave equation based on standard linear solid model, a viscoacoustic wave equation with regularization term is derived, and a stable Q-RTM based on this equation is developed. And the detailed derivation process of the viscoacoustic wave equation containing the regularization term is given. Compared with the commonly used low-pass filtering method, the method based on the regularization term avoids the design of the filter and the selection of the cutoff frequency. We test the Q-RTM method on the BP gas layer model, the Marmousi model and real seismic data. The numerical example results show that the Q-RTM method proposed in this paper can effectively solve the instability problem, compensate the amplitude energy, and obtain a higher resolution seismic profile. (c2022 Elsevier B.V.)

SANTOS BASIN 1,561,490

A SMART MERGE WORKFLOW FOR DUAL-AZIMUTH IMAGES

X.Li, D.Snyder, D.Chu and I.Dura-Gomez (ExxonMobil). *2ND ANNUAL SEG/AAPG APPLIED GEOSCIENCE AND ENERGY INTERNATIONAL MEETING [IMAGE] (Houston, TX, 8/28/2022-9/1/2022) ABSTRACTS* pp.2656-2660, 2022. (ISSN 1949-4645; Available at <http://library.seg.org> as of 10/3/2022; **Expanded abstract**)

In this paper, a smart merge flow for dual azimuth images is proposed. It is implemented by three major steps. First, an attribute volume of image quality is derived for each survey, based on the local image coherence and magnitude. Then the merging weights are assigned based on this attribute: higher image quality will get a larger merging weight. Second, a relative shift controlled by weight is performed to achieve the best alignment dynamically, and third, a final summation with weight is applied. Some common pitfalls during application are discussed and possible solutions are proposed. This flow was successfully applied to a Brazil dual azimuth project. The merged volume was confirmed to achieve a better image quality with enhanced continuity and magnitude over two individual azimuth images.

SANTOS BASIN 1,561,491

LEAST-SQUARES REVERSE TIME MIGRATION: LESSONS LEARNED FROM RECENT APPLICATIONS IN CHALLENGING AREAS OF THE SANTOS BASIN, BRAZIL

J.Rodrigues, F.Duarte, D.Domingos, B.Pereira-Dias and E.Pintas (Petroleo Brasileiro SA). *2ND ANNUAL SEG/AAPG APPLIED GEOSCIENCE AND ENERGY INTERNATIONAL MEETING [IMAGE] (Houston, TX, 8/28/2022-9/1/2022) ABSTRACTS* pp.2699-2703, 2022. (ISSN 1949-4645; Available at <http://library.seg.org> as of 10/3/2022; **Expanded abstract**)

The increase in computing power over the last decade enabled the use of innovative technologies to improve seismic imaging, with significant impact in exploration de-risking and reservoir characterization in complex geological settings. Among these processing and imaging techniques, we highlight the Least-Squares Reverse Time Migration (LSRTM), which became a reality for several projects nowadays. In this work, we present the outcome of recent LSRTM applications in challenging areas on deep-water offshore of the Santos Basin, Brazil. Important benefits are seen, such as illumination compensation in the pre-salt section, more reliable data for quantitative analysis, resolution uplift, and reduction of migration artifacts, aiding the exploratory interpretation and characterization of the carbonate reservoirs.

SANTOS BASIN 1,561,492

EFFECTIVE INTERBED MULTIPLE ATTENUATION WITH EXPLORATION-SCALE STREAMER DATA FROM SANTOS BASIN

X.Jia, H.Wang, A.Baumstein, Y.Cha, X.Li, V.Gottumukkula, I.Dura-Gomez, E.Neunmann and A.Srinivasan (ExxonMobil). *2ND ANNUAL SEG/AAPG APPLIED GEOSCIENCE AND ENERGY INTERNATIONAL MEETING [IMAGE] (Houston, TX, 8/28/2022-9/1/2022) ABSTRACTS* pp.2872-2876, 2022. (ISSN 1949-4645; Available at <http://library.seg.org> as of 10/3/2022; **Expanded abstract**)

If not properly handled during seismic processing, strong interbed multiples pose serious challenges to seismic interpretation in complex subsurface environments such as the Brazil pre-salt. Data-driven interbed multiple prediction methods based on convolution-correlation can produce high quality interbed multiple models. However, they also come with technical difficulties in the handling of billions of seismic traces and have a huge computation cost. We demonstrate a successful interbed multiple attenuation (IMA) project with a dataset from Brazil Santos Basin, where the interbed multiples are very strong and severely contaminate the pre-salt seismic images. With synthetic experiments, we show how the multiple generation mechanism is identified. It is shown that the anhydrite layer along top and base of salt, along with the water bottom are the main multiple generator layers. Then this is followed by a successful application of IMA to exploration-scale dual-azimuth datasets, coupled with advanced image domain adaptive subtraction. The results show that the strong migration swings due to interbed multiples can be removed very effectively, which is critical for the subsequent structural interpretation.

SARATOV VOLGOGRAD AREA 1,561,493

REDUCING DRILLING HAZARD RISK IN A CARBONATE ENVIRONMENT USING SEISMIC PROCESSING, DIFFRACTION IMAGING AND INTERPRETATION

I.Yakovlev, K.Smironov, A.Lushkina, O.Mozgovaya, V.Sablina and A.Firsov. *FIRST BREAK* v.40, no.12, pp.79-84, Dec. 2022. (ISSN 0263-5046; ISSN 1365-2397)

Buried structural anomalies, such as karst sinkholes, within carbonate depositional environments impose significant dangers for borehole integrity and drilling equipment due to rapid changes in rock properties (from tight to porous), potentially resulting in extensive mud loss, drill bit jamming, and other complications. This often leads to delays in well construction planning and sometimes to subsequent sidetrack drilling and a dramatic increase in costs. Thus, paleo-karst localization prior to well planning and construction becomes a critical task for economic optimization. However, this is a non-trivial exercise due to the relatively small

scale and size of karst-type features and anomalies, which are at the limit of the lateral resolution of most standard surface geophysical methods. In this paper, we introduce a methodology for predicting karst based on a combination of targeted 3D seismic processing and integrating the diffracted wavefield anomalies in addition to using conventional seismic attributes. The presented approach has been proven to be efficient at detecting karsts in a real oil field and can be deployed in other regions.

SAUDI ARABIA 1,561,494

MODELING FREQUENCY ATTENUATION DUE TO GAS IN SANDSTONE AND CARBONATE GAS RESERVOIRS

S.Almeshari (Saudi Aramco). *2ND ANNUAL SEG/AAPG APPLIED GEOSCIENCE AND ENERGY INTERNATIONAL MEETING [IMAGE]* (Houston, TX, 8/28/2022-9/1/2022) ABSTRACTS pp.2557-2560, 2022. (ISSN 1949-4645; Available at <http://library.seg.org> as of 10/3/2022; **Expanded abstract**)

Attenuation (1/Q) provides an insight into detecting hydrocarbon from seismic data. However, care should be taken as there are multiple factors that can cause intrinsic attenuation even if the reservoirs are fully saturated with brine. The purpose of this modeling exercise is to use rock physics and VSP Q-analysis to help in viscoacoustic forward modeling and to validate the use of it for more efficient gas characterization.

SEISMIC DATA PROCESSING 1,561,495

SEISMIC SPECKLE AS MULTIPLICATIVE NOISE EXPLAINING LAND REFLECTIONS DISTORTED BY NEAR-SURFACE SCATTERING

A.Bakulin, D.Neklyudov and I.Silvestrov (Saudi Aramco; Russian Academy Sciences). *2ND ANNUAL SEG/AAPG APPLIED GEOSCIENCE AND ENERGY INTERNATIONAL MEETING [IMAGE]* (Houston, TX, 8/28/2022-9/1/2022) ABSTRACTS pp.2601-2605, 2022. (ISSN 1949-4645; Available at <http://library.seg.org> as of 10/3/2022; **Expanded abstract**)

Land seismic challenges are usually attributed to superimposed near-surface noise. We suggest that small-scale near-surface scattering distorts the reflections themselves via a mechanism we refer to as "seismic speckle", similar to speckle noise in optics and acoustics. We describe a simple mathematical model of multiplicative seismic noise that captures the main features of such distortions seen on the field data. The first type of multiplicative noise with random phase perturbations explains the severe coherency loss and a substantial amplitude reduction after stacking. Residual statics is another type of multiplicative noise leading to progressive loss of higher frequencies. Both mechanisms combined quantitatively explain amplitude transformation observed while locally stacking field data. We present field observations confirming seismic speckle and also numerically demonstrate how local stacking can recover the accurate phase of the undistorted signal on synthetic data.

SEISMIC DATA PROCESSING 1,561,496

LARGE-SCALE MARCHENKO IMAGING WITH DISTANCE-AWARE MATRIX REORDERING, TILE LOW-RANK COMPRESSION, AND MIXED-PRECISION COMPUTATIONS

M.Ravasi, Y.Hong, H.Ltaief, D.Keyes and D.Vargas (King Abdullah Univ; Utrecht Univ). *2ND ANNUAL SEG/AAPG APPLIED GEOSCIENCE AND ENERGY INTERNATIONAL MEETING [IMAGE]* (Houston, TX, 8/28/2022-9/1/2022) ABSTRACTS pp.2606-2610, 2022. (ISSN 1949-4645; Available at <http://library.seg.org> as of 10/3/2022; **Expanded abstract**)

A variety of wave-equation-based seismic processing algorithms rely on the repeated application of the Multi-Dimensional Convolution (MDC) operator. For large-scale 3D seismic surveys, this comes with severe computational challenges due to the sheer size of high-density, full-azimuth seismic datasets required by such algorithms. We present a three-fold solution that greatly alleviates the memory footprint and computational cost of 3D MDC by leveraging a combination of: (i) distance-aware matrix reordering; (ii) Tile Low-Rank (TLR) matrix compression; and (iii)

computations in mixed floating-point precision. By applying our strategy to a 3D synthetic dataset, we show that the size of kernel matrices used in the Marchenko redatuming and Multi-Dimensional Deconvolution equations can be reduced by a factor of 34 and 6, respectively. We also introduce a TLR Matrix-Vector Multiplication (TLR-MVM) algorithm that, as a direct consequence of such compression capabilities, is consistently faster than its dense counterpart by a factor of 4.8 to 36.1 (depending on the selected hardware). As a result, the associated inverse problems can be solved at a fraction of cost in comparison to state-of-the-art implementations that require a pass through the entire data at each MDC operation. This is achieved with minimal impact on the quality of the processing outcome.

SEISMIC DATA PROCESSING 1,561,497

S-TTRANSFORM BASED PROCESSING OF NOISY SURFACE WAVE RECORD FOR RECOVERING HIGH-RESOLUTION SPECTRUM

S.Mukherjee, M.Bhaumik and T.Naskar (IIT Madras). *2ND ANNUAL SEG/AAPG APPLIED GEOSCIENCE AND ENERGY INTERNATIONAL MEETING [IMAGE]* (Houston, TX, 8/28/2022-9/1/2022) ABSTRACTS pp.2631-2635, 2022. (ISSN 1949-4645; Available at <http://library.seg.org> as of 10/3/2022; **Expanded abstract**)

Generating high-resolution dispersion spectra is a key part of the multichannel analysis of the surface waves (MASW) method to accurately predict near-surface shear wave velocity profiles. In field acquisitions, a common problem is noise contamination occurring due to defects in sensors, faulty connections, non-source generated waves. The noisy traces distort the dispersion spectra and hamper an accurate dispersion curve selection. The traditional wavefield transformation techniques mute or remove the noisy traces to negate noise-inflicted artifacts in the dispersion spectra. However, valuable information existing apart from the noise is lost in the process. We propose combining the modified S-transform and the high-resolution linear Radon transform in the slant f-k transform flow chart to extract the essential information from the noisy traces. The efficacy of the proposed approach is demonstrated using noisy synthetic and real-world shot-gathers. The proposed approach generated high-resolution, multimodal dispersion spectra while the existing methods failed to produce mode-separated dispersion spectra.

SEISMIC DATA PROCESSING 1,561,498

MULTICHANNEL COMPRESSIVE SENSING FOR SEISMIC DATA RECONSTRUCTION USING JOINT SPARSITY

I.Pawelec, M.Wakin and P.Sava (Colorado Sch Mines). *2ND ANNUAL SEG/AAPG APPLIED GEOSCIENCE AND ENERGY INTERNATIONAL MEETING [IMAGE]* (Houston, TX, 8/28/2022-9/1/2022) ABSTRACTS pp.2636-2640, 2022. (ISSN 1949-4645; Available at <http://library.seg.org> as of 10/3/2022; **Expanded abstract**)

Despite the many advances in data reconstruction technology and significant increase in the number of channels available for recording the particle motion, acquiring non-aliased seismic data at high signal-to-noise ratio remains a challenge. Areas with restricted access, difficult terrain, and slow velocities in the near surface can prevent the acquisition of properly sampled wavefields which in turn significantly complicates the suppression of the near surface related noise. There are two key strategies available for reducing the sampling requirement without loss of information. Recording wavefield and its derivatives yields multiple pieces of information at each sampling point, creating multichannel signal and allowing for an increased distance between samples. Compressive sensing (CS) is an alternative way of data acquisition relying on randomized sampling and known data patterns in some domain. We propose combining the two concepts by using multichannel measurements of wavefield and its derivatives in the compressive sensing framework and solving the joint sparse recovery problem. Our preliminary results show that the multichannel CS approach is more reliable than the single channel CS, and achieves higher SNR and smaller and less coherent differences compared to its single channel counterpart.

SEISMIC DATA PROCESSING 1,561,499

SEISMIC DATA RECONSTRUCTION USING DENOISING CONVOLUTIONAL NEURAL NETWORK COMBINED WITH REGULARIZATION BY DENOISING

N.Lan, K.Sang and F.Zhang (China Univ Petroleum). *2ND ANNUAL SEG/AAPG APPLIED GEOSCIENCE AND ENERGY INTERNATIONAL MEETING [IMAGE] (Houston, TX, 8/28/2022-9/1/2022) ABSTRACTS* pp.2641-2645, 2022. (ISSN 1949-4645; Available at <http://library.seg.org> as of 10/3/2022; **Expanded abstract**)

Seismic data reconstruction (SDR) is a highly ill-posed inverse problem that requires the introduction of suitable priors by regularization methods to obtain unique and accurate reconstruction results. Recently, denoising by regularization (RED) has provided new ideas for solving ill-posed inverse problems using sophisticated denoising priors. In this paper, we introduce RED into the reconstruction field and propose a seismic data reconstruction method based on denoising convolutional neural network (DnCNN). Specifically, we first construct an explicit RED objective defined by DnCNN, which can use the deep denoising priors embedded in this denoising network to improve the reconstruction accuracy of seismic data. Then, we combine the constructed RED objective with a least-squares fidelity term to form a novel SDR model. Finally, under the half quadratic splitting framework, an efficient iterative algorithm for solving the novel SDR model is developed through theoretical derivation. The performance of this algorithm is tested on synthetic and field data. The results demonstrate that the developed method not only has superior computational efficiency but also has state-of-the-art reconstruction performance compared to the widely used data-driven-tight-frame-based reconstruction method.

SEISMIC DATA PROCESSING 1,561,500

PWD-PINN: SLOPE-ASSISTED SEISMIC INTERPOLATION WITH PHYSICS-INFORMED NEURAL NETWORKS

F.Brandolin, M.Ravasi and T.Alkhalifah (King Abdullah Univ). *2ND ANNUAL SEG/AAPG APPLIED GEOSCIENCE AND ENERGY INTERNATIONAL MEETING [IMAGE] (Houston, TX, 8/28/2022-9/1/2022) ABSTRACTS* pp.2646-2650, 2022. (ISSN 1949-4645; Available at <http://library.seg.org> as of 10/3/2022; **Expanded abstract**)

Seismic data can be expressed as a superposition of local plane waves. A gather of traces can be described by the local plane wave differential equation (PDE), that allows to predict each of the traces from the previous one, given the knowledge of the local slope of the events. In the approach presented here, we train a neural network in an unsupervised manner to solve seismic interpolation problems using the local plane wave differential equation and the local slope estimated by the mean of plane wave destruction filters (PWD). The physics-informed neural network (PINN) maps the input grid points in time and space to the amplitudes of the wavefield whilst matching the information contained in the available traces. The proposed approach is tested on two seismic interpolation tasks using synthetic data, specifically, interpolation of data with large gaps and those aliased. Whilst the network shows remarkable interpolation capabilities in both experiments, it tends to struggle fitting aliased data with high frequency content. To mitigate this problem, we propose to include locally adaptive activation functions in the architecture. This leads to improved convergence and reconstruction accuracy.

SEISMIC DATA PROCESSING 1,561,501

REVERSE-TIME MIGRATION OF MOBILE MARINE VIBRATOR DATA

K.Almuteri, P.Sava and J.Shragge (Colorado Sch Mines). *2ND ANNUAL SEG/AAPG APPLIED GEOSCIENCE AND ENERGY INTERNATIONAL MEETING [IMAGE] (Houston, TX, 8/28/2022-9/1/2022) ABSTRACTS* pp.2694-2698, 2022. (ISSN 1949-4645; Available at <http://library.seg.org> as of 10/3/2022; **Expanded abstract**)

Marine vibrators are viable alternatives to seismic air-guns in ocean-bottom acquisition because of their low environmental

impact. They are also advantageous due to their ability to generate more low-frequency content compared to air-guns, and due to their suitability for simultaneous acquisition. However, mobile marine vibrators introduce a unique set of processing and imaging challenges for ocean-bottom acquisition, such as the Doppler effect and the time-dependent source-receiver offsets, which are not features of conventional marine acquisition. Standard seismic data processing and imaging techniques assume stationary sources and are not fully suitable for mobile marine vibrator data without modification. Not accounting for source motion in seismic imaging introduces phase change and mispositioning of imaged structure. Further, ignoring source motion effects may imply apparent poor illumination, velocity errors, and or both. We propose a reverse-time migration approach that considers the source-motion effects and is capable of producing accurate subsurface images. Synthetic examples illustrate the ability of our proposed method to construct accurate subsurface RTM images even for source velocities higher than what is common in typical marine acquisition. Our approach is not limited to mobile marine vibrator data, but is also applicable to streamer data.

SEISMIC DATA PROCESSING 1,561,502

LEAST-SQUARES REVERSE-TIME MIGRATION WITH ANGLE GATHERS THROUGH POINT SPREAD FUNCTIONS

J.Bai and O.Yilmaz (Emerson). *2ND ANNUAL SEG/AAPG APPLIED GEOSCIENCE AND ENERGY INTERNATIONAL MEETING [IMAGE] (Houston, TX, 8/28/2022-9/1/2022) ABSTRACTS* pp.2704-2708, 2022. (ISSN 1949-4645; Available at <http://library.seg.org> as of 10/3/2022; **Expanded abstract**)

Angle-domain common image gathers (ADCIGs) describe reflectivity variations over reflection angles and azimuth for model building and amplitude versus angle (AVA) analysis. The ADCIGs can be obtained from migration, such as reverse-time migration (RTM). In this paper, we present image-domain angle/azimuth-dependent least-squares RTM (LSRTM) with an Lp-norm regularization between the ADCIGs and an angle/azimuth-dependent reflectivity model and with a total-variation regularization of the reflectivity model. The Hessian in the LSRTM is approximated by point spread functions, which are calculated from Born modeling followed by RTM. The method is illustrated through 2D numerical examples with the inaccuracy of migration velocity models. The examples demonstrate that the method improves the ADCIGs and their angle stacks with enhanced resolution, balanced amplitudes, compensated illumination, and energy distribution in extended angular ranges.

SEISMIC DATA PROCESSING 1,561,503

LEAST-SQUARES RTM WITH SHIFTED TOTAL VARIATION REGULARIZATION FOR DEPTH IMAGING OF SPARSE SHORT-OFFSET SEISMIC DATA

T.Zand, A.Gorszczyk, A.Gholami, H.Ghasemzadeh and A.Malcolm (Polish Academy Sciences; Tehran Univ; K N Toosi Univ Technology; Newfoundland Memorial Univ). *2ND ANNUAL SEG/AAPG APPLIED GEOSCIENCE AND ENERGY INTERNATIONAL MEETING [IMAGE] (Houston, TX, 8/28/2022-9/1/2022) ABSTRACTS* pp.2714-2718, 2022. (ISSN 1949-4645; Available at <http://library.seg.org> as of 10/3/2022; **Expanded abstract**)

Least-squares reverse time migration (LSRTM) is a leading tool in imaging complex geological structures. This is because it includes the full-wave equation via reverse time migration (RTM), and solves the linearized wave equation by the least-squares (LS) minimization. To stabilize the LSRTM solution and mitigate the shortcomings that arise from linearization, simplification, approximation in simulation, and imperfection of data acquisition an appropriate regularization must be used. However, the conventional regularization methods such as Tikhonov, total variation (TV), or sparse regularization perform suboptimally, even in recovering structurally simple earth models. Here we introduce a new extension of Tikhonov-TV compound regularization, called shifted TV, to regularize the unknown reflectivity image. This new regularization implemented in the frame of a nonlinear migration allows for high-resolution and stable imaging in the presence of

rough migration velocity models. We demonstrate the performance of our method using a short offset academic-style streamer data generated in the crustal-scale GO-3D-OBS synthetic subduction zone model. The results confirm that the shifted regularization increases the robustness of LSRTM with an imperfect background velocity model and allows us to estimate high-quality reflectivity images of complex geological setting despite the limited streamer length.

.....
SEISMIC DATA PROCESSING **1,561,504**

NORMALIZED ENERGY-NORM IMAGING CONDITION FOR ELASTIC REVERSE-TIME MIGRATION

C.Oren and J.Shragge (Colorado Sch Mines). *2ND ANNUAL SEG/AAPG APPLIED GEOSCIENCE AND ENERGY INTERNATIONAL MEETING [IMAGE]* (Houston, TX, 8/28/2022-9/1/2022) *ABSTRACTS* pp.2719-2723, 2022. (ISSN 1949-4645; Available at <http://library.seg.org> as of 10/3/2022; **Expanded abstract**)

Elastic wavefield imaging of multicomponent seismic data can provide additional information about sub-surface geological structures (e.g., elastic properties and fracture distribution) relative to single-component acoustic imaging. We propose a novel imaging condition for elastic reverse time migration using deconvolution energy normalization. Being derived from the existing energy-norm imaging operator, the proposed approach uses multicomponent seismic data without wave-mode decomposition, outputs a scalar image with attenuated backscattering artifacts and does not suffer from polarity reversal at normal incidence. Realistic numerical experiments show the effectiveness of the normalized energy-norm imaging condition in balancing the image amplitudes as well as enhancing the vertical spatial resolution in comparison with its energy-norm counterpart.

.....
SEISMIC DATA PROCESSING **1,561,505**

ACCELERATED KIRCHHOFF DEPTH MIGRATION ON CPU-GPU HETEROGENEOUS COMPUTING SYSTEMS

Y.Liu, H.Liu, Y.He, F.Qin and Y.Du (Aramco Research Center; Saudi Aramco). *2ND ANNUAL SEG/AAPG APPLIED GEOSCIENCE AND ENERGY INTERNATIONAL MEETING [IMAGE]* (Houston, TX, 8/28/2022-9/1/2022) *ABSTRACTS* pp.2724-2728, 2022. (ISSN 1949-4645; Available at <http://library.seg.org> as of 10/3/2022; **Expanded abstract**)

Kirchhoff Depth Migration (KDMIG) is one of the most reliable seismic techniques for imaging complex geological structures. It has been widely used in production. However, with advances in 3D seismic data acquisition, massive amount of seismic data has been acquired, resulting in dramatically increase of computational cost for KDMIG. An accelerated KDMIG algorithm has been developed based on the CPU-GPU heterogeneous parallel computing system. To fully utilize the power of the supercomputer, we have developed four strategies, including cross-spread sorting, texture interpolation, multi-stream computation, and parallel architecture optimization, to accelerate the KDMIG method. Numerical tests demonstrate that the efficiency has been improved by up to 40x compared to the CPU version without any compromise of the imaging accuracy.

.....
SEISMIC DATA PROCESSING **1,561,506**

DEBLURRING MIGRATION IMAGES WITH POINT SPREAD FUNCTION FILTER

C.Liu, N.Dai, W.Wu, X.Wu, M.Guo and H.Fu (Tsinghua Univ; BGP CNPC). *2ND ANNUAL SEG/AAPG APPLIED GEOSCIENCE AND ENERGY INTERNATIONAL MEETING [IMAGE]* (Houston, TX, 8/28/2022-9/1/2022) *ABSTRACTS* pp.2739-2743, 2022. (ISSN 1949-4645; Available at <http://library.seg.org> as of 10/3/2022; **Expanded abstract**)

Migration images deblurring is an important post-processing procedure to derive a high-resolution geological section and get the success of petroleum exploration. However, conventional migration images deblurring methods are based on a local-layered medium assumption, and require high computational costs to calculate the

deblurring filter for migration images with a limited resolution improvement. To obtain a high-resolution migration image with reduced computational costs, we proposed a point spread function (PSF) filter method. First, we calculated the PSF filter in the wavenumber domain. Then we interpolated PSF filters of the remaining points in each subsection by the adjacent four PSF filters. Finally, we applied all PSF filters to the blurred migration image. Results from the Marmousi model and the 2D filed dataset reveal that our PSF filter method could significantly enhance the spatial resolution of migration images with lower computational cost compared with the conventional deblurring filter method. Moreover, the PSF filter approach is more applicable in practical situations without the local-layered medium assumption.

.....
SEISMIC DATA PROCESSING **1,561,507**

LEAST-SQUARES REVERSE TIME MIGRATION OF SEISMIC SOURCE CODING BASED ON SHEARLET TRANSFORM

Y.Nabi, X.Gong and Z.Xu (Jilin Univ). *2ND ANNUAL SEG/AAPG APPLIED GEOSCIENCE AND ENERGY INTERNATIONAL MEETING [IMAGE]* (Houston, TX, 8/28/2022-9/1/2022) *ABSTRACTS* pp.2744-2748, 2022. (ISSN 1949-4645; Available at <http://library.seg.org> as of 10/3/2022; **Expanded abstract**)

Migration images deblurring is an important post-processing procedure to derive a high-resolution geological section and get the success of petroleum exploration. However, conventional migration images deblurring methods are based on a local-layered medium assumption, and require high computational costs to calculate the deblurring filter for migration images with a limited resolution improvement. To obtain a high-resolution migration image with reduced computational costs, we proposed a point spread function (PSF) filter method. First, we calculated the PSF filter in the wavenumber domain. Then we interpolated PSF filters of the remaining points in each subsection by the adjacent four PSF filters. Finally, we applied all PSF filters to the blurred migration image. Results from the Marmousi model and the 2D filed dataset reveal that our PSF filter method could significantly enhance the spatial resolution of migration images with lower computational cost compared with the conventional deblurring filter method. Moreover, the PSF filter approach is more applicable in practical situations without the local-layered medium assumption.

.....
SEISMIC DATA PROCESSING **1,561,508**

DATA-DRIVEN SEISMIC PRESTACK VELOCITY INVERSION VIA COMBINING RESIDUAL NETWORK WITH CONVOLUTIONAL AUTOENCODER

G.Liu, L.Zhang, Q.Wang and J.Xu (China Nat Eng Res Ctr). *JOURNAL OF APPLIED GEOPHYSICS* v.207, Dec. 2022. (ISSN 0926-9851; Article no.104846)

Seismic full-waveform inversion (FWI) is a powerful imaging approach in exploration geophysics, to estimate high-resolution subsurface geophysical properties via fitting synthetic data to observed seismic records. Nevertheless, there exist several intractable issues, e.g., solution non-uniqueness, cycle-skipping phenomenon, weak robustness and high computational burden. Recently, more attention has been paid to data-driven FWI techniques based on deep neural networks. However, their success greatly depends on an ocean of training instances, which is not available in oil exploration conveniently. To cope with this situation, an effective strategy is to reduce the dimensionality of input and output spaces for given training instances. By exploiting 2D velocity profile nonlinear compressibility, we train a residual convolutional autoencoder under an unsupervised mode using velocity data, where its encoder acts as a velocity dimensionality reduction operator to transform 2D velocity profiles into low-dimensional 1D pseudo-velocity curves. Then, a residual network is trained to build a nonlinear mapping from multi-shot seismic records to 1D pseudo-velocity curves. In the inference stage, the trained decoder converts those predicted 1D curves back to 2D velocity profiles. Therefore, we propose a novel two-stage data-driven seismic inversion technique combining a residual network with a residual convolutional autoencoder. The detailed

experiments on four synthetic data sets (salt body, layered, faulted and salt dome models) illustrate that our proposed method with three different residual network architectures outperforms other approaches including FCNVMB, VelocityGAN and pure residual network, according to four objective evaluation metrics and subjective visualization. (c2022 Elsevier B.V.)

SEISMIC DATA PROCESSING 1,561,509

GPU PERFORMANCE ANALYSIS FOR VISCOACOUSTIC WAVE EQUATIONS USING STENCIL COMPUTATION FROM SYMBOLIC SPECIFICATION

L.Jesus, P.Nogueira, J.Speglich and M.Boratto (SENAI-CIMATEC). *3RD EAGE HPC IN AMERICAS WORKSHOP (Online, 5/17-18/2022) ABSTRACTS 2022*. (Abstract no.WED08; Available at <http://www.earthdoc.org> as of 10/26/2022; 6 pp; **Abstract only**)

Stencil computation is the essence of several applications in high-performance computing, such as computational fluid dynamics, image processing, and geophysical applications that involve solving wave equations. The most common seismic modeling uses acoustic wave equation. However, several other equations that best represent the subsurface can also be used for seismic modeling. Viscoacoustic modeling provides an accurate image with the high resolution of exploratory targets due to including characteristics such as amplitude attenuation and velocity dispersion in the propagation of seismic waves. In this work, we describe the viscoacoustic equations based on the Maxwell, Kelvin-Voigt, and standard linear solid (SLS) rheological models while considering first- and second-order formulations. These equations are in the time-space domain, and the finite-difference method is suitable for solving them. This work also describes the development and implementation of six viscoacoustic equations on the Devito tool.

SEISMIC DATA PROCESSING 1,561,510

PHYSICS-BASED PRECONDITIONED MULTIDIMENSIONAL DECONVOLUTION IN THE TIME DOMAIN

D.Vargas, I.Vasconcelos, M.Ravasi and N.Luiken (Utrecht Univ; King Abdullah Univ). *2ND ANNUAL SEG/AAPG APPLIED GEOSCIENCE AND ENERGY INTERNATIONAL MEETING [IMAGE] (Houston, TX, 8/28/2022-9/1/2022) ABSTRACTS pp.2822-2826, 2022*. (ISSN 1949-4645; Available at <http://library.seg.org> as of 10/3/2022; **Expanded abstract**)

Multi-Dimensional Deconvolution is a data-driven method that is at the center of key seismic processing applications--from suppressing multiples to inversion-based imaging. When posed in an interferometric context, it can grant access to overburden-free seismic virtual surveys at a given datum in the subsurface. As such, it constitutes an essential processing operation that achieves multiple imaging objectives simultaneously in redatuming or target-oriented imaging: e.g., suppressing multiples, removing complex overburden effects, and retrieving amplitude consistent image gathers for impedance inversion. Despite its potential, the deconvolution process relies on the solution of an ill-conditioned linear inverse problem sensitive to noise artifacts due to incomplete acquisition, limited sources, and band-limited data. Typically, this inversion is performed in the Fourier domain where the estimation of optimal regularization parameters hinders accurate waveform reconstruction. We reformulate the problem in the time domain--long believed to be computationally intractable--and introduce several physical constraints that naturally drive the inversion towards a reduced set of reliable, stable solutions. This allows to successfully reconstruct the overburden-free reflection response beneath a complex salt body from noise-contaminated data.

SEISMIC DATA PROCESSING 1,561,511

OPERATOR CHAINS AND SEISMIC DATA DECOMPOSITION

S.Fomel (Texas Univ, Austin). *2ND ANNUAL SEG/AAPG APPLIED GEOSCIENCE AND ENERGY INTERNATIONAL*

MEETING [IMAGE] (Houston, TX, 8/28/2022-9/1/2022) ABSTRACTS pp.2842-2846, 2022. (ISSN 1949-4645; Available at <http://library.seg.org> as of 10/3/2022; **Expanded abstract**)

Chains of elementary operators can be used to approximate more complex operators. I develop a general approach to building such chains and estimating operator parameters. Chaining alternative weights in time and frequency domains can approximate non-stationary filters for matching data with different frequency content. Chaining elementary destruction filters helps decompose seismic data into non-stationary frequency components (in one dimension) or non-stationary slope components (in multiple dimensions). Field data examples confirm the validity of the proposed approach.

SEISMIC DATA PROCESSING 1,561,512

LEAST-SQUARES NON-STATIONARY TRIANGLE SMOOTHING

R.F.Alomar, S.Fomel (Texas Univ, Austin). *2ND ANNUAL SEG/AAPG APPLIED GEOSCIENCE AND ENERGY INTERNATIONAL MEETING [IMAGE] (Houston, TX, 8/28/2022-9/1/2022) ABSTRACTS pp.2847-2851, 2022*. (ISSN 1949-4645; Available at <http://library.seg.org> as of 10/3/2022; **Expanded abstract**)

We propose a fast and accurate method to estimate the radius of non-stationary triangle smoothing for matching two seismic datasets. The smoothing radius is estimated by non-linear least-squares inversion using an iterative Gauss-Newton approach. We derive and implement the derivative of the smoothing operator to compute the gradient for inversion. The proposed method is useful for implementing non-stationary triangle smoothing as a low-cost edge-preserving filter. The efficiency of the proposed method is also confirmed in a field-data application of random noise attenuation by non-stationary local signal-and-noise orthogonalization.

SEISMIC DATA PROCESSING 1,561,513

SEISMIC NOISE ATTENUATION VIA LEARNED AND ANALYTICAL BASIS FUNCTIONS

Y.Guo, R.Lin and M.D.Sacchi (Alberta Univ). *2ND ANNUAL SEG/AAPG APPLIED GEOSCIENCE AND ENERGY INTERNATIONAL MEETING [IMAGE] (Houston, TX, 8/28/2022-9/1/2022) ABSTRACTS pp.2867-2871, 2022*. (ISSN 1949-4645; Available at <http://library.seg.org> as of 10/3/2022; **Expanded abstract**)

Seismic noise attenuation is a long-term problem in seismic data processing. Many methods have been used to deal with this issue. A few can handle the problem of signal leakage created by filtering. We propose an approach that entails modeling the signal via two operators. Specifically, we combine learned global basis function in conjunction with an analytical transform to model seismic signals and capture subtle features that often end in the error or leakage panel. The global basis is extracted from initially filtered data via a Proper Orthogonal Decomposition (POD), while analytical basis functions could be any conventional transform. By promoting sparsity of the analytical basis and iteratively updating the coefficients of the global learned basis, we can model the data with a significant reduction of signal leakage. Synthetic and field data examples are shown to demonstrate the method.

SEISMIC DIFFRACTION 1,561,514

REVEALING THE DISCONTINUITIES BY 3D PRESTACK DIFFRACTION SEPARATION AND IMAGING

C.Li, S.Peng, X.Cui and P.Lin (China Univ Mining Technol). *2ND ANNUAL SEG/AAPG APPLIED GEOSCIENCE AND ENERGY INTERNATIONAL MEETING [IMAGE] (Houston, TX, 8/28/2022-9/1/2022) ABSTRACTS pp.2759-2763, 2022*. (ISSN 1949-4645; Available at <http://library.seg.org> as of 10/3/2022; **Expanded abstract**)

Diffractions are the seismic response of subsurface geological discontinuities, and thus, carry detailed geological information in 3D seismic exploration. It is a challenge to separate weak diffractions from specular reflections, especially when they have

similar kinematical characteristics in the 3D pre-stack case. The conventional pre-stack method often separates diffractions based on the data-driven local slope which is difficult to separate the similar seismic events. Therefore, we parameterize and calculate the local slope through the normal moveout velocity and ray parameter, which can enhance the stability and accuracy of local slopes. In this way, an effective strategy about pre-stack diffraction separation and imaging is proposed for detecting the subsurface discontinuous structure.

SEISMIC DIFFRACTION 1,561,515

SEISMIC DIFFRACTIONS SEPARATION AND IMAGING BASED ON CONVOLUTIONAL NEURAL NETWORK

J.Sun, J.Yang, Z.Li, J.Huang and J.Xu (China Univ Petroleum). *2ND ANNUAL SEG/AAPG APPLIED GEOSCIENCE AND ENERGY INTERNATIONAL MEETING [IMAGE] (Houston, TX, 8/28/2022-9/1/2022) ABSTRACTS* pp.2764-2768, 2022. (ISSN 1949-4645; Available at <http://library.seg.org> as of 10/3/2022; **Expanded abstract**)

In exploration seismology, the reflections have been extensively used for imaging and inversion to detect hydrocarbon and mine resources, which are generated from subsurface continuous impedance interfaces. When the reflectors are not continuous and their size reduces to less than a half wavelength, the reflected wave becomes scattering, which is also known as the diffraction. Both reflection and diffraction can be used to image subsurface structures, and the latter is helpful to resolve small-scale discontinuities, such as fault plane, pinch-out, Karst caves and salt edge. However, the amplitudes of diffractions are usually much weaker than that of reflections. This makes it difficult to directly identify and extract diffractions from common-shot gathers and to apply them for imaging. On the other hand, they have different geometrical characteristics in the dip-angle common-image gathers (DACIGs), which provides us an opportunity to extract diffractions. In this study, we present an efficient and accurate diffraction separation and imaging method in DACIGs using convolutional neural network (CNN). The labeled data of DACIGs are generated using one pass of seismic modeling and migration for velocity models with and without artificial scatterers. Then, a simplified end-to-end CNN is trained to identify and extract reflections from the DACIGs with coupled reflections and diffractions. Next, two adaptive subtraction workflows are used to compute diffractions and stacked image. Numerical experiments for Marmousi-II and Sigsbee models demonstrate that the proposed method can produce accurate reflection and diffraction separation results in DACIGs and the stacked image show a good resolution for subsurface small-scale discontinuities.

SEISMIC EXPLORATION 1,561,516

COMBINED QUASI-NEWTON AND ADAPTIVE GRADIENT OPTIMIZATION SCHEME USED IN SEISMIC DATA PROCESSING

J.McLeman and T.Burgess, asrs. (DownUnder GeoSolutions LLC). *World 2022/212,270A1*, p. 10/6/2022, f. 3/28/2022 (Appl. 2,222,169), pr. U.S. 3/29/2021 (Appl. 63/167,332) (G01V-0001/46; G01V-0001/48; G01V-0001/50).

A method for determining spatial distribution of properties of formations in a subsurface volume using geophysical sensor signals recorded proximate the volume includes inversion processing an initial model of the spatial distribution. The inversion processing comprises at least second order optimizing. The second order optimizing comprises calculating a scalar for the identity matrix in limited memory Broyden-Fletcher-Goldfarb-Shanno (L-BFGS) optimization, modifying the scalar using an adaptive gradient type scheme to estimate an inverse Hessian matrix, and using the modified plurality of scalars to optimize the inversion processing. The method of estimating the inverse Hessian matrix in L-BFGS can be further extended to include convolutional operators.

SEISMIC INTERPRETATION 1,561,517

AUTOMATIC 3D FAULT IDENTIFICATION METHOD DRIVEN BY DATA FROM EXPERT INTERPRETATION SAMPLES AND FORWARD MODELING SAMPLES

H.Yu (Shengli Oilfield Res Inst). *PETROLEUM GEOLOGY AND RECOVERY EFFICIENCY (YOUQI DIZHI YU CAISHOULU)* v.29, no.6, pp.58-66, Nov. 2022. (ISSN 1009-9603; **In Chinese**) [Full article and English abstract available from P.A.]

SEISMIC INTERPRETATION 1,561,518

UPSCALING ACOUSTIC WAVE EQUATION USING RENORMALIZATION GROUP THEORY

A.Malkoti, S.M.Hanasoge and R.E.Plessix (Tata Inst Fundamental Res; Shell Global Solutions Int). *2ND ANNUAL SEG/AAPG APPLIED GEOSCIENCE AND ENERGY INTERNATIONAL MEETING [IMAGE] (Houston, TX, 8/28/2022-9/1/2022) ABSTRACTS* pp.2507-2511, 2022. (ISSN 1949-4645; Available at <http://library.seg.org> as of 10/3/2022; **Expanded abstract**)

Seismic waves interact with a broad range of heterogeneities as they propagate through the Earth. Simulating this full range of scales for wave propagation requires capturing heterogeneities of all scales, which can be computationally unaffordable. In such cases, we rely on macroscopic representations of media obtained through an upscaling process that preserves the effects of small-scale heterogeneities (in comparison to the wavelengths of interest). Here, we discuss the application of the renormalization-group (RG) theory-based upscaling to the two-dimensional acoustic wave equation. The upscaled models obtained using this method show a good consistency for generated waveforms.

SEISMIC INTERPRETATION 1,561,519

SEISMIC RESPONSE ANALYSIS OF THIN COALS

Y.Xi and X.Yin (China Univ Petroleum). *2ND ANNUAL SEG/AAPG APPLIED GEOSCIENCE AND ENERGY INTERNATIONAL MEETING [IMAGE] (Houston, TX, 8/28/2022-9/1/2022) ABSTRACTS* pp.2517-2521, 2022. (ISSN 1949-4645; Available at <http://library.seg.org> as of 10/3/2022; **Expanded abstract**)

For some complex structures with thin interbedded coal or fault, the coal contained in sand reservoirs seriously hinders reservoir description and fluid identification of subsurface formations. The strong shielding effect of coal on sand reflection can easily lead to false bright spots in lithology identification, so that the reservoir position and boundary cannot be accurately described. In particular, the stratigraphic structure characteristics of sand coupled with some thin coals form complex composite reflections. Therefore, in view of the particularity and complexity of the geological sedimentary environment of coal-bearing reservoir, combined with the geological feature of coal development and actual logging data, this paper systematically analyzes the seismic reflection law of coal-bearing reservoirs. The single-well model test and the comparison of synthetics and seismic data prove that using the numerical simulation method to carry out forward modeling analysis and to study the seismic response characteristics of different sand-coal combination models is conducive to eliminating the influence of coal and accurately characterizing the reserve.

SEISMIC INTERPRETATION 1,561,520

ECHO PHONE FOR DIRECT ATTENUATION INDICATION

L.Liu, T.Fei, F.Qin and Y.Luo (Aramco Research Center; Saudi Aramco). *2ND ANNUAL SEG/AAPG APPLIED GEOSCIENCE AND ENERGY INTERNATIONAL MEETING [IMAGE] (Houston, TX, 8/28/2022-9/1/2022) ABSTRACTS* pp.2611-2615, 2022. (ISSN 1949-4645; Available at <http://library.seg.org> as of 10/3/2022; **Expanded abstract**)

Each reservoir has its own characteristic seismic frequency response due to its unique lithology and fluid property. When the seismic waves illuminate the subsurface medium and propagate back to the surface geophones, they bring back the attenuation

information related to the reservoir fluid features. Such information can be reflected by the amplitude and frequency variations of the seismic waves. We propose a novel method of echo phone to directly reveal the subsurface attenuation features. This method first focuses the surface seismic data back on the seal of the target via the wave-equation redatuming approach. This simulates a new data set that can be assumed to be acquired by setting many sources on the seal and associated receivers on the surface. We then isolate all the seismic events passing through the targets by computing the transmitted arrivals from the redatumed source to the surface receivers. Since the wavepath corresponding to these events are all influenced by the reservoir right below the sources, we compute frequency-dependent attributes, including frequency spectrum ratio and centroid frequency, to evaluate the feature of reservoir attenuation. Since the hydrocarbon, especially gas, has stronger attenuation than water, such attributes can be used to distinguish the reservoir feature. Numerical tests on both synthetic and field data sets validate the feasibility of this study.

SEISMIC INTERPRETATION **1,561,521**

LEVERAGING PYTHON CAPABILITIES FOR MULTI-GPU 2D MARCHENKO IMAGING

V.Koehne, M.Santos, T.Oliveira, R.Santos, M.Souza, D.Revelo, J.Speglich, E.Sperandio and D.Barrera (HPC-SENAI-CIMATEC). *3RD EAGE HPC IN AMERICAS WORKSHOP (Online, 5/17-18/2022) ABSTRACTS 2022*. (Abstract no.WED03; Available at <http://www.earthdoc.org> as of 10/26/2022; 5 pp; **Abstract only**)

Some geological settings may have the presence of strong internal multiple events on their surface-recorded seismic reflection response. The underlying single-scattering assumption of conventional imaging algorithms can produce a final result with ghost reflectors due to incorrect handling of multiply scattered events (Behura et al., 2014). This problem can be addressed with the Marchenko method (Broggini et al., 2012), which retrieves Green's functions with receivers at the surface and a virtual source at the desired subsurface point, using as inputs the reflection response and a background velocity model. With the Green's functions and focusing functions, we can apply an imaging condition to estimate the amplitude at the focal point free of the effects of internal multiples due to scattering at the overburden, or a target-oriented image if the process is repeated for a set of points. The implementation aspects of the method were first introduced on 2D media by Thorbecke et al. (2017) and were extended to 3D media by Brackenhoff et al. (2022) using C code and a multi-core OpenMP implementation. Ravasi and Vasconcelos (2020) also address implementation aspects on HPCs and highlight the advantages of using Python as a main language. We discuss these points in this work, with the addition of multi-GPU considerations using the CUDA C language and the pybind11 package. Although Python is slower than compiled languages such as C and Fortran (Gmys et al., 2020) because it is an interpreted language, it can save development time because of the many libraries in its ecosystem. In this abstract, we review the theory of the iterative method and some imaging conditions, discuss their implementation and the advantages of using the Python language and GPUs, and illustrate this with a numerical example.

SEISMIC INTERPRETATION **1,561,522**

FAULT TOLERANCE LIBRARY FOR GEOPHYSICAL NUMERICAL METHODS

C.Santana, I.Sardina and S.Xavier-de-Souza (Rio Grande Norte Fed Univ). *3RD EAGE HPC IN AMERICAS WORKSHOP (Online, 5/17-18/2022) ABSTRACTS 2022*. (Abstract no.WED04; Available at <http://www.earthdoc.org> as of 10/26/2022; 5 pp; **Abstract only**)

High-performance computing (HPC) provides the ability to study problems involving significant computations and data processing, such as full-waveform inversion (FWI) and least-squares migration (LSM). This method estimates the velocity model from the difference between observed and artificially modeled data (Virieux; Operto, 2009). One way to decrease this algorithm's execution time is to make some of its workloads parallel among the supercomputer's nodes. Regardless, each component provides a particular mean time between failures (MTBF); consequently, the

more components the execution employed, the more chance there was for failure. Because of this, supercomputing applications have fault tolerance (FT) methods to avoid failure (Treaster, 2005). Failures in 3D FWI can produce considerable economic impact, as it may take several days or weeks to recompute the lost data. Because of this, we investigate FT techniques that best fit geophysical problems such as FWI. This routine saves the code state of an iteration of FWI with a specific frequency. In the case of failure, the algorithm can be initialized from the most recent checkpoint and the last executed iteration can be restarted. Successively, we employ the checkpoint technique to save the local state of each process. The active nodes save their local state if the application receives any termination signal or if one node stops. This work presents 3D FWI using an FT library implemented in C++ with global and local checkpointing and fault detection with a heartbeat message using UDP. We performed FWI with a synthetic velocity model, and we executed the FWI with failures with and without FT.

SEISMIC MODEL **1,561,523**

AN IMMERSSED ABSORBING BOUNDARY CONDITION FOR SCALAR WAVEFIELD MODELING UNDER TOPOGRAPHY

K.Chen, H.Chen and H.Zhou (China Univ Petroleum). *2ND ANNUAL SEG/AAPG APPLIED GEOSCIENCE AND ENERGY INTERNATIONAL MEETING [IMAGE] (Houston, TX, 8/28/2022-9/1/2022) ABSTRACTS pp.2532-2536, 2022*. (ISSN 1949-4645; Available at <http://library.seg.org> as of 10/3/2022; **Expanded abstract**)

The irregular surface is an important aspect that needs be considered in finite-difference (FD) numerical simulations of seismic waves. To avoid the artificial edge reflections from the irregular surface, an effective absorbing boundary condition (ABC) should be designed with consideration of the topography. However, the FD methods usually use a rectangular grid discretization that causes a staircase problem in approximating the irregular surface. Additionally, the current ABC often assumes a horizontal interface between the interior computational domain and the top absorbing domain, which is the not case when an irregular surface exists. To avoid the spurious scattering caused by the staircase and adjust the ABC to irregular surfaces, we develop an immersed ABC for scalar wavefield modeling. We place the irregular surface at fractional grid nodes according to the true topography and we predict the wavefields at ghost grid points by a plane-wave transmitting boundary condition (BC). The ghost grid points refer to those grid nodes required by the interior FD calculations and the wavefield prediction is implemented along the normal direction of the surface, which means wavefield absorption along the normal direction. Numerical examples are presented to verify the feasibility of our immersed ABC under topography.

SEISMIC MODEL **1,561,524**

REMOVING THE DISCRETIZATION ERRORS FOR THE FRACTIONAL SPATIAL DERIVATIVES BASED CONSTANT-Q VISCOELASTIC WAVE EQUATION MODELING

H.Zhou, J.Wang and Y.Liu (China Univ Petroleum). *2ND ANNUAL SEG/AAPG APPLIED GEOSCIENCE AND ENERGY INTERNATIONAL MEETING [IMAGE] (Houston, TX, 8/28/2022-9/1/2022) ABSTRACTS pp.2537-2541, 2022*. (ISSN 1949-4645; Available at <http://library.seg.org> as of 10/3/2022; **Expanded abstract**)

Recently, the amplitude and phase decoupled viscoelastic wave equation attracts the attention of geophysical researchers because of its convenience for seismic imaging. The wave equation is often solved by the staggered-grid pseudospectral method, which has the spatial spectral accuracy. Further removing the discretization errors from temporal derivatives are desirable for accurately describing the attenuation phenomena. We have derived a new wavenumber-time domain (k-space) viscoelastic equation by the eigenvalue decomposition method and by the solution to the matrix differential equations. The error compensation operators inside our k-space equation can simultaneously correct the discretization errors of different types of temporal derivatives and are wave mode adaptive. In homogeneous media, the accuracy of the k-space wave equation is verified by the viscoelastic analytical solution. In

heterogeneous media, the viscoelastic k-space operators change to the mixed-domain k-space operators, which are effectively represented by the lowrank method. The simulation results from the simple and complex models reveal that our viscoelastic k-space method successfully removes the discretization errors of viscoelastic simulation, and is superior to the conventional staggered-grid pseudospectral method in terms of accuracy.

SEISMIC MODEL

1,561,525

A FINITE-ELEMENT METHOD TO COMPUTE THE SEISMIC RESPONSE IN NON-ISOTHERMAL POROELASTIC MEDIA

J.E.Santos, G.B.Savioli, J.M.Carcione and J.Ba (Buenos Aires Univ; Hohai Univ). *2ND ANNUAL SEG/AAPG APPLIED GEOSCIENCE AND ENERGY INTERNATIONAL MEETING [IMAGE] (Houston, TX, 8/28/2022-9/1/2022) ABSTRACTS* pp.2547-2551, 2022. (ISSN 1949-4645; Available at <http://library.seg.org> as of 10/3/2022; **Expanded abstract**)

We analyze the seismic response in fluid saturated poroelastic media based on the non-isothermal wave equation, which includes the temperature field other than those of stress and deformation. The model, which combines the Biot and Lord-Shulman (LS) theories, predicts the propagation of four waves: two compressional P waves, one fast and one slow, a thermal wave, and a shear wave. An initial boundary-value problem (IBVP) for the thermo-poroelastic wave equation is formulated and solved by applying the finite-element (FE) method. The FE procedure is formulated for the 1D case on an open bounded interval with absorbing boundary conditions at the artificial boundaries. We discretize the solid and fluid displacements and the temperature using piecewise linear globally continuous polynomials. The theory is used to study the propagation of the two compressional P waves and the thermal wave. We compare the coupled and uncoupled cases, including and neglecting viscosity. The algorithms may become useful for a better understanding of the behavior of seismic waves in hydrocarbon reservoirs and crustal rocks, because the assumption of isothermal wave propagation is now removed.

SEISMIC MODEL

1,561,526

A NODAL DISCONTINUOUS GALERKIN METHOD FOR WAVE PROPAGATION IN COUPLED FLUID-SOLID MEDIA

R.Li and Y.Zhang (Xi'an Jiaotong Univ). *2ND ANNUAL SEG/AAPG APPLIED GEOSCIENCE AND ENERGY INTERNATIONAL MEETING [IMAGE] (Houston, TX, 8/28/2022-9/1/2022) ABSTRACTS* pp.2552-2556, 2022. (ISSN 1949-4645; Available at <http://library.seg.org> as of 10/3/2022; **Expanded abstract**)

An accurate solution of the wave equation at an acoustic-elastic interface is important for full wavefield imaging and inversion in marine exploration. The solution requires careful implementation for the acoustic-elastic boundary conditions. In this work, we leverage a nodal discontinuous Galerkin (NDG) method, in which the unstructured uniform triangular meshes are used for the model meshing and an explicit up-wind numerical flux derived from Riemann problem is adopted to handle the boundary conditions at the acoustic-elastic interface. The numerical results demonstrate that the proposed NDG method is effective and accurate for dealing with the coupled acoustic-elastic media.

SEISMIC MODEL

1,561,527

FINITE-DIFFERENCE MODELING OF MARINE VIBRATOR SOURCES

K.Almuteri, J.Shragge and P.Sava (Colorado Sch Mines). *2ND ANNUAL SEG/AAPG APPLIED GEOSCIENCE AND ENERGY INTERNATIONAL MEETING [IMAGE] (Houston, TX, 8/28/2022-9/1/2022) ABSTRACTS* pp.2561-2565, 2022. (ISSN 1949-4645; Available at <http://library.seg.org> as of 10/3/2022; **Expanded abstract**)

Marine vibrators are emerging as an attractive alternative to conventional air-guns in ocean-bottom acquisition due to their ability to generate low-frequency waves and to limit negative

impacts on marine wildlife. Using marine vibrators introduces challenges not found in conventional air-gun-based acquisition, including handling phenomena associated with the Doppler effect due to the source motion, and time-dependent source-receiver offsets when receivers are placed on the ocean bottom. Standard seismic data processing solutions assume stationary sources at ocean-bottom acquisition; however, accurately accounting for source motion effects in processing is critical for optimal subsurface imaging. To address these challenges, we develop a finite-difference approach for modeling full acoustic wavefields in a generalized coordinate system that tracks the moving source. Synthetic examples demonstrate that this technique has the ability to accurately and stably model high-velocity moving sources, and account for the wavefield distortion predicted by the Doppler theory. This approach is not limited to understanding wavefield propagation for a moving source and can be used to develop other advanced processing techniques for marine vibrator data.

SEISMIC MODEL

1,561,528

GPU-BASED 3D ANISOTROPIC ELASTIC MODELING USING MIMETIC FINITE DIFFERENCES

H.Singh, J.Shragge and I.Tsvankin and F.Hoxha (Colorado Sch Mines; NVIDIA). *2ND ANNUAL SEG/AAPG APPLIED GEOSCIENCE AND ENERGY INTERNATIONAL MEETING [IMAGE] (Houston, TX, 8/28/2022-9/1/2022) ABSTRACTS* pp.2566-2570, 2022. (ISSN 1949-4645; Available at <http://library.seg.org> as of 10/3/2022; **Expanded abstract**)

Accurate modeling of elastic wavefields for 3D anisotropic media is important for many applications in seismic processing and inversion. However, efficient wavefield simulation for tilted transversely isotropic (TTI) media and, especially, for orthorhombic and lower symmetries remains challenging. Finite-difference (FD) implementations using centered Taylor-series coefficients on single staggered grids suffer from reduced accuracy due to problems in computing the partial wave-field derivatives in TTI or tilted orthorhombic (TOR) media and in enforcing the free-surface boundary conditions. To address these issues, we develop a 3D mimetic FD (MFD) algorithm for arbitrarily anisotropic media that uses fully staggered grids. This CUDA-based algorithm is implemented on graphics processing units (GPUs) to leverage the massive parallelism of this computer architecture. For multi-GPU parallelization, we employ the CUDA-aware MPI library that exploits the remote direct memory access feature (RDMA) for buffer transfers. Weak- and strong-scaling tests on a single DGX NVIDIA A100 node with eight GPUs demonstrate that our efficient multi-GPU implementation achieves a quasilinear computational speedup.

SEISMIC MODEL

1,561,529

ON THE ABSORBING BOUNDARIES TO REPLICATE SEMI-INFINITE HALF-SPACE IN NUMERICAL SEISMIC ANALYSES USING THE FINITE ELEMENT METHOD

T.R.Hebert, J.M.Bryce and A.P.Chattopadhyay (Marshall Univ). *2ND ANNUAL SEG/AAPG APPLIED GEOSCIENCE AND ENERGY INTERNATIONAL MEETING [IMAGE] (Houston, TX, 8/28/2022-9/1/2022) ABSTRACTS* pp.2576-2580, 2022. (ISSN 1949-4645; Available at <http://library.seg.org> as of 10/3/2022; **Expanded abstract**)

Computational analysis allows for easy replication of seismic tomography using numerical solving techniques. The Finite Element Method (FEM) and the Finite Difference Method (FDM) are the two primary methods which are used for such computational models that have been presented in the literature. One challenge of such analyses is the creation of a semi-infinite half space. In a monolithic, elastic domain, seismic waves propagate without any interruptions in the absence of domain boundaries. However, in a computational study, the geometry is of a finite volume and it is not possible to create a semi-infinite half-space without additional adjustments. To address this, certain boundary conditions which simulate the finite domain to behave like a semi-infinite half space are used. These conditions are enforced on the essential boundaries, which otherwise reflect the transient wave propagation. We call these conditions as absorbing layers, which

trap the outbound waves at these boundaries, thus preventing reflection of the waves back into the domain of analysis. In this study, the efficacy of using different absorbing layers is investigated in the framework of the FEM formulation of the transient wave propagation in monolithic and multi-material linear elastic domains. We test three different methods of implementing absorbing layers into a computational model: Perfectly Matched Layers (PML), Caughey Absorbing Layer Method or Caughey Damping (CD), and Infinite Elements (IE). The assessment of CD and IE were performed in the commercial FEM software ABAQUS and were compared with benchmark computational results of PML from the literature. The quality of absorption was quantified based on the residual strain energy and displacements present in the domain of interest post interaction of the propagating waves with the absorbing layer. It was determined that the Infinite Elements provides an absorbing layer of reasonable accuracy at relative ease of implementation in seismic tomography simulations.

SEISMIC MODEL 1,561,530

SEISMIC REFLECTIVITY INVERSION VIA A REGULARIZED DEEP IMAGE PRIOR

H.Chen, M.D.Sacchi and J.Gao (Alberta Univ; Xi'an Jiaotong Univ). *2ND ANNUAL SEG/AAPG APPLIED GEOSCIENCE AND ENERGY INTERNATIONAL MEETING [IMAGE] (Houston, TX, 8/28/2022-9/1/2022) ABSTRACTS* pp.2586-2590, 2022. (ISSN 1949-4645; Available at <http://library.seg.org> as of 10/3/2022; **Expanded abstract**)

Supervised deep learning methods have been applied for seismic reflectivity inversion. It has been noticed that supervised deep learning for seismic inversion and imaging needs a considerable amount of labeled data that is often only obtainable via synthetic simulations. A regularized Deep Image Prior (DIP) is proposed to perform seismic reflectivity inversion and alleviate the problem above. The weights of the deep neural network are optimized to fit the observed seismic data. Unlike supervised deep learning, the Deep Image Prior approach focuses on a single dataset and does not require pre-training the network with large datasets. In addition, the method uses the network structure as an implicit regularization of the inverse problem leading to reflectivity estimators with improved lateral continuity and vertical resolution. This work conducts synthetic and field data examples to present a regularized Deep Image Prior method that estimates high-resolution (broadband) reflectivity estimates.

SEISMIC MODEL 1,561,531

A HOLISTIC APPROACH TO COMPUTING FIRST-ARRIVAL TRAVELTIMES USING PHYSICS-INFORMED NEURAL NETWORKS

U.B.Waheed, T.Alkhalifah, E.Haghighat and C.Song (King Fahd Univ Petrol Min; King Abdullah Univ; Massachusetts Inst Technol; Imperial Coll, London). *83RD ANNUAL EAGE CONFERENCE (Online and Madrid, Spain, 6/6-9/2022) ABSTRACTS* 2022. (Abstract no.613; Available at <http://www.earthdoc.org> as of 7/7/2022; 5 pp; **Abstract only**)

Since the original algorithm by John Vidale in 1988 to numerically solve the isotropic eikonal equation, there has been tremendous progress on the topic addressing an array of computational challenges, including improvement of the solution accuracy, incorporation of surface topography, the addition of accurate physics by accounting for anisotropy/attenuation in the medium, and speeding up computations. Despite these advances, these algorithms have no mechanism to carry information gained by solving one problem to the next. Moreover, these approaches may breakdown for certain complex forms of the eikonal equation, requiring simplification of the equations to estimate approximate solutions. Therefore, we seek an alternate approach to address these challenges holistically. We propose an algorithm based on the emerging paradigm of physics-informed neural network to solve different forms of the eikonal equation. We show how transfer learning can be used to speed up computations by utilizing information gained from prior solutions. Such an approach makes the implementation of eikonal solvers much simpler and puts us on a much faster path to progress. The method paves the pathway to

solving complex forms of the eikonal equation that have remained unsolved using conventional algorithms or solved using some approximation techniques at best.

SEISMIC MODEL 1,561,532

EMPLOYING GATE-BASED QUANTUM COMPUTING FOR TRAVEL TIME SEISMIC INVERSION

A.Albino, O.Pires, R.Souza, P.Santos, A.Netto and E.Nascimento (SENAI-CIMATEC). *3RD EAGE HPC IN AMERICAS WORKSHOP (Online, 5/17-18/2022) ABSTRACTS* 2022. (Abstract no.WED07; Available at <http://www.earthdoc.org> as of 10/26/2022; 5 pp; **Abstract only**)

Quantum computing can provide an advantage in computational tasks due to the possibility of performing simultaneous calculations in a higher-order space. In geophysics, some works have been carried out that proposed the use of quantum annealing computing to solve important problems such as seismic inversion. However, no works were found in the literature dealing with these problems using gate-based quantum computing. This work aims to apply gate-based quantum computing heuristics to the traveltimes tomography problem. The heuristics used to solve the problem were the quantum approximate optimization algorithm (QAOA) and warm-start QAOA, which are algorithms developed for near-term applications. Both heuristics used found optimal results in the final probability distribution, showing higher probabilities for better solutions. With warm-starting, it was possible to find more approximate solutions due to the contribution of state initialization, making the optimization less complex.

SEISMIC RECORDING 1,561,533

INCREASING IO THROUGHPUT IN SEISMIC WITH NFS OVER RDMA AND NVIDIA GPU DIRECT STORAGE

C.Benedicto, N.Okita and J.Faccipieri Junior (Campinas State Univ). *3RD EAGE HPC IN AMERICAS WORKSHOP (Online, 5/17-18/2022) ABSTRACTS* 2022. (Abstract no.TUE01; Available at <http://www.earthdoc.org> as of 10/26/2022; 5 pp; **Abstract only**)

Several types of seismic methods had their computing time greatly reduced when they were implemented on graphic processing units (GPUs). These methods have a large amount of parallel work when processing large seismic datasets, and therefore they are able to take advantage of the parallelism offered by GPUs. They are usually present in computer nodes from two to up to eight devices. One consequence of this reduction in computing time is that other steps start to become more relevant to the total execution time. Notable examples of this are traveltimes-based seismic regularization methods, which constantly pull samples from a dataset and have relatively inexpensive computation phases depending upon the chosen traveltimes. These types of problems are called IO-bound. To further improve their performance, it is necessary to decrease the time it takes for the data to be copied from storage to the GPU's memory (VRAM). Two new technologies have the potential to increase the performance of IO-bound applications on network storage. They are NFS over remote direct memory access (RDMA) (NFSoRDMA) and NVIDIA's GPU Direct Storage (GDS). Both technologies are based on RDMA, which is the ability of several components (including components located on different nodes) in the system to exchange data without having to pass it through CPU cores. In this work, we modified our existing seismic regularization benchmark to support GDS. We compared the performance benefits of NFSoRDMA and GDS against traditional NFS over TCP. We conducted our experiments with the GPU-accelerated stacking phase of the tool while considering three different traveltimes-normal moveout (NMO), 2D common reflection surface, and 3D common reflection surface--with a real 3D marine dataset.

SEISMIC RECORDING 1,561,534

ENERGY EFFICIENCY OF REVERSE TIME MIGRATION ON HPC ARCHITECTURES

M.Serpa, P.Silva, C.Kunas, A.Carissimi, J.Panetta and P.Naviaux (Rio Grande Sul Fed Univ; NVIDIA; Aeronautics Inst

Technol). *3RD EAGE HPC IN AMERICAS WORKSHOP (Online, 5/17-18/2022) ABSTRACTS 2022*. (Abstract no.TUE02; Available at <http://www.earthdoc.org> as of 10/26/2022; 5 pp; **Abstract only**)

Reverse time migration (RTM) is a preferred solution for modeling and imaging seismic data in areas with complex wave phenomena. It computes numerical solutions to the complete wave equation. Historically, RTM was impractical due to high computational costs. Nevertheless, developers have been importing their simulations to the new high-performance computing (HPC) architecture, providing faster and more accurate results with each new generation. That makes RTM a viable option in the imaging portfolio when it is coupled with more precise velocity model-building workflows. However, there are several challenges to achieving high performance on HPC architecture. The first is related to choosing the architecture that best fits the simulation. Moreover, the API used to implement the simulation affects the performance and portability of the code. This abstract presents two versions of an RTM simulation that reduces floating-point operations by changing the equation derivatives and improving the simulation's energy efficiency. This paper studies optimizations in different multiple core and graphic processing unit (GPU) architectures, investigating the impact of other APIs on the energy efficiency and portability of the code. The energy efficiency results showed that the CUDA implementation running on the Volta architecture has the best energy efficiency for RTM on GPUs, while for multiple cores, the OpenACC version was the best.

SEISMIC VELOCITY COMPUTATN 1,561,535

A ROBUST MIGRATION VELOCITY ANALYSIS METHOD BASED ON ADAPTIVE DIFFERENTIAL SEMBLANCE OPTIMIZATION

Z.Yu and Y.Liu (China Univ Petroleum). *JOURNAL OF APPLIED GEOPHYSICS* v.207, Dec. 2022. (ISSN 0926-9851; Article no.104851)

Migration velocity analysis (MVA) is an efficient tool to reconstruct low wavenumber components of the model. Compared with data domain methods, the MVA methods are implemented in image domain by processing imaging results directly through minimizing moveouts and improving the coherence of the common image gathers (CIGs), such as angle domain common image gathers (ADCIGs) or subsurface offset domain image gathers (ODCIGs). As one of the wave-equation based migration velocity analysis (WEMVA) methods, differential semblance optimization (DSO) can automatically detect the moveout existed in the CIGs and is convenient to implement. However, referring to the CIGs contaminated by spurious imaging artefacts caused by uneven illumination and irregular observation geometry, the traditional DSO method may produce poor velocity update with oscillations, which can prevent rapid convergence to a correct velocity model. To deal with this issue and extend the solution space, we introduce an adaptive DSO (ADSO) method by replacing the traditional image matching with energy distribution matching. By reducing dependence on the imaging results and introducing a variable weighting function in the calculation of the adjoint sources, the amplitude of the inverted model can be evenly distributed and free of artefacts. Three numerical examples show that the ADSO method is robust with little artefacts presenting in the gradients. Combined with the improved gradient, the ADSO can lead to a stable update. (c2022 Elsevier B.V.)

SHANDONG 1,561,536

A NOVEL ENVELOPE ALGORITHM FOR ESTIMATING AND EVALUATING NOISE EFFECT IN STATIONARY CONTROLLED-SOURCE ELECTROMAGNETIC DATA

C.Zhou, Y.Yang, H.Zhang, J.Wang and H.Sun (Shandong Univ). *JOURNAL OF APPLIED GEOPHYSICS* v.207, Dec. 2022. (ISSN 0926-9851; Article no.104864)

Controlled-source electromagnetic (CSEM) is affected by noise during exploration. Moreover, different frequencies in the data are affected differently by noise. However, past evaluation methods, such as the relative root mean square error (RRMSE) method, are not efficient or accurate, especially when there are many frequencies of interest. Therefore, a noise evaluation method based

on a mixed spectrum envelope algorithm containing wavelet decomposition, Hilbert transform and peak envelope was proposed for the first time. This method estimates the upper bound of the noise effect at the frequencies of interest by the amplitude of the adjacent frequencies rather than by estimating its exact value or statistical average. Based on this method, the maximum possible value of noise effect can be obtained, which is then divided by its raw spectrum to obtain a newly defined noise evaluation parameter, "noise ratio". Using this new parameter, the degree of the noise effect at the frequencies of interest can be evaluated more accurately. Furthermore, using an appropriate threshold, a large number of candidate frequencies including harmonics can be filtered out. The performance of the method is tested on synthetic signals and real data from Shandong Province, China. The test results show that the evaluation method based on the envelope algorithm is more stable and effective than the conventional RMSE method. Based on the features of the method, it can be applied to all periodic signals in other stationary scenarios. (c2022 Elsevier B.V.)

SHEAR WAVE SPLITTING 1,561,537

SHEAR WAVE SPLITTING ANALYSIS METHOD BASED ON GRADIENT DESCENT

Z.He, Y.Yang, W.Li and B.Tao (Chengdu Univ Technology). *83RD ANNUAL EAGE CONFERENCE (Online and Madrid, Spain, 6/6-9/2022) ABSTRACTS 2022*. (Abstract no.611; Available at <http://www.earthdoc.org> as of 7/7/2022; 5 pp; **Abstract only**)

Fracture prediction is an important content in the exploration of fractured reservoirs. Shear wave splitting analysis is an important means for fracture prediction. In order to improve the efficiency of shear wave splitting analysis, we propose a new method based on gradient descent. The R component and T component seismic data of fracture medium are synthesized for testing and compared with the conventional method. The results show that the proposed method can effectively obtain shear wave splitting parameters and improve the computational efficiency compared with the conventional method.

SOUTH CAROLINA 1,561,538

DEBLENDABLE LAND ACQUISITION

A.Kumar, J.Fuller, T.Rayment, M.Phillips, D.Monk, C.Ansorger and S.Schmitt (DUG Technology). *2ND ANNUAL SEG/AAPG APPLIED GEOSCIENCE AND ENERGY INTERNATIONAL MEETING [IMAGE] (Houston, TX, 8/28/2022-9/1/2022) ABSTRACTS* pp.2852-2856, 2022. (ISSN 1949-4645; Available at <http://library.seg.org> as of 10/3/2022; **Expanded abstract**)

Given the success of inversion-based deblending algorithms, simultaneous-source seismic acquisition is now a well-established technology used by many acquisition companies. It allows multiple sources to be fired near-simultaneously in a narrow time interval, which can improve the acquisition efficiency and reduce the cost. To be effective, deblending needs to be performed without compromising data quality. In this paper, we address specific challenges that directly affect the quality and efficiency of inversion-based deblending and provide practical recommendations for future simultaneous-source acquisition.

SOUTH CHINA SEA 1,561,539

A RECOGNITION ALGORITHM OF SEISMIC SIGNALS BASED ON WAVELET ANALYSIS

W.Jiang, W.Ding, X.Zhu and F.Hou (Shanghai Jiao Tong Univ; China Ministry Natural Rsc). *JOURNAL OF MARINE SCIENCE AND ENGINEERING* v.10, no.8, Aug. 2022. (ISSN 2077-1312; Article no.1093)

In order to meet the requirements of mobile marine seismometers to observe and record seismic signals, a study of fast and accurate seismic signal recognition was carried out. This paper introduces the use of the wavelet analysis method for seismic signal processing and recognition, and compares and analyzes the abilities of different wavelet basis functions to detect the seismic signal. By denoising and reconstructing the signal, the distribution law of the

wavelet coefficients of seismic signal at different scales was obtained. On this basis, this paper proposes an identification model of seismic signals based on wavelet analysis and thereby solves the conflict between high speed and high accuracy of seismic signal recognition methods. In this study, the simulation was carried out in the Matlab2020b environment, and the feasibility of wavelet recognition algorithm was proven by applying this algorithm to the seismic signal database for experimental verification.

SOUTH CHINA SEA 1,561,540

HIGH-FREQUENCY DEPENDENCE OF ACOUSTIC PROPERTIES OF THREE TYPICAL SEDIMENTS IN THE SOUTH CHINA SEA

J.Wang, Z.Hou, G.Li, G.Kan, B.Liu, X.Meng, Q.Hua and L.Sun (Marine Geology Inst China; Sun Yat-sen Univ). *JOURNAL OF MARINE SCIENCE AND ENGINEERING* v.10, no.9, Sept. 2022. (ISSN 2077-1312; Article no.1295)

The acoustic characteristics of three fine-grained sediments (silty sand, silt, silty clay) in the South China Sea (SCS) were measured and analyzed at high frequency range of 27–247 kHz. The measurement results show that the sound speed dispersion is a positive linear relation at the measured frequency range, and the attenuation follows nonlinear frequency dependence, $\alpha = \kappa f^n$, where n ranges from 0.59 to 0.85 for the three different sediments in the SCS. The frequency dependence of sound speed and attenuation were compared with the published literature. It was found that for silty clay, clayey silt, silt, and silty sand, the dispersion characteristics of these four sediments are basically consistent; in general, the dispersion of coarse particles is significant, and that of fine particles is weak, and permeability is the key parameter that determines the inflection point of high frequency to low frequency. By modeling these sediments with the Biot–Stoll model, it was found that the Biot–Stoll model can better predict the frequency-dependent characteristics of sound attenuation in a high-frequency band under the matching constraints of sound speed dispersion characteristics, indicating that the Biot–Stoll model has good applicability to different types of sediments in a high-frequency band.

TENGIZ OIL FIELD 1,561,541

TENGIZ FIELD FAULT SHADOWS MITIGATION WITH COMBINED JOINT FWI-TOMOGRAPHY, Q-TOMOGRAPHY, AND LEAST-SQUARE MIGRATION

T.Li, K.S.Lee, B.Gong, K.Yang, K.Zhang, A.Bibolova and Z.Katrenov (In-Depth Geophysical; Chevron Technical Ctr; Tengizchevroil). *2ND ANNUAL SEG/AAPG APPLIED GEOSCIENCE AND ENERGY INTERNATIONAL MEETING [IMAGE] (Houston, TX, 8/28/2022-9/1/2022) ABSTRACTS* pp.2581-2585, 2022. (ISSN 1949-4645; Available at <http://library.seg.org> as of 10/3/2022; **Expanded abstract**)

A pilot project consisting of depth model building and depth migration was performed in 2018 for the Tengiz and Korolev fields onshore Kazakhstan. The pilot work focused on image improvement of a subset of the 2009 3D survey where joint FWI-Grid Based Tomography resulted in a high-resolution subsurface velocity model. The successfully completed pilot demonstrated uplifts to the image quality, especially within the target reservoir interval, and led to the planning and execution of the full-field re-processing project in 2019, with the unresolved residual fault shadows being a major target to be mitigated. Q-Tomography, Q-Migration, and Least-Square Migration were proved to be effective in the mitigation of the fault shadow issues, in addition to the overall imaging improvement on Tengiz and Korolev fields.

TENGIZ OIL FIELD 1,561,542

OPTIMIZED STACKING OF MIGRATED OFFSET VECTOR TILES FOR TENGIZ PSDM IMAGE ENHANCEMENT

T.Li, K.S.Lee, B.Gong, K.Yang, K.Zhang, A.Bibolova and Z.Katrenov (In-Depth Geophysical; Chevron Technical Ctr; Tengizchevroil). *2ND ANNUAL SEG/AAPG APPLIED GEOSCIENCE AND ENERGY INTERNATIONAL MEETING*

[IMAGE] (Houston, TX, 8/28/2022-9/1/2022) ABSTRACTS pp.2651-2655, 2022. (ISSN 1949-4645; Available at <http://library.seg.org> as of 10/3/2022; **Expanded abstract**)

In the reprocessing of the giant Tengiz oil field onshore Kazakhstan, it was observed that the illumination of the deep carbonate platform reservoirs exhibited some azimuthal variations. The azimuthal dependent illuminations could be attributed to the complex overburden, which consists of relatively large faults, that causes fault shadows, as well as the overlying dirty salt embedded with anhydrites rafts. Wide azimuth Kirchhoff and RTM depth migration output image gathers were used for the analysis of the azimuthal influences on the migration stack. The azimuthal image optimization workflow was applied to both Kirchhoff OVT gathers and RTM Vector Offset Tiles that leads to some significant improvements in the final reservoir images.

UINTA BASIN 1,561,543

MONUMENT BUTTE 3D - REPROCESSING CASE STUDY IN UINTA BASIN

M.Preston, X.Li, S.Berman, P.Keith, C.Egger, J.Heim, N.Pralica, D.Brookes and J.Beck (TGS). *2ND ANNUAL SEG/AAPG APPLIED GEOSCIENCE AND ENERGY INTERNATIONAL MEETING [IMAGE] (Houston, TX, 8/28/2022-9/1/2022) ABSTRACTS* pp.2665-2669, 2022. (ISSN 1949-4645; Available at <http://library.seg.org> as of 10/3/2022; **Expanded abstract**)

A 3D land seismic survey was processed using amplitude and azimuthal-friendly workflow. The sequence includes multiple iterations of surface consistent amplitude balancing and surface consistent deconvolution, along with the attenuation of various types of noise in several domains at different processing stages. The resulting final PSTM gathers and stack volumes provide uplift compared to previous processing results. These improvements include broader bandwidths in the low and high end of the spectrum, enhanced structural feature imaging, and improved S/N. Furthermore, using 5D interpolation, data was regularized in offset and azimuth domains allowing surface-related multiple reflections to be identified and successfully removed. The azimuth-separated PSTM gathers preserve the azimuthal variations in the data. The azimuthal velocity variation analysis (VVAz) on the PSTM gathers successfully captured stress anisotropy caused by local and regional features. The anisotropy results corroborate drilling-induced tensile fractures and borehole breakouts on image logs.

VELOCITY ANISOTROPY 1,561,544

A STABLE TTI ACOUSTIC WAVE EQUATION

L.Zhang and E.Ohen (Seismic PPS). *2ND ANNUAL SEG/AAPG APPLIED GEOSCIENCE AND ENERGY INTERNATIONAL MEETING [IMAGE] (Houston, TX, 8/28/2022-9/1/2022) ABSTRACTS* pp.2527-2531, 2022. (ISSN 1949-4645; Available at <http://library.seg.org> as of 10/3/2022; **Expanded abstract**)

There are different acoustic wave equations used in TTI reverse time migration. Some equations have strong shear waves which will create artifacts in final RTM images. In this paper, a pure P wave equation is proposed for TTI media based on the dispersion relation. Compared to some TTI wave equations, our new wave equation is not only shear wave free but also stable even when $\epsilon < \delta$. We validate the accuracy of the acoustic wave equation using synthetic velocity models.

VELOCITY ANISOTROPY 1,561,545

PORO-ACOUSTOELASTICITY FD SIMULATION OF ELASTIC WAVE PROPAGATION IN PRESTRESSED POROUS MEDIA

H.Yang and L.Fu (China Univ Petroleum). *2ND ANNUAL SEG/AAPG APPLIED GEOSCIENCE AND ENERGY INTERNATIONAL MEETING [IMAGE] (Houston, TX, 8/28/2022-9/1/2022) ABSTRACTS* pp.2542-2546, 2022. (ISSN 1949-4645; Available at <http://library.seg.org> as of 10/3/2022; **Expanded abstract**)

Insight into wave propagation in prestressed porous media is of

importance to geophysical applications, such as monitoring changes in geopressure. This issue can be approached by the theory of poro-acoustoelasticity that extends the classical acoustoelasticity of solids to porous media. The relevant poro-acoustoelasticity equations can be formulated from anisotropic poroelasticity equations by replacing the poroelastic stiffness matrix with the acoustoelastic stiffness matrix containing both the second-order 2oeC and third-order 3oeC elastic constants. In this study, a rotated staggered-grid finite-difference (RSG-FD) method is used to solve a first-order velocity-stress formulation of poro-acoustoelasticity equations for elastic wave propagation in prestressed porous media. We perform numerical simulations of wave propagation for the model of poro-acoustoelastic homogeneous space under three states of prestress-confining (hydrostatic), uniaxial, and pure shear. The resulting wavefield snapshots show fast P-, S-, and slow P-wave propagations in poro-acoustoelastic media under loading prestresses, which illustrates that the stress-induced velocity anisotropy is of orthotropy that is strongly related to the orientation of prestresses. These examples demonstrate the significant impact of prestress conditions on seismic responses in both velocity and anisotropy.

VELOCITY ANISOTROPY 1,561,546

THE CALCULATION OF FIRST-ARRIVAL P-WAVE TRAVELTIME FOR ATTENUATING TTI MEDIA

M.Wang, J.Chen, Z.Zhao, K.Ji and S.Chang (Tulsa Univ; PetroChina Research Inst). *2ND ANNUAL SEG/AAPG APPLIED GEOSCIENCE AND ENERGY INTERNATIONAL MEETING [IMAGE] (Houston, TX, 8/28/2022-9/1/2022) ABSTRACTS* pp.2571-2575, 2022. (ISSN 1949-4645; Available at <http://library.seg.org> as of 10/3/2022; **Expanded abstract**)

First-arrival P-wave traveltimes play a crucial role in many geophysical applications such as migration and tomography. And the solution of Eikonal equation has been proven effective and accurate for approximating the traveltimes. Eikonal equation for attenuative case can provide not only the information of phase arrival, but also the decay in wave amplitudes resulted from energy absorption by media. By applying the rotation operator to the eikonal equation in attenuating VTI (vertical transversely isotropic) media, the equation in attenuating TTI (titled transversely isotropic) media can be derived directly. However, numerical methods such as fast marching method that has been widely used for eikonal solutions, updating the traveltimes of each grid points by choosing the minimum of traveltimes, cannot be applied to attenuating case due to no minimum value between two complex numbers. In order to address this issue, the perturbation method can be introduced by decomposing the complex-valued eikonal equation into real and imaginary part, called zeroth- and first-order governing equation, respectively. The real part of the complex-valued travel-time corresponds to the phase of waves, while the imaginary part describes the magnitude of attenuation. Thus, by solving these governing equations successively, the real and imaginary part of travel-time can be obtained. Numerical modeling for homogeneous or SEG/ Hess attenuating TTI media demonstrate the effectiveness and accuracy of our technique.

VELOCITY ANISOTROPY 1,561,547

ELASTIC ANISOTROPIC FINITE-DIFFERENCE FULL-WAVE MODELING AND IMAGING OF 2D TILTED TRANSVERSELY ISOTROPIC (TTI) MEDIA

L.Behera (CSIR-NGRI). *JOURNAL OF APPLIED GEOPHYSICS* v.207, Dec. 2022. (ISSN 0926-9851; Article no.104837)

Imaging below the tilted transversely isotropic (TTI) media pose serious problems and distortions of the subsurface geological targets of interest for hydrocarbon exploration, which is very common in fold-thrust belts or active tectonic areas like the Rocky Mountain foothills of the Canada or foothills of the Himalaya. To model and image below the TTI media having symmetry axis orthogonal to dipping anisotropic layers, a 2D TTI thrust sheet is considered for elastic anisotropic finite-difference full-wave modeling and generation of synthetic seismic data using the robust staggered-grid scheme of wave propagation. Free-surface boundary

conditions at the top and absorbing boundary conditions for the other three sides of the model have been imposed to reduce undesirable edge effects and suppress dispersions. The synthetic seismic data generated for the 2D TTI thrust model are migrated using the anisotropic Kirchhoff pre-stack time (PSTM) and depth migration (PSDM) technique followed by the migration velocity analysis (MVA) algorithm. The traveltime computations are made using robust eikonal equations with fourth-order elastic anisotropic finite-difference solutions to handle large tilts (ν) along with anisotropic ray-tracing to image below the TTI thrust sheet. The MVA algorithm adopted also estimates the anisotropic parameters ϵ and δ accurately within the acceptable error limit through successive iterations of inversion and parameter update, which results in sufficient flattening of the reflection events in the common image gathers (CIGs). This is a powerful and stable methodology to handle large tilt ($\nu = 60^\circ$) of the steeply dipping reflectors in complex geological structure like the TTI thrust model without much distortion of CIGs for which the symmetry axis of each TTI block is set orthogonal to the bottom of the reflectors having different tilts. (c2022 Elsevier B.V.)

VELOCITY ANISOTROPY 1,561,548

Q-COMPENSATION IMAGING OF ANISOTROPIC VISCOUS QUASI-ACOUSTIC MEDIA ALONG WAVEFIELD PROPAGATION PATH

B.Zhang and H.Wang (Tongji Univ). *2ND ANNUAL SEG/AAPG APPLIED GEOSCIENCE AND ENERGY INTERNATIONAL MEETING [IMAGE] (Houston, TX, 8/28/2022-9/1/2022) ABSTRACTS* pp.2792-2796, 2022. (ISSN 1949-4645; Available at <http://library.seg.org> as of 10/3/2022; **Expanded abstract**)

In the process of seismic wave propagation in real underground media, seismic wavefield is affected by anisotropy, Q attenuation and other factors. In order to more realistically simulate the propagation process of seismic wave in underground media, it is necessary to consider forward propagation and imaging in complex media. At present, the existing forward modeling and imaging methods can be easily realized in anisotropic and absorption attenuation media respectively, however it is difficult to realize forward modeling and imaging in anisotropic absorption attenuation media. RTM can realize forward modeling and Q-compensation imaging in anisotropic absorption attenuation media based on two-way wave equation, however, the mathematical derivation and numerical implementation of two-way wave equation in anisotropic absorption attenuation media are relatively cumbersome. In this paper, the 15-degree equation in the ray-centered coordinate system of VTI media is solved in the frequency-space domain (Zhang et al., 2021), and the complex velocity is introduced to realize Q-compensation imaging in VTI absorption attenuation media. The numerical experiments verify the effectiveness of this method.

VELOCITY MODEL 1,561,549

Q-LSRTM USING VISCOACOUSTIC VTI WAVE EQUATION BASED ON THE NEARLY CONSTANT Q MODEL

S.S.Zhang, B.L.Gu and Z.C.Li (China Univ Petroleum). *2ND ANNUAL SEG/AAPG APPLIED GEOSCIENCE AND ENERGY INTERNATIONAL MEETING [IMAGE] (Houston, TX, 8/28/2022-9/1/2022) ABSTRACTS* pp.2729-2733, 2022. (ISSN 1949-4645; Available at <http://library.seg.org> as of 10/3/2022; **Expanded abstract**)

In the imaging process, ignoring the effects of attenuation and anisotropy will reduce the quality and resolution of the imaging profile. In this paper, we present a Q-compensated least-squares reverse time migration method in viscoacoustic VTI media (Q-VTI-LSRTM) using the pure qP-wave viscoacoustic VTI wave equation. Based on the adjoint theory, we derive the demigration operator, adjoint operator, and gradient-sensitive kernel. The proposed method can simultaneously handle the anisotropy and viscosity of subsurface media, and it's free of the quasi-SV-wave artifacts. Moreover, the method can compensate for attenuation effects during the iterative process to avoid the instability caused by high-frequency noise. The numerical results show that the proposed

method can compensate the amplitude loss and phase distortion caused by attenuation, and correct the inaccurate position of the reflection interfaces caused by anisotropy, which improves the accuracy and resolution of the imaging profile.

VELOCITY MODEL 1,561,550

OPTIMIZED DOWNWARD CONTINUATION FOR THE ONE-WAY WAVE EQUATION IN TTI MEDIA

C.Macesanu and F.Liu (TGS). *2ND ANNUAL SEG/AAPG APPLIED GEOSCIENCE AND ENERGY INTERNATIONAL MEETING [IMAGE]* (Houston, TX, 8/28/2022-9/1/2022) ABSTRACTS pp.2734-2738, 2022. (ISSN 1949-4645; Available at <http://library.seg.org> as of 10/3/2022; **Expanded abstract**)

This paper proposes an enhancement to the accuracy of the Fourier Finite Difference (FFD) method used in the one-way wave equation. Errors associated with FFD can be magnified in media with strong lateral variations in velocity. To reduce the magnitude of these errors, the reference velocity at each depth may be replaced by a velocity function which is a smooth version of the exact model. An isotropic phase-shift plus interpolation (PSPI) step is first employed to compute the wavefield propagation with this intermediate velocity function, followed by corrections for anisotropy and residual velocity variations implemented using finite difference (FD). To illustrate the accuracy of the method, several migration examples are shown.

VELOCITY MODEL 1,561,551

AN OPTIMAL APERTURE CROSSCORRELATION IMAGING CONDITION FOR MARCHENKO IMAGING

X.Chen, Y.Hu, Y.Wo, W.Cao and X.Huang (Southwest Petroleum Univ). *2ND ANNUAL SEG/AAPG APPLIED GEOSCIENCE AND ENERGY INTERNATIONAL MEETING [IMAGE]* (Houston, TX, 8/28/2022-9/1/2022) ABSTRACTS pp.2787-2791, 2022. (ISSN 1949-4645; Available at <http://library.seg.org> as of 10/3/2022; **Expanded abstract**)

Marchenko imaging is a novel technique to create subsurface images which are free of spurious artifacts related to internal multiples. The foundation of Marchenko imaging is applying a specific imaging condition to the retrieved Green's functions. Crosscorrelation imaging condition is commonly used since holding advantages of straightforward implementations and stable performance, especially in field data applications. However, the image quality from crosscorrelation imaging condition is closely related to migration aperture, which specifies the spatial integration range involved in the crosscorrelation function. By investigating the impact of the migration aperture on crosscorrelation-based Marchenko imaging, we find that a large migration aperture will result in an image with low resolution and uneven energy distribution. To address this problem, we adopt an optimal aperture crosscorrelation Marchenko imaging (OAC-MI) method which imposes a constraint on spatial range of the integration. Synthetic tests demonstrate that the proposed approach improves the image resolution while keeps the energy distributed more evenly.

VERTICAL SEISMIC PROFILING 1,561,552

EFFECTS OF SOURCE MISPOSITIONING ON REPEATABILITY FOR ONSHORE DAS VSP DATA

R.Isaenkov, K.Tertyshnikov, A.Yurikov and R.Pevzner (Curtin Univ). *83RD ANNUAL EAGE CONFERENCE (Online and Madrid, Spain, 6/6-9/2022) ABSTRACTS* 2022. (Abstract no.614; Available at <http://www.earthdoc.org> as of 7/7/2022; 5 pp; **Abstract only**)

4D seismic is an established approach in monitoring hydrocarbon reservoir production carbon storage. To reliably detect and track changes in the subsurface, time-lapse seismic data should achieve a high level of repeatability during acquisition. The repeatability is affected by many factors. The mispositioning--the distance between a source or receiver location of the baseline data and monitor surveys--is one of the key factors during acquisition and significant effort is usually applied to maintain it as low as

possible. Repeatability might be drastically reduced by the mispositioning of just a few meters. The borehole seismic with distributed acoustic sensing (DAS) with the permanently installed optical fibre in a well eliminates the mispositioning for the receivers. However, source points on the surface are still prone to misposition errors. To study the effect of mispositioning, we designed a dedicated experiment and acquired a DAS VSP survey at the Curtin GeoLab facility using a vibroseis source. Pairwise comparison of 76 shot points spread from 0.1 to 25 m apart showed a significant repeatability decrease due to small positioning errors as well as a strong effect of rapid spatial near-surface variations on repeatability.

VIKING GRABEN 1,561,553

WAVE-EQUATION DECONVOLUTION: A SHORT-PERIOD DEMULTIPLE TOOL FOR STREAMER, OBN AND LAND ENVIRONMENTS

G.Poole, M.Farshad, Z.Jin and B.Li (Cie Generale Geophysique). *FIRST BREAK* v.40, no.12, pp.59-64, Dec. 2022. (ISSN 0263-5046; ISSN 1365-2397)

Short-period multiple attenuation is often challenging, as the multiple generators are typically not sufficiently well recorded as primary events for SRME approaches to be successful. Model-based approaches have traditionally been used to circumvent this problem, but they may only model multiples generated by key events, such as the water bottom. Deconvolution-based alternatives offer the possibility of modeling multiples from more short-period multiple generators, but, in practice, many acquisition geometries are not well suited to higher-dimensional deconvolution implementations. We discuss a wave-equation deconvolution (WEDecon) approach that derives its prediction operator from the image domain. The image is then used to predict multiples, which are removed from the data. We highlight the flexibility of the WEDecon approach using data examples from towed-streamer, ocean-bottom node (OBN), and land geometries. The WEDecon approach has successfully significantly reduced the levels of residual multiples present in all these data types. We acknowledge, however, that short-period multiple attenuation is still a challenging topic and that further work is necessary in this area.

WAVE ATTENUATION 1,561,554

PRE-MIGRATION ATTENUATION ANALYSIS AND MAPPING TO IMAGE DOMAIN BY WEIGHTED MIGRATIONS

Y.Sun, C.Wu, M.Fan and Z.Tan (Chevron). *2ND ANNUAL SEG/AAPG APPLIED GEOSCIENCE AND ENERGY INTERNATIONAL MEETING [IMAGE]* (Houston, TX, 8/28/2022-9/1/2022) ABSTRACTS pp.2591-2595, 2022. (ISSN 1949-4645; Available at <http://library.seg.org> as of 10/3/2022; **Expanded abstract**)

A conventional approach to attenuation compensation for seismic imaging is to pick attenuated time t^* from depth-migrated data and to invert t^* in tomography for spatially varying Q . The drawbacks of the approach include workflow complexity and spectral distortions by depth migrations. We propose picking t^* from pre-migration data, computing a data-domain $1/Q$ to approximately to the partial derivation of t^* with respect to t , and mapping t^* and $1/Q$ to image domain by depth migrations. For low-dip and gently varying earth models, test results show that common-image-point (CIP) gathers of $1/Q$ so obtained yield reasonable $1/Q$ models. If required, the CIP gathers of t^* so mapped can be used in tomography to invert for more general Q models.

DRILLING (WELL)

BALANCED PRESSURE DRILLING 1,561,555

PREDICTION OF OVERPRESSURE ZONES IN MARINE SEDIMENTS USING ROCK-PHYSICS AND OTHER APPROACHES

N.Dubinya, I.Bayuk, A.Hortov, K.Myatchin, A.Pirogova and P.Shchuplov (Russian Academy Sciences; Novye Proekty LLC; Lomonosov Moscow St Univ). *JOURNAL OF MARINE SCIENCE AND ENGINEERING* v.10, no.8, Aug. 2022. (ISSN 2077-1312; Article no.1127)

The paper discusses the problem of localizing zones of high pore pressure in sub-bottom sediments (first tens of meters under the seafloor). Prediction of the overpressure zones in the near-surface is required for the mitigation of risks at the early stages of the offshore hydrocarbon field exploration and development. The results of seismic data interpretation generally serve as the main source of information for this kind of problems, yet there are other methods to predict overpressure zones in the subsurface. The paper presents the results of the overpressure zone prediction using a set of methods including empirical ones, and the approach based on rock-physics modeling that features the soft-sand model of unconsolidated media effective properties. While the rock-physics modeling grants the most reliable result, it is also the most demanding method to the input data. Hence, it can be used to verify other methods of the overpressure zone prediction. We present the results of the overpressure zone prediction at the research site on the Black Sea shelf. The mitigation of the drilling risks via changing the drilling conditions is discussed in detail. As the drilling through the overpressure zones is often a necessity, the engineering solutions proposed in the paper can be applied elsewhere when facing similar problems typical for offshore exploration.

BIT (ROCK) 1,561,556

DRILLING BIT NOZZLE BASED SENSING SYSTEM

A.Alshaikh, B.Li, G.Zhan and T.E.Moellendick, asrs. (Saudi Arabian Oil Co; Aramco Services Co). World 2022/204,183A1, p. 9/29/2022, f. 3/22/2022 (Appl. 2,221,387), pr. U.S. 3/22/2021 (Appl. 208,361) (E21B-0010/00; E21B-0010/60).

A system for gathering downhole measurements includes a drill bit, at least one nozzle receptacle located on the drill bit, and a sensor system. The sensor system has a sensor housing, a flow path extending through the sensor housing, wherein the flow path allows fluid to flow through the sensor housing, and an internal cavity provided within the sensor housing separate from the flow path. The internal cavity contains components that include at least one sensor for gathering data about drill bit conditions and downhole conditions, a powering unit, a printed circuit board, and an electrical conductor, wherein the sensor housing is installed in the at least one nozzle receptacle.

BIT (ROCK) 1,561,557

CHARGING AND COMMUNICATION INTERFACE FOR DRILL BIT NOZZLE-BASED SENSING SYSTEM

B.Li, A.Alshaikh, C.P.Gooneratne, G.Zhan and T.E.Moellendick, asrs. (Saudi Arabian Oil Co; Aramco Services Co). World 2022/204,170A1, p. 9/29/2022, f. 3/22/2022 (Appl. 2,221,374), pr. U.S. 3/22/2021 (Appl. 208,333) (E21B-0010/60).

A method includes utilizing a charging and communication interface and a sensor system to gather downhole measurements. The method further includes charging and activating the sensor system using the charging and communication interface, installing the sensor system into a nozzle of a drill bit, running the drill bit into a wellbore, conducting measurements using the sensor system, pulling the drill bit out of the wellbore, and contacting the charging and communication interface with the sensor system to retrieve the measurements from the sensor system.

DIRECTIONAL DRILLING 1,561,558

HIGH-RELIABILITY FLEXIBLE DRILL ROD

X.Wan, Z.Xu, Z.Yang and X.Wan. World 2022/206,896A1, p. 10/6/2022, f. 3/31/2022 (Appl. 2,284,419), pr. China 4/2/2021 (Appl. 2021-10,362,324) (E21B-0017/02; E21B-0007/06; E21B-0017/16). (Assigned to X.Wan; **In Chinese**)

The present disclosure relates to a high-reliability flexible drill rod comprising a plurality of transmission units that are connected end to end. Each transmission unit comprises a drill collar housing, a mandrel, a bit pressure transmission structure and a torque transmission structure, wherein the bit pressure transmission structure and the torque transmission structure are arranged independently from each other to achieve separate transmission of bit pressure and torque of a directional drilling tool. The structure is simple, and the development costs of a multilayer oil field are significantly reduced. A deflection center of the bit pressure transmission structure and a deflection center of the torque transmission structure coincide with each other, and during design, the length of the transmission unit can be shortened to the greatest extent, such that the requirements of short-radius and ultra-short-radius drilling are met, the difficulty of well deviation control in a rotary drilling process is reduced while high-build-rate rotary directional drilling is achieved, and the reliability and the deflecting stability of an apparatus are improved.

DRILLING ACTIVITY 1,561,559

69TH ANNUAL RIG CENSUS 2022

J.Rovig (NOV Inc). *ANNUAL IADC GENERAL MEETING (New Orleans, LA, 11/2-4/2022) PROCEEDINGS 2022*. (Available at <http://www.iadc.org> as of 11/15/2022; 24 pp)

[Copy of visual presentation available from P.A.]

DRILLING ACTIVITY 1,561,560

PROJECTILE DRILLING SYSTEM

M.C.Russell, L.D.Underwood, L.Vanstone, P.Bailey, D.E.Bernhard, T.Cutshall, K.J.Durkee, K.Newberg and A.J.Abeyta, asrs. (HyperSciences Inc). World 2022/213,074A1, p. 10/6/2022, f. 3/29/2022 (Appl. 2,271,422), pr. U.S. 3/30/2021 (Appl. 63/168,133) and U.S. 3/23/2022 (Appl. 656,133) (E21B-0007/16; E21B-0007/00; E21B-0017/18).

Geologic material in a borehole is weakened by accelerating a projectile into contact with the material. A drill bit is then used to bore through the weakened material. To accelerate the projectile, an endcap is placed in a conduit using a source of gas. The endcap isolates the conduit from the external environment. A projectile is then positioned in the conduit above the endcap. Movable members within the conduit are operated in sequence to enable single endcaps and projectiles to be moved into the conduit. Gas from the conduit is evacuated into an annulus between the conduit and a surrounding conduit, and a propellant material is provided into the conduit. The propellant material applies a force to the projectile to accelerate the projectile into contact with the geologic material. A fluid is circulated down a second annulus outside of the surrounding conduit to contact the drill bit and remove debris.

DRILLING ACTIVITY 1,561,561

SELF-EXCITATION SHAFT PUNCHING AND INDUCED UNLOADING COUPLING ROCK BREAKING DRILL BIT AND DRILLING SPEED-UP METHOD

Y.Liu, X.Liu, J.Liu, Z.Guan, D.Zou, H.Liao, S.Weil, Z.Zhang and X.He, asrs. (China Univ Petroleum). World 2022/205,546A1, p. 10/6/2022, f. 4/26/2021 (Appl. 2,189,849), pr. China 3/30/2021 (Appl. 2021-10,338,814) (E21B-0010/16; E21B-0010/43). (**In Chinese**)

A self-excitation shaft punching and induced unloading coupling rock breaking drill bit comprises a drill bit body; an external annular rock breaking part is provided at a drilling end of the drill bit body, and the middle part of a head end of the external annular rock breaking part is concaved inwards to form a central rock breaking part; a plurality of blades and a plurality of cones embedded with cone cutting teeth are provided on the external

annular rock breaking part in the circumferential direction; a plurality of outer ring cutting teeth are provided on the radial outer end surfaces of the blades in a generatrix direction; central cutting teeth are provided on a bottom end surface of the central rock breaking part; and a drill bit nozzle is provided on the drill bit body.

DRILLING EQUIPMENT 1,561,562

PREDICT DRILLING EQUIPMENT FAILURE USING AI-BASED SOUND WAVE ANALYSIS METHODOLOGY

S.A.Alsaif and T.Saud Alothman (King Saud Univ). *OFFSHORE TECHNOLOGY CONFERENCE [OTC] (Houston, TX, 5/2-5/2022) PROCEEDINGS 2022*. (ISBN 978-1-61399-852-6; OTC-31828; Available at <http://www.onepetro.org> as of 6/23/2022; 6 pp)

This paper focuses on using AI-based sound-wave analysis of drilling equipment to assess its health conditions, to predict equipment failure by detecting anomalous sound patterns in both time and frequency domains, and to apply predictive maintenance. Machines can produce noise with frequencies higher than the upper audible limit of human hearing; these frequencies are referred to as ultrasounds (or ultrasonic sounds). Thus, by listening to a wider sound spectrum, a better understanding of the equipment's state is achieved, which will lead to more accurate failure prediction methods. The process starts by capturing sounds via microphone. Then, short-time Fourier Transform is used to convert time-domain sound waves to its corresponding frequency domain. Both time- and frequency-domain signals are combined to form a two-dimensional spectrogram. This spectrogram is trained using an AI model to learn the difference between normal and abnormal equipment sounds. After training, the system identifies anomalous sounds the equipment might produce. This generates an alert to the operational team to take action, preventing equipment failure. Compared to the human auditory system, the experimental results showed that the proposed method achieved significant improvements in anomalous sound detection only for machines that can produce noise in the ultrasound region, while other machines achieved worse results compared to the audible sound region. (Copyright 2022 OTC)

DRILLING EQUIPMENT 1,561,563

FLUID INLET SLEEVES FOR IMPROVING FLUID FLOW IN EARTH-BORING TOOLS, EARTH-BORING TOOLS HAVING FLUID INLET SLEEVES, AND RELATED METHODS

J.M.Bilen and J.Morin, asrs. (Baker Hughes Oilfield LLC). *World 2022/204,407A1*, p. 9/29/2022, f. 3/24/2022 (Appl. 2,221,749), pr. U.S. 3/24/2021 (Appl. 211,522) (E21B-0010/61; E21B-0010/42; E21B-0010/60).

An earth-boring tool includes a nozzle port extending from an external surface to an internal fluid plenum of a tool body. A fluid inlet sleeve is disposed within the nozzle port of the tool body. The fluid inlet sleeve includes a hollow cylinder having a longitudinal end oriented within the internal fluid plenum. The longitudinal end of the fluid inlet sleeve includes one surface oriented at an angle within a range from greater than 0 degrees to about 90 degrees relative to a plane to which a longitudinal axis of the fluid inlet sleeve is normal.

DRILLING FLUID SYSTEM 1,561,564

FILTER TOOLS AND METHODS OF FILTERING A DRILLING FLUID

A.H.Al-Bayat and O.M.Alhamid, asrs. (Saudi Arabian Oil Co; Aramco Services Co). *World 2022/211,826A1*, p. 10/6/2022, f. 4/22/2021 (Appl. 2,128,568), pr. U.S. 3/29/2021 (Appl. 215,322) (E21B-0027/00; E21B-0021/00; E21B-0021/10).

A filter tool for a wellbore may include an outer housing, a filtration system, at least one filter tool sensor, and a filter motor. The outer housing may have an interior wall comprising at least one port and an exterior wall defining an exterior surface of the filter tool. The exterior wall may be movable between a first position in which the exterior wall covers the at least one port in the interior wall and a second position in which the exterior wall

uncovers the at least one port in the interior wall. The interior wall of the outer housing and the filtration system may cooperate to define a collection chamber. The filter motor may move the exterior wall of the outer housing between the first position and the second position. Embodiments also include systems and methods employing the filter tool.

DRILLING OPTIMIZATION 1,561,565

SUCCESSFUL DRILLING OPTIMIZATION IN CARBONIFEROUS FORMATION SETS NEW BENCHMARK PERFORMANCE STANDARDS FOR THE SUBANDEAN AREA OF BOLIVIA

J.P.Tocantins, C.Vazquez Carrizo, J.Creamer, D.Mendoza, G.Ortuno and R.Duran (Schlumberger; Repsol). *OFFSHORE TECHNOLOGY CONFERENCE [OTC] (Houston, TX, 5/2-5/2022) PROCEEDINGS 2022*. (ISBN 978-1-61399-852-6; OTC-31824; Available at <http://www.onepetro.org> as of 6/23/2022; 18 pp)

The Margarita-10 well is located in the Caipipendi block of southern Bolivia. This block accounts for 30% of the gas production for the entire country. An operator faced a unique challenge to reduce well construction costs for this well while drilling through a harsh Carboniferous formations sequence. The Carboniferous interval is extremely hard and abrasive with unconfining compressive strength (UCS) values ranging from 12,000 psi to 24,000 psi, averaging 20,000 psi with 32,000-psi peaks. This interval is a complex drilling environment consisting of interbedded, conglomeratic, hard, and abrasive lithologies that presents several drilling obstacles, such as formation heterogeneity and multiple geological uncertainties. These obstacles often impact drilling operations, including the bit's cutting structure being prematurely damaged that can cause nonproductive time typically related to the low rate of penetration (ROP) and poor drillstring dynamic behavior with severe levels of shocks; thus, multiple unwanted bottomhole assembly (BHA) trips. The operator's major objective was to reduce the high well-construction costs in this environment; hence, motivating the search for a novel drill-bit cutting structure design that would produce a step change in drilling performance. To accurately determine the environmental factors that influence bit performance, a detailed formation mapping analysis was performed using geological data from nearby wells. To comprehend the causes of previous failure modes, an engineering program for rock-strength identification was used to identify the rock types and lithology characteristics, such as rock UCS, expected formation abrasion, and impact indexes. This information was used to adjust the digital rock file and better reproduce the actual drilling conditions in the Carboniferous strata virtually to develop a suitable cutting structure, predict drillstring vibrations, and recommend optimal drilling parameters to maximize the performance of the product downhole. The operator successfully deployed the novel drill-bit cutting structure, achieving above field average results in terms of ROP and footage. (Copyright 2022 OTC)

DRILLING PLATFORM 1,561,566

COST EFFECTIVE FIXED OFFSHORE PLATFORM IN SHALLOW WATER WITHOUT JACKET

P.K.Chatterjee and J.Shah (Dragon Oil Holdings Ltd). *OFFSHORE TECHNOLOGY CONFERENCE [OTC] (Houston, TX, 5/2-5/2022) PROCEEDINGS 2022*. (ISBN 978-1-61399-852-6; OTC-31841; Available at <http://www.onepetro.org> as of 6/23/2022; 16 pp)

This paper proposes an alternative design of small wellhead platforms in shallow water that require permanent manning due to operational requirements. The proposed structure is a combination of two monopods of moderate diameter (54 in.) connected rigidly by structural members. Multiple wells can be drilled through one of the two piles by using conductor sharing wellhead technology. The inadequate structural stability of the twin-pile platform without a jacket against environmental loads will be ensured by a few tie members connected to seabed with help of specially-designed small concrete foundations. Tie members will be bolted to the pile and the foundation. Each tie member will be lifted offshore together with the concrete foundation for quick installation and correct

positioning of the foundation on the seabed. The pre-fabricated deck will be welded to the top of the pile. Numerical studies include structural design of a platform at 20 m water depth for omnidirectional waves of 10.5 m height as per API RP 2A working stress design method. The analytical method is provided to simulate interaction of concrete foundations with soil that can be easily implemented in structural analysis. The results indicate that the proposed structure has considerable reserve strength against failure due to extreme environmental loads and impact from medium-sized boats. (Copyright 2022 OTC)

DRILLING PLATFORM 1,561,567

OFFSHORE DRILLING PLATFORM ENGINE ROOM VENTILATION EXPERIMENTAL DEVICE

H.Liu, S.Guo, B.Tian and P.Zhao, asrs. (Tangshan Ship Tech Co Ltd). World 2022/198,542A1, p. 9/29/2022, f. 3/25/2021 (Appl. 2,182,888) (B63B-0071/00; F24F-0007/00; G01M-0099/00). (In Chinese)

The present invention relates to the technical field of offshore equipment, and in particular to an offshore drilling platform engine room ventilation experimental device. For the problems that the existing experimental devices are inconvenient to use, and the experimental results are not accurate because the experimental conditions cannot be changed, the following solution is proposed: the device comprises a box body; two supports are symmetrically fixed to the bottom of the box body; two air outlets are symmetrically formed on the box body; a mounting plate is slidably installed on the bottom inner wall of the box body; a rotating rod is rotatably installed on the mounting plate; a plurality of fan blades are fixedly installed on the rotating rod; a first drive motor is fixedly installed on one side of the mounting plate; a drive shaft is fixedly installed on the output shaft of the first drive motor; one end of the drive shaft is fixedly connected to the rotating rod; and a support column is rotatably installed on the bottom inner wall of the box body. The present invention is convenient to use, can ensure ventilation effect, and allows for change of the experimental environment, thereby effectively improving the accuracy of test results.

DRILLING RIG 1,561,568

SYSTEMS AND METHODS FOR GENERATION OF ELECTRICAL POWER AT A DRILLING RIG

A.B.Bodishbaugh and C.J.Murtland, asrs. (ICE Thermal Harvesting LLC). World 2022/213,115A1, p. 10/6/2022, f. 3/31/2022 (Appl. 2,271,486), pr. U.S. 4/2/2021 (Appl. 63/200,908), U.S. 7/2/2021 (Appl. 305,293), U.S. 7/2/2021 (Appl. 305,294), U.S. 7/2/2021 (Appl. 305,296), U.S. 7/2/2021 (Appl. 305,297), U.S. 7/2/2021 (Appl. 305,298), U.S. 9/22/2021 (Appl. 481,658), U.S. 9/24/2021 (Appl. 63/261,601), U.S. 10/6/2021 (Appl. 494,936), U.S. 1/19/2022 (Appl. 578,520), U.S. 1/19/2022 (Appl. 578,528), U.S. 1/19/2022 (Appl. 578,550), U.S. 1/19/2022 (Appl. 578,542), U.S. 2/11/2022 (Appl. 650,811), U.S. 2/14/2022 (Appl. 670,827), U.S. 2/28/2022 (Appl. 682,126), U.S. 3/18/2022 (Appl. 63/269,572), U.S. 3/24/2022 (Appl. 63/269,862), U.S. 3/29/2022 (Appl. 657,011), U.S. 3/29/2022 (Appl. 657,009) and U.S. 3/29/2022 (Appl. 657,015) (E21B-0041/00; F01D-0015/10; F01K-0007/16; F01K-0007/30; F01K-0025/00; F01K-0025/06; F01K-0027/00; F01K-0027/02).

Embodiments of systems and methods for generating power in the vicinity of a drilling rig are disclosed. During a drilling operation, heat generated by drilling fluid flowing from a borehole, exhaust from an engine, and/or fluid from an engine's water (or other fluid) jacket, for example, may be utilized by corresponding heat exchangers to facilitate heat transfer to a working fluid. The heated working fluid may cause an ORC unit to generate electrical power.

DRILLING RIG 1,561,569

SYSTEMS AND METHODS FOR GENERATION OF ELECTRICAL POWER AT A DRILLING RIG

A.B.Bodishbaugh and C.J.Murtland, asrs. (ICE Thermal Harvesting LLC). World 2022/213,114A1, p. 10/6/2022, f. 3/31/2022

(Appl. 2,271,484), pr. U.S. 4/2/2021 (Appl. 63/200,908), U.S. 7/2/2021 (Appl. 305,294), U.S. 7/2/2021 (Appl. 305,296), U.S. 7/2/2021 (Appl. 305,293), U.S. 7/2/2021 (Appl. 305,297), U.S. 7/2/2021 (Appl. 305,298), U.S. 9/22/2021 (Appl. 481,658), U.S. 9/24/2021 (Appl. 63/261,601), U.S. 10/6/2021 (Appl. 494,936), U.S. 1/19/2022 (Appl. 578,520), U.S. 1/19/2022 (Appl. 578,528), U.S. 1/19/2022 (Appl. 578,550), U.S. 1/19/2022 (Appl. 578,542), U.S. 2/11/2022 (Appl. 650,811), U.S. 2/14/2022 (Appl. 670,827), U.S. 2/28/2022 (Appl. 682,126), U.S. 3/18/2022 (Appl. 63/269,572), U.S. 3/24/2022 (Appl. 63/269,862), U.S. 3/29/2022 (Appl. 657,011), U.S. 3/29/2022 (Appl. 657,009) and U.S. 3/29/2022 (Appl. 657,015) (E21B-0036/00; E21B-0047/07; F03G-0007/04).

Embodiments of systems and methods for generating power in the vicinity of a drilling rig are disclosed. During a drilling operation, heat generated by drilling fluid flowing from a borehole, exhaust from an engine, and/or fluid from an engine's water (or other fluid) jacket, for example, may be utilized by corresponding heat exchangers to facilitate heat transfer to a working fluid. The heated working fluid may cause an ORC unit to generate electrical power.

DRILLING RIG 1,561,570

SYSTEMS AND METHODS FOR GENERATION OF ELECTRICAL POWER AT A DRILLING RIG

A.B.Bodishbaugh and C.J.Murtland, asrs. (ICE Thermal Harvesting LLC). World 2022/213,113A1, p. 10/6/2022, f. 3/31/2022 (Appl. 2,271,482), pr. U.S. 4/2/2021 (Appl. 63/200,908), U.S. 7/2/2021 (Appl. 305,294), U.S. 7/2/2021 (Appl. 305,296), U.S. 7/2/2021 (Appl. 305,293), U.S. 7/2/2021 (Appl. 305,297), U.S. 7/2/2021 (Appl. 305,298), U.S. 9/22/2021 (Appl. 481,658), U.S. 9/24/2021 (Appl. 63/261,601), U.S. 10/6/2021 (Appl. 494,936), U.S. 1/19/2022 (Appl. 578,520), U.S. 1/19/2022 (Appl. 578,528), U.S. 1/19/2022 (Appl. 578,550), U.S. 1/19/2022 (Appl. 578,542), U.S. 2/11/2022 (Appl. 650,811), U.S. 2/14/2022 (Appl. 670,827), U.S. 2/28/2022 (Appl. 682,126), U.S. 3/18/2022 (Appl. 63/269,572), U.S. 3/24/2022 (Appl. 63/269,862), U.S. 3/29/2022 (Appl. 657,011), U.S. 3/29/2022 (Appl. 657,009) and U.S. 3/29/2022 (Appl. 657,015) (F03G-0007/04; E21B-0021/01; E21B-0021/06; F03G-0004/00; F24T-0050/00).

Embodiments of systems and methods for generating power in the vicinity of a drilling rig are disclosed. During a drilling operation, heat generated by drilling fluid flowing from a borehole, exhaust from an engine, and/or fluid from an engine's water (or other fluid) jacket, for example, may be utilized by corresponding heat exchangers to facilitate heat transfer to a working fluid. The heated working fluid may cause an ORC unit to generate electrical power.

DRILLING SHIP 1,561,571

ENSURING THE ENVIRONMENTAL FRIENDLINESS OF DRILLSHIPS DURING THEIR OPERATION IN SPECIAL ECOLOGICAL REGIONS OF NORTHERN EUROPE

S.Sagin, O.Kuropyatnyk, A.Sagin, I.Tkachenko, O.Fomin, V.Pistek and P.Kucera (Odessa National Univ; Ukraine State Univ; Brno Univ Technology). *JOURNAL OF MARINE SCIENCE AND ENGINEERING* v.10, no.9, Sept. 2022. (ISSN 2077-1312; Article no.1331)

The features of the operation of the drillship-type vessels in special ecological regions of Northern Europe are considered. The main gap in the study of these systems is to determine the optimal degree of recirculation. The requirements of the International Maritime Organization for the emission of nitrogen oxides from the exhaust gases of marine diesel engines are given. The aim of the study is to determine the optimal degree of recirculation of exhaust gases of a 16V32 STX-MAN marine diesel. During the research, the optimal degree of exhaust gas recirculation varied in the range of 0–21%, the load on the diesel—in the range of 35–95% of the rated power. It was established that in this case, the emission of nitrogen oxides decreases up to 7.7–33.6%, the specific fuel consumption increases up to 0.2–3.5%. It was also found that the use of gas recirculation in the range of 18–21% at loads of 35–55% leads to a critical increase in exhaust gas temperature. It is advisable to use exhaust gas recirculation in the range of 6–15% to ensure the environmental friendliness of the operation of the drillships. In

these modes, the maximum reduction in nitrogen oxide emissions is ensured with a minimum increase in specific fuel consumption. Future studies should be directed at the development of the criteria for the environmental stability of sea vessels.

DRILLING (WELL) 1,561,572

SYNTHESIS AND USE OF GRAFTED GRAPHENE IN WELLBORE CONSTRUCTION FLUIDS FOR LUBRICATION AND CORROSION INHIBITION

A.Santra and C.Thaeamlitz, asrs. (Aramco Services Co). World 2022/212,664A1, p. 10/6/2022, f. 3/31/2022 (Appl. 2,222,770), pr. U.S. 3/31/2021 (Appl. 63/168,412) (C09K-0008/03; C09K-0008/12).

A composition of matter including a mono-facial polymer-grafted graphene particle and an aqueous-based drilling fluid is provided. In the composition, a first side of the graphene particle has a grafted polymer. A method of lubricating a tool surface using the composition of matter is also provided. The method includes providing an aqueous-based drilling fluid, the aqueous-based drilling fluid having a mono-facial polymer-grafted graphene particle and introducing the aqueous-based drilling fluid into a wellbore such that it contacts a tool surface to form a coated tool. A drilling tool having a mono-facial polymer-grafted graphene particle adhered to its surface is also provided.

DRILLING (WELL) 1,561,573

DRILLING SYSTEM WITH GAS DETECTION SYSTEM FOR USE IN DRILLING A WELL

M.D.Rowe and T.H.T.Blakey, asrs. (Halliburton Energy Service). World 2022/203,672A1, p. 9/29/2022, f. 3/25/2021 (Appl. 2,124,033), pr. U.S. 3/24/2021 (Appl. 211,118) (E21B-0047/12; E21B-0004/02; E21B-0043/12).

A drilling system for drilling a well is disclosed herein. The drilling system may include a drillstring, a gas detector, and a computer system. The drillstring may include a downhole motor operable to rotate a drill bit and the downhole motor may include a stator and a rotor, at least one of the stator or the rotor comprising an elastomer compound. The gas detector may be operable to detect a gas indicative of deterioration of the elastomer compound. The computer system may be programmed to generate an indication based on the detection of the gas indicative of the deterioration by the gas detector.

DRILLING (WELL) 1,561,574

SURFACTANT-BASED FORMULATION AND USE THEREOF AS A DISSOLVING AGENT FOR POLYMERS AND ORGANIC MATERIAL DERIVED FROM OILFIELD DRILLING [FORMULACION ESPUMANTE Y SU USO COMO AGENTE TENSOACTIVO VISCOELASTICO EN YACIMIENTOS DE BAJA PERMEABILIDAD]

J.C.Jimenez Osorio, asr. (Chemiservis SA de CV). World 2022/203,494A1, p. 9/29/2022, f. 3/23/2022 (Appl. 2,250,027), pr. Mex. 3/26/2021 (Appl. 21,003,595) (C09K-0008/524; C09K-0008/584). (In Spanish)

The present invention relates to a foaming formulation and to the use thereof as a viscoelastic surfactant in low-permeability reservoirs, the formulation being designed to be used in low-pressure reservoirs where the use of low-density systems is required as a result of the characteristics of the reservoirs. The present invention can likewise be adapted to densities of 0.5 to 0.2 g/cm³ without losing its viscoelastic diverting properties.

FLANGE 1,561,575

FLANGE SHIELD

G.Myung and M.Cogill, Jr., asrs. (Comy LLC). World 2022/211,784A1, p. 10/6/2022, f. 3/30/2021 (Appl. 2,124,794), pr. World 3/30/2021 (Appl. 2,124,794) (F16L-0017/00; E21B-0017/02; E21B-0019/00; F16B-0007/00; F16J-0009/00; F16L-0023/02; F16L-0055/00).

Disclosed is a flange shield for separating flanges including a polymeric fabric having a disk shape and sandwiched between the

flanges and apertures inwardly spaced a distance from a circumferential edge of the polymeric fabric and able to receive fasteners that secure the flanges and the polymeric fabric together. Disclosed is a method of protecting a first flange and a second flange by separation including contacting a polymeric fabric with one of the first and the second flange and contacting the polymeric fabric that is contacted with the first or the second flange with the other of the first and the second flange. The method further includes securing the polymeric fabric between the first and the second flange by using fasteners that extend through apertures of the first and the second flange and apertures of the polymeric fabric with the first and the second flange to form a flange joint.

FORMATION EVALUATION 1,561,576

ESTIMATIONS OF RESERVOIR PARAMETERS WITH A MULTIPLE-STORAGE PHENOMENON IN DRILL STEM TESTS FOR NO PRODUCTION AT SURFACE

N.M.A.Rahman, asr. (Saudi Arabian Oil Co; Aramco Services Co). World 2022/204,403A1, p. 9/29/2022, f. 3/24/2022 (Appl. 2,221,744), pr. U.S. 3/24/2021 (Appl. 211,245) (E21B-0043/00; E21B-0049/08; G01V-0011/00).

A method of estimating reservoir properties is disclosed. The method includes obtaining downhole pressure data during a drill stem test in a wellbore penetrating a reservoir, computing a first linearity measure of a first diagnostic plot, wherein the first diagnostic plot represents a first dependency of the downhole pressure data on a linear-scale with respect to inverse time on a linear-scale, determining, based at least on the first linearity measure, data sufficiency of the drill stem test, and generating, from the downhole pressure data and based at least on the data sufficiency, an estimation of the reservoir properties.

MANAGED PRESSURE DRILLING 1,561,577

INTERNET OF THINGS IN MANAGED PRESSURE DRILLING OPERATIONS

E.Mammadov and S.Cody, asrs. (Opla Energy Ltd). World 2022/204,821A1, p. 10/6/2022, f. 4/1/2022 (Appl. 2,250,500), pr. U.S. 4/1/2021 (Appl. 63/169,684) (E21B-0044/00; E21B-0021/08; G05D-0016/20).

A control system for a pressure management apparatus (PMA) of a drilling system has an onsite device in close proximity to and in communication with the PMA and an offsite device at a remote location. Both the onsite and offsite devices are connected to a network, such as the Internet, through which the devices can communicate with one another. The onsite device receives data in real-time from the PMA and the offsite device can access the data in real-time via the network. The offsite device can generate a command based on the data or user input at the offsite device and send the command to the onsite device to modify one or more settings of the PMA. A control panel is displayed on the user interface of the offsite device to allow an operator to remotely control the PMA.

MUD ADDITIVE 1,561,578

USE OF SYNTHETIC CALCIUM CARBONATE PARTICLES AS AN ADDITIVE IN WATER-BASED DRILLING FLUIDS

Y.Villada, C.Busatto, N.Casis and D.Estenez (INTEC). *COLLOIDS AND SURFACES A: PHYSICOCHEMICAL AND ENGINEERING ASPECTS* v.652, 11/5/2022. (ISSN 0927-7757; Article no.129801)

The design and formulation of drilling fluids are essential for a successful drilling operation performance. In this work, the incorporation of calcium carbonate particles (CaCO₃) as a novel additive of water-based drilling fluids (WBMs) was evaluated. CaCO₃ particles were synthesized by the precipitation method and characterized in terms of morphological, thermal and structural properties. WBM systems were prepared containing three different viscosifier additives such as xanthan gum, (XGD), guar gum (GG) or corona gum (GEC). The addition of CaCO₃ particles on the rheological, filtration, thermal and structural properties of WBMs was investigated. It was found that fluids containing XGD and

CaCO₃ particles exhibited significant improvements on their functional properties. This behavior was mainly attributed to surface interactions between bentonite with polymers, as well as bentonite with CaCO₃. For all systems, the addition of particles resulted in a reduction in the volume of filtrate. Moreover, the Sisko and Herschel Bulkley model were employed in order to describe theoretical the rheological behaviour. (c2022 Elsevier B.V.)

MUD ADDITIVE 1,561,579

TUNING THE RHEOLOGICAL PROPERTIES OF KAOLIN SUSPENSIONS USING BIOPOLYMERS

A.Shakeel, W.Ali, C.Chassagne and A.Kirichek (Freiburg Univ; Delft Univ Technol). *COLLOIDS AND SURFACES A: PHYSICO-CHEMICAL AND ENGINEERING ASPECTS* v.654, 12/5/2022. (ISSN 0927-7757; Article no.130120)

Kaolin based suspensions have wide range of applications such as slurry wall, drilling fluids, adhesives, cosmetics, refractories and pharmaceuticals, due to their abundance in nature, low cost and non-swelling nature. On the other hand, the unique properties (i.e., biodegradability) of biopolymers make them suitable candidate for variety of applications including modification of clay suspensions. In this study, the rheological properties of kaolin suspensions modified with different biopolymers (xanthan gum (XG), sodium carboxymethyl cellulose (CMC), potato starch (PS), chitosan (Ch) and apple fibre (AF)) have been investigated by varying the biopolymer type, content and clay content. The main objective of the present study is to propose a substitute for the natural mud sample. Frequency sweep tests, stress ramp-up tests and time-dependent tests were performed by using the Couette geometry (coaxial cylinders) for the prepared suspensions. The rheological results showed that both viscosity and moduli were significantly influenced by adding different biopolymers into the kaolin suspensions. For instance, an increase in viscosity of modified suspensions was observed: 3 - 4 orders of magnitude by adding xanthan gum (1 wt%) or sodium carboxymethyl cellulose (5 wt%) and 6 orders of magnitude by adding apple fibre (5 wt%). Likewise, the incorporation of different biopolymers significantly affected the complex modulus of modified clay suspensions. For example, similar or higher values of complex modulus than the pure kaolin suspension were observed at low xanthan gum or sodium carboxymethyl cellulose content (0.1 wt%). In case of chitosan, the complex modulus of the modified suspensions was higher than the complex modulus of pure kaolin suspension, even at very low polymer content (1 wt%). In the case of potato starch, a decrease in complex modulus by increasing polymer content till 10 wt% was observed followed by an increase in complex modulus with polymer content. The shear rate ramp-up and ramp-down experiments showed that the time-dependent behaviour of kaolin suspensions was not strongly influenced by adding different biopolymers. This knowledge will provide a base to choose a suitable substitute for the natural mud sample. (c2022 The Authors. Elsevier B.V.)

MUD SYSTEM 1,561,580

WELL SYSTEM INCLUDING A DOWNHOLE PARTICLE MEASUREMENT SYSTEM

M.D.Rowe and S.P.Lawrence, asrs. (Halliburton Energy Service). *World* 2022/203,692A1, p. 9/29/2022, f. 3/29/2021 (Appl. 2,124,654), pr. U.S. 3/26/2021 (Appl. 214,420) (E21B-0043/12; E21B-0037/08; E21B-0047/12).

A well system for handling downhole particles is disclosed herein. The well system may include a mud pump, a shaker including a corrugated shaker screen, a drill string, an imaging device, and a data acquisition system that may include a processor. The processor may be programmed to determine a cross-sectional area of a portion of the corrugated shaker screen occupied by the downhole particles in a first image of the images based on the first image, on a known profile of corrugations of the corrugated shaker screen and a known distance and angle between the imaging device and the corrugated shaker screen to determine a volume of the downhole particles on the portion of the corrugated shaker screen in the first image based on the cross sectional area occupied by downhole particles, a velocity of the downhole particles moving across the corrugated shaker screen, and an image generation rate.

OFFSHORE WELL 1,561,581

SEAWATER-BASED DIRECT EMULSION FLUID WITH AN INVERSE OIL/WATER RATIO FOR AREAS WITH A LOW PRESSURE GRADIENT AND HIGH TEMPERATURE [FLUIDO DE EMULSION DIRECTA BASE AGUA DE MAR CON RELACION ACEITE/AGUA INVERTIDA PARA ZONAS DE BAJO GRADIENTE DE PRESION Y ALTA TEMPERATURA]

B.Romero Morales, J.G.Torres De La Cruz, A.Hernandez Velazquez, asrs. (Chemiservis SA de CV). *World* 2022/203,496A1, p. 9/29/2022, f. 3/24/2022 (Appl. 2,250,029), pr. Mex. 3/25/2021 (Appl. 21,003,521) (C09K-0008/26; C09K-0008/28). (In Spanish)

The aim of the invention is to use natural resources in offshore well drilling, repair and completion operations, eliminating the use of borehole water, reducing the use of diesel oil, and therefore reducing the use of supply vessels, leading to a reduction in costs. This also leads to the ability to continue to operate even under adverse weather conditions. Independently of its use in offshore operations, the invention can also be used in onshore wells. The invention relates to a system comprising low-density direct emulsion fluids modified in the continuous phase, dispersed phase, an emulsifier and additional heat-polymerised materials to withstand high temperatures, offering excellent well stability at a low cost. The invention is intended for use in drilling, repair and completion works on offshore and onshore wells in extremely harsh environments and at high temperatures.

OIL BASE MUD 1,561,582

PROBING THE STATE OF WATER IN OIL-BASED DRILLING FLUIDS

W.Di, C.Zhao, T.Geng, Q.Sun, Z.Xu and D.Sun (Shandong Univ; State Key Laboratory China; China Oilfield Svcs Ltd; Alberta Univ). *COLLOIDS AND SURFACES A: PHYSICO-CHEMICAL AND ENGINEERING ASPECTS* v.651, 10/20/2022. (ISSN 0927-7757; Article no.129770)

Oil-based drilling fluids, also referred to as "invert emulsion drilling fluids", have been widely accepted as mixtures of water-in-oil (W/O) emulsions and inorganic particles, in which the water droplet-particle interaction has not been considered. Probing the state of water plays an important role in optimizing the performance of oil-based drilling fluids. In this work, hydrophilic BaSO₄ and hydrophobic polytetrafluoroethylene (PTFE) particles were added to W/O emulsions. The microstructures of the water droplets and particles in the oil phase were studied using an optical microscope. The state of water was characterized by T2 nuclear magnetic resonance (NMR) and low-temperature differential scanning calorimetry (LT-DSC). Finally, the state of water in actual invert emulsion drilling fluids was verified by two-dimensional T1-T2 NMR. The results showed that the water droplets bound to the hydrophilic BaSO₄ particles formed hydrated particle aggregates in the oil phase, while the water droplets and hydrophobic PTFE particles were suspended individually in the oil phase. Thus, the so-called invert emulsion drilling fluids are in fact colloidal suspensions of hydrated particle aggregates in continuous oil phase, rather than W/O emulsions. The findings of this work provide new insights into the formulation and utilization of oil-based drilling fluids. (c2022 Elsevier B.V.)

POLYCRYSTALLINE DIAMND BIT 1,561,583

EVOLUTION IN THE DEVELOPMENT OF PRE-SALT CARBONATE DRILL BITS IN THE SANTOS BASIN

F.M.Lima and A.Passos (Petroleo Brasileiro SA). *OFFSHORE TECHNOLOGY CONFERENCE [OTC] (Houston, TX, 5/2-5/2022) PROCEEDINGS* 2022. (ISBN 978-1-61399-852-6; OTC-31832; Available at <http://www.onepetro.org> as of 6/23/2022; 9 pp)

The pre-salt reserves offshore from Santos basin represent a great opportunity and probably the most important recent oil discovery in Brazil. These carbonate reservoirs are currently drilled with various types of drill bits, and have proven to be a challenging environment. Since their discovery, there has been an incessant search for the development of drill bits that are able to drill these hard and, in some cases, very abrasive formations in a single run

and with optimized drilling rates. In this way, the costs for wells construction would be increasingly reduced, which would further increase the attractiveness of the development of these fields in Santos basin. This paper presents the technological evolution employed in drill bits, from the beginning of the exploratory campaign in Santos basin until newer developments, newer PDC bits designs, and geometric cutters currently used in pre-salt carbonate drilling. In addition, the contractual improvements and results are also presented, showing consistent evolution of ROP and perforated extension over the years, with the development and use of new drill bits in Petrobras. (Copyright 2022 OTC)

REAMER (WELL) 1,561,584

REAMERS WITH IMPROVED DURABILITY AND/OR STABILITY

G.Mensa-Wilmot, asr. (Chevron USA Inc). World 2022/211,782A1, p. 10/6/2022, f. 3/29/2021 (Appl. 2,124,735) (E21B-0010/26; E21B-0010/32; E21B-0010/43).

A reamer for use in enlarging a borehole in a drilling operation comprises an elongate body defining a rotational axis about which the reamer is rotated in the drilling operation and a plurality of reamer blocks configured to extend radially outwards from the elongate body relative to the rotational axis, wherein each reamer block comprises at least a first row of cutters configured to engage a formation in which the borehole is being drilled with a given back rake in the drilling operation, a given portion of each first row extending longitudinally along its reamer block, a longitudinal direction being substantially parallel to the rotational axis; each back rake of said cutters is either a high back rake or a low back rake; and for at least one first row of cutters, the respective back rakes of the cutters alternate along the given portion of the row between one or more high back rakes and one or more low back rakes.

ROTARY DRIVE 1,561,585

DOWNHOLE ROTARY DRIVE APPARATUS

A.Phillips, T.J.Walerianczyk and M.Garza, asrs. (Steel Space Drilling Ltd). World 2022/208,095A1, p. 10/6/2022, f. 3/31/2022 (Appl. 2,250,813), pr. Gr. Brit. 4/1/2021 (Appl. 2,104,767) (E21B-0004/00; E21B-0004/02).

A downhole rotary drive apparatus for driving a bit used to drill or ream a borehole comprises a body configured for coupling to, or forming part of, a tubular string for running into the borehole and an output shaft at least partially disposed within and rotatably mounted to the body. A plurality of rotary drives are disposed around the body, each having a rotor. The apparatus further comprises a transmission arrangement comprising a drive component mounted on at least one of the rotors of the rotary drives and a driven component mounted on the output shaft. The driven component is disposed radially inwards of the drive component such that an inner surface of the drive component engages an outer surface of the driven component, rotation of the driven component by the drive component driving rotation of the output shaft. The rotary drives and/or the transmission arrangement of the rotary drive apparatus are disposed within blade portions disposed on or formed in the body.

ROTARY STEERABLE SYSTEM 1,561,586

FILTERING OF RSS PAD NOISE IN MUD PULSE TELEMETRY SYSTEMS AND DETECTION OF RSS PAD LEAKS

L.Zhang, B.Paravastu, M.Mehta, R.Sobhana and F.C.O.Chagas, asrs. (Halliburton Energy Service). World 2022/203,661A1, p. 9/29/2022, f. 3/24/2021 (Appl. 2,123,809), pr. U.S. 3/23/2021 (Appl. 209,859) (E21B-0047/18; E21B-0047/10; G01V-0003/18).

The present disclosure relates to systems and methods for adaptive filtering of rotary steerable system (RSS) pad noise and the detection of RSS pad seal leakage in real-time.

ROTARY STEERABLE SYSTEM 1,561,587

ROTARY STEERING DRILLING TOOL HAVING SELF-ADAPTIVE SUPPORT STRUCTURE

X.Wan, Z.Xu, Z.Yang and K.Zheng. World 2022/199,666A1, p. 9/29/2022, f. 3/24/2022 (Appl. 2,282,831), pr. China 3/25/2021 (Appl. 2021-10,321,614) (E21B-0007/06; E21B-0007/04; E21B-0017/10; E21B-0041/00; E21B-0044/00). (Assigned to X.Wan; **In Chinese**)

A rotary steering drilling tool having a self-adaptive support structure is disclosed herein. By adding a centralizing sleeve and passing a flexible shaft through the inside of the centralizing sleeve, an original direct connection between the tail of a central shaft and an outer sleeve becomes an indirect connection by means of the centralizing sleeve, and the distance of the arm of force during the deformation of the flexible shaft is increased without significantly lengthening a flexible joint, thereby reducing a working pressure of a bias control mechanism, and improving use stability of the tool and stratum adaptability.

SEMISUBMERSIBLE DRLG BARGE 1,561,588

PERFORMANCE OF AN ADVANCED INTELLIGENT CONTROL STRATEGY IN A DYNAMIC POSITIONING (DP) SYSTEM APPLIED TO A SEMISUBMERSIBLE DRILLING PLATFORM

M.Alremeihi, R.Norman, K.Pazouki, A.Dev and M.Bashir (Newcastle Univ; Liverpool John Moores Univ). *JOURNAL OF MARINE SCIENCE AND ENGINEERING* v.9, no.4, April 2021. (ISSN 2077-1312; Article no.399)

Oil drilling and extraction platforms are currently being used in many offshore areas around the world. Whilst those operating in shallow seas are secured to the seabed, for deeper water operations, dynamic positioning (DP) is essential for the platforms to maintain their position within a safe zone. Operating DP requires intelligent and reliable control systems. Nearly all DP accidents have been caused by a combination of technical and human failures; however, according to the International Marine Contractors Association (IMCA) DP Incidents Analysis, DP control and thruster system failures have been the leading causes of incidents over the last ten years. This paper will investigate potential operational improvements for DP system accuracy by adding a predictive neural network (PNN) control algorithm in the thruster allocation along with a nonlinear proportional integral derivative (PID) motion control system. A DP system's performance on a drilling platform in oil and gas deep-water fields and subject to real weather conditions is simulated with these advanced control methods. The techniques are developed for enhancing the safety and reliability of DP operations to improve the positioning accuracy, which may allow faster response to a critical situation during DP drilling operations. The semisubmersible drilling platform's simulation results using the PNN strategy show improved control of the platform's positioning.

THREAD (MECHANICAL) 1,561,589

SIZING A THREAD AXIAL CLEARANCE [DIMENSIONNEMENT D'UN JEU AXIAL DE FILETAGE]

T.Mathon, L.Boufflers and M.Luongo, asrs. (Vallourec Oil & Gas France; Nippon Steel Corp). World 2022/207,995A1, p. 10/6/2022, f. 3/21/2022 (Appl. 2,250,508), pr. Fr. 3/31/2021 (Appl. 2,103,327) (F16L-0015/06; E21B-0017/042). (**In French**)

The invention relates to a tubular threaded seal for drilling, the exploitation of hydrocarbon wells, the transport of petroleum and gas, carbon capture or geothermal energy, comprising a male tubular element and a female tubular element, each of said male tubular element and female tubular element respectively comprising a male threaded portion and a female threaded portion. Either the male threaded portion or female threaded portion optionally comprises a solid anti-corrosion and/or lubricating coating, said male threaded portion and female threaded portion respectively comprising at least one male thread tooth or one female thread tooth and a thread axial clearance TAG providing a space, in the installed state, between an engagement flank of said male thread tooth and a bearing flank of said female thread tooth, characterised in that said thread axial clearance TAG is greater than or equal to a minimum clearance TAGmin.

WATER BASE MUD 1,561,590

ON THE USE OF ESPINA CORONA GUM AS A POLYMERIC ADDITIVE IN WATER-BASED DRILLING FLUID

Y.Villada, M.E.Taverna, J.M.Maffi, S.Giletta, N.Casis and D.Estenez (Litoral Nacional Univ; Buenos Aires Technol Inst). *COLLOIDS AND SURFACES A: PHYSICOCHEMICAL AND ENGINEERING ASPECTS* v.650, 10/5/2022. (ISSN 0927-7757; Article no.129601)

The aim of this work is to evaluate the espina corona gum (ECG) as a sustainable viscosifier or filtration reducer additive in water-based drilling fluids (WBM) as a potential replacement of guar gum (GG). ECG is a galactomannan isolated from leguminous seeds of *Gleditsia amorphoides*, trees that grow in South America with viscosifier properties and applications in the food area. ECG was characterized by FTIR, Z potential, intrinsic viscometry, TGA, and steady and oscillatory shear rheological analysis. Moreover, its effect on the main functional properties of WBM was studied. Fluids containing bentonite (BT), polyanionic cellulose (PAC), GG or ECG were prepared, and rheological, filtration, thermal and structural properties were determined. In order to study the theoretical rheological behavior, several models such as power law, Sisko and Herschel-Bulkley were evaluated. The rheological studies revealed that WBM containing ECG exhibit higher viscosities in comparison with those with GG. Herschel-Bulkley parameters indicated that the WBM with high ECG concentration showed higher yield stress. In addition, the presence of ECG improves the thermal stability and filtration properties. The results indicate that ECG can be considered as an innovative, renewable and non-toxic alternative to partially or totally replace GG in WBM. (c2022 Elsevier B.V.)

WATER BASE MUD 1,561,591

SURFACTANT-BASED FORMULATION AND USE THEREOF AS A POLYMER-REMOVAL AGENT [FORMULACION A BASE DE SURFACTANTES Y SU USO COMO AGENTE DE REMOCION DE POLIMEROS]

J.C.Jimenez Osorio, asr. (Chemiservis SA de CV). World 2022/203,491A1, p. 9/29/2022, f. 3/23/2022 (Appl. 2,250,023), pr. Mex. 3/26/2021 (Appl. 21,003,613) (C09K-0008/52; C09K-0008/52; C09K-0008/58; C09K-0008/60; C09K-0008/74). (In Spanish)

The present invention relates to a surfactant-based formulation and the use thereof as a polymer-removal agent for cleaning the majority of water-based oil well drilling fluids, significantly reducing the viscosity of the polymer-based drilling fluid remnants left over in the deposits used during well drilling and/or completion operations.

WELL LOGGING & SURVEYING

GAMMA GAMMA LOGGING 1,561,592

APPARATUS AND METHOD FOR CHARACTERIZING LINER AND ANNULUS PROPERTIES WITH A GAMMA-GAMMA TOOL

L.Mosse, asr. (Schlumberger Technol Corp; Schlumberger Canada Ltd; Schlumberger Serv Petrol; Schlumberger Technol BV). World 2022/203,918A1, p. 9/29/2022, f. 3/16/2022 (Appl. 2,220,568), pr. U.S. 3/22/2021 (Appl. 63/164,205) (E21B-0049/00; E21B-0047/125; E21B-0047/18; G01V-0001/52; G01V-0013/00).

Embodiments presented provide for an apparatus and method for characterizing linear and annulus properties using a gamma-gamma tool.

SAMPLE ANALYSIS 1,561,593

THE COMBINED DISCRETE GAUSSIAN ANALYSIS OF MICP AND NMR T2 DISTRIBUTIONS OF MULTI-MODAL CARBONATE ROCKS

J.Gao, H.T.Kwak and M.M.Alsinan, asrs. (Saudi Arabian Oil Co; Aramco Services Co). World 2022/204,297A1, p. 9/29/2022, f.

3/23/2022 (Appl. 2,221,571), pr. U.S. 3/23/2021 (Appl. 209,824) (G01N-0024/08; G01N-0015/08; G01R-0033/44).

A method includes screening heterogeneity of a rock sample using nuclear magnetic resonance testing to determine a composition of the rock sample, drilling at least one smaller rock sample representative of the determined composition, and testing the at least one smaller rock sample with mercury-injection capillary pressure to obtain a capillary pressure distribution of the at least one smaller rock sample. The method further includes decomposing a T2 distribution from the nuclear magnetic resonance testing and the capillary pressure distribution using Gaussian fitting to identify multiple pore systems, where the small ends of the Gaussian fitted T2 distribution and the Gaussian fitted, capillary pressure distribution are overlapped for at least one of the identified pore systems.

WELL LOGGING 1,561,594

WELLBORE DATA DEPTH MATCHING USING CHANGE POINT ALGORITHMS

S.Wlodarczyk, asr. (Schlumberger Technol Corp; Schlumberger Canada Ltd; Schlumberger Serv Petrol; GeoQuest Systems BV). World 2022/203,702A1, p. 9/29/2022, f. 5/27/2021 (Appl. 2,134,537), pr. U.S. 3/26/2021 (Appl. 63/200,772) (G01V-0005/04; G01V-0001/40; G01V-0001/48; G01V-0003/18).

A method includes receiving a well log having a signal. The method also includes identifying in the signal a first change point that demarcates a first signal region and a second signal region. The method also includes determining that the first signal region is inconsistent in comparison to the second signal region. The method also includes producing a modified well log by removing the first signal region from the signal in response to determining that the first signal region is inconsistent in comparison to the second signal region.

WELL COMPL SERV & WORKOVER

ABANDONMENT 1,561,595

WIRELINE PLUG SYSTEM

C.Kruger, asr. (Welltec A/S). World 2022/200,559A1, p. 9/29/2022, f. 3/25/2022 (Appl. 2,257,898), pr. Europe. 3/26/2021 (Appl. 21,165,336) (E21B-0023/06; E21B-0033/12; E21B-0033/127; E21B-0033/134).

The present invention relates to a wireline plug system for setting a permanent plug in a well for plugging and abandonment that comprises a wireline pumping tool comprising a pump powered from the surface via a wireline. The pump comprises a pump inlet and a pump outlet, with the wireline pumping tool having a first end connected to the wireline and a second end, a plugging and abandonment plug comprising a first plug end and an opening in the first plug end, and an engagement tool for releasably connecting the plug to the wireline pumping tool. The engagement tool has a through-bore fluidly connecting the opening in the first plug end with the pump outlet, wherein the plugging and abandonment plug comprises a tubular metal part and an expandable metal sleeve surrounding and connected to an outer face of the tubular metal part. The tubular metal part has an expansion aperture fluidly connecting an inside of the tubular metal part and a cavity between the expandable metal sleeve and the tubular metal part. The invention also relates to a wireline plug setting method for setting a permanent plug in a well for plugging and abandonment on the wireline.

ACID CLEANING (WELL) 1,561,596

ACID FORMULATION AND USE THEREOF AS AN AGENT FOR REMOVING CALCIUM CARBONATE-BASED SCALE [FORMULACION ACIDA Y SU USO COMO AGENTE DE REMOCION DE INCRUSTACIONES A BASE DE CARBONATO DE CALCIO]

J.C.Jimenez Osorio, asr. (Chemiservis SA de CV). World

2022/203,490A1, p. 9/29/2022, f. 3/23/2022 (Appl. 2,250,022), pr. Mex. 3/26/2021 (Appl. 21,003,593) (C09K-0008/52; C09K-0008/03; C09K-0008/52; C09K-0008/72; C09K-0008/74; C09K-0008/86; E21B-0037/06). (In Spanish)

Less than 10% of oil wells occur naturally, while 90% are created by some type of artificial system and many of these are equipped with an electrical submersible pump, formed by Cr 13- and SCr 13-type alloys, which easily corrode in the presence of conventional acid systems prepared with hydrochloric acid (HCl). For this reason, the present invention relates to a liquid-based acid formulation prepared with an organic synthetic acid fluid designed with nanotechnology, which significantly reduces corrosive effects, and the use thereof as an agent for removing calcium carbonate-based scale, specifically in cleaning operations with stimulation in oil wells.

ACIDIZING

1,561,597

PHYSICOCHEMICAL EVALUATION OF THE USE OF ALCOHOLIC MICELLAR SOLUTIONS CONTAINING NONYLPHENOL AND ETHANOL FOR THE ACIDIZING OF CARBONATE MATRICES

G.M.Arruda, D.C.Silva, G.S.Azevedo, E.R.V.Galvao, M.A.F.Rodrigues and A.O.Wanderley Neto (Rio Grande Norte Fed Univ). *COLLOIDS AND SURFACES A: PHYSICOCHEMICAL AND ENGINEERING ASPECTS* v.652, 11/5/2022. (ISSN 0927-7757; Article no.129821)

Acid stimulation presents a great challenge when it comes to reducing the reaction rate between hydrochloric acid and carbonate rock, which makes it possible to increase the depth of the injected solutions. The surfactants are excellent candidates to reduce the reaction rate and make the rock water-wettable. However, high temperatures and the presence of salts as a product of the acidizing reaction can affect the performance of surfactants under reservoir conditions. In the present study, acidified alcoholic micellar solutions were obtained containing nonylphenol surfactant of 100, 40, and 11 ethoxylated bonds and ethanol as an amphi-solvent to assist the maintenance of the surfactant properties under adverse conditions. The solutions were characterized before and after the acidizing reactions (absence and presence of salt, respectively), evaluating the cloud point, surface tension, and kinematic viscosity. The experiments revealed that ethanol assisted in maintaining or improving the cloud point of the formulations, reaching above 70 °C. In addition, concerning nonylphenol 11EO formulations, the alcohol did not alter the effect of reducing the reaction rate and could partially substitute the surfactant in the active substance of the formulation. (c2022 Elsevier B.V.)

BUBBLE

1,561,598

SUB-MILLIMETRIC VISUALIZATION AND STABILITY MEASUREMENT FOR SUPERCRITICAL CO2 FOAMS: EFFECT OF IONIC COMPLEXATION ON TUBULAR AND DIVERGING FLOWS

H.Hosseini, J.S.Tsau and R.B.Ghahfarokhi (Kansas Univ). *COLLOIDS AND SURFACES A: PHYSICOCHEMICAL AND ENGINEERING ASPECTS* v.653, 11/20/2022. (ISSN 0927-7757; Article no.129988)

Development of natural gas resources as fuel for energy transition requires sustainable recovery processes with manageable amount of water used for unconventional stimulation of wellbores to protect the environment. To manage stability issues and bubble morphological alternations within the waterless fluids such as dry foams, microstructure and physicochemical properties were correlated to ionic complexation, bubble local plastic deformation (T1 event) in vicinity of constriction and elastoplastic behavior of CO2-water interface travelling from wellbore to fracture and flow back. This work presents facile sub-millimetric observation and step by step image analysis protocol for dry scCO2 foam transport and stability evaluation across the vertical view cell (tubular flow) and after constriction (diverging flow) and highlights the effect of viscoelastic components of interface on bubble plastic deformation and interfacial stability. The scCO2 foam's microscopic structure was stabilized with (i) Zwitterionic Surfactants (ZS) and (ii) ZS-conjugated Polyelectrolyte Complex Nanoparticles (PECNP).

PECNP-Surfactant scCO2 foam structure was noticeably affected by confinement ratio between the feeding tube and view cell, thus excessive lamella breakup and rearrangement of scCO2 bubbles occurred with higher rate in widening flow, which contributed to formation of less uniform dispersion of scCO2 droplets in PECNP-Surfactant scCO2 foam. However, the PECNP-Surfactant complexes residing in CO2-water lamella stabilized the deformed microstructure for significantly longer time. Bubble shape deformity was attributed to bubble elongation due to elastoplastic properties of lamella interface originated by the presence PECNP nanoparticle verified by higher dilatational elasticity at interface. Stability of deformed bubbles in pattern of PECNP-surfactant scCO2 foam with longer resistivity to lamella breakage, coalescence, and gravity drainage (up to 160 min) were compared to sudden bubble growth and expansion (after 30 min) detected for narrower distribution of smaller scCO2 bubbles stabilized in mixtures of ZS in high salinity brine (33.3 kppm). Higher resistance to morphological change (coalescence, rupture, burst) was observed for viscous lamella of PECNP-surfactant in scCO2 foam originated from higher viscosity and dilatational elasticity of lamella interface. (c2022 Elsevier B.V.)

CARBON DIOXIDE FLOODING

1,561,599

CO2-RESPONSIVE GEL PARTICLES AND WORMLIKE MICELLES COUPLING SYSTEM FOR CONTROLLING CO2 BREAKTHROUGH IN ULTRA-LOW PERMEABILITY RESERVOIRS

D.Du, B.Chen, W.Pu, X.Zhou, R.Liu and F.Jin (Southwest Petroleum Univ; Tuha Drilling Co). *COLLOIDS AND SURFACES A: PHYSICOCHEMICAL AND ENGINEERING ASPECTS* v.650, 10/5/2022. (ISSN 0927-7757; Article no.129546)

CO2 flooding in ultra-low permeability reservoirs is an effective means to boost oil production, while the complex fractures formed by fracturing in the initial development stage induce severe CO2 channeling. Therefore, a CO2-responsive coupling system which coupled CO2-responsive gel particles (CRPGP) with CO2-responsive wormlike micelles (CTWM) was prepared to restrain CO2 breakthrough. To testify the EOR capacity during CO2 flooding of the responsive coupling system, the interaction between CRPGP and CTWM, and responsiveness of coupling system was investigated, followed by core flooding and rock slab flooding experiments. Experiment results showed that after the coupling system was exposed with CO2, the particle size of CRPGP increased, spherical micelles of CTWM transformed to wormlike micelles, CRPGP and CTWM were integrated through hydrophobic association among wormlike micelles and hydrophobic chains in CRPGP, and the coupling system's apparent viscosity increased from 10.4 mPa.s to 2339 mPa.s. Moreover, 0.5 pore volume (PV) CO2-responsive coupling system injection and further CO2 flooding could dramatically boost oil production in fractured cores and rock slabs, which was primarily ascribed to the aggrandizement of sweeping volume resulting from the plugging effect of CRPGP and mobility ratio improvement of the coupling system. Compared with single slug plugging of fractures, multi-stage regulation of fractures could establish a higher-pressure gradient, and more crude oil in the matrix was activated with enhanced oil recovery (EOR) of 22.8%. All the experimental results demonstrated that the CO2-responsive coupling system has great EOR capacity during CO2 flooding, which provided novel insights for ultra-low permeability reservoirs EOR technology that incorporated with CO2 resource utilization and storage. (c2022 Elsevier B.V.)

CASING (WELL)

1,561,600

PRESSURE-DAMPENING CASING TO REDUCE STRESS LOAD ON CEMENT SHEATH

A.H.Al-Oqaili, A.M.Al-Abduljabbar and A.J.Shaikh, asrs. (Saudi Arabian Oil Co; Aramco Services Co). *World* 2022/204,306A1, p. 9/29/2022, f. 3/23/2022 (Appl. 2,221,580), pr. U.S. 3/23/2021 (Appl. 209,896) (E21B-0017/00; F16L-0009/12; F16L-0009/147; F16L-0058/10).

A casing may have a tubular body formed by a wall extending axially from a first end to a second end, the tubular body having a bore therein throughout. The wall may radially extend from an

inner surface of the tubular body to an outer surface of the tubular body. The wall may include a base layer and one or more secondary layers attached to the base layer. The one or more secondary layers may be a rubber or smart foam.

CEMENT ADDITIVE **1,561,601**

EFFECT OF MAGNETIC NANOPARTICLES ON STRENGTH DEVELOPMENT AND MICROSTRUCTURAL PROPERTIES OF CEMENT SLURRY

T.M.M.Alvim, F.D.S.Maranhao, J.H.G.Batista, O.A.M.Reales, F.G.Souza Junior and R.D.Toledo Filho (Rio de Janeiro Fed Univ; Repsol Sinopec Brasil). *OFFSHORE TECHNOLOGY CONFERENCE [OTC] (Houston, TX, 5/2-5/2022) PROCEEDINGS* 2022. (ISBN 978-1-61399-852-6; OTC-31810; Available at <http://www.onepetro.org> as of 6/23/2022; 12 pp)

The typical solution in the cement industry to respond to the application challenges is the use chemical additives to adapt cement characteristics to the scenario. However, this approach may weaken cement integrity especially in long term. The use of physical properties to obtain similar performance may be a new frontier as cement can be kept without changes and the new additives are inert to the mixture. A proof-of-concept study was carried out on using magnetic nanoparticles (MNP) and an oscillating magnetic field source to replace chemical additives in the objective of reducing Waiting on Cement (WOC) time during cementing operations in oil and gas wells. A rigorous process was executed to select the most promising particles and several experiments testing different cement slurries designs were executed to confirm the feasibility of this patented technology. Magnetite nanoparticles were blended in 15.9 ppg class G Portland cement slurries in amounts of 0.25% and 0.50% by weight of cement (BWOC). The slurries were cured in atmospheric conditions up to seven days and characterized to determine the influence of the nanoparticles on early age compressive strength development and microstructural properties. Compressive strength development was tested both by destructive testing and by ultrasonic cement analyzer (UCA). Microstructural properties were determined by isothermal calorimetry, scanning electron microscopy, X-ray diffraction and thermogravimetric analysis. Destructive testing of samples cured at atmospheric conditions up to 168 hours showed that the use of magnetic nanoparticles did not affect the compressive strength of cement. UCA experiments, carried out in temperatures similar to those obtainable by magnetically induced heating, confirmed the potential of the technology to accelerate strength development. Isothermal calorimetry results showed that the presence of MNP did not interfere with the normal hydration reaction of cement, a fact that was confirmed by the thermogravimetric analyses. (Copyright 2022 OTC)

CEMENT SLURRY **1,561,602**

A CALCULATION MODEL FOR THE TEMPERATURE FIELD OF THE SHALLOW SUBMARINE STRATA CONSIDERING THE HEAT OF HYDRATION OF CEMENT SLURRY

H.Diao, H.Fan, B.J.Leira, S.Sangesland, Y.Ye, Y.Liu, F.Zhou, B.Wu, L.C.Sevillano et al. (China Univ Petroleum). *OFFSHORE TECHNOLOGY CONFERENCE [OTC] (Houston, TX, 5/2-5/2022) PROCEEDINGS* 2022. (ISBN 978-1-61399-852-6; OTC-31812; Available at <http://www.onepetro.org> as of 6/23/2022; 19 pp)

During offshore oil and gas resource exploration, the large amount of heat generated by cement hydration will cause the hydrates around the wellbore to decompose, leading to cementing operation failure or more serious types of accidents. Therefore, the influence of the heat on temperature of hydrate layer, overlying and underlying strata during the cementing process is studied in this paper. A calculation model for the temperature field of deep-water hydrate layer cementing is established. The model considers the influence of cement slurry hydration heat release, hydrate decomposition, and heat transfer between hydrate layer, overlying and underlying strata on temperature distribution of the hydrate layer, overlying and underlying strata. Using MATLAB language programming, the partial differential equations were solved by the difference method, and numerical simulations were carried out

through simulated wells. The temperature distribution of drilling fluid, cement slurry, hydrate layer and strata during the deep-water cementing process is calculated. Through analysis, the following conclusions are obtained. (1) The cement hydration in the cementing process generates a lot of heat, which severely destroys the stable temperature and pressure conditions of the hydrate layer and causes a large amount of decomposition of the hydrate. (2) The decomposition of hydrate is a long-term process comparing with the cement hydration process. Therefore, the decomposition of hydrate during the cementing operation and for a period of time after completion will bring safety threats to the drilling and completion operations. (3) Considering the heat transfer between the hydrate layer and the overlying and underlying strata more accurately reflects the temperature change of the hydrate layer during the cementing process than only considering the heat exchange between the cement column and the hydrate layer. (Copyright 2022 OTC)

CENTRALIZER **1,561,603**

VARIABLE STIFFNESS CENTRALIZER

D.Arsoski, asr. (Downhole Products Ltd). World 2022/201,028A1, p. 9/29/2022, f. 3/22/2022 (Appl. 2,252,612), pr. U.S. 3/24/2021 (Appl. 63/165,234) (E21B-0017/10).

A centralizer for use in a wellbore includes a body for disposing around a periphery of a downhole tubular. The body has a plurality of bow springs biased toward an expanded position and a pair of end rings connecting the bow springs. The centralizer further includes an indentation or row of indentation segments formed in a surface of and along each bow spring. The indentations or indentation segments are operable to reduce a stiffness of the centralizer as the bow springs move from the expanded position to a restricted position.

CORROSION INHIBITOR **1,561,604**

N-DOPED AND Cu,N-DOPED CARBON DOTS AS CORROSION INHIBITOR FOR MILD STEEL CORROSION IN ACID MEDIUM

S.Padhan, T.K.Rout and U.G.Nair (IIT Dhanbad; Tata Steel Ltd). *COLLOIDS AND SURFACES A: PHYSICO-CHEMICAL AND ENGINEERING ASPECTS* v.653, 11/20/2022. (ISSN 0927-7757; Article no.129905)

In the present study, N-doped carbon dots (N-CDs) and Cu,N-doped carbon dots (Cu,N-CDs) with various Cu doping amounts were explored as corrosion inhibitors for mild steel substrate. Material characterizations of synthesized materials were performed using UV-Vis, FTIR and XRD, TEM and XPS techniques. Electrochemical corrosion testing showed enhanced corrosion inhibition performance for Cu,N-CDs relative to N-CDs. The inhibition efficiencies were directly proportional to concentrations of N-CDs and Cu,N-CDs, with more than 97% achieved at 100 ppm of Cu,N-CDs. Gravimetric measurements at temperatures ranging from 40 to 70 °C revealed a slight increase in inhibition efficiencies from 99.5 % to 99.7 % for higher Cu doped Cu,N-CDs. Protective nature of N-CDs and Cu,N-CDs was accredited to physicochemical adsorption and inhibitor film formation. In addition, the growth of an electroless like Cu deposit on the mild steel surface contributed to better inhibition performances of Cu,N-CDs. The inhibition mechanism was supported by surface characterization of inhibited steel substrate. (c2022 Elsevier B.V.)

ENHANCED RECOVERY **1,561,605**

METHOD AND DEVICE FOR HEATING FORMATION WATER DIRECTIONALLY AND QUANTITATIVELY IN DELAYED MANNER

W.Yu, asr. (Beijing Energy Technol Ltd). World 2022/206,713A1, p. 10/6/2022, f. 3/28/2022 (Appl. 2,283,517), pr. China 3/29/2021 (Appl. 2021-10,330,593) (E21B-0043/24; E21B-0036/04). (In Chinese)

A method for heating formation water is disclosed herein. The formation water is heated by using a horizontal well heater that has a special structural design, in such a way that the water course

above a horizontal well is heated directionally and quantitatively in a delayed manner, which prevents heat energy from being transferred downwards so as to reduce the mining energy consumption of mineral resources. The horizontal well electric heater structurally comprises an α -angle structure of a slotted screen pipe, a heat insulation system and a heating system, wherein $\alpha = \arctan(\text{horizontal well depth}/r)$, the horizontal well depth is the distance from a horizontal section of the heating horizontal well to an overlying mineral resource reservoir, and r is half of the well distance of the heating well.

FRACTURING 1,561,606

FRACTURING SYSTEM, CONTROL SYSTEM FOR FRACTURING SYSTEM, AND CONTROL METHOD

K.Liu, X.Li, S.Cui, Z.Mao, W.Liu, L.Li, P.Zhang and D.Zhao, asrs. (Yantai Jereh Petrol Co Ltd). World 2022/205,401A1, p. 10/6/2022, f. 4/2/2021 (Appl. 2,185,184) (E21B-0043/26; E21B-0043/267). (In Chinese)

A fracturing system, a control system for a fracturing system, and a method for controlling a fracturing system during well site work are disclosed herein. The control system comprises: a fracture control apparatus, the fracture control apparatus being able to acquire a target fracturing pressure of a fracturing device, perform closed-loop control on the fracturing device using the target fracturing pressure as a control target, and set a target sand mixing pressure for a sand mixing device; and a sand mixing control apparatus, the sand mixing control apparatus performing closed-loop control on the sand mixing device using the target sand mixing pressure as a control target.

FRACTURING EQUIPMENT 1,561,607

PURGING SYSTEM AND PURGING METHOD FOR TURBINE FRACTURING DEVICE GROUP, AND TURBINE FRACTURING DEVICE GROUP

J.Wang, R.Zhang, F.Li, Z.Mao, P.Zhang and J.Wang, asrs. (Yantai Jereh Petrol Co Ltd). World 2022/198,780A1, p. 9/29/2022, f. 5/25/2021 (Appl. 2,195,798), pr. China 3/23/2021 (Appl. 2021-10,306,134) (F02C-0007/22; B08B-0005/00; E21B-0043/26; F02C-0007/232). (In Chinese)

Provided are a purging system for a turbine fracturing device group and a turbine fracturing device group comprising the purging system, and also provided is a purging method of the purging system. The turbine fracturing device group comprises a plurality of gas turbines, and each gas turbine comprises a plurality of fuel supply pipelines. The purging system comprises: a first air compressor and a purging pipeline, wherein the purging pipeline is communicated with the first air compressor and the plurality of fuel supply pipelines of each gas turbine in the turbine fracturing device group; the first air compressor is configured to supply compressed air to at least some fuel supply pipelines, which are stopped from supplying fuel, for purging, in a state that at least some fuel supply pipelines in the plurality of fuel supply pipelines are stopped from supplying the fuel. The purging system can simultaneously purge fuel pipelines and nozzles of a plurality of gas turbines, such that the maintenance by the purging system is more centralized and convenient, and workloads of on-site personnel are reduced.

FRACTURING FLUID ADDITIVE 1,561,608

DESIGN OF SALT-RESPONSIVE LOW-VISCOSITY AND HIGH-ELASTICITY HYDROPHOBIC ASSOCIATION POLYMERS AND STUDY OF ASSOCIATION STRUCTURE CHANGES UNDER HIGH-SALT CONDITIONS

J.Mao, H.Cao, H.Zhang, A.Du, J.Xue, C.Lin, X.Yang, Q.Wang, J.Mao et al. (Southwest Petroleum Univ). COLLOIDS AND SURFACES A: PHYSICOCHEMICAL AND ENGINEERING ASPECTS v.650, 10/5/2022. (ISSN 0927-7757; Article no.129512)

A hydrophobic associative water-soluble polymer, SRHV, was designed and synthesized in this study. The CAC of SRHV was 0.072 wt% and 0.2 wt%. The scanning electron microscopy tests showed that the polymer demonstrated a multilayer network

structure. Rheological tests revealed that polymer solution exhibited low-viscosity and high-elasticity rheological behaviors under high-salinity conditions and this salt-responsive behavior persists at high temperatures. Fluorescent probe tests confirmed that salt addition promoted the formation of hydrophobic association networks. Through molecular dynamics simulation, various parameters, such as mean square displacement (MSD), radius of gyration (Rg), and radial distribution function (RDF), were analyzed to further explain the salt-tolerance mechanism of SRHV and the effect of salt ions on the hydrophobic association structure. The results showed that the viscosity and elasticity of polymers were not necessarily correlated. In addition, elasticity dominated when the positive effect of salt-promoted association exceeded the negative effect of salt-coiled molecular chains and polymer relies on elasticity to achieve an excellent sand-carrying effect at this time. In general, SRHV exhibits great potential for application in oil fields with high salt environment, which could effectively reduce the waste of freshwater resources. Furthermore, this work provides some support for suspending sand relying on elastic. (c2022 Elsevier B.V.)

GRIPPER (PIPE) 1,561,609

TUBULAR GRIPPING APPARATUS

R.Gomez and K.T.Page, asrs. (Weatherford Technology LLC). World 2022/212,962A1, p. 10/6/2022, f. 1/19/2022 (Appl. 2,270,246), pr. U.S. 3/29/2021 (Appl. 216,313) (E21B-0019/16; E21B-0019/10).

A tubular gripping apparatus includes a housing having a bore and a plurality of gripping members movable between a gripping position and a release position. The apparatus may also include a shield having a tubular inner body movable relative to an outer body. The tubular inner body is movable between a retracted position, in which the tubular inner body is positioned above the plurality of gripping members, and an extended position, in which the inner body is at least partially positioned interiorly of the plurality of gripping members.

HYDRATE CONTROL 1,561,610

DOWNHOLE PUMPING TOOL

A.Faraoun, asr. (Welltec A/S). World 2022/200,245A1, p. 9/29/2022, f. 3/21/2022 (Appl. 2,257,280), pr. Europe. 3/22/2021 (Appl. 21,164,020) (E21B-0037/00; E21B-0041/00; E21B-0043/12; E21B-0049/08).

The present invention relates to the use of a downhole pumping tool for removing a hydrate formation forming a hydrate plug in a tubing in a well, the downhole pumping tool comprising a pump having a pump inlet and a pump outlet, an electric motor for driving the pump, a wireline for powering the electric motor, the pump having a first end arranged closest to the wireline and a second end facing the hydrate plug, wherein the pump inlet is arranged in the second end, and the pump inlet contacts a first face of the hydrate plug, the pump providing suction to remove at least part of a plurality of gas molecules from the hydrate plug for dissolving at least part of the hydrate formation. The invention also relates to a hydrate removal method for removing hydrate formation forming a hydrate plug in a tubing.

HYDRAULIC FRACTURING 1,561,611

THE SPONTANEOUS IMBIBITION MECHANISMS FOR ENHANCED OIL RECOVERY BY GEL BREAKING FLUID OF CLEAN FRACTURING FLUID

M.Zhao, S.Liu, Z.Gao, Y.Wu and C.Dai (China Univ Petroleum; China Offshore Oil Eng Co). COLLOIDS AND SURFACES A: PHYSICOCHEMICAL AND ENGINEERING ASPECTS v.650, 10/5/2022. (ISSN 0927-7757; Article no.129568)

The quick flowback treatment after conventional fracturing construction can waste a lot of energy from fracturing fluid. Meanwhile, spontaneous imbibition has great application potential for enhanced oil recovery (EOR). In this work, based on pre-developed silica nanoparticle-reinforced CO₂-sensitive fracturing fluid system, the imbibition factors of the gel breaking fluid were studied. In addition, the HNMR technology, AFM, contact angle

test, and interfacial tension (IFT) test were used to explore the mechanism of spontaneous imbibition. The results show that imbibition mainly occurs in the small pores, and the adsorption of components can reduce roughness and flow resistance. Meanwhile, the adsorption layer was formed by surfactants and nanoparticles, changing wettability from oil-wet to water-wet, reducing the IFT between oil and water. The synergistic effect of multi-component improves the imbibition effect. We expect that this study can broaden the application of multi-component gel breaking fluid in low permeability reservoirs. (c2022 Elsevier B.V.)

HYDRAULIC FRACTURING 1,561,612

SAND CONVEYING APPARATUS AND CONTROL METHOD THEREFOR AND APPARATUS AND STORAGE MEDIUM

K.Liu, D.Zhao and Z.Mao, asrs. (Yantai Jereh Petrol Co Ltd). World 2022/205,590A1, p. 10/6/2022, f. 5/25/2021 (Appl. 2,195,645), pr. China 4/2/2021 (Appl. 2021-10,361,552) (B66C-0013/08; B65G-0065/00; B65G-0065/32; B66C-0001/16; B66C-0005/02; B66C-0009/02; B66C-0009/08; B66C-0009/14; B66C-0011/00; B66C-0013/46; B66C-0013/48; B66C-0013/50; B66C-0019/00). (In Chinese)

A sand conveying apparatus and a control method therefor and an apparatus and a storage medium are disclosed herein. The sand conveying apparatus comprises a material storage device, a conveying device and a hoisting device, wherein the material storage device is located above an area where sand needs to be input; the conveying device is connected to the material storage device, and the conveying device is configured to convey the sand to the material storage device; the hoisting device is located above the conveying device, the hoisting device transports the sand in a hoisted sand accommodating portion to the conveying device by means of the action of a hoist, and between a first position where the hoist of the hoisting device is located and the position where a hopper is located, simultaneous movement along a plurality of line segments in different directions is achieved, such that linear movement is achieved.

HYDRAULIC FRACTURING 1,561,613

PLUNGER, HYDRAULIC END AND PLUNGER PUMP

B.Wang, H.Li, H.Cui, X.Li, W.Cui and P.Li, asrs. (Yantai Jereh Petrol Co Ltd). World 2022/205,583A1, p. 10/6/2022, f. 5/20/2021 (Appl. 2,194,872), pr. China 3/31/2021 (Appl. 2021-10,347,506) (F04B-0053/14; F04B-0053/10). (In Chinese)

A plunger, a hydraulic end, and a plunger pump are disclosed herein. The plunger comprises a plunger body, a first liquid intake hole and a first valve assembly; the plunger body comprises a runner located inside the plunger body; the first liquid intake hole is located on the plunger body and passes through a side wall of the plunger body; the plunger body comprises a first end part and a second end part; the runner in the interior of the plunger body extends from the first end part of the plunger body to the second end part of the plunger body; the portion of the runner in the interior of the plunger body close to the first end part is sealed; the runner in the interior of the plunger body extends to the second end part, and a first opening is formed at the second end part; the first liquid intake hole communicates with the runner; and the first valve assembly is located at the first opening, and is configured to allow fluid to flow out from the runner at the first opening, and prevents fluid from flowing back into the runner from the outside. Thus, the plunger may improve the durability of a plunger pump and reduce the cost of the plunger pump.

HYDRAULIC FRACTURING 1,561,614

CONTROL METHOD AND CONTROL APPARATUS APPLIED TO ELECTRICALLY DRIVEN FRACTURING EQUIPMENT

K.Liu, X.Li, Z.Mao, S.Cui and S.Zhang, asrs. (Yantai Jereh Petrol Co Ltd). World 2022/198,818A1, p. 9/29/2022, f. 6/25/2021 (Appl. 2,102,406), pr. China 3/25/2021 (Appl. 2021-10,318,395) (F04B-0049/06; E21B-0043/26; F04B-0049/20). (In Chinese)

A control method and control apparatus applied to electrically

driven fracturing equipment are disclosed herein. The electrically driven fracturing equipment comprises a plunger pump and a first motor for driving the plunger pump. The control method comprises acquiring a preset displacement of the plunger pump; acquiring a rotational speed of the first motor and a discharge pressure of the plunger pump; determining a real-time displacement of the plunger pump on the basis of the rotational speed of the first motor and the discharge pressure of the plunger pump and adjusting the real-time displacement; and, when the real-time displacement reaches the preset displacement, keeping the first motor in a stable state. According to the control method, better adaptation to the site can be achieved by controlling the rotational speed of the first motor by means of the displacement, and the real-time displacement of the plunger pump is determined on the basis of the rotational speed of the first motor and the discharge pressure of the plunger pump, thus the displacement of the plunger pump can be corrected in real time, thereby ensuring accurate calculation, thus improving the calculation accuracy of the pump efficiency of the plunger pump.

OPEN HOLE COMPLETION 1,561,615

OPEN HOLE MULTI-ZONE SINGLE TRIP COMPLETION SYSTEM

A.C.Hammer and D.Q.Napier, asrs. (Baker Hughes Oilfield LLC). World 2022/212,154A1, p. 10/6/2022, f. 3/24/2022 (Appl. 2,221,644), pr. U.S. 3/29/2021 (Appl. 63/167,368) (E21B-0034/10; E21B-0023/06; E21B-0034/08).

A multi-zone single trip open hole completion system includes an outer tubular assembly including an uphole end, a downhole end, an inner tubular assembly, an anchor arranged on the outer tubular assembly, and an anchor setting assembly provided on one of the outer tubular assembly and the inner tubular assembly. The anchor setting assembly is operable to selectively set the anchor. An isolation flow path is in the outer tubular. A flow control system is arranged on the inner tubular assembly. The flow control system selectively blocks flow through the inner tubular assembly. A remotely operated valve is arranged in one of the inner tubular assembly and the outer tubular assembly. The remotely operated valve is operable to close fluid flow through the tubular. An isolation packer is arranged along the outer tubular assembly. Closing the remotely operated valve enables the anchor, and the isolation packer to be set.

ORIENTED PERFORATING 1,561,616

ORIENTATION RING

J.J.Constantine, R.Hand and N.Adams, asrs. (ConocoPhillips Co). World 2022/204,402A1, p. 9/29/2022, f. 3/24/2022 (Appl. 2,221,742), pr. U.S. 3/24/2021 (Appl. 63/165,414) (E21B-0017/00; E21B-0017/02; E21B-0017/05; E21B-0017/10; E21B-0017/14; E21B-0019/16).

Implementations described and claimed herein provide systems and methods for increasing accuracy of firing perforating charges in an oil well casing. In one implementation, a body of an orientation device has a first portion and a second portion. An opening extends through a center of the body from a first lateral surface to a second lateral surface, and the opening is configured to receive a perforating gun string. An outer perimeter surface extends about the center of the body from the first lateral surface to the second lateral surface. The outer perimeter surface has a first shape associated with the first portion and a second shape associated with the second portion. The second shape forms a base portion configured to maintain the perforating gun string in an orientation by preventing rotation of the perforating gun string. The orientation corresponds to a predetermined perforating charge direction of the perforating gun string.

PACKER 1,561,617

OPTIMIZATIONS OF DOWNHOLE SEALING DEVICES AND THEIR VALIDATIONS

A.Zhong, Z.Fan, A.Purohit and B.P.J.Mothilal (Halliburton). OFFSHORE TECHNOLOGY CONFERENCE [OTC] (Houston, TX, 5/2-5/2022) PROCEEDINGS 2022. (ISBN 978-1-61399-852-6;

OTC-31830; Available at <http://www.onepetro.org> as of 6/23/2022; 11 pp)

Due to complexity and strong nonlinear behavior, design of sealing devices such as packer elements has heavily relied on empirical knowledge for many years. Since downhole environments continue to grow harsher, especially in high-pressure, high-temperature (HPHT) conditions, there are large gaps between existing empirical knowledge and the notable challenges faced in the sealing element development process. These gaps have often led to a trial-and-error approach to design, extending development time through frequent delays and resulting in significant cost overruns. Moreover, empirical knowledge gained through the process for a particular design has very limited application to other designs. To overcome these deficiencies of a traditional development approach, a combination of computational modeling, materials science, and small-scale tests was used in the early stage of a development project to optimize sealing element design, which substantially reduced the number of physical tests and ultimately reduced the overall development cycle time and cost. The main feature of this optimization/improvement of sealing element design is to use engineering mechanics principles, primarily via computational modeling, as guidelines for sealing device development instead of relying heavily on empirical knowledge. The computational models are calibrated and validated through small scale physical tests, which ensure the fidelity of the computational models. The optimum packer element designs are obtained through a systematic numerical scheme along with machine lessons. Considering the approximations and limitations of numerical models, the numerically determined optimum design is further evaluated, examined against real application conditions, and adjusted as needed, before being finalized. The result is an efficient, physically calibrated and validated computational model for packer element behavior. This model along with machine learning algorithms is applied to the optimization of a 9-5/8 in. packer element which successfully passed both API 11D1 type V3 and V0 testing on the first attempt. (Copyright 2022 OTC)

PARTICLE VELOCITY 1,561,618

TRUE PARTICLE VELOCITY WAVEFIELD PROCESSING IN FIBER OPTICS - PARTICLE MOTION SENSOR HYBRID ARRAY

T.Mizuno and J.H.Le Calvez, asrs. (Schlumberger Technol Corp; Schlumberger Canada Ltd; Schlumberger Serv Petrol; Schlumberger Technol BV). World 2022/203,945A1, p. 9/29/2022, f. 3/18/2022 (Appl. 2,220,858), pr. U.S. 3/24/2021 (Appl. 211,429) (G01V-0001/22; G01D-0005/35; G01H-0009/00; G01V-0001/24; G01V-0001/30; G01V-0008/24; G01V-0013/00).

Systems and methods may be used to reconstruct particle velocity wavefields from coupling-calibrated fiber-optic data that subsequently enables physically valid construction of the particle velocity wavefields for a hybrid sensor array including both fiber-optic and particle motion sensors. These systems and methods may be used in a variety of borehole geophysical applications, such as structure and reservoir imaging, impedance inversion, attenuation tomography, micro-seismic fracture imaging, focal mechanism analysis, and so on. The systems and methods may also be used in other applications such as geothermal and CO2 storage monitoring.

PLUGGING AGENT 1,561,619

STUDY OF ADHESIVE SELF-DEGRADING GEL FOR WELLBORE SEALING

Y.Wang, D.Liu, R.Liao, G.Zhang, M.Zhang and X.Li (Yangtze Univ; China National Petrol Corp). *COLLOIDS AND SURFACES A: PHYSICO-CHEMICAL AND ENGINEERING ASPECTS* v.651, 10/20/2022. (ISSN 0927-7757; Article no.129567)

In this study, a self-degrading gel with high adhesion was synthesized by acrylamide, acrylic acid and an unstable cross-linker. It was used for the pressurized operation of oil and gas wells. The degradation time, adhesion and plugging performance of the gel were investigated by degradation experiments, adhesion experiments and plugging experiments. To a certain extent, it was found that the concentration of the reactants had different effects on the degradation time and adhesion friction of the gels. In

addition, the adhesion friction varies due to compressional deformation of the gel by compression. The blocking ability of the gels was mainly related to the adhesion friction. The blocking capacity of high-strength horizontal gels is linearly related to the adhesion friction. The sealing capacity of low strength horizontal gel is non-linearly related to the adhesion friction. Compared with conventional gel blocking operation, the gel breaking operation at the end of gel blocking operation does not require additional injection of gel breaking agent due to the introduction of unstable crosslinker. The gel degradation time can be controlled by designing the formulation to achieve rapid gel breakage and rejection. It saves time cost and economic cost. The highly viscous self-degrading gel can be used as a wellbore pressure packer for oil and gas wells under pressure. (c2022 Elsevier B.V.)

PLUGGING AGENT 1,561,620

DESIGN, PREPARATION AND PROPERTIES OF NEW POLYACRYLAMIDE BASED COMPOSITE NANO-MICROSPHERES WITH LIKE "BALL IN BALL" STRUCTURE

X.Ma, Y.Zhou, P.Yi, S.Zhou, Y.Wang and D.Yang (Beijing Univ Chem Technol; Changqing Oilfield Co). *COLLOIDS AND SURFACES A: PHYSICO-CHEMICAL AND ENGINEERING ASPECTS* v.654, 12/5/2022. (ISSN 0927-7757; Article no.130037)

Recently, polymer gel nano-microspheres as a new kind of depth profile control agent have achieved preliminary effects in enhancing oil recovery (EOR), especially, for some low-permeability reservoirs that are difficult to enter by conventional polymer flooding. To synergistically improve the water-oil mobility ratio on the basis of blocking pore throat and adjusting water flooding profile by microgel, a new polyacrylamide composite nano-microspheres with like "ball in ball" structure are designed and prepared via inverse microemulsion polymerization in the case of pre-introducing hyperbranched polyacrylamide (HBPAM) in the water phase. Like-spheroid (HBPAM) with high rheological properties are gradually released from microspheres to achieve the synergistic effects of plugging pore throat of reservoir and viscosity improvement of the dispersion. This article uses FTIR, SEM, TEM, TGA and laser particle size analyzer to characterize the structure, morphology, thermo-stability and particle size distribution of composite microspheres. The swelling dynamics, temperature, and salt resistance of the composite microspheres are then analyzed. More importantly, the rheological properties, dispersion stability, thickening ability, emulsifying property, and oil displacement mechanism of microspheres are systematically studied. The plugging rate and oil displacement efficiency are analyzed by simulated core experiments to evaluate the application effect of microspheres. The composite microspheres designed in this paper are expected to solve the challenge that conventional polyacrylamide used in EOR is difficult to be injected in low permeability reservoirs and synergistically enhance the profile control and EOR effect of nanospheres. (c2022 Elsevier B.V.)

PLUGGING AGENT 1,561,621

SYNTHESIS OF POLYSTYRENE/SILICA AND POLY(STYRENE-CO-BUTYL ACRYLATE)/SILICA NANOCOMPOSITE PARTICLES BY PICKERING EMULSION POLYMERIZATION WITH NON-FUNCTIONALIZED SILICA NANOPARTICLES

H.T.Ip, L.Liu, L.Hong and T.Ngai (Hong Kong Chinese Univ; South China Univ Technol). *COLLOIDS AND SURFACES A: PHYSICO-CHEMICAL AND ENGINEERING ASPECTS* v.654, 12/5/2022. (ISSN 0927-7757; Article no.130104)

Organic-inorganic nanocomposite particles can be prepared by Pickering emulsion polymerization. Attempts to prepare polystyrene/silica nanocomposite particles without the addition of auxiliary comonomers, surface modification of silica sols or alcoholic silica sols or use of functionalized silica nanoparticles have not yielded satisfactory results. In this study, we demonstrated a versatile approach to prepare polystyrene/silica and poly(styrene-co-butyl acrylate)/silica nanocomposite particles by subjecting commercially available non-functionalized silica nanoparticles through Pickering emulsion polymerization. Monodisperse

nanocomposite particles with a high silica incorporation efficiency were fabricated. We investigated the effects of the silica content, initiator content and pH value on the properties of the prepared nanocomposite particles. Mechanistic investigations of the system showed that the silica nanoparticles did not require surface polymerization. Two aspects facilitated the adhesion of silica nanoparticles onto the growing latex particles: wetting of hydrophilic silica nanoparticles by more hydrophobic oligomers, and electrostatic interaction between the silica nanoparticles and oppositely charged oligoradicals. (c2022 Elsevier B.V.)

SCALE INHIBITOR 1,561,622

SURFACTANT-BASED ACID FORMULATION AND USE THEREOF AS A CALCIUM CARBONATE AND DOLOMITE DISSOLVING AGENT TO PREVENT THE FORMATION OF SCALING IN THE OIL INDUSTRY [FORMULACION ACIDA A BASE DE SURFACTANTES Y SU USO COMO AGENTE DISOLVENTE DE CARBONATO DE CALCIO Y DOLOMIA PARA PREVENIR LA FORMACION DE INCRUSTACIONES EN LA INDUSTRIA PETROLERA]

J.C.Jimenez Osorio, asr. (Chemiservis SA de CV). World 2022/203,492A1, p. 9/29/2022, f. 3/23/2022 (Appl. 2,250,025), pr. Mex. 3/26/2021 (Appl. 21,003,591) (C09K-0008/04; C09K-0008/52; C09K-0008/72; C09K-0008/74). (In Spanish)

The present invention relates to a surfactant-based acid formulation and to the use thereof as a calcium carbonate and dolomite dissolving agent to prevent the formation of scaling in the oil industry, which is used in stimulation work in calcium carbonate and dolomite formations, and has the secondary function of eliminating the fouling produced by seawater-based drilling fluids containing high concentrations of organic or synthetic polymers in oilfields.

SCALE INHIBITOR 1,561,623

SYNTHETIC ACID FORMULATION AND USE THEREOF AS A CALCIUM CARBONATE DISSOLVING AGENT TO PREVENT THE FORMATION OF SCALING IN THE OIL INDUSTRY [FORMULACION SINTETICA ACIDA Y SU USO COMO AGENTE DISOLVENTE DE CARBONATO DE CALCIO PARA PREVENIR LA FORMACION DE INCRUSTACIONES EN LA INDUSTRIA PETROLERA]

J.C.Jimenez Osorio, asr. (Chemiservis SA de CV). World 2022/203,489A1, p. 9/29/2022, f. 3/23/2022 (Appl. 2,250,021), pr. Mex. 3/26/2021 (Appl. 21,003,594) (C09K-0008/52; C09K-0008/52; E21B-0037/06). (In Spanish)

The present invention relates to a synthetic acid formulation and the use thereof as a calcium carbonate dissolving agent to prevent the formation of scaling in the oil industry, which offers highly effective stimulation and can also be used in the removal of scaling from fractures and the removal of scaling from rigging, and which performs equally to hydrochloric acid, providing exceptional calcium carbonate solubility of up to 99.9%, but without the highly hazardous exposure and without the highly corrosive properties of same. It is thermally stable up to 190°C and is compatible with light and extra heavy oils.

SIMULATION 1,561,624

WELL INTERVENTION PERFORMANCE SYSTEM

P.Mukerji, N.W.Hoyer, G.Lillehammer and R.K.Thakur, asrs. (Schlumberger Technol Corp; Schlumberger Canada Ltd; Schlumberger Serv Petrol; Schlumberger Technol BV). World 2022/204,718A1, p. 9/29/2022, f. 3/25/2022 (Appl. 2,271,339), pr. U.S. 3/25/2021 (Appl. 63/166,105) (E21B-0047/12; E21B-0044/00; E21B-0047/26).

A method can include receiving inputs for a well; generating scenarios for the well using the inputs; instructing a simulator to simulate generated scenarios; receiving simulation results for at least some of the generated scenarios; and assessing the received simulation results for implementation of one or more well actions for the well.

SOLIDS CONTROL 1,561,625

ACOUSTIC SAND MONITOR

L.D.Rhyne, P.Crowder and H.Janakiram Subramani, asrs. (Chevron USA Inc). World 2022/212,797A1, p. 10/6/2022, f. 3/31/2022 (Appl. 2,222,965), pr. U.S. 4/2/2021 (Appl. 63/170,156) (E21B-0043/34; G01N-0015/00; G01N-0015/06; G01N-0029/04; D21B-0043/00).

An acoustic sand monitor system includes an exciter assembly and a receiver that are configured to be coupled to an accumulator vessel. Separating equipment separates sand from a fluid stream produced by a well. The accumulator vessel collects the sand separated from the fluid stream. The exciter assembly causes vibrations of the accumulator vessel and the receiver measures audio signals generated by the vibrations of the accumulator vessel. A control system analyzes the audio signal to determine the amount of sand collected in the accumulator vessel.

WATER SHUTOFF 1,561,626

A SELECTIVE WATER CONTROL AND GAS AUGMENTATION METHOD BASED ON APR GEL

L.Chen, H.Zeng, X.Liang, J.Yi, Z.Mao, G.Li, L.Liu and Y.Hu (Yangtze Univ; CNOOC Research Inst). *COLLOIDS AND SURFACES A: PHYSICOCHEMICAL AND ENGINEERING ASPECTS* v.653, 11/20/2022. (ISSN 0927-7757; Article no.129980)

Water production will seriously affect the economics of gas well in the development of oil field. However, the conventional water shutoff agent is easy to block the gas flow channel at the same time of plugging the water. In this paper, a temperature and salt resistant polymer gel system composed of acrylamide/acryloyl morpholine/vinylpyrrolidone terpolymer (APR) and polyethyleneimine/modified alumina nanoparticle cross-linker was developed. At the same time, a selective water control and gas augmentation method based on APR gel was established. The effect of gel composition on its performance was mainly studied, and the water & gas shutoff performance in harsh environment was also researched by sandpack flow experiment. The gelation time could be controlled within 2–14 h by adjusting the concentration of the polymer, cross-linker, and deoxidant. In addition, the dehydration rate of the gel was only 2.6% after 180 days heat aging at 107°C and 230,000 mg/L mineralization. The scanning electron microscope (SEM) showed that the uniform distribution of the network structure resulted in the gel with excellent stability in harsh environments. Sand filling experiments indicated that the plugging rate of gel for sand filling models with different permeability was all above 90% in harsh environment (107°C, 230,000 mg/L salinity). Besides, laboratory experiments have illustrated that the injection pattern of the gel has a significant influence on its water & gas shutoff performance. Injecting 0.5PV gel solution first, then injecting 6PV N₂, the shutoff performance of gel for water was nine times as good as that of gas. The research provides technical guidance for the water shutoff of high-temperature and high-salt gas reservoirs. (c2022 Elsevier B.V.)

WELL COMPLETION 1,561,627

CONTRACTION JOINT FOR INTELLIGENT COMPLETION AND DOWNHOLE COMPLETION SYSTEM

W.Lai, R.Musayev, A.Bahl, D.Deleon and L.Yu, asrs. (Schlumberger Technol Corp; Schlumberger Canada Ltd; Schlumberger Serv Petrol; Schlumberger Technol BV). World 2022/212,810A1, p. 10/6/2022, f. 4/1/2022 (Appl. 2,222,999), pr. U.S. 4/2/2021 (Appl. 63/170,090) (E21B-0017/043; E21B-0017/07; E21B-0034/08).

A contraction joint includes a mandrel at least partially disposed within an upper tubular member, the upper tubular member being capable of moving uphole and downhole to change a length of the contraction joint. The contraction joint also includes a nipple housing connected to the upper tubular member, a piston housing connected to the nipple housing, a support piston disposed in the piston housing, the support piston being affixed to an upper mandrel sub of the mandrel via at least one piston retaining device, a lock housing disposed between the upper tubular member and the upper mandrel sub, and a stroke locking mechanism disposed

within the lock housing, the stroke locking mechanism including a profile that engages the nipple housing.

WELL COMPLETION 1,561,628

DOWNHOLE TOOL SECURABLE IN A TUBULAR STRING

J.Kellner, T.Tinnin and B.Griffith, asrs. (Innovex Downhole Solut Inc). World 2022/212,447A1, p. 10/6/2022, f. 3/30/2022 (Appl. 2,222,462), pr. U.S. 4/2/2021 (Appl. 220,987) (E21B-0023/00; E21B-0034/06).

A downhole tool includes a tubular, an inner valve assembly positioned in the tubular, and a body positioned radially between the inner valve assembly and the tubular, the body at least partially made from a bonding agent configured to secure the inner valve assembly in the tubular.

WELL COMPLETION 1,561,629

REDUNDANT TRIGGER SYSTEM

M.F.Tafur, B.Chen, Y.Dufour, B.Walther, B.Swenson and S.E.Buchanan, asrs. (Schlumberger Technol Corp; Schlumberger Canada Ltd; Schlumberger Serv Petrol; Schlumberger Technol BV). World 2022/204,284A1, p. 9/29/2022, f. 3/23/2022 (Appl. 2,221,548), pr. U.S. 3/26/2021 (Appl. 63/166,506) (E21B-0034/14; E21B-0034/06; E21B-0034/10).

A redundant trigger section that actuates a device between operational positions in response to a controlled signal includes a housing including an internal through passage and a plurality of chambers formed in a wall of the housing, a pilot piston disposed within the internal through passage, an actuating piston connected to the pilot piston, and a plurality of triggers connected to the actuating piston. Upon receipt of the controlled signal by a first tubing pressure chamber of the plurality of chambers, at least one trigger of the plurality of triggers activates the actuating piston, which pushes the pilot piston within the internal through passage from an initial position to a final position.

WELL COMPLETION 1,561,630

REGENERATING SOLVENT MIXTURES THAT ARE USED FOR ELEMENTAL SULFUR REMOVAL WITHIN HYDROCARBON WELLS

P.S.Northrop and K.A.Harnsberry, asrs. (ExxonMobil Upstream Res Co). World 2022/203,912A1, p. 9/29/2022, f. 3/16/2022 (Appl. 2,220,495), pr. U.S. 3/26/2021 (Appl. 63/166,379) (C09K-0008/53; E21B-0021/06).

Methods for utilizing and regenerating solvent mixtures for dissolving elemental sulfur within hydrocarbon wells are described herein. One method includes providing a solvent mixture including an elemental sulfur solvent fraction including disulfide compound(s), as well as an odorant fraction including a lactate ester solvent. The method also includes injecting the solvent mixture into a hydrocarbon well such that the elemental sulfur solvent fraction dissolves elemental sulfur deposited on well components, as well as collecting the resulting spent solvent mixture, which includes thiols and residual lactate ester solvent, within a spent solvent separator. The method further includes sparging the spent solvent mixture with oxidizer within the spent solvent separator to allow for oxidation of the thiols to produce the disulfide compound(s) using the residual lactate ester solvent (and, optionally, additional lactate ester solvent), as well as regenerating the solvent mixture using at least a portion of the produced disulfide compound(s).

WELL COMPLETION 1,561,631

WATER-DISPERSIBLE POLYMER POWDER COMPOSITIONS FOR CEMENTING IN SUBTERRANEAN FORMATION, THEIR MANUFACTURE AND USE

C.Schmidtke, A.Assmann, M.Winklbauer and L.Wolferstetter, asrs. (BASF SE). World 2022/200,156A1, p. 9/29/2022, f. 3/17/2022 (Appl. 2,256,923), pr. Europe. 3/23/2021 (Appl. 21,164,356) (C04B-0028/04; C04B-0040/00; C09K-0008/467; C09K-0008/487; C04B-0103/46).

The present disclosure relates to a water-dispersible polymer powder composition for use as additive in cementing in subterranean formations comprising at least particles of a styrene-butadiene polymer, a water-soluble polymer, and a non-ionic emulsifier, wherein the styrene-butadiene polymer particles are at least partly covered by and/or embedded in a composition comprising at least the water-soluble polymer, process of making such compositions, by spray-drying an aqueous dispersion comprising said particles of a styrene-butadiene polymer and a water-soluble polymer, wherein at least one non-ionic emulsifier is added before or after spray-drying, and the use of such water-dispersible polymer powder compositions for cementing in subterranean formations penetrated by at least a well bore.

WELL INTEGRITY 1,561,632

FIELD LIFE EXTENSION: REAL TIME WELL INTEGRITY MANAGEMENT

P.E.Aranha, E.Schnitzler, N.Moreira, L.E.Duccini, A.L.Martins, A.B.Falchetto and J.L.Anjos (Petroleo Brasileiro SA). *OFFSHORE TECHNOLOGY CONFERENCE [OTC] (Houston, TX, 5/2-5/2022) PROCEEDINGS 2022*. (ISBN 978-1-61399-852-6; OTC-31816; Available at <http://www.onepetro.org> as of 6/23/2022; 19 pp)

This article aims to present the evolution of well design and well integrity monitoring throughout their life cycle and life-extension analysis. The motivation comes from the need to make a decision to extend the life of wells while accounting for both green and brownfields. Petrobras' design practices were updated to meet the Well Integrity National Regulatory requirements and to support the life extension analysis. In order to assess the well integrity during the production lifetime, a digital twin of the well was developed that is capable of modelling the physics of permanent and transient fluid flow and the corresponding behavior of trapped annuli with thermo-structural coupling to the mechanical structure. Also, as part of the monitoring process, additional information will be provided by new sensors to be installed in the A and B annuli, aiming to improve monitoring capability. This paper will present the results of the new well design and life extension analysis practices for retrofit projects. Besides that, a discussion on new challenging scenarios faced by the company is included. The well integrity case study of a deep-water field in Brazilian offshore using a real-time digital-twin approach will highlight the main technological solutions developed to ensure well operations within the envelope during its lifetime. Adopting this strategy allows us to optimize procedures with the goal of maximizing production or injection rates while sticking to safety requirements. The availability of additional annuli sensors can improve the system capability. With the well integrity surveillance digital twin, Petrobras successfully implemented a unique monitoring integrity system for offshore production units in Brazil, increasing our understanding of the well structure's behavior and, consequentially, the asset's operational safety during its lifetime. In addition, this initiative aims to push the industry towards the development of wet X-mas trees according to API RP 17V requirements. (Copyright 2022 OTC)

WELL PLUG 1,561,633

ISOLATION PLUG TOOL AND METHOD

G.Kelbie, asr. (Baker Hughes Oilfield LLC). World 2022/204,082A1, p. 9/29/2022, f. 3/22/2022 (Appl. 2,221,256), pr. U.S. 3/22/2021 (Appl. 208,325) (E21B-0023/01; E21B-0033/12; E21B-0033/12; E21B-0033/14; E21B-0034/14).

The present disclosure relates to an isolation plug tool including a mandrel, an anchor assembly disposed on the mandrel, a seal assembly disposed on the mandrel having a seal, and a sleeve removably disposed radially outwardly of the seal.

WELL PLUGGING 1,561,634

METHOD AND APPARATUS FOR USE IN PLUG AND ABANDON OPERATIONS

J.Rutherford, asr. (ConocoPhillips Co). World 2022/213,022A1, p. 10/6/2022, f. 3/22/2022 (Appl. 2,271,262), pr. U.S. 3/29/2021 (Appl.

63/167,228) and U.S. 3/22/2022 (Appl. 655,885) (C09K-0008/42; E21B-0033/13; E21B-0033/12).

The invention relates to the use of a casing or liner with pre-formed, selectively openable apertures, in plug and abandon operations at the end of life of a hydrocarbon well. The casing or liner is installed at the start of the well's life and the apertures are provided over a length of the casing/liner above the reservoir where a permanent plug would normally be formed when the well is abandoned at the end of its life. Associated with the apertures are sliding sleeve closure members which are designed to remain operational over the 20-30 year lifetime of the well.

WELL PLUGGING 1,561,635

SYSTEMS AND METHODS FOR PLUGGING A WELL

T.E.Harms, asr. (Halliburton Energy Service). World 2022/211,788A1, p. 10/6/2022, f. 3/30/2021 (Appl. 2,124,831), pr. U.S. 3/29/2021 (Appl. 215,227) (E21B-0033/134; E21B-0023/06; E21B-0033/16; E21B-0043/116).

A plugging system for plugging a cased well in a single trip downhole is disclosed herein. The plugging system may include a tool string positionable within the cased well and including a bore and a downhole tool coupled to the tool string. The downhole tool may include a first perforating gun, an upper resettable packer, a lower resettable packer, and a flow-through assembly. The first perforating gun may be operable to perforate the casing of the cased well. When the downhole tool is positioned in the cased well, the upper resettable packer may be uphole of the first perforating gun. When the downhole tool is positioned in the cased well, the lower resettable packer may be downhole of the first perforating gun. The flow-through assembly may be positioned between the upper resettable packer and the lower resettable packer and operable to flow fluids into a bore of the cased well.

WELL STIMULATION 1,561,636

METHOD FOR SINGLE-STAGE TREATMENT OF SILICEOUS SUBTERRANEAN FORMATIONS

H.Zhao, M.Ziauddin, T.I.Yusuf, P.Abin and J.C.Santa-Maria, asrs. (Schlumberger Technol Corp; Schlumberger Canada Ltd; Schlumberger Serv Petrol; Schlumberger Technol BV). World 2022/204,339A1, p. 9/29/2022, f. 3/24/2022 (Appl. 2,221,630), pr. U.S. 3/25/2021 (Appl. 63/166,072) (C09K-0008/74; C09K-0008/72; E21B-0043/26).

Methods and compositions for treating a siliceous geologic formation are described herein. An aqueous treatment composition for treating such formations includes an acid having molecular weight less than about 200, or an ammonium or sodium salt thereof, an HF source, and from about 0.1 wt% to about 2.0 wt% of a fluoride scale inhibitor, the aqueous treatment composition having a pH from about 1.0 to about 3.0.

WELL TOOL 1,561,637

DEBRIS BARRIER FOR RETRIEVABLE DOWNHOLE TOOL USING EXPANDABLE METAL MATERIAL

R.T.Murphy, S.Martinez, M.L.Fripp and R.B.Falconer, asrs. (Halliburton Energy Service). World 2022/211,802A1, p. 10/6/2022, f. 3/31/2021 (Appl. 2,125,101), pr. U.S. 3/30/2021 (Appl. 217,213) (E21B-0023/06; E21B-0033/04; E21B-0043/10).

A system is described for forming a debris barrier downhole in a wellbore. The system may include a mandrel, a retrievable downhole tool, and a debris ring. The mandrel may be positionable within a wellbore. The retrievable downhole tool may be positionable around the mandrel to perform tasks downhole in the wellbore. The debris ring may include an expandable material positionable around the mandrel to form a debris barrier. The debris barrier may be formed in response to exposing the expandable material to wellbore fluid.

WELL TOOL 1,561,638

WELLBORE DART WITH SEPARABLE AND EXPANDABLE TOOL ACTIVATOR

B.Gao, L.C.Helms, A.Gadre, Y.Hu and G.J.Makowiecki, asrs. (Halliburton Energy Service). World 2022/211,772A1, p. 10/6/2022, f. 3/28/2021 (Appl. 2,124,543), pr. U.S. 3/28/2021 (Appl. 214,878) (E21B-0034/14; E21B-0023/04; E21B-0034/10).

A wellbore dart can be used to activate a downhole tool within a wellbore to perform a function, such as shifting a sleeve. The dart includes a tool activator that is releasably connected to a body of the dart. After the downhole tool has been activated, the body can be released from the tool activator to open a fluid flow path within the downhole tool. A device can be pumped and land on the tool activator. The tool activator can include multiple sections that expand radially away from each other when force from the device is exerted on the sections. Expansion of the sections allows the device to pass through the tool activator. The dart can also include a retracting device that moves the sections back together after the device has passed through the tool activator.

WELL WORKOVER 1,561,639

EXTENDED RELEASE ASPHALTENE INHIBITOR COMPOSITION

R.Tomson, P.Guraieb, K.Powell and R.Jayawickramage, asrs. (Tomson Technologies LLC). World 2022/208,322A1, p. 10/6/2022, f. 3/28/2022 (Appl. 2,252,856), pr. U.S. 3/29/2021 (Appl. 63/167,445) (C09K-0008/52; C09K-0008/03).

A nanoparticle for well-treatment applications and compositions and methods of making and using the same are disclosed. The nanoparticle can include a carrier material and an asphaltene inhibitor. The asphaltene inhibitor is capable of being released from the carrier material. The nanoparticle can have a size of 10 nanometers (nm) to 500 nm.

PRODUCING OIL & GAS

ACTIVATED CHARCOAL 1,561,640

ACTIVATED CARBON FROM POLYURETHANE RESIDUES AS MOLECULAR SIEVES FOR KINETIC ADSORPTION/SEPARATION OF CO₂/CH₄

O.F.Cruz, Jr., I.C.Gomez, M.M.Escandell, C.R.Rambo and J.Silvestre-Albero (Inst Nac Pesquisas Amazon; Alicante Univ; Santa Catarina Fed Univ). *COLLOIDS AND SURFACES A: PHYSICO-CHEMICAL AND ENGINEERING ASPECTS* v.652, 11/5/2022. (ISSN 0927-7757; Article no.129882)

Activated carbon-based molecular sieves were synthesized, characterized and their kinetics of adsorption were evaluated to be used in separation processes of CO₂/CH₄ mixtures. Polyurethane (PU) foams were used as carbon precursors and the PU-derived carbons were physical activated with CO₂. All the samples present a preferential adsorption of CO₂ over methane in kinetic adsorption experiments. Samples activated at 800 °C during 6 h exhibited the highest selectivity due to the absence of methane adsorption at lower resident times, which makes those samples very interesting for industrial processes of natural gas purification. Kinetic studies were performed to explain the kinetic profiles obtained, confirming that in the samples with smallest pore size, intraparticle diffusion was the limiting step, evidencing that certain oxygen groups favour CO₂ adsorption, whereas adsorption was the limiting step in the samples with wider pores. (c2022 Elsevier B.V.)

ANCHOR (STRUCTURAL) 1,561,641

DYNAMIC PENETRATION PROCESS OF TORPEDO ANCHORS INTO SAND FOUNDATION

G.Li, J.Zhang, J.Niu, J.Liu and Y.Yang (Xijing Univ; Dalian Univ Technol; Chang'an Univ). *JOURNAL OF MARINE SCIENCE AND ENGINEERING* v.10, no.8, Aug. 2022. (ISSN 2077-1312; Article no.1097)

Torpedo anchors are a new type of anchoring system in deepwater that is much more economical than conventional anchoring methods. The dynamic penetration process is vitally important to the installation of torpedo anchors. Based on the spherical cavity expansion theory, the dynamic response characteristics of pressure-locked soils are analyzed using the Mohr-Coulomb criterion. The equations for the penetration of torpedo anchors with bullet-shaped heads are established considering rod friction. Subsequently, the analytical solutions for velocity, acceleration, and final penetration depth and the approximate analytical solution for penetration depth vs. time are obtained. The established penetration equation is solved using MATLAB software to obtain a semi-analytical solution, and the model tests on the penetration of a torpedo anchor with different initial velocities into saturated sand with different densities were conducted. A comparison of the test results shows that the analytical solution and the semi-analytical solution can well predict the model test results, indicating that the established analytical method can be used to analyze the penetration process of torpedo anchors. The research results can provide a guideline to the installation of torpedo anchors into the seabed in actual engineering.

ARTIFICIAL LIFT 1,561,642

LARGE-STROKE WALKING BEAM PUMPING UNIT

C.Zhang, J.Zhang and Y.Y.Song, asrs. (Apex Oilfld Equip Co Ltd). World 2022/205,538A1, p. 10/6/2022, f. 4/22/2021 (Appl. 2,188,826), pr. China 3/31/2021 (Appl. 2021-10,346,141) (E21B-0043/00). (In Chinese)

The present disclosure relates to a large-stroke walking beam pumping unit, comprising a base and a driving mechanism, which is fixedly installed at one end of the base, wherein a walking beam is provided at another end of the base by means of a support mechanism, so as to form a walking beam structure; a horsehead is installed at the front end of the walking beam; the rear end of the walking beam is connected to the driving mechanism by means of a connecting rod, so as to form a crank-connecting rod structure; a middle seat is installed on the walking beam in a sliding manner; the middle seat and the support mechanism are, by means of a stress arc device, connected to each other; and the support mechanism comprises a front support and a rear support, the top ends of which are connected to each other by means of a hinge member, and other ends of the front support and the rear support are both installed on two sides of the base in a sliding manner.

AUTONOMOUS UNDERWATER VEHC 1,561,643

REGION-SEARCHING OF MULTIPLE AUTONOMOUS UNDERWATER VEHICLES: A DISTRIBUTED COOPERATIVE PATH-MANEUVERING CONTROL APPROACH

T.Chen, X.Qu, Z.Zhang and X.Liang (Harbin Engineering Univ; Dalian Maritime Univ). JOURNAL OF MARINE SCIENCE AND ENGINEERING v.9, no.4, April 2021. (ISSN 2077-1312; Article no.355)

In this article, a distributed cooperative path-maneuvering control approach is developed for the region-searching of multiple autonomous underwater vehicles under both dynamic uncertainties and ocean currents. Salient contributions are as follows: (1) by virtue of boustrophedon motions and trigonometric functions, the coverage path-planning design is first proposed to generate multiple parameterized paths, which can guarantee that the region-searching is successfully completed by one trial; (2) combining with sliding mode and adaptive technique, distributed maneuvering control laws for surge and yaw motions are employed to drive vehicles to track the assigned paths, thereby contributing to the cooperative maneuvering performance with high accuracy; (3) by the aid of graph theory, the distributed signal observer-based consensus protocols are developed for path parameter synchronization, and successfully apply to maintain the desired formation configuration. The globally asymptotical stability of the closed-loop signals is analyzed via the direct Lyapunov approach, and simulation studies on WL-II are conducted to illustrate the remarkable performance of the proposed path-maneuvering control approach.

AUTONOMOUS UNDERWATER VEHC 1,561,644

A PERFORMANCE ANALYSIS OF FEATURE EXTRACTION ALGORITHMS FOR ACOUSTIC IMAGE-BASED UNDERWATER NAVIGATION

A.J.Oliveira, B.M.Ferreira and N.A.Cruz (Porto Univ). JOURNAL OF MARINE SCIENCE AND ENGINEERING v.9, no.4, April 2021. (ISSN 2077-1312; Article no.361)

In underwater navigation, sonars are useful sensing devices for operation in confined or structured environments, enabling the detection and identification of underwater environmental features through the acquisition of acoustic images. Nonetheless, in these environments, several problems affect their performance, such as background noise and multiple secondary echoes. In recent years, research has been conducted regarding the application of feature extraction algorithms to underwater acoustic images, with the purpose of achieving a robust solution for the detection and matching of environmental features. However, since these algorithms were originally developed for optical image analysis, conclusions in the literature diverge regarding their suitability to acoustic imaging. This article presents a detailed comparison between the SURF (speeded-up robust features), ORB (oriented FAST and rotated BRIEF), BRISK (binary robust invariant scalable key points), and SURF-Harris algorithms, based on the performance of their feature detection and description procedures, when applied to acoustic data collected by an autonomous underwater vehicle. Several characteristics of the studied algorithms were taken into account, such as feature point distribution, feature detection accuracy, and feature description robustness. A possible adaptation of feature extraction procedures to acoustic imaging is further explored through the implementation of a feature selection module. The performed comparison has also provided evidence that further development of the current feature description methodologies might be required for underwater acoustic image analysis.

AUTONOMOUS UNDERWATER VEHC 1,561,645

THE AUV-FOLLOWER CONTROL SYSTEM BASED ON THE PREDICTION OF THE AUV-LEADER MOVEMENT USING DATA FROM THE ONBOARD VIDEO CAMERA

D.Yukhimets and V.Filaretov (Sevastopol State Univ). JOURNAL OF MARINE SCIENCE AND ENGINEERING v.10, no.8, Aug. 2022. (ISSN 2077-1312; Article no.1141)

The paper proposes a new method for the synthesis of spatial motion control systems of the AUV-leader and a group of AUV-followers during their cooperative movement in a desired formation. This system allows the provision of an accurate positioning of the followers relative to the leader using information received with a low frequency only from their onboard video cameras. To improve the accuracy of the created system it proposes a method of estimation of the parameters of the movement of the AUV-leader (its speeds and accelerations) to predict its movement relative to the AUV-follower in the time intervals between the updates of information received from video cameras.

AUTONOMOUS UNDERWATER VEHC 1,561,646

HYPERPARAMETER OPTIMIZATION FOR THE LSTM METHOD OF AUV MODEL IDENTIFICATION BASED ON Q-LEARNING

D.Wang, J.Wan, Y.Shen, P.Qin and B.He (China Ocean Univ; Qilu Univ Technology). JOURNAL OF MARINE SCIENCE AND ENGINEERING v.10, no.8, Aug. 2022. (ISSN 2077-1312; Article no.1002)

Accurate mathematical models are the basis for controlling and estimating the state of an autonomous underwater vehicle (AUV) system, so how to improve their accuracy is a fundamental problem in the field of automatic control. However, AUV systems are complex, uncertain, and highly non-linear, and it is not easy to obtain improved accuracy through traditional modeling methods. We fit an accurate dynamic AUV model in this study using the long short-term memory (LSTM) neural network approach. As hyperparameter values have a significant impact on LSTM performance, it is important to select the optimal combination of hyper-

parameters. The present research uses the improved Q-learning reinforcement learning algorithm to achieve this aim by improving its recognition accuracy on the verification dataset. To improve the efficiency of action exploration, we improve the Q-learning algorithm and choose the optimal initial state according to the Q table in each round of learning. This can effectively avoid the ineffective exploration of the reinforcement learning agent between the poor-performing hyperparameter combinations. Finally, the experiments based on simulated or actual trial data demonstrate that the proposed model identification method can effectively predict kinematic motion data and, more importantly, that the modified Q-learning approach can optimize the network hyperparameters in the LSTM.

AUTONOMOUS UNDERWATER VEHIC 1,561,647

ADAPTIVE FORMATION CONTROL OF MULTIPLE UNDERACTUATED AUTONOMOUS UNDERWATER VEHICLES

B.K.Sahu and B.Subudhi (Nat Inst Technol Rourkela). *JOURNAL OF MARINE SCIENCE AND ENGINEERING* v.10, no.9, Sept. 2022. (ISSN 2077-1312; Article no.1233)

In this paper, we present a 3D formation control scheme for a group of torpedo-type underactuated autonomous underwater vehicles (AUVs). These multiple AUVs combined with an unmanned surface vessel (USV) construct a sort of star-topology acoustic communication network where the USV is at the center point. Due to this kind of topological feature, this paper applies a virtual school concept. This is a geometric graph where each node is taken as a virtual leader for each specific AUV and assigned its own reference trajectory. For each individual vehicle, its formation strategy is simple: just follow the trajectory of its corresponding virtual leader so as for multiple AUVs to compose the given formation. As for the formation subject, this paper mainly focuses on the formation tracking problem rather than the formation producing. For the torpedo-type vehicle considered in this paper, there are only three control inputs (surge force, pitch, and yaw moments) available for its underwater 3D motion and therefore this is a typical underactuated system. For the following vehicle's trajectory, a sort of potential field method is used for obstacle avoidance, and a neural network-based adaptive scheme is applied to on-line approximate the vehicle's unknown nonlinear dynamics, and the uncertainty terms including modeling errors, measurement noises, and external disturbances are handled by the properly designed robust scheme. The proposed formation method can guarantee the uniform ultimate boundedness (UUB) of the closed-loop system. Numerical studies are also carried out to verify the effectiveness of the proposed scheme.

AUTONOMOUS UNDERWATER VEHIC 1,561,648

THREE-DIMENSIONAL PATH PLANNING FOR AUVS BASED ON STANDARD PARTICLE SWARM OPTIMIZATION ALGORITHM

B.Zhan, S.An, Y.He and L.Wang (Qingdao Univ Sci & Technol). *JOURNAL OF MARINE SCIENCE AND ENGINEERING* v.10, no.9, Sept. 2022. (ISSN 2077-1312; Article no.1253)

This paper proposes an improved standard particle swarm optimization 2011 for autonomous underwater vehicles (AUVs). A mutation operator with a threshold is introduced to solve the problem of particles falling into the local extreme, and a nonlinear adaptive parameter strategy is introduced to accelerate the convergence speed. The proposed algorithm considers "path length", "path safety", "path smoothness" and "physical constraints" synthetically. For the specific navigation environment of AUVs, the path planning simulation is conducted based on MATLAB/Simulink, and the navigation guidance and control closed-loop simulation system is established. Simulation results show the effectiveness of the proposed algorithm.

CABLE 1,561,649

YOLO-SUBMARINE CABLE: AN IMPROVED YOLO-V3 NETWORK FOR OBJECT DETECTION ON SUBMARINE

CABLE IMAGES

Y.Li, X.Zhang and Z.Shen (Hangzhou Dianzi Univ). *JOURNAL OF MARINE SCIENCE AND ENGINEERING* v.10, no.8, Aug. 2022. (ISSN 2077-1312; Article no.1143)

Due to the strain on land resources, marine energy development is expanding, in which the submarine cable occupies an important position. Therefore, periodic inspections of submarine cables are required. Submarine cable inspection is typically performed using underwater vehicles equipped with cameras. However, the motion of the underwater vehicle body, the dim light underwater, and the property of light propagation in water lead to problems such as the blurring of submarine cable images, the lack of information on the position and characteristics of the submarine cable, and the blue-green color of the images. Furthermore, the submarine cable occupies a significant portion of the image as a linear entity. In this paper, we propose an improved YOLO-SC (YOLO-Submarine Cable) detection method based on the YOLO-V3 algorithm, build a testing environment for submarine cables, and create a submarine cable image dataset. The YOLO-SC network adds skip connections to feature extraction to make the position information of submarine cables more accurate, a top-down downsampling structure in multi-scale special fusion to reduce the network computation and broaden the network perceptual field, and lightweight processing in the prediction network to accelerate the network detection. Under laboratory conditions, we illustrate the effectiveness of these modifications through ablation studies. Compared to other algorithms, the average detection accuracy of the YOLO-SC model is increased by up to 4.2%, and the average detection speed is decreased by up to 1.616 s. The experiments demonstrate that the YOLO-SC model proposed in this paper has a positive impact on the detection of submarine cables.

CARBON DIOXIDE CORROSION 1,561,650

EFFECT OF CORROSION PRODUCTS ON THE INHIBITORY PERFORMANCE OF IMIDAZOLIUM IONIC LIQUID TOWARD CARBON STEEL IN CO2-SATURATED NaCl BRINE

Y.Guo, J.Xue, J.Zhang, Q.Chen, L.Fan, C.Tang, K.Rei, A.Fu and Q.Bi (Xi'an Univ Architecture). *COLLOIDS AND SURFACES A: PHYSICOCHEMICAL AND ENGINEERING ASPECTS* v.651, 10/20/2022. (ISSN 0927-7757; Article no.129135)

Carbon steel corrosion represents an intractable problem during oil and gas exploitation. An imidazolium-based ionic liquid, 1-dodecyl-3-methyl imidazolium hydrogen sulfate (abbreviated as DMIMHS), was used as a corrosion inhibitor for carbon steel in the CO2-saturated NaCl brine at 313 K in this study. The inhibitive effects and mechanisms of the pre-corroded product on the anti-corrosion behavior of DMIMHS were investigated by electrochemical measurements, surface characterizations, quantum calculation and molecular dynamics simulations. The results showed that DMIMHS had remarkable inhibition efficacy on freshly abraded steel, with a 94.46% inhibition efficiency in the presence of 30 mg/L DMIMHS, and corrosion products can slightly decelerate the corrosion behavior. More importantly, the addition of DMIMHS favored the remarkably enhanced inhibitive properties for carbon steel after pre-corroded, namely the corrosion resistance increased with the extension of corrosion time. According to the experimental results and theoretical calculations, the inhibitive mechanisms of DMIMHS toward carbon steel in the CO2-saturated NaCl brine were proposed. (2022 Elsevier B.V.)

CENTRIFUGAL PUMP 1,561,651

CAVITATING FLOW IN THE VOLUTE OF A CENTRIFUGAL PUMP AT FLOW RATES ABOVE THE OPTIMAL CONDITION

Q.Hu, Y.Yang, W.Shi, W.Cao and Y.Shi (Jiangsu Univ; Zhejiang LBX Pump Ind Ltd). *JOURNAL OF MARINE SCIENCE AND ENGINEERING* v.9, no.4, April 2021. (ISSN 2077-1312; Article no.446)

Cavitation is regarded as a considerable factor causing performance deterioration of pumps under off-design conditions, especially at overload conditions. To investigate the unsteady cavitation evolution around the tongue of a pump volute, and its

influence on the flow field within passages of the impeller, numerical calculations and several hydraulic tests were performed on a typical centrifugal pump with a shrouded impeller. Emphasis was laid on the cavitation evolution and blade-loading distribution at flow rates above the optimal value. Results indicated that vapor is likely to first emerge from the tongue of the volute rather than at the leading edge of the blades at overload conditions. In contrast to the designed condition, the flow distribution in each passage is obviously different. The flow rate of the passage reaches a maximum just past the location of the tongue, while the minimum flow rate value is projected to appear at the passage upstream. The cavitation at the tongue squeezes the flow area at the outlet of the corresponding flow passage of the tongue, thereby causing a huge growth in the flow rate at the impeller outlet.

CENTRIFUGAL PUMP 1,561,652

NUMERICAL AND EXPERIMENTAL STUDY ON THE EFFECT OF ROTOR-STATOR DISTANCE ON ROTOR-STATOR INTERACTION STRENGTH WITHIN MIXED-FLOW CENTRIFUGAL PUMPS

F.Han, X.Chen, Y.Yang and C.Wang (Hohai Univ; Yangzhou Univ). *JOURNAL OF MARINE SCIENCE AND ENGINEERING* v.10, no.8, Aug. 2022. (ISSN 2077-1312; Article no.1114)

In this article, the influence of rotor-stator distance on the pump performance and rotor-stator interaction strength within mixed-flow centrifugal pump was investigated based on numerical calculation and test verification. Firstly, the performances of mixed-flow centrifugal pumps with two different rotor-stator distances were obtained and compared with the numerical results, which confirms the high accuracy of the numerical simulation. Next, the performances of mixed-flow centrifugal pumps with five different rotor-stator distances were compared and analyzed. It was found that the hydraulic performance of the mixed-flow centrifugal pump varies slightly as the rotor-stator distance increases. The mean values of the standard deviation of the head and efficiency of the mixed-flow centrifugal pump at each rotor-stator distance under full flow conditions are only 0.16 m and 0.11%, respectively. Then, the strengths of the rotor-stator interaction with different rotor-stator distances were analyzed. It was found that the strengths of the shock interaction, the wake interaction, and the potential interaction were all reduced with increasing rotor-stator distance. Moreover, when the rotor-stator distance is 1.5 mm, the pressure distribution in the circumferential direction of the rotor-stator interference zone shows obvious unstable characteristics: the pressure change amplitude is significantly greater than the other rotor-stator distance of the pressure change amplitude, the maximum and minimum pressure amplitude difference being 56.9 kPa, and with the increase in the rotor-stator distance, the maximum and minimum pressure amplitude difference gradually decreases, with an average value of 32.3 kPa. These findings could provide useful insight into prospects for the improvement of the operational stability of mixed-flow centrifugal pumps, and the results of this study can be extended to all centrifugal pumps using diffusers in the form of vanes as the pressure chamber, which has strong practical application and theoretical value.

COATING MATERIAL 1,561,653

FUNCTIONALIZED GRAPHENE OXIDE DISPERSED POLYVINYL ALCOHOL-EPOXIDIZED LINSEED OIL COMPOSITE: AN ECO-FRIENDLY AND PROMISING ANTICORROSION COATING MATERIAL

A.M.Madhusudhana, K.N.S.Mohana, M.B.Hegde, S.R.Nayak, K.Rajitha and M.C.S.Kumar (Mysore Univ). *COLLOIDS AND SURFACES A: PHYSICO-CHEMICAL AND ENGINEERING ASPECTS* v.650, 10/5/2022. (ISSN 0927-7757; Article no.129382)

Polyvinyl alcohol (PVA) is an extensively used biodegradable polymer including corrosion inhibition, but it fails to withstand long time protection due to water solubility. The present work emphasized an efficient way to transform PVA to hydrophobic nature and further modification for corrosion protection of mild steel (MS). In this backdrop, PVA was blended with varying amounts of the synthesized amine-functionalized graphene oxide (AGO) and then assimilated with the epoxidized linseed oil (ELO).

The fabricated composite material was coated on MS surface by the doctor's blade technique, and their adhesion character, roughness, wettability, and sustainability in saline media were confirmed by atomic force microscopy (AFM), contact angle, and electrochemical techniques. The chemical bonding as well as structural interactions of the prepared AGO were ascertained by Fourier-transform infrared (FT-IR), X-ray powder diffraction (XRD), and X-ray photoelectron spectroscopy (XPS) methods. Electrochemical impedance spectroscopy (EIS) measurements of the PVA coatings showed improved Nyquist semicircle diameter by increasing the AGO content, and the potentiometric polarization (PP) data supports the EIS results. The different weight percentages of AGO dispersed PVA/ELO composite coatings revealed enormous changes in their Nyquist, Bode, and phase angle plots. The highest impedance and charge transfer resistance of PVA/ELO-AGO (0.25 wt%) coating are found to be $10\text{ E}+08.6\ \Omega\ \text{cm}^2$ and $4.541 \times 10\ \text{E}+08\ \Omega\ \text{cm}^2$, respectively. Further, the composite coating was sustained for 20 days in 3.5 wt% NaCl solution showing its enhanced barrier property. This can be ascribed due to the strong cross-linkages in PVA/ELO-AGO that makes it a durable and promising anti-corrosion coating material. (c2022 Elsevier B.V.)

COATING MATERIAL 1,561,654

LOADING HALLOYSITE NANOTUBES ON MXENE AS FUNCTIONAL COMPOSITE FILLER TOWARDS A POLYBENZOXAZINE ANTICORROSION COATING

Y.Deng, G.Song, T.Zhang, Z.Lang, P.Wu and D.Zheng (Xiamen Univ; Wuhan Univ). *COLLOIDS AND SURFACES A: PHYSICO-CHEMICAL AND ENGINEERING ASPECTS* v.650, 10/5/2022. (ISSN 0927-7757; Article no.129498)

Although MXene as an attractive two-dimensional additive can enhance the corrosion protection performance of an organic coating, it does not appear to have a beneficial effect on the longer-term corrosion resistance of polybenzoxazine framework due to its high electrical conductivity. Therefore, in this work, the composite sheets and polybenzoxazine resin were prepared using some natural and renewable materials for a sustainable purpose. A novel polybenzoxazine (PCD) was firstly synthesized from green curcumin, 1,2-bis(2-aminoethoxy)ethane and paraformaldehyde through thermal polymerization with the polymerized high crosslinking network as an inhibitor carrier. Secondly, the sustainable and naturally renewable halloysite nanotubes were loaded onto the external surfaces or intercalated into the interstratified interfaces of the MXene carrier as a MXene@halloysite (MH) composite inhibitor. The MH could not only efficiently enhance the anticorrosion performance of the PCD coating, but also effectively reduce the aggregation of the nanotubes. When the MH was introduced into the PCD framework, the PCD-MH composite coating exhibited great corrosion protection performance compared with the other coatings. This work may lead to many promising applications of MXene-based nano-sheets in the field of metal-protection. (c2022 Elsevier B.V.)

COATING MATERIAL 1,561,655

GREEN AND RAPID FABRICATION OF SUPERHYDROPHILIC AND UNDERWATER SUPEROLEOPHOBIC COATINGS FOR SUPER ANTI-CRUDE OIL FOULING AND CRUDE OIL-WATER SEPARATION

W.Zhou, X.Hu, B.Zhan, S.Li, Z.Chen and Y.Liu (Jilin Univ; Ansteel Group Res Inst). *COLLOIDS AND SURFACES A: PHYSICO-CHEMICAL AND ENGINEERING ASPECTS* v.652, 11/5/2022. (ISSN 0927-7757; Article no.129805)

The development of surfaces with super anti-crude oil-fouling behavior and crude oil-water separation properties is still a global challenge owing to the high viscosity of crude oil. Herein, superhydrophilic and underwater superoleophobic surfaces were successfully prepared by a simple, green and environmentally friendly one-step dip coating method. In the whole process, microcrystalline cellulose with hydrophilic hydroxyl functional groups was introduced into the coating with the help of inorganic adhesives, water was the only solvent, and no other organic solvents or surface modifiers was added. Besides being highly

resistant to low viscosity oils and achieving effective oil-water separation (more than 98.3% separation efficiency after 30 cycles), the surface effectively resisted crude oil adhesion and achieved high viscosity crude oil-water separation. In addition, the underwater oil contact angle can still reach 147.5° and 152.5° after 20 cycles of sandpaper friction tests and 50 cycles of finger pressure tests, respectively, which indicates excellent durability. Furthermore, the method can achieve excellent superhydrophilicity and underwater superoleophobicity on varieties of substrates (such as copper foil, aluminum sheet and glass), showing very extensive applicability. It is expected that such fabrication strategy can provide a low cost, green and environmentally friendly approach to construct a series of superhydrophilic and underwater superoleophobic surfaces to achieve super anti-crude oil-fouling and (crude) oil-water separation. (c2022 Elsevier B.V.)

COATING MATERIAL 1,561,656

SYNERGISTIC CONTROL OF WETTING RESISTANCE AND CORROSION INHIBITION BY CERIUM TO ENHANCE CORROSION RESISTANCE OF SUPERHYDROPHOBIC COATING

K.An, Y.Sui, Y.Wang, Y.Qing, C.Long, X.Liu, Y.Shang and C.Liu (Northeastern Univ, China; Qingdao Univ Technology). *COLLOIDS AND SURFACES A: PHYSICO-CHEMICAL AND ENGINEERING ASPECTS* v.653, 11/20/2022. (ISSN 0927-7757; Article no.129874)

Superhydrophobic coatings have attracted significant attention in the anti-corrosion protection. However, their long-term corrosion resistance is still challenging under the penetration of corrosive media. In this work, we report an one-step electrodeposition method to fabricate a cerium-based superhydrophobic (CS) coating on the surface of Al alloy. The effects of cerium ions on the morphology, roughness, anti-wettability and anti-corrosion property of the coatings were investigated in detail. The results indicated that cerium ions can effectively control the anti-wetting properties of the coating surface by regulating surface micro/nanostructure during electrodeposition process. The obtained CS coating has the best corrosion protection when the cerium ion concentration is 0.0125 mol/L, and its impedance modulus changes slightly, reaching $3.16 \times 10^6 \Omega \text{ cm}^2$ after immersing in 3.5 wt% NaCl solution for 192 h. Notably, the CS coating could form a Ce-rich passive layer during the immersion to prevent further corrosion, exhibiting excellent long-term corrosion resistance. Consequently, cerium ions can enhance the corrosion inhibition behavior of such coating through the synergistic effect of regulating the surface micro/nanostructure and the active inhibition of cerium. (c2022 Elsevier B.V.)

COMMUNICATION SYSTEM 1,561,657

IDENTIFICATION OF ORBITAL ANGULAR MOMENTUM BY SUPPORT VECTOR MACHINE IN OCEAN TURBULENCE

X.Li, J.Huang and L.Sun (Guilin Univ Electr Technol). *JOURNAL OF MARINE SCIENCE AND ENGINEERING* v.10, no.9, Sept. 2022. (ISSN 2077-1312; Article no.1284)

With the advancement of underwater communication technology, the traditional modulation dimension has been introduced, developed and utilized. In addition, orbital angular momentum (OAM) is utilized as the modulation dimension for optical underwater communication to obtain larger spectrum resources. The OAM features are extracted using a histogram of oriented gradient and trained using the support vector machine method with a gradient direction histogram feature. The topological charge value of the OAM was used to identify the classification labels, and the ocean turbulence caused by different temperatures and salinity were analyzed. Experimentation results showed that the recognition accuracy for the OAM under the Laguerre-Gaussian beam rates of 1-5, 1-6, 1-7, 1-8, 1-9, and 1-10 was 98.93%, 98.89%, 97.33%, 96.66%, 95.40%, and 95.33%, respectively. The proposed method achieved a high recognition accuracy and performed efficiently under strong turbulence. Our research explored a new technique that provides a new idea for the demodulation of OAM in optical underwater communication.

CORROSION 1,561,658

N-DOPED CARBON DOTS AS A MULTIFUNCTIONAL PLATFORM FOR REAL-TIME CORROSION MONITORING AND INHIBITION

Z.Liu, R.Jia, Y.Jian, F.Chen, G.Yan and D.He (Chengdu Univ Technology). *COLLOIDS AND SURFACES A: PHYSICO-CHEMICAL AND ENGINEERING ASPECTS* v.650, 10/5/2022. (ISSN 0927-7757; Article no.129499)

The occurrence of corrosion can't be completely eliminated. To prevent the failure of structural materials, corrosion has to be easily identified, visualized and detected at early-stage, in order to intervene at the point where it is necessary. In this view, fluorescent N-doped CDs have been synthesized to synergistically inhibit and monitor corrosion of iron. The as-prepared CDs were fabricated by simple solvothermal process using citric acid as carbon source and ammonia as dopant. It is found that the active groups on the surface of the CDs promote the formation of adsorption film of CDs on iron plates and effective fluorescence emission. As a result, the CDs could readily inhibit the corrosion of iron and exhibit an inhibition efficiency of 88 % at 180 mg/L. As the degree of corrosion increases, the CDs-adsorption film can sensitively, visually and effectively respond to released Fe³⁺ due to the complexation between CDs and Fe³⁺. Due to this dual function of CDs for corrosion monitoring and inhibition, they can readily trace early-stage corrosion and prevent its development. This is a synergistic strategy to prevent critical engineering failures and to ensure the safety of structural metal materials. (c2022 Elsevier B.V.)

CORROSION CONTROL 1,561,659

REFRESHABLE SELF-POLISHING SUPERHYDROPHOBIC COATING ON Mg ALLOY TO PROHIBIT CORROSION AND BIOFOULING IN MARINE ENVIRONMENT

B.Li, L.Wang, Y.Su, R.Qiu, Z.Zhang and Y.Ouyang (Shandong Univ Sci Technol; Luoyang Research Inst; Chongqing Research Inst; Dalian Univ Technol). *COLLOIDS AND SURFACES A: PHYSICO-CHEMICAL AND ENGINEERING ASPECTS* v.651, 10/20/2022. (ISSN 0927-7757; Article no.129693)

Corrosion susceptibility is a critical obstacle for Mg alloy usage in harsh environments. Bioinspired superhydrophobic surface (SHS) affords a new way to combat corrosion. However, problems, e.g., water vapor condensation and air dissolution, ceaselessly hurdle practical usage of SHS for long-term corrosion inhibition. In this report, targeting the corrosion inhibition of Mg alloy in seawater, a refreshable self-polishing superhydrophobic coating is bound onto AZ31 Mg alloy bridging via a ceramic/paraffin buffer layer to solve the two problems encountered by traditional SHS. Firstly, the liquid paraffin is injected into the porous ceramic structure constructed by micro-arc oxidation (MAO). Then, carbon soot (CS) is grown onto the ceramic/paraffin layer via a combustion method. The internal CS layer is firmly bonded due to the molten paraffin. Meanwhile, the external superhydrophobic CS layer is soft and floppy to perform self-polishing property under dynamic water flow condition. The refreshable feature endows the regeneration of SHS. Using water jet flush (5.8 m/s) and immersion test up to 168 h, Mg alloy covered ceramic layer and carbon soot (MMAO-CS) coating demonstrates excellent stability. Using diatoms as target organisms to illustrate seawater anti-biofouling property, a few diatoms are found on MMAO-CS even after immersion for 10 d due to the low modulus and self-polishing of the external superhydrophobic layer invaded by the water phase and bio-organisms. For prohibiting corrosion in seawater environment, MMAO-CS coating possesses prominent resistance with $|Z|0.01 \text{ Hz} (2.82 \times 10^7 \Omega \text{ cm}^2)$ of 6 orders of magnitude larger than bare AZ31 ($42.9 \Omega \text{ cm}^2$), enabling its potential usage in marine environment. (c2022 Elsevier B.V.)

CORROSION CONTROL 1,561,660

ENHANCED EFFECT OF PHENYL SILANE-MODIFIED HEXAGONAL BORON NITRIDE NANOSHEETS ON THE CORROSION PROTECTION BEHAVIOR OF POLY(ARYLENE ETHER NITRILE) COATING

Y.Xia, S.Zhang, L.Tong, G.Lin, Z.Bai and X.Liu (China Univ Electronic Sci). *COLLOIDS AND SURFACES A: PHYSICO-CHEMICAL AND ENGINEERING ASPECTS* v.652, 11/5/2022. (ISSN 0927-7757; Article no.129869)

Developing alternative protective coating with long serve life under complicated aggressive condition possesses desperate need in corrosion protection filed. Herein, a high performance functional polymer called poly(arylene ether nitrile) (PEN) was employed as a novel organic corrosion protection coating for preservation of P110 steel in this work. The phenyl silane functionalized hexagonal boron nitride (h-BN-MPDTS) synthesized via silylation reaction was introduced into PEN, forming a more efficient protection coating system with superior corrosion resistance. The obtained EIS experimental consequences confirmed that impedance of h-BN-MPDTS PEN coating ($1.036 \times 10^8 \text{ E}+08 \text{ } \Omega \text{ cm}^2$) was promoted by two orders of magnitude when compared to the neat coating ($2.226 \times 10^6 \text{ E}+06 \text{ } \Omega \text{ cm}^2$) with one time constant remained throughout the immersion process of 80 days. Meantime, less rust was seen from the artificial scratches of h-BN-MPDTS sample during the salt spray experiment, further demonstrating better corrosion resistance of h-BN-MPDTS PEN coating. Thus, this study provides a neoteric feasibility of high-performance polymer in anticorrosion coatings field. (c2022 Elsevier B.V.)

CORROSION CONTROL 1,561,661

HIGH BARRIER AND DURABLE SELF-HEALING COMPOSITE COATING: BORON NITRIDE COMBINED WITH CYCLODEXTRIN FOR ENHANCING THE CORROSION PROTECTION PROPERTIES OF WATERBORNE EPOXY COATING

R.Zou, G.Xiao, C.Chen, C.Chen, Z.Yang, F.Zhong, M.Wang and Y.Li (Southwest Petroleum Univ; Chengdu Univ). *COLLOIDS AND SURFACES A: PHYSICO-CHEMICAL AND ENGINEERING ASPECTS* v.653, 11/20/2022. (ISSN 0927-7757; Article no.129896)

In recent years, a great deal of research has been devoted to designing smart anti-corrosion coatings with diverse self-healing capabilities, effective passive barrier properties, and long-lasting protection. Herein, the tetraethyl orthosilicate (TEOS) was used as a pH response guardian encapsulated on a BTA-loaded β -cyclodextrin (β -CD) nanocavity shells (CD(BTA)@TEOS), which would be ineffective in acidic environments, thus causing the release of BTA. Meanwhile, the polydopamine (PDA) was coated on the hexagonal boron nitride (h-BN) nanosheets (h-BN@PDA) to enhance its dispersibility and provide reactive sites. Further, the h-BN@PDA-CD(BTA)@TEOS (BPCT) hybrids were synthesized by linking CD(BTA)@TEOS nanocavity shells and h-BN@PDA nanosheets through PDA and KH560 as bridging agents. The dispersion of BPCT in waterborne epoxy coating (WEC) can effectively fill the coating defects and prolong the diffusion path of corrosive media, showing excellent barrier properties due to the excellent barrier properties of h-BN@PDA nanosheets against corrosive media. Meanwhile, the excellent self-healing properties of the composite coating under corrosive conditions were mainly derived from the released BTA and stripped PDA in response to pH variation. The corrosion resistance of the composite coating was tested by electrochemical, salt spray tests and microscopic corrosion morphology, and the self-healing properties of the coating were demonstrated by scratch electrochemistry. The expiration time of the BPCT/WEC sample was extended by 15 d, the persistence time in the salt spray test increased by 100 h, and the self-healing properties appeared after 4 h of coating rupture compared to the control WEC. The results proved that the WEC loaded with BPCT nanocontainers had a high barrier effect along with self-healing function and durable corrosion resistance. (c2022 Elsevier B.V.)

DRILLING (WELL) 1,561,662

DOWNHOLE MECHANICAL ACTUATOR

W.Hughes, asr. (Hughes Tool Co LLC). World 2022/212,817A1, p. 10/6/2022, f. 4/1/2022 (Appl. 2,223,014), pr. U.S. 4/2/2021 (Appl. 63/170,025) and U.S. 3/30/2022 (Appl. 709,210) (E21B-0033/00; E21B-0034/00).

Disclosed herein are various embodiments of well control system for drilling an oil or gas well safely and efficiently by

providing a mechanical actuator capable of transmitting a rotational force downhole, and converting the rotational force to an axial force for the purpose of operating downhole equipment, including subsurface safety valves, compressible bladder valves, and sliding sleeve valves. Because the actuator is mechanical and not hydraulic as in conventional equipment, the force applied is independent of the depth at which it is applied, overcoming a major deficiency seen in comparable hydraulic systems.

ELECTRIC SUBMERSIBLE PUMP 1,561,663

UNDERSTANDING ESP PERFORMANCE UNDER HIGH VISCIOUS APPLICATIONS AND EMULSION PRODUCTION

L.Pastre, J.Biazussi, W.M.Verde, J.Marins, A.Melchuna, M.Cowie, L.Vergara, I.Navarro, D.Lemos et al. (Campinas State Univ). *OFFSHORE TECHNOLOGY CONFERENCE [OTC] (Houston, TX, 5/2-5/2022) PROCEEDINGS 2022*. (ISBN 978-1-61399-852-6; OTC-31839; Available at <http://www.onepetro.org> as of 6/23/2022; 31 pp)

Although being widely used as an artificial lift method for heavy oil field developments, Electrical Submersible Pump (ESP) system performance in high viscous applications is not fully understood. A miscomprehension of challenges and equipment performance in such conditions might lead to operation inefficiencies and equipment failures. This paper presents results of single-phase and multiphase tests performed by University of Campinas (UNICAMP). It also presents operation data, lessons learned, and failure examples gathered over 10 years of ESP operation in Peregrino field which is a heavy oil, high viscous oilfield offshore Brazil operated by Equinor. Affinity laws commonly used for ESP simulations don't hold true for high viscosity applications. Hydraulic performance of centrifugal pumps is affected by fluid parameters like viscosity and density; operation parameters such as flow rate and rotational speed; and specific stage design characteristics. To determine degradation in head and efficiency as well as power requirement increase in viscous applications, Equinor performs one-phase high-viscosity flow-loop test to qualify each stage type prior to deployment in Peregrino field. For the qualification of ESPs, single-phase qualification tests are performed using mineral oil with viscosities specifically chosen to cover the viscosity range of the specific field. Each stage type is qualified using a prototype with reduced number of stages due to flow loop limitations. Qualification tests for the Peregrino field confirmed that affinity laws are not accurate for high-viscous applications and provided important insights regarding pump performance that are used in equipment specification and system surveillance. The UNICAMP research team has designed and performed multiphase-flow tests to evaluate emulsion formation inside centrifugal pump stages and effective viscosity behavior. Phase inversion phenomenon investigation was also included in studies. Studies performed using a prototype stage allowed visualization and evaluation of oil drops dynamics inside the impeller in different rotational speeds. (Copyright 2022 OTC)

ELECTRIC SUBMERSIBLE PUMP 1,561,664

ROTOR BEARING DESIGN FOR DOWNHOLE MOTORS

R.Ekambaram, Y.C.Jee, A.I.Watson and P.Mahadevan, asrs. (Schlumberger Technol Corp; Schlumberger Canada Ltd; Schlumberger Serv Petrol; Schlumberger Technol BV). World 2022/212,660A1, p. 10/6/2022, f. 3/31/2022 (Appl. 2,222,765), pr. U.S. 3/31/2021 (Appl. 63/168,804) (E21B-0004/00; E21B-0004/02; E21B-0017/046; E21B-0043/12).

Rotor bearings are provided. The motor bearing can be used in an electric submersible pump motor. The bearing can include a body and one or more anti-rotation pins disposed partially in a groove in an outer surface of the body and configured to be received in a corresponding keyway in an inner diameter of a stator. The anti-rotation pin prevents or inhibits rotation of the bearing relative to the stator.

ELECTRIC SUBMERSIBLE PUMP 1,561,665

INTERLOCKING DIFFUSER ARRANGEMENT IN ELECTRICAL SUBMERSIBLE PUMP

Z.Ye and M.Paquette, asrs. (Baker Hughes Oilfield LLC). World 2022/204,659A1, p. 9/29/2022, f. 3/18/2022 (Appl. 2,271,216), pr. U.S. 3/22/2021 (Appl. 208,817) (F04D-0029/44; E21B-0043/12; F04D-0013/10; F04D-0029/22; F04D-0029/42).

An electrical submersible well pump has upper and lower diffusers non-rotatably mounted in a housing. A rotatable impeller between the upper and lower diffusers has a bottom shroud. An outward-facing wall is on an upper end of the lower diffuser. A lower end of the upper diffuser has an inward-facing wall that fits closely around the outward-facing wall of the lower diffuser. A key mounted between the inward-facing and outward-facing walls prevents relative rotation between the diffusers. The key extends axially above an upper end of the neck and radially inward from the inward-facing wall of the upper diffuser into close proximity to the bottom shroud, creating a sand dam.

FINGERPRINTING 1,561,666

4D CHEMICAL FINGERPRINT WELL MONITORING

A.C.Cavazos Sepulveda and D.P.San Roman Alerigi, asrs. (Saudi Arabian Oil Co; Aramco Services Co). World 2022/212,535A1, p. 10/6/2022, f. 3/30/2022 (Appl. 2,222,588), pr. U.S. 3/30/2021 (Appl. 217,069) (G01N-0021/552; G01N-0021/35; G01N-0021/45).

A sensing system for monitoring a composition of a downhole fluid in a well, where the sensing system includes: a light source, a waveguide, an evanescent field sensing element that is indirect contact with a downhole fluid, and a detector. The light source is operable for emitting a beam and includes a frequency comb generator configured to modify at least a portion of the beam into a sensing comb beam. The evanescent field sensing element provides attenuated internal reflection of the sensing comb beam at the interface between the evanescent field sensing element and the downhole fluid, and the portion of the sensing comb beam interacts with the downhole fluid to form at least a portion of an interacted beam. The detector obtains a spectral distribution of the interacted beam.

FLOAT 1,561,667

SOLITARY WAVE INTERACTION WITH A FLOATING PONTOON BASED ON BOUSSINESQ MODEL AND CFD-BASED SIMULATIONS

S.C.Mohapatra, H.Islam, T.S.Hallak and C.G.Soaes (Lisbon Univ; Maritime Res Inst Neth; CENTEC). *JOURNAL OF MARINE SCIENCE AND ENGINEERING* v.10, no.9, Sept. 2022. (ISSN 2077-1312; Article no.1251)

A mathematical model of solitary wave interaction with a pontoon-type rigid floating structure over a flat bottom is formulated based on Boussinesq-type equations under weakly nonlinear dispersive waves. Based on the higher-order Boussinesq equations, the solitary wave equation is derived, and a semi-analytical solution is obtained using the perturbation technique. On the other hand, brief descriptions of the application of wave2Foam and OceanWave3D on the aforementioned problem are presented. The analytical solitary wave profiles in the outer region are compared with Computational Fluid Dynamics (CFD) and OceanWave 3D model simulations in different cases. The comparison shows a good level of agreement between analytical, wave2Foam, and OceanWave3D. In addition, based on the wave2Foam and coupled OceanWave3D model, the horizontal, vertical wave forces, and the pressure distributions around the pontoon are analysed. Further, the effect of the Ursell number, pontoon length, and water depth on the solitary wave profiles are analysed based on the analytical solution. The paper validates each of the three models and performs intercomparison among them to assess their fidelity and computational burden.

FLOATING PRODUCTN PLATFORM 1,561,668

RESEARCH ON RISK ASSESSMENT METHOD OF STEEL CATENARY RISER BASED ON INFORMATION FUSION

P.Yang, L.Jia, Z.Kang and J.Kang (Harbin Engineering Univ; CNOOC Research Inst). *OCEAN ENGINEERING* v.259, 9/1/2022. (ISSN 0029-8018; Article no.111890)

The Steel Catenary Riser (SCR) is an essential component connecting the subsea production system and the offshore floating platform and SCR malfunction leads to disastrous consequences. In order to ensure operation safety, the operating company monitors SCR motion response in real time by installing sensors. This paper aims to develop a multi-sensor information fusion algorithm for SCR risk assessment. The algorithm generates basic probability assignment (BPA) function based on known information. Then, the intuitionistic fuzzy multi-attribute decision matrix is constructed by BPA to evaluate the dynamic reliability of the sensor. Finally, the focal element credibility is calculated to reduce the conflict between evidences, and the improved Desert-Smarandache (DSm) theory fusion rule is utilized to evaluate the SCR risk through decision fusion. The feasibility of this method is verified by the case study. The corresponding risk control strategy is also provided. (c2022 Elsevier Ltd.)

FLOWLINE 1,561,669

DESIGN AND ANALYSIS OF ELECTRICALLY HEAT-TRACED FLOWLINE (EHTF) PIPELINE END MANIFOLD (PLEM) USING SEVEN VEGA

A.Gautam, D.Du and F.H.De Ligny (Subsea 7). *OFFSHORE TECHNOLOGY CONFERENCE [OTC] (Houston, TX, 5/2-5/2022) PROCEEDINGS 2022*. (ISBN 978-1-61399-852-6; OTC-31817; Available at <http://www.onepetro.org> as of 6/23/2022; 9 pp)

This paper presents the successful design and installation of the electrically heat-traced flowline (EHTF) pipeline end manifold (PLEM) using the newly built, highly capable pipelay vessel *Seven Vega*. This was achieved by taking advantage of *Seven Vega's* reel-lay firing-line capabilities. The EHTF PLEM is an essential component of the EHTF system, which combines the thermal performance of pipe-in-pipe (PiP) flowline with electrical heating capability. The EHTF PLEM is a complex structure that is designed to flow production fluid from well jumpers and from an extension flowline through a flowline jumper and that also extends electrical heating functionality to the extension flowline. It has three hubs, six gate valves, eight electric flying leads, the piping header, and the termination of the electrical system all in one structure. The final design resulted in major reductions in overall length and weight. The creative design went through multiple iterations to achieve the desired results while the vessel was still being built. *Seven Vega* is designed to install rigid flowlines, including PiP systems and electrical trace heating, in water depths of up to 3,000 m. Most reel-lay vessels have small PLET manipulator assembly (PMA) systems in the firing line. However, *Seven Vega's* bigger envelope and weight accommodates both the first and second ends. Avoiding the need for cross-haul reduces cost and adds flexibility to the schedule. The result was an overall reduction in the weight of the PLEM, flexibility in the schedule, and a successful design of the recoverable EHTF PLEM within *Seven Vega's* PMA capacity. This paper showcases the advanced capabilities of the newly built *Seven Vega* and focuses on optimization and installation of the essential PLEM structure of the EHTF technology. (Copyright 2022 OTC)

FLOWMETER 1,561,670

SUBSEA MULTIPHASE FLOW METER MEASUREMENT PERFORMANCE ASSURANCE WITH AN APPLIED DATA VALIDATION AND RECONCILIATION SURVEILLANCE METHODOLOGY

E.Graham, L.Castillo, J.Yi, T.Mooney, T.Jadot and A.Amin (BP International Ltd; BP America Inc; Belsim Engineering SA; Belsim Engineering USA Inc). *OFFSHORE TECHNOLOGY CONFERENCE [OTC] (Houston, TX, 5/2-5/2022) PROCEEDINGS 2022*. (ISBN 978-1-61399-852-6; OTC-31836; Available at <http://www.onepetro.org> as of 6/23/2022; 33 pp)

Measurement performance assurance for subsea multiphase

flow meters (MPFM) can derive motivation from several sources of technical and/or business need, ranging from well surveillance to flow assurance monitoring, to production allocation among commingled sources of varying royalty, taxation, or ownership. Often, the more sensitive the subsea MPFM measurement is to a technical or business driver the more difficult it can be to initiate a comparison to a reference measurement or reference fluids such as topside measurement. Thus, providing assurance for subsea MPFM measurement performance requires a coordinated effort of MPFM performance surveillance--a combination of data and activities that can enable continuous indication of MPFM measurement performance, with or without periodic comparisons with reference measurements. However, utilizing MPFM performance surveillance information--which can come from a multitude of sources--can be confusing and potentially misinformative if a rigorous methodology to systematize the information isn't applied. It was in this context that a surveillance methodology using data validation and reconciliation (DVR) was chosen to leverage the disparate surveillance information available and provide quantitative measurement performance assurance results for a subsea MPFM. DVR was applied to assess the performance of a subsea MPFM incorporated within a subsea/topside field. Multiple sources of surveillance data and information were utilized in the application including the subsea MPFM, independent water-liquid ratio measurement, pressures and temperatures throughout the network, fluid properties, inlet separator flow measurements, and well test results. Three main objectives were established to demonstrate efficacy of the applied DVR methodology for subsea MPFM measurement performance assurance: (1) quantified DVR results for direct MPFM validation via well test; (2) continuous DVR condition-based monitoring (CBM) of the subsea MPFM within a defined subsea/topsides topology during normal operations, and (3) DVR-derived uncertainty estimates for the subsea MPFM. Several case studies using DVR surveillance are presented to address subsea measurement performance assurance. (Copyright 2022 OTC)

GAS LIFT DESIGN (WELL) 1,561,671

HYBRID HYDROCARBON LIFT SYSTEM AND METHOD

J.Xiao, asr. (Saudi Arabian Oil Co; Aramco Services Co). World 2022/212,729A1, p. 10/6/2022, f. 3/31/2022 (Appl. 2,222,864), pr. U.S. 3/31/2021 (Appl. 219,641) (E21B-0043/12; F04F-0005/24; F04F-0005/42).

A system for hybrid gas lifting may include a gas-lift completion arranged to inject high-pressure gas into production tubing of a well. The system may include a downhole annular jet pump. The downhole annular jet pump may include an annular nozzle arranged to receive the injected high-pressure gas. The injected high-pressure gas exits the annular nozzle as an annular high-velocity gas jet. The downhole annular jet pump may include a throat section arranged to receive the annular high-velocity gas jet, and to mix the annular high-velocity gas jet with a low-pressure production fluid. The downhole annular jet pump may include a diffuser section arranged to facilitate conversion of kinetic energy into pressure energy in a mixture of the annular high-velocity gas jet and the low-pressure production fluid, and to produce the mixture to a surface via the production tubing.

GAS LIFT (WELL) 1,561,672

PROCESSES FOR INCREASING HYDROCARBON PRODUCTION

E.Block, M.L.Crane and D.Zachariah, asrs. (Extract Management Co LLC). World 2022/212,875A1, p. 10/6/2022, f. 4/1/2022 (Appl. 2,223,104), pr. U.S. 4/1/2021 (Appl. 220,470) (E21B-0043/12).

Systems and methods for increasing hydrocarbon production using an electrical submersible pump are described. The methods typically include, for example, configuring an electrical submersible pump comprising a gas separator to induce a gas lift effect in a well comprising a tubing within a casing. Hydrocarbon production from the well is therefore increased using the electrical submersible pump.

GAS LIFT (WELL) 1,561,673

GAS LIFT SYSTEM AND METHOD

S.L.Wildman, Sr., W.D.Wildman and M.R.Wildman, asrs. (Sam and Gail LLC). World 2022/212,320A1, p. 10/6/2022, f. 3/29/2022 (Appl. 2,222,274), pr. U.S. 3/29/2021 (Appl. 63/167,297) (E21B-0043/12; E21B-0034/08; F04F-0001/20; F16K-0031/122; F16K-0031/126).

A gas lift system for lifting oil with a production tube positioned inside a well casing with manifolds in the production tube spaced apart from each other is disclosed herein. The system includes including valve assemblies on the manifolds that each have an open position and a closed position; each of the valve assemblies includes a biasing device that biases the valve towards the closed position, where pressurizing each valve assembly with a control fluid generates a force that acts against the biasing force of the biasing device to open the valve, and a means to selectively control the pressure of the control fluid in the control line, where each of the valve assemblies includes different biasing forces in each valve, with a topmost valve having a highest biasing force and each sequentially lower valve having a lower biasing force. A method for using the gas lift system is also included.

GAS LIQUID SEPARATION 1,561,674

PUMP SYSTEM WITH PASSIVE GAS SEPARATION

D.J.Brown, T.A.Kopecky and C.L.Newport, asrs. (Halliburton Energy Service). World 2022/211,902A1, p. 10/6/2022, f. 2/4/2022 (Appl. 2,215,170), pr. U.S. 3/31/2021 (Appl. 219,834) (E21B-0043/12; E21B-0021/06; E21B-0033/12).

Apparatus and method for passive gas separation in a through-tubing-conveyed (TTC) pump system comprise abruptly reversing a flow direction of wellbore fluids from flowing up the wellbore to down into a liquids reservoir. The generally annular liquids reservoir is formed between a production tubing and a pump of the TTC pump system. Wellbore fluids flowing up the production tubing are diverted into the annulus via one or more outlet ports in the production tubing. The wellbore fluids flow up the annulus until encountering one or more inlet ports in the production tubing, which redirects the wellbore fluids from the annulus down into the liquids reservoir. The reversal of flow direction causes gas in the wellbore fluids to separate from liquids as the gas continues moving up the wellbore instead of changing direction with the liquids. The substantially gas free liquids are then pumped by the pump up to the surface.

GAS PROCESSING 1,561,675

LNG PRODUCTION USING ETHYLENE, PROPANE AND AMMONIA CASCADE REFRIGERATION

A.El-Khashab, M.Faraq, M.M.F.Morgan and A.A.H.Abdel Gelil, asrs. (ENPPI). World 2022/207,055A2, p. 10/6/2022, f. 4/1/2021 (Appl. 2,100,010).

LNG production is a high-energy-consumption industry, as it generally depends on cooling the feed gas to liquify the gas stream. Thus, reducing the required energy in this industry, which leads directly to increasing the profit, is always a challenge. A traditional LNG production plant usually consists of different techniques using cascade refrigerant of propane and ethylene to cool the gas inlet stream and decreasing the gas pressure using control valve for deep cooling to decrease the temperature and hence produce gas liquid. The present invention offers significant efficiency advantages over the traditional LNG production plant, as in the idea presented here that will significantly reduce LNG plant CAPEX and OPEX as reflected in plant installed and operating power. This invention shows how using ammonia absorption refrigeration integrated with compressor gas turbine waste heat recovery (WHRU) and compressor discharge hot stream cascaded with propane mechanical refrigeration will enhance LNG plant heat optimization and will provide a refrigerant required in the cooling of the LNG. In addition, utilizing a one-stage high inlet pressure liquid expander to produce a high percentage of LNG at high inlet pressure gas (above 80 bar) led to reducing the recycle gas flow rate. This invention is applicable for new LNG plants and for upgrading existing LNG plants.

GAS PROCESSING 1,561,676

METHODS, APPARATUS AND SYSTEM FOR UTILISING COLD ENERGY RECOVERED FROM A LIQUEFIED NATURAL GAS FEED IN A NATURAL GAS LIQUID EXTRACTION PROCESS

W.S.Chong, J.K.J.Lim, H.W.Kim and W.Y.Ho, asrs. (Singapore LNG Corp Pte Ltd). World 2022/203,600A1, p. 9/29/2022, f. 3/22/2022 (Appl. 2,250,154), pr. SG 3/22/2021 (Appl. 202,102,929) (F25J-0003/02; C10L-0003/10; F17C-0009/04; F25J-0001/00).

Disclosed herein is a natural gas liquids (NGL) extraction process utilising cold energy recovered from a supplemental liquid natural gas (LNG) feed, and an apparatus and system for the process. The process comprises separating NGL from a rich LNG feed to provide a lean LNG stream and a NGL stream; and performing a first thermal exchange between the lean LNG stream and the supplemental LNG feed in a supplemental heat exchanger, wherein the lean LNG stream is cooled and the supplemental LNG feed is heated, wherein the supplemental LNG feed is distinct from the rich LNG feed. The apparatus and system each comprises a supplemental heat exchanger and a distillation column configured to perform the process.

GAS PROCESSING PLANT 1,561,677

NGL EXTRACTION/GAS TREATMENT UTILIZING WASTE HEAT RECOVERY CASCADE REFRIGERATION

A.El-Khashab, M.Farag, T.Zein El-Din, M.Haggag and A.Ahmed, asrs. (ENPPI). World 2022/207,056A2, p. 10/6/2022, f. 4/1/2021 (Appl. 2,100,011).

Natural gas liquids (NGLs) extraction from natural gas is a high-energy-consumption industry, as it generally depends on chilling the feed gas to liquify the targeted hydrocarbons, reducing the required energy in this industry is always a challenge which leads directly to increasing the profit. A traditional NGL recovery plant usually consists of feed chilling exchangers combined with a gas expansion or mechanical refrigeration cycle followed by gas expansion using turbo expanders for deep chilling. The chilled gas stream is routed to a de-methanizer where the methane is separated as a top product which normally compressed and routed to downstream users as a sales gas and the heavier components are separated into bottom product NGLs before entering the fractionation train to separate ethane and other products. This invention shows how by using either standalone ammonia absorption refrigeration or ammonia absorption refrigeration and propane cascade refrigeration integrated with a sales gas compressor waste heat recovery unit (WHRU) plant, CAPEX and OPEX can be dramatically decreased. Furthermore, with either of these refrigeration techniques, a significant increase in NGL recovery can be achieved. This invention is also applicable to gas treatment or conditioning plants.

GAS SEPARATOR 1,561,678

DEVICE AND METHOD FOR MONITORING OPERATIONAL PERFORMANCE OF GAS SEPARATOR BY USING VIBRATION ACCELERATION VALUE MEASUREMENT

Y.H.No and J.S.Ki (GeoScan Co Ltd). World 2022/203,121A1, p. 9/29/2022, f. 6/17/2021 (Appl. 217,613), pr. Korea 3/25/2021 (Appl. 2021-0,038,858) (G01M-0099/00; E21B-0043/38; F04D-0013/08; G01M-0007/02; G01P-0015/02; G06F-0015/16; G08B-0021/18). (In Korean)

The present invention relates to a device and a method capable of precisely and accurately monitoring whether a gas separator properly performs a role and function of separating a liquid and a gas by monitoring the operational performance of the gas separator in real time on the basis of a vibration acceleration value measured by a vibration sensor installed in the gas separator during operation of an ESP system.

GAS WELL DEWATERING 1,561,679

EXCELLENT FOAMING PROPERTIES OF ANIONIC-ZWITTERIONIC-GEMINI CATIONIC COMPOUND

SURFACTANTS FOR GAS WELL DELIQUIFICATION: EXPERIMENTAL AND COMPUTATIONAL INVESTIGATIONS

W.Han, J.Fan, H.Lu, Y.Yan, C.Liu and S.Dong (Xi'an Shiyu Univ; China Univ Petroleum). COLLOIDS AND SURFACES A: PHYSICO-CHEMICAL AND ENGINEERING ASPECTS v.653, 11/20/2022. (ISSN 0927-7757; Article no.129944)

Foams are often employed as an efficient and cleaner method to remove the liquid accumulated at the bottom of the gas wells and promote the production of natural gas. However, the extreme conditions (e.g., high content of condensate, high salinity, high temperature, etc.) in the wells would retard the performance of the foaming agents. Usually, mixtures of different foaming surfactants were used to achieve high performances under those extreme conditions. In this paper, foams stabilized by surfactant mixtures containing alpha-olefin sulfonate (AOS), synthesized green cocamidopropyl betaine (CAPB) and modified quaternary ammonium Gemini surfactant (CAGB) in a proportion of 0.2:0.2:0.2 (wt%/wt%/wt%) were developed to evaluate their industrial application potential in gas well deliquification. The ternary surfactant (CAPB-CAGB-AOS) foam exhibited higher stability than the other dual surfactant foams and singular surfactant foams. Additionally, the foaming efficiency (defined as the ratio of the mass of water converted into foam to the mass of the initial liquid) and liquid unloading efficiency of the CAPB-CAGB-AOS mixture could be improved with the presence of condensate. Salts and methanol had a weak influence on the performance of the CAPB-CAGB-AOS foam. The introduction of ethylenediamine tetraacetic acid disodium (EDTA-2Na) can enhance the performance of the CAPB-CAGB-AOS foam against salts. The temperature (> 60 °C) favored the foaming efficiency and liquid unloading efficiency of the CAPB-CAGB-AOS mixture, which reached up to 100% and 88.5% at 90 °C. These results indicated that the synergy effect of these three surfactants on the stability and liquid unloading efficiency of the foam can be confirmed. Moreover, the synergy effect can also be confirmed by the surface tension test, the foam's microstructure observation and the computational studies on calculated binding energies and electrostatic interactions. (c2022 Elsevier B.V.)

GLYCOL DEHYDRATION 1,561,680

MERCURY REMOVAL BY INJECTION OF REAGENTS IN GAS PHASE

R.A.Jadhav and R.Owen, asrs. (Chevron USA Inc). World 2022/208,417A1, p. 10/6/2022, f. 3/31/2022 (Appl. 2,252,992), pr. U.S. 4/1/2021 (Appl. 63/169,775) (B01D-0053/64; C10L-0003/10).

The present disclosure relates to removing mercury from a gas phase by injecting a scavenger solution into the gas phase.

HEAVE COMPENSATOR 1,561,681

IMPROVED FRACTIONAL-ORDER PID CONTROLLER OF A PMSM-BASED WAVE COMPENSATION SYSTEM FOR OFFSHORE SHIP CRANES

H.Chen, X.Wang, M.Benbouzid, J.F.Charpentier, N.Al-Ahmed and J.Han (Shanghai Maritime Univ; Ecole Navale (France); Nantes Univ). JOURNAL OF MARINE SCIENCE AND ENGINEERING v.10, no.9, Sept. 2022. (ISSN 2077-1312; Article no.1238)

Wave compensation technology is crucial to the safety of the ship operation and the accurate placement of load. Its compensation efficiency and the gentle change of the rope tension are particularly important. In this paper, we adopt permanent magnet synchronous machine (PMSM) as the actuator to construct the basic wave compensation system. Firstly, the motion model of ship and load under wave action is established, and the fractional-order PID (FOPID) controller for the position loop of the PMSM is introduced. Then, the parameters of FOPID are optimized by genetic algorithm-particle swarm optimization (GAPSO) algorithm, which is based on genetic algorithms (GA) and particle swarm optimization (PSO) algorithms for better compensation performance. The wave synchronization strategy is used to simulate the load, when it needs to be taken into the water. The non-linear dynamic equations of the rope are solved by Lagrange mechanics and the heave displacement is obtained by time series

prediction algorithm. Finally, the effect of wave compensation and wave synchronization strategy are verified on MATLAB/Simulink. The results show that after the compensation, the crane load can follow the set height value very well, the compensation efficiency can reach more than 94%, and the wave synchronization strategy significantly reduces the change of the rope tension.

HYDRATE FORMATION 1,561,682

STUDY ON THE RHEOLOGY OF CO₂ HYDRATE SLURRY BY USING THE CAPILLARY METHOD

W.Fu, W.We, H.Wang, B.Huang and Z.Wang (China Univ Mining Technol; CNPC Research Inst; China Univ Petroleum). *JOURNAL OF MARINE SCIENCE AND ENGINEERING* v.10, no.9, Sept. 2022. (ISSN 2077-1312; Article no.1224)

The rheological properties of the CO₂ hydrate slurry are experimentally investigated by using a new flow loop with an inner diameter of 50 mm. The pressure drops of the CO₂ hydrate slurry are measured experimentally under the volumetric hydrate fraction (ranging from 1.4 to 17.2 vol%) and the shear rate (ranging from 40 to 590 per second). Using the capillary method, the rheology of the CO₂ hydrate slurry is analyzed based on the pressure drop. The CO₂ hydrate slurry is identified as a power-law fluid and exhibits strong shear-thickening behavior. The increase in the volumetric hydrate concentration not only ascends the apparent viscosity, but also makes the non-Newtonian behavior of the hydrate slurry become more obvious. The non-Newtonian index and the consistence factor of fluid increase exponentially with the volumetric hydrate concentration increasing. A Herschel-Bulkley-type rheological model of the CO₂ hydrate slurry is correlated from experimental data. The developed model performs with an average discrepancy of less than 16.3% within the range of the experiment.

HYDRATE INHIBITOR 1,561,683

DUAL FUNCTIONALITY OF ULTRALOW LEVELS OF A MODEL KINETIC HYDRATE INHIBITOR ON HYDRATE PARTICLE MORPHOLOGY AND INTERPARTICLE FORCE

J.E.Worley, J.G.Delgado-Linares and C.A.Koh (Colorado Sch Mines). *COLLOIDS AND SURFACES A: PHYSICOCHEMICAL AND ENGINEERING ASPECTS* v.652, 11/5/2022. (ISSN 0927-7757; Article no.129825)

Gas hydrate plug formation is a major concern in oil and gas exploitation efforts, wherein line blockages can pose major safety, economic, and environmental risks. Kinetic hydrate inhibitors (KHIs) are a promising class of hydrate management chemicals, which are potentially cleaner, cheaper, and greener than traditional thermodynamic hydrate inhibitors (THIs). Therefore, understanding the effects that KHIs have on hydrate particles is vital to their application. In this study, polyvinylpyrrolidone (PVP), a model KHI, was investigated at ultralow concentrations to determine its effect on the properties of hydrates and elucidate when nucleation and growth inhibition begins. It was found that PVP can adsorb at the hydrate particle surface to reduce interparticle force by 40–54 %. Low concentration PVP continues to affect interparticle forces at prolonged contact times, reducing forces at 30-minutes to 1-hour of contact by 20–40 % and reducing sintering rate. PVP also reduces film growth rates by 30–50 % depending on the concentration of PVP in the water phase. The onset of major nucleation and growth effects was observed to occur at 0.01 wt% PVP in the water phase, two orders of magnitude below concentrations typically employed in hydrate management. It was discovered that low dosage PVP can cause major morphological changes to the hydrate particles in both the short and long term, which can influence interparticle forces and particle agglomeration, and may serve as a morphological screening tool for KHIs. A proposed mechanism for the observed morphology changes explains how the heterogenous adsorption of chemicals at the particle surface can lead directly to the newly observed particle morphology. The results presented in this paper show that ultralow concentrations of KHIs (0.0005 wt%) can have combined effects on the interfacial activity and crystal growth and morphology of hydrates, showing KHIs to be a dual function inhibitor of both interparticle interactions and hydrate growth. These results can inform KHI applications from industrial flow assurance to carbon

dioxide transport for unimpeded carbon capture and sequestration. (c2022 Elsevier B.V.)

LUBRICATING OIL 1,561,684

FOAMABILITY AND FOAM STABILITY OF OILY MIXTURES

T.Arnaudova, Z.Mitrinova, N.Denkov, D.Grownov, R.Brenda and S.Tcholakova (Sofia Univ; Lubrizol Ltd). *COLLOIDS AND SURFACES A: PHYSICOCHEMICAL AND ENGINEERING ASPECTS* v.653, 11/20/2022. (ISSN 0927-7757; Article no.129987)

Lubricating oils consist of base oil, containing different hydrocarbons, and modifying components (additives) which improve the application performance. Some of these additives are able to stabilize entrained air bubbles, potentially causing serious problems for engines, transmissions and hydraulic systems. Here we evaluate the foamability and foam stability of model mineral oils (hexadecane, light oil, heavy oil and their mixtures) in the presence and in the absence of nanoparticles as additives, at several temperatures. The results allow us to categorize the systems studied into three groups: (1) Oils unable to entrap any air during the stirring period; (2) Oils able to entrap air during stirring, but unable to retain it after stopping the stirring; (3) Oils which form stable bubbles and foams. Hexadecane, with and without nanoparticles, falls into the first group. Heavy oil in the presence of nanoparticles falls into the third group, whereas all other mixtures are in the second group. The inability of hexadecane to entrain air is related to its low viscosity and very low foam film stability which leads to instantaneous coalescence of the bubbles formed. The increased foamability of heavy and light oils and their mixtures is explained by: (1) their higher viscosity as compared to hexadecane which leads to slower foam film thinning and (2) the presence of long chain alkanes in these oils which create weak steric repulsion between the foam film surfaces. The addition of nanoparticles increases the foamability and the foam stability of heavy oil, without changing significantly the foam properties of the light oil and hexadecane. The latter effect is explained by the inability of the particles to attach to the light oil-air and hexadecane-air interfaces, whereas the same particles adsorb on the heavy oil-air interface and create additional steric repulsion between the air bubbles, thus allowing the formation of stable foam. (c2022 Elsevier B.V.)

MAGNETIC PERMEABILITY 1,561,685

FLUIDS HAVING INCREASED MAGNETIC PERMEABILITY FOR SUBTERRANEAN TOOL ACTIVATION

P.J.Jones and G.T.Werkheiser, asrs. (Halliburton Energy Service). *World* 2022/211,800A1, p. 10/6/2022, f. 3/31/2021 (Appl. 2,125,081), pr. U.S. 3/30/2021 (Appl. 217,250) (E21B-0047/13; E21B-0047/09).

Fluid flows, such as slurries, conditioning fluids, spacer fluids, or the like, may be modified to carry materials having high magnetic permeability characteristics that can be detected by a magnetic permeability sensing apparatus positioned along the fluid flow path in wellbores or downhole tools. Sensed presence of the high magnetic permeability material by the sensing apparatus positioned in the fluid flow path may result in initiation of an operational event. The operational event may include, but not limited to closing or opening a valve, moving a component, conveying a signal, activating or deactivating a device, or the like.

MARINE FOULING 1,561,686

HYDRATION AND ANTIBIOFOULING OF TMAO-DERIVED ZWITTERIONIC POLYMERS SURFACES STUDIED WITH ATOMISTIC MOLECULAR DYNAMICS SIMULATIONS

P.Sarker, G.T.Chen, M.S.J.Sajib, N.W.Jones and T.Wei (Howard Univ; Florida Univ). *COLLOIDS AND SURFACES A: PHYSICOCHEMICAL AND ENGINEERING ASPECTS* v.653, 11/20/2022. (ISSN 0927-7757; Article no.129943)

Zwitterionic polymers have emerged as a class of highly effective ultralow fouling materials for critical marine coating and biomedical applications. The recently developed trimethylamine N-oxide (TMAO)-derived zwitterionic polymers have demonstrated

excellent antibiofouling capability in various chemical environments; however, it remains unclear how they interact with proteins at the microscopic level. To further investigate the antifouling mechanisms, we performed atomistic molecular dynamics (MD) simulations in combination with free-energy computations to provide an in-depth molecular understanding of the interactions of TMAO polymer brush (pTMAO) surfaces with proteins of opposite charges (positively charged lysozyme and negatively charged barnacle cement protein) in aqueous environments (pure water and saline solution). Our simulations revealed ordered structures of a condensed hydration water layer on the pTMAO surfaces in pure and saline water. The quantitative free energy analyses showed that the pTMAO surface has small protein desorption energy, but with a strong hydration energy barrier near the polymer surfaces to resist protein adsorption compared to other biofouling surfaces. The addition of salts only has a slight effect on the pTMAO surface's exclusion of proteins due to the small interference of the structure of interfacial water. This study provides detailed knowledge of the strong surface hydration of zwitterionic polymers and its relation to salt impact, protein adsorption, and antibiofouling behavior of these important materials. (c2022 Elsevier B.V.)

MOORING **1,561,687**

MOORING INTEGRITY ISSUES AND LESSONS LEARNED DATABASE: DEEPSTAR(R) PROJECT 20401

R.Spong, R.Garrity, C.Thompson, X.Yan, O.Gabrielsen, D.LHostis, C.Heyl, J.Minnebo, M.Naciri et al. (Spire Engineering). *OFFSHORE TECHNOLOGY CONFERENCE [OTC] (Houston, TX, 5/2-5/2022) PROCEEDINGS* 2022. (ISBN 978-1-61399-852-6; OTC-31823; Available at <http://www.onepetro.org> as of 6/23/2022; 13 pp)

Mooring failures have been a recurring issue in the offshore industry, and failures continue to occur across the offshore Floating Production System (FPS) fleet. Many of these recurring failures appear to be from similar degradation mechanisms as past events. To better understand these trends and learn from these events, DeepStar(R) Project 20401: Database of Mooring Integrity Issues and Lessons Learned was initiated. The project primarily consisted of the collection and assessment of mooring integrity data on failures, pre-emptive replacements and repairs observed on FPS permanent mooring systems. Additionally, chain corrosion/wear data was collected and summarized as part of the project. When available the data was collected from published sources. However, most of the integrity data came from the eight operator and mooring consultancies companies participating in the project. This paper describes the project data collection, the deliverables and key observations from the mooring integrity database developed as part of the project. The observations presented within the paper provide unique insight into predominate degradation mechanisms, observed consequences and estimated failure rates of mooring lines. (Copyright 2022 OTC)

MOORING **1,561,688**

NUMERICAL MODELLING FOR SYNTHETIC FIBRE MOORING LINES TAKING ELONGATION AND CONTRACTION INTO ACCOUNT

I.Catipovic, N.Alujevic, S.Rudan and V.Slapnicar (Zagreb Univ). *JOURNAL OF MARINE SCIENCE AND ENGINEERING* v.9, no.4, April 2021. (ISSN 2077-1312; Article no.417)

Synthetic fibre mooring lines are used as an alternative to traditional steel wire ropes due to their higher strength to weight ratio. Benefits are also found in relative ease of handling, and therefore the marine industry has largely accepted this type of mooring line. By rules and regulations, the design of mooring lines should be based on a coupled dynamic analysis of a particular mooring system and moored vessel. This approach incorporates damping and inertial forces (i.e., hydrodynamic reactions) acting directly on the mooring lines due to their motion through the seawater. On the basis of the outer diameter of the synthetic fibre rope, the Morison equation gives estimations of the mooring line hydrodynamic reactions. In comparison to the traditional steel wire ropes, the synthetic mooring lines usually have relatively larger

elongations and consequently larger reductions of the outer diameter. Furthermore, the lower diameter certainly leads to reduced values of damping and added mass (of mooring lines) that should be considered in the coupled model. Therefore, the aim of this study was to develop a new numerical model that includes diameter changes and axial deformations when estimating the hydrodynamic reactions. The development of the model is carried out with a nonlinear finite element method for mooring lines with the assumption of large three-dimensional motions. The obtained results show the effectiveness of the newly developed model as a more accurate approach in calculation of hydrodynamic reactions.

MOORING **1,561,689**

COMPOSITE SPRINGS FOR MOORING TENSIONERS: A SYSTEMATIC REVIEW OF MATERIAL SELECTION, FATIGUE PERFORMANCE, MANUFACTURING, AND APPLICATIONS

Y.Cai, M.Bazli, A.P.Basnayake, M.Veidt and M.T.Heltzmann (Queensland Univ). *JOURNAL OF MARINE SCIENCE AND ENGINEERING* v.10, no.9, Sept. 2022. (ISSN 2077-1312; Article no.1286)

Ocean energy is an underutilized renewable energy source compared with hydropower and wind power. Therefore, the development of economical and efficient wave energy converters (WECs) is important and crucial for offshore power generation. The mooring tensioner is a critical device that can be used in point-absorber-type WECs, semisubmersible floats for oil and gas drilling, and floating wind turbines. A mooring tensioner is a system used to create, reduce, or maintain tension within the mooring lines by applying a force to the mooring line. Composite springs as mooring tensioners have several advantages compared to metal springs, such as corrosion resistance, high specific strain energy, appropriate fatigue performance, and the ability to flexibly adjust the spring constant without changing the overall dimensions. This paper reviews in detail the fatigue performance, seawater durability, and manufacturing methods of different composite materials as well as the current and potential applications of composites springs. In addition, recommendations for future research and opportunities for composite mooring tensioners are presented.

MOORING **1,561,690**

SHORT AND LONG TERM CREEP BEHAVIOUR OF POLYAMIDE ROPES FOR MOORING APPLICATIONS

L.Civier, Y.Chevillotte, G.Bles, F.Montel, P.Davies and Y.Marco (UMR-CNRS; Ifremer). *OCEAN ENGINEERING* v.259, 9/1/2022. (ISSN 0029-8018; Article no.111800)

Polyamide 6 fibres are of interest for mooring lines of floating wind turbines and these are continuously loaded throughout their service life. Such applications require the long term response of polyamide 6 ropes in water to be characterized. This paper presents results describing the long term creep behaviour of polyamide 6 sub-ropes with tests that lasted 2 years. A specially designed experimental set-up for long term creep test in water is presented first. Then, a kinetic study comparing creep and recovery is performed using a logarithmic identification of the strain rate. The need for performing long term creep tests is evaluated by comparing the long term creep results to those from short term creep tests lasting 3 h. The results show that a 3 h long creep test provides a reasonable prediction of long term creep strain using a single logarithmic linear law. Finally, a latch-based Weibull model is compared to a single linear logarithmic law to describe and predict creep and recovery response. It is shown that the Weibull model allows a better description of the recovery behaviour of polyamide 6 but is less well adapted for the description of creep. (c2022 Elsevier Ltd.)

MOORING **1,561,691**

AN EFFECTIVE BIDIRECTIONAL SOLVING METHOD FOR THE MOTION AND MOORING TENSION OF MOORED FLOATERS

F.Zeng, N.Zhang, G.Huang, W.Pan and M.He (Dalian Univ Technol; Tianjin Research Inst). *OCEAN ENGINEERING* v.259, 9/1/2022. (ISSN 0029-8018; Article no.111924)

With more and more moored floaters having been applied in ocean engineering globally, the security of moored floaters is becoming a key concern. Although there are extensive studies on the motion and mooring tension of moored floaters, few of them addressed the direct relation between the motion and mooring tension of floaters. This study establishes a direct relation between floater motion and mooring tension through the fairlead position and proposes a new effective bidirectional solving method on the floater motion and mooring tension in time domain. Noted that this method is independent to specific environmental factors. To validate the proposed method, analytical solutions are firstly obtained and then compared with the 2-D experimental measurements and 3-D numerical simulations. The comparison shows that the predictions by the proposed method match well with the measurements and simulations. Therefore, given the time history on either motion or mooring tension of floaters, the other can be predicted by the proposed method efficiently. For operational environments offshore, this method can be used to predict the motion or mooring tension, which is also saving in cost and time. (c2022 Elsevier Ltd.)

MULTIPHASE FLOW 1,561,692

SYSTEM FOR MEASURING MULTIPHASE FLOW IN DOWNHOLE CONDITIONS AND FLOW REGIMES

S.Sherrit, L.P.Tosi, K.V.Sherrill, M.Rais-Zadeh, J.R.Hall, J.F.Tims, M.Fradet, R.M.Briggs and C.Yahnker, asrs. (California Inst Technol). World 2022/212,240A1, p. 10/6/2022, f. 3/28/2022 (Appl. 2,222,115), pr. U.S. 3/31/2021 (Appl. 63/168,877) (E21B-0047/00; G01F-0001/7086; G01F-0001/712; G01F-0001/74; G01N-0030/00).

Systems and methods for measuring multiphase flow of a fluid mixture in a downhole pipe of an oil/gas/water well are presented. According to one aspect, time-series measurement of the flow velocity and composition at a plurality of discrete azimuths of the pipe are measured. Measured time-correlated velocity and composition data are used to identify fluid components present in the pipe and estimate cross-sectional area and velocity of each of the fluid components. According to another aspect, pressure and temperature at the downhole pipe are measured, and used to calculate the mass density of each fluid component. For each of the fluid components, the cross-sectional area, velocity, and mass density are used to generate a corresponding mass flow rate. An algorithm with a set of parameters tuned to specific flow regimes is used to map the sensed data from the time-series measurements into the mass flow rate of each fluid component.

OFFSHORE EQUIPMENT 1,561,693

RISER CLAMP

J.M.Johnsen and P.Nilsson, asrs. (MHWirth AS). World 2022/203,516A1, p. 9/29/2022, f. 3/22/2022 (Appl. 2,250,071), pr. Norw. 3/23/2021 (Appl. 20,210,372) (E21B-0017/01; E21B-0017/02; E21B-0017/10; F16L-0003/22).

A riser clamp for supporting fluid pipes in parallel with and spaced from an external surface of a tubular riser is disclosed herein. The riser clamp comprises one or more body portion(s) that form a generally circular or partially circular clamp body that encircles a clamp axis, with the one or more body portion(s) each having a radially outwardly facing external surface and a radially inwardly facing internal surface. The riser clamp further comprises a separate, generally planar pipe saddle part that extends radially outwardly of the clamp body.

OFFSHORE STRUCTURE 1,561,694

FRACTIONAL-ORDER ELASTOPLASTIC MODELING OF SANDS CONSIDERING CYCLIC MOBILITY

L.Wu, W.Cheng and Z.Zhu (Zhejiang Univ; Paris-Est Univ). *JOURNAL OF MARINE SCIENCE AND ENGINEERING* v.9, no.4, April 2021. (ISSN 2077-1312; Article no.354)

Seabed soil may experience a reduction in strength or even liquefaction when subjected to cyclic loadings exerted by offshore structures and environmental loadings such as ocean waves and earthquakes. A reasonable and robust constitutive soil model is indispensable for accurate assessment of such structure-seabed interactions in marine environments. In this paper, a new constitutive model is proposed by enriching subloading surface theory with a fractional-order plastic flow rule and multiple hardening rules. A detailed validation of both stress- and strain-controlled undrained cyclic test results of medium-dense Karlsruhe fine sand is provided to demonstrate the robustness of the present constitutive model to capture the non-associativity and cyclic mobility of sandy soils. The new fractional cyclic model is then implemented into a finite element code based on a two-phase field theory via a user subroutine, and a numerical case study on the response of seabed soils around a submarine pipeline under cyclic wave loadings is presented to highlight the practical applications of this model in structure-seabed interactions.

OFFSHORE STRUCTURE 1,561,695

EFFECT OF VARIATION IN THE MASS RATIO ON VORTEX-INDUCED VIBRATION OF A CIRCULAR CYLINDER IN CROSSFLOW DIRECTION AT REYNOLDS NUMBER = 10 E+04: A NUMERICAL STUDY USING RANS MODEL

M.U.Anwar, M.M.A.Lashin, N.B.Khan, A.Munir, M.Jameel, R.Muhammad, K.Guedri and A.M.Galal (Nat Univ Sci & Technol; Princess Nourah Univ). *JOURNAL OF MARINE SCIENCE AND ENGINEERING* v.10, no.8, Aug. 2022. (ISSN 2077-1312; Article no.1126)

This study reports on the numerical analysis of the impact of mass ratio on the vortex-induced vibration (VIV) phenomenon of an elastically rigid cylinder, oscillating freely in a crossflow direction. Reynolds-averaged Navier-Stokes (RANS) equations with (k- ω SST) model were used to analyze the flow behavior, amplitude ratio and vortex shedding patterns. The study was performed at a constant Reynolds number (Re) of 10 E+04, with reduced velocity (Ur) ranging from 2 to 14 and mass ratio (m) ranging from 2.4 to 11. The mass ratio was defined as the ratio between the mass of the vibrating cylinder and mass of the fluid displaced. It was found that increasing the mass ratio from 2.4 to 11 resulted in decreases in amplitude response by 80%, 71% and 31% at the initial branch, the upper to lower transition region, and the lower branch, respectively. However, the amplitude in the upper branch decreased by only 8% at a high mass ratio. The peak amplitude observed in the present study was lower than previous experimental and DES results. However, the RANS k- ω SST well captured the vortex shedding modes of 2S, 2P, P + S, and 2T. In 2S mode, two single pairs of vortices were formed, whereas in 2P mode two pairs were generated in single oscillation. Similarly, P + S meant one pair and one individual vortex, whereas 2T mode meant two triplets of vortices generated in one oscillation. The study concluded that an increase in mass ratio results in a shortened lock-in region and decreased amplitude response.

OFFSHORE STRUCTURE 1,561,696

A REVIEW ON RECENT DEVELOPMENT OF NUMERICAL MODELING OF LOCAL SCOUR AROUND HYDRAULIC AND MARINE STRUCTURES

M.Zhao (Western Sydney Univ). *JOURNAL OF MARINE SCIENCE AND ENGINEERING* v.10, no.8, Aug. 2022. (ISSN 2077-1312; Article no.1139)

This paper reviews the recent development of numerical modelling of local scour around hydraulic and marine structures. The numerical models for simulating local scour are classified into five categories: sediment transport rate models, two-phase models, CFD-DEM models, equilibrium scour models and depth-averaged models. The sediment transport rate models are the most popularly used models because of their high calculation speed and availability of empirical formulae for predicting sediment transport rates. Two-phase models were developed to simulate sediment transport in the format of sheet flow under strong current velocity or strong turbulence. The CFD-DEM model simulates the motion of every individual sediment particle. Its speed is the slowest, but it

provides the opportunity to understand fundamental mechanisms of flow-particle interaction and particle-particle interaction using small-scale simulations. Equilibrium scour models predict the final scour profile at the equilibrium stage but cannot predict scour history. The depth-averaged models that were developed early are not recommended for local scour problems because they are not able to predict three-dimensional features around structures. Although many numerical models have been developed and many studies have been conducted to investigate local scour, some challenging problems remain to be solved, for example, the effects from scaling and sediment gradation. In addition, people's understanding of local scour of cohesive sand is still very shallow, and more experimental and numerical research in this area is needed.

OFFSHORE STRUCTURE 1,561,697

MACHINE LEARNING MODELING FOR THE NEAR-WAKE MEAN VELOCITY DEFICIT PROFILES BEHIND A ROUGH CIRCULAR CYLINDER

J.Mi, S.Laima, X.Jin and H.Li (Harbin Inst Technology). *OCEAN ENGINEERING* v.259, 9/1/2022. (ISSN 0029-8018; Article no.111791)

This study proposes a machine-learning framework to model the near-wake mean velocity profile, illustrating the similarity in the near wake of a circular cylinder. A dataset comprising the near-wake velocity field and wall pressure of the rough circular cylinder, ranging from the subcritical to supercritical flow regimes, is obtained via the wind tunnel test. Then, singular value decomposition of the mean velocity deficit matrixes is performed to obtain the left- and right-singular vectors. The generalized basis and coordinate are finalized by analyzing the scatter of the singular vectors, the correlation of the singular vectors with inputs, and the energy distribution of different generalized basis and coordinates. Next, the random forests (RF) algorithm is applied with the asymmetry of the wall pressure coefficient, drag force coefficient, Reynolds number, and spatial coordinate as inputs, and outputs the generalized coordinates. Finally, the importance of inputs is investigated through Shapley Additive Explanation (SHAP), which enhances the interpretability of the model. The test results show that the RF model can accurately predict the near-wake mean velocity deficit profiles at various Reynolds numbers. The SHAP evaluation indicates that the asymmetry of the pressure coefficient is crucial for modeling the velocity fields among different regimes. (c2022 Elsevier Ltd.)

OFFSHORE STRUCTURE 1,561,698

ANALYTICAL SOLUTION OF PARAMETRICALLY INDUCED PAYLOAD NONLINEAR PENDULATION IN OFFSHORE LIFTING

B.Chilinski, A.Mackojc and K.Mackojc (Warsaw Univ Technology; Fathom Group Ltd). *OCEAN ENGINEERING* v.259, 9/1/2022. (ISSN 0029-8018; Article no.111835)

This paper presents a concept of analytical modelling methodology of a parametrically induced payload pendulation. A nonlinear analytical approximated solution was found for the considered 3-DOF model by simplifying to an elliptically excited Mathieu oscillator. The dynamic responses of the parametric pendulum being excited by bidirectional regular waves applied as kinematic functions at the crane tip were studied by means of the perturbation method. In order to investigate the model's dynamic properties, an analytical first order solution was formulated through the utilisation of multiple-scale analysis. The accuracy of the solution derived was validated for two scenarios -- payload oscillations outside the resonant region and on the resonance curve. The approximate analytical solution was examined for different sets of the system excitation curve parameters. The authors conducted numerical analyses (direct integration of a nonlinear governing equation) in order to give a satisfactory confirmation of the proposed methodology and evaluate the robustness of the obtained solution. Using the first order approximation, the results are found to be more conservative comparing to the simulations however, for all of the presented cases, the solution achieves a very good correspondence with the numerical results. The studies were summarised with an examination of the stability assessment of the lifted object. (c2022 Elsevier Ltd.)

OFFSHORE STRUCTURE 1,561,699

NUMERICAL STUDY OF VORTEX-INDUCED VIBRATIONS OF A CIRCULAR CYLINDER AT DIFFERENT INCIDENCE ANGLES

Y.Gao, Z.Jiang, L.Ma, S.Fu, G.He and C.Shi (Harbin Inst Technology; Massachusetts Inst Technol; Shanghai Jiao Tong Univ). *OCEAN ENGINEERING* v.259, 9/1/2022. (ISSN 0029-8018; Article no.111858)

The effects of four different incidence angles (α) on the vortex-induced vibration (VIV) response of a two degrees-of-freedom cylinder were studied using the two-dimensional unsteady Reynolds-averaged Navier-Stokes equation and shear stress transport $k-\omega$ model, combined with the fourth-order Runge-Kutta method. The VIV characteristics, including the structural vibration amplitude, vibration frequency, lock-in regime, the pattern of vortex shedding, Strouhal number, hydrodynamic coefficient, and power conversion efficiency were systematically researched. The numerical results showed that a change of the incidence angle made the VIV response of the cylinder display multifrequency characteristics. As the incidence angle increased, the amplitude in the y direction gradually decreased; comparatively, the amplitude in the x direction gradually increased. The VIV responses for different incidence angles all presented an obvious lock-in phenomenon; however, the width of lock-in region changed slightly with variation of the incidence angle. As the incidence angle increased, the root-mean-square value of the hydrodynamic force coefficient in the y direction and the mean value of the hydrodynamic force coefficient in the x direction both had a decreasing tendency. (c2022 Elsevier Ltd.)

OFFSHORE STRUCTURE 1,561,700

ON THE COMPLEMENTARITY OF THE SLENDER-BODY AND NEWMAN'S APPROXIMATIONS FOR DIFFERENCE-FREQUENCY SECOND-ORDER WAVE LOADS ON SLENDER CYLINDERS

L.H.S.Carmo and A.N.Simos (Sao Paulo Univ). *OCEAN ENGINEERING* v.259, 9/1/2022. (ISSN 0029-8018; Article no.111905)

As reported in the literature, Newman's and the slender-body approximations for second-order wave loads (the latter often referred to as Rainey's equation) present an interesting complementarity for the case of a bottom mounted vertical cylinder, indicating that each one captures different physical aspects of the problem. In light of that result, the present work aims at analyzing this complementarity by inspecting the different components that constitute the second-order wave loads, including the ones due to body motions, and by relating them to the incident and diffracted waves. This is done by analyzing the case of a single surface piercing cylinder under the action of long-crested bichromatic waves, first considered to be bottom mounted and then in floating condition. It is also shown that the second-order terms from Rainey's formulation are indeed relevant, reminding one that the common practice of analyzing second-order loads by simply applying Morison's equation with second-order wave kinematics is not strictly correct. In order to include the effects of body motions, Rainey's equation, which can be seen as an extension of the inertial part of Morison's equation to include nonlinear terms, is combined with Pinkster's approach for the low-frequency second-order loads on floating bodies. This combination is made in order to allow the evaluation of the forces considering the mean body position, in opposition to the original approach that considers the instantaneous body position, allowing an IFFT algorithm to efficiently compute second-order wave loads in a real sea condition directly in time domain. As a drawback of the slender-body approximation, end effects due to the extremities of the cylinder and effects due to wave scattering and radiation are lost, as is the case when using Morison's equation to evaluate first-order loads, and the question is to what extent they can be neglected when dealing with second-order wave loads. (c2022 Elsevier Ltd.)

OFFSHORE STRUCTURE 1,561,701

USING ANN TO STUDY VIV OF FLEXIBLE CYLINDERS IN UNIFORM AND SHEAR FLOWS

J.Song, W.Chen, S.Guo and D.Yan (Beijing Inst Mechanics). *OCEAN ENGINEERING* v.259, 9/1/2022. (ISSN 0029-8018; Article no.111909)

The ANN model trained on experimental datasets is developed, especially based on the characteristics of flexible cylinder's VIV, the Bayesian regularization back propagation algorithm is employed to train the presented neural network. Nine intuitive physical parameters are selected according to the governing equations of cylinder dynamics. The results show that the neural network trained with intuitive physical quantity can acceptable predictions predict VIV, and the linear regression value is 0.940. In addition, the range of model parameters is limited in the trained neural network, with around 20% error. (c2022 Elsevier Ltd.)

OFFSHORE STRUCTURE 1,561,702

STUDY ON HYSTERETIC PERFORMANCE OF WELDED T-JOINTS CIRCULAR TUBE ON PLATFORM CONSIDERING SEAWATER CORROSION

Y.Yang, X.Chen, Y.Liu, T.Xu, P.Chen and Z.He (Dalian Univ Technol). *OCEAN ENGINEERING* v.259, 9/1/2022. (ISSN 0029-8018; Article no.111942)

In this study, the macroscopic hysteretic mechanical behaviour of welded circular tube T-joints corroded by seawater was evaluated through hysteretic mechanical performance tests. Full immersion accelerated electrochemical corrosion tests with a proportioned seawater medium were conducted on steel specimens obtained from tube joints. The generalised degradation rule of the mechanical performance of the material with the development of corrosion was obtained via a monotonic tensile test of steel specimens. The hysteresis test of corroded joints revealed that corrosion and cyclic loading have degradation effects on joint strength, stiffness, bearing capacity, and energy dissipation. At a low number of cycles, the effect of corrosion is generally greater than that of cyclic loading. A hysteretic skeleton model that can determine the ultimate load of the corroded joint was established based on the load-displacement curve. Moreover, the hysteretic rules that describe the degradation characteristics of the loading and unloading stiffness were established. Finally, the hysteresis model of corrosion joints was proposed. The model was validated using experimental results, and we demonstrated that it can accurately reflect the effect of the degree of corrosion and loading process on the hysteretic characteristics of joints. (c2022 Elsevier Ltd.)

OFFSHORE STRUCTURE 1,561,703

INSTABILITY AND FAILURE OF SUBSEA STRUCTURES

F.P.Gao and Z.Y.Yin (Chinese Academy Sciences; Hong Kong Polytechnic Univ). *JOURNAL OF MARINE SCIENCE AND ENGINEERING* v.10, no.8, Aug. 2022. (ISSN 2077-1312; Article no.1001)

Subsea engineering structures are evolutive systems with high diversity--e.g., submarine pipelines, foundations for offshore platforms or wind turbines, deep-sea submersibles, and underwater tunnels. Such subsea engineering structures are generally designed to have a reasonably long and safe operational life. Nevertheless, they are vulnerable to extreme marine environmental conditions, such as breaking waves, submarine landslides, and operational loads. As such, the safety and resilience of the subsea infrastructural developments are extremely dependent on the stability, deformability, ductility and strength of subsea structures or materials. The complicated interactions between the environmental fluids, subsea structures and the seabed could bring numerous geohazards, foundation instabilities, structural or material failures. This special issue on the instability and failure of subsea structures includes eighteen contributions focusing on fundamental and applied studies that may contribute to an understanding of and improvement in subsea structures (e.g., pile or monopile foundations); spudcan foundations, suction caissons, subsea mattress, deep-water anchors, submarine pipelines, underwater tunnel linings, and subsea shuttle tanker, and seabed

soils or materials for deep-sea submersibles (e.g., marine sands, soft soils, gas hydrate-bearing sediments, and Ti-6Al-4V ELI alloys). A brief overview of all the contributions is given that emphasizes the main topics and the findings of their analyses.

OIL IN WATER EMULSION 1,561,704

THE ATTRACTION BETWEEN LIKE-CHARGED OIL-IN-WATER EMULSION DROPLETS INDUCED BY IONIC MICELLES

S.Liu, Y.Hu, J.Xia, N.Li, H.Fan and M.Duan (Southwest Petroleum Univ; Harvard Univ; China Univ Petroleum). *COLLOIDS AND SURFACES A: PHYSICOCHEMICAL AND ENGINEERING ASPECTS* v.654, 12/5/2022. (ISSN 0927-7757; Article no.130143)

Although extensive work has been reported that micelles can induce depletion attraction between two solid spheres or a sphere and a plate, the effect of different micelles on the depletion between two soft surfaces has been rarely reported. Optical tweezers were used to measure the forces between two oil-in-water emulsions in solutions of sodium dodecylbenzenesulfonate (SDBS), cetyltrimethylammonium bromide (CTAB), and octylphenol polyoxyethylene ether with ten oxyethylene glycol ether (OP-10) at varying concentrations. When the concentration of surfactant below their critical micelle concentration (cmc), force profiles between two emulsion droplets were purely repulsive. As the concentration of SDBS or CTAB above its cmc, the attraction between like-charged O/W emulsion droplets was dominant. The coalescence of the like-charged O/W emulsion droplets is observed. For nonionic surfactants OP-10, even if the cmc had been reached, the attractive force between O/W emulsion droplets couldn't be measured. Results shows that attractive forces between two like-charged emulsion droplets of several microns in solution can also be induced by ionic micelles and the depletion was enhanced by counterion osmotic pressure. Our work suggests that the effect of micelle-induced depletion on the force between two solid surfaces can be used to predict forces between several micrometers of emulsion droplets. (c2022 Elsevier B.V.)

OIL PRODUCING 1,561,705

MULTI-PHASE REGULATION AND CONTROL MULTI-WELL PUMPING UNIT

X.Wu, X.Han, H.Liang, H.Chen, M.Han, Y.Zhang, Z.Jiao and Y.Zhang, asrs. (China Recovery Tech Co Ltd). *World* 2022/205,773A1, p. 10/6/2022, f. 9/8/2021 (Appl. 2,117,064), pr. China 4/1/2021 (Appl. 2021-20,665,562) (E21B-0043/00). (In Chinese)

The present invention provides a multi-phase regulation and control multi-well pumping unit, which relates to an oil exploitation installation and comprises: a power portion outputting torque via a rotating shaft; a crank portion comprising at least two crank mechanisms, the two crank mechanisms being fixedly connected to two ends of the rotating shaft respectively, and free ends of the crank mechanisms being connected to power flexible ropes; and a power output portion comprising a plurality of power flexible rope guide assemblies which are uniformly distributed along the circumference of the power output portion, and the multiple power flexible rope guide assemblies being fixed on a power output rack. The free end of the crank mechanism is fixedly connected to one end of the power flexible rope, and the other end of the power flexible rope provides power output to the outside by means of the power flexible rope guide assembly. According to the pumping unit system, the two ends of the rotating shaft drive the double cranks to serve as power sources, and the multiple power flexible ropes lead from double crank power output mechanisms to drive multiple pumping wells to operate by means of the uniformly distributed guide assemblies, such that the energy consumption of the multi-well pumping unit system can be effectively reduced, thereby improving the productivity.

OIL PRODUCING 1,561,706

TEXTURED RESILIENT SEAL FOR A SUBSURFACE SAFETY VALVE

R.G.Dusterhoft, S.W.J.Ng and J.D.Vick, Jr., asrs. (Halliburton Energy Service). *World* 2022/203,695A1, p. 9/29/2022, f. 4/6/2021 (Appl. 2,126,019), pr. U.S. 3/26/2021 (Appl. 213,668) (E21B-0034/10; E21B-0021/10; F16J-0015/02).

A resilient seal includes an annular body portion and a seating surface defined by the annular body portion and configured to interface with a seat of a subsurface safety valve. The resilient seal further includes a plurality of sealing surfaces defined by the annular body portion. Each sealing surface of the plurality of sealing surfaces is positioned to interface with a flapper of the subsurface safety valve in a closed position of the flapper of the subsurface safety valve. Additionally, the resilient seal includes at least one annular channel defined by the annular body portion between adjacent sealing surfaces of the plurality of sealing surfaces.

OIL RECOVERY 1,561,707

GOLF-TYPE GAS LIFT BALL, GAS LIFT OIL RECOVERY DEVICE, CONTROL SYSTEM, AND CONTROL METHOD

Z.Wu. *World* 2022/199,639A1, p. 9/29/2022, f. 3/23/2022 (Appl. 2,282,620), pr. China 3/25/2021 (Appl. 2021-10,321,616), China 3/25/2021 (Appl. 2021-20,613,582), China 8/18/2021 (Appl. 2021-10,950,759), China 8/18/2021 (Appl. 2021-21,944,884) and China 12/6/2021 (Appl. 2021-11,477,316) (E21B-0043/12; E21B-0047/12). (Assigned to Z.Wu; **In Chinese**)

A golf-type gas-lift ball is used to lift oil and gas by relying on high-pressure gas to provide power in a gas-lift tubing. The gas-lift tubing is a tee pipe, and it comprises a gas supply pipe, a lift pipe, and a tail pipe. The golf-type gas-lift ball comprises a body and a plurality of protrusions provided on an outer side wall of the body. The protrusions are hard pointed blocks or soft burrs. The diameter of the body is less than the inner diameter of the gas supply pipe, and the diameter of the body is less than the inner diameter of the lift pipe. A gas-lift oil recovery device having a gas-lift ball and an oil recovery device control system and control method are also disclosed herein. The gas-lift oil recovery device having a gas-lift ball comprises a golf-type gas-lift ball, a ball collecting and pitching device, and a staged starting device. The gas-lift oil recovery device having a gas-lift ball can effectively improve the efficiency of oil and gas lifting.

OIL WATER SEPARATION 1,561,708

MAGNETICALLY SEPARABLE MESOPOROUS Fe₃O₄@g-C₃N₄ AS A MULTIFUNCTIONAL MATERIAL FOR METALLIC ION ADSORPTION, OIL REMOVAL FROM THE AQUEOUS PHASE, PHOTOCATALYSIS, AND EFFICIENT SYNERGISTIC PHOTOACTIVATED FENTON REACTION

H.Mao, Q.Zhang, F.Cheng, Z.Feng, Y.Hua, S.Zuo, A.Cui and C.Yao (Changzhou Univ). *INDUSTRIAL & ENGINEERING CHEMISTRY RESEARCH* v.61, no.25, pp.8895-8907, 6/29/2022. (ISSN 0888-5885; ISSN 1520-5045)

Water pollution is a global problem. Therefore, efficient methods for oil/water separation, degradation of organic dyes, and adsorption of metal ions from wastewater are urgently needed for environmental protection. Herein, mesoporous g-C₃N₄, nanosized Fe₃O₄, and aminopropyl triethoxysilane were used as raw materials to assemble a multifunctional magnetic water purification material (MPG-C₃N₄/Fe₃O₄/NH₂). The homogeneously dispersed Fe₃O₄ particles and hydrophobic hydrocarbon chain on the surface endows it with excellent magnetic oil/water separation properties even after 10 cycles. MPG-C₃N₄/Fe₃O₄/NH₂ possesses a prominent adsorption capacity of as high as 93.45 mg/ for Cu-metallic ions. The adsorption of Cu²⁺ on MPG-C₃N₄/Fe₃O₄/NH₂ is in accordance with the second-order kinetic model and the Langmuir monolayer adsorption model. Notably, MPG-C₃N₄/Fe₃O₄/NH₂ can degrade organic pollutants because of its photocatalytic ability due to the heterojunction formation between MPG-C₃N₄ and Fe₃O₄ nanoparticles. The hydrophobic surface allows more oxygen to enter the heterogeneous degradation system,

improving the efficiency of O₂ to receive photogenerated electrons to convert into superoxide anion radicals (O₂(dot)-). Surprisingly, MPG-C₃N₄/Fe₃O₄/NH₂ can be used as a heterogeneous photoactivated Fenton catalyst with brilliant degradation rates and efficiency (as high as 95% within 40 min) toward complicated organic pollutants—for example, RhB, phenol, and BPA—with favorable reusability.

OIL WATER SEPARATOR 1,561,709

THE IMPACT OF RISER-INDUCED SLUGS ON THE DOWNSTREAM DEOILING EFFICIENCY

S.Pedersen and M.V.Bram (Aalborg Univ). *JOURNAL OF MARINE SCIENCE AND ENGINEERING* v.9, no.4, April 2021. (ISSN 2077-1312; Article no.391)

In oil and gas productions, the severe slug is an undesired flow regime due to the negative impact on the production rate and facility safety. This study examines the severe riser-induced slugs' influence on a typical separation process, consisting of a 3-phase gravity separator physically linked to a deoiling hydrocyclone. Four inflow scenarios are compared: uncontrolled, open-loop, feasible, and infeasible closed-loop anti-slug control, respectively. Three PID controllers' coefficients are kept constant for all the tests: the separator pressure, water level, and hydrocyclone pressure-drop-ratio (PDR) controllers. The simulation results show that the separation efficiency is significantly larger in the closed-loop configuration, probably due to the larger production rates which provide a preferable operation condition for the hydrocyclone. It is concluded that both slug elimination approaches improve the separation efficiency consistency, but that the closed-loop control provides the best overall separation performance.

OIL WATER SEPARATOR 1,561,710

A BIOMIMETIC JANUS DELIGNIFIED WOOD MEMBRANE WITH ASYMMETRIC WETTABILITY PREPARED BY THIOL-OL CHEMISTRY FOR UNIDIRECTIONAL WATER TRANSPORT AND SELECTIVE OIL/WATER SEPARATION

K.Wang, X.Liu, Y.Dong, S.Zhang and J.Li (Nanjing Forestry Univ; Beijing Forestry Univ). *COLLOIDS AND SURFACES A: PHYSICO-CHEMICAL AND ENGINEERING ASPECTS* v.652, 11/5/2022. (ISSN 0927-7757; Article no.129793)

Inspired by the amazing intelligent water manipulation behavior of cactus, spiders, and desert beetles, tremendous efforts have been devoted to developing intelligent Janus membrane materials with asymmetric wettability for unidirectional water transport and selective water/oil separation. However, the remaining challenges include tedious procedures, harsh conditions, expensive devices, and scaling-up problems. Inspired by the oriented tubular porosity and hierarchical scaffold of wood, biomimetic Janus wood membranes with asymmetric wettability were prepared by direct ultraviolet-induced thiol-ol chemistry. The delignified wood membranes were first prepared by the partial removal of hemicellulose and lignin from the natural balsa wood. Subsequently, an octadecanethiol/ethanol solution was sprayed onto the one side of the delignified wood membrane surfaces. After ultraviolet irradiation under ambient conditions, Janus wood membranes with asymmetric wettability were successfully prepared. The resultant Janus wood membranes exhibited unidirectional water-transport ability and selective oil/water separation; both heavy oil/water and light oil/water mixtures could be separated by merely changing the orientation of the membrane. In addition, the Janus wood membranes showed excellent separation efficiency and recyclability. This novel, facile, scalable, and low-cost strategy for preparing Janus membranes holds great potential for applications in several fields, such as droplet manipulation, multi-liquid separation, purification of industrial wastewater, and microfluidics. (c2022 Elsevier B.V.)

PILING 1,561,711

PILE DRIVING IN HEAVILY OVERCONSOLIDATED CLAYS

R.F.Stevens, C.Millan, U.Gupta and G.Park (Fugro USA Marine Inc; BHP; McDermott Inc). *OFFSHORE TECHNOLOGY*

CONFERENCE [OTC] (Houston, TX, 5/2-5/2022) PROCEEDINGS 2022. (ISBN 978-1-61399-852-6; OTC-31834; Available at <http://www.onepetro.org> as of 6/23/2022; 24 pp)

Results are presented for the driving of 48-inch-diameter, open-ended piles in heavily overconsolidated clay for a fixed offshore platform located about 28 miles off the northeast coast of Trinidad. A comparison of observed and predicted blow counts, measured maximum driving stresses, the energy transmitted to the pile, and the soil resistance to driving for different damping factors are presented. The results of signal-matching analyses are also presented. (Copyright 2022 OTC)

PILING 1,561,712

DYNAMIC RESPONSE OF A FOUR-PILE GROUP FOUNDATION IN LIQUEFIABLE SOIL CONSIDERING NONLINEAR SOIL-PILE INTERACTION

Y.Yu, X.Bao, Z.Liu and X.Chen (Shenzhen Univ). *JOURNAL OF MARINE SCIENCE AND ENGINEERING* v.10, no.8, Aug. 2022. (ISSN 2077-1312; Article no.1026)

Piles, which are always exposed to dynamic loads, are widely used in offshore structures. The dynamic response of the pile-soil-superstructure system in liquefiable soils is complicated, and the interaction between the pile and soil and the pile volume effect are the key influencing factors. In this study, a water-soil fully coupled dynamic finite element-finite difference (FE-FD) method was used to numerically simulate the centrifuge shaking table (CST) test of a four-pile group in saturated sand soil. An interface contact model was proposed to simulate the pile-soil interaction, and a solid element was used to consider the volume effect of the pile. The acceleration responses of the soil and pile, settlement deformation, excess pore water pressure, and bending moment were examined. The results show that the bending moment response of the two piles parallel to the shaking direction show minor differences, while the two piles perpendicular to the shaking direction show almost the same distribution. The values of excess pore water pressure at the same depth but different azimuth angles around the pile are also different. The numerical simulation can accurately reproduce soil deformation and pile internal force during and after dynamic loading.

PLATFORM JACKET 1,561,713

AN EFFICIENT MONTE-CARLO SIMULATION FOR THE DYNAMIC RELIABILITY ANALYSIS OF JACKET PLATFORMS SUBJECTED TO RANDOM WAVE LOADS

W.Lin and C.Su (South China Univ Technol). *JOURNAL OF MARINE SCIENCE AND ENGINEERING* v.9, no.4, April 2021. (ISSN 2077-1312; Article no.380)

The growing demand for the application of jacket platforms in deep water requires more attention on the assessment of structural reliability. This paper is devoted to the dynamic reliability analysis of jacket platforms subjected to random wave loads with the Monte-Carlo simulation (MCS), in which a sample size of the order of magnitude of 10⁴ to 10⁵ for repeated time-history analyses is required for small failure probability problems, and a duration time up to three hours needs to be considered in the time-history analyses for a specific sea condition. To tackle the difficulty involved in the MCS, the explicit time-domain method (ETDM) is used for the required time-history analyses of jacket platforms, in which truncated explicit expressions of critical responses with regards to the contributing loading terms are first established and then used for numerous repeated sample analyses. The use of ETDM greatly enhances the computational efficiency of MCS, making it feasible for the dynamic reliability analysis of jacket platforms under random wave loads. A jacket platform with 11,688 degrees of freedom was analyzed for the evaluation of dynamic reliability under a given sea condition, indicating the accuracy and efficiency of the present approach and its feasibility to practical structures.

PLATFORM JACKET 1,561,714

THE EFFECTS OF INSTALLATION ON THE ELASTIC STIFFNESS COEFFICIENTS OF SPUDCAN FOUNDATIONS

W.L.Lin, Z.Wang, F.Liu and J.T.Yi (Chongqing Univ). *JOURNAL OF MARINE SCIENCE AND ENGINEERING* v.9, no.4, April 2021. (ISSN 2077-1312; Article no.429)

Subjected to pre-load, spudcan foundations, widely utilized to support offshore jack-up rigs, may penetrate in a few diameters into soft clays before mobilizing sufficient resistance from soil. While its stress-strain behavior is known to be affected by the embedment condition and soil backflow, the small-strain calculation with wished-in-place assumption was previously adopted to analyze its elastic stiffness coefficients. This study takes advantage of a recently developed dual-stage Eulerian-Lagrangian (DSEL) technique to re-evaluate the elastic stiffness coefficients of spudcans after realistically modelling the deep, continuous spudcan penetration. A numerical parametric exercise is conducted to investigate the effects of strength non-homogeneity, embedment depths, and the spudcan's size on the elastic stiffness. On these bases, an expression is provided such that the practicing engineers can conveniently factor the installation effects into the estimation of elastic stiffness coefficients of spudcans.

PLATFORM JACKET 1,561,715

DYNAMIC PERFORMANCE AND CRASHWORTHINESS ASSESSMENT OF HONEYCOMB REINFORCED TUBULAR PIPE IN THE JACKET PLATFORM UNDER SHIP COLLISION

H.Lin, C.Han, L.Yang, H.Karampour, H.Luan, P.Han, H.Xu and S.Zhang (China Univ Petroleum; Griffith Univ). *JOURNAL OF MARINE SCIENCE AND ENGINEERING* v.10, no.9, Sept. 2022. (ISSN 2077-1312; Article no.1194)

The collision between the pipe legs of jacket platforms and bypassing ships is of great concern for the safety assessment of platforms. Honeycomb structures have been widely used owing to their unique deformation and mechanical properties under dynamic impact loads. In this paper, two typical honeycomb structures, namely hexagonal honeycomb and arrow honeycomb, were constructed for the impact protection of inclined pipe legs in jacket platforms, and the present study aimed to assess the dynamical performance and crushing resistance of the designed honeycomb reinforced structure under ship collision by using the numerical simulation software ANSYS/LS-DYNA. The dynamical performance of the honeycomb reinforced pipe leg was investigated considering various influential parameters, including the impact velocity and impact direction. The crashworthiness of the two types of honeycomb was evaluated and compared by different criteria, namely the maximum impact depth (δ_{max}), specific energy absorption (SEA) and the proposed index offset sliding (OS). The results demonstrated that both the hexagonal honeycomb structure and the arrow honeycomb structure can reduce the damage of inclined pipe legs caused by ship collision, while the hexagonal honeycomb can provide the better anti-collision capacity, which can well reduce the offset sliding and better protect the pipe leg from ship collision.

PLATFORM JACKET 1,561,716

IMPACT OF DESIGN PARAMETERS ON THE DYNAMIC RESPONSE AND FATIGUE OF OFFSHORE JACKET FOUNDATIONS

A.Marjan and P.Hart (Cranfield Univ). *JOURNAL OF MARINE SCIENCE AND ENGINEERING* v.10, no.9, Sept. 2022. (ISSN 2077-1312; Article no.1320)

The lifetime of offshore foundations is governed by a combination of harsh environmental conditions and complex service loads. The fatigue limit state (FLS) analysis needs to be performed in the time domain to capture the complex phenomenon. This study aims to investigate different parameters and design modifications that can impact the design life of an offshore jacket foundation. An OC4 jacket foundation is designed in industrial software from DNV and reduced to a super-element model. The super-element model is connected to an NREL 5-MW wind turbine designed in Bladed. The

time-series loads are used to compute the fatigue damages faced by the foundation during the service life. The impact of soil non-linearity, marine growth, scour size, the mass of the transition piece, and the grouted connection's design on the dynamic response and fatigue damages are compared. A 30% increase in life was observed by replacing the concrete transition piece with a lightweight steel configuration. The fatigue damages were considerably greater for the inclined pile in the leg grouted connection than for the leg in the pile concept. The study provides a different perspective by analysing the effect of design parameters and design changes in the complex and computationally expensive time-series domain.

PLATFORM JACKET 1,561,717

MODEL TESTS ON JACKING INSTALLATION AND LATERAL LOADING PERFORMANCE OF JACKET FOUNDATION IN SAND

J.Liu, J.Chen, X.Huang, W.Zhou and Z.Guo (Qingdao Univ Technology; Zhejiang Univ). *OCEAN ENGINEERING* v.259, 9/1/2022. (ISSN 0029-8018; Article no.111738)

The long-term dynamic behavior of pile under cyclic loads is important for the stability and safety characteristics of jacket supported offshore wind turbine. In this study, large-scale indoor model tests were carried out on the jacking installation and lateral loading of jacket foundation in sand. For the process of pile installation, it shows that the linear growth of pile tip resistance during installation can be divided into two stages, and its critical depth (the depth at which the growth rate of pile tip resistance begins to decrease significantly) is 11D (diameter). The jacking resistance of latter pile is significantly greater than that of former pile. Under static load, the maximum bending moment point of front row pile is higher than that of back row pile. The depth of bending moment reverse point is also 11D for front and back row piles. Under cyclic loads, the displacement at tower top undergoes two stages: rapid growth stage and slow growth stage. The friction resistance of back row pile increases first and then decreases along depth, showing an oblique "V" shape. The natural frequency varies with different load frequencies and cyclic load ratios. The evolution trend of system damping ratio and natural frequency is roughly opposite. (c2022 Elsevier Ltd.)

PLATFORM JACKET 1,561,718

SCOUR EFFECTS ON THE BEARING CAPACITY OF MULTI-BUCKET JACKET FOUNDATION FOR OFFSHORE WIND TURBINES

J.Li, Y.Guo, J.Lian and H.Wang (Tianjin Univ). *OCEAN ENGINEERING* v.259, 9/1/2022. (ISSN 0029-8018; Article no.111848)

The Multi-Bucket Jacket Foundation (MBJF) is presently being installed in Chinese wind farms with increasing numbers. Compared to monopiles, MBJF is a shallow foundation and the effect of scouring on the bearing capacity is more significant. This research proposes a universal three-dimensional model of the MBJF with local scour to efficiently estimate the effect of scouring on the MBJF bearing capacity. Firstly, using the proposed model, the ultimate bearing capacity is calculated under a single load, and the discounting effect of different scour ranges and scour depths on the ultimate bearing capacity is evaluated. Furthermore, the fixed load-displacement approach is used to calculate the failure envelope of the foundation under composite loading mode, and the influence of different scour patterns on the failure envelope is compared. The findings reveal that when the scour extent and depth increase, the foundation's bearing capacity decreases non-linearly, and the foundation bearing envelope line gradually shrinks. Under the condition that the ultimate vertical load is not exceeded, a rise in vertical load can enhance the ultimate load capacity after scouring to a certain extent. Finally, the calculated envelopes are integrated with engineering applications to quantify the safety redundancy of the MBJF bearing capacity for different seabed morphologies. The method and results can provide methodological support for the accurate prediction and efficient assessment of the MBJF's post-scour bearing capacity. (c2022 Elsevier Ltd.)

PRODUCING EQUIPMENT 1,561,719

RESULTS OF APPLICATION DEMONSTRATION OF AUTONOMOUS OFFSHORE POWER SYSTEM SUPPORTING MULTIPLE MOBILE AND STATIC ASSETS

A.R.Lesemann and E.J.Hammagren (C-Power). *OFFSHORE TECHNOLOGY CONFERENCE [OTC] (Houston, TX, 5/2-5/2022) PROCEEDINGS* 2022. (ISBN 978-1-61399-852-6; OTC-31818; Available at <http://www.onepetro.org> as of 6/23/2022; 14 pp)

Over the last decade, several technology trends have dominated the innovation cycle within the terrestrial economy. Electrification, cloud computing, decarbonization, digitization, and autonomy are representative examples of macro trends that have had a rapid and fundamental impact; an impact felt not only in user-facing technologies, such as electric vehicles and software-as-a-service, but also in the infrastructure required to deliver those technologies. However, the scale of the impact and rollout has not been felt equally between the terrestrial and ocean economies. The innovation cycle in the ocean economy is significantly slower. What accounts for the difference and are there solutions to this issue? One obvious cause is the increased time, complexity, risk, and cost of offshore operations compared to similar activities on land. These differences impede the rapid development, demonstration, and field deployment of innovative technologies offshore. However, by their nature, high cost, long duration offshore operational activities, coupled with unrelenting competitive, policy and environmental pressures, create attractive opportunities to reduce cost, complexity, and risk. These operational improvement opportunities are now coupled with the ever-increasing external push and internal pull around decarbonization and the goal of net zero operations. Said another way, there is much to gain through technological innovation offshore. However, a major obstacle stands in the way: reliable power supplies at sea. The traditional methods of providing power, which must always be brought on site, are through expensive infrastructure: ships, platforms, and subsea umbilicals. Even unattended energy storage, i.e., batteries, which represent a step forward, is not a comprehensive solution. Constrained energy availability, coupled with the need for retrieval and replacement, dampen the cost, complexity, and carbon savings of this pathway. (Copyright 2022 OTC)

PRODUCING WELL 1,561,720

MONITORING DEPOSITION IN FLUID FLOWLINES THAT CONVEY FLUIDS DURING WELLBORE OPERATIONS

D.Bennett, S.Daly, C.Fudge, D.Latiolais, S.Horner, P.Prince and O.Ogundare, asrs. (Halliburton Energy Service). *World* 2022/212,117A1, p. 10/6/2022, f. 3/22/2022 (Appl. 2,221,283), pr. U.S. 4/1/2021 (Appl. 220,496) (E21B-0047/06; E21B-0047/26; G06N-0020/00).

A system can control a transmission of a pressure signal subsea into a flowline comprising a fluid. The system can receive sensor data indicating one or more properties of a first reflection signal corresponding to the pressure signal in the flowline. The system can adjust a model based on the one or more properties of the first reflection signal. The model can be configured for determining a presence of a material deposition in the flowline. The system can determine, based on a second reflection signal and the adjusted model, a presence of the material deposition in the flowline. The system can output a command configured to initiate a remediation operation to reduce the material deposition in the flowline.

PRODUCING WELL 1,561,721

METHODS TO USE CHEMO-RESISTIVE SENSORS FOR WELLBORE PRODUCTION

D.E.Jamison, W.Shumway and P.A.May, asrs. (Halliburton Energy Service). *World* 2022/211,817A1, p. 10/6/2022, f. 4/1/2021 (Appl. 2,125,447), pr. U.S. 3/31/2021 (Appl. 219,114) (G01N-0033/00; G01N-0021/3504; G01N-0027/04; G01N-0027/407; G01N-0033/24).

The disclosure provides a method for determining a composition of a fluid. The method comprises diverting a sample of a portion of the fluid to a test chamber. The method further comprises actuating a heat source disposed around the test chamber to increase the temperature within the test chamber to produce vapors from the

sample of the portion of the fluid and directing the vapors from the sample of the portion of the fluid to a chemical sensor array comprising one or more chemical sensors. The method further comprises determining a composition of the vapors from the sample of portion of the fluid, wherein the composition of the vapors is associated with the composition of the fluid.

PRODUCTION ALLOCATION 1,561,722

DECOMPOSITION AND ALLOCATION METHOD OF ENERGY CONSUMPTION QUOTA FOR OIL ENTERPRISES BASED ON REASONABLE ENERGY CONSUMPTION OF OIL RESERVOIR: A CASE OF SHENGLI OILFIELD

Z.Li, D.Li, S.Bing, W.Xiao, H.Zhang, Y.Xu, W.Zheng and X.Yang (Shengli Oilfield Co; Shengli Oilfield Res Inst). *PETROLEUM GEOLOGY AND RECOVERY EFFICIENCY (YOUQI DIZHI YU CAISHOULU)* v.29, no.6, pp.77-84, Nov. 2022. (ISSN 1009-9603; In Chinese)

[Full article and English abstract available from P.A.]

PRODUCTION PLATFORM 1,561,723

REVIEW ON FIXED AND FLOATING OFFSHORE STRUCTURES: PART I: TYPES OF PLATFORMS WITH SOME APPLICATIONS

C.V.Amaechi, A.Redda, H.O.Butler, I.A.Ja'e and C.An (Lancaster Univ; Curtin Univ; Denmark Tech Univ; Petronas Univ; China Univ Petroleum). *JOURNAL OF MARINE SCIENCE AND ENGINEERING* v.10, no.8, Aug. 2022. (ISSN 2077-1312; Article no.1074)

Diverse forms of offshore oil and gas structures are utilized for a wide range of purposes and in varying water depths. They are designed for unique environments and water depths around the world. The applications of these offshore structures require different activities for proper equipment selection, design of platform types, and drilling/production methods. This paper will provide a general overview of these operations as well as the platform classifications. In this paper, a comprehensive review is conducted on different offshore petroleum structures. This study examines the fundamentals of all types of offshore structures (fixed and floating), as well as the applications of these concepts for oil exploration and production. The study also presents various design parameters for state-of-the-art offshore platforms and achievements made in the industry. Finally, suitable types of offshore platforms for various water depths are offered for long-term operations. An extension of this study (Part II) covers sustainable design approaches and project management on these structures; this review helps designers in understanding existing offshore structures, and their uniqueness. Hence, the review also serves as a reference data source for designing new offshore platforms and related structures.

PRODUCTION PLATFORM 1,561,724

OFFSHORE HYBRID GAS EXPORT SYSTEMS AND METHODS

M.I.L.Souza, R.L.Bodanese and L.G.Bodanese, asrs. (Horton Brasil Tecnol Ltda). *World* 2022/198,294A1, p. 9/29/2022, f. 3/23/2022 (Appl. 2,250,104), pr. U.S. 3/23/2021 (Appl. 63/164,927) (B63B-0035/44; B63B-0035/00; B65D-0088/78; E21B-0043/01).

An offshore system for producing and exporting hydrocarbon gas comprises a production platform configured to receive the hydrocarbon gas from one or more subsea wells in an offshore production field; a subsea manifold; a fluid transfer conduit extending from the production platform to the subsea manifold, wherein the fluid transfer conduit is configured to supply the hydrocarbon gas from the production platform to the subsea manifold; a first subsea gas storage device in selective fluid communication with the subsea manifold, wherein the first subsea gas storage device is configured to temporarily store the hydrocarbon gas; a first gas export assembly coupled to the subsea manifold and in selective fluid communication with the subsea manifold, wherein the first gas export assembly is configured to supply the hydrocarbon gas from the manifold to a first export vessel releasably coupled to the first gas export assembly.

RISER PIPE 1,561,725

TEST SYSTEM DEVELOPMENT AND EXPERIMENTAL STUDY ON THE FATIGUE OF A FULL-SCALE STEEL CATENARY RISER

J.Yu, F.Wang, Y.Yu, X.Liu, P.Liu and Y.Su (Tianjin Univ). *JOURNAL OF MARINE SCIENCE AND ENGINEERING* v.10, no.9, Sept. 2022. (ISSN 2077-1312; Article no.1325)

This paper presents a full-scale deep-water steel catenary riser fatigue test system. The proposed system can carry out fatigue tests on steel catenary risers, hoses, and subsea pipelines up to 21 m in length, ranging from 8 to 24 inches in diameter. The test system was realized by mechanical loading with loading control systems, and could carry out axial tension and compression, bending moment, torsion, and internal pressure to simulate all load types on deep-water steel catenary risers or subsea pipelines. The counterforce was sustained by a counterforce frame. Through mechanical simulation analysis, the authors determined the size of the counterforce frame and designed the connection form of the counterforce frame and loading system. According to the required loading capacity, the appropriate cylinder thickness and diameter were obtained through calculation. After the design and construction of the test system, the authors designed a fatigue test to confirm the loading capacity and accuracy of the test system. The authors performed full-scale testing to assess the fatigue performance of pipe-to-pipe mainline 5G girth welds fabricated to BS 7608. This test was designed according to the stress level of pipelines in the Lingshui 17-2 gas field, and the test results were compared with the calculation results of the S-N curve.

RISER PIPE 1,561,726

ASSESSMENT OF NEW MATERIALS IN UNBONDED FLEXIBLE PIPES

L.C.Bayout, F.Migeon and F.Sarrasin (Bureau Veritas Marine). *OFFSHORE TECHNOLOGY CONFERENCE [OTC] (Houston, TX, 5/2-5/2022) PROCEEDINGS* 2022. (ISBN 978-1-61399-852-6; OTC-31811; Available at <http://www.onepetro.org> as of 6/23/2022; 15 pp)

The present paper is related to the assessment of new materials for use in unbonded flexible pipes designed and manufactured as per API 17J. Unbonded flexible pipes are a key solution in the oil and gas industry that are used as subsea static flowlines and dynamic risers to convey various types of fluids at high-pressure, high-temperature conditions and in deepwater environments. In view of the increasingly challenging applications these pipes must withstand, unbonded flexible pipes are complex in terms of design, fabrication, and installation aspects, which leads to generally tailor-made designs. Consequently, this drives flexible pipe manufacturers to constantly develop, optimize, and qualify new solutions, including new materials for the different layers and components of the flexible pipe. This paper focuses on the process followed for incorporating new materials in the flexible pipe type approval certificate (TAC) upon verification of conformity versus API 17J. Firstly, a new material is developed or assessed, or an existing material is assessed in a new environment, with the help of methods to qualify the new technology through functional analysis and qualification - failure modes, effects, and criticality analysis (Q-FMECA), allowing us to establish the qualification program. Secondly, the API 17J requirements for qualifying a new material are outlined; these include procurement; the manufacturing process; quality assurance; small-, medium-, and full-scale tests, and the aspects of design rules. Finally, the involvement of the independent verification agent (IVA) and the IVA deliverables will be described. (Copyright 2022 OTC)

SUBSEA PRODUCTION SYSTEM 1,561,727

SYSTEMS ENGINEERING OF SUBSEA PRODUCTION SYSTEMS

A.Marcotulli and D.Wilkinson (Saipem; Endeavor Management). *OFFSHORE TECHNOLOGY CONFERENCE [OTC] (Houston, TX, 5/2-5/2022) PROCEEDINGS* 2022. (ISBN 978-1-61399-852-6; OTC-31827; Available at <http://www.onepetro.org> as of 6/23/2022; 10 pp)

Subsea production systems (SPS) are widely used throughout the upstream oil and gas industry, and can range in complexity from simple, single-well tiebacks, in shallow water, through to multi-well developments (involving subsea processing), linked back to purpose-built host facilities, in deep water and/or harsh environments. As the complexity (and cost) of the SPS being deployed has increased over the past few decades, the requirement for a more rigorous and systematic approach toward the engineering of such systems has increased. Whilst it is true that many SPS are based on "industry standard" components (when viewed at a sufficiently granular level), the reality is that every SPS is in some way unique, primarily due to the large number of boundary conditions that drive the design--be it the reservoir characteristics, produced fluid properties, water depth, seabed topography/soil conditions, environmental conditions, etc. SPS are also somewhat unusual in the upstream oil and gas industry, insofar as they typically involve the transport of multiphase flowstreams over relatively long distances, which directly impacts the complexity of the system. The inherent complexity of managing multiphase flowstreams (and/or operating subsea processing facilities) using remotely operated equipment, leads to systems where many elements of the design are "tightly coupled," as a minor change in one part of the system has the potential to significantly impact the design and operation of another part of the system, even though these "system components" may be widely separated physically. Similarly, complex systems used in other industries have been found to greatly benefit from the application of formal systems engineering (SE) processes. Whilst it is acknowledged that SE has been informally practiced in the upstream oil and gas industry for many years, the approach has typically been relatively unstructured as the various SE processes are scattered throughout existing engineering and project management processes. (Copyright 2022 OTC)

TENSION LEG PLATFORM **1,561,728**

HYDRODYNAMIC ANALYSIS OF A MODULAR FLOATING STRUCTURE WITH TENSION-LEG PLATFORMS AND WAVE ENERGY CONVERTERS

N.Ren, H.Wu, K.Liu, D.Zhou and J.Ou (Hainan Univ; Dalian Univ Technol; South China Univ Technol). *JOURNAL OF MARINE SCIENCE AND ENGINEERING* v.9, no.4, April 2021. (ISSN 2077-1312; Article no.424)

This work presents a modular floating structure, which consists of five inner tension-leg platforms and two outermost wave energy converters (denoted as MTLPW). The hydrodynamic interaction effect and the mechanical coupling effect between the five inner tension-leg platforms (TLP) and the two outermost wave energy converters (WEC) are taken into consideration. The effects of the connection modes and power take-off (PTO) parameters of the WECs on the hydrodynamic performance of the MTLPW system are investigated under both operational and extreme sea conditions. The results indicate that the hydrodynamic responses of the MTLPW system are sensitive to the connection type of the outermost WECs. The extreme responses of the bending moment of connectors depend on the number of continuously fixed modules. By properly utilizing hinge-type connectors to optimize the connection mode for the MTLPW system, the effect of more inner TLP modules on the hydrodynamic responses of the MTLPW system can be limited to be acceptable. Therefore, the MTLPW system can be potentially expanded to a large degree.

TENSION LEG PLATFORM **1,561,729**

STABILITY ANALYSIS OF A TLP WITH INCLINED TENSION LEGS UNDER DIFFERENT MARINE SURVIVAL CONDITIONS

N.Weï, Z.Zhang, X.Xu and W.Yao (Shanghai Univ; Shandong Power Eng Co Ltd). *JOURNAL OF MARINE SCIENCE AND ENGINEERING* v.10, no.8, Aug. 2022. (ISSN 2077-1312; Article no.1058)

To verify that inclined tension legs can improve the stability of the tension leg platform, this paper established the dynamic equation of a tension leg platform (TLP) under marine environmental loads by using the modified Morrison equation

considering the influence of ocean currents on wave forces. Additionally, the velocity and acceleration of random wave water particles were simulated via the JONSWAP spectrum. In addition, a three-dimensional model of a tension leg platform with inclined tension legs was established by AQWA, and its dynamic responses under variable survival conditions were compared and analyzed. The results showed that the surge and heave were more sensitive to the sea current, while the pitch was more sensitive to the wind. There is a significant difference in tendon tensions between the atypical TLP with inclined tension legs established in this study and the typical International Ship and Offshore Structures Committee (ISSC) TLP.

ULTRASONIC FLOWMETER **1,561,730**

ULTRASONIC FLOW METER

R.Konishi (Panasonic IP Mgmt Co Ltd). World 2022/202,275A1, p. 9/29/2022, f. 3/8/2022 (Appl. 229,910), pr. Japan 3/25/2021 (Appl. 2021-050,923) (G01F-0001/66). (In Japanese)

This ultrasonic flow meter includes: a cylindrical flow path having a rectangular cross section through which a fluid to be measured flows; a pair of ultrasonic transceivers located upstream and downstream of the cylindrical flow path; a measurement unit; a calculation unit; and a partition plate. The measurement unit measures the propagation time it takes for ultrasonic waves to propagate from one of the ultrasonic transceivers to the other one. The calculation unit calculates the flow velocity and flow rate of the fluid to be measured on the basis of the propagation time measured by the measurement unit. The partition plate is disposed in the cylindrical flow path so as to be parallel to the flow direction of the fluid to be measured and divides the cylindrical flow path into a plurality of divided flow paths. Moreover, the partition plate is provided with a notch part or opening part that allows communication between the division flow paths in a short-circuit path that short-circuits a normal propagation path in which the ultrasonic waves propagate along a regular path from one of the ultrasonic transceivers to the other one.

UNDERWATER PIPELINE **1,561,731**

MODELING AND DYNAMIC ANALYSIS OF A TRIPLE-TAGLINE ANTI-SWING SYSTEM FOR MARINE CRANES IN AN OFFSHORE ENVIRONMENT

M.Sun, S.Wang, G.Han, L.An, H.Chen and Y.Sun (Dalian Maritime Univ). *JOURNAL OF MARINE SCIENCE AND ENGINEERING* v.10, no.8, Aug. 2022. (ISSN 2077-1312; Article no.1146)

Payload lifting is inefficient and high-risk under rough sea conditions. Thus, it is not easy to achieve precise assembly, and the swing payload is liable to collide with other structures on deck and cause damage. In this paper, to explore the complex dynamic characteristics of a triple-tagline anti-swing system (TTAS) for marine cranes in an offshore environment, an irregular wave model was first integrated into a dynamic system model of TTAS, and the TTAS for offshore payload lifting was simplified as a constrained-pendulum system with moving base excitations. Further, the dynamic system model was established by applying the methods in robotics. Meanwhile, the dynamic characteristics were simulated and analyzed using Matlab/Simulink. The simulation results show that the in-plane angle and out-of-plane angle of the payload can be effectively suppressed, and the range of the two-dimensional trajectory of the payload is greatly reduced. The research results provide a theoretical basis for optimizing the mechanical structures of TTAS or similar equipment.

UNDERWATER PIPELINE **1,561,732**

CAPTURING THE TURNING HOOK OF STRESS-DILATANCY CURVE OF CRUSHABLE CALCAREOUS SAND

W.Jin, Y.Tao and R.Chen (Zhejiang Univ Sci Technol). *JOURNAL OF MARINE SCIENCE AND ENGINEERING* v.10, no.9, Sept. 2022. (ISSN 2077-1312; Article no.1269)

For crushable calcareous sand, the stress-dilatancy curve has a significant turning hook around the peak stress ratio, the hook

contains the main features of the loading process, including the phase transformation point and the peak stress ratio point. However, more than half of this turning hook, i.e., the line after the peak stress ratio point, is usually ignored by known stress-dilatancy models. It is difficult to directly establish the stress-dilatancy model with such turning hook characteristics, since such turning hook demonstrates that the dilatancy is not a single-valued function of the stress ratio. Based on the first law of thermodynamic, we related dilatancy to breakage energy. Then, we mapped breakage energy from the stress-energy plane to the strain-energy plane to avoid the non-single-valued function problem. Then, the stress-dilatancy model was conveniently established. Compared with the other four existing stress-dilatancy models, the benefit of our modeling process is that it can easily capture the turning hook of the stress-dilatancy curve. Our model is also verified by simulating colloidal-silica-stabilized and MICP-stabilized calcareous sands, as well as three types of calcareous sands, respectively.

UNMANNED VEHICLE 1,561,733

NUMERICAL STUDY ON HYDRODYNAMIC COEFFICIENT ESTIMATION OF AN UNDERACTUATED UNDERWATER VEHICLE

L.Hong, X.Wang, D.Zhang and H.Xu (Harbin Inst Technology). *JOURNAL OF MARINE SCIENCE AND ENGINEERING* v.10, no.8, Aug. 2022. (ISSN 2077-1312; Article no.1049)

Hydrodynamic coefficient estimation is crucial to the shape design, dynamic modeling, and control of underwater vehicles. In this paper, we conduct a numerical study on the hydrodynamic coefficient estimation of an underactuated underwater vehicle (actuated only in the surge, heave, and yaw degrees of freedom) by adopting the computational fluid dynamics (CFD) approach. Firstly, the mechanical structure of an underactuated underwater vehicle is briefly introduced, and the dynamic model of the underwater vehicle with hydrodynamic effects is established. Then, steady and unsteady Reynolds Averaged Navier-Stokes (RANS) simulations are carried out to numerically simulate the towing test, rotating arm test, and Planar Motion Mechanism (PMM) test of the underwater vehicle numerically. To simulate unsteady motions of the underactuated underwater vehicle, a sliding mesh model is adopted to simulate flows in the computational fluid domain that contain multiple moving zones and capture the unsteady interactions between the underwater vehicle and the flow field. Finally, the estimated hydrodynamic coefficients of the underwater vehicle are validated in a physical experiment platform, and the results show that the numerical estimates are in good agreement with the experimental data.

UNMANNED VEHICLE 1,561,734

VIRTUAL UNDERWATER DATASETS FOR AUTONOMOUS INSPECTIONS

I.Polymentis, M.Haroutunian, R.Norman and D.Trodden (Newcastle Univ). *JOURNAL OF MARINE SCIENCE AND ENGINEERING* v.10, no.9, Sept. 2022. (ISSN 2077-1312; Article no.1289)

Underwater vehicles have become more sophisticated, driven by the offshore sector and the scientific community's rapid advancements in underwater operations. Notably, many underwater tasks, including the assessment of subsea infrastructure, are performed with the assistance of autonomous underwater vehicles (AUVs). There have been recent breakthroughs in artificial intelligence (AI) and, notably, in deep-learning (DL) models and applications, which have widespread usage in a variety of fields, including aerial unmanned vehicles, autonomous car navigation, and other applications. However, they are not as prevalent in underwater applications due to the difficulty of obtaining underwater datasets for a specific application. In this sense, the current study utilises recent advancements in the area of DL to construct a bespoke dataset generated from photographs of items captured in a laboratory environment. Generative adversarial networks (GANs) were utilised to translate the laboratory object dataset into the underwater domain by combining the collected images with photographs containing the underwater

environment. The findings demonstrated the feasibility of creating such a dataset, since the resulting images closely resembled the real underwater environment when compared with real-world underwater ship hull images. Therefore, the artificial datasets of the underwater environment can overcome the difficulties arising from the limited access to real-world underwater images and are used to enhance underwater operations through detecting and classifying underwater object images.

UNMANNED VEHICLE 1,561,735

DESIGN AND CONTROL OF AN UNDERWATER ROBOT BASED ON HYBRID PROPULSION OF QUADROTOR AND BIONIC UNDULATING FIN

X.Zeng, M.Xia, Z.Luo, J.Shang, Y.Xu and Q.Yin (National Univ Technology; Changsha Univ Sci Technol). *JOURNAL OF MARINE SCIENCE AND ENGINEERING* v.10, no.9, Sept. 2022. (ISSN 2077-1312; Article no.1327)

Stable, quiet, and efficient propulsion methods are essential for underwater robots to complete their tasks in a complex marine environment. However, with a single propulsion method, such as propeller propulsion and bionic propulsion, it is difficult to achieve high efficiency and high mobility at the same time. Based on the advantages of the high-efficiency propulsion of a bionic undulating fin and the stable control of the propeller, an underwater robot based on the hybrid propulsion of a quadrotor and undulating fin is proposed in this paper. This paper first introduces the mechanical implementation of the underwater robot. Then, based on kinematic modeling and theoretical derivation, the underwater motion and attitude of the robot are analyzed and the 6-DOF dynamic equation of the robot is established. Finally, the underwater motion performance of the robot is verified through field experiments. The experimental results show that the robot can realize the heave motion, surge motion, and in-situ steering motion independently and can hover stably. When the undulating frequency is 6 Hz, the maximum propulsion speed of the robot can reach up to 1.2 m/s (1.5 BL/s).

VALVE 1,561,736

TRIMS FOR PRODUCING PRESSURE DROPS IN SUBJECT FLUIDS AND RELATED VALVES AND METHODS

H.C.Stibbe, asr. (Baker Hughes Oilfield LLC). World 2022/213,045A1, p. 10/6/2022, f. 3/25/2022 (Appl. 2,271,352), pr. U.S. 3/30/2021 (Appl. 217,494) (F16K-0001/36; F16K-0025/00; F16K-0047/04).

Valves configured to induce a pressure drop in a subject fluid may include an inlet, a seat, an outlet, and a valve trim located around the seat and interposed between the inlet and tire outlet. The valve trim may include an annulus including a monolithic, unitary, porous material defining a tortuous, interconnected space extending radially through the annulus. Pores at an exterior of the monolithic, unitary, porous material being arranged in a close-packed hexagonal space lattice.

VISCOUS OIL RECOVERY 1,561,737

DOWNHOLE TOOL ACTUATOR WITH VISCOUS FLUID CLEARANCE PATHS

R.G.Dusterhoft, B.R.Pickle, L.G.Collins, A.E.Beck, M.L.Apicioneck and M.W.Meaders, asrs. (Halliburton Energy Service). World 2022/211,823A1, p. 10/6/2022, f. 4/6/2021 (Appl. 2,126,014), pr. U.S. 3/29/2021 (Appl. 216,066) (E21B-0021/08; E21B-0034/08).

A flow tube is axially moveable within an actuator body between a first axial position and a second axial position for actuating a downhole tool, such as for closing a subsurface safety valve. The flow tube includes an interior flow bore for conveying fluids from the tubing string through the actuator body. An external flow tube profile defined on the flow tube includes an upper shoulder for engagement with a wiper in the first axial position, a lower shoulder for engagement with the wiper in the second axial position, and a clearance path between the upper and lower shoulders for allowing viscous flow past the wiper when the flow tube is moved between the first and second axial positions.

WALKING BEAM 1,561,738

LARGE-STROKE WALKING BEAM-TYPE OIL PUMPING UNIT

C.Zhang, asr. (Apex Oilfld Equip Co Ltd). World 2022/206,167A1, p. 10/6/2022, f. 1/29/2022 (Appl. 2,274,870), pr. China 3/31/2021 (Appl. 2021-10,346,141) (E21B-0043/00). (In Chinese)

A large-stroke walking beam-type oil pumping unit is comprised of a base and a driving mechanism fixedly installed at one end of the base, wherein a walking beam is arranged at the other end of the base by means of a support mechanism to form a walking beam type structure, a horsehead is installed at a front end of the walking beam, a rear end of the walking beam is connected to the driving mechanism by means of a connecting rod to form a crank connecting rod structure, a middle base is installed on the walking beam, the support mechanism comprises a front support and a rear support, wherein top ends of the front support and the rear support are connected to each other, and the other end of the front support and the other end of the rear support are installed on two sides of the base. By means of the oil pumping unit, the included angle between the oil pumping unit and a connecting line of a hinge member and a projection point is adjusted by adjusting the component dimensions and optimizing the support mechanism, such that stress concentration is reduced, thereby providing a service for using the crank connecting rod structure in the large-stroke walking beam-type oil pumping unit.

WATER IN OIL EMULSION 1,561,739

EFFECTS OF PARAFFIN WAX CONTENT AND TEST TEMPERATURE ON THE STABILITY OF WATER-IN-MODEL WAXY CRUDE OIL EMULSIONS

X.Xia, Z.Zhao, W.Cai, C.Li, F.Yang, B.Yao and G.Sun (China Univ Petroleum). *COLLOIDS AND SURFACES A: PHYSICOCHEMICAL AND ENGINEERING ASPECTS* v.652, 11/5/2022. (ISSN 0927-7757; Article no.129815)

Waxy crude oil is important fossil energy containing both paraffin wax and some asphaltene. The interactions between paraffin wax and asphaltene not only affect the crude oil rheology, but also the stability of crude oil emulsion. To further understand the influences of paraffin waxes on the W/O emulsion stability, in the course of this work, the effects of paraffin wax content and test temperature on the stability of W/O emulsions (with fixed asphaltene concentration of 0.5 wt%) were investigated grounded on the physical property tests of the oils, macroscopic stability measurement of the emulsions, microscopic observation of the emulsions and oil-water interfacial properties test. The results indicated that increasing the paraffin content enhances the WAT of the oils but weakens the asphaltene stability in the oil phase thus leading to the aggregation of asphaltene into a bigger size. The rheology of the model waxy oils deteriorates greatly with increasing the content of paraffin wax. The emulsion stability is outstandingly affected by the test temperature. At 30 °C (much more than the WAT), increasing the paraffin wax content benefits the asphaltene adsorption at the oil-water interface, which then reduces the interfacial tension but increases the strength of the asphaltene film formed at the interface, this facilitates the formation of smaller water droplets and improves the stability of the emulsion to some extent. At a test temperature of 15 °C (well below the WAT), increasing the content of paraffin wax also facilitates the formation of a stronger network structure of wax crystals, which dramatically improves the emulsion stability by immobilizing water droplets in the network. Meanwhile, the water droplets in the emulsion containing 15 wt% paraffin wax have the smallest size and largest number, and can efficiently act as the wax crystal nucleators thus dramatically changing the precipitated wax crystals into very small particles and facilitating the development of a wax crystal film around the droplets. This film also helps to improve the stabilization of the emulsion. (c2022 Elsevier B.V.)

WELL TESTING 1,561,740

WELL TEST ANALYSIS METHOD FOR FRACTURE-CAVITY RESERVOIRS OF BEADS-ON-STRING STRUCTURE WITH WELLBORE-CAVE CONNECTION

C.We, S.Cheng, Z.Li, J.Song, Y.Wang and J.Wu (China Univ Petroleum; China Offshore Oil Eng Co; China Nat Aviation Co Ltd). *PETROLEUM GEOLOGY AND RECOVERY EFFICIENCY (YOUQI DIZHI YU CAISHOULU)* v.29, no.6, pp.85-94, Nov. 2022. (ISSN 1009-9603; In Chinese)

[Full article and English abstract available from P.A.]

RESERVOIR ENG & REC METHOD

ASPHALTENE 1,561,741

INTERFACIAL MICRO AND MACRO RHEOLOGY OF FRACTIONATED ASPHALTENES

R.K.Moghaddam, H.W.Yarranton and G.Natale (Calgary Univ). *COLLOIDS AND SURFACES A: PHYSICOCHEMICAL AND ENGINEERING ASPECTS* v.651, 10/20/2022. (ISSN 0927-7757; Article no.129659)

Asphaltenes are a fraction of crude oil that can stabilize undesirable water/crude oil emulsions. Only a small fraction of the asphaltenes plays an active role in emulsion stabilization and this fraction has a relatively high heteroatom content. However, the transient behavior and the microstructural evolution of these asphaltene fractions at the water/oil interfaces are not fully understood. In this study, interfacial rheology and microstructural evolution of Athabasca asphaltene and its subfractions at the water/toluene interface were studied using passive microrheology and dilatational rheology. Asphaltenes (labeled A) were fractionated based on their surface activity via an emulsion-based method to obtain interfacially active (IA) and partially active (PA) subfractions. The passive microrheology experiments demonstrated that the IA asphaltenes adsorbed much faster at the water/toluene interface than A and PA asphaltenes. The IA asphaltenes formed rigid interfacial films within a few minutes which fully immobilized the probe particles. The same adsorption trend was observed in the interfacial pressure measurements and dilatational rheology experiments. Particle tracking microrheology over the entire interface showed that, during the adsorption process, asphaltene films grew heterogeneously and eventually turned into homogeneous structures at longer aging times. The IA asphaltene films were more homogeneous than the other asphaltene films offering fewer weak points for coalescence. The drop size distributions in emulsions prepared using IA and PA asphaltene showed significant coalescence after 1.5 h in the PA fraction but not the IA fraction, confirming the ability of IA asphaltenes to stabilize emulsions. (c2022 Elsevier B.V.)

CORE ANALYSIS 1,561,742

NOVEL METHODS AND RELATED SYSTEMS TO ESTIMATE WATER CONTENT OF SUBTERRANEAN CORE SAMPLES

A.Kumar, R.M.Fyfe, A.Mittal and L.Arguello, asrs. (Core Laboratories LP). World 2022/204,616A1, p. 9/29/2022, f. 5/4/2022 (Appl. 2,227,699), pr. U.S. 3/26/2021 (Appl. 63/166,779) (G01N-0033/28; E21B-0049/08; G01N-0033/24).

A method of processing a core sample includes the steps of: hermetically sealing the core sample in a chamber of an enclosure, comminuting the core sample while the chamber is hermetically sealed, injecting a hydrophilic agent into the chamber, wherein a slurry is formed by at least the hydrophilic agent and water released by the core sample, extracting at least a portion of the slurry from the chamber, separating a fluid from the slurry, analyzing the separated fluid to estimate an amount of water in the fluid, and estimating a water content of the core sample using the estimated amount of water in the fluid.

DISSOLVED GAS

1,561,743

PROCESSES AND SYSTEMS FOR MONITORING ONE OR MORE GASES DISSOLVED IN A LIQUID

R.Sharma, Q.K.Elias and T.Ramakrishnan, asrs. (Schlumberger Technol Corp; Schlumberger Canada Ltd; Schlumberger Serv Petrol; Schlumberger Technol BV). World 2022/212,344A1, p. 10/6/2022, f. 3/29/2022 (Appl. 2,222,306), pr. U.S. 3/29/2021 (Appl. 63/167,412) (G01N-0021/65; G01J-0003/44; G01N-0021/31; G01N-0021/3504; G01N-0021/53; G01N-0033/28).

Processes and systems for monitoring one or more gases dissolved in a liquid. In some embodiments, the process can include introducing a fluid into an inlet of a sample cell, where the fluid includes at least one gas dissolved in a liquid. The fluid can flow through the sample cell such that at least a portion of the fluid flows past an optical window such that the fluid is viewable within the sample cell through the optical window. The fluid can be recovered from an outlet of the sample cell. An electromagnetic radiation signal can be emitted into the sample cell through the optical window for at least a portion of the time the fluid is viewable through the optical window. The fluid can be contacted with the electromagnetic radiation signal within the sample cell. A scattered electromagnetic radiation signal that can include elastic scattered radiation and inelastic scattered radiation emitted from the sample cell through the optical window can be directed into a filter to remove at least a portion of the elastic scattered radiation to produce a primarily inelastic scattered radiation signal. The primarily inelastic scattered radiation signal can be directed to a detector to detect a Raman signal indicating the presence of the at least one dissolved gas in the liquid.

DRILLING FLUID SYSTEM

1,561,744

CONTROL SYSTEMS AND METHODS FOR ROCK CUTTINGS IDENTIFICATION

V.Solovyeva, K.Katterbauer, A.F.Marsala and N.M.Jabri, asrs. (Saudi Arabian Oil Co). World 2022/211,659A1, p. 10/6/2022, f. 4/1/2021 (Appl. 2,100,139) (E21B-0047/04). (Also assigned to V.Solovyeva)

Techniques for correlating a depth of drill bit cuttings include circulating a drilling fluid into a wellbore during a drilling process to form the wellbore in a subterranean formation; circulating a portion of uniquely identifiable particles from a container into the drilling fluid during the drilling process; circulating a return drilling fluid that includes the drilling fluid, cuttings from the subterranean formation, and the uniquely identifiable particles; separating the drilling fluid from the cuttings from the subterranean formation and the uniquely identifiable particles; capturing at least one image of the separated cuttings and the uniquely identifiable particles; and determining, based on the image, a depth of the subterranean formation.

DROP

1,561,745

ROLE OF SURFACTANT-INDUCED MARANGONI EFFECTS IN DROPLET DYNAMICS ON A SOLID SURFACE IN SHEAR FLOW

X.Shang, Z.Luo, G.Hu and B.Bai (Zhejiang Univ; Xi'an Jiaotong Univ). *COLLOIDS AND SURFACES A: PHYSICOCHEMICAL AND ENGINEERING ASPECTS* v.654, 12/5/2022. (ISSN 0927-7757; Article no.130142)

We address the dynamics of a surfactant-laden droplet on a solid surface in simple shear flow numerically. Our analysis uses the front-tracking method to take surfactant transport into account. The interfacial tension and the slip coefficient, both of which depend heavily on the surfactant concentration, are fully integrated into the generalized Navier boundary condition to model the moving contact lines. Accurate prediction of droplet motion indicates that the surfactant can change droplet behavior drastically. Surfactant-induced effects, such as interfacial tension reduction, the Marangoni stress, and wettability alternation, are investigated for various capillary numbers, surface wettabilities, elasticity numbers, and surface Péclet numbers. Deformation and motion of a sliding droplet are enhanced by the Marangoni effect, which is associated with an interfacial tension gradient. When the

capillary number reaches a critical value, the sliding-to-detachment and detachment-to-pinch-off transitions occur. Both transitions can be triggered and accelerated by a surfactant, especially when convection is dominant. As a result, the critical capillary number decreases, but exhibits a non-monotonic relationship with the elasticity number and Péclet number. The mechanisms that underlie the effect of Marangoni stress are discussed by analyzing the distributions of the surfactant concentration and the hydrodynamic forces exerted on the droplet. Accumulation of surfactants near the receding contact line reverses the local concentration gradient, attempts to change its direction along the interface, and delays droplet detachment. Furthermore, the strong surfactant dilution reduces both the surfactant concentration and the interfacial tension gradient, and thereby increasing the critical value for droplet pinch-off. (c2022 Elsevier B.V.)

EMULSION

1,561,746

PROBING THE GENERATION MECHANISM OF EMULSION BASED ON SHEARING ACTIONS BETWEEN MULTIPHASE FLUIDS IN POROUS MEDIA

Z.Wang, G.Cao, Y.Bai, P.Wang, X.Liu and X.Wang (Northeast Petroleum Univ; Zhejiang Univ). *COLLOIDS AND SURFACES A: PHYSICOCHEMICAL AND ENGINEERING ASPECTS* v.653, 11/20/2022. (ISSN 0927-7757; Article no.129997)

The generation, migration, and coalescence processes of emulsions in porous media of the actual formations are relatively complex. However, few studies have been reported about the generation mechanism of emulsions under shearing action, especially under shearing action between multiphase fluids. In this paper, the concept of emulsification caused by fluid shearing was proposed for the first time. An oil-water two phases flow model in porous media was established to study the generation process of emulsion caused by shearing actions between oil and water. Fluid flow velocity, pressure and distribution characteristics of oil and water during this process were recorded. The effects of flow velocity and oil-water interface properties on the generation process of emulsion were investigated. Combined with the microscopic visualization oil displacement model, the generation characteristics of emulsions in porous media were further explored. The results indicated that the complex flow between oil and water in porous media would cause shear emulsification of crude oil. With the increase of flow velocity of oil-water two phases, the shear emulsification capacity was gradually enhanced. The generation capacity of emulsion in the micro shearing unit was mainly affected by the flow velocity of the displacing phase, and the particle size of the emulsion was mainly affected by the flow velocity of the shearing phase. When the interfacial tension between oil and water was lower than 10 E-01 mN/m, the shear emulsification rate did not change significantly. These results are of great significance for the supplement and improvement of the generation mechanism of emulsions in porous media, providing theoretical guidance for further enhancing oil recovery by regulating emulsification. (c2022 Elsevier B.V.)

ENHANCED RECOVERY

1,561,747

METHODOLOGY FOR MODELING ELECTROKINETIC EFFECTS AND IDENTIFYING CARBONATED WATER INJECTION PARAMETERS

M.A.Alsaud, S.Ayirala and A.Yousef, asrs. (Saudi Arabian Oil Co; Aramco Services Co). World 2022/204,022A1, p. 9/29/2022, f. 3/21/2022 (Appl. 2,221,136), pr. U.S. 3/22/2021 (Appl. 208,195) (E21B-0043/20; E21B-0021/06; E21B-0043/16).

A method for recovering hydrocarbons from a hydrocarbon-containing formation is disclosed herein. The method may include determining the hydrocarbon-containing formation pressure, temperature, and other properties such as the total acid number and total base number of the hydrocarbons, rock type, and brine ionic composition. The method may also include determining a desired amount of wettability alteration of the formation and modeling the formation. Modeling the formation may be based on the determined pressure, temperature, total acid number and total base number of the hydrocarbons, rock type, and brine ionic composition. The method may also include preparing an aqueous

wellbore fluid based on the estimated wellbore fluid composition and injecting the aqueous wellbore fluid into the hydrocarbon-containing formation.

ENHANCED RECOVERY

1,561,748

FOAMING FORMULATION AND USE THEREOF AS A VISCOELASTIC SURFACTANT IN LOW-PERMEABILITY RESERVOIRS [FORMULACION ESPUMANTE Y SU USO COMO AGENTE TENSOACTIVO VISCOELASTICO EN YACIMIENTOS DE BAJA PERMEABILIDAD]

J.C.Jimenez Osorio, asr. (Chemiservis SA de CV). World 2022/203,493A1, p. 9/29/2022, f. 3/23/2022 (Appl. 2,250,026), pr. Mex. 3/26/2021 (Appl. 21,003,590) (C09K-0008/58). (In Spanish)

The present invention relates to a foaming formulation and to the use thereof as a viscoelastic surfactant in low-permeability reservoirs, the formulation being designed to be used in low-pressure reservoirs where the use of low-density systems is required as a result of the characteristics of the reservoirs. The present invention can likewise be adapted to densities of 0.5 to 0.2 g/cm³ without losing its viscoelastic diverting properties.

FOAM

1,561,749

ASSESSING THE PERFORMANCE OF FOAMS STABILIZED BY ANIONIC/NONIONIC SURFACTANT MIXTURE UNDER HIGH TEMPERATURE AND PRESSURE CONDITIONS

Z.Xu, Z.Li, S.Cui, B.Li, Q.Zhang, L.Zheng and M.M.Husein (China Univ Petroleum; PetroChina; Calgary Univ). *COLLOIDS AND SURFACES A: PHYSICO-CHEMICAL AND ENGINEERING ASPECTS* v.651, 10/20/2022. (ISSN 0927-7757; Article no.129699)

Foam flooding is an effective tertiary recovery method for oil and gas reservoirs. However, foam performance is very sensitive to the reservoir temperature and pressure. In this study, the formation and collapse of a water-based foam stabilized by a mixed ionic and nonionic surfactant system under typical reservoir conditions (up to 150 °C and 50 MPa) were investigated. A multifunctional foam analyzer, an interfacial rheometer, and a coiled tube are used to assess foam microstructure, surface tension and bulk viscosity under 25 – 80 °C and 0.1 – 10 MPa. Results show that the foam comprehensive value is highest under low temperature and high pressure. With increasing temperature, the gas bubbles become larger, fewer in number, and more irregular in shape coupled with a thinner liquid film. Increased pressure, on the other hand, decreases the bubble size, increases the number of bubbles and contributes to a more uniform and dense foam. At constant temperature, the surface tension decreases as the pressure increases, while at constant pressure, a minimum surface tension is observed with increasing temperature, which in turn increased with increasing pressure. Foam viscosity displayed an opposite trend to that of the surface tension. Understanding the variation of foam properties with temperature and pressure is key toward successful application of foam flooding. (c2022 Elsevier B.V.)

FOAM

1,561,750

THE FORMATION OF SOY PROTEIN FIBRILS-CHITIN NANOWHISKER COMPLEX COACERVATES: RELATIONSHIP TO MIXED FOAM STABILITY

X.Y.Li, G.Y.Li, Q.Z.Zeng, D.X.Su, S.He, X.Q.Yang, A.Nag, J.Li and Y.Yuan (Guangzhou Univ). *COLLOIDS AND SURFACES A: PHYSICO-CHEMICAL AND ENGINEERING ASPECTS* v.652, 11/5/2022. (ISSN 0927-7757; Article no.129783)

The effects of protein fibrillation modifications on foam properties and the foaming and stabilization ability of soy protein fibrils (SPF) and chitin nanowhisker (CNW) complex systems were investigated and evaluated. The results showed that the structure of SPF stretched significantly with the increase of heating time, probably due to the unfolding and rearrangement of protein structure. The foaming ability and stability of SPF were significantly higher than those of natural protein. The SPF and CNW coacervates effectively increased the foam strength, probably due to the interaction between the "worm-like" SPF structure and the short crystal structure of CNW. In addition, the samples

containing salt had higher foaming ability, stability and viscosity compared to those without salt, resulting in a significant improvement in foaming properties. This study provided a new idea for studying the functional properties of modified protein-modified polysaccharides complex coacervates. (c2022 Elsevier B.V.)

FORMATION EVALUATION

1,561,751

FORMATION EVALUATION BASED ON PULSE POWER ELECTRODE DISCHARGE MEASUREMENTS

M.E.Cammack and B.Wiecek, asrs. (Halliburton Energy Service). World 2022/203,675A1, p. 9/29/2022, f. 3/25/2021 (Appl. 2,124,256), pr. U.S. 3/24/2021 (Appl. 211,817) (E21B-0021/08; E21B-0004/14; E21B-0047/18).

A first characteristic of a first discharge of electrodes of a pulse power drilling assembly in a borehole of a subterranean formation is determined. The first characteristic is based on a measurement of the first discharge. A second characteristic of a second discharge of the electrodes is determined. The second discharge occurs after the first discharge, and the second characteristic is based on a measurement of the second discharge. A difference between the first characteristic and the second characteristic is determined. A boundary layer of the subterranean formation is determined based on the difference.

FORMATION TESTING

1,561,752

IDENTIFYING ASPHALTENE PRECIPITATION AND AGGREGATION WITH A FORMATION TESTING AND SAMPLING TOOL

R.Naveena-Chandran, S.M.F.Hamza, G.M.Hashmi, J.Rogers, C.M.Jones and A.H.Vanzuilekom, asrs. (Halliburton Energy Service). World 2022/211,913A1, p. 10/6/2022, f. 2/11/2022 (Appl. 2,216,166), pr. U.S. 4/1/2021 (Appl. 63/169,417) and U.S. 1/31/2022 (Appl. 589,336) (E21B-0017/10; E21B-0049/08; E21B-0043/12; E21B-0047/06; G01L-0019/08; G01N-0021/84).

A system and method for a fluid sampling tool are disclosed herein. The fluid sampling tool may include a probe section. The probe section may include one or more probes, one or more stabilizers, and a housing that houses a bidirectional piston pump. The method may include disposing a fluid sampling tool into a wellbore at a first depth, pressing the one or more probes into a surface of the wellbore, drawing a reservoir fluid from the wellbore through the one or more probes, placing the reservoir fluid into the housing, isolating the housing from the one or more modules of the fluid sampling tool with one or more shut-in valves, depressurizing the housing with the bidirectional piston pump, and measuring the asphaltene precipitation of the reservoir fluid within the housing.

GAS WATER CONTACT

1,561,753

METHANE AT THE GAS/WATER INTERFACE: MOLECULAR SIMULATIONS OF SURFACE ADSORPTION AND SECOND SURFACE VIRIAL COEFFICIENTS

Y.Wang, O.Allen, E.Collins and H.S.Ashbaugh (Tulane Univ; Ark Univ, Pine Bluff; Dillard Univ). *COLLOIDS AND SURFACES A: PHYSICO-CHEMICAL AND ENGINEERING ASPECTS* v.652, 11/5/2022. (ISSN 0927-7757; Article no.129725)

Liquid surface tensions are moderated by the adsorption of species like surfactants and gases at interfaces. In order to disentangle the competing polar and nonpolar interactions that oppose/favor adsorption at a gas/water interface and gain molecular insights into the role of inter-solute interactions on moderating the surface tension, we report here molecular simulations of purely nonpolar methane adsorption onto aqueous surfaces over a broad range of temperatures (0–50°C) and bulk gas pressures (up to ca 750 bar). As expected, positive methane adsorption at the interface significantly lowers the surface tension with increasing pressure, although this effect is not without bound as plateaus/minima in the surface tension are observed near 500 bar. The excess surface adsorption of methane directly observed from simulation agrees quantitatively with those determined from the surface tension following Gibbs adsorption isotherm, giving confidence in the thermodynamic consistency of the simulation results and Gibbs'

interpretation of the effect of solute adsorption. From the simulation results we were able to evaluate surface adsorption coefficients and second surface virial coefficients for methane's sitting at the interface. The second virial coefficients determined from simulation were found to be slightly more attractive than those predicted from statistical thermodynamic integrals for two-dimensional gases, suggesting water could help drive methane interactions in the interface. Generalizing the statistical thermodynamic integral for the second surface virial coefficient to that for a gas confined to a pseudo-two-dimensional slit, however, near quantitative agreement with the simulation results is observed, indicating water plays effectively no role. Comparisons of the simulation results with experiment are generally favorable, although the simulations appear to under predict net adsorption likely as a result of the neglect of methane polarization interactions. (c2022 Elsevier B.V.)

HYDRATE FORMATION 1,561,754

MODELING THE MECHANICAL BEHAVIOR OF METHANE HYDRATE-BEARING SAND USING THE EQUIVALENT GRANULAR VOID RATIO

J.Shen, A.C.F.Chiu and C.W.W.Ng (Hohai Univ; Shantou Univ; Hong Kong Univ Sci Technol). *JOURNAL OF MARINE SCIENCE AND ENGINEERING* v.10, no.8, Aug. 2022. (ISSN 2077-1312; Article no.1040)

For the safe extraction of methane from hydrate reservoirs, modeling the mechanical behavior of the methane hydrate-bearing soil properly is crucial in order to enable designers to analysis hydrate-dissociation-induced geotechnical failures. Hydrate morphology is one of major factors affecting the mechanical behavior of soil containing hydrate. This paper presents a new constitutive model for methane hydrate-bearing sand (MHBS) using the equivalent granular void ratio as a state variable, which can quantify the effects of the pore-filling and load-bearing hydrate morphology under a unifying framework. The proposed model is a combination of generalized plasticity and an elastic damage model so as to take into account the observed frictional and bonding aspects of MHBS, respectively. By using the concept of state-dependent dilatancy, the equivalent granular void ratio is formulated and adopted in the generalized plasticity model. In addition, a nonlinear damage function is implemented to elucidate the degradation of hydrate bonds with respect to shearing. Compared with the basic generalized plasticity model for host sand, only three additional parameters are required to capture key mechanical behaviors of MHBS. By comparing the triaxial test results of MHBS synthesized from a range of host sands with a predicted behavior by the proposed model, it is demonstrated that the new model can satisfactorily capture the stress-strain and volumetric behavior of MHBS under different hydrate saturations, confining pressures, and void ratios.

HYDRATE FORMATION 1,561,755

DISCRETE ELEMENT SIMULATION OF THE MACRO-MESO MECHANICAL BEHAVIORS OF GAS-HYDRATE-BEARING SEDIMENTS UNDER DYNAMIC LOADING

Y.Jiang, M.Li, H.Luan, Y.Shi, S.Zhang, P.Yan and B.Li (Shandong Univ Sci Technol). *JOURNAL OF MARINE SCIENCE AND ENGINEERING* v.10, no.8, Aug. 2022. (ISSN 2077-1312; Article no.1042)

Under the action of dynamic loadings such as earthquakes and volcanic activities, the mechanical properties of gas-hydrate-bearing sediments will deteriorate, leading to a decrease in the stability of hydrate reservoirs and even inducing geological disasters such as submarine landslides. In order to study the effect of dynamic loading on the mechanical properties of hydrate sediments, triaxial compression tests of numerical specimens were carried out by using particle flow code (PFC2D), and the macro-meso mechanical behaviors of specimens were investigated. The results show that the loading frequency has a small effect on the stiffness of the hydrate sediment, while it has a large effect on the peak strength. The peak strength increases and then decreases with the increase in loading frequency. Under the same loading frequency, the peak strength of the hydrate sediment increases

with the increase in loading amplitude, and the stiffness of the specimen decreases with the increase in loading amplitude. The maximum shear expansion of the specimen changes with the movement of the phase change point and the rearrangement of the particles. The maximum shear expansion of the specimen changes with the movement of the phase change point and the change of the bearing capacity of the particles after the rearrangement, and the more forward the phase change point is, the stronger the bearing capacity of the specimen in the plastic stage. The shear dilatancy angle and the shear dilatancy amount both increase linearly with the increase in loading amplitude. The influence of loading frequency and amplitude on the contact force chain, displacement, crack expansion, and the number of cementation damage inside the sediment is mainly related to the average axial stress to which the specimen is subjected, and the number of cracks and cementation damage of the sediment specimen increases with the increase in the average axial stress to which the sediment specimen is subjected. As the rate of cementation damage increases, the distribution of shear zones becomes more obvious.

HYDRAULIC FRACTURING 1,561,756

FRACTURE INTERACTION IN MULTIWELL CONFIGURATION'S USING ADVANCED GEOMECHANICAL NUMERICAL MODELLING

E.I.Martinez, J.A.Iglesias, L.M.Ramasesha, N.Frechette, J.M.S.Serra, N.A.G.Molano, N.R.Morillas and P.E.V.Mendoza (Repsol). *83RD ANNUAL EAGE CONFERENCE (Online and Madrid, Spain, 6/6-9/2022) ABSTRACTS 2022*. (Abstract no.608; Available at <http://www.earthdoc.org> as of 7/7/2022; 5 pp; **Abstract only**)

In unconventional assets, hydraulic fracture interaction between wells is an important issue that could compromise well productivity. Initial state of stress within a reservoir and its variation with production is part of the information needed to answer important development questions, such as: What is the optimum distance between wells? What is the critical distance to reduce frac hit risk? What is the effect of reservoir depletion on the optimum distance between wells? The stress state after depletion depends on the drainage network and is difficult to estimate due to large well counts, complex well geometry and completion parameters, depletion time (more than 50 years) and the lateral variation of reservoir properties. Different scenarios were considered: well location, well spacing, fracture to fracture location (fracture face tip to tip or offset), and fracture asymmetry due to pore pressure variations. Models cover 5 years of production on the parent wells. The results show that the most import variable on fracture propagation and interaction is pore pressure depletion. The obtained information is used in new well location planning (well spacing, frac stage locations, etc.) to optimize frac placement and avoid fracture interaction events between wells.

IMBIBITION 1,561,757

CHARACTERISTICS AND MECHANISM OF IMBIBITION OIL RECOVERY IN THE ULTRA-LOW-PERMEABILITY VOLCANIC OIL RESERVOIR IN THE SANTANGHU BASIN

S.Li, S.Yang, X.Gao, M.Wang, B.Shen and J.Yu (State Key Laboratory China; PetroChina; China Univ Petroleum; Tuha Oilfield Co). *COLLOIDS AND SURFACES A: PHYSICO-CHEMICAL AND ENGINEERING ASPECTS* v.652, 11/5/2022. (ISSN 0927-7757; Article no.129838)

Imbibition oil recovery (IOR) is an important method to improve the recovery factor (RF) of low-permeability reservoirs. To explore the characteristics and mechanism of IOR in ultra-low-permeability volcanic oil reservoirs (ULPVRs) in the Santanghu Basin, this study conducted various imbibition experiments under NMR monitoring using actual cores from the reservoir, including spontaneous imbibition (SI) and forced imbibition (FI) experiments involving different rock sample sizes. Further, we obtained the IOR characteristics of ultra-low-permeability volcanic rocks (ULPVRs). Meanwhile, based on the experimental test results of the pore structure and casting thin section, combined with imbibition theory, the mechanism of the IOR in ULPVRs was obtained. The results demonstrated that the IOR characteristics of the ULPVRs are

significantly different from those of conventional tight sandstone and shale. Conventional tight sandstone and shale evenly produce oil on the rock surface during IOR, whereas ULPVRs exhibits extremely few and scattered oil production points on the rock surface during IOR. Unlike conventional tight sandstone and shale plunger cores where the RF of SI is generally approximately 30%, the IOR of ULPVRs is particularly poor, with RFs of SI being 4.59% and 2.70% for plunger and full-diameter cores, respectively, and the RF of FI is only 10.19% for the plunger core. In addition, ULPVRs are extremely heterogeneous, and the pore structure and production characteristics of IOR are extremely complicated. The oil produced by SI in the plunger and full-diameter cores comes from middle pores ($0.01 \mu\text{m} < r < 0.1 \mu\text{m}$) and large pores ($r > 0.1 \mu\text{m}$), respectively, while the oil produced by FI in the plunger core comes from large pores. Conventional tight sandstone and shale are not conducive to seepage owing to their small pore sizes, however, their compatibility between the pore and throat sizes makes them favorable for IOR. The extremely poor matching between the pore and throat sizes of the ULPVRs is unfavorable for seepage, and is primarily responsible for its poor IOR effect. For the ULPVRs in the Santanghu Basin, the key to EOR is to improve the seepage capacity of the reservoir throat, such as further large-scale volume fracturing, rather than implementing too many measures for IOR. The results of this study can provide a reference and basis for the efficient development of ULPVRs. (c2022 Elsevier B.V.)

IMMISCIBLE DISPLACEMENT 1,561,758

DISCREPANCY OF SIMULATING SNAP-OFF PROCESSES IN 2D AND 3D PORE-THROATS

L.He, S.Han, Y.Yuan and Y.Yuan (Shaanxi Univ Sci & Technol; Hunan Univ). *COLLOIDS AND SURFACES A: PHYSICO-CHEMICAL AND ENGINEERING ASPECTS* v.653, 11/20/2022. (ISSN 0927-7757; Article no.129978)

3D pore-throats with uniform thickness were commonly used to explore snap-off processes in experimental studies, and always simplified as 2D areal models in simulation of snap-off processes. However, 3D effects of capillary force, viscous force and wall cannot be neglected. We assume that snap-off processes in 2D and 3D pore-throats may exist discrepancy. Snap-off processes in both 2D and 3D pore-throats were simulated with various capillary numbers Ca , viscosity ratios μ_r and size ratios M of throat and pore. The results showed: (1) snap-off was more prone to occur with the same M in 3D pore-throats due to the larger capillary pressure difference; (2) the increase of M inhibited occurrence of snap-off, and the inhibition effect of M was more obvious in 2D pore-throats; (3) snap-off only occurred with $M < 7/35$ in 2D pore-throats, which was significant different from the Roof theory ($M < 1/2$). These findings indicate that 2D areal models are not suitable to simplify the 3D pore-throat in simulating snap-off processes. (c2022 Elsevier B.V.)

INTERMOLECULAR FORCE 1,561,759

EFFECTS OF INORGANIC CATIONS ON THE STERIC FORCE BETWEEN POLYACRYLAMIDE LAYER PHYSICALLY ADSORBED ON SiO₂ WAFER AND POLY (ETHYLENE OXIDE) LAYER

Q.Li, Y.Li, X.Zhai, M.Chen, M.Ding and Y.Wang (China Univ Petroleum; Sinopec Research Inst). *COLLOIDS AND SURFACES A: PHYSICO-CHEMICAL AND ENGINEERING ASPECTS* v.654, 12/5/2022. (ISSN 0927-7757; Article no.130031)

The physical adsorption of polyacrylamide on the SiO₂ wafer in high salty solutions was investigated by an improved AFM steric force measurement. The colloid probe was modified by poly (ethylene oxide) layer and used to determine the steric force between adsorbed polyacrylamide and poly (ethylene oxide) layer in NaCl, KCl, MgCl₂ and CaCl₂ solutions. Assuming the adsorbed polyacrylamide complies with the self-similar model, the surface excesses, the thicknesses of the proximal regions, and "free energies of sticking" were estimated. Take the case of 5000 mg/L NaCl for example. The concentration profile was deduced from the corresponding steric force profile. The polyacrylamide concentration next to the SiO₂ wafer was estimated to be about 147 g/L and the average concentration in the proximal region was estimated to be about 100 g/L. Based on the above estimations, interaction strength

between the adsorbed cations and polyacrylamide was established, $\text{Mg}^{2+} > \text{Ca}^{2+} > \text{K}^{+} > \text{Na}^{+}$. Moreover, the conformations of the adsorbed polyacrylamide were changed from "lying flat" to folded ones by the stronger interactions between the adsorbed cations and polyacrylamide." (c2022 Elsevier B.V.)

KEROGEN 1,561,760

COMBINED EFFECTS OF THE CHEMICAL STRUCTURE AND NANOPORE DEVELOPMENT ON WATER VAPOR/LIQUID ADSORPTION IN SHALE KEROGEN

C.Zhang, Y.Yao, R.Swennen and H.Wu (China Univ Geosci, Beijing; Leuven Katholieke Univ). *COLLOIDS AND SURFACES A: PHYSICO-CHEMICAL AND ENGINEERING ASPECTS* v.653, 11/20/2022. (ISSN 0927-7757; Article no.129920)

The interaction between water/gas and rock plays an important role in evaluating initial fluid storage in shale gas reservoirs. It is challenging to understand the co-occurrence relationships of water, chemical structure, and nanopore in shale kerogen due to the fact that both pore-forming material and water adsorption are related to the chemical structure. In this study, we did water vapor adsorption (WVA) experiments on seven Longmaxi Formation shale kerogen, and then analyzed the vapor-liquid equilibrium process. Results show that water is preferentially adsorbed in micropores ($< 2 \text{ nm}$) through monolayer coverage when the relative humidity (RH) is less than 75%, while mesopores (2–50 nm) contribute dominantly to the total water adsorption when the RH is greater than 75%. Furthermore, based on grand canonical Monte Carlo simulations, we constructed water-contained molecular models with the same adsorption amounts as the WVA experiments to simulate the water adsorption process. Simulation results show that water can exist in hydrophilic oxygen-containing structures in the form of monolayer coverage, and in hydrophobic carbon structures in the form of water clusters. Under low RH, the narrow ultra-micropores (mainly $< 0.35 \text{ nm}$) within the hydrophilic oxygen-containing structures are the primary adsorption centers for water adsorption, which results in a monolayer coverage of water molecules. With increasing RH, the hydrophobic carbon structures can adsorb water molecules because the residual oxygen-containing structures bonded to aliphatic/aromatic carbons provide connecting sites for the formation and growth of water clusters. Based on the acquired results, a molecular model showing the co-occurrence relationships among water, chemical structure, and nanopore was constructed, which helps to understand the microscopic mechanism of fluids-rock interactions. (c2022 Elsevier B.V.)

MADRID BASIN 1,561,761

GEOHERMAL POTENTIAL OF MADRID BASIN FROM INTEGRATED GEOPHYSICAL AND WELL DATA ANALYSIS (CENTRAL SPAIN)

M.A.B.Llamosas, A.M.Martin, A.J.O.Campos and G.Z.Valcarce (Madrid Complutense Univ; Repsol Exploracion SA). *83RD ANNUAL EAGE CONFERENCE (Online and Madrid, Spain, 6/6-9/2022) ABSTRACTS 2022*. (Abstract no.615; Available at <http://www.earthdoc.org> as of 7/7/2022; 5 pp; **Abstract only**)

New energy demand linked to world population growth and awareness about climate change have brought out the need to develop new forms of energy guided by the urgency of an ecological transition. In this context geothermal resources have the potential of contributing significantly to sustainable use in many parts of the world. In Spain, during the 1980s, oil and gas explorations carried out in the Madrid Basin confirmed the existence of two geothermal reservoirs. Here we present diverse geological features of the basin essential in geothermal exploration. We use airborne radiogenic and magnetic data to characterize the basement. Detailed ground concentration estimates of the heat producing elements are used to calculate the heat production and heat flow in the near surface. The distribution pattern of both parameters is heterogeneous with two main areas separated by southward prolongation of the Berzosa Fault. The eastern sector is characterized by both low heat production and heat flow rates while the western area is distinguished by high values as a response of the exposed granites. In addition, we build one 3D geological model and one 3D isothermal model with leapfrog geothermal from seismic, well data, and mapping information.

NANOPARTICLE

1,561,762

A NOVEL HYBRID HYPERBRANCHED NANOWIRE CNTs FOR ENHANCING OIL RECOVERY THROUGH INCREASING VISCOELASTICITY AND HIGH-VISCOUS EMULSIONS TO COMPENSATE RESERVOIR HETEROGENEITY

R.Gou, W.Pu, R.Liu, Y.Chen, T.Zhang and X.Lin (Southwest Petroleum Univ; Chongqing Univ). *COLLOIDS AND SURFACES A: PHYSICO-CHEMICAL AND ENGINEERING ASPECTS* v.654, 12/5/2022. (ISSN 0927-7757; Article no.130118)

Polymer flooding was one of the most cost-effective methods for enhanced oil recovery (EOR). It was the key for enhancing oil recovery that studying novel polymer could cope with harsh reservoir conditions. In this work, a hyperbranched nanowire (O-20 @PAM@CNTs) for polymer flooding was synthesized by in situ polymerization with monomers and hybrid carbon nanotubes (CNTs). FT-IR, ¹H NMR, TEM, gel permeation chromatograph (GPC) and rheometer were used to characterize the composition, micro-morphology, MWD (molecular weight distribution) and rheological properties of O-20 @PAM and O-20 @PAM@CNTs. Compared with O-20 @PAM, O-20 @PAM@CNTs showed excellent viscosification, temperature resistance, anti-shear and viscoelastic properties. The hyperbranched nanowire had the best performance with the content of hybrid CNTs of 0.2% w/w and which molecular weight (741999) was about half that of O-20 @PAM (1330629). Enhanced performance of the O-20 @PAM@CNTs could be attributed to the hybrid CNTs provided polymer a hyperbranched structure to build more compact and complex network and boost the association between polymer chains. Besides, the fatty alcohol polyoxyethylene ether(O-20) on the chains of O-20 @PAM@CNTs raised the viscosity of flooding liquid by emulsification and that partly compensated the heterogeneity of the core, thus improved the displacement efficiency markedly. Core Flooding Experiments shown that 0.3 times of pore volume O-20 @PAM@CNTs-0.2 increased oil recovery by 17.5% contrasting only 11.6% for 0.4 times of pore volume O-20 @PAM, in the same solution concentration (2000 ppm). O-20 @PAM@CNTs had more obvious advantage in performance and more economical than O-20 @PAM, which indicated a better application of O-20 @PAM@CNTs in EOR. (c2022 Elsevier B.V.)

OIL AND GAS MIGRATION

1,561,763

STRUCTURES IN SHALLOW MARINE SEDIMENTS ASSOCIATED WITH GAS AND FLUID MIGRATION

G.Ma, L.Zhan, H.Lu and G.Hou (Peking Univ). *JOURNAL OF MARINE SCIENCE AND ENGINEERING* v.9, no.4, April 2021. (ISSN 2077-1312; Article no.396)

Geological structure changes, including deformations and ruptures that developed in shallow marine sediments, are well recognized but were not systematically reviewed in previous studies. These structures, generally developed at a depth less than 1000 m below seafloor, are considered to play a significant role in the migration, accumulation, and emission of hydrocarbon gases and fluids, and the formation of gas hydrates, and they are also taken as critical factors affecting carbon balance in the marine environment. In this review, these structures in shallow marine sediments are classified into over-pressure-associated structures, diapir structures and sediment ruptures based on their geometric characteristics and formation mechanisms. Seepages, pockmarks, and gas pipes are the structures associated with over-pressure, which is generally induced by gas/fluid pressure changes related to gas and/or fluid accumulation, migration and emission. The mud diapir and salt diapir are diapir structures driven by gravity slides, gravity spread and differential compaction. Landslides, polygonal faults and tectonic faults are sediment ruptures, which are developed by gravity, compaction forces and tectonic forces, respectively. Their formation mechanisms can be attributed to sediment diagenesis, compaction, and tectonic activities. The relationships between the different structures, between structures and gas hydrates, and between structures and authigenic carbonate are also discussed.

POROSITY DISTRIBUTION

1,561,764

TRIANGULATION OF PORE STRUCTURAL CHARACTERISATION OF DISORDERED MESOPOROUS SILICA USING NOVEL HYBRID METHODS INVOLVING DUAL-PROBE POROSIMETRIES

S.Mousa, K.Baron, R.S.Fletcher and S.P.Rigby (Nottingham Univ; Johnson Matthey). *COLLOIDS AND SURFACES A: PHYSICO-CHEMICAL AND ENGINEERING ASPECTS* v.653, 11/20/2022. (ISSN 0927-7757; Article no.130026)

The key issue, in applying indirect pore structure characterisation methods to disordered materials, is that usually some physical assumptions are necessary to probe pore size, such as concerning the mode of the phase transition used, which determines meniscus geometry or kernel type. This issue often undermines the relative advantages of indirect methods, over direct methods like imaging, from both the wider range of pores sizes that can be probed in a single experiment and the much better statistical representativeness of the data, which are essential for highly heterogeneous disordered materials. Further, parameter calibrations provided using supposedly the same model ordered porous materials are often conflictual. However, this work introduces dual-liquid thermoporometry, and also dual-probe, serial water sorption and mercury intrusion, to complement multi-adsorbate, serial gas sorption, to overcome this issue by triangulating the data for three key probe molecules used in three different porosimetries, namely liquid intrusion, gas sorption, and thermoporometry. It has been found that augmenting one porosimetry, using just one probe molecule, to a dual-probe experiment removes the aforementioned, key drawback of indirect methods. The alternative, complementary dual-probe porosimetries can also cross-validate this approach for each other. This allows indirect methods to stand alone, without the need for direct imaging methods to inform or validate prior assumptions. Further, the dual-probe experiments allow additional information on pore structure to be obtained beyond that provided by single-probe experiments. For example, dual-liquid thermoporometry also allows the probing for the presence and nature of the advanced melting effect, and serial water adsorption and mercury porosimetry delivers information on network filling mechanisms during adsorption in disordered media. (c2022 The Authors. Elsevier B.V.)

RESERVOIR CHARACTERIZATION

1,561,765

MICRO-SCALE NUMERICAL STUDY OF WATER FLOOD IN AN OIL-WET CARBONATE ROCK

S.H.Talebian and A.Fahimifar (Amirkabir Univ Technology). *83RD ANNUAL EAGE CONFERENCE (Online and Madrid, Spain, 6/6-9/2022) ABSTRACTS 2022*. (Abstract no.618; Available at <http://www.earthdoc.org> as of 7/7/2022; 5 pp; **Abstract only**)

Micro-scale simulation of brine injection into a porous media saturated with oil was performed using COMSOL Multiphysics. The rock and fluid properties are exported from a carbonate reservoir to investigate water-based enhanced oil recovery (EOR) in the rock-fluid system. The impact of interfacial tension, permeability alteration, capillary entry pressure, and velocity and density of injection brine on the fluids flow pattern in micromodel pore network is investigated. It was observed from the results that in the oil-wet porous system with light crude oil, velocity and wettability alteration are the most important displacement mechanisms and IFT reduction and capillary entry pressure are the second important factors in the enhanced oil recovery process.

RESERVOIR ENGINEERING

1,561,766

EMULSIFIED FOAMING FORMULATION AND USE THEREOF AS AN ORGANIC MATERIAL DISSOLVING AGENT IN LOW-PRESSURE OIL WELLS [FORMULACION EMULSIONADA ESPUMANTE Y SU USO COMO AGENTE DISOLVENTE DE MATERIAL ORGANICO EN POZOS PETROLIFEROS CON BAJA PRESION]

J.C.Jimenez Osorio, asr. (Chemiservis SA de CV). *World 2022/203,495A1*, p. 9/29/2022, f. 3/23/2022 (Appl. 2,250,028), pr. Mex. 3/26/2021 (Appl. 21,003,601) (C09K-0008/58). **(In Spanish)**

The present invention relates to an emulsified foaming

formulation and the use thereof as an organic material dissolving agent in low-pressure oil wells, since the properties of the foam of the present invention are useful in wells where it is necessary for the hydrostatic head generated by the system to be also low in order to better control the placement of the system where it is required, due to which its foam quality is 65%.

RESERVOIR MODEL 1,561,767

VISUALIZING FLUID FLOW THROUGH POROUS MEDIA IN VIRTUAL REALITY

J.Proctor, D.D'Angelo and N.Derzhi, asrs. (Halliburton Energy Service). World 2022/204,692A1, p. 9/29/2022, f. 3/23/2022 (Appl. 2,271,280), pr. U.S. 3/26/2021 (Appl. 63/166,882) and U.S. 3/23/2022 (Appl. 656,077) (G01V-0001/30; E21B-0049/08; G01V-0001/50; G02B-0027/01; G06T-0019/00).

Systems and methods for visualizing fluid flows in a virtual reality (VR) environment are disclosed. A digital volume image representing a reservoir formation sample is obtained from an imaging device. The digital volume is segmented by assigning hydraulic properties of the formation sample to each volume element based on image properties associated with that volume element. Fluid flow is simulated using the segmented digital volume. A vector field representing flow properties at different points along one or more flow lines through the pore space is generated. An interactive visualization of a three-dimensional (3D) virtual environment representing the formation sample with the flow line(s) is provided via a VR display. Responsive to receiving user input specifying an area of the environment to view at a selected level of detail, the specified area is rendered at the selected level of detail and a current view of the interactive visualization is updated accordingly.

RESERVOIR MODEL 1,561,768

AUTOMATIC SUBSURFACE PROPERTY MODEL BUILDING AND VALIDATION

A.Abubakar, H.Di, T.Zhao, Z.Li and C.Li, asrs. (Schlumberger Technol Corp; Schlumberger Canada Ltd; Schlumberger Serv Petrol; GeoQuest Systems BV). World 2022/204,682A1, p. 9/29/2022, f. 3/22/2022 (Appl. 2,271,266), pr. U.S. 3/22/2021 (Appl. 63/164,259) (G01V-0001/30; G06N-0003/02; G06N-0020/00).

A method for modeling a subsurface property for a subterranean volume of interest includes receiving input measurement data representing a subterranean volume of interest, predicting a subsurface property based at least in part on the input measurement data using a first machine learning model, predicting a subsurface property model based at least in part on the subsurface property, the input measurement data, or both, using a second machine learning model, predicting synthetic measurement data based at least in part on the subsurface property model using a third machine learning model, a physics-based model, or both, comparing the synthetic measurement data and the input measurement data, and training the first machine learning model, the second machine learning model, or both based at least in part on the comparing.

SHALE RESERVOIR 1,561,769

METHOD AND DEVICE FOR PREDICTING ELASTIC PARAMETERS OF SHALE RESERVOIR, AND STORAGE MEDIUM

X.Yin, L.Yin, Z.Zong, G.Wu, G.Zhang, D.Cao, F.Zhang, K.Liang, J.Zhang et al., asrs. (China Univ Petroleum). World 2022/198,363A1, p. 9/29/2022, f. 3/22/2021 (Appl. 2,182,006) (G01V-0001/50; G01V-0001/30). (In Chinese)

The present application provides a method and device for predicting elastic parameters of a shale reservoir, and a storage medium. The method comprises: acquiring well logging data of shale; using a SCA model to determine the effective elastic modulus of a background matrix; performing free gas addition on hard pores by using an inclusion model, so as to determine the effective elastic modulus of the background matrix containing hard pores; using a micro-nano pore model that uses an adsorption gas ratio and the

elastic modulus of an adsorption gas as surface elastic parameters to determine the effective elastic modulus of a nano-porous organic substance considering the adsorption gas, the surface effect of micro-nano pores in the micro-nano pore model being positively correlated with the adsorption gas ratio; using a Gassmann equation to determine the effective elastic modulus of a saturated nanoporous organic substance; using an anisotropic inclusion model to obtain an equivalent elastic matrix of the shale; and determining, according to the equivalent elastic matrix and density of the shale, the equivalent longitudinal wave velocity and the equivalent transverse wave velocity of the shale. Thus, the reasonable prediction of elastic parameters of a shale reservoir is achieved.

SOIL ANALYSIS 1,561,770

NORMALIZED STRESS-STRAIN BEHAVIOR OF DEEP-SEA SOFT SOILS IN THE NORTHERN SOUTH CHINA SEA

Y.Yang, H.Kou, Z.Li, Y.Jia and C.Zhu (China Ocean Univ). *JOURNAL OF MARINE SCIENCE AND ENGINEERING* v.10, no.8, Aug. 2022. (ISSN 2077-1312; Article no.1142)

The study of the physical and mechanical properties of marine soil is of great importance for marine geohazard prediction, submarine energy extraction, and submarine foundation design. In this study, a series of basic geotechnical tests and triaxial compression tests are performed on samples taken from the Shenhu sea area in the South China Sea (SCS). Physical and mechanical properties, particularly normalized stress-strain behavior, are investigated. The microstructural and mineralogical characterization is carried out, through scanning electron microscopy (SEM), and X-ray diffraction (XRD). The results indicated that the sample could be classified as high-plasticity silt (MH) with high water content and high compressibility, that the soil has the highest quartz content in its mineral composition, a loose skeleton composed of flocculent structures under the microscope and is distributed with the remains of marine organisms. Furthermore, a new stress-strain-normalized condition is theoretically derived, based on the hyperbola function. In this condition, the concept of standard normalized factor, which is defined as the ultimate value of principal stress difference, is introduced. Meanwhile, the normalized stress-strain relationship of soft soil from the SCS is established under consolidated undrained conditions and the results of the model are compared with the experimental results, with a good normalization effect. It is believed that the work presented in this paper could contribute to the design and construction of offshore engineering.

SURFACE ACTIVE AGENT 1,561,771

A MOLECULAR STUDY ON THE BEHAVIOR OF POLYETHOXYLATED ALKYL ETHERS SURFACTANTS IN A WATER/N-ALKANE INTERFACE

A.M.Luz, T.J.dos Santos, G.D.Barbosa, C.L.Camargo and F.W.Tavares (Rio de Janeiro Fed Univ; Rice Univ; Alabama Univ, Tuscaloosa). *COLLOIDS AND SURFACES A: PHYSICOCHEMICAL AND ENGINEERING ASPECTS* v.651, 10/20/2022. (ISSN 0927-7757; Article no.129627)

Advanced oil recovery in oil/water and water/oil emulsions is a scientific and technological challenge, and efficient technologies depend on the water/oil interface properties. Due to their amphiphilic nature, surfactants are used to modify these interfacial properties to increase oil recovery and stabilize droplets in emulsification processes. Poly-(oxyethylene) alkyl ethers are a class of non-ionic surfactants often used as reference detergents due to their relatively simple structure compared to typical commercial surfactants. This tunable structure allows a design to tailor the substance's properties to the desired application. Here, we conduct molecular dynamics simulations to obtain both macroscopic and microscopic properties of water/n-heptane interfacial systems in the presence of these surfactants. We evaluated the effect of both temperature and modifications to the structure of the surfactant model, varying the number of ethylene oxide units in the head group. We verify that their structural properties are specific to maximize stabilizing interactions such as hydrogen bonds with water molecules, adopting a folded structure and parallel

orientation in regards to the interface. We analyze the Potential of Mean Force (PMF) that shows the affinity of the surfactant to the interface is enhanced as the number of ethoxylated units increases, which is related to the decrease in interfacial tension. (c2022 Elsevier B.V.)

SURFACE ACTIVE AGENT

1,561,772

COMPARATIVE STUDY ON THE AMPHIPHILICITY, EMULSIFYING AND FOAMING PROPERTIES OF SAPONINS EXTRACTED FROM *FURCRAEA FOETIDA*

T.H.Randriamamonjy, J.F.Ontiveros, M.T.Andrianjafy, P.Samiez, A.Berlioz-Barbier, V.Nardello-Rataj, J.Aubry, V.Ramanandraibe and M.Lemaire (Antananarivo Univ). *COLLOIDS AND SURFACES A: PHYSICO-CHEMICAL AND ENGINEERING ASPECTS* v.653, 11/20/2022. (ISSN 0927-7757; Article no.129923)

A sustainable surfactant was obtained as a by-product of waste from the production of fibers from *Furcraea foetida* (FF). The extraction process is described and the chemical constituents (flavonoids, saponins and others) in the hemp of Mauritius in Madagascar were determined using ultra-performance liquid chromatography coupled to high resolution hybrid mass spectrometer. The hypothesis of surface-active behavior of this crude mixture was corroborated by surface tension measurements and these results were compared with 2 commercial *Quillaja saponaria* (QS) samples: S0019 (TCI) and Q-Naturale 200 V. The critical micellar concentration of the FF saponins is 0.025 wt%. The hydrophilicity-lipophilicity radius was determined by the PIT-slope method and all saponins are more hydrophilic than the C10E4, the polyethoxylated reference surfactant. The hydrophilicity decreasing order is as follows: Q-Naturale 200 V > FF > S0019. Oil in water (O/W) emulsions were formulated with isopropyl myristate as oil and their size distribution and stability during 7 days are equivalents for the three saponins. There is no coalescence, and creaming phenomena can be reduced increasing the oil fraction. Nanoemulsions were obtained with FF using ultrasounds and reducing the oil content. Foaming properties were also studied and the stability of foams is similar between the 3 saponins (higher than the foam formulated with sodium laureth sulfate). These findings show that FF is a new source of saponins that can be used as promising emulsifier and foam agent with properties equivalent to those quantified for available commercial saponins and equal or better than typical benchmark surfactants as Tween 40 (emulsifier) or sodium laureth sulfate (foaming agent). (c2022 Elsevier B.V.)

SURFACE ACTIVE AGENT

1,561,773

MICROSCOPIC MECHANISMS OF $MgCl_2$ AFFECTING ANIONIC SURFACTANT ADSORPTION KINETICS ON THE AIR-WATER INTERFACE

X.Cao, W.Xia, P.Zhang, H.Cao, X.Li and X.Zhang (China Univ Petroleum). *COLLOIDS AND SURFACES A: PHYSICO-CHEMICAL AND ENGINEERING ASPECTS* v.653, 11/20/2022. (ISSN 0927-7757; Article no.129925)

Inorganic salts can significantly affect the interfacial tension (IFT) of surfactant solutions, which is a key factor influencing the interphase mass transfer and reaction in multiphase systems. The change in IFT is directly related to the adsorption behavior of surfactants. However, the mechanisms underlying the effects of salt on surfactant IFT and adsorption kinetics are not yet clear. Here, taking $MgCl_2$ and sodium dodecyl sulfate (SDS) as examples, the IFT characteristics of surfactant solutions under different salt concentrations were investigated, and the adsorption behavior and interface characteristics of SDS with or without $MgCl_2$ were further analyzed by molecular dynamics simulations. We find that surfactant adsorption involves mixed diffusion-kinetic controlled adsorption. The addition of $MgCl_2$ can obviously accelerate the adsorption kinetics and increase the adsorption capacity of SDS. Under the influence of magnesium ions, more "vacant sites" exist on the interface. Meanwhile, the orientation of the headgroups can be rapidly changed during the adsorption process to achieve a reasonable adsorption configuration faster, and the double electric layer (EDL) becomes thinner, reducing the electrostatic barrier. In addition, our findings offer new insights into anionic surfactant adsorption kinetics in a saline environment. (c2022 Elsevier B.V.)

SURFACE ACTIVE AGENT

1,561,774

INVESTIGATION ON NOVEL REDOX-RESPONSIVE FERROCENYL SURFACTANTS WITH REVERSIBLE INTERFACIAL BEHAVIOR AND THEIR RECYCLING APPLICATION FOR ENHANCED OIL RECOVERY

H.Jia, J.He, Q.Wang, Y.Xu, L.Zhang, H.Jia, L.Song, Y.Wang, Q.Xie et al. (China Univ Petroleum). *COLLOIDS AND SURFACES A: PHYSICO-CHEMICAL AND ENGINEERING ASPECTS* v.653, 11/20/2022. (ISSN 0927-7757; Article no.129971)

Stimuli responsive surfactants with reversible properties may effectively solve the problems of traditional surfactants (the switching of interfacial activity and the demulsification difficulty of emulsions) in enhanced oil recovery (EOR). In the present study, we fabricate brand-new redox-responsive double-tailed ferrocenyl surfactants 1,1'-ferrocenedicarboxylic acid-(N,N-dimethyldodecylamine)2 (FDA-(DMDA)2) via the dynamic supramolecular assembly. The reversible redox-responsive interfacial behaviors of ferrocenyl surfactants are estimated by measuring the interfacial tension reduction capacity, emulsifying performance, and wettability reversal ability. Compared with oxidized single-tailed ferrocenyl surfactant (FA-DMDA-Ox), oxidized double-tailed ferrocenyl surfactant (FDA-(DMDA)2-Ox) displays higher interfacial activity, which can be accurately switched by redox trigger. Cyclic micromodel flooding tests show that the FDA-(DMDA)2-Ox can in-situ emulsify the kerosene in pore media, and the addition of Na_2SO_3 to the produced fluid can achieve the recycle of the surfactants. Oil displacement tests demonstrate that the developed double-tailed ferrocenyl surfactants possess the potential in EOR and recycling. (c2022 Elsevier B.V.)

SURFACE ACTIVE AGENT

1,561,775

PORE-SCALE IMBIBITION COMPARISONS BETWEEN CAPILLARY AND GRAVITY FORCES REVEAL DISTINCT DRAINAGE MECHANISMS AND RESIDUAL OIL DISTRIBUTIONS

Q.Ma, W.Zhu, W.Bu, Z.Song, H.Li and Y.Liu (Beijing Univ Sci & Technol). *COLLOIDS AND SURFACES A: PHYSICO-CHEMICAL AND ENGINEERING ASPECTS* v.653, 11/20/2022. (ISSN 0927-7757; Article no.129981)

Capillary and gravity forces are considered two important drivers for enhanced oil recovery (EOR) in low-permeability reservoirs. To better understand the residual oil distribution and oil displacement mechanisms of these two driven systems, core- and pore-scale imbibition experiments were conducted in this work. The core-scale results indicated that the imbibition of surfactin (capillary force-driven) and an anionic gemini surfactant (AG, gravity-driven) solutions were comparable (only 0.6% original oil-in-place (OOIP) difference). And pore-scale results showed that surfactin and AG systems exhibited different dominant forces, cocurrent imbibition and countercurrent imbibition. Regarding the residual oil during imbibition, the surfactin solution creates an obvious oil-water-solid interface in the microtube and pushes the residual oil to coalesce into a "cluster" near the outlet. In contrast, the AG solution leaves residual oil films on the microtube wall during imbibition. It was concluded that the interface mechanisms of these differences are revealed by the investigations of contact angles and solid-liquid interfacial forces, which indicated that the original hydrophilic solid wall is exposed by surfactin, leading to capillary force-dominated imbibition, while the AG molecules only absorbed on the oil film that attach to the pore wall, instead of peeling it, could not establish significant capillary forces and must depend on gravity for severe imbibition. These findings explain the micro mechanisms and residual oil distribution features of different imbibition systems, which is helpful to optimize oil producing processes at a given reservoir during given development stages. (c2022 Elsevier B.V.)

THICKENER

1,561,776

TUG-OF-WAR BETWEEN HYDROGEN BOND AND HYDROPHOBIC INTERACTION OF BISFUNCTIONALIZED GRAPHENE OXIDE/HYDROLYZED POLYACRYLAMIDE

ALLOWS THICKENING AND SALT-RESISTANCE IN ENHANCED OIL RECOVERY

J.Cao, G.Xu, X.Wang, H.Wang, J.Zhang and C.Liu (China Univ Petroleum; State Key Laboratory China; Johns Hopkins Univ). *COLLOIDS AND SURFACES A: PHYSICO-CHEMICAL AND ENGINEERING ASPECTS* v.653, 11/20/2022. (ISSN 0927-7757; Article no.129909)

Polymer flooding is the most commonly used method to enhance oil recovery. Due to the harsh stratum environment, it is particularly important to prepare polymer systems with high viscosity and salt resistance. Here, we present a tug-of-war strategy that can easily control polymer system viscosity and salt resistance. By introducing hydroxyl and phenyl groups to the surface of GO, we successfully synthesized a series of Diethanolamine-Diphenylpropylamine Graphene Oxide (DDGO) with different ratio of hydroxyl and phenyl, as confirmed by TGA, ATR-FTIR and XPS analysis. ¹H NMR demonstrated the three DDGOs have different phenyl/hydroxyl ratio. TEM images showed DDGO maintained 2D nanostructure upon modification. We mixed partially hydrolyzed polyacrylamide (HPAM) with DDGO to form a hybrid system. The surface hydroxyl groups of DDGOs are bridged with HPAM through hydrogen bonds to improve network structures, whereas phenyl groups are conducive to self-association by π - π interaction. The properties of the hybrid systems are regulated by the tug of war of functional groups on the surface of nanoparticles. The results from oil displacement experiments showed that the enhanced oil recovery ratio jumped to 21.5% for HPAM/DDGO system, while it was only 7.7% for HPAM solution, which provides an alternative thought of EOR. (c2022 Elsevier B.V.)

WATERFLOODING

1,561,777

DYNAMICS OF ELECTROSTATIC INTERACTION AND ELECTRODIFFUSION IN A CHARGED THIN FILM WITH NANOSCALE PHYSICO-CHEMICAL HETEROGENEITY: IMPLICATIONS FOR LOW-SALINITY WATERFLOODING

A.Pourakaberian, H.Mahani and V.Niasar (Sharif Univ Technology; Manchester Univ). *COLLOIDS AND SURFACES A: PHYSICO-CHEMICAL AND ENGINEERING ASPECTS* v.650, 10/5/2022. (ISSN 0927-7757; Article no.129514)

The slow kinetics of wettability alteration toward a more water-wetting state by low-salinity waterflooding (LSWF) in oil-brine-rock (OBR) systems is conjectured to be pertinent to the electrokinetic phenomena in the thin brine film. We hypothesize that the nanoscale physicochemical heterogeneities such as surface roughness and surface charge heterogeneity at the rock/brine interface control further the dynamics of electrodiffusion and electrostatic disjoining pressure (Π_{el}), thus the time-scale and the magnitude of the low salinity effect (LSE). In this regard, film-scale computational fluid dynamics (CFD) simulations were performed. The coupled Poisson-Nernst-Planck (PNP) equations were solved numerically in a thin water film confined between a solid surface and oil, both negatively charged. The solid surface is representative of sandstone (quartz/kaolinite) with patchwise physicochemical heterogeneity. The electrical properties of the oil are representative of a crude-oil sample. The OBR system was initially under chemical equilibrium with high salinity (HS) brine, then was exposed to low salinity (LS) brine. The time-scale of reaching chemical equilibrium under LS, and the spatio-temporal evolution of electric potential were investigated. We find that surface roughness (introduced by quartz patches on quartz surface) increases the diffusion time up to 3-fold due to increased tortuosity. However the effect of surface roughness and surface charge heterogeneity (introduced by kaolinite patches on quartz surface) on the effective diffusion coefficient ($Deff$) is minor. While surface roughness and surface charge heterogeneity affect the disjoining pressure (Π_{el}) significantly, the influence of surface roughness on Π_{el} is more pronounced under HS than LS condition. In contrast, the effect of surface charge heterogeneity is more appreciable under LS than HS. Our findings imply that the LS effect can be enhanced in rough, heterogeneously charged systems like clayey sandstone, although its magnitude depends on the charge density of the roughness and its variation with salinity. We introduce two scaling factors, namely the effective diffusion coefficient ($Deff$) and the retardation coefficient (ω), to upscale the nanoscale results to pore-scale and beyond. (c2022 Elsevier B.V.)

WATERFLOODING

1,561,778

STUDY ON INTERFACE REGULATION EFFECTS OF JANUS NANOFUID FOR ENHANCED OIL RECOVERY

J.Cao, Y.Chen, G.Xu, X.Wang, Y.Li, S.Zhao, C.Liu and X.Wang (China Univ Petroleum; China Oilfield Svcs Ltd). *COLLOIDS AND SURFACES A: PHYSICO-CHEMICAL AND ENGINEERING ASPECTS* v.653, 11/20/2022. (ISSN 0927-7757; Article no.129880)

In this paper, Janus silica nanoparticles (JNS) were fabricated through a facile in-situ modification way. The hydrophilic-hydrophobic balance of Janus silica was regulable by changing the grafting amount of alkyl chains. In contrast to unmodified silica, Janus silica with amphiphilic features similar to surfactants had remarkable interface regulation effects at liquid-liquid and solid-liquid interfaces. JNS nanofluid lowered the interfacial tension and increased the interfacial modulus. It was also found that JNS had excellent emulsifying abilities. Moreover, JNS nanofluid could reverse the strongly oil-wet rock into water-wet, converting the capillary resistance into the driving force. The formation of disjoining pressure and reduced adhesion work of JNS nanofluid facilitated oil film stripping. The core flooding result showed that JNS nanofluid effectively enhanced oil recovery by 15.9 % with low dosages. The finding of this paper would help further understand the interface regulation effects of Janus nanofluid and construct an efficient nanofluid flooding system for enhanced oil recovery. (c2022 Elsevier B.V.)

WATERFLOODING

1,561,779

WATERFLOODING CHARACTERISTICS AND IMPROVEMENT MEASURES OF FRACTURE-CAVITY CARBONATE RESERVOIRS IN TAHE OILFIELD

S.Zheng, Z.Kang, X.Cheng, X.Li, S.Zhang, S.Cui and L.Jiang (Sinopec Research Inst; Sinopec). *PETROLEUM GEOLOGY AND RECOVERY EFFICIENCY (YOUQI DIZHI YU CAISHOULU)* v.29, no.6, pp.95-104, Nov. 2022. (ISSN 1009-9603; **In Chinese**)

[Full article and English abstract available from P.A.]

WATERFLOODING

1,561,780

WATER FLOODING EXPERIMENT AND LAW OF CARBONATE RESERVOIR CORES WITH DIFFERENT FRACTURE OCCURRENCES

H.Guo, L.Cheng, P.Wang and P.Jia (China Univ Petroleum). *PETROLEUM GEOLOGY AND RECOVERY EFFICIENCY (YOUQI DIZHI YU CAISHOULU)* v.29, no.6, pp.105-112, Nov. 2022. (ISSN 1009-9603; **In Chinese**)

[Full article and English abstract available from P.A.]

WATERFLOODING

1,561,781

A NEW CHARACTERIZATION METHOD FOR PREDOMINANT FLOW FIELD OF RESERVOIRS BASED ON OIL-TO-FLUX RATIO

K.Ma, H.Cai, Y.Gao and R.Jiang (China Nat Offshor Oil Corp; China Univ Petroleum). *PETROLEUM GEOLOGY AND RECOVERY EFFICIENCY (YOUQI DIZHI YU CAISHOULU)* v.29, no.6, pp.113-120, Nov. 2022. (ISSN 1009-9603; **In Chinese**)

[Full article and English abstract available from P.A.]

WATERFLOODING

1,561,782

APPLICATION OF PROBABILISTIC NEURAL NETWORK IN SALINE WATER FLOODED LAYER IDENTIFICATION

J.Li, M.Yang, Y.Du, H.Shen, L.Liu and Q.Sun (Shengli Oilfield Res Inst; China Univ Petroleum). *PETROLEUM GEOLOGY AND RECOVERY EFFICIENCY (YOUQI DIZHI YU CAISHOULU)* v.29, no.6, pp.121-129, Nov. 2022. (ISSN 1009-9603; **In Chinese**)

[Full article and English abstract available from P.A.]

WATERFLOODING 1,561,783

FEASIBILITY AND TECHNOLOGIES FOR IMPROVING RECOVERY AT EXTRA-HIGH WATER CUT DEVELOPMENT STAGE IN WATERFLOODING RESERVOIRS

X.Lue and W.Li (C & C Reservoirs; Daqing Oilfield Co Ltd). *PETROLEUM GEOLOGY AND RECOVERY EFFICIENCY (YOUQI DIZHI YU CAISHOULU)* v.29, no.6, pp.130-137, Nov. 2022. (ISSN 1009-9603; **In Chinese**)

[Full article and English abstract available from P.A.]

WATERFLOODING 1,561,784

SIMULATION AND PREDICTION OF WATER-FLOODING RESERVOIR RELATIVE PERMEABILITY CURVE BASED ON MACHINE LEARNING

C.Li, X.Cao, L.Zhang, X.Jiang, J.Liu, C.Jin, F.Wang and H.Yang (Shengli Oilfield Res Inst; Shengli Oilfield Co). *PETROLEUM GEOLOGY AND RECOVERY EFFICIENCY (YOUQI DIZHI YU CAISHOULU)* v.29, no.6, pp.138-142, Nov. 2022. (ISSN 1009-9603; **In Chinese**)

[Full article and English abstract available from P.A.]

WATERFLOODING 1,561,785

THE INTERPLAY BETWEEN MICROBIAL RESERVOIR SOURING AND BARITE PRECIPITATION DURING WATERFLOODING OIL AND GAS RESERVOIRS

A.Mahmoodi, M.Alizadeh Kiapi, M.Jahanbani Veshareh and H.Maghani Nick (Danish Hydrocarbon Res Ctr). *83RD ANNUAL EAGE CONFERENCE (Online and Madrid, Spain, 6/6-9/2022) ABSTRACTS* 2022. (Abstract no.631; Available at <http://www.earthdoc.org> as of 7/7/2022; 5 pp; **Abstract only**)

Seawater flooding is a common strategy of improved oil recovery, during which seawater, containing sulfate (SO₄²⁻), is injected into oil reservoirs to maintain reservoir pressure and sweep out oil. The presence of sulfate in an oil reservoir may trigger two harmful mechanisms, namely microbial reservoir souring and sulfate scales deposition. Microbial reservoir souring is a process in which sulfate reducing bacteria (SRB) consume sulfate and produce hydrogen sulfide (H₂S). Scale formation, occurs if, for instance, seawater, containing sulfate, mix with a Ba²⁺-rich formation brine to form barite (BaSO₄) scale. Due to the possible competition of these processes on consuming sulfate ions, an inclusive simulation of these processes is desired. This study utilizes a model that is capable of simulating reservoir souring and mitigation strategies along with scale formation inside the reservoir. The model simulates multi-phase flow using a commercial reservoir simulator, the chemical species transport, and the chemical reactions. It is shown that higher reservoir souring reduces the total barite formed in the reservoir. Conversely, barite formation has minimal effect on reservoir souring unless the injected sulfate concentration is low. Furthermore, if more barite is formed deep in the reservoir, less barite is formed around the production well.

WATER INJECTION 1,561,786

HOW SUBSEA PRODUCED WATER MANAGEMENT CAN REDUCE OVERALL CARBON FOOTPRINT OF SUBSEA-TO-SHORE OIL DEVELOPMENTS

S.Anres, S.Shaiek, F.Bacati, R.Giolo, W.Zid, E.La Sorda, M.Rondon, P.Pedenaud, G.Skivington et al. (Saipem). *OFFSHORE TECHNOLOGY CONFERENCE [OTC] (Houston, TX, 5/2-5/2022) PROCEEDINGS* 2022. (ISBN 978-1-61399-852-6; OTC-31822; Available at <http://www.onepetro.org> as of 6/23/2022; 22 pp)

A new subsea-to-shore oil field architecture is presented where produced water is separated, treated and re-injected locally. This solution reduces the overall power consumption and the global CO₂e footprint of the development compared to an architecture where the whole production is sent to shore. The paper will present the results of a study for the development of a 200,000 bpd oil field requiring 300,000 bpd water injection located 150 km from shore in 1,500 m water depth and with a field life of 15 years. Preliminary design work performed covers flow assurance, subsea process,

subsea equipment, subsea layout as well as CO₂e footprint comparison with a scenario where all the production is sent to shore. The system incorporates a gravity-based liquid-liquid separator for bulk oil-water separation, produced water is then treated, mixed with desulfated seawater and re-injected. Oil, gas and residual produced water are sent to shore via a single wet-insulated line with continuous injection of low-dosage hydrate inhibitors. This scenario has two main advantages compared to a subsea-to-shore without subsea processing. The first is that the power required to boost production is significantly reduced. The second is that the volume of produced water to be treated onshore is also significantly reduced, which is advantageous, not only in terms of cost, but also in terms of reducing the shore operation's footprint. Particular focus will be made on the produced water treatment design which is a two-stage design using two different technologies for increased robustness in order to reach a specification of 30 ppm oil-in-water for injection water. (Copyright 2022 OTC)

WATER IN OIL EMULSION 1,561,787

EFFECT OF ELECTROLYTES IN THE WATER PHASE ON THE STABILITY OF W1/O/W2 DOUBLE EMULSIONS

E.Kwak, J.Lee, Y.Jo and M.Choi (Konkuk Univ; Gangneung-Wonju Nat Univ). *COLLOIDS AND SURFACES A: PHYSICO-CHEMICAL AND ENGINEERING ASPECTS* v.650, 10/5/2022. (ISSN 0927-7757; Article no.129471)

This study aimed to improve the physicochemical stability of water-in-oil-in-water (W1/O/W2) double emulsions using different formulations that influence the inner emulsion fraction (water-in-oil (W/O) type: 10%, 20%, 30%, 40%, and 50%) and osmotic agents (NaCl, KCl, MgCl₂, and Na₂CO₃). The stabilities of the double emulsions were analyzed for 60 d based on the droplet size, charge, viscosity, and encapsulation efficiency (EE). From the results of the inner emulsion fraction, the double emulsions showed the smallest droplet size at 50% inner emulsion fraction, regardless of the osmotic agent. The viscosity and EE of the double emulsions increased as the inner emulsion fraction increased. The droplet size of the double emulsion increased in the following order: nonelectrolyte (control) < Na₂CO₃ < MgCl₂ < KCl < NaCl, according to osmotic agents. The double emulsions with NaCl and MgCl₂ exhibited higher EEs than the other emulsions. The EE of the double emulsion decreased from 81% (MgCl₂) to 0%. Therefore, our results concluded that the best formulation for a stable double emulsion was NaCl or MgCl₂ at 50% of the inner emulsion fraction. (c2022 Elsevier B.V.)

WELL CONTROL 1,561,788

ASSISTANCE SYSTEM AND METHOD FOR INTELLIGENT WELL CONTROL

Q.Zeng, D.Xie and Y.Gao, asrs. (Vertechs Oil & Gas Co Ltd). *World* 2022/198,547A1, p. 9/29/2022, f. 3/25/2021 (Appl. 2,182,907), pr. China 3/24/2021 (Appl. 2021-10,313,135) (G06F-0003/14; E21B-0021/08; G06F-0003/01; G06F-0003/16; G06T-0019/00). (**In Chinese**)

An assistance system and method for intelligent well control are disclosed herein. The system comprises AR glasses, a server, and a first sensor group. The first sensor group is configured to collect real-time data of a wellbore and the ground, and transmit the real-time data to the server. The server is configured to analyze a target pressure value of a throttling valve inlet of the ground according to the real-time data, acquire an actual pressure value of the throttling valve inlet of the ground from the real-time data, and transmit the actual pressure value and the target pressure value to the AR glasses. The AR glasses are configured to dynamically display the actual pressure value and the target pressure value in real time. The first sensor group and the server enable an operator to receive an actual pressure value and a target pressure value which are real-time and accurate; and the AR glasses can display the actual pressure value and the target pressure value in the field of view of the operator, and follows the line of sight of the operator, so that the operator can perform a well control operation more intently, thereby improving the security in a well control operation.

WELL MODEL

1,561,789

EXPERIMENTAL APPARATUS FOR SIMULATING SUBSTANCE EXCHANGE BETWEEN WELLBORE AND FORMATION

J.Deng, F.Xu, J.Zhou, L.Zhang, D.Chen, Y.Wang, Y.Ji, X.Sun et al., asrs. (China Coalbed Corp Ltd; China Univ Petroleum). World 2022/199,701A1, p. 9/29/2022, f. 3/25/2022 (Appl. 2,283,177), pr. China 3/26/2021 (Appl. 2021-10,327,751) (E21B-0047/10). (In Chinese)

An experimental apparatus for simulating substance exchange between a wellbore and a formation is disclosed herein. The experimental apparatus comprises: a wellbore simulation system, a wellbore liquid injection system, a formation simulation system, a formation fluid injection system, and a data acquisition system; the wellbore simulation system comprises a vertically arranged wellbore body for simulating a wellbore; the formation simulation system comprises a horizontally arranged sealing body for simulating a formation and a mortar filler filled in the sealing body; the wellbore liquid injection system is connected to the upper end of the wellbore body so as to inject a wellbore liquid into the wellbore body; the formation fluid injection system is connected to one end of the sealing body so as to inject a formation fluid into the sealing body; the other end of the sealing body is communicated with the bottom of the wellbore body; and the data acquisition system is electrically connected to the wellbore simulation system and the formation simulation system so as to acquire simulation data.

WETTABILITY

1,561,790

A MECHANISTIC COMPARISON OF FORMATE, ACETATE, AND GLYCINE AS WETTABILITY MODIFIERS FOR CARBONATE AND SHALE FORMATIONS

I.Baghisov, G.A.Abeykoon, M.Wang, O.P.Oyenowo, F.J.Arguelles-Vivas and R.Okuno (Texas Univ, Austin). *COLLOIDS AND SURFACES A: PHYSICO-CHEMICAL AND ENGINEERING ASPECTS* v.652, 11/5/2022. (ISSN 0927-7757; Article no.129849)

Previous studies indicated the efficacy of the simplest amino acid, glycine, as a wettability modifier that enhances the imbibition of water in carbonate reservoirs. The objective of this research was to compare the performance of formate, acetate, and glycine as wettability modifiers for carbonate and shale formations. Formate and acetate were studied for the first time as novel wettability modifiers. Note that the aminomethyl and amino groups are the only structural differences between formate and glycine, and acetate and glycine, respectively. The experiments consisted of contact-angle measurements on oil-aged calcite and shale plates, and imbibition displacements (spontaneous and forced). The comparison among these additives was made with/without adding hydrogen chloride (HCl) for adjusting the pH of the solutions. Amott indexes of glycine and formate + HCl solutions were noticeably higher than the rest of the cases in the imbibition experiments. We found that formate can be very effective in altering the wettability of carbonate rocks to water-wet state when the pH of the solution is reduced. This indicates the synergy of pH adjustment and the attraction of formate to the rock surface, which resulted in an improvement of the oil recovery. Glycine showed a superior behavior as a wettability modifier in comparison to formate and acetate for all the experimental conditions of this study. This indicated that the amino group, in the presence of the carboxyl group, plays a key role in altering the rock wettability. We demonstrated that the ability of glycine to alter wettability comes from two factors: one is the chelate effect caused by the amino group as an electron donor in the presence of the carboxyl group. The chelate effect makes glycine entropically more favorable for binding to calcium cation in the brine, which triggers calcite dissolution, and/or attaching directly to the calcite surface. The other factor is the calcite dissolution induced by pH reduction, followed by the attraction of glycine to the rock surface. (c2022 Elsevier B.V.)

WETTABILITY

1,561,791

DROPLET AND BUBBLE WETTING BEHAVIORS: THE ROLES OF SURFACE WETTABILITY AND ROUGHNESS

Y.Xiao, J.Zheng, Y.He and L.Wang (Chengdu Univ Technology). *COLLOIDS AND SURFACES A: PHYSICO-CHEMICAL AND ENGINEERING ASPECTS* v.653, 11/20/2022. (ISSN 0927-7757; Article no.130008)

Droplet and bubble wettability are important parameters for characterizing the wetting propensity of solid surface. Recent studies have shown significant differences between the wetting behaviors of droplet and bubble, specifically apparent contact angle (ACA) and contact angle hysteresis (CAH). However, very few studies have systematically investigated and examined the differences. Additionally, there is a lack of comprehensive knowledge and experimental observations about the effects of surface roughness on the droplet and bubble wetting behaviors under different wetting states. These knowledge gaps restrict our understanding of the wetting dynamic process. In this study, by varying surface roughness and modifying wettability with silane coupling agent KH-550, we evaluated droplet and bubble CAHs from strong hydrophilicity to hydrophobicity using a novel gas-driven method and the moving needle method, and analyzed the measurements using the friction force model. Young contact angle (YCA) was calculated to characterize the intrinsic wettability of three-phase system and experimental observations were interpreted in detail. The results show that the impact of roughness on droplet CAH varies in different wetting states caused by coupled effect between solid-liquid affinity and rough microstructure. A critical YCA for effective spreading is observed in bubble wetting behaviors for the first time, above which bubble ACA and CAH abruptly change. The increase of roughness reduces bubble ACA and CAH. With a critical Young contact angle as the turning point, the difference between droplet and bubble wetting behaviors as well as the effect of roughness vary. Additionally, after bubble fully spreads, its advancing angles are equal to droplet ACAs, and its ACAs are equal to droplet receding angles on relatively smooth surface. These intriguing findings are supplementary to current knowledge about droplet and bubble wetting behaviors. (c2022 Elsevier B.V.)

PIPELINING, SHIP & STORAGE**FLEXIBLE PIPE**

1,561,792

THERMOPLASTIC POLYMER BLENDS

L.Chen and C.Xu, asrs. (Covestro LLC). World 2022/211,994A1, p. 10/6/2022, f. 3/9/2022 (Appl. 2,219,550), pr. U.S. 4/1/2021 (Appl. 220,003) (C08L-0075/04; B32B-0001/08; B32B-0027/40; E21B-0043/01; F16L-0011/00).

The present disclosure is directed to thermoplastic polymer blends. The blends can include a first thermoplastic polyurethane and a second thermoplastic polyurethane, wherein the blend includes from 10 wt% to 50 wt% of the second thermoplastic polyurethane based on a total weight of the thermoplastic polymer blend. The first thermoplastic polyurethane can include a reaction product of a first reaction mixture consisting of or consisting essentially of an aliphatic diisocyanate and an aliphatic isocyanate-reactive component. The second thermoplastic polyurethane can include a reaction product of a second reaction mixture including a polyisocyanate, an isocyanate-reactive component having a number average molecular weight of from 500 g/mol to 10,000 g/mol, and a chain extender having a number average molecular weight of from 60 g/mol to 450 g/mol.

GAS HYDRATE

1,561,793

A REVIEW OF NATURAL GAS HYDRATE FORMATION WITH AMINO ACIDS

B.Li, Y.Y.Lu and Y.L.Li (Chongqing Univ). *JOURNAL OF MARINE SCIENCE AND ENGINEERING* v.10, no.8, Aug. 2022. (ISSN 2077-1312; Article no.1134)

Natural gas is a kind of low-carbon energy source with abundant reserves globally and high calorific value. It is cleaner and more efficient than oil and coal. Enlarging the utilization of natural gas is also one of the important ways to reduce carbon emissions in the world. Solidified natural gas technology (SNG) stores natural gas in solid hydrates, which is a prospective, efficient, safe and environmental-friendly strategy of natural gas storage and transport. However, the slow growth rate and randomness of nucleation during natural gas hydrate formation in pure water hinder the industrial application of this technology. As a kind of new and potential additives, biodegradable amino acids can be adopted as favorable kinetic promoters for natural gas hydrate synthesis. Compared with other frequently used chemical additives, amino acids are usually more friendly to the environment, and are capable of avoiding foam formation during complete decomposition of gas hydrates. In this paper, we have reviewed the research progress of gas hydrate generation under the promotion of amino acids. The formation systems in which amino acids can enhance the growth speed of gas hydrates are summarized, and the impact of the concentration in different systems and the side chains of amino acids on hydrate growth have been illustrated. The thermodynamic and kinetic behaviors as well as the morphology properties of hydrate formation with amino acids are summarized, and the promotion mechanism is also analyzed for better selection of this kind of potential additives in the future.

MOORING 1,561,794

A SEMI-SUPERVISED MACHINE-LEARNING MODEL TO FORECAST MOVEMENTS OF MOORED VESSELS

E.Romano-Moreno, A.Tomas, G.Diaz-Hernandez, J.L.Lara, R.Molina and J.Garcia-Valdecasas (Cantabria Univ; Madrid Politecnica Univ; Oritia & Boreas). *JOURNAL OF MARINE SCIENCE AND ENGINEERING* v.10, no.8, Aug. 2022. (ISSN 2077-1312; Article no.1125)

Good performance of port activities in terminals is mainly conditioned by the dynamic response of the moored ship system at a berth. An adequate definition of the highly multivariate processes involved in the response of a moored ship at a berth is crucial for an appropriate characterization of port operability. The availability of an efficient forecast system of the movements of moored ships is essential for the planning, performance, and safety of the development of port operations. In this paper, an inference model to predict moored ship motions based on a semi-supervised machine-learning methodology is presented. A comparison with different supervised and unsupervised machine-learning techniques, as well as with existing deep learning-based models for predicting moored ship motions, has been performed. The highest performance of the semi-supervised machine learning-based model has been obtained. Additionally, the influence of infragravity wave parameters introduced as predictor variables in the model has been analyzed and compared with the typical ocean waves, wind, and sea level as predictor variables. The prediction model has been developed and validated with an available dataset of measured data from field campaigns in the Outer Port of Punta Langosteira (A Coruna, Spain).

PIPELINE 1,561,795

PREDICTION OF RUPTURE AND PERFORATION LIMITS OF PRESSURISED X80 PIPELINES USING BP NEURAL NETWORKS AND GENERALISED ADDITIVE MODELS

Y.Zhou and S.Zhang (Hohai Univ). *OCEAN ENGINEERING* v.259, 9/1/2022. (ISSN 0029-8018; Article no.111839)

Impact resistance of in-service pressurised X80 pipelines is one of the top safety priorities in the petrochemical industry. Based on impact limits, including the rupture and perforation limits, the failure threshold can be identified and the impact resistance of target structures can be assessed. In this study, backpropagation neural networks (BPNNs) and generalised additive models (GAMs) were developed to predict the rupture and perforation limits of pressurised X80 pipelines. First, an explicit dynamic model was established to provide comprehensive training datasets considering the effects of various dominant parameters. Interdependencies between the impact limits and various dominant parameters were

analysed using the Pearson correlation coefficient. Then, BPNN models optimised by the backpropagation algorithm and neuron numbers were trained to predict the impact limits. Based on the optimal smooth functions and smoothing coefficients, the GAMs then provided two integrated regression functions for impact limits. Finally, the predictive stabilities of the BPNN and GAM on impact limits were discussed using a random dataset. The BPNNs and GAMs were in a strong agreement with the expectations, and the predictive accuracy of the BPNNs was approximately three times that of GAMs. The findings of this study can be used as guidelines for protection design and risk assessment of pressurised X80 pipelines. (c2022 Elsevier Ltd.)

PIPELINE 1,561,796

PIPELINE INSPECTION ROBOT WITH VARIABLE TRACKS AND CONTROL METHOD THEREFOR

A.Song, T.Miao, B.Shao, B.Xu, G.Song, B.Xu, S.Liu and J.Min, asrs. (Southeast Univ). World 2022/198,714A1, p. 9/29/2022, f. 4/1/2021 (Appl. 2,184,851), pr. China 3/24/2021 (Appl. 2021-10,312,255) (F16L-0055/32; B62D-0055/065; B62D-0055/08; B62D-0055/116). (In Chinese)

Disclosed are a pipeline inspection robot with variable tracks and a control method therefor. The pipeline inspection robot of the present invention comprises a robot main body, track assemblies symmetrically arranged on left and right sides of the robot main body, and a forward driving mechanism, wherein the robot main body is connected to the track assemblies on the left and right sides of the robot main body by means of a track fixing frame, and a track angle adjusting mechanism is respectively connected between the robot main body and the track assemblies on the left and right sides thereof. By means of the present invention, an inclination angle of the track can be adjusted, and each set of track angle adjusting mechanisms is independent, and thus the robot has good flexibility to adapt to different pipeline environments.

PIPELINE FLOW 1,561,797

FORMATION AND FLOW CHARACTERISTICS OF METHANE HYDRATES IN HIGH-PRESSURE PIPELINES

S.Huang, G.Ma, C.Zang, Y.Wang and X.Wang (Liaoning Petrochem Univ). *INDUSTRIAL & ENGINEERING CHEMISTRY RESEARCH* v.61, no.25, pp.8738-8751, 6/29/2022. (ISSN 0888-5885; ISSN 1520-5045)

To ensure the safe flow of the hydrate slurry in the pipeline, a high-pressure flow loop with visual capability was designed, and flow characteristics and growth kinetics of methane (CH₄) hydrates from the pure water system were investigated. Experiment results showed that with an increase in the flow rate, the induction time first increased and subsequently decreased. When the flow rate was higher than 360 L/h, the loop was not blocked. The effect of NaCl on polyvinylpyrrolidone (PVP) as the kinetic inhibitor on the nucleation and growth of methane hydrates was studied by measuring the hydrate induction time and gas consumption. The results show that the addition of PVP was found to significantly prolong the hydrate induction time and decrease the amount of gas consumption; the presence of NaCl enhanced the inhibition strength of PVP. Through the focused beam reflectance measurement (FBRM), the results indicated that the hydrate particle size in the loop decreases with an increase of flow rate, and the added PVP to the system led to smaller average particle size. Based on the analysis of pressure difference and flow rate, the mechanism of pipe clogging in the pure water system was put forward. We believe that this research can provide theoretical support for the industrial application of CH₄ hydrate slurry flow to some extent.

PIPELINE INDUSTRY 1,561,798

COMBINED DRILLING AND STOPPING SYSTEM

M.U.Qasim, Y.Li and R.F.Larson, asrs. (Mueller International LLC). World 2022/204,538A1, p. 9/29/2022, f. 3/25/2022 (Appl. 2,221,989), pr. U.S. 3/26/2021 (Appl. 63/166,436) (F16L-0041/00; F16K-0043/00; F16L-0041/06; F16L-0055/10; F16L-0055/11;

F16L-0055/12).

A machine includes a tool housing defining a housing cavity; a first tool coupled to a first linear drive mechanism, the first tool linearly repositionable along an axis by the first linear drive mechanism about and between a first retracted position and an extended position, the first tool positioned within the housing cavity in the first retracted position, the first tool positioned external to the housing cavity in the extended position; and a second tool coupled to a second linear drive mechanism, the second tool linearly repositionable along the axis by the second linear drive mechanism about and between a second retracted position and a sealing position, the second tool positioned within the housing cavity in the second retracted position, the second tool positioned external to the housing cavity in the sealing position.

PIPELINE TRANSPORTATION 1,561,799

SOLID DRAG REDUCTION ADDITIVE AND METHODS OF USING SAME

B.M.Vittur, asr. (Baker Hughes Oilfield LLC). World 2022/203,819A1, p. 9/29/2022, f. 2/28/2022 (Appl. 2,218,201), pr. U.S. 3/26/2021 (Appl. 214,164) (C08F-0020/18; C08F-0002/00; C08F-0002/22).

Methods of reducing drag in a flowing hydrocarbon include introducing to the flowing hydrocarbon an amount of a solid drag reducing additive effective to improve the flow, the solid drag reducing additive including a polymer particle prepared from at least one polar monomer and a percent by weight (wt%) of liquid of 50 wt% or less. Methods also include producing a solid drag reducing additive that includes forming a polymer from at least one polar monomer by emulsion polymerization; and disrupting the emulsion by adding at least one demulsifier and at least one anti-blocking agent to form the solid drag reducing additive. Compositions include a solid drag reducing additive comprising a polymer prepared from at least one polar monomer and having an average particle size in a range of about 100 pm to about 500 pm, wherein the solid drag reducing additive comprises less than 50 wt% of liquid.

PIPELINE TRANSPORTATION 1,561,800

ANTICORROSIVE COMPOSITION

O.Hamza, R.Mattsson, A.L.Paulsen, M.O.Hansen, asrs. (RockWool A/S). World 2022/200,535A1, p. 9/29/2022, f. 3/24/2022 (Appl. 2,257,838), pr. Europe 3/25/2021 (Appl. 21,164,922) (C23F-0011/08; C03C-0025/007; C03C-0013/06; F16L-0058/04; C04B-0028/26; D04H-0001/64; F16L-0059/14; C09D-0005/00; C23F-0011/06; C23F-0011/18; C23F-0011/12; F16L-0059/147; C09D-0001/04; C09D-0007/61; C08K-0003/32; C08K-0003/34; C09D-0007/63; C08K-0005/092).

The present invention relates to an anticorrosive composition and the use of such a composition for imparting anticorrosive properties to a material, and a material comprising such a composition.

SHIP 1,561,801

MULTICRITERIA SHIP ROUTE PLANNING METHOD BASED ON IMPROVED PARTICLE SWARM OPTIMIZATION-GENETIC ALGORITHM

W.Zhao, Y.Wang, Z.Zhang and H.Wang (Jilin Univ). JOURNAL OF MARINE SCIENCE AND ENGINEERING v.9, no.4, April 2021. (ISSN 2077-1312; Article no.357)

With the continuous prosperity and development of the shipping industry, it is necessary and meaningful to plan a safe, green, and efficient route for ships sailing far away. In this study, a hybrid multicriteria ship route planning method based on improved particle swarm optimization-genetic algorithm is presented, which aims to optimize the meteorological risk, fuel consumption, and navigation time associated with a ship. The proposed algorithm not only has the fast convergence of the particle swarm algorithm but also improves the diversity of solutions by applying the crossover operation, selection operation, and multigroup elite selection operation of the genetic algorithm and improving the Pareto

optimal frontier distribution. Based on the Pareto optimal solution set obtained by the algorithm, the minimum-navigation-time route, the minimum-fuel-consumption route, the minimum-navigation-risk route, and the recommended route can be obtained. Herein, a simulation experiment is conducted with respect to a container ship, and the optimization route is compared and analyzed. Experimental results show that the proposed algorithm can plan a series of feasible ship routes to ensure safety, greenness, and economy and that it provides route selection references for captains and shipping companies.

SHIP 1,561,802

COOPERATIVE MANEUVERING MATHEMATICAL MODELING FOR MULTI-TUGS TOWING A SHIP IN THE PORT ENVIRONMENT

G.Wu, X.Zhao, Y.Sun and L.Wang (Shanghai Maritime Univ; Harbin Engineering Univ). JOURNAL OF MARINE SCIENCE AND ENGINEERING v.9, no.4, April 2021. (ISSN 2077-1312; Article no.384)

The towing operation of multi-tug-assisted ship navigation mainly relies on the experience of the captain, and there is no set of effective operation methods. Therefore, it is difficult to achieve accurate assisted navigation when multiple tugboats work in coordination. The calculation method of maneuverability of the towing system with multi-tug-assisted navigation is proposed in this paper. In view of the complexity of multi-tug-assisted large ship maneuvering, this article focuses on solving the problems of force analysis and maneuvering modeling between the multi-tug and ship systems. Firstly, a maneuvering mathematic model for towing ships is established, and the hydrodynamic force of the hull, rope force of the tugs, and force of wind interference are analyzed. The thrust and moment of the ducted azimuthal propeller are calculated, and the mathematical model of the tug's cable tension is discussed. Then, the fourth-order Runge-Kutta method is used to solve the differential equations of the maneuvering motion of the ships and each tug. Based on the ship-towing process by multiple tugs, a multi-tug-assisted ship towing simulation platform was built by using the Visual Studio development tool. Finally, on the simulation platform, multi-tug longitudinal-towing-simulation experiments at different speeds were carried out, and the simulation of turning towing maneuvers under the influence of wind was done. The simulation results showed that as the towing speed increases, the initial towing speed fluctuates greatly. There is a significant drift effect on the ships by the wind force. And the wind will cause a fluctuation in the tug's rope force. The simulation of the multi-tugs towing a ship entering the port was carried out in the port environment. The results showed that the multi-tug towing system and simulation platform may be used for the safety training of the tug's crew.

SHIP 1,561,803

SHIP ROLL PREDICTION ALGORITHM BASED ON BI-LSTM-TPA COMBINED MODEL

Y.Wang, H.Wang, D.Zou and H.Fu (Harbin Engineering Univ). JOURNAL OF MARINE SCIENCE AND ENGINEERING v.9, no.4, April 2021. (ISSN 2077-1312; Article no.387)

When ships sail on the sea, the changes of ship motion attitude presents the characteristics of non-linearity and high randomness. Aiming at the problem of low accuracy of ship roll angle prediction by traditional prediction algorithms and single neural network model, a ship roll angle prediction method based on bidirectional long short-term memory network (Bi-LSTM) and temporal pattern attention mechanism (TPA) combined deep learning model is proposed. Bidirectional long short-term memory network extracts time features from the forward and reverse of the ship roll angle time series, and temporal pattern attention mechanism extracts the time patterns from the deep features of a bidirectional long short-term memory network output state that are beneficial to ship roll angle prediction, ignore other features that contribute less to the prediction. The experimental results of real ship data show that the proposed Bi-LSTM-TPA combined model has a significant reduction in MAPE, MAE, and MSE compared with the LSTM model and the SVM model, which verifies the effectiveness of the proposed algorithm.

SHIP **1,561,804**

DEVELOPMENT OF ALGORITHMS FOR IDENTIFYING PARAMETERS OF THE MARITIME VESSEL MOTION MODEL IN OPERATING CONDITIONS WITH ELEMENTS OF INTELLECTUAL ANALYSIS

N.Ivanovskii, S.G.Chernyi, A.Zhilentov and V.Emelianov (Kerch State Marine Univ; St Petersburg Marine Univ; Russian Fed Financial Univ). *JOURNAL OF MARINE SCIENCE AND ENGINEERING* v.9, no.4, April 2021. (ISSN 2077-1312; Article no.418)

The article examines the synthesis of algorithms for the estimation of the random parameters of ship movement models, based on measured information in field tests. In addition, accuracy analysis of the synthesized algorithms is provided. The derived algorithms are relatively simple and allow highly precise unknown parameters for estimation of ship motion models at the non-real-time scale to be obtained using the measurements recorded in field tests. The results can be used in the construction of automated ship control systems, or in the development of navigation simulators and the creation of ship models.

SHIP **1,561,805**

A VELOCITY OBSTACLE-BASED REAL-TIME REGIONAL SHIP COLLISION RISK ANALYSIS METHOD

P.Chen, M.Li and J.Mou (Wuhan Univ Technology). *JOURNAL OF MARINE SCIENCE AND ENGINEERING* v.9, no.4, April 2021. (ISSN 2077-1312; Article no.428)

Maritime accidents such as ship collisions pose continuous risks to individuals and society with due to their severe consequences on human life, economic and environmental losses, etc. Supervising the maritime traffic in the different regions and maintaining its safety level is an essential task for stakeholders such as maritime safety administrations. In this research, a new ship collision risk analysis method is developed with the utilisation of AIS (automatic identification system) data. A velocity obstacle-based risk measurement is applied to measure the risk of collision between multiple ships from the velocity perspective, based on which, the collision risk and the complexity of the encounter situation are obtained at the same time. Secondly, a density-based clustering technique is introduced to identify the hot spots of ship traffic in the region as an indicator for maritime safety operators. A case study using historical AIS data was implemented to verify the effectiveness of the proposed approach in a manner that simulates the real-time data scenario. Furthermore, a comparison between existing risk analysis method is conducted to validate the proposed method.

SHIP **1,561,806**

FINITE-TIME CONTROLLER DESIGN FOR THE DYNAMIC POSITIONING OF SHIPS CONSIDERING DISTURBANCES AND ACTUATOR CONSTRAINTS

Y.Zhang, C.Liu, N.Zhang, Q.Ye and W.Su (Wuxi Inst Technology; China Ship Sci Res Center). *JOURNAL OF MARINE SCIENCE AND ENGINEERING* v.10, no.8, Aug. 2022. (ISSN 2077-1312; Article no.1034)

Focusing on dynamic positioning (DP) systems for ships, which are subject to environmental disturbances and actuator constraints, this paper presents a finite-time controller that uses a disturbance observer with the aid of a backstepping technique. First, to estimate the time-varying and unknown environmental disturbances in finite time, two sliding-mode disturbance observers are constructed. Specifically, an adaptive disturbance observer (ADO) effectively decreases undesired chattering without the need for prior information on environmental disturbances. Then, to handle the actuator constraints, the designed control forces are distributed into multiple actuators using a control allocation algorithm to obtain the actual forces. Next, an auxiliary dynamic system is built to compensate for velocity tracking errors induced by the mismatch of the DP control law and thruster forces. Then, with the designed ADO and the auxiliary dynamic system, a finite-time controller with a fast exponential-reaching law is designed; this ensures that the positioning errors and the sliding surface

converge to zero at a fast convergence rate. Finally, numerical simulations are presented: these present a cable-laying ship experiencing wind, currents, and waves in different sea states. The results show the effectiveness of the presented control scheme.

SHIP **1,561,807**

STUDY ON SLOSHING CHARACTERISTICS IN A LIQUID CARGO TANK UNDER COMBINATION EXCITATION

Q.Zhang, B.Shui and H.Zhu (Wuhan Univ Technology). *JOURNAL OF MARINE SCIENCE AND ENGINEERING* v.10, no.8, Aug. 2022. (ISSN 2077-1312; Article no.1100)

Sloshing is a common flow phenomenon in liquid cargo tanks and has a great negative impact on the stability and safety of ship navigation. It is important to understand the sloshing process of tanks under the excitation of complex external conditions for the transportation of liquid cargo. In this paper, the sloshing characteristics of a liquid cargo tank are studied under the combination excitation conditions of roll and surge. The pressure distribution characteristics at different positions of the cargo tank are discussed, along with the influence of different excitation conditions on the pressure of the cargo tank. The results show that under the condition of combination excitation, the fluid sloshes along the diagonal direction of the tank, and the peak liquid height and peak pressure are located on the diagonal corner of the tank. The peak pressure at the lowest point on the diagonal of the tank is proportional to the amplitude of the roll angle and surge, and the change in roll angle amplitude has a significant impact on the pressure and liquid height at different positions.

SHIP **1,561,808**

REAL-TIME WEIGHT OPTIMIZATION OF A NONLINEAR MODEL PREDICTIVE CONTROLLER USING A GENETIC ALGORITHM FOR SHIP TRAJECTORY TRACKING

D.Yu, F.Deng, H.Wang, X.Hou, H.Yang and T.Shan (Qingdao Univ Sci & Technol). *JOURNAL OF MARINE SCIENCE AND ENGINEERING* v.10, no.8, Aug. 2022. (ISSN 2077-1312; Article no.1110)

This paper presents a weight optimization method for a nonlinear model predictive controller (NMPC) based on the genetic algorithm (GA) for ship trajectory tracking. The weight coefficients Q and R of the objective function in NMPC are obtained via the real-time optimization of the genetic algorithm instead of the trial and error method, which improves the efficiency and accuracy of the controller. In addition, targeted improvements are made to the internal crossover operator, mutation operator, crossover rate, and mutation rate of the genetic algorithm. The simulation comparison of trajectory tracking between NMPC with real-time-optimized weight coefficients and the one with constant coefficients is performed. Finally, the simulation result shows that the controller with real-time-optimized weight coefficients has a better trajectory tracking effect than that with constant weight coefficients.

SHIP **1,561,809**

DEVELOP A COMPREHENSIVE METHOD TO EVALUATE THE MENTAL WORKLOAD OF SHIP OPERATORS

S.Yan, Y.Weil, F.Li and C.C.Tran (Harbin Engineering Univ; Vietnam National Univ). *JOURNAL OF MARINE SCIENCE AND ENGINEERING* v.10, no.8, Aug. 2022. (ISSN 2077-1312; Article no.1133)

Mental workload has become an important factor affecting the human error of ship operators. Controlling the mental workload of operators within a reasonable range can reduce human errors. The purpose of this study is to develop an evaluation method to evaluate the ship operator's mental workload. First, the evaluation indices system was constructed according to three types of mental workload measurements. Second, the criteria importance through intercriteria correlation (CRITIC) method and analytic hierarchy process (AHP) method were used to determine the relative weight of each index. Finally, the fuzzy theory was used to calculate ship operator's mental workload. The experiment results indicated that subjective workload assessment technique, physiological

measurement (eye response), and error rate can be integrated into the comprehensive evaluation method to assess the mental workload of ship operators. Thus, this method can be used to comprehensively evaluate the mental workload level and improve the reliability of the assessment results.

SHIP **1,561,810**

DESIGN AND SAFETY ASSESSMENT OF RECOMMENDED ROUTE OFF THE WESTERN COAST OF IZU O SHIMA ISLAND

R.Miyake and H.Itoh (National Maritime Res Inst). *JOURNAL OF MARINE SCIENCE AND ENGINEERING* v.10, no.8, Aug. 2022. (ISSN 2077-1312; Article no.1060)

Ship routing systems (e.g., traffic separation schemes) have been established worldwide to ensure ship traffic safety. There are no specific measures to establish an effective ship route. We have previously proposed a method to design and assess the route comparison with the present traffic flow in the interest to establish an effective ship routing system, particularly for recommended routes. The method consists mainly of the following procedures: understanding the existing phenomena and the issues in the target area by analyzing target traffic flow; designing safety measures; assessing the safety measures; and determining the optimal safety measure. This method was used to design and assess the recommended route off the western coast of Izu O Shima Island. This route has been in service since January 2018. The purpose of this study is to validate the proposed method. First, the technical details of the method are described. An automatic identification system (AIS) observation was conducted before and after the implementation to validate the effectiveness of the recommended route for reducing collisions. The results show that the recommended route effectively reduces the risk of collisions. More specifically, the proposed method was found to be useful when establishing an effective recommended route.

SHIP **1,561,811**

A REVIEW OF PROGRESS AND APPLICATIONS OF AUTOMATED VACUUM MOORING SYSTEMS

K.Yan, S.Zhang, J.Oh and D.W.Seo (Kunsan National Univ). *JOURNAL OF MARINE SCIENCE AND ENGINEERING* v.10, no.8, Aug. 2022. (ISSN 2077-1312; Article no.1085)

Compared with the traditional mooring system, the automated vacuum mooring system can meet the development needs of large-scale ship automation, port automation, and environmental protection. This review describes the latest research focuses, progress, applications, and future perspectives regarding the automated vacuum mooring system. First, the components, working principles, advantages, limits, and risks of the automated vacuum mooring system are discussed. Secondly, typical application cases of automated vacuum mooring systems are introduced, looking at two aspects of the ship-based system and shore-based system. Then, the routine maintenance of the automated vacuum mooring system is introduced. Finally, a discussion on the challenges and future perspectives of the automated vacuum mooring system is provided in this review. The advantages of an automated vacuum mooring system make it a potentially highly effective and economical option for a wider range of ship mooring than a traditional mooring system.

SHIP **1,561,812**

FAST MULTIGRID ALGORITHM FOR NON-LINEAR SIMULATION OF INTACT AND DAMAGED SHIP MOTIONS IN WAVES

Z.Wang, T.Li, Q.Jin, H.Guo, J.Zhao and J.Qi (Wuhan Univ Technology; Marine Design & Res Inst; Three Gorges Navigation). *JOURNAL OF MARINE SCIENCE AND ENGINEERING* v.10, no.8, Aug. 2022. (ISSN 2077-1312; Article no.1101)

This paper proposes a fast multigrid algorithm to simulate the non-linear motion of ships in both intact and damaged conditions. The simulations of ship motions in waves are known to require much time to calculate due to the strong non-linear interactions

between ship and waves. To improve the calculation efficiency while retaining the accuracy, a prediction-correction strategy was designed to accelerate the simulation through three sets of locally refined meshes. The flow field was first estimated in a coarse mesh and then mapped to a locally refined mesh for further higher-fidelity corrections. A partitioned radial basis function (PRBF) method is proposed to interpolate and reconstruct the flow field for the refined mesh. A new two-phase flow solver was developed with a fast multigrid algorithm based on the Reynolds-averaged Navier-Stokes equations (RANSE). The new solver was applied to study the non-linear behavior of a damaged ship in beam waves and the effect of damaged compartments on ship rolling motion. Validation against the solution with the original method of single set meshes and experimental data indicates that the proposed algorithm yields satisfactory results while saving 30-40% of the computational time.

SHIP **1,561,813**

AVAILABLE MANEUVERING MARGINS-BASED SHIP COLLISION ALERT SYSTEM

L.Du, O.A.V.Banda and Z.Sui (Wuhan Univ Technology; Aalto Univ). *JOURNAL OF MARINE SCIENCE AND ENGINEERING* v.10, no.8, Aug. 2022. (ISSN 2077-1312; Article no.1123)

The timing of a ship taking evasive maneuvers is crucial for the success of collision avoidance, which is affected by the perceived risk by the navigator. Therefore, we propose a collision alert system (CAS) based on the perceived risk by the navigator to trigger a ship's evasive maneuvers in a timely manner to avoid close-quarters situations. The available maneuvering margins (AMM) with ship stability guarantees are selected as a proxy to reflect the perceived risk of a navigator; hence, the proposed CAS is referred to as an AMM-based CAS. Considering the dynamic nature of ship operations, the non-linear velocity obstacle method is utilized to identify the presence of collision risk to further activate this AMM-based CAS. The AMM of a ship are measured based on ship maneuverability and stability models, and the degree to which they violate the risk perception-based ship domain determines the level of collision alert. Several typical encounter scenarios are selected from AIS data to demonstrate the feasibility of this AMM-based CAS. The promising results suggest that this proposed AMM-based CAS is applicable in both ship pair encounter and multi-vessel encounter scenarios. Thus, the collision risk can be accurately detected, and then a collision alert consistent with the risk severity is issued. This proposed AMM-based CAS has the potential to assist autonomous ships in understanding the risk level of the encounter situation and determining the timing for evasive maneuvers. The advantages and limitations of this proposed method are discussed.

SHIP **1,561,814**

RESEARCH ON SHIP COLLISION PROBABILITY MODEL BASED ON MONTE CARLO SIMULATION AND BI-LSTM

S.Vuksa, P.Vidan, M.Bukljias and S.Pavic (Split Univ; Zagreb Univ). *JOURNAL OF MARINE SCIENCE AND ENGINEERING* v.10, no.8, Aug. 2022. (ISSN 2077-1312; Article no.1124)

The efficiency and safety of maritime traffic in a given area can be measured by analyzing traffic density and ship collision probability. Maritime traffic density is the number of ships passing through a given area in a given period of time. It can be measured using vessel tracking systems, such as the Automatic Identification System (AIS). The information provided by AIS is real-time data designed to improve maritime safety. However, the AIS data can also be used for scientific research purposes to improve maritime safety by developing predictive models for collisions in a research area. This article proposes a ship collision probability estimation model based on Monte Carlo simulation (MC) and bidirectional long short-term memory neural network (Bi-LSTM) for the maritime region of Split. The proposed model includes the processing of AIS data, the verification of AIS data, the determination of ports and ship routes, MC and the collision probability, the Bi-LSTM learning process based on MC, the ship collision probability for new or existing routes, and the traffic density. The results of MC, i.e., traffic/vessel route and density, and collision probability for the study area can be used for Bi-LSTM training with the aim of

estimating ship collision probability. This article presents the first part of research that includes MC in detail, followed by a preliminary result based on one day of processed AIS data used to simulate MC and propose a model architecture that implements Bi-LSTM for ship collision probability estimation.

SHIP 1,561,815

MULTI-OBJECTIVE WEATHER ROUTING ALGORITHM FOR SHIPS: THE PERSPECTIVE OF SHIPPING COMPANY'S NAVIGATION STRATEGY

J.Szlapczynska (Gdynia Maritime Univ). *JOURNAL OF MARINE SCIENCE AND ENGINEERING* v.10, no.9, Sept. 2022. (ISSN 2077-1312; Article no.1212)

Ship weather routing has always been an important issue in the research field of navigation, and many scholars have been devoted to this research for a long time. To study the route strategies of different shipping companies, this paper proposes an improved multi-objective ant colony optimization (IMACO) algorithm based on the Technique for Order Preference by Similarity to Ideal Solution (TOPSIS). It can comprehensively consider ship navigation risk and fuel consumption cost under complex sea conditions. First, the grid method is used to model the marine environment. Then, we calculate the fuel consumption and the ship navigation risk of each grid and use the TOPSIS method to evaluate these two indicators for each grid. The results show that due to the different strictness of navigation management requirements of different companies, different routes are selected in the same sea area at the same time. Compared with the single-objective ant colony optimization (SACO) algorithm, the algorithm proposed in this paper can more comprehensively and effectively solve the problem of route strategy selection of shipping companies, which has great practical significance for ship operations management.

SHIP 1,561,816

SPOT CHARTER RATE FORECAST FOR LIQUEFIED NATURAL GAS CARRIERS

D.V.Lyridis (Athens Univ). *JOURNAL OF MARINE SCIENCE AND ENGINEERING* v.10, no.9, Sept. 2022. (ISSN 2077-1312; Article no.1270)

Recent maritime legislation demands the transformation of the transportation sector to be greener and more energy efficient. Liquefied natural gas (LNG) seems a promising alternative fuel solution that could replace the conventional fuel sources. Various studies have focused on the prediction of the LNG price; however, no previous work has been carried out on the forecast of the spot charter rate of LNG carrier ships, an important factor for the maritime industries and companies when it comes to decision-making. Therefore, this study is focused on the development of a machine-learning pipeline to address the aforementioned problem by (i) forming a dataset with variables relevant to LNG; (ii) identifying the variables that impact the freight price of LNG carrier; and (iii) developing and evaluating regression models for short and mid-term forecast. The results showed that the general regression neural network presented a stable overall performance for forecasting periods of 2, 4, and 6 months ahead.

SHIP 1,561,817

EXTENDED STATE OBSERVER-BASED PARAMETER IDENTIFICATION OF RESPONSE MODEL FOR AUTONOMOUS VESSELS

M.Zhu, W.Sun, Y.Wen and L.Huang (Wuhan Univ Technology; Sunwin Intelligent Co Ltd). *JOURNAL OF MARINE SCIENCE AND ENGINEERING* v.10, no.9, Sept. 2022. (ISSN 2077-1312; Article no.1291)

Identification of parameters involved in the linear response model with high precision is a highly cost-effective, as well as a challenging task, in developing a suitable model for the verification and validation (V+V) of some key techniques for autonomous vessels in the virtual testbed, e.g., guidance, navigation, and control (GNC). In order to deal with this identification problem, a novel

identification framework is proposed in this paper by introducing the extended state observer (ESO), and the well-evaluated robust weighted least square support vector regression algorithm (RW-LSSVR). A second-order linear response model is investigated in this study due to its wide use in controller designs. Considering the highly possible situation that only limited states could be measured directly, the required but immeasurable states in identifying parameters contained in the response model are approximately estimated by the ESO. Theoretical analysis of the stability is given to show and improve the applicability of the ESO. Simulation studies based on linear response models with predefined parameter values of a cargo vessel and a patrol vessel maneuvering in an open water area are carried out, respectively. Results show that the proposed approach not only estimates immeasurable states with high accuracy but also ensures good performance on the parameter identification of the response model with very close values to the nominal ones. The proven identified approach is economic because it only requires limited kinds of low-cost sensors.

SHIP 1,561,818

AUTOMATIC IDENTIFICATION SYSTEM (AIS) DATA SUPPORTED SHIP TRAJECTORY PREDICTION AND ANALYSIS VIA A DEEP LEARNING MODEL

X.Chen, C.We, G.Zhou, H.Wu, Z.Wang and S.A.Biancardo (Huaiyin Inst Technology; Shanghai Maritime Univ; Napoli Federico II Univ). *JOURNAL OF MARINE SCIENCE AND ENGINEERING* v.10, no.9, Sept. 2022. (ISSN 2077-1312; Article no.1314)

Automatic Identification System (AIS) data-supported ship trajectory analysis consistently helps maritime regulations and practitioners make reasonable traffic controlling and management decisions. Significant attentions are paid to obtain an accurate ship trajectory by learning data feature patterns in a feedforward manner. A ship may change her moving status to avoid potential traffic accident in inland waterways, and thus, the ship trajectory variation pattern may differ from previous data samples. The study proposes a novel ship trajectory exploitation and prediction framework with the help of the bidirectional long short-term memory (LSTM) (Bi-LSTM) model, which extracts intrinsic ship trajectory features with feedforward and backward manners. We have evaluated the proposed ship trajectory performance with single and multiple ship scenarios. The indicators of mean absolute error (MAE), mean absolute percentage error (MAPE) and mean square error (MSE) suggest that the proposed Bi-LSTM model can obtained satisfied ship trajectory prediction performance.

SHIP 1,561,819

FUZZY LOGIC-BASED MODELING METHOD FOR REGIONAL MULTI-SHIP COLLISION RISK ASSESSMENT CONSIDERING IMPACTS OF SHIP CROSSING ANGLE AND NAVIGATIONAL ENVIRONMENT

Z.Shi, R.Zhen and J.Liu (Jimei Univ; Wuhan Univ Technology). *OCEAN ENGINEERING* v.259, 9/1/2022. (ISSN 0029-8018; Article no.111847)

The ship crossing angle and navigational environment have significant impact on the precisely modeling of regional ship collision risk, but the existed studies seldom consider this problem. In order to realize the perception of regional multi-ship collision risk, this paper proposes a fuzzy logic-based modelling method for regional multi-ship collision risk assessment considering impact of ship crossing angle and navigational environment. The method incorporates the impact factors of DCPA, TCPA, ship crossing angle and navigational environment in multi-ship encounter situation by using fuzzy logic theory. We use Analytic Hierarchy Process (AHP) to obtain the risk weights of different ships versus single ships, and then obtain the value of multi-ship collision risk. In order to verify the validity of the model, data from the Taiwan Strait is used for verification, and the results show that this method can realize the early warning of regional multi-ship collision risk. The method can provide an important basis for maritime collision risk monitoring and ship navigation risk assessment for maritime administration departments and shore-based center of maritime autonomous ships. (c2022 Elsevier Ltd.)

SHIP 1,561,820

TOWARDS THE EVALUATION OF DATE/TIME FEATURES IN A SHIP ROUTE PREDICTION MODEL

A.Lo Duca and A.Marchetti (Natl Res Council (Italy)). *JOURNAL OF MARINE SCIENCE AND ENGINEERING* v.10, no.8, Aug. 2022. (ISSN 2077-1312; Article no.1130)

Ship route prediction (SRP) is an algorithm that allows us to assess the future position of a ship using historical data extracted from AIS messages. In an SRP task, it is very important to select the set of input features used to train the model. In this paper, we try to evaluate whether time-dependent features are relevant to an SRP model based on a K-nearest neighbor classifier through a practical experiment. In practice, we build two models--one with and one without the date/time features--and we calculate some performance metrics and the SHAP value for both models. Tests show that although the model with the date/time features outperforms the other model in terms of the evaluation metrics, it does not in the practical experiments.

TANK 1,561,821

EFFECTIVE CONFIGURATION OF PERFORATED BAFFLE PLATE FOR EFFICIENT SLOSH DAMPING IN LIQUID RETAINING TANKS UNDER LATERAL EXCITATION

P.Nimisha, B.R.Jayalekshmi and K.Venkataramana (Nat Inst Technol (India)). *OCEAN ENGINEERING* v.259, 9/1/2022. (ISSN 0029-8018; Article no.111855)

Perforated baffle plates are used as an anti-slosh mechanism in various fields owing to the need for slosh suppression and weight reduction. However, there is an uncertainty in the selection of configuration of perforated baffle plate due to the several influencing parameters for slosh damping efficiency. Therefore, the present study focuses on the development of an efficient slosh damping configuration for the perforated baffle plate. For this, nonlinear dynamic analysis under seismic ground motions with different PGA/PGV ratios has been carried out in the time domain using the concepts of Computational Fluid Dynamics (CFD) in the numerical models of liquid tanks with perforated baffle plates of different configurations. The response of the system under impulsive and convective modes is analysed by observing the free surface elevation, hydrodynamic pressure, turbulence kinetic energy and turbulence eddy dissipation as the response parameters. The study developed an effective baffle configuration for efficient slosh damping, considering the various response parameters. (c2022 Elsevier Ltd.)

ULTRASONIC TESTING 1,561,822

AUGMENTED REALITY IN ULTRASONIC INSPECTION

D.Werner, P.Buschke, D.van de Ven and W.Zhang, asrs. (Baker Hughes Holdings LLC). World 2022/213,105A1, p. 10/6/2022, f. 3/31/2022 (Appl. 2,271,465), pr. U.S. 3/31/2021 (Appl. 63/168,983) and U.S. 3/25/2022 (Appl. 705,249) (G01N-0027/90; G01N-0029/06; G01N-0029/04; G01N-0029/24; G01N-0029/26; G06V-0020/20).

Systems and methods for improved visualization of non-destructive testing (NDT) measurements are provided. A probe can be employed to acquire NDT measurements of a target. Images of the target can also be captured during testing. The captured images can be analyzed to identify selected objects therein (e.g., the target, the probe, etc.) Graphical user interfaces (GUIs) including the NDT measurements can be further generated for viewing in combination with the target. In one aspect, the GUI can be viewed as a hologram within a display of an augmented reality device when viewing the target. In another aspect, the GUI can be projected upon the target. The GUI can be configured to overlay the NDT measurements at the location where the NDT measurements are acquired. This display of the NDT measurements can help an inspector more easily relate the NDT measurements to the target and improve reporting of the NDT measurements.

UNDERWATER PIPELINE 1,561,823

SHEDDING DAMAGE DETECTION OF METAL UNDERWATER PIPELINE EXTERNAL ANTICORROSIVE COATING BY ULTRASONIC IMAGING BASED ON HOG+SVM

X.Hong, L.Huang, S.Gong and G.Xiao (South China Univ Technol). *JOURNAL OF MARINE SCIENCE AND ENGINEERING* v.9, no.4, April 2021. (ISSN 2077-1312; Article no.364)

Underwater pipelines are the channels for oil transportation in the sea. In the course of pipeline operation, leakage accidents occur from time to time for natural and man-made reasons which result in economic losses and environmental pollution. To avoid economic losses and environmental pollution, damage detection of underwater pipelines must be carried out. In this paper, based on the histogram of oriented gradient (HOG) and support vector machine (SVM), a non-contact ultrasonic imaging method is proposed to detect the shedding damage of the metal underwater pipeline external anti-corrosion layer. Firstly, the principle of acoustic scattering characteristics for detecting the metal underwater pipelines is introduced. Following this, a HOG+SVM image-extracting algorithm is used to extract the pipeline area from the underwater ultrasonic image. According to the difference of mean gray value in the horizontal direction of the pipeline project area, the shedding damage parts are identified. Subsequently, taking the metal underwater pipelines with three layers of polyethylene outer anti-corrosive coatings as the detection object, an autonomous surface vehicle (ASV) for underwater pipelines defect detection is developed to verify the detection effect of the method. Finally, the underwater ultrasonic image which used to detect the metal underwater pipeline shedding damage is obtained by acoustic sensor. The results show that the shedding damage can be detected by the proposed method. With the increase of shedding damage width, the effect of pipeline defect location detection is better.

UNDERWATER PIPELINE 1,561,824

INVESTIGATIONS ON THE EFFECTIVENESS OF PROTECTION METHODS FOR A SUBMARINE PIPELINE EXPOSED TO THE IMPACT OF A FALLING ANCHOR

C.Zhang, Z.Zang, M.Zhao, Y.Chen and J.Zhang (Tianjin Univ; Western Sydney Univ; China Univ Petroleum). *JOURNAL OF MARINE SCIENCE AND ENGINEERING* v.10, no.8, Aug. 2022. (ISSN 2077-1312; Article no.1159)

The occurrence of a buried submarine pipeline crossing a channel becoming damaged by the impact of a falling anchor is becoming more common. It is important to analyze the dynamic response of pipelines exposed to such impact and develop effective protection methods to ensure the safe operation of the pipelines exposed to the impact of falling anchors. In this study, different protection methods, including pure rock, concrete mattress + rock, concrete mattress + rock + rubber pad, and compound flexible pad + rock, are physically tested. The strains at the impacting point and along the pipeline were measured with the fiber Bragg grating (FBG) sensors. The effectiveness of the protection methods is analyzed based on the maximum strain and its affected length on the pipeline. Then, a theoretical model is established to analyze the deformation and strain of a pipeline. Through curve-fitting the experimental results, the bearing capacity coefficients for different protection methods are determined. The protection method of compound flexible pad + rock has the best performance to protect the pipeline from the impact of a falling anchor.

UNDERWATER PIPELINE 1,561,825

CFD INVESTIGATION ON SECONDARY FLOW CHARACTERISTICS IN DOUBLE-CURVED SUBSEA PIPELINES WITH DIFFERENT SPATIAL STRUCTURES

F.Han, Y.Liu, Q.Lan, W.Li and Z.Wang (Dalian Maritime Univ). *JOURNAL OF MARINE SCIENCE AND ENGINEERING* v.10, no.9, Sept. 2022. (ISSN 2077-1312; Article no.1264)

Double-curved pipes are widely employed as essential components of subsea pipeline systems. Considering the layout

flexibility and application diversity, there are various spatial structures for the double-curved combinations. However, few studies have compared the flow characteristics in different double-curved pipes. The dissipations of the corresponding downstream flow have not been thoroughly investigated, which are crucial for the measurement accuracy and flow assurance. In this paper, the turbulent flow in double-curved pipes with different spatial structures (i.e., Z, U, and spatial Z types) was numerically studied by employing the ω -Reynolds stress model. The major purpose was to develop an in-depth knowledge on the secondary flow characteristics in different double-curved pipes and quantify the dissipations of the downstream flow. The effects of the spatial angle and interval distance of the two curves on the flow fields are taken into consideration, and the swirl intensity Si is introduced to evaluate the secondary flow dissipation. It is found that the secondary flows in the Z- and U-type structures are in opposite directions when the interval distance is short (3D), and the secondary flow in the spatial Z type exhibits an oblique symmetric form. Only in the Z-type pipe with a short interval distance the secondary flow exhibits an exponential dissipation, and the fully developed flow is easier to achieve than the other cases. However, as the interval distance increases, the directions of the secondary flow in the U- and Z-type structures are the same, and the flow dissipations in all the structures return to the exponential types. The obtained dissipation rates for the secondary flow downstream of Z, U, and spatial Z pipes with the 9D interval distance were 0.40, 0.25, and 0.20, respectively. The results are expected to guide the design of pipeline layouts and provide a reference for the arrangement of flowmeters in a complex subsea pipeline system.

ALT FUELS & ENERGY SOURCES

ANATOLIA

1,561,826

RESERVOIR ROCK CHARACTERIZATION IN EDREMIT GEOTHERMAL FIELD: GEOCHEMICAL IMPLICATIONS FOR POSSIBLE FAULT ZONES

S.Elidemir, N.Gulec, K.Deniz and Y.K.Kadioglu (Middle East Technical Univ; Ankara Univ). *APPLIED GEOCHEMISTRY* v.143, Aug. 2022. (ISSN 0883-2927; Article no.105388)

Reservoir lithology of Edremit geothermal field from western Anatolia is investigated by means of mineralogic-petrographic and geochemical analyses. Drill cuttings that belong to reservoir levels are analyzed macroscopically and microscopically, followed by the techniques of X-Ray Diffraction (XRD), Confocal Raman Spectroscopy (CRS) and Electron Probe Micro Analysis (EPMA) for detailed mineral characterizations. In the samples, dominant rock fragments are identified as granitic rocks while quartz, feldspars (plagioclase, orthoclase), micas (biotite, muscovite), carbonates (calcite, dolomite, ankerite) and amphiboles (actinolite, richterite, pargasite, hornblende, edenite) constitute the main mineral phases. CRS and EPMA studies reveal that the composition of plagioclase feldspars ranges from Ca-rich (bytownite) to Na-rich (oligoclase). The effects of cataclasis and alteration which are the indications of faulting and hydrothermal fluid activity, respectively, are detected from textural characteristics of the samples. These textures include cataclastic, mylonitic and mortar textures. The observed alterations are metasomatism and secondary uranization. The changes in major and trace element concentrations along the well bore are deduced from the results of X-Ray Fluorescence (XRF) analyses. It was observed that changes in textural features which are associated with various grain sizes from coarse to fine, closely coincide with chemical variations with depth, leading to the identification of three distinctive zones at depth intervals of 900-928 m, 930-974 m and 976-1038 m. The correlation of geochemical findings regarding hydrothermal fluid effect (such as pyrite abundance, alteration features) with the information of a probable water leakage around 930 m depth, suggests that the middle part of these three zones is the potential passageway for the fluid. The litho-geochemical results also suggest that the fluids are likely to be Si-rich and (in deeper levels) Ca-rich which are in accordance with the hydrogeochemistry of the system that is previously investigated. This study points out the importance and

practicality of geochemical studies as significant indicators utilized in geothermal exploration. (c2022 Elsevier Ltd.)

BITUMEN

1,561,827

MECHANISM OF MODIFICATION OF BITUMEN ZETA POTENTIAL BY SODIUM CITRATE: INTERACTIONS BETWEEN BITUMEN METAL CONTENT AND LIGANDS

T.Bai, B.Xiang, M.Li, R.Manica and Q.Liu (Alberta Univ). *COLLOIDS AND SURFACES A: PHYSICOCHEMICAL AND ENGINEERING ASPECTS* v.653, 11/20/2022. (ISSN 0927-7757; Article no.130007)

Sodium citrate (Na_3Cit) has been proved to significantly increase the negative charges on bitumen surfaces, which enhances bitumen liberation and prevents slime coating in the bitumen recovery process. To understand the in-depth theory of Na_3Cit modifying the bitumen zeta potential, different assumptions of Na_3Cit interacting with bitumen were proposed and experimentally verified in this study. Accordingly, chemicals with similar properties were selected and compared with Na_3Cit to confirm the mechanisms. We found that adding ethylenediaminetetraacetic acid (EDTA) and phosphate (PO_4^{3-}), which act like citrate as a ligand, resulted in a more negatively charged bitumen surface at pH 8.5 compared with sodium chloride ($NaCl$). However, even though the sulfate ion (SO_4^{2-}) carries multiple negative charges, increasing the concentration of sodium sulfate (Na_2SO_4) led to less negatively charged bitumen surfaces at the same pH, a trend similar to $NaCl$. Meanwhile, Na_3Cit and EDTA promoted the release of metal cations from bitumen to the aqueous solution. However, the concentration of metal ions released by sodium phosphate dibasic (Na_2HPO_4) was much smaller than expected. Adsorption of Na_3Cit , EDTA, and Na_2HPO_4 on the bitumen surface was observed through mainly outer-sphere complexation and minor inner-sphere complexation. Our study revealed that ligands such as Na_3Cit could remove metal ions from bitumen and adsorb onto the bitumen surface, which were the dominant reasons for modifying the zeta potential at the bitumen/water interface. (c2022 Elsevier B.V.)

FLOCCULATING

1,561,828

THE INHIBITORY EFFECTS OF SYNTHETIC POLYACRYLIC ACID AND HUMIC SUBSTANCES ON THE INITIAL STAGE OF COLLOIDAL FLOCCULATION INDUCED BY POLYCATIONIC FLOCCULANT WITH LOW CHARGE DENSITY

V.H.Lim, Y.Yamashita, K.Ogawa and Y.Adachi (Tsukuba Univ). *COLLOIDS AND SURFACES A: PHYSICOCHEMICAL AND ENGINEERING ASPECTS* v.653, 11/20/2022. (ISSN 0927-7757; Article no.129930)

Humic substances (HS) coexisting with colloidal particles are inevitable in water bodies. Since the cationic flocculant used for flocculation treatment in such water bodies interacts electrostatically with HS and colloidal particles, the efficiency of the flocculant tends to be lower than in water bodies containing only colloidal particles. The colloidal flocculation mechanism by polycation with low charge density is dominated by bridging effects rather than charge neutralization effects. Furthermore, the polyionic complex formation of low charge density polycations with HS is not stoichiometric, based on the oppositely charged groups. Therefore, it was unclear how HS affects the flocculation of colloidal particles by polycation with low charge density. In this study, the effects of two naturally occurring HS and two synthetic polyanions on the flocculation behavior of negatively charged polystyrene latex (PSL) particles induced by polycationic flocculant with low charge density (4 %) were investigated under standardized mixed fluid conditions. Considering the flocculation inhibition effect in terms of the molar concentration ratio of flocculant-derived cations to polyanion-derived anions, it was found that polyanions less inhibit the flocculation of PSL particles by flocculant with low charge density compared to flocculant with high charge density. The relationship between the degree of inhibition of flocculation and the affinity of polyanions for polycations obtained from electrophoretic mobility experiments was verified, and the effectiveness of using low charge density polycations as particle flocculants in water

bodies containing particles and HS was discussed. (c2022 Elsevier B.V.)

FLOTATION 1,561,829

MOLECULAR DYNAMICS SIMULATION OF BULK NANOBUBBLES

S.A.Hewage and J.N.Meegoda (New Jersey Inst Technology). *COLLOIDS AND SURFACES A: PHYSICOCHEMICAL AND ENGINEERING ASPECTS* v.650, 10/5/2022. (ISSN 0927-7757; Article no.129565)

The long-term stability of nanobubbles with high internal gas pressure is a puzzling question for nanobubble researchers. The classical Molecular Dynamics simulation based on LAMMPS software was used to evaluate the performance of an oxygen nanobubble with high gas density. This research consists of two main cases. In the first case, bubble behavior was examined with 3247 O2 molecules embedded in a 4.5 nm radius spherical volume to represent the bubble and was surrounded by 438,490 H2O molecules with 1 g/cm3 density. In the second case, the parametric study was conducted while maintaining the same parameters where the amount of O2 molecules changed at the initial configuration. Hence six different O2 bubble configurations were simulated under two different temperature settings, 20°C and 30°C. The Lennard Jones potentials are used for molecular interactions. The simulations were run first under the NVT and then changed to the NPT ensemble. Simulation results were analyzed for bubble size, pressure, surface tension, gas diffusion, the influence of internal initial gas densities, gas concentration, and temperature conditions. The high initial gas concentration with high initial internal gas density causes a more stable bubble condition under both NVT and NPT ensembles. This stability can be attributed to the gas supersaturation conditions. The systems with low initial internal gas densities transferred to a smaller radius gas cluster with a high internal density as they shifted to the NPT ensemble. The system with a higher temperature causes elevated system pressures at NVT and volume expansion during NPT. Under NVT simulation, bubble size was higher at lower temperatures. Under NPT conditions, bubble size increases for larger initial density cases and decreases for lower density cases. Further increased temperature causes faster gas diffusion, and higher internal bubble pressure leads to unstable conditions. (c2022 Elsevier B.V.)

FLOTATION 1,561,830

EFFECT OF PARTICLE SHAPE ON PARTICLE-BUBBLE INTERACTION BEHAVIOR: A COMPUTATIONAL STUDY USING DISCRETE ELEMENT METHOD

Y.Chen, L.Zhuang and Z.Zhang (China Univ Mining Technol). *COLLOIDS AND SURFACES A: PHYSICOCHEMICAL AND ENGINEERING ASPECTS* v.653, 11/20/2022. (ISSN 0927-7757; Article no.130003)

A three-dimensional Discrete Element Method (DEM) simulation model of particle-bubble interaction behavior based on particle-bubble mechanics theory was developed, and six kinds of irregular shape particle models were designed. The interaction behavior of spherical and irregular-shaped coal particles with the particle size of 0.1 mm and densities of -1.3, 1.4-1.5, + 1.7 g/cu.cm and a fixed bubble in quiescent water was simulated. The simulation results show that the interaction between spherical and irregular shape particles with the bubble can be divided into five stages: free settling, flow around the bubble surface, sliding with a liquid film, film rupture & three-phase contact line (TPCL) formation, sliding with a TPCL. Irregular shape particles have a larger critical collision angle and capture probability than spherical particles. The critical induction time of irregular particles is smaller than that of spherical particles. Irregular particles with edges and corners can promote the thinning and rupture of the liquid film between bubble and particle, thereby reducing the induction time and increasing the capture probability. (c2022 Elsevier B.V.)

GEOHERMAL EXPLORATION 1,561,831

GEOHERMAL ENERGY BASICS/EDUCATION FOR A SUSTAINABLE FUTURE

S.Nash and C.Dietl. *OFFSHORE TECHNOLOGY CONFERENCE [OTC] (Houston, TX, 5/2-5/2022) PROCEEDINGS* 2022. (ISBN 978-1-61399-852-6; OTC-31829; Available at <http://www.onepetro.org> as of 6/23/2022; 7 pp)

This paper presents a road map for providing training to experienced geoscientists, engineers, and data scientists who seek to participate in geothermal energy exploration, development, and integration. The road map starts by identifying the foundational skills and knowledge base of experienced geoscientists and engineers and then specifically discusses which elements are of direct value in geothermal energy development. The paper then discusses the best strategies for upscaling skills and closing knowledge gaps, as well as pathways for immediate implementation of the knowledge in the form of planning documents and projects. The final stage of the road map includes assessing and designing collaborative challenges so that teams learn how best to work together and achieve their goals. The final section of the paper includes brief case studies of two examples of retooled geothermal education offered by the American Association of Petroleum Geologists (AAPG). (Copyright 2022 OTC)

BUSINESS & ECONOMICS

DRILLING ACTIVITY 1,561,832

DRILLER'S OUTLOOK: NABORS' PERSPECTIVE ON SUCCESSFULLY NAVIGATING THE CURRENT AND FUTURE ENERGY LANDSCAPES

S.Saxena (Nabors Drilling Solutions). *ANNUAL IADC GENERAL MEETING (New Orleans, LA, 11/2-4/2022) PROCEEDINGS* 2022. (Available at <http://www.iadc.org> as of 11/15/2022; 10 pp)

[Copy of visual presentation available from P.A.]

FIELD DEVELOPMENT 1,561,833

A REALISTIC AND INTEGRATED MODEL FOR EVALUATING OFFSHORE OIL DEVELOPMENT

R.Qiu, Z.Li, Q.Zhang, X.Yao, S.Xie, Q.Liao and B.Wang (China Univ Petroleum; Zhejiang Petroleum Co Ltd; CNPC Research Inst). *JOURNAL OF MARINE SCIENCE AND ENGINEERING* v.10, no.8, Aug. 2022. (ISSN 2077-1312; Article no.1155)

With the rising consumption of oil resources, major oil companies around the world have increasingly engaged in offshore oil exploration and development, and offshore oil resources have accounted for an increasing proportion. Offshore oil engineering projects are capital-intensive, and the development of offshore oil fields faces a tough battle, especially in a period of low oil prices. Thus, a comprehensive evaluation model is highly needed to help assess economic benefits and provide meaningful and valuable information for operators and investors to make sensible decisions. This study firstly proposed a realistic and integrated evaluation model for offshore oil development based on actual historical project data. This evaluation model incorporated modules from the underwater system to the platform system and processes from oil reservoir extraction to oil, gas and water treatment. The uncertain parameters in the evaluation process are dealt with by sensitivity analysis and Monte Carlo simulation. The proposed model is applied to a typical offshore oil development project in Bohai Bay, China. The results reveal that the recovery factor and oil price have the greatest impact on the economic benefits. In the case of deterministic analysis, the breakeven oil price of the project is US\$40.59/bbl. After considering the uncertainty of project parameters, the higher the oil price, the greater the probability of NPV > 0. When the oil price is higher than US\$70/bbl, even with uncertain project parameters, the probability of NPV > 0 can still be as high as 97.39%.

GULF COAST 1,561,834

2023 GULF COAST ENERGY OUTLOOK

G.Upton (Louisiana State Univ). *ANNUAL IADC GENERAL MEETING (New Orleans, LA, 11/2-4/2022) PROCEEDINGS 2022*. (Available at <http://www.iadc.org> as of 11/15/2022; 39 pp)
 [Copy of visual presentation available from P.A.]

HYDRAULIC FRACTURING 1,561,835

NORTH AMERICAN MARKET OUTLOOK: S&P GLOBAL - COMMODITY INSIGHTS; COSTS AND SUPPLY CHAIN

S.Landes (S&P Global). *ANNUAL IADC GENERAL MEETING (New Orleans, LA, 11/2-4/2022) PROCEEDINGS 2022*. (Available at <http://www.iadc.org> as of 11/15/2022; 14 pp)
 [Copy of visual presentation available from P.A.]

PETROLEUM INDUSTRY 1,561,836

STANDARDIZATION OF PROCUREMENT EQUIPMENT SPECIFICATIONS: ESTABLISHING A STRONG FOUNDATION FOR OIL AND GAS CAPITAL PROJECT DEVELOPMENT AND DELIVERY

A.Postema, D.Harris and D.Berry. *OFFSHORE TECHNOLOGY CONFERENCE [OTC] (Houston, TX, 5/2-5/2022) PROCEEDINGS 2022*. (ISBN 978-1-61399-852-6; OTC-31843; Available at <http://www.onepetro.org> as of 6/23/2022; 10 pp)

Operators need industry-wide standardization to manage the US\$3 trillion in CAPEX expenditure forecast for 2018-2025 (Global Data, 2018), while maintaining competitiveness and mitigating risks. With the backing of the World Economic Forum, Joint Industry Program 33 (JIP 33) was initiated to drive industry-level standardization for procuring equipment items, moving the industry structurally--across the value chain--towards common engineering designs and solutions, established by means of cross-company and value-chain collaboration. By 2022, over 50 standardized, freely available specifications will have been delivered. Their adoption by 12 major operators is being measured and is progressing well. This enables the program to capture and evaluate successes, challenges, key learnings and feedback. The program has also established a process for future maintenance of JIP33 specifications in order to achieve sustained benefits. The success of JIP33 is measured, within the operating companies and the wider industry, by the extent of adoption and use of the JIP33 specifications. This requires aligning corporate engineering and procurement processes with JIP33 methodology, embedding the JIP33 specifications in company systems, and using JIP33 specifications as default on projects, with a policy of "no deviations." In 2019-2021 JIP33 specifications have been downloaded over 110,000 times from the IOGP website. Supplier feedback indicates cost savings of up to 50% and a potential reduction of 65% in supplier engineering hours could be achieved if the specifications become industry standard designs. Key information that is filtered through constructive feedback from vendors during the purchase process, has led to a series of recommendations for further improving existing JIP33 specifications. These now become part of a structured maintenance process. JIP33 is closely collaborating with standards development organisations to ensure that valuable learning can be included in updates of the international parent standards. Industry networks have been established to engage with engineering contractors and suppliers to create awareness of JIP33. (Copyright 2022 OTC)

PROFIT 1,561,837

MARKET OUTLOOK

J.K.Wicklund (Wicklund & Associates). *ANNUAL IADC GENERAL MEETING (New Orleans, LA, 11/2-4/2022) PROCEEDINGS 2022*. (Available at <http://www.iadc.org> as of 11/15/2022; 45 pp)
 [Copy of visual presentation available from P.A.]

REGULATION 1,561,838

THE REGULATORS' PERSPECTIVE: BOEM OVERVIEW

W.Cruikshank (BOEM). *ANNUAL IADC GENERAL MEETING (New Orleans, LA, 11/2-4/2022) PROCEEDINGS 2022*. (Available at <http://www.iadc.org> as of 11/15/2022; 9 pp)
 [Copy of visual presentation available from P.A.]

HEALTH, SAFETY & ENVIRON

BENTHONIC ORGANISM 1,561,839

LONG-TERM CHANGES IN THE MACROBENTHIC ASSEMBLAGES AT A HARBOUR SEDIMENT DISPOSAL SITE IN THE SOUTHERN NORTH SEA

A.R.Boon and J.van Dalen (Avans Univ Applied Sci). *MARINE ENVIRONMENTAL RESEARCH* v.178, June 2022. (ISSN 0141-1136; Article no.105663)

This study focussed on the long-term, sediment-driven changes of macrobenthic assemblages in dredged harbour sediment from Rotterdam harbour disposed of in excavated sand extraction pits off the Dutch coast. Macrobenthic species and sediment grain size composition were studied in samples from two disposal sites and the surrounding environment over ten years after the cessation of disposal activities. There was a strong association between the sediment granulometry and the benthic assemblage composition. Shortly after the last discharge, the top layer of the sediments in the pits contained 20%–60% mud (particles <63 µm) and was colonised by benthic species typical for these sediments. The pit sediments and benthic assemblages contrasted strongly with the surrounding medium-coarse sediment, extremely low in mud (<0.01%). Over eight to ten years, the top layers of the disposal sites became significantly less muddy (ca. 5%–15% mud), and the benthic assemblages changed over this period from mud-favouring species dominated by annelids to species preferring fine sand with relatively low mud percentages dominated by molluscs. The two different disposal sites converged in sediment composition and benthic assemblages over the ten years of monitoring. The contrast with the medium-coarse sediments with very low mud percentages remained even after this period. The use of sand extraction pits as disposal sites for dredged harbour sediments may be seen as an economically sound beneficial use option in dredged material management, albeit with long-term ecological effects. (c2022 The Authors. Elsevier Ltd.)

CARBON DIOXIDE REMOVAL 1,561,840

PROCEEDINGS OF THE CARBON CAPTURE TECHNOLOGY EXPO - NORTH AMERICA

CARBON CAPTURE TECHNOLOGY EXPO - NORTH AMERICA (Houston, TX, 6/14-15/2022) PROCEEDINGS 2022. (Available at <http://www.ccus-expo.com> as of 8/16/2022) (Abstract only)

The Carbon Capture Technology Expo, held June 14-15, 2022, featured three tracks: carbon capture, utilization, and storage (CCUS); hydrogen production, storage, and infrastructure development; and fuel cell design, development, and manufacturing. CCUS topics included accelerating the adoption of CCUS projects; technologies used to enable net-zero emissions; making large-scale CCUS projects affordable; ways to capture CO2 and direct air; developing large-scale CCUS infrastructure; funding for CCUS projects; ensuring that CCUS projects are economically sustainable; and details about different CCUS projects, such as Project Tundra in North Dakota, the Coastal Bend Carbon Management Partnership in Corpus Christi, and projects in Texas. Hydrogen topics include how hydrogen production intersects with CCUS and the role of hydrogen in the energy transition. Fuel-cell topics focus on hydrogen as an alternative fuel source. (Table of contents and individual abstracts available from P.A.)

CHEMICAL INJECTION

1,561,841

THERMOPHILIC HYDROCARBON-UTILIZING BACILLI FROM MARINE SHALLOW HYDROTHERMAL VENTS AS PRODUCERS OF BIOSURFACTANTS

V.Zammuto, A.Spano, M.S.Nicolo, E.Grillo, M.T.Caccamo, S.Magazu, S.Cappello and C.Gugliandolo (Messina Univ; ATHENA). *JOURNAL OF MARINE SCIENCE AND ENGINEERING* v.10, no.8, Aug. 2022. (ISSN 2077-1312; Article no.1077)

The exploitation of thermophilic hydrocarbon-utilizing bacilli could provide novel environmentally friendly surfactants. In this work, 80 thermophilic bacilli isolated from shallow hydrothermal vents of the Eolian Islands (Italy) were screened for their ability to utilize hydrocarbons and produce biosurfactants (BSs). Among them, 15 strains grew with kerosene or gasoline (2% v/v) as the only carbon and energy source, and most of them were positive to the methylene blue agar as prescreening assay for BSs production and displayed emulsifying activity. The cell-free supernatants (CFSs) from two selected strains, *Bacillus licheniformis* B3-15 and *Bacillus horneckiae* SBP3, were both surface active and able to emulsify different hydrocarbons and vegetable oils. BSs from B3-15 (910 mg/L) and SBP3 (950 mg/L) were chemically different surfactin-like lipopeptides, with specific mineral, castor, and crude oil removal ability from the cotton matrix. CFSs from the 15 thermophilic strains, which harbor both lipolytic and surfactant abilities, could be suitable for industrial-based applications and environmental issues, such as oil recovery and removal from polluted areas or surfaces, (e.g., oil pipelines, bilge tankers, or industrial silos), whereas the crude BSs, as high-value compounds, may be used in different fields of application, such as the detergent, cosmetic, and pharmaceutical industries.

CRUSTACEAN

1,561,842

SMALL SUSPENSION-FEEDING AMPHIPODS PLAY A PIVOTAL ROLE IN CARBON DYNAMICS AROUND OFFSHORE MAN-MADE STRUCTURES

N.Mavraki, J.W.P.Coolen, D.A.Kapasakali, S.Degraer, J.Vanaverbeke and J.Beermann (Wageningen Marine Res; Royal Belgian Inst; Alfred Wegener Inst). *MARINE ENVIRONMENTAL RESEARCH* v.178, June 2022. (ISSN 0141-1136; Article no.105664)

The establishment of artificial hard substrates (i.e. offshore wind farms and oil and gas platforms) on marine soft sediments increases the available habitat for invertebrate communities that would otherwise be restricted to natural hard bottoms. Suspension feeding invertebrates clear a significant amount of particles from the water column and release organic matter in the form of feces, influencing the basis of marine food webs and affecting surrounding environments. Artificial structures in the southern North Sea are dominated by a suspension-feeding crustacean in terms of abundance and sometimes even biomass: the amphipod *Jassa herdmani*. Animal densities of this tiny biofouler are known to exceed 1 million individuals per m². Despite their small body sizes and their simple filter apparatus, we hypothesized that *J. herdmani* is a highly effective suspension feeder with a significant impact on neighboring communities due to its high abundances. In a feeding experiment, individuals of *J. herdmani* were provided with either an algal or an animal diet under two different temperature regimes. Clearance rates and fecal-pellet carbon (FPC) were measured. The results revealed high clearance rates and subsequent FPC, which were more pronounced at the higher temperature. Furthermore, clearance rates and FPC varied insignificantly with different food items. We further used the current findings for upscaling calculations to the total number of offshore windfarms and oil and gas platforms in the southern North Sea. Our calculations indicated that *J. herdmani* alone clears 0.33–4.71 km³ water per year in the southern North Sea. At the same time, these amphipods release 255–547 tons of carbon per year by means of defecation, thus enriching the surrounding soft sediments with organic matter. Our study highlights that tiny amphipods can mediate indirect effects of man-made structures in the North Sea, which could have a profound impact on pelagic and benthic habitats. (c2022 The Authors. Elsevier Ltd.)

DEMULSIFIER

1,561,843

FUNCTIONAL GRAPHENE OXIDE COATED DIATOMITE FOR EFFICIENT AND RECYCLABLE DEMULSIFICATION OF CRUDE OIL-IN-WATER EMULSION

H.Xu, X.Yang, Y.Qin and Y.Wang (Sichuan Agricultural Univ; Sichuan Univ). *COLLOIDS AND SURFACES A: PHYSICO-CHEMICAL AND ENGINEERING ASPECTS* v.650, 10/5/2022. (ISSN 0927-7757; Article no.129559)

The separation of micro-sized oil droplets from crude oil-in-water (O/W) emulsion is urgently required by petroleum industry and the environmental protection. Herein, we demonstrate a magnetically recyclable diatomite-graphene oxide (M-DM-GO) composite relying on the superior adsorption performance of graphene oxide (GO) and cost-effectiveness of diatomite (DM). Combining the improved positive surface charge by chemical grafting polyethyleneimine (PEI) on the GO surface, the as-prepared M-DM-GO exhibited high demulsification efficiency (Ed) of 96.8% for crude O/W emulsion with pH 6.0 at optimal dosage of 350 mg/L. Importantly, M-DM-GO displayed favorable demulsification performances under broaden pH conditions, suggesting its wide application scopes. Meanwhile, due to the magnetic response capability, M-DM-GO ensured efficient demulsification performance with Ed > 90% after 5 cycles. The efficiency, recyclability and wide pH application conditions make the M-DM-GO have universal application prospects in the management of crude O/W emulsion. (c2022 Elsevier B.V.)

EXPLOSION

1,561,844

NUMERICAL VALIDATION OF THE TWO-WAY FLUID-STRUCTURE INTERACTION METHOD FOR NON-LINEAR STRUCTURAL ANALYSIS UNDER FIRE CONDITIONS

D.Woo and J.K.Seo (Pusan National Univ). *JOURNAL OF MARINE SCIENCE AND ENGINEERING* v.9, no.4, April 2021. (ISSN 2077-1312; Article no.400)

Fire accidents on ships and offshore structures lead to complex non-linear material and geometric behavior, which can cause structural collapse. This not only results in significant casualties, but also environmental catastrophes such as oil spills. Thus, for the fire safety design of structures, precise prediction of the structural response to fire using numerical and/or experimental methods is essential. This study aimed to validate the two-way fluid-structure interaction (FSI) method for predicting the non-linear structural response of H-beams to a propane burner fire by comparison with experimental results. To determine the interaction between a fire simulation and structural analysis, the Fire-Thermomechanical Interface model was introduced. The Fire Dynamics Simulator and ANSYS Parametric Design Language were used for computational fluid dynamics and the finite element method, respectively. This study validated the two-way FSI method for precisely predicting the non-linear structural response of H-beams to a propane burner fire and proposed the proper time increment for two-way FSI analysis.

GEOLOGIC SEQUESTRATION

1,561,845

THE IMPORTANCE OF CO₂ COMPOSITION SPECIFICATION IN THE CCUS CHAIN

D.D.Erickson, H.Haghighi and C.Phillips (Wood plc). *OFFSHORE TECHNOLOGY CONFERENCE [OTC] (Houston, TX, 5/2-5/2022) PROCEEDINGS* 2022. (ISBN 978-1-61399-852-6; OTC-31844; Available at <http://www.onepetro.org> as of 6/23/2022; 13 pp)

Carbon capture and storage (CCS) has seen growing momentum as a crucial strategy for meeting CO₂ emission reduction targets. However, it comes with different technical and strategic challenges. One of the major challenges associated with CCS is the multi-actor value chain, which, based on individual actor requirements, may not be necessarily aligned with each other and therefore requires coordination and agreement. An important design consideration is the quality of the CO₂ stream as it moves through the CCS process. Various industries still consider CO₂ as a waste stream, and as such, it only has limited quality control based on local regulations. This paper will discuss the various issues

associated with CO₂ quality in the various elements of the CCS chain, from collection through transportation to storage. Various technologies provide discrete solutions for different elements of the CCS chain. However, for a cost-effective CCS design, a holistic approach should be applied. At custody transfer points within a CCS chain, CO₂ will need to meet specification criteria for type and quantity of allowable impurities. Impurities may be inherent in the captured CO₂ or carried over from processes or reaction by-products. Some impurities may have significant impact on the behaviour of CO₂-rich fluid even in small ppm quantities and may adversely affect the integrity or operation of the CCS chain. If CO₂ does not meet specification criteria, it risks non-acceptance at custody transfer points. This paper addresses the critical considerations for CO₂ quality at each of the CCS chain interface points. This paper will provide a high-level overview of how impurities can significantly affect the calculation of CO₂-rich fluid properties and behaviour, chemical reactions, corrosion risk, etc. Additionally, some of the gaps in the current understanding and standards and their possible economic impact on CCS chain design and operation will be addressed. (Copyright 2022 OTC)

GEOLOGIC SEQUESTRATION 1,561,846

ACCELERATING MINERAL CARBONATION IN HYDRAULIC FRACTURING FLOWBACK AND PRODUCED WATER USING CO₂-RICH GAS

B.Zhu, S.A.Wilson, M.J.Raudsepp, C.J.Vessey, N.Zeyen, S.Safari, K.N.Snihur, B.Wang, S.Riechelmann et al. (Alberta Univ). *APPLIED GEOCHEMISTRY* v.143, Aug. 2022. (ISSN 0883-2927; Article no.105380)

Mineral carbonation is a Carbon Capture Utilization and Storage (CCUS) technique that can be used to remove or divert carbon dioxide (CO₂) from the atmosphere and store it in carbonate minerals. Hydraulic fracturing flowback and produced water (FPW) is Ca- and Mg-rich wastewater generated by the petroleum industry that can be used to sequester CO₂ in benign minerals. Here, we describe the rate and efficiency of mineral carbonation achieved by sparging 10% CO₂/90% N₂ gas into pH-adjusted FPW, collected from the Duvernay Formation in the Western Canadian Sedimentary Basin. Our results indicate that calcite (CaCO₃) precipitated at the expense of brucite [Mg(OH)₂] dissolution following CO₂ injection; as such, no Mg-carbonate precipitates were formed. The carbonation reaction reached steady state within 1 h and 14.2% of the aqueous Ca in the FPW was precipitated as calcite, sequestering 1.56 ± 0.33 g CO₂/L of FPW. Our dissolved inorganic carbon measurements, geochemical models, and stable carbon isotope results indicate that CO₂ mineralization can be maximized by maintaining solution at pH ≥ 10 during CO₂ sparging. If all of the Ca and Mg in the FPW could be carbonated, it would offer a greater CO₂ sequestration potential of 12.5 ± 0.3 g CO₂/L. (c2022 Elsevier Ltd.)

GEOLOGIC SEQUESTRATION 1,561,847

PERIDOTITE DISSOLUTION IN THE PRESENCE OF GREEN MICROALGAE: IMPLICATIONS FOR A GEOENGINEERING STRATEGY OF CO₂ SEQUESTRATION

T.Xie, L.Zhao and Y.Wu (Southwest Univ Sci Technol; Guizhou Academy Sciences; Guiyang Inst Geochemistry). *JOURNAL OF ASIAN EARTH SCIENCES* v.241, Jan. 2023. (ISSN 1367-9120; Article no.105486)

Enhanced silicate dissolution has been recognized as a potentially promising geoengineering strategy to help remove CO₂ from the atmosphere by applying crushed minerals to aquatic systems. However, it has not yet been fully quantified in the presence of eukaryotic green microalgae. Here, we studied the interaction of peridotite with *Chlamydomonas reinhardtii* (C.R.) and *Chlorella pyrenoidosa* (C.P.). We found that the peridotite dissolution rate was significantly enhanced by green microalgae. Meanwhile, the interaction between peridotite and green microalgae showed two stages with first-order reaction in the early stage (0-4 or 5 days). The amount of Mg²⁺ released per algal chlorophyll-a biomass and unit time in the early stage is about an order of magnitude higher than that in the late stage (4 or 5-9 days). The quantified effect of C.P. on the dissolution rate of

peridotite is about two times higher than that for C.R. in the early stage. Based on the stoichiometric relation of peridotite dissolution, it is estimated that one milligram chlorophyll-a biomass of C.R. and C.P. can remove 0.44 and 0.24 mg CO₂ from the atmosphere in one day via accelerating dissolution, respectively. Besides, the Mg²⁺ ion released from peridotite can promote the growth of green microalgae in turn. Thus, green microalgae play a positive role in CO₂ sequestration via the artificial adding peridotite to aquatic systems, but the issue related to the great deceleration of peridotite dissolution rate after a period of time has to be solved to improve the efficiency of CO₂ sequestration in the future. (c2022 Elsevier Ltd.)

GEOLOGIC SEQUESTRATION 1,561,848

METHOD OF GEOLOGIC STORAGE OF CARBON DIOXIDE, METHOD OF DEVELOPING CARBON DIOXIDE-CONTAINING NATURAL GAS FIELDS, AND METHOD OF OCEAN WATER STORAGE OF CARBON DIOXIDE

T.Yamada (Japan Petrol Explor Co Ltd). World 2022/201,424A1, p. 9/29/2022, f. 3/25/2021 (Appl. 2,112,525) (B01J-0019/00). (In Japanese)

This method of geologic storage of carbon dioxide generates carbon dioxide supersaturated water by the dispersion of nanometer-size microbubbles of a carbon dioxide fluid, and injects the microbubble-containing carbon dioxide supersaturated water into the stratum water in a geologic layer. At that time, by adjusting the particle size and dispersion amount of the microbubbles in the carbon dioxide supersaturated water, a sinking current of the microbubble-containing carbon dioxide supersaturated water is formed in the stratum water. In this way, geologic storage of carbon dioxide can be performed regardless of an upper seal (a sealing layer).

INDUCED SEISMICITY 1,561,849

UNDERSTANDING DELAWARE BASIN INDUCED SEISMICITY USING FORT WORTH BASIN SEISMICITY

B.L.Rader. *WEST TEXAS GEOLOGICAL SOCIETY BULLETIN* v.62, no.2, pp.7-12, Nov.-Dec. 2022. (ISSN 0739-5957)

Seismic activity in the Fort Worth Basin (FWB) has been studied since the first earthquake was felt in late 2008 at the Dallas-Fort Worth (DFW) International airport. To explain seismic activity in the FWB, seismologists looked towards the disposal of wastewater from oil and gas activities by saltwater disposal (SWD) wells. Wastewater injection through SWD wells has been correlated as inducing these earthquakes. Seismologists have proposed that as injection continues, the associated pressure will continue to build and generate earthquakes. Injection has continued in the FWB to the present day; however, since mid-2015, earthquake occurrence has nearly stopped. Seismologists struggle to explain why earthquakes are associated with some faults and not others in the region. They have focused mainly on the pore-pressure component on induced earthquakes. A FWB research paper suggests that there is a fluid component that appears to impact the frequency, magnitude, and location of the induced earthquakes. By applying the same methodology to the seismicity in the Delaware Basin, we may develop an understanding to earthquake location, frequency, and magnitude currently experienced in the Pecos, Texas area. Recent seismicity has been focused in an area northwest of Pecos with some magnitudes exceeding M4.0. This area has few SWD wells but experienced most of the recent larger-magnitude earthquakes. Can the same fluid factor explanation for FWB seismicity also explain the earthquake pattern, frequency, and location in the Delaware Basin? This article explores that question.

MEMBRANE PERMEATION 1,561,850

FLUOROPOLYMER-BASED HYBRID SUPERHYDROPHOBIC NANOCOMPOSITE COATING WITH ANTIFOULING AND SELF-CLEANING PROPERTIES FOR EFFICIENT OIL/WATER SEPARATION

P.O.Lartey, D.Li, J.Li, W.Qin, K.Guo and J.Ma (Taiyuan Univ Technology). *COLLOIDS AND SURFACES A:*

PHYSICO-CHEMICAL AND ENGINEERING ASPECTS v.650, 10/5/2022. (ISSN 0927-7757; Article no.129504)

The production of industrial and domestic effluents possessing oily contaminated water has become a global concern as a result of environmental contamination and pollution. Newly synthesized organic-inorganic hybrid nanocomposites with special wetting and anti-wetting properties have been adopted in recent times to address this problem. However, this method has faced a few setbacks in curbing the situation, which leaves the problem persistent. In order to realize the full potential of hybrid composites in combating oil/water contamination, we synthesize a robust organic-inorganic superhydrophobic hybrid nanocomposite containing Polyvinylidene fluoride (PVDF) and silicon hydroxide (SiO₂) to coat cellulose filter paper for effective and efficient separation of oil/water mixtures. With a simple dip-coating technique, the superhydrophobic hybrid composite obtain a superhydrophobicity with a water contact angle as high as 161° on the filter paper. The coated membrane possessed a robust mechanical property as well as chemical stability which withstands a sandpaper abrasion test of up to 80 cycles and could retain its superhydrophobicity in acidic, neutral and alkaline media after 24 hrs of immersion respectively. Moreover, the coated surface possessed nanopores which allows it to be used in oil water separation applications both under pressure and gravity with a separation efficiency of up to 99.7 % and can also be recycled many times for use. The excellent antifouling and self-cleaning ability of the coated membrane also prevents the adhesion of contaminants from the surface. The outstanding performance of the facilely and cost-effective fabricated superhydrophobic hybrid composite reveals a great potential for curbing the problems of oil contamination while addressing some existing barriers to the full potential realization of hybrid composites. (c2022 Elsevier B.V.)

OIL SPILL

1,561,851

UTILIZING COMPUTATIONAL FLUID DYNAMICS TO ESTIMATE DRIFT EXTENT FROM AERIAL SPRAYING OF DISPERSANTS

V.Ryan, H.Thurumella, N.D'Arcy-Evans, N.Boustead, E.Jal, A.Kilner and C.Dillon-Gibbons (AMOG Consulting). *OFFSHORE TECHNOLOGY CONFERENCE [OTC] (Houston, TX, 5/2-5/2022) PROCEEDINGS 2022*. (ISBN 978-1-61399-852-6; OTC-31826; Available at <http://www.onepetro.org> as of 6/23/2022; 13 pp)

Aerial application of dispersants is an effective means of responding to oil spills in coastal waters and the deeper waters of the Outer Continental Shelf or the Gulf of Mexico. To ensure the safety of responders and nearby wildlife, a buffer area is put in place around the spilled oil to be treated, within which spraying operations are conducted. In 2015, a research project was initiated to develop a prototype decision support tool (DST) designed specifically for estimating the spray drift during the aerial application of dispersants on an oil spill. In 2019, an initiative was undertaken to further develop the DST, to address known data gaps in the modeling used in the prototype, to expand on the aircraft included in the tool, and to include a contour plot output of dispersant deposition. The DST has been designed specifically for estimating the spray drift during the aerial application of dispersants on an oil spill through the use of complex computational fluid dynamics (CFD) modeling. The DST program's operational space was developed based on direct input from oil spill response operators (OSROs) for ten airframes currently used in the United States for aerial response operations, including both turbo propeller and turbo fan engine types. The DST employs a database of results generated using the latest in CFD modeling technology to examine flow structures and drift effects created by various operating conditions, coupled with specific configurations of different oil spill response aircraft and their spray systems (boom and nozzle configurations). The DST uses a response surface curve (RSC) for each airframe to predict the drift extent of dispersant particles and mass deposition concentration, the RSC for each airframe was derived from a database of results generated using the latest CFD modeling technology. (Copyright 2022 OTC)

OIL SPILL

1,561,852

2D NANONEEDLE-LIKE ZnO/SiO₂ JANUS MEMBRANE WITH ASYMMETRIC WETTABILITY FOR HIGHLY EFFICIENT SEPARATION OF VARIOUS OIL/WATER MIXTURES

Y.Xu, X.Zeng, L.Qiu and F.Yang (Hubei Univ). *COLLOIDS AND SURFACES A: PHYSICO-CHEMICAL AND ENGINEERING ASPECTS* v.650, 10/5/2022. (ISSN 0927-7757; Article no.129352)

The offshore oil spills and the discharge of oily wastewater are not only doing harm to the economy but also disrupting our aquatic and biotic environment. In order to alleviate this serious situation, researchers have developed super-wettability membranes to achieve efficient oil-water separation. Among them, asymmetric wettability Janus membranes with unique selective permeable properties have received widespread attention. However, utilizing a facile and environment-friendly method to endow a material with Janus super wettability to realize high oil-water separation efficiency and selectivity is still a challenge. Herein, a low-cost strategy is used to electrodeposit flake Zn on the copper mesh. Super-hydrophilic ZnO can be grown on it by a simple hydrothermal method, and then the Janus membrane with asymmetric wettability can be obtained by spraying SiO₂ and octadecanethiol modification. It is worth noting that at a suction pressure of 4 kPa, the separation efficiency of the light oil-water mixture can reach more than 99.99%, and the flux is up to 13067.5 L/m²/h. Under the action of gravity, the separation efficiency of the heavy oil-water mixture can reach more than 99.80%, and the flux is about 2000 L/m²/h. Undoubtedly, the Janus membrane can simplify the operation to achieve on-demand oil-water separation. Last but not least, it can still maintain good performance after acid-base corrosion, wear, and cyclic tests, thereby showing broad potential in the field of oil-water separation and environmental protection. (c2022 Elsevier B.V.)

OIL SPILL

1,561,853

MODELING OF ACCIDENTAL OIL SPILLS AT DIFFERENT PHASES OF LNG TERMINAL CONSTRUCTION

B.Na, S.Son and J.C.Choi (Korea Univ; Daewoo Eng & Construction). *JOURNAL OF MARINE SCIENCE AND ENGINEERING* v.9, no.4, April 2021. (ISSN 2077-1312; Article no.392)

Accidental oil spills not only deteriorate biodiversity but also cause immediate threats to coastal environments. This study quantitatively investigates the initial dispersion of spilled oil using the environmental fluid dynamics code (EFDC) model, loosely coupled with an endorsed oil spill model (MEDSLIK-II) accounting for time-dependent advection, diffusion, and physiochemical weathering of the surface oil slick. Focusing on local contributing factors (i.e., construction activities) to oil dispersion, the current model is applied to likely oil spills occurring at three different phases of the Songdo LNG terminal construction on a reclaimed site in South Korea. Applied phases pose detailed ship collision scenarios generated based on a proposed construction plan of the terminal. The effects of permeable revetments, required for reclamation, on the currents were also investigated and applied in subsequent oil spill modeling. For each scenario, the simulated results showed distinct patterns in the advection, dispersion, and transformation of the oil slick. Oil absorption into the coast, which causes immense damage to the coastal communities, is found to be highly dependent on the tidal currents, volume of oil spilled, and nearby construction activities.

OIL SPILL

1,561,854

APPLICATION OF PHASE-SELECTIVE ORGANOGELATORS (PSOGs) FOR MARINE OIL SPILL REMEDIATION

H.Bi, C.An, C.N.Mulligan, Z.Chen, K.Lee, J.Wen, Z.Qu and X.Chen (Concordia Univ; Fisheries & Oceans Canada). *JOURNAL OF MARINE SCIENCE AND ENGINEERING* v.10, no.8, Aug. 2022. (ISSN 2077-1312; Article no.1111)

Oil spill incidents frequently cause serious impacts on the ecosystem, society, and economy. To cope with this problem, the use

of phase-selective organogelators (PSOGs) has been developed in recent years as a promising oil spill response tool, which can congeal oils from biphasic systems, accelerating oil removal and recovery and reducing impacts on the environment. This article systematically reviews reported technologies for the use of PSOGs for potential oil spill remediation in the literature from January 2016 to May 2022. It discusses several kinds of PSOGs based on molecular structures which are possible for gelling oil in the presence of water/seawater. Their mechanisms for phase-selective gelation are summarized, including hydrogen bonding, π - π stacking interactions, van der Waals force, hydrophobic interactions, etc. The currently possible deployment methods for the application of PSOGs are explored; carrier solvents and powder form are frequently used. Moreover, the challenges and the corresponding recommendations regarding standardized testing protocols and evaluation framework, gelation selectivity, as well as challenges in field tests, are further discussed.

OIL SPILL 1,561,855

A COMPREHENSIVE REVIEW OF CANADIAN MARINE OIL SPILL RESPONSE SYSTEM THROUGH THE LENS OF DECANTING REGULATIONS AND PRACTICES

N.S.Daisy, M.H.Hafezi, L.Liu and K.Lee (Dalhousie Univ; Fisheries & Oceans Canada). *JOURNAL OF MARINE SCIENCE AND ENGINEERING* v.10, no.9, Sept. 2022. (ISSN 2077-1312; Article no.1310)

Marine oil spill response operations could generate a large volume of liquid oily wastes (e.g., emulsified oil, non-emulsified oil, and wastewater) that can be up to 30 to 40 times greater than the original volume of spilled oil. Oil decanting technologies are used globally for recovering spilled oil and handling liquid wastes. Canada follows the standards set out in the MARPOL 73/78 Annex 1 International regulations in most areas, with more strict discharge requirements in certain locations. For instance, inland waters discharge should not exceed 5 ppm, and in special areas, such as the Great Lakes, the discharge standard is under 0 ppm. In the event of an oil spill, decanted seawater should be barged to shore for disposal, which significantly constrains the response capacity and efficiency of oil recovery by skimmers due to limited temporary storage space in barges and the long time and high cost of transportation. This has become one of the greatest challenges the Canadian governments and oil spill response industries are facing in Canada. Moreover, when the spill response team decides that decanting is an appropriate way to handle the spilled oil, the approval process may take a long time, which negatively impacts the spill that has already occurred. Moreover, Canada uses a 10,000-tonne planning standard for oil spill preparedness, whereas the United States uses a worst-case scenario, and Europe uses a 60,000 m3 planning standard. The existing planning threshold in Canada can cause the country to be not fully prepared when it comes to responding to a very large oil spill if one should occur. This study conducted a comprehensive review of the current Canadian oil spill response system and framework, regulations, roles and responsibilities of federal and provincial governments, existing decanting capabilities, and capacities of Canadian oil spill responders. More importantly, this study identified the gaps in the current oil spill response system and regulatory and technological barriers to oil decanting. Marine oil decanting regulations and practices in the US and selected European countries have also been reviewed to support addressing the challenges and improving the Canadian experience. It is expected that this study would help the stakeholders and professionals to better understand the oil spill response system and oil decanting status quo in Canada and facilitate Canadian governments and industries to better address the challenges in oil spill regulations and practices.

OIL SPILL 1,561,856

EFFECT OF ACTIVATION TIME ON SULFUR-DOPED POROUS CARBON FOR EFFICIENT DEGRADATION OF ORGANIC POLLUTANTS WITH PERSULFATE

Y.Guo, K.Xuan, Y.Li, C.Pu, Z.Zeng, Z.Huang, Y.Guo, H.Ruan and J.Li (East China Univ Technology). *COLLOIDS AND SURFACES A: PHYSICOCHEMICAL AND ENGINEERING*

ASPECTS v.651, 10/20/2022. (ISSN 0927-7757; Article no.129612)

Metal-free catalysis by using carbonaceous materials has propelled to the forefront in investigation of persulfate (PS) activation for green degradation of aqueous organic pollutants. Herein, sulfur-doped porous carbons (S-AC) were feasibly produced by chemical activation of Poly (phenylene sulphide) with KOH as activator. The influences of activation time on the porous structure, sulfur doping level, and chemical functionality of the as-prepared carbons were investigated by various characterization means. The S-AC samples were employed as metal-free catalysts to activate PS for phenol removal. Experiments results demonstrated that sulfur doping enhanced the catalytic activity of S-AC, and the S-AC-2 sample prepared by carbonization activation of 2 h was demonstrated to be a promising alternative to common metal oxides and other advanced carbon-based materials. Moreover, the S-AC-2/PS system could efficiently degrade various organics, which can be a green material for wastewater treatment and environmental remediation. In addition, the effects of various reaction parameters on phenol removal were discussed. It was found that S-AC-2 still presented an outstanding performance in a wide pH range. Furthermore, the PS activation mechanism over S-AC-2 was investigated by a series of classical radical quenching tests, EPR and Linear Sweep Voltammetry. (c2022 Elsevier B.V.)

OIL WASTE 1,561,857

REVIEW OF HOLLOW FIBER (HF) MEMBRANE FILTRATION TECHNOLOGY FOR THE TREATMENT OF OILY WASTEWATER: APPLICATIONS AND CHALLENGES

M.K.Hosseini, L.Liu, P.K.Hosseini, A.Bhattacharyya, K.Lee, J.Miao and B.Chen (Dalhousie Univ; Fisheries & Oceans Canada; Newfoundland Memorial Univ). *JOURNAL OF MARINE SCIENCE AND ENGINEERING* v.10, no.9, Sept. 2022. (ISSN 2077-1312; Article no.1313)

Oily wastewater has been recognized as a threat to the environment due to its hazardous nature and it can negatively affect the ecosystem, and threaten wildlife and human health. Physical, chemical, and biological technologies demonstrated a mixed performance in oily wastewater treatment, and, therefore, a proper treatment technology for oily wastewater needs to be addressed. Membrane filtration using a hollow fiber (HF) membrane is a promising alternative to remove emulsified oil from oily wastewater. This review discusses different sources of oily wastewater, various treatment methods, and membrane technology. The assessment has been focused on the parameters affecting HF membrane performance and applications of HF membrane-based technology to treat oily wastewater. This review paper reveals that HF membrane filtration systems have been previously used for the treatment of oily wastewater in bench-scale studies and few pilot-scale applications, which proved to be favorable in the treatment of recalcitrant wastewater containing oil and high salinity. Limitations associated with membrane fouling and the reduction of membrane permeability and membrane lifespan can be tackled and alleviated through modifying membrane chemistry and adjusting operational parameters. The compilation of studies showed that a low food/microorganism (F/M) ratio, long solid retention time (SRT) with high sludge age, long hydraulic retention time (HRT), and moderate aeration were the preferred operational parameters when treating oily wastewater. Based on this review, future studies should focus on optimizing the hydrodynamic conditions of the HF system, the commercialization of modified HF membranes, and the utilization of green technology in HF membrane construction to broaden HF membrane technology applications.

OIL WATER SEPARATION 1,561,858

CALCIUM-BASED CATALYST FOR OZONE CATALYTIC OXIDATION FOR ADVANCED TREATMENT OF HIGH SALT ORGANIC WASTEWATER

G.Shao, Z.Zhou, Y.Tu, J.Chen, F.Zhang, S.Tian and Z.Ren (Beijing Univ Chem Technol). *COLLOIDS AND SURFACES A: PHYSICOCHEMICAL AND ENGINEERING ASPECTS* v.654, 12/5/2022. (ISSN 0927-7757; Article no.130149)

From a green and efficient point of view, a novel calcium-based catalyst (Al2O3-PDA-SA-CaxOy) was prepared in this work using

Al₂O₃ as the supporter, Ca²⁺ as the main active component and polydopamine (PDA) and sodium alginate (SA) as the modifying substances by a simple impregnation method. The prepared Al₂O₃-PDA-SA-CaxOy catalyst showed a higher treatment performance for high salt organic wastewater, and removal rate of chemical oxygen demand (COD) was enhanced from 29.81 % to 66.39 % comparing with single ozonation. It showed a good catalytic performance compared with other catalysts reported in the literature. The carboxyl group in SA was cross-linked with Ca²⁺ for loading more metal Ca, and the N-doped graphitic carbon layer was obtained by PDA carbonization. The carbon layer had a strong aiming effect on metal ions, inhibiting the migration and agglomeration of Ca and facilitating the formation of dispersed calcium active sites (Ca-O). Electron paramagnetic resonance (EPR) and radical quenching tests showed that hydroxyl radical (xOH) and superoxide radical (O₂x⁻) were the reactive oxygen species (ROS) for organics degradation. In conclusion, the Al₂O₃-PDA-SA-CaxOy catalyst showed a good catalytic performance and used for advanced treatment of high-salt organic wastewater. (c2022 Elsevier B.V.)

OIL WATER SEPARATOR 1,561,859

EMULSION TEMPLATED POROUS FUNNEL FROM POLYPROPYLENE WASTE FOR EFFICIENT OIL SEPARATION AND SPILLAGE MANAGEMENT

S.Rani, D.Kumar, B.Nandan and R.K.Srivastava (IIT Delhi). *COLLOIDS AND SURFACES A: PHYSICO-CHEMICAL AND ENGINEERING ASPECTS* v.650, 10/5/2022. (ISSN 0927-7757; Article no.129563)

A huge surge in waste polypropylene (PP) generation, seen after the outburst of coronavirus, has created additional challenges for plastic waste management, which has been a difficult issue to deal with for the past few decades. A novel approach to create a value-added product out of waste PP from face mask and sack is reported here in which an emulsion templated, sacrificial 3D printed porous funnel was developed for efficient oil-water separation. A hitherto unexplored water-in-oil emulsion of PP was formulated for this purpose which was used as a template to create the porous samples. Emulsion templated porous samples showed mesoporous morphology and a specific surface area of more than 170 m²/g, as confirmed by BET and SAXS analysis. A high oil adsorption capacity of 7.5 g/g of the porous sample was observed for petrol which was found to be comparable with a commercial nonwoven PP absorbent pad (8.8 g/g). A 3D printed funnel was fabricated via sacrificial templating, and it was used for the separation of oil (petrol) from contaminated water. The separation efficiency of 99.8% for petrol/water mixture was obtained without any decline in performance, hydrophobicity, and structural integrity of the funnel for ten cycles of use. The approach used in this research can further be extended at a scaled-up level to attain commercial viability of the process and may additionally be used for plastic waste other than PP. (c2022 Elsevier B.V.)

OIL WATER SEPARATOR 1,561,860

NONFLAMMABLE, ROBUST AND RECYCLABLE HYDROPHOBIC ZEOLITIC IMIDAZOLATE FRAMEWORKS/SPONGE WITH HIGH OIL ABSORPTION CAPACITY FOR EFFICIENT OIL/WATER SEPARATION

W.Xiang and Z.Guo (Minnan Normal Univ). *COLLOIDS AND SURFACES A: PHYSICO-CHEMICAL AND ENGINEERING ASPECTS* v.650, 10/5/2022. (ISSN 0927-7757; Article no.129570)

Developing robust sponge-based materials with high oil capacity and excellent flame resistance for oil spill cleanup is significant. Herein, a highly hydrophobic composite sponge material for oil-water separation, containing a melamine-formaldehyde (MF) sponge substrate and zeolitic imidazolate framework-8 (ZIF-8) coating was fabricated through the simple amino-assisted in-situ growth of ZIF-8 onto the strut surface of MF sponge. The successful integration of MF sponge and ZIF-8 nanoparticles in one composite material was confirmed by scanning electron microscopy, X-ray diffraction and nitrogen sorption. The synergistic effect of the MF substrate and ZIF-8 coating significantly improved its flame resistance. Combining the

advantage of the MF substrate and the hydrophobic ZIF-8 nanocrystals, the ZIF-8/MF composite sponge showed high porosity and good hydrophobicity with a water contact angle of 130°. A high adsorption capacity towards various oils was achieved in the range of 76-164 g/g. Besides, the ZIF-8/MF composite sponge exhibited excellent separation performance for light oil/heavy oil-water mixtures via adsorption and/or gravity-driven separation. In addition, owing to its compressibility and mechanical stability, the ZIF-8/MF composite sponge could be easily regenerated by a simple squeezing method and showed excellent recyclability for the oil adsorption. These features make the ZIF-8/MF composite sponge promising for highly efficient oil-water separation. (c2022 Elsevier B.V.)

PETROLEUM INDUSTRY 1,561,861

STRATEGIC ROADMAP FOR DIGITALIZED ASSET LIFECYCLE MANAGEMENT

M.Kusumawardhani, J.V.Johansen and T.Markedset (Yinson Production; Stavanger Univ). *OFFSHORE TECHNOLOGY CONFERENCE [OTC] (Houston, TX, 5/2-5/2022) PROCEEDINGS 2022*. (ISBN 978-1-61399-852-6; OTC-31837; Available at <http://www.onepetro.org> as of 6/23/2022; 11 pp)

The oil and gas industry is facing an increasingly complex world, characterized by the diffusion of digital emergence, sustainability awakening, and the seemingly continuous pandemic. To keep their competitive advantage, companies need to map their organizational strategy to prepare for what lies ahead. Asset lifecycle management (ALM) is an integral part of oil and gas facilities and could not escape from this diffusion as well. Digital advancement in ALM has been proliferating for years as companies strive to catch up with current development while anticipating future requirements. The pandemic has massively accelerated the pace of digital advancement of the organization and changed the role of ALM in the organization and the way it's executed. Thus, this paper arises from the motivation to share knowledge in ALM digital efforts with companies of mutual background. In the paper, we will discuss the current drivers in asset management and how these drivers stir the transformation of asset integrity management (AIM) into ALM. The paper will also discuss how the holistic lifecycle approach and sustainability are retrofitted as part of the organization's transformation that is needed for long-term competitive advantage in the digital age. Finally, a fit-for-purpose roadmap for strategic ALM digitalization will be presented, along with the possibility for further research. (Copyright 2022 OTC)

PHOTODEGRADATION 1,561,862

INGENIOUS CONSTRUCTION OF Ni(DMG)2/TiO2-DECORATED POROUS NANOFIBERS FOR THE HIGHLY EFFICIENT PHOTODEGRADATION OF POLLUTANTS IN WATER

H.Lu, M.Zhang, P.Wang, X.Xu, Y.Liu and D.G.Yu (Shanghai Univ Sci Technol). *COLLOIDS AND SURFACES A: PHYSICO-CHEMICAL AND ENGINEERING ASPECTS* v.650, 10/5/2022. (ISSN 0927-7757; Article no.129561)

Dyes and metal ions which are the major components of effluents from industries such as textile, paper, leather, cosmetics and plastic, prove to be the most harmful and toxic of all the contaminants. Especially, Ni²⁺ as colorant and methylene blue (MB) are contained in the wastewater of printing and dyeing plant. Herein, novel porous dimethylglyoxime (DMG)/TiO₂/polyacrylonitrile (PAN) nanofiber mats were prepared via electrospinning to treat Ni²⁺ and MB mixture pollutants. The formation of red and virgulate Ni(DMG)₂ on the nanofiber surface indicated that the composite possessed visible adsorption capacity (48.6895 mg/g in 120 min) as a benefit of the capability of DMG to sense Ni²⁺. Most importantly, the DMG/TiO₂-decorated PAN nanofiber mats exhibited excellent photocatalytic MB degradation efficiency (97 % within 60 min) owing to the construction of heterojunctions between Ni(DMG)₂ and TiO₂ nanoparticles and the shortening of electron and hole transport paths by hierarchical structures. The skillful use of Ni(DMG)₂ as an intermediate for photocatalytic MB degradation suggested that these functionalized nanofiber mats are promising candidates for practical application

in sensing, heavy metal ion adsorption, and photocatalytic organic pollutant degradation. (c2022 Elsevier B.V.)

PLATFORM JACKET 1,561,863

EVIDENCE OF FISH FOLLOWING TOWED OIL AND GAS PLATFORMS TO A REEFING SITE AND RAPID COLONISATION

M.J.Marnane, K.D.Schramm, D.Driessen, L.A.Fullwood, B.J.Saunders, S.Songploy, J.Kettratad, P.Sitaworawet, S.Chaiyakul et al. (Chevron Energy Technol Co). *MARINE ENVIRONMENTAL RESEARCH* v.180, Sept. 2022. (ISSN 0141-1136; Article no.105728)

We investigated the composition and abundance of fish assemblages associated with seven offshore oil and gas platform jackets in the Gulf of Thailand before (pre-lift and pre-tow), and immediately after relocation (post-tow and reefed). Jackets were cut, lifted until partly out of the water, and attached to the rear of a heavy lift vessel. They were towed at speeds of 2.7 – 3.3 knots for between 133.9 and 205.4 km before being placed on the seafloor at an artificial reef site. Sixteen species of fish were observed both before and after jacket towing. We believe these species have sought refuge in the complex structures out of the current and have remained with the jackets. Ten species of fish were observed before towing, but not after. A further seven species of fish were only observed after the jackets were relocated onto the seafloor and were assumed to be early colonisers to the structures. The paper provides empirical evidence of a much-discussed paradigm that fish can swim great distances following moved structures, and further evidence of the ability of fish to rapidly colonise reefed structures. (c2022 The Authors. Elsevier Ltd.)

RISK ANALYSIS 1,561,864

REDUCING HAZARDS AND RISK THROUGH VIRTUAL RISK ASSESSMENT

L.Boyd, L.Mills, A.Jacintho and G.Martinez (Siemens Energy AG). *OFFSHORE TECHNOLOGY CONFERENCE [OTC] (Houston, TX, 5/2-5/2022) PROCEEDINGS 2022*. (ISBN 978-1-61399-852-6; OTC-31838; Available at <http://www.onepetro.org> as of 6/23/2022; 6 pp)

For companies with worksites around the globe, assessing risks can be a challenge, particularly when different countries might adhere to different rules and regulations regarding workplace operations. This paper reviews a novel risk assessment template designed to evaluate a wide variety of risks on a "level playing field" for each manufacturing site office, offshore platform, and other work locations. The template, which is completed by qualified personnel at the specific site, ranks facilities based upon their environmental, health, and safety (EHS) risks as well as ISO requirements incorporating quality and EHS standards. (Copyright 2022 OTC)

SHIP 1,561,865

DECARBONIZATION IN SHIPPING INDUSTRY: A REVIEW OF RESEARCH, TECHNOLOGY DEVELOPMENT, AND INNOVATION PROPOSALS

G.Malloppas and E.A.Yfantis (Cyprus Marine Inst). *JOURNAL OF MARINE SCIENCE AND ENGINEERING* v.9, no.4, April 2021. (ISSN 2077-1312; Article no.415)

This review paper examines the possible pathways and possible technologies available that will help the shipping sector achieve the International Maritime Organization's (IMO's) deep decarbonization targets by 2050. There has been increased interest from important stakeholders regarding deep decarbonization, evidenced by market surveys conducted by Shell and Deloitte. However, deep decarbonization will require financial incentives and policies at an international and regional level given the maritime sector's approximately 3% contribution to greenhouse gas (GHG) emissions. This review paper, based on research articles and grey literature, discusses techno-economic problems and/or benefits for technologies that will help the shipping sector achieve the IMO's targets. This review presents a discussion on the recent literature regarding alternative fuels (nuclear, hydrogen, ammonia,

methanol), renewable energy sources (bio-fuels, wind, solar), the maturity of technologies (fuel cells, internal combustion engines) as well as technical and operational strategies to reduce fuel consumption for new and existing ships (slow steaming, cleaning and coating, waste heat recovery, hull and propeller design). The IMO's 2050 targets will be achieved via radical technology shift together with the aid of social pressure, financial incentives, regulatory and legislative reforms at the local, regional, and international levels.

SHIP 1,561,866

MEGA-SHIP-GENERATED TSUNAMI: A FIELD OBSERVATION IN TAMPA BAY, FLORIDA

P.Wang and J.Cheng (South Florida Univ). *JOURNAL OF MARINE SCIENCE AND ENGINEERING* v.9, no.4, April 2021. (ISSN 2077-1312; Article no.437)

The displacement of a large amount of water in a moderate-sized estuary by a fast-moving mega-ship can generate tsunami-like waves. Such waves, generated by cruise ships, were observed in Tampa Bay, Florida, USA. Two distinct, long tsunami-like waves were measured, which were associated with the passage of a large cruise ship. The first wave had a period of 5.4 min and a height of 0.40 m near the shoreline. The second wave had a period of 2.5 min and was 0.23 m high. The peak velocity of the onshore flow during the second wave reached 0.65 m/s. The shorter, second wave propagated considerably faster than the first wave in the breaking zone. The measured wave celerity was less than 50% of the calculated values, using the shallow water approximation of the dispersion equation, suggesting that nonlinear effects play an important role. A fundamental similarity among the generation of tsunamis, as induced by mega-ships, landslides or earthquakes, is a process that causes a vertical velocity at the sea surface, where a freely propagating wave is produced. This mega-ship-generated tsunami provides a prototype field laboratory for systematically studying tsunami dynamics, particularly the strong turbulent flows associated with the breaking of a tsunami wave in the nearshore, and tsunami-land interactions. It also provides a realistic demonstration for public education, which is essential for the preparation and management of this unpreventable hazard.

SHIP 1,561,867

A SHIP FIREFIGHTING TRAINING SIMULATOR WITH PHYSICS-BASED SMOKE

R.Tao, H.Ren and Y.Zhou (Dalian Maritime Univ; CNOOC Energy Technl Svcs). *JOURNAL OF MARINE SCIENCE AND ENGINEERING* v.10, no.8, Aug. 2022. (ISSN 2077-1312; Article no.1140)

Under the current background of navigation education, students generally lack a comprehensive grasp of ship firefighting equipment's operation. Therefore, we develop a novel ship firefighting training simulator with a multi-sensory human-computer interaction function for teaching and training marine students. In the simulator, we consider a container ship of 1.8w containers as the prototype ship, and the entire ship models are built using three-dimensional modeling technology. We design various interactive modes and realize a full-process operation simulation of several standard ship firefighting equipment. Furthermore, we propose a purely Lagrangian vortex dynamics framework to simulate smoke and flame in fire scenarios. In this framework, we model fluids using velocity and vorticity fields discretized on discrete vortex segments. The main components of the framework include a stable geometric stretching solution and particle strength exchange method for solving the diffusion term. The simulation results show that the simulator has good behavioral realism and scene immersion and can be applied to ship firefighting training. To the best of our knowledge, this is the first study on real-time smoke simulation using a physics-based method in a firefighting training simulator.

SHIP 1,561,868**CONSIDERATIONS ON THE EFFECT OF SLOW-STEAMING TO REDUCE CARBON DIOXIDE EMISSIONS FROM SHIPS**

D.Glujić, P.Kralj and J.Dujmović (Rijeka Univ). *JOURNAL OF MARINE SCIENCE AND ENGINEERING* v.10, no.9, Sept. 2022. (ISSN 2077-1312; Article no.1277)

Carbon dioxide emissions have become a growing problem worldwide. Global institutions are addressing this problem and developing solutions. Countries that are aware of this problem are implementing regulations that affect global industry and, in particular, maritime transport. Considering that the combustion process—namely, for diesel—remains the main energy conversion process on board ships, the question arises: what is the best solution for reducing pollutant emissions? Coastal countries have taken various measures to reduce the emission of harmful gases into the marine environment. The problem with these measures is that it is difficult to accurately predict their impact. This paper looks at one of these measures (slow-steaming) to determine how it affects carbon dioxide emissions from different types of ships and their modes of operation. Engine room simulators were used to study two marine power plants under different operating conditions. Fuel consumption was measured—such as flows from heavy fuel oil and diesel oil service tanks to all consumers—and carbon emissions were calculated accordingly. The study showed a large reduction in carbon dioxide emissions in the case of a modern power plant ship and large deviations when all operating modes were compared.

SHIP 1,561,869**PRIMARY FACTORS AFFECTING THE EFFICIENCY OF THERMOELECTRIC POWER GENERATION SHEETS FOR WASTE-HEAT RECOVERY FROM THE SHIP'S EXHAUST GAS**

X.Liu, C.Zhao, H.Guo and Z.Wang (Shanghai Maritime Univ). *JOURNAL OF MARINE SCIENCE AND ENGINEERING* v.10, no.9, Sept. 2022. (ISSN 2077-1312; Article no.1281)

In order to investigate the effect of different influencing factors on the application of temperature differential power generation in the ship exhaust gas and to explore the potential of waste heat recovery and the utilization of exhaust gas during ship travel, an experimental system based on the temperature differential power generation of ship exhaust gas in the marine environment was established. The maximum output power and the maximum efficiency of each temperature-difference power generation module were theoretically calculated. The results showed that the insulation material and the salt water (seawater) had little effect on the efficiency of the temperature differential power generation modules. Conversely, the installation pressure, the heat transfer oil, the cooling water temperature (seawater temperature), and the heat source temperature (exhaust gas pipe temperature) had a great influence on the open-circuit voltage and the maximum output power. The thermally conductive silicone grease and the cooling water temperature of 10°C increased the open-circuit voltage by 31.54% and 18.95%, respectively, and increased the maximum output power by 82.05% and 51.79%, respectively. The maximum output of a single temperature differential power generator reached 63.5% when using an installation pressure of 3 bar, a cooling water temperature of 20°C, double-layer aluminum insulation, and thermally conductive silicone grease. Finally, this study provides relevant data support for using temperature differential power generation devices for ship exhaust gas.

SOLID ADSORBENT 1,561,870**PREPARATION AND CO₂ ADSORPTION PROPERTIES OF TEPA-FUNCTIONALIZED MULTI-LEVEL POROUS PARTICLES BASED ON SOLID WASTE**

H.Su, H.Zhang, G.Qi, W.Lu and M.Wang (Shandong Univ Sci Technol). *COLLOIDS AND SURFACES A: PHYSICOCHEMICAL AND ENGINEERING ASPECTS* v.653, 11/20/2022. (ISSN 0927-7757; Article no.130004)

In this paper, tetraethylenepentamine (TEPA)-functionalized solid waste-based porous particles were prepared by the wet

impregnation method, and their functionalization characteristics and CO₂ adsorption performances at different TEPA loadings were investigated. Through a scanning electron microscope test and a N₂ adsorption/desorption test, it is found that, as the TEPA loading increases from 4 wt% to 20 wt%, the specific surface area and pore volume of the samples decrease slowly and micropores gradually disappear. Besides, the CO₂ adsorption capacity of the samples was tested by a fixed-bed adsorption experimental device at 298 K and 0–1 bar. The results show that the CO₂ adsorption capacity reaches the maximum (71.29 mg/g) at a 12 wt% TEPA loading, which is attributed to the high content of affinity sites in CO₂. Furthermore, the effect of temperature (298–398 K) was investigated at 1 bar. It is concluded that an appropriate increase in adsorption temperature can enhance the flexibility of TEPA and greatly reduce its diffusion resistance. The highest adsorption capacity (83.05 mg/g) is achieved at 348 K. Then, the effect of pressure (0–40 bar) was analyzed at the optimal temperature (348 K) and optimal TEPA loading (12 wt%), and the results suggest that the adsorption capacity gradually strengthens with the increase in pressure, ultimately reaching a peak of 204.06 mg/g. The adsorption selectivities of CO₂/N₂ and CO₂/H₂ are 14.88 and 9.66, respectively, indicating that the porous particles have a stronger affinity for CO₂ than for N₂ and H₂. The infrared spectra prove the formation of carbamates, which confirms that CO₂ is sequestered in porous particles by chemical adsorption. The adsorption kinetics and adsorption thermodynamics results reveal the presence of both physical and chemical adsorptions of 12 wt% TEPA-porous particles in the adsorption process, and the chemical one is dominant. (c2022 Elsevier B.V.)

SUSTAINABILITY 1,561,871**VALORIZATION OF POLYETHYLENE TEREPHTHALATE (PET) PLASTIC WASTES AS NANOFIBROUS MEMBRANES FOR OIL REMOVAL: SUSTAINABLE SOLUTION FOR PLASTIC WASTE AND OIL POLLUTION**

F.Topuz, D.G.Oldal and G.Szekely (King Abdullah Univ). *INDUSTRIAL & ENGINEERING CHEMISTRY RESEARCH* v.61, no.25, pp.9077-9086, 6/29/2022. (ISSN 0888-5885; ISSN 1520-5045)

The accumulation of plastic wastes has become a global environmental issue, because of their ever-growing production, slow degradation, and potential environmental hazards. Consequently, reducing their presence in the environment by upcycling has sparked tremendous research interest. Herein, we report the valorization of poly(ethylene terephthalate) (PET) plastic wastes to produce nanofibrous adsorptive membranes for their applications in oil removal. In this study, plastic wastes derived from PET bottles were dissolved in trifluoroacetic acid (TFA) or a TFA/dichloromethane (DCM) binary solvent system and then electrospun into nanofibrous recycled PET (rPET) membranes. The nanofiber morphology was tuned by adjusting the polymer concentration. The nanofibers produced via electrospinning from TFA solutions were more uniform than those produced using TFA/DCM. The influence of acid-mediated recycling on the PET structure was explored via thermogravimetric and X-ray photoelectron spectroscopy analyses. A dynamic mechanical analysis showed that the membranes exhibited high flexibility with effective Young's moduli. The sorption capacities of the nanofibrous PET membranes for crude oil, diesel, gasoline, and pump oil were 22.9 ± 2, 19.6 ± 1.8, 11.1 ± 1, and 19.3 ± 1.6 g/g, respectively. The membrane could be recycled by squeezing and reused five times for oil removal while maintaining an sorption capacity of >75%. After the sorption tests, an apparent increase in the fiber diameter was observed due to the oil uptake into the fiber matrix. The present study provides a sustainable solution to plastic and oil pollution management, minimizing the production of new carbon-based materials and lowering carbon emissions. This work aligns with the United Nations' Sustainable Development Goals—specifically goal 12 on responsible consumption and production and goal 14 on life under water.

WATER POLLUTION

1,561,872

OCEAN WATER QUALITY MONITORING USING REMOTE SENSING TECHNIQUES: A REVIEW

F.Mohseni, F.Saba, S.M.Mirmazloumi, M.Amani, M.Mokhtarzade, S.Jamali and S.Mahdavi (K N Toosi Univ Technology; CTTC; Wood Envir Infrastructure). *MARINE ENVIRONMENTAL RESEARCH* v.180, Sept. 2022. (ISSN 0141-1136; Article no.105701)

Ocean Water Quality (OWQ) monitoring provides insights into the quality of water in marine and near-shore environments. OWQ measurements can contain the physical, chemical, and biological characteristics of oceanic waters, where low OWQ values indicate an unhealthy ecosystem. Many parameters of water can be estimated from Remote Sensing (RS) data. Thus, RS offers significant opportunities for monitoring water quality in estuaries, coastal waterways, and the ocean. This paper reviews various RS systems and techniques for OWQ monitoring. It first introduces the common OWQ parameters, followed by the definition of the parameters and techniques of OWQ monitoring with RS techniques. In this study, the following OWQ parameters were reviewed: chlorophyll-a, colored dissolved organic matter, turbidity or total suspended matter/solid, dissolved organic carbon, Secchi disk depth, suspended sediment concentration, and sea surface temperature. This study presents a systematic analysis of the capabilities and types of spaceborne systems (e.g., optical and thermal sensors, passive microwave radiometers, active microwave scatterometers, and altimeters) which are commonly applied to OWQ assessment. The paper also provides a summary of the opportunities and limitations of RS data for spatial and temporal estimation of OWQ. Overall, it was observed that chlorophyll-a and colored dissolved organic matter are the dominant parameters applied to OWQ monitoring. It was also concluded that the data from optical and passive microwave sensors could effectively be applied to estimate OWQ parameters. From a methodological perspective, semi-empirical algorithms generally outperform the other empirical, analytical, and semi-analytical methods for OWQ monitoring. (c2022 Elsevier Ltd.)

WATER TREATING

1,561,873

REVIEW OF BIOLOGICAL PROCESSES IN A MEMBRANE BIOREACTOR (MBR): EFFECTS OF WASTEWATER CHARACTERISTICS AND OPERATIONAL PARAMETERS ON BIODEGRADATION EFFICIENCY WHEN TREATING INDUSTRIAL OILY WASTEWATER

A.Bhattacharyya, L.Liu, K.Lee and J.Miao (Dalhousie Univ; Fisheries & Oceans Canada). *JOURNAL OF MARINE SCIENCE AND ENGINEERING* v.10, no.9, Sept. 2022. (ISSN 2077-1312; Article no.1229)

Oily wastewater is generated from various sources within the petrochemical industry, including extraction, refining and processing, storage, and transportation. Over the years, large volumes of oily wastewater from this industry have made their way into the environment, negatively affecting the environment, human health, and the economy. The raw waters from the petrochemical industry can differ significantly and have complex features, making them difficult to treat. Membrane bioreactors (MBR) are a promising treatment option for complex wastewater; it is a combined physical and biological treatment. The biological component of the MBR is one of the main contributing factors to its success. It is important to know how to control the parameters within the bioreactor to promote the biodegradation of hydrocarbons to improve the treatment efficiency of the MBR. There have been many reviews on the effects of the biological factors of membrane fouling; however, none have discussed the biodegradation process in an MBR and its impact on effluent quality. This review paper investigates the hydrocarbon biodegradation process in an aerobic MBR system by gathering and analyzing the recent academic literature to determine how oily wastewater characteristics and operational parameters affect this process.

SCIENCE & ENGINEERING

COMPLEXING AGENT

1,561,874

CHELATING AGENT-BASED FORMULATION AND USE THEREOF AS AN AGENT FOR DISSOLVING INORGANIC DEPOSITS IN OIL FIELDS [FORMULACION A BASE DE AGENTE QUELANTE Y USO DEL MISMO COMO AGENTE DE DISOLUCION DE DEPOSITOS INORGANICOS EN CAMPOS PETROLEROS]

J.C.Jimenez Osorio, asr. (Chemiservis SA de CV). *World* 2022/203,497A1, p. 9/29/2022, f. 3/24/2022 (Appl. 2,250,030), pr. Mex. 3/26/2021 (Appl. 21,003,592) (C09K-0008/00). (In Spanish)

The present invention relates to a non-acid liquid formulation designed to remove scale or inorganic deposits (formed by CaSO₄, iron, calcium, strontium, barium, carbonates, sulphates or oxides). The formulation is based on a chelating agent, which, in addition to preventing scale precipitation, is also used to remove unwanted scale and has low chemical material consumption and slower carbonate dissolution rates at high temperatures, allowing for deeper penetration and removal of gypsum and magnesium used in the preparation of drilling fluids. Moreover, it combines the advantages of conventional acids without their drawbacks, meaning that it has very low levels of corrosion and it can be used in a temperature range from 80°C to 204°C, thereby improving well productivity.

DATA MANAGEMENT

1,561,875

ADVANCED DATA DISCOVERY AND VISUALIZATION FOR ENERGY DATA SOURCES

Y.Zeng, L.Lu, B.Vinta, C.Hans, Z.Mai and W.Qiu, asrs. (Schlumberger Technol Corp; Schlumberger Canada Ltd; Schlumberger Serv Petrol; GeoQuest Systems BV). *World* 2022/212,441A1, p. 10/6/2022, f. 3/30/2022 (Appl. 2,222,451), pr. U.S. 3/30/2021 (Appl. 63/168,198), U.S. 3/30/2021 (Appl. 63/168,200) and U.S. 3/30/2021 (Appl. 63/168,201) (G06F-0003/04842; G06F-0008/30; G06F-003/04817; G06F-0003/0482; G06F-0016/29; G06N-0020/00).

A method implements advanced data discovery and visualization for energy data sources. The method includes presenting a map view displaying multiple data locations, receiving a selection identifying a subset of the map view, and selecting multiple application components corresponding to the data locations from the subset of the map view. The method further includes updating, responsive to selecting the application components, a toolbar displayed on the map view to include multiple icons corresponding to the application components. The method further includes presenting a visualization component, of the application components, displaying data, corresponding to a data location, in response to a selection from the toolbar. The method further includes creating, using a workflow component of the application components, a project workspace. The data presented with the visualization component is automatically imported to the project workspace.

DATA MANAGEMENT

1,561,876

INTEGRATED ENERGY DATA SCIENCE PLATFORM

Y.Zeng, B.Vinta, C.Hans, L.Lu, Y.Ma and A.Perozo, asrs. (Schlumberger Technol Corp; Schlumberger Canada Ltd; Schlumberger Serv Petrol; GeoQuest Systems BV). *World* 2022/212,438A1, p. 10/6/2022, f. 3/30/2022 (Appl. 2,222,443) pr. U.S. 3/30/2021 (Appl. 63/168,198), U.S. 3/30/2021 (Appl. 63/168,200) and U.S. 3/30/2021 (Appl. 63/168,201) (G06F-0003/048; G06F-0008/00; G06F-0021/00; G06N-0020/00).

A method implements an integrated energy data science platform. The method includes presenting a data discovery component, including a map view to select data using the map view. The method further includes presenting a model selection component to select a machine learning model configured with deployment settings and configured to use the data, wherein the deployment settings identify sample features of the data. The method further includes authorizing access to the machine learning

model and the data, deploying the machine learning model using the deployment settings, and presenting results generated from the sample features using the machine learning model, wherein the sample features are extracted from the data.

ELECTRIC GENERATOR 1,561,877

DOWNHOLE ELECTRICAL GENERATOR

A.B.M.Aguiar, T.A.C.Maia, O.A.Faria, R.L.P.Martins and N.K.Pai, asrs. (Halliburton Energy Service). World 2022/211,808A1, p. 10/6/2022, f. 3/31/2021 (Appl. 2,125,258), pr. U.S. 3/30/2021 (Appl. 217,657) (E21B-0041/00; H02K-0001/14; H02K-0001/27; H02K-0007/18).

Apparatuses, systems and methods for implementing a downhole alternator assembly are disclosed. In some embodiments, a downhole alternator assembly comprises a casing; a turbine disposed within the casing and actuated by a drilling fluid flow; and a rotor disposed within the casing. The rotor includes a cylindrical rotor core rotated by the turbine; a plurality of permanent magnets disposed in the cylindrical rotor core; and a drilling fluid channel extending axially through the center of the cylindrical rotor core. The downhole alternator assembly includes a stator disposed within the casing. The stator includes a cylindrical stator core disposed concentrically between the cylindrical rotor core and the casing; conductor windings within the cylindrical stator core; and a plurality of radially distributed fluid channels extending axially within the cylindrical stator core between a front end of the cylindrical stator core and a back end of the cylindrical stator core.

FIELD EQUIPMENT 1,561,878

FIELD EQUIPMENT DATA SYSTEM

G.Sridhar, S.K.Subbiah, M.Ibrahim, A.E.Rodriguez Herrera, N.Alhamad, G.S.Gupta et al., asrs. (Schlumberger Technol Corp; Schlumberger Canada Ltd; Schlumberger Serv Petrol; GeoQuest Systems BV). World 2022/204,723A1, p. 9/29/2022, f. 3/25/2022 (Appl. 2,271,353), pr. U.S. 3/26/2021 (Appl. 63/200,756) (E21B-0049/02; G01V-0001/46; G01V-0001/50; G06N-0003/04; G06N-0020/00).

A method can include receiving real-time, time series data from equipment at a wellsite that includes a wellbore in contact with a fluid reservoir, processing the time series data as input to a trained machine learning model to predict a future solids event related to influx of solids into the wellbore from the fluid reservoir, and outputting a time of the future solids event.

GLACIER 1,561,879

BROKEN ICE CIRCUMFERENTIAL CRACK ESTIMATION VIA IMAGE TECHNIQUES

J.Cai, S.Ding, Q.Zhang, R.Liu, D.Zeng and L.Zhou (Jiangsu Univ Sci & Technol; Norwegian Meteorology Inst). OCEAN ENGINEERING v.259, 9/1/2022. (ISSN 0029-8018; Article no.111735)

The identification and digitization of floating ice are of great significance to developing numerical ice load model of ships and marine structures in managed ice fields. The circumferential crack method is a commonly-used method to simulate the level ice breaking process for a polar ship. The crack size, including radius and open-angle, is an import parameter that should be considered in the analysis of ice-structure interactions. It is usually determined by the empirical formulas, which may introduce many uncertainties in the selection of input parameters. In this paper, we adopt a deep learning YOLACT model to identify broken ice blocks from an image, where an image processing algorithm is newly developed to estimate circumferential crack size for each identified ice blocks. The numerical simulation shows that the accuracy of the radius and open-angle estimated by the present method can reach up to 97.37% and 96.66%, respectively. The present tool could be used to assist design and operations for marine structures in ice-infested waters. (c2022 Elsevier Ltd.)

GLACIER 1,561,880

HYDROELASTIC POTENTIAL FLOW SOLVER SUITED FOR NONLINEAR WAVE DYNAMICS IN ICE-COVERED WATERS

M.C.Hartmann, M.Onorato, F.De Vita, G.Clauss, S.Ehlers, F.B.und Polach, L.Schmitz, N.Hoffmann and M.Klein (Hamburg Univ Technology). OCEAN ENGINEERING v.259, 9/1/2022. (ISSN 0029-8018; Article no.111756)

The aim of this paper is to introduce a fully nonlinear numerical finite element solver for the simulation of nonlinear wave processes in the presence of a solid ice sheet. In this study, solid ice cover referred to the size of the ice sheet and denoted that the length of the ice sheet was many times larger than the longest relevant wavelength. The complexity of the ice sheet characteristics was assumed to be homogeneous, isotropic and in the linear elastic plate regime so that the deformation process could be modeled by the Kirchhoff-Love plate ansatz. The method presented was verified and validated for different ice dimensions and wave scenarios. At the beginning, the implementation of the flexural rigidity to the free surface boundary condition was verified by comparing the analytical wave-ice dispersion relation to simulation results with small amplitude regular waves and varying ice dimensions. Afterwards, the general applicability was validated by means of wave-ice experiments. The experiments were performed in the ice tank at Hamburg Ship Model Basin HSVA comprising regular waves and transient wave groups. (c2022 Elsevier Ltd.)

HORIZONTAL WELL 1,561,881

DRIVE AND STEERING OF A DOWNHOLE ROBOT

K.V.Sherrill, J.F.Tims and S.J.Moreland, asrs. (California Inst Technol). World 2022/212,670A1, p. 10/6/2022, f. 3/31/2022 (Appl. 2,222,776), pr. U.S. 4/2/2021 (Appl. 63/170,385) (E21B-0023/00; F16L-0055/30).

Systems and methods for driving and steering of a robot, or mobile vessel, for operation in a downhole pipe of an oil/gas/water well are presented. According to one aspect, the mobile vessel includes a plurality of wheels arranged outwardly from the mobile vessel so that each wheel may contact the inner wall of the casing. According to another aspect, the plurality of wheels may include respective wheel-centerlines that intersect the centerline of the casing that is at an offset from a centerline of the mobile vessel. The plurality of wheels includes at least two drive wheels and at least one passive wheel. According to a further aspect, the drive wheels are configured to rotate about their respective wheel-centerlines to steer the mobile vessel during traversal of the casing. In one case, the mobile vessel includes two drive and steering wheels and one passive wheel.

HURRICANE 1,561,882

NEAR-INERTIAL WAVES INDUCED BY TYPHOON MEGI (2010) IN THE SOUTH CHINA SEA

A.Cao, Z.Guo, Y.Pan, J.Song, H.He and P.Li (Zhejiang Univ; Zhejiang Ocean Univ; China Ministry Natural Rsc). JOURNAL OF MARINE SCIENCE AND ENGINEERING v.9, no.4, April 2021. (ISSN 2077-1312; Article no.440)

Near-inertial waves (NIWs) are a kind of internal wave and are usually generated by synoptic wind forcing and play an important role in the oceanic energy budget. However, the lack of in situ observations limits our understanding of NIWs to some extent. Through a comparison with in situ observations, in this study, we first showed that the hybrid coordinate ocean model reanalysis results could reasonably reproduce the typhoon-induced NIWs, and we then adopted these data to investigate the NIWs induced by typhoon Megi in 2010 in the South China Sea (SCS). The results indicate that Megi-induced near-inertial kinetic energy was mainly concentrated in the SCS Basin. In the vertical direction, Megi-induced NIWs could propagate to a depth of 1000 m. The damping and modal content of Megi-induced NIWs were site-dependent: In the region near Megi's track, NIWs were dominated by the first three baroclinic modes and damped quickly; whereas in two zones to the west of the Luzon Island and Luzon Strait, the e-folding time of Megi-induced NIWs could be longer than 20 days and higher modes (mode 4 to mode 7) were enhanced several days after the

Megi passed by. The possible mechanisms of these phenomena were also explored in this study.

ICEBERG **1,561,883**

EFFECTS OF WIND, WAVES, AND CURRENTS ON ICEBERGS AND SURFACE FLOATS IN THE LABRADOR SEA: A MODELING STUDY

J.Parayil, E.K.Demirov and Y.Afanasyev (Newfoundland Memorial Univ). *JOURNAL OF MARINE SCIENCE AND ENGINEERING* v.10, no.9, Sept. 2022. (ISSN 2077-1312; Article no.1167)

This article presents a model study of the dynamics of icebergs and surface floats in the Labrador Sea. The model was forced with data on the wind above the ocean surface, surface waves, and ocean currents. These data were obtained from the reanalysis of near-surface characteristics of the ocean and atmosphere for the year 2008. Icebergs and floats launched in an area north of the Labrador coast and to the east of Greenland generally move southeastward until they reach a boundary current "highway". After that, they are carried by ocean currents into the central part of the subpolar North Atlantic. Simulations demonstrated that, for smaller icebergs, the primary balance is between the air and water drag, while for larger icebergs, it is between three forces: the air and water drag and the combined Coriolis and pressure forces. Floats, on the other hand, are driven mostly by the Ekman component of the surface velocity, while the geostrophic and Stokes components are less important. The significant variability in the motion of icebergs and floats is due to storms passing over the Labrador Sea, since these high-wind events introduce time-dependent dynamics.

MODEL **1,561,884**

ADVANCED APPLICATION OF MODEL OPERATIONS IN ENERGY

C.Hans, B.Vinta, Y.Zeng, L.Lu and J.Zhang, asrs. (Schlumberger Technol Corp; Schlumberger Canada Ltd; Schlumberger Serv Petrol; GeoQuest Systems BV). World 2022/212,445A1, p. 10/6/2022, f. 3/30/2022 (Appl. 2,222,458), pr. U.S. 3/30/2021 (Appl. 63/168,198), U.S. 3/30/2021 (Appl. 63/168,200) and U.S. 3/30/2021 (Appl. 63/168,201) (G06F-0003/0482; G06F-0008/60; G06F-0008/71; G06F-0016/26; G06N-0020/00).

A method implements advanced application of model operations in energy. The method includes presenting an inspection view with a model list. The method further includes receiving a selection of a list entry, corresponding to a model, from the model list, wherein the model of the list entry is a champion model selected from multiple challenger models corresponding to the list entry. The method further receiving deployment settings of the model, presenting a deployment view with a deployment list with the model, and updating a deployment status of the model in the deployment view.

OFFSHORE STRUCTURE **1,561,885**

MONITORING THE CLEANLINESS OF AN UNDERWATER SURFACE OF A STATIONARY OBJECT

J.Costa, A.Krapp, S.Paereli, K.T.Boman, S.M.Jackson and M.Levantis, asrs. (Jotun A/S). World 2022/200,430A1, p. 9/29/2022, f. 3/23/2022 (Appl. 2,257,632), pr. Europe. 3/23/2021 (Appl. 21,860,022) and Europe. 7/6/2021 (Appl. 21,386,042) (B63B-0059/08; B63B-0059/10; G05D-0001/02).

A computer-implemented method of monitoring the cleanliness of an underwater surface of a stationary object is disclosed herein. The method is performed on a computing device and comprises retrieving environmental data from memory of the computing device, the environmental data associated with environment conditions of the stationary object; determining a fouling value indicative of a level of fouling that the surface is exposed to based on at least the environmental data; determining a fouling protection value defining a tolerance to fouling associated with a surface of the stationary object; and identifying a level of risk of fouling on the surface of the stationary object by determining a fouling risk value using the fouling protection value and the fouling value.

PETROLEUM INDUSTRY **1,561,886**

VERIFICATION OF AN ENVIRONMENTAL IMPACT ASSESSMENT USING A MULTIVARIATE STATISTICAL MODEL

W.R.Chou, H.Y.Hsieh, G.K.Hong, F.C.Ko, P.J.Meng and K.S.Tew (Nat Museum Marine Taiwan; National Dong Hwa Univ). *JOURNAL OF MARINE SCIENCE AND ENGINEERING* v.10, no.8, Aug. 2022. (ISSN 2077-1312; Article no.1023)

Environmental impact assessments are a means of preventing and mitigating the adverse effects of economic development activities on the natural environment. It is meant to ensure that decision-makers have sufficient information to consider environmental impacts before proceeding with new projects. Despite their important role in public policy, environmental impact assessments have seldom been verified. In this study, we used principal component analysis (PCA) to identify the major sources of influence on the coastal waters adjacent to a major tourist facility (an aquarium) in southern Taiwan, followed by the construction of a structural equation model (SEM) to determine the direct and indirect effects of the abiotic factors on phytoplankton and zooplankton density and diversity. Based on the loading of principal components 1-3, we identified that river input, suspended matter, and seasonal changes were the major factors affecting the coastal area. The SEM further suggested that phytoplankton density and diversity were affected directly by seasonal changes and suspended matter, but only indirectly by river input, owing to the latter's effect on suspended matter. In contrast, the SEM suggested that zooplankton density and diversity were affected directly by seasonal changes, but indirectly by both river input and suspended matter owing to their effects on phytoplankton density and diversity. Q2 was the season with the highest number of visitors to the aquarium, but none of the abiotic or biotic parameters showed particular differences, implying that the variations in those parameters in the adjacent coastal waters were not related to the visitors. We suggest that PCA and SEM be used in the future in other contexts to verify environmental impact assessments.

SHIP **1,561,887**

ANALYSIS OF DANGEROUS SEA STATES IN THE NORTHWESTERN MEDITERRANEAN AREA

A.Innocenti, M.Onorato and C.Brandini (LaMMA Consortium Lab; Torino Univ). *JOURNAL OF MARINE SCIENCE AND ENGINEERING* v.9, no.4, April 2021. (ISSN 2077-1312; Article no.422)

Extreme sea waves, although rare, can be notably dangerous when associated with energetic sea states and can generate risks for the navigation. In the last few years, they have been the object of extensive research from the scientific community that helped with understanding the main physical aspects; however, the estimate of extreme waves probability in operational forecasts is still debated. In this study, we analyzed a number of sea-states that occurred in a precise area of the Mediterranean sea, near the location of a reported accident, with the objective of relating the probability of extreme events with different sea state conditions. For this purpose, we performed phase-resolving simulations of wave spectra obtained from a WaveWatch III hindcast, using a Higher Order Spectral Method. We produced statistics of the sea-surface elevation field, calculating crest distributions and the probability of extreme events from the analysis of a long time-series of the surface elevation. We found a good matching between the distributions of the numerically simulated field and theory, namely Tayfun second- and third-order ones, in contrast with a significant underestimate given by the Rayleigh distribution. We then related spectral quantities like angular spreading and wave steepness to the probability of occurrence of extreme events finding an enhanced probability for high mean steepness seas and narrow spectra, in accordance with literature results, finding also that the case study of the reported accident was not amongst the most dangerous. Finally, we related the skewness and kurtosis of the surface elevation to the wave steepness to explain the discrepancy between theoretical and numerical distributions.

WAVE FORCE

1,561,888

THE IMPACT OF WAVE MODEL SOURCE TERMS AND COUPLING STRATEGIES TO RAPIDLY DEVELOPING WAVES ACROSS THE NORTH-WEST EUROPEAN SHELF DURING EXTREME EVENTS

N.G.Valiente, A.Saulter, J.M.Edwards, H.W.Lewis, J.M.Castillo Sanchez, D.Bruciaferri, C.Bunney and J.Siddorn (Met Office; Southampton Oceanogr Ctr). *JOURNAL OF MARINE SCIENCE AND ENGINEERING* v.9, no.4, April 2021. (ISSN 2077-1312; Article no.403)

Predicting severe natural hazards requires accurate forecasting systems. Recently, there has been a tendency towards more integrated solutions, where different components of the Earth system are coupled to explicitly represent the physical feedbacks between them. This study focuses on rapidly developing waves under extra tropical storms to understand the impact of different wave source term parameterisations in the WAVEWATCH III (WWIII) model (ST4 and ST6) and coupling strategies (surface roughness closure versus surface stress closure) on the accuracy of the Met Office regional atmosphere-ocean-wave coupled research system for the northwest (NW) European shelf (UKC4). Results of a study focused on simulations during the winter of 2013-2014 demonstrate that ST6 allows for a faster wave growth than the ST4 parameterisation but might degrade low to mid energy wave states. The difference between ST6 and ST4 in wave growth is larger for higher wind speeds and short fetches. The experiment with ST4 and roughness closure consistently under-predicts the wave growth in those locations where fetch dependence is an important factor (i.e., seas to the east of Ireland and the UK for storms coming from the NW-WNW). The implementation in the wave model of ST6 physics with the stress closure coupling strategy appears to improve growth of young wind-seas, reducing bias in those locations where the storms are underestimated. The slower wave growth when using surface roughness closure seems to be related to an underestimation of the momentum transfer computed by the wave model when coupling the wind speeds. For very young to young wind seas, this can be overcome when the surface stress is computed by the atmospheric model and directly passed to the ocean.

WAVE FORCE

1,561,889

PREDICTION OF WAVE ENERGY FLUX IN THE BOHAI SEA THROUGH AUTOMATED MACHINE LEARNING

H.Yang, H.Wang, Y.Ma and M.Xu (Dalian Maritime Univ; Sun Yat-sen Univ). *JOURNAL OF MARINE SCIENCE AND ENGINEERING* v.10, no.8, Aug. 2022. (ISSN 2077-1312; Article no.1025)

The rational assessment of regional energy distribution provides a scientific basis for the selection and siting of power generation units. This study, which focused on the Bohai Sea, set 31 research coordinate points in the Bohai sea for assessing the potential/trends of wave energy flux (WEF). We applied a point-to-point time series prediction method which modelled the different geographical coordinate points separately. Subsequently, we evaluated the performance of three traditional machine learning methods and three automated machine learning methods. To estimate WEF, the best model was applied to each research coordinate points, respectively. Then, the WEF was calculated and predicted based on the data of MWP, SWH, and water depth. The results indicate that, for all coordinates in the Bohai Sea, the H2O-AutoML algorithm is superior to the other five algorithms. Gradient boosting machine (GBM), extreme gradient boosting (XGBoost), and stacked ensemble models yielded the best performance out of the H2O algorithms. The significant wave height (SWH), the mean wave period (MWP), and the WEF in the Bohai Sea tended to be concentrated in the center of the sea and dispersed in the nearshore areas. In the year 2000, 2010, 2020, and 2030, the maximum annual average WEF at each research coordinate in the Bohai Sea is around 1.5 kW/m, with a higher flux in autumn and winter. In summary, the results provide ocean parameter characterization for the design and deployment of wave energy harvesting devices. Moreover, the automated machine learning introduced herein has potential for use in more applications in ocean engineering.

WAVE HEIGHT

1,561,890

PREDICTION METHOD FOR OCEAN WAVE HEIGHT BASED ON STACKING ENSEMBLE LEARNING MODEL

Y.Zhan, H.Zhang, J.Li and G.Li (Wuhan Univ Technology; CSSC Marine Technol Co Ltd). *JOURNAL OF MARINE SCIENCE AND ENGINEERING* v.10, no.8, Aug. 2022. (ISSN 2077-1312; Article no.1150)

Wave heights are important factors affecting the safety of maritime navigation. This study proposed a stacking ensemble learning method to improve the prediction accuracy of wave heights. We analyzed the correlation between wave heights and other oceanic hydrological features, according to eleven features, such as measurement time, horizontal velocity, temperature, and pressure, as the model inputs. A fusion model consisting of two layers was established according to the principle of stacking ensemble learning. The first layer used the extreme gradient boosting algorithm, a light gradient boosting machine, the random forest technique, and adaptive boosting to determine the deep relations between the wave heights and the input features. The second layer used a linear regression model to fit the relation between the first layer outputs and the actual wave heights, using the data from the four models of the first layer. The fusion model was trained based on the five-fold cross-verification algorithm. This paper used real data to test the performances of the proposed fusion model, and the results showed that the mean absolute error and the mean squared error of the fusion model were at least 35.79% and 50.52% better than those of the four models.

WAVE HEIGHT

1,561,891

REVIEW OF THE APPLICATION OF ARTIFICIAL NEURAL NETWORKS IN OCEAN ENGINEERING

N.Portillo Juan and V.Negro Valdecantos (Madrid Politecnica Univ). *OCEAN ENGINEERING* v.259, 9/1/2022. (ISSN 0029-8018; Article no.111947)

Artificial Neural Networks (ANNs) were firstly used to model ocean engineering problems in the decade of 1990s. Since then, this soft-modelling technique has proved several advantages against traditional approaches. In this article, the application of ANNs in ocean and maritime engineering from its beginnings until today is reviewed. After reviewing more than 90 studies, some general rules to apply in ANNs in ocean engineering are concluded, the most common and advantageous methods are summed up and research gaps in the application of ANNs are identified. (c2022 The Authors. Elsevier Ltd.)

WAVE (WATER)

1,561,892

EXPERIMENTAL INVESTIGATION ON THE VERTICAL STRUCTURE CHARACTERISTICS OF INTERNAL SOLITARY WAVES

P.Peng, H.Du, G.Wei, S.Wang, P.Xuan, S.Cai and J.Xie (National Univ Technology; South China Sea Inst Ocean). *JOURNAL OF MARINE SCIENCE AND ENGINEERING* v.10, no.8, Aug. 2022. (ISSN 2077-1312; Article no.1045)

An experimental investigation of the vertical structure characteristics of internal solitary waves (ISWs) was systematically carried out in a large gravitationally stratified fluid flume. Four different stratifications were established, and basic elements of ISWs were measured by a conductivity probe array. The vertical distributions of the amplitude, characteristic frequency and waveform of two types of ISWs under different stratifications were obtained, and the experimental results were compared with the theoretical model. The study shows that most vertical structures of the amplitude under different stratifications agree with those of the theoretical model, while there are some deviations for ISWs with large amplitudes. Neither the two-layer model nor the continuously stratified model can effectively describe the variation in the characteristic frequency at different depths with amplitude. For a single small-amplitude ISW, the characteristic frequency first increases and then decreases with increasing depth. The characteristic frequency is largest at the depth of the maximum buoyancy frequency. For an ISW with a relatively large amplitude, there is likely to be a local minimum of the characteristic frequency

near the depth where the maximum buoyancy frequency lies. In different stratifications, the sech2 function of KdV theory can describe the waveforms of ISWs at different depths well.

.....

WIND FORCE

1,561,893

SENSITIVITIES IN WIND DRIVEN SPECTRAL WAVE MODELING FOR THE BELGIAN COAST

F.van Eeden, G.Klonaris, J.Verbeurgt, P.Troch and A.De Wulf (Gent Univ). *JOURNAL OF MARINE SCIENCE AND ENGINEERING* v.10, no.8, Aug. 2022. (ISSN 2077-1312; Article no.1138)

This paper presents the analysis of spectral wind-wave modeling (using SWAN) of the North Sea focusing on the modeled wave parameters along the Belgian coast. Two wind databases were used to drive the model: ECMWF-ERA5 reanalysis and the Dutch Offshore Wind Atlas. The models were calibrated with measured data at various stations along the Belgian coastline. The accuracy in terms of wave parameter statistics was compared for the calibrated and uncalibrated models. It was found that a calibrated SWAN model does, in general, produce more accurate results when compared to measured data for stations along the Belgian coastline even though not by any significant margin. Comparing the two wind databases, on the modeling scale conducted in this study, there is no advantage observed in using a spatially finer scale wind database over a coarser database to force the model. The grid sizes were varied in the models and marginal differences were observed in the modeled data. The long-term extreme value statistics were calculated for various grid sizes and compared to published values. It is shown that the extreme value statistics are relatively insensitive to the grid density and thus much time can be saved on long-term modeling on this model scale. In addition, a benefit to the practice of grid nesting is demonstrated when considering complex bathymetric effects that have an influence on wave transformation in the shallower areas of the coast, especially along the Belgian coastline demarcated with its numerous sandbanks.

.....

ZETA POTENTIAL

1,561,894

THE ZETA POTENTIAL OF QUARTZ. SURFACE COMPLEXATION MODELLING TO ELUCIDATE HIGH SALINITY MEASUREMENTS

P.Leroy, A.Maineult, S.Li and J.Vinogradov (Bureau Rech Geol Min (Fr); Sorbonne Univ; China Univ Geosci, Wuhan; Aberdeen Univ). *COLLOIDS AND SURFACES A: PHYSICOCHEMICAL AND ENGINEERING ASPECTS* v.650, 10/5/2022. (ISSN 0927-7757; Article no.129507)

The zeta potential is a measureable electrical potential of paramount importance to understand the electrochemical properties of rocks. However, the zeta potential remains poorly understood because it takes place at the nanoscale of the electrical double layer on the mineral surface. Streaming potential measurements on quartz-rich Fontainebleau and Lochaline sandstones carried out at high salinity (above 0.1 M NaCl) yield surprisingly high zeta potential values, which cannot be correctly reproduced by a traditional surface complexation model considering that the shear plane is located at the beginning of the diffuse layer. We found that placing the shear plane, where the zeta potential is defined, slightly closer to the mineral surface than the Stern plane significantly improves the predictions of the zeta potential and surface charge density of quartz at high salinity as well as the values of the equilibrium constant describing sodium adsorption in the Stern layer. Our results have strong implications for the modelling of the electrochemical properties of minerals in contact with highly saline solutions. (c2022 Elsevier B.V.)

.....

Aalborg Univ	1,561,709	Alsinan, M M	1,561,593	Atchley, S C	1,561,161
Aalto Univ	1,561,813	Altanshagai, G	1,561,113	ATHENA	1,561,841
Abbasi, I A	1,561,248	Alujevic, N	1,561,688	Athens Univ	1,561,816
Abdel Gelil, A A H	1,561,675	Alvim, T M M	1,561,601	Aubry, J	1,561,772
Aberdeen Univ	1,561,102	Amaechi, C V	1,561,723	Auckland Univ	1,561,245
Aberdeen Univ	1,561,105	Amani, M	1,561,872	Automated Analytics LLC	1,561,481
Aberdeen Univ	1,561,894	American Museum	1,561,128	Avans Univ Applied Sci	1,561,839
Abeykoon, G A	1,561,790	Amin, A	1,561,670	Axen, G J	1,561,098
Abeyta, A J	1,561,560	Aming, A	1,561,446	Ayirala, S	1,561,747
Abivin, P	1,561,636	Amirkabir Univ Technology	1,561,765	Aze, T	1,561,273
Abolhassani, S	1,561,440	AMOG Consulting	1,561,851	Azevedo, G S	1,561,597
Abubakar, A	1,561,768	An, C	1,561,723	Azizi, A	1,561,225
ACTeQ	1,561,460	An, C	1,561,854	Aznar, J	1,561,456
Adachi, Y	1,561,828	An, K	1,561,656	Ba, J	1,561,525
Adams, N	1,561,616	An, L	1,561,731	Baardman, R H	1,561,480
Adeel, K	1,561,450	An, S	1,561,648	Babila, T L	1,561,219
Adroit, B	1,561,135	Anderson, J E	1,561,423	Bacati, F	1,561,786
Aerden, D	1,561,111	Anderson, R P	1,561,178	Baeten, G	1,561,456
Aeronautics Inst Technol	1,561,534	Anderson, R P	1,561,329	Baghishov, I	1,561,790
Afanasyev, Y	1,561,883	Andrew Dufrane, S	1,561,302	Bahia, B	1,561,461
Agnon, A	1,561,153	Andrianjafy, M T	1,561,772	Bahia Federal Univ	1,561,279
Aguado, R	1,561,112	Andrieu, S	1,561,101	Bahl, A	1,561,627
Aguiar, A B M	1,561,877	Angielczyk, K D	1,561,202	Bai, B	1,561,407
Ahmadi, R	1,561,391	Angrand, P	1,561,101	Bai, B	1,561,745
Ahmed, A	1,561,677	Anjos, J L	1,561,632	Bai, J	1,561,502
Ahmed Abbasi, I	1,561,249	Ankara Univ	1,561,826	Bai, T	1,561,827
Aix Marseille Univ	1,561,109	Anres, S	1,561,786	Bai, Y	1,561,746
Alabama Univ, Tuscaloosa	1,561,771	Ansorger, C	1,561,538	Bai, Z	1,561,660
Al-Abduljabbar, A M	1,561,600	Ansteel Group Res Inst	1,561,655	Bailey, P	1,561,560
Al-Ahmed, N	1,561,681	Antananarivo Univ	1,561,772	Baina, R	1,561,474
Alai, R	1,561,429	Antcliffe, J B	1,561,139	Baker Hughes Holdings LLC	1,561,822
Al-Bayat, A H	1,561,564	Antonarakou, A	1,561,388	Baker Hughes Oilfield LLC	1,561,563
Alberta Univ	1,561,461	Anwar, M U	1,561,695	Baker Hughes Oilfield LLC	1,561,615
Alberta Univ	1,561,513	Apache Egypt Companies	1,561,280	Baker Hughes Oilfield LLC	1,561,633
Alberta Univ	1,561,530	Apex Oilfld Equip Co Ltd	1,561,642	Baker Hughes Oilfield LLC	1,561,665
Alberta Univ	1,561,582	Apex Oilfld Equip Co Ltd	1,561,738	Baker Hughes Oilfield LLC	1,561,736
Alberta Univ	1,561,827	Apicioneck, M L	1,561,737	Baker Hughes Oilfield LLC	1,561,799
Alberta Univ	1,561,846	Arad, A	1,561,481	Bakulin, A	1,561,468
Albino, A	1,561,532	Aramco Overseas Co BV	1,561,480	Bakulin, A	1,561,495
Aldega, L	1,561,285	Aramco Research Center	1,561,465	Baldock, S	1,561,439
Alfred Wegener Inst	1,561,462	Aramco Research Center	1,561,505	Baldock, S	1,561,470
Alfred Wegener Inst	1,561,842	Aramco Research Center	1,561,520	Balochistan Univ	1,561,173
Algeo, T	1,561,190	Aramco Services Co	1,561,556	Balsamo, F	1,561,285
Al-Ghafri, A S M	1,561,248	Aramco Services Co	1,561,557	Balthasar, U B	1,561,383
Alhamad, N	1,561,878	Aramco Services Co	1,561,564	Banda, O A V	1,561,813
Alhamid, O M	1,561,564	Aramco Services Co	1,561,572	Banerjee, S	1,561,394
Al-Harthy, A	1,561,249	Aramco Services Co	1,561,576	Bankole, O M	1,561,336
Ali, A	1,561,249	Aramco Services Co	1,561,593	Bansal, R	1,561,425
Ali, G	1,561,441	Aramco Services Co	1,561,600	Bao, L	1,561,150
Ali, M	1,561,280	Aramco Services Co	1,561,666	Bao, L	1,561,186
Ali, W	1,561,579	Aramco Services Co	1,561,671	Bao, X	1,561,712
Alicante Univ	1,561,640	Aramco Services Co	1,561,747	Barago, N	1,561,096
Alizadeh Kiapi, M	1,561,785	Aranha, P E	1,561,632	Barago, N	1,561,308
Aljinovic, D	1,561,117	Arasanipalai, S	1,561,477	Baratoux, L	1,561,196
Alkhalifah, T	1,561,459	Aretz, M	1,561,324	Barberon, V	1,561,264
Alkhalifah, T	1,561,468	Arguelles-Vivas, F J	1,561,790	Barbosa, G D	1,561,771
Alkhalifah, T	1,561,500	Arguello, L	1,561,742	Barnes, N	1,561,231
Alkhalifah, T	1,561,531	Aristotle Univ	1,561,388	Baron, K	1,561,764
Allaire, N	1,561,127	Arizona Univ	1,561,262	Barreiro, J G	1,561,189
Allaire, N	1,561,225	Ark Univ, Pine Bluff	1,561,753	Barrera, D	1,561,521
Allen, O	1,561,753	Armentrout, D	1,561,429	Barrera Nabor, P	1,561,428
Almeida, G M	1,561,123	Armijo, R	1,561,180	Barski, M	1,561,405
Almeshari, S	1,561,494	Arnaudova, T	1,561,684	BASF SE	1,561,631
Almubarak, M S	1,561,464	Arnot, M J	1,561,337	Bashir, M	1,561,588
Almuteri, K	1,561,501	Arruda, G M	1,561,597	Basnayake, A P	1,561,689
Almuteri, K	1,561,527	Arsoski, D	1,561,603	Basso, M	1,561,290
Alomar, R F	1,561,512	Asahara, Y	1,561,184	Basu, P	1,561,155
Al-Oqaili, A H	1,561,600	Ashbaugh, H S	1,561,753	Bathula, L	1,561,488
Alremeihi, M	1,561,588	Ashouri, A R	1,561,330	Batista, J C	1,561,279
Alsaif, S A	1,561,562	Assemat, A	1,561,224	Batista, J H G	1,561,601
Alsaud, M A	1,561,747	Assis, P C	1,561,432	Bault, V	1,561,239
Alshaikh, A	1,561,556	Assmann, A	1,561,631	Baumberger, R	1,561,182
Alshaikh, A	1,561,557	Atakul-Ozdemir, A	1,561,141	Baumstein, A	1,561,492

Baxter, E F	1,561,111	Block, E	1,561,672	British Antarctic Survey	1,561,293
Baylor Univ	1,561,161	Bocking, M	1,561,118	British Geological Survey	1,561,138
Bayout, L C	1,561,726	Bodanese, L G	1,561,724	British Geological Survey	1,561,157
Bayri, H	1,561,450	Bodanese, R L	1,561,724	British Geological Survey	1,561,255
Bayuk, I	1,561,555	Bodishbaugh, A B	1,561,568	British Geological Survey	1,561,268
Bazli, M	1,561,689	Bodishbaugh, A B	1,561,569	British Geological Survey	1,561,342
Beck, A E	1,561,737	Bodishbaugh, A B	1,561,570	Brito, D	1,561,474
Beck, J	1,561,543	Boehme, M	1,561,389	Brno Univ Technology	1,561,571
Becker, R T	1,561,284	BOEM	1,561,838	Bronner, M	1,561,204
Beermann, J	1,561,842	Bohai Oilfield Res Inst	1,561,115	Brookes, D	1,561,429
Behera, L	1,561,547	Bohai Oilfield Res Inst	1,561,185	Brookes, D	1,561,543
Beihang Univ	1,561,433	Bohai Oilfield Res Inst	1,561,479	Brotzer, A	1,561,462
Beijing Energy Technol Ltd	1,561,605	Bojanowski, M	1,561,405	Brown, D J	1,561,674
Beijing Forestry Univ	1,561,710	Bolat, Y	1,561,136	Browne, G H	1,561,337
Beijing Inform Technl Univ	1,561,433	Boligon, A	1,561,279	Bruciaferri, D	1,561,888
Beijing Inst Geol Geophys	1,561,334	Bollen, E M	1,561,114	Bruguier, O	1,561,196
Beijing Inst Geology	1,561,358	Bolton, C T	1,561,109	Brune, S	1,561,097
Beijing Inst Mechanics	1,561,701	Boman, K T	1,561,885	Brunel Univ	1,561,303
Beijing Museum	1,561,099	Bond, D P G	1,561,323	Brussels Vrije Univ	1,561,284
Beijing Univ	1,561,433	Bonini, L	1,561,308	Bryce, J M	1,561,529
Beijing Univ Chem Technol	1,561,620	Boon, A R	1,561,839	Brytik, V	1,561,425
Beijing Univ Chem Technol	1,561,858	Booth, G A	1,561,248	Bu, Q	1,561,444
Beijing Univ Sci & Technol	1,561,775	Boratto, M	1,561,509	Bu, W	1,561,775
Bell, G L	1,561,175	Bordeaux Univ	1,561,146	Buchanan, S E	1,561,629
Bellas, S	1,561,388	Bornemann, A	1,561,320	Buenos Aires Technol Inst	1,561,590
Belsim Engineering SA	1,561,670	Bose, S	1,561,396	Buenos Aires Univ	1,561,264
Belsim Engineering USA Inc	1,561,670	Bosnia Academy Sci & Arts	1,561,117	Buenos Aires Univ	1,561,525
Ben Hassine, A	1,561,474	Boston Coll	1,561,111	Bukljas, M	1,561,814
Benbouzid, M	1,561,681	Boston Univ	1,561,111	Bunney, C	1,561,888
Bendoraitis, D P	1,561,419	Bosworth, W	1,561,280	Bureau Rech Geol Min (Fr)	1,561,101
Benedicto, C	1,561,533	Botsyun, S	1,561,389	Bureau Rech Geol Min (Fr)	1,561,894
Bennett, C	1,561,342	Botting, J P	1,561,347	Bureau Veritas Marine	1,561,726
Bennett, D	1,561,720	Botziolis, C	1,561,388	Burgess, T	1,561,516
Bennion, R	1,561,292	Bouchaala, F	1,561,280	Burren, J	1,561,430
Benton, M J	1,561,255	Bouchakour, M	1,561,235	Burtz, O	1,561,423
Benzerara, K	1,561,406	Bouchal, J M	1,561,135	Busatto, C	1,561,578
Berger, A	1,561,182	Bouchal, J M	1,561,325	Buschke, P	1,561,822
Berglar, K	1,561,462	BouDagher-Fadel, M K	1,561,259	Butler, A D	1,561,120
Bergman, S	1,561,401	Boufflers, L	1,561,589	Butler, H O	1,561,723
Bergman, S C	1,561,162	Boustead, N	1,561,851	Butterfield, N J	1,561,233
Bergmann, K D	1,561,329	Bouybaouene, M	1,561,111	Butterfield, N J	1,561,269
Berlin Museum	1,561,104	Bowling Green State Univ	1,561,100	Butterfield, N J	1,561,291
Berlin Museum	1,561,195	Bowling Green State Univ	1,561,175	C & C Reservoirs	1,561,783
Berlin Museum	1,561,221	Bowman, V C	1,561,293	Cabral, T S	1,561,419
Berlioz-Barbier, A	1,561,772	Boxtel Museum	1,561,169	Caccamo, M T	1,561,841
Berman, S	1,561,543	Boyd, J L	1,561,157	Caggiati, M	1,561,158
Bern Univ	1,561,182	Boyd, L	1,561,864	Caggiati, M	1,561,217
Bernard, S	1,561,169	Bozetti, G	1,561,256	Cai, C	1,561,409
Bernhard, D E	1,561,560	BP	1,561,455	Cai, H	1,561,781
Berry, D	1,561,836	BP America Inc	1,561,670	Cai, J	1,561,879
Betts, M J	1,561,113	BP International Ltd	1,561,670	Cai, S	1,561,892
Bezerra, F H R	1,561,285	Bram, M V	1,561,709	Cai, W	1,561,739
BGP CNPC	1,561,420	Brand, P	1,561,342	Cai, Y	1,561,689
BGP CNPC	1,561,506	Brandini, C	1,561,887	Calgary Univ	1,561,125
Bhattacharyya, A	1,561,857	Brandolin, F	1,561,500	Calgary Univ	1,561,143
Bhattacharyya, A	1,561,873	Brandon, A D	1,561,401	Calgary Univ	1,561,741
Bhaumik, M	1,561,497	Brasilia Univ	1,561,123	Calgary Univ	1,561,749
BHP	1,561,711	Brasilia Univ	1,561,124	Calif Univ, Santa Barbara	1,561,344
Bi, H	1,561,854	Bremen Univ	1,561,271	Calif Univ, Santa Cruz	1,561,129
Bi, Q	1,561,650	Brenda, R	1,561,684	Calif Univ, Santa Cruz	1,561,219
Biancardo, S A	1,561,818	Bretagne Univ	1,561,385	Calif Univ, Santa Cruz	1,561,466
Biazussi, J	1,561,663	Briggs, D E G	1,561,140	California Inst Technol	1,561,404
Bibolova, A	1,561,541	Briggs, D E G	1,561,194	California Inst Technol	1,561,692
Bibolova, A	1,561,542	Briggs, R M	1,561,692	California Inst Technol	1,561,881
Bilen, J M	1,561,563	Brika, N	1,561,450	Calner, M	1,561,359
Bing, S	1,561,722	Bristol Univ	1,561,112	Calvert, A J	1,561,368
Birnie, C	1,561,468	Bristol Univ	1,561,141	Camargo, C L	1,561,771
Birnie, C E	1,561,459	Bristol Univ	1,561,149	Camargo, M M	1,561,290
Blackbourn, G A	1,561,340	Bristol Univ	1,561,231	Cambridge Univ	1,561,110
Blackbourn Geoconsulting	1,561,340	Bristol Univ	1,561,255	Cambridge Univ	1,561,164
Blakey, T H T	1,561,573	Bristol Univ	1,561,268	Cambridge Univ	1,561,231
Blard, P H	1,561,404	Bristol Univ	1,561,271	Cambridge Univ	1,561,232
Bles, G	1,561,690	Bristol Univ	1,561,393	Cambridge Univ	1,561,233

Cambridge Univ	1,561,260	Chanvry, E	1,561,136	Chen, Y	1,561,252
Cambridge Univ	1,561,269	Charbonnier, S	1,561,169	Chen, Y	1,561,360
Cambridge Univ	1,561,281	Charpentier, J F	1,561,681	Chen, Y	1,561,762
Cambridge Univ	1,561,291	Chassagne, C	1,561,579	Chen, Y	1,561,778
Cambridge Univ	1,561,292	Chatterjee, P K	1,561,566	Chen, Y	1,561,824
Cambridge Univ Museum	1,561,342	Chattopadhyay, A P	1,561,529	Chen, Y	1,561,830
Cammack, M E	1,561,751	Chaudhary, S	1,561,155	Chen, Z	1,561,655
Campbell, K A	1,561,245	Chemingui, N	1,561,477	Chen, Z	1,561,854
Campi, A L	1,561,432	Chemiservis SA de CV	1,561,574	Chen, Z Q	1,561,178
Campinas State Univ	1,561,290	Chemiservis SA de CV	1,561,581	Chen, Z Y	1,561,369
Campinas State Univ	1,561,533	Chemiservis SA de CV	1,561,591	Cheng, F	1,561,708
Campinas State Univ	1,561,663	Chemiservis SA de CV	1,561,596	Cheng, H	1,561,282
Campos, A J O	1,561,761	Chemiservis SA de CV	1,561,622	Cheng, J	1,561,866
Canada Geological Survey	1,561,351	Chemiservis SA de CV	1,561,623	Cheng, L	1,561,187
Cantabria Univ	1,561,794	Chemiservis SA de CV	1,561,748	Cheng, L	1,561,780
Cao, A	1,561,882	Chemiservis SA de CV	1,561,766	Cheng, R H	1,561,244
Cao, B	1,561,386	Chemiservis SA de CV	1,561,874	Cheng, S	1,561,740
Cao, D	1,561,769	Chen, A	1,561,365	Cheng, W	1,561,484
Cao, G	1,561,746	Chen, B	1,561,121	Cheng, W	1,561,694
Cao, H	1,561,608	Chen, B	1,561,599	Cheng, X	1,561,482
Cao, H	1,561,773	Chen, B	1,561,629	Cheng, X	1,561,779
Cao, J	1,561,160	Chen, B	1,561,857	Cheng, Y	1,561,431
Cao, J	1,561,776	Chen, C	1,561,108	Chengdu Univ	1,561,661
Cao, J	1,561,778	Chen, C	1,561,312	Chengdu Univ Technology	1,561,162
Cao, Q	1,561,130	Chen, C	1,561,661	Chengdu Univ Technology	1,561,166
Cao, S C	1,561,428	Chen, C	1,561,661	Chengdu Univ Technology	1,561,183
Cao, W	1,561,551	Chen, D	1,561,445	Chengdu Univ Technology	1,561,217
Cao, W	1,561,651	Chen, D	1,561,789	Chengdu Univ Technology	1,561,237
Cao, X	1,561,773	Chen, F	1,561,215	Chengdu Univ Technology	1,561,276
Cao, X	1,561,784	Chen, F	1,561,658	Chengdu Univ Technology	1,561,362
Cao, Y	1,561,206	Chen, G	1,561,251	Chengdu Univ Technology	1,561,365
Cappello, S	1,561,841	Chen, G	1,561,300	Chengdu Univ Technology	1,561,403
Carbone, C	1,561,247	Chen, G T	1,561,686	Chengdu Univ Technology	1,561,413
Carcione, J M	1,561,525	Chen, H	1,561,523	Chengdu Univ Technology	1,561,434
Carissimi, A	1,561,534	Chen, H	1,561,530	Chengdu Univ Technology	1,561,537
Carmo, L H S	1,561,700	Chen, H	1,561,681	Chengdu Univ Technology	1,561,658
Caron, J B	1,561,250	Chen, H	1,561,705	Chengdu Univ Technology	1,561,791
Caron, J B	1,561,350	Chen, H	1,561,731	Chernyi, S G	1,561,804
Carrapa, B	1,561,262	Chen, J	1,561,148	Chevillotte, Y	1,561,690
Casis, N	1,561,578	Chen, J	1,561,241	Chevron	1,561,554
Casis, N	1,561,590	Chen, J	1,561,373	Chevron Energy Technol Co	1,561,863
CASP	1,561,102	Chen, J	1,561,546	Chevron Technical Ctr	1,561,437
CASP	1,561,265	Chen, J	1,561,717	Chevron Technical Ctr	1,561,541
Castillo, L	1,561,670	Chen, J	1,561,858	Chevron Technical Ctr	1,561,542
Castillo Sanchez, J M	1,561,888	Chen, K	1,561,361	Chevron USA Inc	1,561,584
Castrejon-Martinez, R F	1,561,457	Chen, K	1,561,523	Chevron USA Inc	1,561,625
Castro, J M	1,561,112	Chen, L	1,561,159	Chevron USA Inc	1,561,680
Catipovic, I	1,561,688	Chen, L	1,561,306	Chilinski, B	1,561,698
Cavalazzi, B	1,561,272	Chen, L	1,561,626	China Coalbed Corp Ltd	1,561,789
Cavazos Sepulveda, A C	1,561,666	Chen, L	1,561,792	China Geological Survey	1,561,361
Cawood, P A	1,561,364	Chen, M	1,561,163	China Geological Survey	1,561,387
C-DAC	1,561,488	Chen, M	1,561,759	China Ministry Natural Rsc	1,561,294
Ceia, M A R	1,561,432	Chen, P	1,561,702	China Ministry Natural Rsc	1,561,539
CENTEC	1,561,667	Chen, P	1,561,805	China Ministry Natural Rsc	1,561,882
Central South Univ (China)	1,561,473	Chen, Q	1,561,650	China Nat Aviation Co Ltd	1,561,740
Ceriani, A	1,561,280	Chen, R	1,561,732	China Nat Eng Res Ctr	1,561,508
Cesca, S	1,561,153	Chen, S	1,561,205	China Nat Offshor Oil Corp	1,561,353
Cevallos-Ferriz, S R S	1,561,105	Chen, S	1,561,431	China Nat Offshor Oil Corp	1,561,781
Cha, Y	1,561,492	Chen, S	1,561,487	China National Petrol Corp	1,561,619
Cha, Y H	1,561,424	Chen, T	1,561,643	China Ocean Univ	1,561,103
Cha, Y H	1,561,425	Chen, W	1,561,413	China Ocean Univ	1,561,339
Chagas, F C O	1,561,586	Chen, W	1,561,701	China Ocean Univ	1,561,367
Chaiyakul, S	1,561,863	Chen, X	1,561,366	China Ocean Univ	1,561,646
Chakrabarti, R	1,561,155	Chen, X	1,561,463	China Ocean Univ	1,561,770
Chakraborty, P P	1,561,191	Chen, X	1,561,551	China Offshore Oil Eng Co	1,561,611
Chang, J	1,561,332	Chen, X	1,561,652	China Offshore Oil Eng Co	1,561,740
Chang, S	1,561,546	Chen, X	1,561,702	China Oilfield Svcs Ltd	1,561,451
Chang'an Univ	1,561,166	Chen, X	1,561,712	China Oilfield Svcs Ltd	1,561,582
Chang'an Univ	1,561,641	Chen, X	1,561,818	China Oilfield Svcs Ltd	1,561,778
Changqing Oilfield Co	1,561,620	Chen, X	1,561,854	China Recovery Tech Co Ltd	1,561,705
Changsha Univ Sci Technol	1,561,735	Chen, Y	1,561,103	China Ship Sci Res Center	1,561,806
Changzhou Univ	1,561,428	Chen, Y	1,561,144	China Univ Electronic Sci	1,561,660
Changzhou Univ	1,561,708	Chen, Y	1,561,179	China Univ Geosci, Beijing	1,561,212

China Univ Geosci, Beijing	1,561,230	China Univ Petroleum	1,561,486	Clauss, G	1,561,880
China Univ Geosci, Beijing	1,561,241	China Univ Petroleum	1,561,499	CNOOC (China) Co Ltd	1,561,375
China Univ Geosci, Beijing	1,561,242	China Univ Petroleum	1,561,515	CNOOC China Ltd	1,561,215
China Univ Geosci, Beijing	1,561,298	China Univ Petroleum	1,561,519	CNOOC (China) Ltd	1,561,421
China Univ Geosci, Beijing	1,561,335	China Univ Petroleum	1,561,523	CNOOC Energy Technl Svcs	1,561,867
China Univ Geosci, Beijing	1,561,385	China Univ Petroleum	1,561,524	CNOOC Ltd	1,561,133
China Univ Geosci, Beijing	1,561,386	China Univ Petroleum	1,561,535	CNOOC Ltd	1,561,371
China Univ Geosci, Beijing	1,561,412	China Univ Petroleum	1,561,545	CNOOC Research Inst	1,561,414
China Univ Geosci, Beijing	1,561,414	China Univ Petroleum	1,561,549	CNOOC Research Inst	1,561,626
China Univ Geosci, Beijing	1,561,418	China Univ Petroleum	1,561,561	CNOOC Research Inst	1,561,668
China Univ Geosci, Beijing	1,561,760	China Univ Petroleum	1,561,602	CNOOC Research Inst Co Ltd	1,561,215
China Univ Geosci, Wuhan	1,561,107	China Univ Petroleum	1,561,611	CNOOC Research Inst Ltd	1,561,294
China Univ Geosci, Wuhan	1,561,172	China Univ Petroleum	1,561,679	CNPC Research Inst	1,561,682
China Univ Geosci, Wuhan	1,561,177	China Univ Petroleum	1,561,682	CNPC Research Inst	1,561,833
China Univ Geosci, Wuhan	1,561,178	China Univ Petroleum	1,561,704	Cody, S	1,561,577
China Univ Geosci, Wuhan	1,561,179	China Univ Petroleum	1,561,715	Coe, A L	1,561,168
China Univ Geosci, Wuhan	1,561,208	China Univ Petroleum	1,561,723	Cogill, M Jr	1,561,575
China Univ Geosci, Wuhan	1,561,257	China Univ Petroleum	1,561,739	Cohen, O B	1,561,153
China Univ Geosci, Wuhan	1,561,261	China Univ Petroleum	1,561,740	Coimbra Univ	1,561,216
China Univ Geosci, Wuhan	1,561,274	China Univ Petroleum	1,561,749	Colchis Petro Consult Ltd	1,561,371
China Univ Geosci, Wuhan	1,561,277	China Univ Petroleum	1,561,757	Collins, E	1,561,753
China Univ Geosci, Wuhan	1,561,301	China Univ Petroleum	1,561,759	Collins, L G	1,561,737
China Univ Geosci, Wuhan	1,561,306	China Univ Petroleum	1,561,769	Collinson, J D	1,561,340
China Univ Geosci, Wuhan	1,561,360	China Univ Petroleum	1,561,773	Colorado Sch Mines	1,561,286
China Univ Geosci, Wuhan	1,561,363	China Univ Petroleum	1,561,774	Colorado Sch Mines	1,561,426
China Univ Geosci, Wuhan	1,561,364	China Univ Petroleum	1,561,776	Colorado Sch Mines	1,561,438
China Univ Geosci, Wuhan	1,561,366	China Univ Petroleum	1,561,778	Colorado Sch Mines	1,561,498
China Univ Geosci, Wuhan	1,561,375	China Univ Petroleum	1,561,780	Colorado Sch Mines	1,561,501
China Univ Geosci, Wuhan	1,561,390	China Univ Petroleum	1,561,781	Colorado Sch Mines	1,561,504
China Univ Geosci, Wuhan	1,561,402	China Univ Petroleum	1,561,782	Colorado Sch Mines	1,561,527
China Univ Geosci, Wuhan	1,561,403	China Univ Petroleum	1,561,789	Colorado Sch Mines	1,561,528
China Univ Geosci, Wuhan	1,561,411	China Univ Petroleum	1,561,824	Colorado Sch Mines	1,561,683
China Univ Geosci, Wuhan	1,561,894	China Univ Petroleum	1,561,833	Combee, L	1,561,475
China Univ Mining Technol	1,561,176	China Univ Sci & Technol	1,561,339	Comy LLC	1,561,575
China Univ Mining Technol	1,561,304	Chinelatto, G F	1,561,290	Concordia Univ	1,561,854
China Univ Mining Technol	1,561,317	Chinese Academy Geol Sci	1,561,126	Connecticut Univ	1,561,118
China Univ Mining Technol	1,561,458	Chinese Academy Geol Sci	1,561,240	Connecticut Univ, Storrs	1,561,119
China Univ Mining Technol	1,561,514	Chinese Academy Geol Sci	1,561,255	Connecticut Univ, Storrs	1,561,263
China Univ Mining Technol	1,561,682	Chinese Academy Geol Sci	1,561,431	ConocoPhillips Co	1,561,616
China Univ Mining Technol	1,561,830	Chinese Academy Geol Sci	1,561,443	ConocoPhillips Co	1,561,634
China Univ Petroleum	1,561,150	Chinese Academy Sciences	1,561,211	Consorti, L	1,561,096
China Univ Petroleum	1,561,152	Chinese Academy Sciences	1,561,240	Constantine, J J	1,561,616
China Univ Petroleum	1,561,154	Chinese Academy Sciences	1,561,319	Coolen, J W P	1,561,842
China Univ Petroleum	1,561,156	Chinese Academy Sciences	1,561,359	Cooper, R	1,561,449
China Univ Petroleum	1,561,163	Chinese Academy Sciences	1,561,392	Cope, T D	1,561,335
China Univ Petroleum	1,561,186	Chinese Academy Sciences	1,561,703	Copenhagen Univ	1,561,268
China Univ Petroleum	1,561,200	Chiu, A C F	1,561,754	Core Laboratories LP	1,561,742
China Univ Petroleum	1,561,205	Cho, E	1,561,471	Cornee, J J	1,561,388
China Univ Petroleum	1,561,206	Cho, T	1,561,348	Corradetti, A	1,561,096
China Univ Petroleum	1,561,210	Choi, J C	1,561,853	Corradini, C	1,561,324
China Univ Petroleum	1,561,228	Choi, M	1,561,787	Corti, G	1,561,097
China Univ Petroleum	1,561,229	Chong, W S	1,561,676	Coskun, G	1,561,429
China Univ Petroleum	1,561,241	Chongqing Research Inst	1,561,659	Cosovic, V	1,561,415
China Univ Petroleum	1,561,282	Chongqing Univ	1,561,714	Costa, J	1,561,885
China Univ Petroleum	1,561,295	Chongqing Univ	1,561,762	Cote d'Azur Univ	1,561,441
China Univ Petroleum	1,561,296	Chongqing Univ	1,561,793	Coutand, I	1,561,264
China Univ Petroleum	1,561,315	Chou, W R	1,561,886	Covelli, S	1,561,096
China Univ Petroleum	1,561,318	Chrisman, R	1,561,455	Covelli, S	1,561,308
China Univ Petroleum	1,561,326	Christian Albrechts Univ	1,561,138	Covestro LLC	1,561,792
China Univ Petroleum	1,561,332	Christian Albrechts Univ	1,561,245	Cowie, M	1,561,663
China Univ Petroleum	1,561,333	Chu, D	1,561,363	C-Power	1,561,719
China Univ Petroleum	1,561,355	Chu, D	1,561,490	CPRM	1,561,124
China Univ Petroleum	1,561,366	Chu, Y	1,561,319	Craddock, J P	1,561,352
China Univ Petroleum	1,561,374	Chuang, Y	1,561,392	Crame, J A	1,561,293
China Univ Petroleum	1,561,376	CICESE	1,561,134	Crane, M L	1,561,672
China Univ Petroleum	1,561,377	Cie Generale Geophysique	1,561,553	Cranfield Univ	1,561,716
China Univ Petroleum	1,561,380	Cifelli, F	1,561,285	Creamer, J	1,561,565
China Univ Petroleum	1,561,407	Cincinnati Univ	1,561,190	Cronier, C	1,561,127
China Univ Petroleum	1,561,452	Civier, L	1,561,690	Cronier, C	1,561,239
China Univ Petroleum	1,561,463	Clack, J A	1,561,292	Crowder, P	1,561,625
China Univ Petroleum	1,561,483	Clapham, M E	1,561,129	Cruciani, G	1,561,158
China Univ Petroleum	1,561,484	Clark Energy Group	1,561,140	Cruickshank, W	1,561,838
China Univ Petroleum	1,561,485	Clausen, S	1,561,226	Cruz, N A	1,561,644

Cruz, O F Jr	1,561,640	de Souza Bazerra, M	1,561,426	Downhole Products Ltd	1,561,603
Cruz Roque, D	1,561,428	de Souza Bezerra, M	1,561,438	DownUnder GeoSolutions LLC	1,561,516
CSIR-NGRI	1,561,547	de Vicente, G	1,561,189	Dragon Oil Holdings Ltd	1,561,566
CSSC Marine Technol Co Ltd	1,561,890	De Vita, F	1,561,880	Draskovic, G	1,561,283
CTTC	1,561,872	De Vleeschouwer, D	1,561,271	Dreossi, D	1,561,272
Cui, A	1,561,708	De Vleeschouwer, D	1,561,284	Driessen, D	1,561,863
Cui, H	1,561,613	De Wulf, A	1,561,893	Du, A	1,561,608
Cui, S	1,561,606	Debrie, J	1,561,406	Du, D	1,561,599
Cui, S	1,561,614	Decarlis, A	1,561,280	Du, D	1,561,669
Cui, S	1,561,749	Deeds, J	1,561,437	Du, G	1,561,252
Cui, S	1,561,779	Degraer, S	1,561,842	Du, H	1,561,892
Cui, W	1,561,613	Deleon, D	1,561,627	Du, J	1,561,400
Cui, X	1,561,458	Delft Inversion	1,561,417	Du, L	1,561,813
Cui, X	1,561,514	Delft Univ Technol	1,561,433	Du, Y	1,561,217
Cui, Y	1,561,116	Delft Univ Technol	1,561,440	Du, Y	1,561,364
Cui, Y	1,561,187	Delft Univ Technol	1,561,465	Du, Y	1,561,505
Cui, Y	1,561,252	Delft Univ Technol	1,561,579	Du, Y	1,561,782
Cui, Y	1,561,367	Delgado-Linares, J G	1,561,683	Duan, M	1,561,704
Cui, Y	1,561,410	Delhi Univ	1,561,191	Duarte, F	1,561,491
Cuong, N Q	1,561,370	Dell'Anno, J	1,561,096	Dubicka, Z	1,561,405
Curtin Univ	1,561,385	Demirov, E K	1,561,883	Dubinya, N	1,561,555
Curtin Univ	1,561,552	Deng, B	1,561,317	Duccini, L E	1,561,632
Curtin Univ	1,561,723	Deng, F	1,561,808	Dufour, Y	1,561,629
Cutshall, T	1,561,560	Deng, J	1,561,789	DUG Technology	1,561,538
Cvetkovic, M	1,561,429	Deng, S	1,561,236	Dujmovic, J	1,561,868
Cvetovic, M	1,561,478	Deng, S	1,561,315	Dukalski, M	1,561,465
Cyprus Marine Inst	1,561,865	Deng, Y	1,561,341	Dumais, M A	1,561,204
Czarniecka, U	1,561,370	Deng, Y	1,561,375	Dunkel, C A	1,561,100
Dadi, K	1,561,391	Deng, Y	1,561,654	Dunn, F S	1,561,232
Daewoo Eng & Construction	1,561,853	Deniz, K	1,561,826	Dunn, F S	1,561,260
Dahm, T	1,561,153	Denk, T	1,561,325	Duprat, V	1,561,474
Dai, C	1,561,611	Denkov, N	1,561,684	Dura-Gomez, I	1,561,425
Dai, M X	1,561,339	Denmark Greenland Geol Sur	1,561,462	Dura-Gomez, I	1,561,490
Dai, N	1,561,506	Denmark Tech Univ	1,561,723	Dura-Gomez, I	1,561,492
Daisy, N S	1,561,855	Denver Museum	1,561,382	Duran, R	1,561,565
Dalhousie Univ	1,561,855	DePauw Univ	1,561,335	Durkee, K J	1,561,560
Dalhousie Univ	1,561,857	Derby Univ	1,561,349	Durska, E	1,561,370
Dalhousie Univ	1,561,873	Derzhi, N	1,561,767	Dusterhoft, R G	1,561,706
Dalian Maritime Univ	1,561,643	Dev, A	1,561,588	Dusterhoft, R G	1,561,737
Dalian Maritime Univ	1,561,731	Di, H	1,561,768	Dyer, L	1,561,453
Dalian Maritime Univ	1,561,825	Di, W	1,561,582	Earth Science Analytics	1,561,472
Dalian Maritime Univ	1,561,867	Diao, H	1,561,602	East China Univ Technology	1,561,339
Dalian Maritime Univ	1,561,889	Diaz, S G	1,561,260	East China Univ Technology	1,561,856
Dalian Univ Technol	1,561,641	Diaz-Hernandez, G	1,561,794	Ecole Navale (France)	1,561,681
Dalian Univ Technol	1,561,659	Dietl, C	1,561,831	Edge Hill Univ	1,561,382
Dalian Univ Technol	1,561,691	Dillard Univ	1,561,753	Edwards, J M	1,561,888
Dalian Univ Technol	1,561,702	Dillinger, A	1,561,136	Egger, C	1,561,543
Dalian Univ Technol	1,561,728	Dillon-Gibbons, C	1,561,851	Ehlers, S	1,561,880
Daly, S	1,561,720	Ding, M	1,561,759	Ehlers, T A	1,561,389
d'Amico, L	1,561,272	Ding, S	1,561,879	Eitel Kemgang Ghomsi, F	1,561,427
Dang, Z	1,561,176	Ding, W	1,561,212	Ekambaram, R	1,561,664
D'Angelo, D	1,561,767	Ding, W	1,561,414	El-Albani, A	1,561,336
Danise, S	1,561,188	Ding, W	1,561,539	El-Attar, M	1,561,437
Danish Hydrocarbon Res Ctr	1,561,785	Ding, Y	1,561,463	Eldrett, J S	1,561,162
Dantas, E L	1,561,123	Djamali, M	1,561,135	Eldrett, J S	1,561,401
Dantas, E L	1,561,124	Dobrovolskiy, A	1,561,436	El-Emam, A	1,561,450
Daqing Oilfield Co Ltd	1,561,783	Domeier, M	1,561,288	El-Ghali, M A K	1,561,249
D'Arcy-Evans, N	1,561,851	Domeier, M	1,561,482	El-Hariri, K	1,561,225
Darroch, S A F	1,561,227	Domingos, D	1,561,491	Elias, Q K	1,561,743
Darroch, S A F	1,561,232	Dong, C	1,561,156	Elidemir, S	1,561,826
Darroch, S A F	1,561,260	Dong, S	1,561,679	El-Khashab, A	1,561,675
Das, K	1,561,191	Dong, S W	1,561,240	El-Khashab, A	1,561,677
Dashtgard, S E	1,561,331	Dong, W G	1,561,379	Elmola, A A	1,561,336
Davies, N S	1,561,164	Dong, Y	1,561,710	El-Nady, M M	1,561,397
Davies, P	1,561,690	Donnadieu, Y	1,561,109	Elrick, M	1,561,190
Davies, S	1,561,342	Donoghue, P C J	1,561,141	Eltayieb, M	1,561,433
Davydenko, M	1,561,467	Donoghue, P C J	1,561,271	Emelianov, V	1,561,804
De Baets, K	1,561,127	Donovan, A D	1,561,422	Emerson	1,561,502
De Baets, K	1,561,143	Dorjnamjaa, D	1,561,113	Emile-Geay, J	1,561,316
de Gea, G A	1,561,112	dos Santos, T J	1,561,771	Emsbo, P	1,561,399
de Gelder, G	1,561,180	Doublier, M P	1,561,368	Endeavor Management	1,561,727
de Leon, A C	1,561,134	Doubrawa, M	1,561,219	Endo, Y	1,561,408
De Ligny, F H	1,561,669	Dowding, E M	1,561,288	Enhkbaatar, B	1,561,113

ENPPI	1,561,675	Ferrara Univ	1,561,158	Gangneung-Wonju Nat Univ	1,561,787
ENPPI	1,561,677	Ferreira, B M	1,561,644	Gans, C	1,561,424
Eotvos Lorand Univ	1,561,310	Field Museum (Chicago)	1,561,202	Gao, B	1,561,638
Erbacher, J	1,561,320	Fielding, C	1,561,118	Gao, F P	1,561,703
Erickson, D D	1,561,845	Fielding, C	1,561,119	Gao, J	1,561,318
Erlangen Nuernberg Univ	1,561,399	Filaretov, V	1,561,645	Gao, J	1,561,416
Escandell, M M	1,561,640	Filipek, A	1,561,370	Gao, J	1,561,530
Escarguel, G	1,561,135	Firenze Univ	1,561,097	Gao, J	1,561,593
Esteno, D	1,561,578	Firsov, A	1,561,493	Gao, M	1,561,107
Esteno, D	1,561,590	Fisheries & Oceans Canada	1,561,854	Gao, R	1,561,431
Esteve, I	1,561,406	Fisheries & Oceans Canada	1,561,855	Gao, X	1,561,757
Etherington, R	1,561,478	Fisheries & Oceans Canada	1,561,857	Gao, Y	1,561,166
Evans, J E	1,561,100	Fisheries & Oceans Canada	1,561,873	Gao, Y	1,561,312
Evans, N J	1,561,196	Fletcher, R S	1,561,764	Gao, Y	1,561,313
Evora Univ	1,561,145	Flores Lopez, F A	1,561,428	Gao, Y	1,561,334
Ewin, T A M	1,561,165	Florida Univ	1,561,686	Gao, Y	1,561,414
Extract Management Co LLC	1,561,672	Fomel, S	1,561,511	Gao, Y	1,561,699
Extremadura Univ	1,561,222	Fomel, S	1,561,512	Gao, Y	1,561,781
Extremadura Univ	1,561,322	Fomin, O	1,561,571	Gao, Y	1,561,788
ExxonMobil	1,561,424	Fontaine, C	1,561,336	Gao, Z	1,561,611
ExxonMobil	1,561,425	Forschungsinst Senckenberg	1,561,181	Garb, M P	1,561,393
ExxonMobil	1,561,490	Fosdick, J C	1,561,263	Garcia, M	1,561,109
ExxonMobil	1,561,492	Foster, W J	1,561,188	Garcia Muro, V J	1,561,122
ExxonMobil Integr Solut Co	1,561,423	Foucher, F	1,561,272	Garcia-Valdecasas, J	1,561,794
ExxonMobil Upstream Res Co	1,561,423	Fradet, M	1,561,692	Garrity, R	1,561,687
ExxonMobil Upstream Res Co	1,561,630	Franceschi, M	1,561,096	Garwood, R	1,561,120
Faccipieri Junior, J	1,561,533	Franceschi, M	1,561,217	Garwood, R J	1,561,164
Fahimifar, A	1,561,765	Franceschi, M	1,561,308	Garza, M	1,561,585
Falchetto, A B	1,561,632	Francis, D A	1,561,245	Garzanti, E	1,561,259
Falconer, R B	1,561,637	Francis, J E	1,561,293	Gautam, A	1,561,669
Fan, H	1,561,215	Frank, T	1,561,118	Gawade, M	1,561,488
Fan, H	1,561,602	Frank, T D	1,561,119	Gdynia Maritime Univ	1,561,815
Fan, H	1,561,704	Frechette, N	1,561,756	Ge, Z	1,561,215
Fan, J	1,561,679	Freiburg Tech Univ	1,561,164	Geier, C	1,561,325
Fan, L	1,561,650	Freiburg Univ	1,561,579	Geissler, W H	1,561,462
Fan, M	1,561,554	Friedrich Alexander Univ	1,561,127	Geng, J	1,561,466
Fan, R	1,561,236	Friedrich Alexander Univ	1,561,142	Geng, T	1,561,582
Fan, T	1,561,412	Friedrich Alexander Univ	1,561,143	Geng, W	1,561,484
Fan, Y	1,561,355	Friedrich Alexander Univ	1,561,147	Gent Univ	1,561,893
Fan, Z	1,561,617	Friedrich Alexander Univ	1,561,271	GeoForschungsZentr Potsdam	1,561,153
Fang, L	1,561,241	Friedrich Alexander Univ	1,561,343	GeoForschungsZentrum	1,561,104
Fang, X	1,561,211	Friedrich Schiller Univ	1,561,246	GEOMAR Helmholtz-Zentrum	1,561,128
Fang, X	1,561,236	Frijia, G	1,561,096	GeoQuest Systems BV	1,561,594
Farag, M	1,561,677	Fripp, M L	1,561,637	GeoQuest Systems BV	1,561,768
Faranda, C	1,561,180	Fu, A	1,561,650	GeoQuest Systems BV	1,561,875
Faraoun, A	1,561,610	Fu, H	1,561,506	GeoQuest Systems BV	1,561,876
Faraq, M	1,561,675	Fu, H	1,561,803	GeoQuest Systems BV	1,561,878
Faria, O A	1,561,877	Fu, L	1,561,545	GeoQuest Systems BV	1,561,884
Farley, K A	1,561,404	Fu, S	1,561,699	George Mason Univ	1,561,190
Farrell, T P	1,561,111	Fu, W	1,561,682	George, S C	1,561,414
Farshad, M	1,561,553	Fu, X	1,561,133	GeoScan Co Ltd	1,561,678
Fathima, A	1,561,385	Fu, X	1,561,276	Geoscience Australia	1,561,368
Fathom Group Ltd	1,561,698	Fuck, R A	1,561,123	Geosciences Envir Toulouse	1,561,101
Fauquette, S	1,561,135	Fudge, C	1,561,720	GeoZentrum Nordbayern	1,561,284
Faure, M	1,561,319	Fugro	1,561,428	Gernigone, L	1,561,204
Fed Inst Geosci Nat Rscs	1,561,320	Fugro USA Marine Inc	1,561,711	Ghaderi, A	1,561,104
Fed Inst Geosci Nat Rscs	1,561,462	Fuller, J	1,561,538	Ghaderi, A	1,561,195
Fei, L	1,561,289	Fullwood, L A	1,561,863	Ghaderi, A	1,561,221
Fei, T	1,561,520	Funck, T	1,561,462	Ghaderi, A	1,561,330
Feijth, J	1,561,447	Fustic, M	1,561,136	Ghahfarokhi, R B	1,561,598
Feng, J	1,561,108	Fuzhou Univ	1,561,373	Ghasemzadeh, H	1,561,503
Feng, J	1,561,253	Fyfe, R M	1,561,742	Ghiglione, M C	1,561,263
Feng, K	1,561,133	Gabrielsen, O	1,561,687	Ghiglione, M C	1,561,264
Feng, X	1,561,178	Gadoev, M	1,561,262	Ghnahalla, M	1,561,336
Feng, X	1,561,420	Gadre, A	1,561,638	Gholami, A	1,561,503
Feng, Z	1,561,708	Gaiser Geophysical Consult	1,561,426	Ghosh, S	1,561,396
Ferdowsi Univ	1,561,195	Gaiser Geophysical Consult	1,561,438	Giannoukos, K	1,561,272
Ferdowsi Univ	1,561,221	Gaiser, J	1,561,426	Gianolla, P	1,561,158
Ferdowsi Univ	1,561,330	Gaiser, J	1,561,438	Gianolla, P	1,561,217
Fernandes, R L	1,561,419	Galal, A M	1,561,695	Gibson, B M	1,561,232
Fernandez, C	1,561,189	Galante, A C	1,561,432	Gibson, B M	1,561,260
Fernandez, R D	1,561,189	Galvao, E R V	1,561,597	Gibson, T M	1,561,329
Fernandez-Blanco, D	1,561,180	Galy, A	1,561,211	Gil, Y	1,561,316

Author and Affiliation Index

Giletta, S	1,561,590	Guo, M	1,561,476	Han, Z	1,561,362
Gill, F L	1,561,138	Guo, M	1,561,506	Hanasoge, S M	1,561,518
Gilleaudeau, G	1,561,190	Guo, P J	1,561,379	Hand, R	1,561,616
Gingerich, P D	1,561,274	Guo, S	1,561,567	Hangzhou Dianzi Univ	1,561,649
Ginot, S	1,561,127	Guo, S	1,561,701	Hanif, M	1,561,173
Giolo, R	1,561,786	Guo, W	1,561,303	Hannigan, R	1,561,221
Girard, C	1,561,224	Guo, Y	1,561,254	Hans, C	1,561,875
Gisolf, A	1,561,417	Guo, Y	1,561,307	Hans, C	1,561,876
Gliwa, J	1,561,104	Guo, Y	1,561,307	Hans, C	1,561,884
Globe Inst Physique	1,561,180	Guo, Y	1,561,513	Hansen, M O	1,561,800
Glujic, D	1,561,868	Guo, Y	1,561,650	Hao, G	1,561,378
GNS Science	1,561,337	Guo, Y	1,561,718	Hao, M	1,561,166
Golding, M L	1,561,351	Guo, Y	1,561,856	Hao, Y	1,561,305
Gomez, I C	1,561,640	Guo, Y	1,561,856	Harbin Engineering Univ	1,561,643
Gomez, R	1,561,609	Guo, Z	1,561,717	Harbin Engineering Univ	1,561,668
Gomi, E	1,561,442	Guo, Z	1,561,860	Harbin Engineering Univ	1,561,802
Goncalves, J E	1,561,419	Guo, Z	1,561,882	Harbin Engineering Univ	1,561,803
Gong, B	1,561,541	Gupta, G S	1,561,878	Harbin Engineering Univ	1,561,809
Gong, B	1,561,542	Gupta, U	1,561,711	Harbin Inst Technology	1,561,697
Gong, F	1,561,359	Guraieb, P	1,561,639	Harbin Inst Technology	1,561,699
Gong, Q	1,561,132	Gutierrez-Marco, J C	1,561,225	Harbin Inst Technology	1,561,733
Gong, S	1,561,823	Gyllenhammar, C F	1,561,469	Harms, T E	1,561,635
Gong, X	1,561,507	Hafezi, M H	1,561,855	Harnsberry, K A	1,561,630
Gong, Y	1,561,360	Haffinger, P	1,561,417	Haroutunian, M	1,561,734
Gonzalez-Guzman, R	1,561,134	Hafid, A	1,561,225	Harrichhausen, N	1,561,344
Gooneratne, C P	1,561,557	Hagadorn, J W	1,561,382	Harris, D	1,561,836
Gorszczyk, A	1,561,503	Hager, E	1,561,475	Hart, M	1,561,439
Gottumukkula, V	1,561,424	Haggag, M	1,561,677	Hart, P	1,561,716
Gottumukkula, V	1,561,492	Haghighat, E	1,561,531	Hartmann, J	1,561,148
Gou, R	1,561,762	Haghighi, H	1,561,845	Hartmann, M C	1,561,880
Goudemand, N	1,561,127	Hail Hakimi, M	1,561,397	Harvard Univ	1,561,247
Graham, E	1,561,670	Hainan Univ	1,561,728	Harvard Univ	1,561,275
Granada Univ	1,561,111	Haj Messaoud, J	1,561,203	Harvard Univ	1,561,704
Granada Univ	1,561,175	Hall, J R	1,561,692	Harvey, T H P	1,561,291
Gray, E	1,561,109	Hallak, T S	1,561,667	Harvey, T H P	1,561,345
Greinert, J	1,561,245	Halliburton	1,561,617	Hashmi, G M	1,561,752
Griffith, B	1,561,628	Halliburton Energy Service	1,561,573	Hassler, J	1,561,437
Griffith Univ	1,561,715	Halliburton Energy Service	1,561,580	Hatcher, R D	1,561,114
Grillo, E	1,561,841	Halliburton Energy Service	1,561,586	Hathorn, L A	1,561,481
Grimsson, F	1,561,135	Halliburton Energy Service	1,561,635	Haugland, T	1,561,460
Grimsson, F	1,561,325	Halliburton Energy Service	1,561,637	Hawke, M	1,561,471
Gross, M	1,561,325	Halliburton Energy Service	1,561,638	Haywood, A M	1,561,157
Growney, D	1,561,684	Halliburton Energy Service	1,561,674	He, B	1,561,646
Grujic, D	1,561,264	Halliburton Energy Service	1,561,685	He, D	1,561,658
Gu, B L	1,561,549	Halliburton Energy Service	1,561,706	He, G	1,561,699
Gu, Z	1,561,466	Halliburton Energy Service	1,561,720	He, H	1,561,882
Guadalupe National Park	1,561,175	Halliburton Energy Service	1,561,721	He, J	1,561,362
Guan, Q	1,561,395	Halliburton Energy Service	1,561,737	He, J	1,561,774
Guan, X	1,561,103	Halliburton Energy Service	1,561,751	He, L	1,561,758
Guan, Z	1,561,561	Halliburton Energy Service	1,561,752	He, M	1,561,133
Guangyu, W	1,561,486	Halliburton Energy Service	1,561,767	He, M	1,561,691
Guangzhou Marine Geol Surv	1,561,108	Halliburton Energy Service	1,561,877	He, S	1,561,750
Guangzhou Univ	1,561,750	Hamburg Univ	1,561,148	He, T	1,561,220
Guedri, K	1,561,695	Hamburg Univ Technology	1,561,880	He, X	1,561,561
Guenser, P	1,561,146	Hamiel, Y	1,561,153	He, Y	1,561,424
Guenser, P	1,561,271	Hammagren, E J	1,561,719	He, Y	1,561,505
Gugliandolo, C	1,561,841	Hammer, A C	1,561,615	He, Y	1,561,648
Guilin Univ Electr Technol	1,561,657	Hamza, O	1,561,800	He, Y	1,561,791
Guilin Univ Technology	1,561,434	Hamza, S M F	1,561,752	He, Z	1,561,537
Guiyang Inst Geochemistry	1,561,847	Han, C	1,561,715	He, Z	1,561,702
Guizar-Sicarios, M	1,561,141	Han, F	1,561,652	Hearst, J M	1,561,175
Guizhou Academy Sciences	1,561,847	Han, F	1,561,825	Hebert, T R	1,561,529
Gulec, N	1,561,826	Han, G	1,561,731	Hecht, L	1,561,134
Guo, B	1,561,376	Han, J	1,561,681	Hefei Univ Technology	1,561,366
Guo, G	1,561,441	Han, M	1,561,705	Hegde, M B	1,561,653
Guo, H	1,561,106	Han, P	1,561,715	Hegge, R F	1,561,480
Guo, H	1,561,780	Han, S	1,561,758	Hegna, S	1,561,448
Guo, H	1,561,812	Han, W	1,561,211	Heim, J	1,561,543
Guo, H	1,561,869	Han, W	1,561,305	Helmholtz Centre Potsdam	1,561,097
Guo, J	1,561,381	Han, W	1,561,679	Helms, L C	1,561,638
Guo, K	1,561,850	Han, X	1,561,705	Heltzmann, M T	1,561,689
Guo, L	1,561,103	Han, Y	1,561,305	Henan Aero Geophys Survey	1,561,360
Guo, L	1,561,367	Han, Z	1,561,183	Henderson, C M	1,561,125

Henderson, C M	1,561,143	Hsieh, A I	1,561,331	IIT Madras	1,561,497
Herguera-Garcia, J C	1,561,134	Hsieh, H Y	1,561,886	Illinois State Univ	1,561,352
Hernandez Velazquez, A	1,561,581	Hu, D	1,561,420	Imperial Coll, London	1,561,531
Hernandez-Jaramillo, S	1,561,457	Hu, G	1,561,745	Imre, G	1,561,415
Hernandez-Villalobos, J C	1,561,457	Hu, H	1,561,294	In-Depth Geophysical	1,561,541
Hersi, O S	1,561,249	Hu, J	1,561,314	In-Depth Geophysical	1,561,542
Herwegh, M	1,561,182	Hu, J	1,561,409	Indian Inst Science	1,561,155
Hesselbo, S P	1,561,346	Hu, K	1,561,354	Ingenieros Geo Mexicanos	1,561,428
Hewage, S A	1,561,829	Hu, Q	1,561,651	Ingrams, S	1,561,102
Heward, A P	1,561,248	Hu, X	1,561,259	Innocenti, A	1,561,887
Heyde, I	1,561,462	Hu, X	1,561,362	Innovex Downhole Solut Inc	1,561,628
Heyl, C	1,561,687	Hu, X	1,561,655	Inst Geol & Min Espana	1,561,189
Hickman-Lewis, K	1,561,272	Hu, Y	1,561,409	Inst Mexicano Petroleo	1,561,428
Hinnov, L	1,561,162	Hu, Y	1,561,551	Inst Nac Pesquisas Amazon	1,561,640
Hiroshima Inst	1,561,191	Hu, Y	1,561,626	Inst Paleontol (Mongolia)	1,561,113
Hiroshima Univ	1,561,191	Hu, Y	1,561,638	INTEC	1,561,578
Hite, D	1,561,460	Hu, Y	1,561,704	Iowa State Univ	1,561,271
Ho, W Y	1,561,676	Hua, Q	1,561,540	Iowa Univ	1,561,194
Hoare, R D	1,561,175	Hua, Y	1,561,708	Ip, H T	1,561,621
Hobbs, N F	1,561,098	Hua, Z	1,561,326	Isaenkov, R	1,561,552
Hoffmann, J	1,561,393	Huayin Inst Technology	1,561,818	Ishikawa, H	1,561,447
Hoffmann, N	1,561,880	Huan, J	1,561,371	Ishwar-Kumar, C	1,561,155
Hofstetter, A	1,561,153	Huang, B	1,561,682	Islam, H	1,561,667
Hohai Univ	1,561,525	Huang, C	1,561,172	Islam, N	1,561,455
Hohai Univ	1,561,652	Huang, C	1,561,483	Israel Geological Survey	1,561,153
Hohai Univ	1,561,754	Huang, G	1,561,691	Issa, A	1,561,450
Hohai Univ	1,561,795	Huang, J	1,561,256	Issautier, B	1,561,101
Holler, M	1,561,141	Huang, J	1,561,303	Istanbul Technical Univ	1,561,249
Hollingworth, S	1,561,165	Huang, J	1,561,515	ISTerre	1,561,180
Holmden, C	1,561,401	Huang, J	1,561,657	Istituto Scienze Marine	1,561,280
Holm-Denoma, C S	1,561,286	Huang, L	1,561,106	Itoh, H	1,561,810
Holmer, L E	1,561,120	Huang, L	1,561,381	Ivanovic, R F	1,561,157
Holmer, L E	1,561,218	Huang, L	1,561,384	Ivanovskii, N	1,561,804
Holmer, L E	1,561,350	Huang, L	1,561,817	Izquierdo-Lopez, A	1,561,250
Hong, G K	1,561,886	Huang, L	1,561,823	Jaavold, V	1,561,475
Hong, H	1,561,274	Huang, S	1,561,797	Jabri, N M	1,561,744
Hong Kong Chinese Univ	1,561,621	Huang, S Q	1,561,240	Jacintho, A	1,561,864
Hong Kong Polytechnic Univ	1,561,703	Huang, W	1,561,108	Jackson, S M	1,561,885
Hong Kong Univ Sci Technol	1,561,754	Huang, X	1,561,354	Jadavpur Univ	1,561,396
Hong, L	1,561,621	Huang, X	1,561,551	Jadhav, R A	1,561,680
Hong, L	1,561,733	Huang, X	1,561,717	Jadot, T	1,561,670
Hong, X	1,561,823	Huang, Y	1,561,230	Ja'e, I A	1,561,723
Hong, Y	1,561,496	Huang, Y	1,561,236	Jaen Univ	1,561,112
Hood, A S	1,561,095	Huang, Z	1,561,856	Jahanbani Veshareh, M	1,561,785
Hood, S D	1,561,245	Huanggang Normal Univ	1,561,257	Jahangir-Oghli, H	1,561,330
Horner, S	1,561,720	Hubei Geological Bureau	1,561,187	Jal, E	1,561,851
Hornig, C S	1,561,331	Hubei Univ	1,561,852	Jamali, S	1,561,872
Horton Brasil Tecnol Ltda	1,561,724	Hughes Tool Co LLC	1,561,662	Jameel, M	1,561,695
Hortov, A	1,561,555	Hughes, W	1,561,662	James, A	1,561,316
Hossam, O	1,561,437	Hui, J	1,561,126	Jamison, D E	1,561,721
Hosseini, S A	1,561,441	Hui, Z	1,561,434	Jan, A	1,561,283
Hosseini, H	1,561,598	Hull Univ	1,561,323	Janakiram Subramani, H	1,561,625
Hosseini, M K	1,561,857	Humboldt Univ	1,561,134	Janjuhah, H T	1,561,388
Hosseini, P K	1,561,857	Hunan Univ	1,561,758	Japan Petrol Explor Co Ltd	1,561,848
Hou, D	1,561,414	Huo, C	1,561,115	Jarochowska, E	1,561,142
Hou, F	1,561,539	Husein, M M	1,561,749	Jarochowska, E	1,561,143
Hou, G	1,561,763	Husom, V	1,561,475	Jarochowska, E	1,561,147
Hou, J	1,561,150	Husson, J M	1,561,351	Jarochowska, E	1,561,271
Hou, J	1,561,186	HYDROCHINA Xibei Eng Corp	1,561,473	Jarochowska, E	1,561,343
Hou, X	1,561,808	HyperSciences Inc	1,561,560	Jayalekshmi, B R	1,561,821
Hou, Y	1,561,177	IANIGLA-CONICET	1,561,122	Jayawickramage, R	1,561,639
Hou, Z	1,561,354	Ibrahim, M	1,561,878	Jee, Y C	1,561,664
Hou, Z	1,561,540	Ibrahim, O	1,561,472	Jenkyns, H C	1,561,346
Houphouet-Boigny Univ	1,561,196	ICE Thermal Harvesting LLC	1,561,568	Jensen, S	1,561,322
Houston Univ	1,561,262	ICE Thermal Harvesting LLC	1,561,569	Jeong, C	1,561,283
Houston Univ	1,561,401	ICE Thermal Harvesting LLC	1,561,570	Jerusalem Hebrew Univ	1,561,153
Houston Univ	1,561,481	Ifremer	1,561,690	Jesus, L	1,561,509
Hoving, H J	1,561,128	IGG-CNR	1,561,097	Ji, C	1,561,099
Howard Univ	1,561,686	Iglesias, J A	1,561,756	Ji, C	1,561,384
Hoxha, F	1,561,528	IIT Bombay	1,561,394	Ji, K	1,561,274
Hoyer, N W	1,561,624	IIT Delhi	1,561,859	Ji, K	1,561,546
HPC-SENAL-CIMATEC	1,561,521	IIT Dhanbad	1,561,604	Ji, N	1,561,205
Hrvatovic, H	1,561,117	IIT Kanpur	1,561,155	Ji, Y	1,561,789

Author and Affiliation Index

Jia, H	1,561,774	Johnsen, J M	1,561,693	King Abdullah Univ	1,561,500
Jia, H	1,561,774	Johnson, A L A	1,561,349	King Abdullah Univ	1,561,511
Jia, L	1,561,409	Johnson Matthey	1,561,764	King Abdullah Univ	1,561,531
Jia, L	1,561,668	Johnson, T	1,561,429	King Abdullah Univ	1,561,871
Jia, P	1,561,130	Johnston, D T	1,561,247	King Fahd Univ Petrol Min	1,561,531
Jia, P	1,561,780	Jolley, D W	1,561,102	King Saud Univ	1,561,562
Jia, R	1,561,658	Jones, C M	1,561,752	Kireev, A	1,561,437
Jia, X	1,561,492	Jones, N W	1,561,686	Kirichek, A	1,561,579
Jia, Y	1,561,770	Jones, P J	1,561,685	Kislitsyn, R	1,561,264
Jian, Y	1,561,658	Jotun A/S	1,561,885	Klein, M	1,561,880
Jiang, D	1,561,099	Ju, P	1,561,230	Klimes, B	1,561,202
Jiang, F	1,561,295	Jurkovsek, B	1,561,117	Klonaris, G	1,561,893
Jiang, H	1,561,179	Jurkovsek, B	1,561,311	Kneller, B	1,561,105
Jiang, H	1,561,277	KN Toosi Univ Technology	1,561,503	Ko, F C	1,561,886
Jiang, H	1,561,308	KN Toosi Univ Technology	1,561,872	Kochnev, B B	1,561,302
Jiang, H	1,561,360	Kaboth-Bahr, S	1,561,331	Koehne, V	1,561,521
Jiang, J	1,561,259	Kader, U F A	1,561,437	Koffi, A Y	1,561,196
Jiang, L	1,561,779	Kadioglu, Y K	1,561,826	Koh, C A	1,561,683
Jiang, N	1,561,482	Kampouris, G E	1,561,250	Kolar-Jurkovsek, T	1,561,117
Jiang, R	1,561,781	Kan, G	1,561,540	Kolar-Jurkovsek, T	1,561,311
Jiang, S	1,561,103	Kane, I A	1,561,105	Komatsu, T	1,561,197
Jiang, S H	1,561,339	Kang, J	1,561,444	Komatsu, T	1,561,345
Jiang, W	1,561,539	Kang, J	1,561,668	Kong, J T	1,561,244
Jiang, X	1,561,784	Kang, Z	1,561,668	Kong, Z	1,561,420
Jiang, Y	1,561,755	Kang, Z	1,561,779	Konishi, R	1,561,730
Jiang, Z	1,561,278	Kanrar, A	1,561,437	Konkuk Univ	1,561,787
Jiang, Z	1,561,479	Kansas Univ	1,561,598	Kontakiotis, G	1,561,388
Jiang, Z	1,561,699	Kapasakali, D A	1,561,842	Kopecky, T A	1,561,674
Jiangsu Oilfield Co	1,561,251	Karadi, V	1,561,310	Koptev, A	1,561,389
Jiangsu Univ	1,561,651	Karampour, H	1,561,715	Korea Inst Geosci Min Rscs	1,561,207
Jiangsu Univ Sci & Technol	1,561,879	Kaskes, P	1,561,284	Korea Polar Research Inst	1,561,268
Jianguo, S	1,561,486	Katco JV LLP	1,561,136	Korea Univ	1,561,853
Jiao, H	1,561,159	Katrenov, Z	1,561,541	Korn, D	1,561,104
Jiao, Y	1,561,257	Katrenov, Z	1,561,542	Korn, D	1,561,195
Jiao, Z	1,561,705	Katterbauer, K	1,561,744	Korn, D	1,561,221
Jilin Normal Univ	1,561,312	Kaurova, O K	1,561,302	Korte, C	1,561,221
Jilin Oilfield Res Inst	1,561,315	Kayama, M	1,561,191	Kou, H	1,561,770
Jilin Univ	1,561,244	Kazan Federal Univ	1,561,287	Kouamelan, A N	1,561,196
Jilin Univ	1,561,312	Kearsey, T	1,561,342	Kouraiss, K	1,561,225
Jilin Univ	1,561,313	Keele Univ	1,561,197	Kralj, P	1,561,868
Jilin Univ	1,561,314	Keir, D	1,561,097	Krapp, A	1,561,885
Jilin Univ	1,561,378	Keith, P	1,561,543	Kruger, C	1,561,595
Jilin Univ	1,561,434	Kelbie, G	1,561,633	Kruta, I	1,561,128
Jilin Univ	1,561,435	Kellner, J	1,561,628	Kuang, H	1,561,255
Jilin Univ	1,561,454	Kelly, S R	1,561,265	Kucera, P	1,561,571
Jilin Univ	1,561,507	Kelly, S R A	1,561,102	Kuiper, Y D	1,561,286
Jilin Univ	1,561,655	Kemp, A I	1,561,196	Kukowski, N	1,561,246
Jilin Univ	1,561,801	Kemp, D B	1,561,403	Kumar, A	1,561,538
Jimei Univ	1,561,819	Kennington, C G	1,561,231	Kumar, A	1,561,742
Jimenez Osorio, J C	1,561,574	Kennington, C G	1,561,233	Kumar, D	1,561,455
Jimenez Osorio, J C	1,561,591	Kennan, L	1,561,162	Kumar, D	1,561,859
Jimenez Osorio, J C	1,561,596	Kennedy, A E	1,561,168	Kumar, M C S	1,561,653
Jimenez Osorio, J C	1,561,622	Kentucky Univ	1,561,114	Kunas, C	1,561,534
Jimenez Osorio, J C	1,561,623	Kerch State Marine Univ	1,561,804	Kunming Prosp Design Inst	1,561,407
Jimenez Osorio, J C	1,561,748	Kershaw, S	1,561,303	Kunsan National Univ	1,561,811
Jimenez Osorio, J C	1,561,766	Kesarwani, H	1,561,201	Kurmann, E	1,561,182
Jimenez Osorio, J C	1,561,874	Kettratad, J	1,561,863	Kuropyatnyk, O	1,561,571
Jin, C	1,561,784	Keyes, D	1,561,496	Kusumawardhani, M	1,561,861
Jin, F	1,561,599	Khalfi, C	1,561,391	Kuvshinov, B	1,561,456
Jin, Q	1,561,812	Khalifa Univ Sci & Technol	1,561,280	Kuwait Oil Co	1,561,450
Jin, W	1,561,732	Khan, D	1,561,296	Kuznetsov, A B	1,561,302
Jin, X	1,561,217	Khan, M	1,561,281	Kvacek, J	1,561,216
Jin, X	1,561,308	Khan, N B	1,561,695	Kwak, E	1,561,787
Jin, X	1,561,403	Khider, D	1,561,316	Kwak, H T	1,561,593
Jin, X	1,561,697	Khudoley, A K	1,561,302	Kyungpook National Univ	1,561,207
Jin, X	1,561,282	Ki, J S	1,561,678	La Sorda, E	1,561,786
Jin, Z	1,561,553	Kiessling, W	1,561,104	Lacassin, R	1,561,180
Jing, Y	1,561,178	Kilner, A	1,561,851	Lacchia, A	1,561,299
Jo, Y	1,561,787	Kim, H W	1,561,676	Laflamme, M	1,561,227
Johannes Gutenberg Univ	1,561,240	King Abdullah Univ	1,561,203	Laforest, C	1,561,336
Johansen, J V	1,561,861	King Abdullah Univ	1,561,459	Lai, W	1,561,627
Johansen, S E	1,561,204	King Abdullah Univ	1,561,468	Lai, X	1,561,179
Johns Hopkins Univ	1,561,776	King Abdullah Univ	1,561,496	Lai, X	1,561,277

Author and Affiliation Index

Laima, S	1,561,697	Leonhard, I	1,561,343	Li, L	1,561,606
LaMMA Consortium Lab	1,561,887	Lepvrier, C	1,561,319	Li, M	1,561,212
Lamsdell, J C	1,561,194	Lerosey-Aubril, R	1,561,225	Li, M	1,561,213
Lamyman, G	1,561,273	Leroy, P	1,561,894	Li, M	1,561,230
Lan, N	1,561,499	Lesemann, A R	1,561,719	Li, M	1,561,254
Lan, Q	1,561,825	Leuven Katholieke Univ	1,561,219	Li, M	1,561,366
Lancaster Univ	1,561,723	Leuven Katholieke Univ	1,561,760	Li, M	1,561,755
Landers, J	1,561,316	Levantis, M	1,561,885	Li, M	1,561,805
Landes, S	1,561,835	Lewis, H W	1,561,888	Li, M	1,561,827
Landman, N H	1,561,128	L'Hostis, D	1,561,687	Li, N	1,561,704
Landman, N H	1,561,393	Li, B	1,561,403	Li, P	1,561,116
Landucci, C	1,561,308	Li, B	1,561,553	Li, P	1,561,613
Lane, P D	1,561,197	Li, B	1,561,556	Li, P	1,561,882
Lang, Z	1,561,654	Li, B	1,561,557	Li, Q	1,561,759
Lantmateriet	1,561,427	Li, B	1,561,659	Li, R	1,561,526
Lanzhou City Univ	1,561,253	Li, B	1,561,749	Li, S	1,561,103
Lapen, T J	1,561,262	Li, B	1,561,755	Li, S	1,561,305
Lara, J L	1,561,794	Li, B	1,561,793	Li, S	1,561,373
Large, J	1,561,456	Li, C	1,561,334	Li, S	1,561,655
Larson, R F	1,561,798	Li, C	1,561,335	Li, S	1,561,757
Lartey, P O	1,561,850	Li, C	1,561,418	Li, S	1,561,894
Lashin, A	1,561,397	Li, C	1,561,444	Li, S Y	1,561,297
Lashin, M M A	1,561,695	Li, C	1,561,458	Li, S Z	1,561,339
Lasseur, E	1,561,101	Li, C	1,561,514	Li, T	1,561,541
Latiolais, D	1,561,720	Li, C	1,561,739	Li, T	1,561,542
Lau, C H	1,561,190	Li, C	1,561,768	Li, T	1,561,812
Lau, K V	1,561,401	Li, C	1,561,784	Li, W	1,561,152
Laugier, B	1,561,446	Li, D	1,561,294	Li, W	1,561,253
Lausanne Univ	1,561,331	Li, D	1,561,420	Li, W	1,561,431
Lawrence, S P	1,561,580	Li, D	1,561,487	Li, W	1,561,537
Le Calvez, J H	1,561,618	Li, D	1,561,722	Li, W	1,561,783
Le Good, M	1,561,455	Li, D	1,561,850	Li, W	1,561,825
Leary, R	1,561,098	Li, F	1,561,384	Li, X	1,561,230
Lechte, M A	1,561,095	Li, F	1,561,607	Li, X	1,561,251
Leda, L	1,561,195	Li, F	1,561,809	Li, X	1,561,256
Lee, C	1,561,207	Li, G	1,561,113	Li, X	1,561,258
Lee, J	1,561,787	Li, G	1,561,148	Li, X	1,561,424
Lee, K	1,561,854	Li, G	1,561,244	Li, X	1,561,425
Lee, K	1,561,855	Li, G	1,561,540	Li, X	1,561,490
Lee, K	1,561,857	Li, G	1,561,626	Li, X	1,561,492
Lee, K	1,561,873	Li, G	1,561,641	Li, X	1,561,543
Lee, K K	1,561,429	Li, G	1,561,890	Li, X	1,561,606
Lee, K S	1,561,541	Li, G Y	1,561,750	Li, X	1,561,613
Lee, K S	1,561,542	Li, H	1,561,187	Li, X	1,561,614
Lee, M	1,561,268	Li, H	1,561,277	Li, X	1,561,619
Lee, S	1,561,423	Li, H	1,561,373	Li, X	1,561,657
Leeds Univ	1,561,138	Li, H	1,561,376	Li, X	1,561,773
Leeds Univ	1,561,157	Li, H	1,561,387	Li, X	1,561,779
Leeds Univ	1,561,220	Li, H	1,561,445	Li, X Y	1,561,750
Leeds Univ	1,561,270	Li, H	1,561,451	Li, Y	1,561,242
Leeds Univ	1,561,273	Li, H	1,561,613	Li, Y	1,561,262
Leeds Univ	1,561,277	Li, H	1,561,697	Li, Y	1,561,303
Leeds Univ	1,561,293	Li, H	1,561,775	Li, Y	1,561,334
Leeds Univ	1,561,323	Li, J	1,561,166	Li, Y	1,561,354
Lefebvre, B	1,561,225	Li, J	1,561,187	Li, Y	1,561,356
Legrand, J	1,561,345	Li, J	1,561,214	Li, Y	1,561,377
Lehnert, O	1,561,359	Li, J	1,561,259	Li, Y	1,561,409
Lei, J Z X	1,561,351	Li, J	1,561,333	Li, Y	1,561,411
Leibniz Inst Appl Geophys	1,561,331	Li, J	1,561,358	Li, Y	1,561,412
Leicester Univ	1,561,197	Li, J	1,561,483	Li, Y	1,561,433
Leicester Univ	1,561,291	Li, J	1,561,484	Li, Y	1,561,435
Leicester Univ	1,561,342	Li, J	1,561,710	Li, Y	1,561,459
Leicester Univ	1,561,345	Li, J	1,561,718	Li, Y	1,561,649
Leicester Univ	1,561,349	Li, J	1,561,750	Li, Y	1,561,661
Leira, B J	1,561,602	Li, J	1,561,782	Li, Y	1,561,759
Lekam, A	1,561,171	Li, J	1,561,850	Li, Y	1,561,778
Lemaire, M	1,561,772	Li, J	1,561,856	Li, Y	1,561,798
Lemos, D	1,561,663	Li, J	1,561,890	Li, Y	1,561,856
Leng, M J	1,561,349	Li, K	1,561,378	Li, Y L	1,561,793
Leng, Y	1,561,159	Li, K	1,561,380	Li, Z	1,561,116
Lenz, O K	1,561,181	Li, L	1,561,113	Li, Z	1,561,206
Leonard, L J	1,561,344	Li, L	1,561,353	Li, Z	1,561,256
Leonhard, I	1,561,142	Li, L	1,561,359	Li, Z	1,561,278

Author and Affiliation Index

Li, Z	1,561,358	Liu, C	1,561,679	Liu, Y	1,561,212
Li, Z	1,561,452	Liu, C	1,561,776	Liu, Y	1,561,255
Li, Z	1,561,463	Liu, C	1,561,778	Liu, Y	1,561,317
Li, Z	1,561,463	Liu, C	1,561,806	Liu, Y	1,561,334
Li, Z	1,561,483	Liu, D	1,561,341	Liu, Y	1,561,366
Li, Z	1,561,515	Liu, D	1,561,411	Liu, Y	1,561,434
Li, Z	1,561,722	Liu, D	1,561,619	Liu, Y	1,561,505
Li, Z	1,561,740	Liu, F	1,561,411	Liu, Y	1,561,524
Li, Z	1,561,749	Liu, F	1,561,429	Liu, Y	1,561,535
Li, Z	1,561,768	Liu, F	1,561,550	Liu, Y	1,561,561
Li, Z	1,561,770	Liu, F	1,561,714	Liu, Y	1,561,602
Li, Z	1,561,833	Liu, G	1,561,508	Liu, Y	1,561,655
Li, Z C	1,561,549	Liu, H	1,561,198	Liu, Y	1,561,702
Liakopoulos, S	1,561,180	Liu, H	1,561,256	Liu, Y	1,561,775
Lian, J	1,561,718	Liu, H	1,561,505	Liu, Y	1,561,825
Liang, C	1,561,212	Liu, H	1,561,567	Liu, Y	1,561,862
Liang, C	1,561,296	Liu, H P	1,561,194	Liu, Z	1,561,116
Liang, H	1,561,705	Liu, J	1,561,103	Liu, Z	1,561,476
Liang, J	1,561,108	Liu, J	1,561,126	Liu, Z	1,561,658
Liang, K	1,561,303	Liu, J	1,561,318	Liu, Z	1,561,712
Liang, K	1,561,769	Liu, J	1,561,326	Liverpool John Moores Univ	1,561,588
Liang, X	1,561,215	Liu, J	1,561,332	Llamosas, M A B	1,561,761
Liang, X	1,561,626	Liu, J	1,561,355	Lo Duca, A	1,561,820
Liang, X	1,561,643	Liu, J	1,561,561	Lomonosov Moscow St Univ	1,561,555
Liang, Y	1,561,431	Liu, J	1,561,641	London Museum	1,561,165
Liao, H	1,561,561	Liu, J	1,561,717	London Museum	1,561,188
Liao, Q	1,561,833	Liu, J	1,561,784	London Museum	1,561,260
Liao, R	1,561,619	Liu, J	1,561,819	London Museum	1,561,272
Liaoning Petrochem Univ	1,561,797	Liu, K	1,561,156	London Univ Coll	1,561,259
Lieffroy, T	1,561,224	Liu, K	1,561,318	Long, C	1,561,656
Liege Univ	1,561,122	Liu, K	1,561,332	Lord, A R	1,561,165
Ligi, M	1,561,280	Liu, K	1,561,606	Lorraine Univ	1,561,211
Lille Univ	1,561,226	Liu, K	1,561,612	Lorraine Univ	1,561,404
Lille Univ	1,561,239	Liu, K	1,561,614	Losso, S R	1,561,275
Lillehammer, G	1,561,624	Liu, K	1,561,728	Lotfy, N M	1,561,397
Lim, A	1,561,204	Liu, L	1,561,520	Louisiana State Univ	1,561,834
Lim, J K J	1,561,676	Liu, L	1,561,621	Lourens, L J	1,561,274
Lim, V H	1,561,828	Liu, L	1,561,626	Ltaief, H	1,561,496
Lima, F M	1,561,583	Liu, L	1,561,782	Lu, C	1,561,210
Lima Neto, I A	1,561,432	Liu, L	1,561,855	Lu, C	1,561,387
Lima, O A L	1,561,279	Liu, L	1,561,857	Lu, F	1,561,409
Lima, S S	1,561,123	Liu, L	1,561,873	Lu, H	1,561,433
Lin, A T	1,561,331	Liu, P	1,561,150	Lu, H	1,561,443
Lin, C	1,561,156	Liu, P	1,561,725	Lu, H	1,561,679
Lin, C	1,561,608	Liu, Q	1,561,827	Lu, H	1,561,763
Lin, F	1,561,276	Liu, R	1,561,599	Lu, H	1,561,862
Lin, G	1,561,660	Liu, R	1,561,762	Lu, L	1,561,875
Lin, H	1,561,715	Liu, R	1,561,879	Lu, L	1,561,876
Lin, J	1,561,305	Liu, S	1,561,099	Lu, L	1,561,884
Lin, M	1,561,214	Liu, S	1,561,468	Lu, R	1,561,423
Lin, M	1,561,380	Liu, S	1,561,611	Lu, W	1,561,213
Lin, P	1,561,458	Liu, S	1,561,704	Lu, W	1,561,870
Lin, P	1,561,514	Liu, S	1,561,796	Lu, X	1,561,387
Lin, R	1,561,513	Liu, S A	1,561,241	Lu, Y	1,561,236
Lin, T	1,561,454	Liu, T	1,561,326	Lu, Y	1,561,420
Lin, W	1,561,319	Liu, W	1,561,606	Lu, Y Y	1,561,793
Lin, W	1,561,713	Liu, X	1,561,115	Lu, Z	1,561,431
Lin, W L	1,561,714	Liu, X	1,561,276	Luan, H	1,561,715
Lin, X	1,561,762	Liu, X	1,561,315	Luan, H	1,561,755
Ling, X	1,561,367	Liu, X	1,561,326	Luan, X	1,561,359
Linyi Univ	1,561,211	Liu, X	1,561,367	Lubrizol Ltd	1,561,684
Lippert, K	1,561,409	Liu, X	1,561,418	Lue, S	1,561,306
Lisbon Univ	1,561,667	Liu, X	1,561,561	Lue, W	1,561,159
Litoral Nacional Univ	1,561,590	Liu, X	1,561,656	Lue, X	1,561,783
Little, C T S	1,561,138	Liu, X	1,561,660	Luiken, N	1,561,510
Liu, A G	1,561,233	Liu, X	1,561,710	Luo, G	1,561,261
Liu, B	1,561,443	Liu, X	1,561,725	Luo, J	1,561,278
Liu, B	1,561,540	Liu, X	1,561,746	Luo, Y	1,561,326
Liu, C	1,561,106	Liu, X	1,561,869	Luo, Y	1,561,520
Liu, C	1,561,444	Liu, Y	1,561,103	Luo, Z	1,561,735
Liu, C	1,561,452	Liu, Y	1,561,150	Luo, Z	1,561,745
Liu, C	1,561,506	Liu, Y	1,561,160	Luongo, M	1,561,589
Liu, C	1,561,656	Liu, Y	1,561,186	Luoyang Research Inst	1,561,659

Lushkina, A	1,561,493	Manchester Univ	1,561,120	McLoughlin, S	1,561,118
Luz, A M	1,561,771	Manchester Univ	1,561,164	McLoughlin, S	1,561,119
Lynch, E M	1,561,344	Manchester Univ	1,561,777	McMahon, W J	1,561,164
Lynch, E P	1,561,382	Mangalath, N	1,561,488	Meaders, M W	1,561,737
Lyon Ecole Normale Super	1,561,127	Manica, R	1,561,827	Meegoda, J N	1,561,829
Lyon I Univ	1,561,404	Manjarrez-Juarez, R	1,561,134	Mehta, M	1,561,586
Lyon Univ	1,561,127	Mann, T	1,561,320	Melbourne Univ	1,561,095
Lyridis, D V	1,561,816	Mannik, P	1,561,359	Melchuna, A	1,561,663
Ma, B	1,561,452	Manral, S	1,561,453	Mendes, M M	1,561,216
Ma, C	1,561,162	Mantilla-Pimiento, A	1,561,447	Mendoza, D	1,561,565
Ma, G	1,561,763	Mao, H	1,561,708	Mendoza, P E V	1,561,756
Ma, G	1,561,797	Mao, J	1,561,608	Meng, C	1,561,416
Ma, J	1,561,850	Mao, J	1,561,608	Meng, J	1,561,309
Ma, K	1,561,781	Mao, Z	1,561,606	Meng, J	1,561,420
Ma, L	1,561,121	Mao, Z	1,561,607	Meng, L	1,561,319
Ma, L	1,561,699	Mao, Z	1,561,612	Meng, P J	1,561,886
Ma, Q	1,561,775	Mao, Z	1,561,614	Meng, Q	1,561,444
Ma, W	1,561,400	Mao, Z	1,561,626	Meng, X	1,561,540
Ma, X	1,561,160	Maranhao, F D S	1,561,601	Menguy, N	1,561,406
Ma, X	1,561,236	Maravelis, A G	1,561,388	Menier, D	1,561,385
Ma, X	1,561,261	Marchetti, A	1,561,820	Mensa-Wilmot, G	1,561,584
Ma, X	1,561,620	Marco, Y	1,561,690	Mersch, A	1,561,114
Ma, Y	1,561,381	Marcotulli, A	1,561,727	Messina Univ	1,561,841
Ma, Y	1,561,876	Marine Design & Res Inst	1,561,812	Met Office	1,561,888
Ma, Y	1,561,889	Marine Geology Inst China	1,561,540	Metcalfe, I	1,561,187
Ma, Z	1,561,373	Marins, J	1,561,663	Methner, K	1,561,389
Ma, Z	1,561,421	Maritime Res Inst Neth	1,561,667	Meunier, A	1,561,336
Macalester Coll	1,561,352	Marjan, A	1,561,716	Mexico Nac Auton Univ	1,561,134
Macdonald, A	1,561,439	Markeset, T	1,561,861	Meyers, S R	1,561,162
Macdonald, F A	1,561,247	Marnane, M J	1,561,863	MHWirth AS	1,561,693
Macesanu, C	1,561,550	Marone, F	1,561,141	Mi, J	1,561,697
MacGabhann, B A	1,561,382	Marques, J C	1,561,105	Miao, J	1,561,857
MacGregor, L	1,561,449	Marsala, A F	1,561,744	Miao, J	1,561,873
Macintyre, H	1,561,456	Marshall Univ	1,561,529	Miao, T	1,561,796
Mackojc, A	1,561,698	Martin, A M	1,561,761	Middle East Technical Univ	1,561,173
Mackojc, K	1,561,698	Martin, E L O	1,561,225	Middle East Technical Univ	1,561,338
Macquarie Univ	1,561,350	Martin, P G	1,561,141	Middle East Technical Univ	1,561,826
Macquarie Univ	1,561,414	Martinez, E I	1,561,756	Mietto, P	1,561,217
Madhusudhana, A M	1,561,653	Martinez, G	1,561,864	Migeon, F	1,561,726
Madrid Complutense Univ	1,561,189	Martinez, S	1,561,637	Milano-Bicocca Univ	1,561,259
Madrid Complutense Univ	1,561,761	Martinod, J	1,561,264	Millan, C	1,561,711
Madrid Politecnica Univ	1,561,321	Martinot, C	1,561,109	Miller, B V	1,561,422
Madrid Politecnica Univ	1,561,794	Martins, A L	1,561,632	Miller, C G	1,561,165
Madrid Politecnica Univ	1,561,891	Martins, R L P	1,561,877	Miller, C G	1,561,345
Maestrelli, D	1,561,097	Marton, E	1,561,415	Millikin, A E G	1,561,329
Maffi, J M	1,561,590	Marusin, V V	1,561,302	Mills, L	1,561,864
Magazu, S	1,561,841	Marz, C	1,561,138	Millward, D	1,561,342
Maghami Nick, H	1,561,785	Masaki, H	1,561,232	Min, J	1,561,796
Mahadevan, P	1,561,664	Masoomzadeh, H	1,561,470	Minisini, D	1,561,162
Mahajan, B	1,561,488	Mass Univ, Boston	1,561,221	Minnan Normal Univ	1,561,860
Mahani, H	1,561,777	Massachusetts Inst Technol	1,561,531	Minnebo, J	1,561,687
Maharaja Sayajirao Univ	1,561,192	Massachusetts Inst Technol	1,561,699	Miot, J	1,561,169
Mahatma, A A	1,561,286	Matador Resources Co	1,561,161	Mirmazloui, S M	1,561,872
Mahdavi, S	1,561,872	Mather, T A	1,561,346	Missagia, R M	1,561,432
Mahfoudh, F	1,561,283	Matheson, E J	1,561,137	Missouri Univ	1,561,382
Mahmoodi, A	1,561,785	Mathon, T	1,561,589	Mitchell, E G	1,561,110
Mahon, E M	1,561,095	Matteini, M	1,561,124	Mitchell, E G	1,561,231
Mai, Z	1,561,875	Matthews, K J	1,561,346	Mitchell, E G	1,561,232
Maia, T A C	1,561,877	Mattioli, E	1,561,404	Mitchell, E G	1,561,233
Maineult, A	1,561,894	Mattsson, R	1,561,800	Mitchell, E G	1,561,260
Mair, D	1,561,182	Mavraki, N	1,561,842	Mitrinova, Z	1,561,684
Makled, W A	1,561,397	Maxwell Dynamics Inc	1,561,451	Mittal, A	1,561,742
Mako, C A	1,561,114	May, P A	1,561,721	Miyake, R	1,561,810
Makowiecki, G J	1,561,638	Mays, C	1,561,118	Mizuno, T	1,561,618
Makri, P	1,561,388	Mays, C	1,561,119	Mo, T	1,561,206
Malcolm, A	1,561,503	Mbarki, N	1,561,391	Moecher, D P	1,561,114
Malkoti, A	1,561,518	McArthur, A D	1,561,105	Moellendick, T E	1,561,556
Malkowski, M A	1,561,263	McCauley, C M	1,561,167	Moellendick, T E	1,561,557
Mallouppas, G	1,561,865	McCoy, V E	1,561,140	Moghaddam, R K	1,561,741
Malone, D H	1,561,352	McDermott Inc	1,561,711	Mohaghegh, S	1,561,330
Malone, J R	1,561,352	McGairy, A	1,561,345	Mohamed, A	1,561,450
Maloney, K M	1,561,227	McGill Univ	1,561,095	Mohamed, A B	1,561,391
Mammadov, E	1,561,577	McLeman, J	1,561,516	Mohana, K N S	1,561,653

Author and Affiliation Index

Mohapatra, S C	1,561,667	Naciri, M	1,561,687	Nguyen, P D	1,561,345
Mohibullah, M	1,561,173	Nag, A	1,561,750	Niasar, V	1,561,777
Mohseni, F	1,561,872	Nagarajan, R	1,561,385	Nicchio, M A	1,561,285
Moissette, P	1,561,388	Nagoya Univ	1,561,184	Nicholls, J	1,561,449
Mokhtarzade, M	1,561,872	Nair, U G	1,561,604	Nicoll, R	1,561,118
Molano, N A G	1,561,756	Nakamoto, G	1,561,447	Nicoll, R S	1,561,119
Molina, R	1,561,794	Nandan, B	1,561,859	Nicolo, M S	1,561,841
Monash Univ	1,561,364	Nanjing Agricultural Univ	1,561,384	Nie, Y	1,561,276
Mondal, D	1,561,439	Nanjing Forestry Univ	1,561,710	Nielsen, A T	1,561,268
Monk, D	1,561,460	Nanjing Inst Geol Palaeont	1,561,099	Nielsen, M L	1,561,268
Monk, D	1,561,538	Nanjing Inst Geol Palaeont	1,561,170	Niigata Univ	1,561,155
Monnet, C	1,561,127	Nanjing Inst Geol Palaeont	1,561,214	Nikashin, K	1,561,287
Monnet, C	1,561,239	Nanjing Inst Geol Palaeont	1,561,241	Nilsson, P	1,561,693
Montclair State Univ	1,561,410	Nanjing Inst Geol Palaeont	1,561,303	Nimisha, P	1,561,821
Montel, F	1,561,690	Nanjing Inst Geol Palaeont	1,561,330	Ninomiya, A	1,561,447
Montevocchi, N	1,561,477	Nanjing Inst Geol Palaeont	1,561,369	Niocaill, C M	1,561,346
Montpellier Univ	1,561,101	Nanjing Univ	1,561,148	Nippon Steel Corp	1,561,589
Montpellier Univ	1,561,224	Nanjing Univ	1,561,160	Niu, J	1,561,641
Mooney, T	1,561,670	Nanjing Univ	1,561,259	Niu, P	1,561,126
Moreira, J	1,561,442	Nanjing Univ	1,561,304	Niu, T	1,561,215
Moreira, N	1,561,632	Nanjing Univ	1,561,362	No Car Univ, Chapel Hill	1,561,349
Moreland, S J	1,561,881	Nantes Univ	1,561,681	No, Y H	1,561,678
Morell, K D	1,561,344	Napier, D Q	1,561,615	Nobes, D C	1,561,339
Moreno-Martin, D	1,561,189	Napoli Federico II Univ	1,561,818	Nogueira, F C C	1,561,285
Morgan, M M F	1,561,675	Narbonne, G M	1,561,247	Nogueira, P	1,561,509
Mori, A	1,561,182	Nardello-Rataj, V	1,561,772	Nohl, T	1,561,284
Morillas, N R	1,561,756	Nascimento, E	1,561,532	Norman, R	1,561,588
Morin, J	1,561,563	Nash, S	1,561,831	Norman, R	1,561,734
Morrison, L	1,561,382	Naskar, T	1,561,497	NORSAR	1,561,460
Mosse, L	1,561,592	Nat Inst Technol (India)	1,561,821	North Bengal Univ	1,561,396
Mothilal, B P J	1,561,617	Nat Inst Technol Rourkela	1,561,647	North Dakota Geol Survey	1,561,398
Mou, J	1,561,805	Nat Museum Marine Taiwan	1,561,886	North Dakota Univ	1,561,398
Mouri, T	1,561,447	Nat Univ Sci & Technol	1,561,695	Northeast Petroleum Univ	1,561,116
Mousa, S	1,561,764	Natale, G	1,561,741	Northeast Petroleum Univ	1,561,375
Moysiuk, J	1,561,250	National Dong Hwa Univ	1,561,886	Northeast Petroleum Univ	1,561,746
Mozgovaya, O	1,561,493	National Maritime Res Inst	1,561,810	Northeastern Univ, China	1,561,656
Mueller International LLC	1,561,798	National Univ Technology	1,561,735	Northern Arizona Univ	1,561,344
Mueller, W E G	1,561,240	National Univ Technology	1,561,892	Northrop, P S	1,561,630
Mughal, S	1,561,329	Natl Res Council (Italy)	1,561,158	Northumbria Univ	1,561,157
Muhammad, R	1,561,695	Natl Res Council (Italy)	1,561,820	Northwest Univ, China	1,561,106
Muir, L A	1,561,347	Naujokaityte, J	1,561,393	Northwest Univ, China	1,561,113
Muirhead, D	1,561,105	Navarro, I	1,561,663	Northwest Univ, China	1,561,120
Mukerji, P	1,561,624	Navaux, P	1,561,534	Northwest Univ, China	1,561,144
Mukherjee, S	1,561,497	Naveena-Chandran, R	1,561,752	Northwest Univ, China	1,561,218
Mukhopadhyay, S	1,561,396	Nayak, S R	1,561,653	Northwest Univ, China	1,561,230
Mukhopadhyay, S K	1,561,328	Nazarbayev Univ	1,561,136	Northwest Univ, China	1,561,253
Mulch, A	1,561,181	Negro Valdecantos, V	1,561,891	Northwest Univ, China	1,561,278
Mulligan, C N	1,561,854	Neklyudov, D	1,561,495	Northwest Univ, China	1,561,350
Muluneh, A A	1,561,097	Nelson, C S	1,561,245	Northwest Univ, China	1,561,482
Munir, A	1,561,695	NERC Isotope Geosci Lab	1,561,349	Norway Geological Survey	1,561,204
Munnecke, A	1,561,147	Nesheim, T O	1,561,398	Norwegian Meteorology Inst	1,561,879
Munnecke, A	1,561,399	Nestell, G P	1,561,117	Norwegian Univ Sci Technol	1,561,204
Murdock, D	1,561,343	Nestell, G P	1,561,167	Nottingham Univ	1,561,764
Murphy, J B	1,561,137	Nestell, M K	1,561,167	NOV Inc	1,561,559
Murphy, R T	1,561,637	Neto, A	1,561,532	Novye Proekty LLC	1,561,555
Murray, J	1,561,382	Neunmann, E	1,561,492	NVIDIA	1,561,528
Murtland, C J	1,561,568	New Jersey Inst Technology	1,561,829	NVIDIA	1,561,534
Murtland, C J	1,561,569	New Mex Inst Mining Technl	1,561,098	NWGI	1,561,258
Murtland, C J	1,561,570	New Mexico Univ	1,561,190	Nyman, S L	1,561,245
Mus, M M	1,561,222	New South Wales Geol Surv	1,561,369	Ocean Floor Geophysics Inc	1,561,449
Mus, M M	1,561,322	Newberg, K	1,561,560	O'Connell, B	1,561,095
Musayev, R	1,561,627	Newcastle Univ	1,561,588	Odessa National Univ	1,561,571
Musso Piantelli, F	1,561,182	Newcastle Univ	1,561,734	Ogawa, K	1,561,828
Mutz, S G	1,561,389	Newell, A J	1,561,255	Ogg, J G	1,561,360
Myatchin, K	1,561,555	Newfoundland Memorial Univ	1,561,503	Ogretmen, N	1,561,180
Myers, C E	1,561,393	Newfoundland Memorial Univ	1,561,857	Ogundare, O	1,561,720
Myers, M	1,561,481	Newfoundland Memorial Univ	1,561,883	Oh, J	1,561,811
Mysore Univ	1,561,653	Newfoundland Oil Gas Corp	1,561,477	Ohen, E	1,561,544
Myung, G	1,561,575	Newport, C L	1,561,674	Ohta, T	1,561,348
Na, B	1,561,853	Newton, R J	1,561,293	Oikonomou, D	1,561,472
Naafs, B D A	1,561,112	Ng, C W W	1,561,754	Oimuhammadzoda, I	1,561,262
Nabi, Y	1,561,507	Ng, S W J	1,561,706	Oji, T	1,561,197
Nabors Drilling Solutions	1,561,832	Ngai, T	1,561,621	O'Keefe, C	1,561,138

Okita, N	1,561,533	Pau Univ	1,561,474	Pires, O	1,561,532
Okuno, R	1,561,790	Paul Sabatier Univ	1,561,324	Pirogova, A	1,561,555
Oldal, D G	1,561,871	Paulsen, A L	1,561,800	Pistek, V	1,561,571
Olesen, O	1,561,204	Pavic, S	1,561,814	Pitra, P	1,561,196
Oliveira, A	1,561,442	Pavlov, D	1,561,425	Plessix, R E	1,561,518
Oliveira, A J	1,561,644	Pavoni, E	1,561,308	Plymouth Univ	1,561,188
Oliveira, A R	1,561,432	Pawelec, I	1,561,498	Plymouth Univ	1,561,383
Oliveira, T	1,561,521	Pazouki, K	1,561,588	Poitiers Univ	1,561,336
Omer Yilmaz, I	1,561,173	Pecorari, M	1,561,158	Poitiers Univ	1,561,406
Omer Yilmaz, I	1,561,338	Pedenaud, P	1,561,786	Pokrovsky, B G	1,561,302
Onorato, M	1,561,880	Pedersen, S	1,561,709	Polish Academy Sciences	1,561,405
Onorato, M	1,561,887	Peking Univ	1,561,099	Polish Academy Sciences	1,561,503
Ontiveros, J F	1,561,772	Peking Univ	1,561,230	Polymenis, I	1,561,734
Onwumelu, C J	1,561,398	Peking Univ	1,561,443	Poole, G	1,561,553
Open Univ	1,561,168	Peking Univ	1,561,763	Pope, M C	1,561,422
Open Univ	1,561,266	Peng, P	1,561,892	Portillo Juan, N	1,561,891
OPERA	1,561,474	Peng, S	1,561,458	Porto Univ	1,561,644
Opla Energy Ltd	1,561,577	Peng, S	1,561,463	Postema, A	1,561,836
OQ Explor & Prod LLC	1,561,248	Peng, S	1,561,514	Poulton, S	1,561,270
Orano	1,561,136	Peng, X	1,561,371	Poulton, S W	1,561,138
Oren, C	1,561,504	Peng, Y	1,561,177	Pound, M J	1,561,157
Oritia & Boreas	1,561,794	Peng, Z	1,561,106	Pourakabarian, A	1,561,777
Ortega-Hernandez, J	1,561,275	Pennsylvania State Univ	1,561,401	Powell, K	1,561,639
Ortuno, G	1,561,565	Percival, L	1,561,284	Powell, N E	1,561,114
Oslo Univ	1,561,288	Pereira, E	1,561,122	Prague National Museum	1,561,216
Otago Univ	1,561,234	Pereira-Dias, B	1,561,491	Pralica, N	1,561,543
Ou, J	1,561,728	Perez, C M	1,561,141	Pramudito, A	1,561,422
Ouabed, N	1,561,171	Periyar Univ	1,561,385	Preston, M	1,561,543
Ouali, J A	1,561,391	Pernambuco Federal Univ	1,561,123	Pret, D	1,561,406
Ouyang, Y	1,561,659	Perozo, A	1,561,876	Prince, P	1,561,720
Ouyang, Z	1,561,253	Peryt, D	1,561,405	Princess Nourah Univ	1,561,695
Ouyang, Z	1,561,277	Peshawar Univ	1,561,173	Priyatkina, N S	1,561,302
Owen, R	1,561,680	Petersen, S V	1,561,393	Proctor, J	1,561,767
Oxford Univ	1,561,139	Petit, G	1,561,169	Pu, C	1,561,856
Oxford Univ	1,561,164	Petranich, E	1,561,096	Pu, W	1,561,599
Oxford Univ	1,561,178	Petranich, E	1,561,308	Pu, W	1,561,762
Oxford Univ	1,561,197	PetroChina	1,561,132	Pufahl, P K	1,561,137
Oxford Univ	1,561,232	PetroChina	1,561,170	Purdue Univ	1,561,360
Oxford Univ	1,561,260	PetroChina	1,561,251	Purohit, A	1,561,617
Oxford Univ	1,561,329	PetroChina	1,561,749	Pusan National Univ	1,561,844
Oxford Univ	1,561,343	PetroChina	1,561,757	Qasim, M U	1,561,798
Oyenowo, O P	1,561,790	PetroChina Research Inst	1,561,131	Qi, G	1,561,870
Ozcan, E	1,561,249	PetroChina Research Inst	1,561,209	Qi, J	1,561,812
Padhan, S	1,561,604	PetroChina Research Inst	1,561,252	Qian, S	1,561,159
Paereli, S	1,561,885	PetroChina Research Inst	1,561,341	Qiang, Q Y	1,561,379
Page, K T	1,561,609	PetroChina Research Inst	1,561,355	Qiao, B	1,561,130
Pai, N K	1,561,877	PetroChina Research Inst	1,561,546	Qiao, P	1,561,403
Palacharla, G	1,561,424	Petroleo Brasileiro SA	1,561,419	Qie, W	1,561,303
Palacharla, G	1,561,425	Petroleo Brasileiro SA	1,561,491	Qilu Univ Technology	1,561,646
Palacios, T	1,561,322	Petroleo Brasileiro SA	1,561,583	Qin, F	1,561,505
Pan, R	1,561,309	Petroleo Brasileiro SA	1,561,632	Qin, F	1,561,520
Pan, S	1,561,381	Petroleos Mexicanos	1,561,457	Qin, N	1,561,463
Pan, W	1,561,691	Petroleum Develop Oman Co	1,561,249	Qin, P	1,561,646
Pan, Y	1,561,882	Petronas Carigali Sdn Bhd	1,561,429	Qin, S	1,561,301
Pan, Z	1,561,375	Petronas Univ	1,561,723	Qin, W	1,561,850
Panasonic IP Mgmt Co Ltd	1,561,730	Petryshen, W	1,561,143	Qin, X	1,561,387
Pancost, R D	1,561,112	Pett, W	1,561,271	Qin, Y	1,561,843
Pandit, M K	1,561,193	Pevzner, R	1,561,552	Qing, W Y	1,561,131
Panetta, J	1,561,534	PGS	1,561,430	Qing, Y	1,561,656
Papanastassiou, D	1,561,180	PGS	1,561,448	Qingdao Inst Marine Geol	1,561,444
Paquette, M	1,561,665	PGS	1,561,477	Qingdao Univ Sci & Technol	1,561,648
Para Federal Univ	1,561,427	Pha, P D	1,561,370	Qingdao Univ Sci & Technol	1,561,808
Paravastu, B	1,561,586	Phadke, S	1,561,488	Qingdao Univ Technology	1,561,367
Parayil, J	1,561,883	Pham, L T	1,561,427	Qingdao Univ Technology	1,561,656
Paris Museum	1,561,169	Phillips, A	1,561,585	Qingdao Univ Technology	1,561,717
Paris-Est Univ	1,561,694	Phillips, C	1,561,845	Qinghai Oilfield Co	1,561,130
Paris-Sorbonne Univ	1,561,406	Phillips, G	1,561,393	Qinghai Univ	1,561,278
Park, G	1,561,711	Phillips, M	1,561,538	Qiu, L	1,561,210
Park, T Y S	1,561,268	Pickle, B R	1,561,737	Qiu, L	1,561,296
Parma Univ	1,561,285	Piepjohn, K	1,561,462	Qiu, L	1,561,297
Passos, A	1,561,583	Pierre & Marie Curie Univ	1,561,169	Qiu, L	1,561,852
Pastre, L	1,561,663	Pige, N	1,561,404	Qiu, R	1,561,659
Patel, S	1,561,192	Pintas, E	1,561,491	Qiu, R	1,561,833

Qiu, W	1,561,875	Res Inst Petrol Explor Dev	1,561,333	Ryan, V	1,561,851
Qu, J	1,561,126	Res Inst Petrol Explor Dev	1,561,379	Ryu, I C	1,561,207
Qu, W	1,561,166	Res Inst Petrol Explor Dev	1,561,381	Saavedra-Castaneda, D	1,561,457
Qu, X	1,561,643	Revelo, D	1,561,521	Saba, F	1,561,872
Qu, Y	1,561,381	Rexiti, Y	1,561,378	Sabar, M S	1,561,336
Qu, Y	1,561,452	Rhyne, L D	1,561,625	Sabba, M	1,561,173
Qu, Y	1,561,483	Ribeiro-Filho, N	1,561,427	Sabbatino, M	1,561,096
Qu, Y	1,561,485	Rice Univ	1,561,771	Sablina, V	1,561,493
Qu, Z	1,561,854	Richards, K R	1,561,292	Sacchi, M D	1,561,461
Queen's Univ, Kingston	1,561,137	Riding, J B	1,561,138	Sacchi, M D	1,561,513
Queen's Univ, Kingston	1,561,247	Riding, J B	1,561,157	Sacchi, M D	1,561,530
Queensland Univ	1,561,689	Riding, J B	1,561,346	Saccomano, G	1,561,272
Quijano, M L	1,561,112	Ridyard, D	1,561,460	Safari, S	1,561,846
Rabat Univ	1,561,111	Riechelmann, S	1,561,846	Sagar, M W	1,561,337
Racicot, R A	1,561,260	Riegel, W	1,561,181	Sagin, A	1,561,571
Rader, B L	1,561,849	Rigby, S P	1,561,764	Sagin, S	1,561,571
Radwan, A E	1,561,397	Rigo, M	1,561,217	Sahu, B K	1,561,647
Ragalla, C	1,561,344	Rijeka Univ	1,561,868	Saint Martin, J P	1,561,406
Rahim, A	1,561,397	Rio de Janeiro Fed Univ	1,561,601	Saipem	1,561,727
Rahman, I A	1,561,232	Rio de Janeiro Fed Univ	1,561,771	Saipem	1,561,786
Rahman, I A	1,561,260	Rio de Janeiro State Univ	1,561,122	Sajeev, K	1,561,155
Rahman, N M A	1,561,576	Rio Grande Norte Fed Univ	1,561,522	Sajib, M S J	1,561,686
Rais-Zadeh, M	1,561,692	Rio Grande Norte Fed Univ	1,561,597	Salamanca Univ	1,561,189
Rajasthan Univ	1,561,193	Rio Grande Sul Fed Univ	1,561,105	Salgadoe, M	1,561,445
Rajitha, K	1,561,653	Rio Grande Sul Fed Univ	1,561,534	Sam and Gail LLC	1,561,673
Rajiv Gandhi Inst Technol	1,561,201	Risi, C	1,561,389	Samanta, P	1,561,396
Ramadan, F S	1,561,397	Roberts, K	1,561,442	Samiez, P	1,561,772
Ramakrishnan, T	1,561,743	Robin, N	1,561,169	San Roman Alerigi, D P	1,561,666
Ramanandraibe, V	1,561,772	Robinson, A C	1,561,262	Sanchez, I C	1,561,322
Ramasesha, L M	1,561,756	Robinson, M M	1,561,219	Sang, K	1,561,499
Rambo, C R	1,561,640	RockWool A/S	1,561,800	Sangesland, S	1,561,602
Ramkumar, M	1,561,385	Rodrigues, J	1,561,491	Sani, F	1,561,097
Ramos, M E	1,561,264	Rodrigues, M A F	1,561,597	Sans-Jofre, P	1,561,406
Randriamamonjy, T H	1,561,772	Rodriguez Herrera, A E	1,561,878	Santa Catarina Fed Univ	1,561,640
Rani, S	1,561,859	Rogers, J	1,561,752	Santa Catharina, A	1,561,105
Ras, P	1,561,467	Roghi, G	1,561,217	Santa-Maria, J C	1,561,636
Rastogi, R	1,561,488	Rojas, A	1,561,202	Santana, C	1,561,522
Ratnakar, V	1,561,316	Roma III Univ	1,561,285	Santos, J E	1,561,525
Rau, E G	1,561,161	Romano-Moreno, E	1,561,794	Santos, L A	1,561,419
Raudsepp, M J	1,561,846	Romans, B W	1,561,263	Santos, M	1,561,521
Ravasi, M	1,561,496	Romero, J	1,561,472	Santos, P	1,561,532
Ravasi, M	1,561,500	Romero Morales, B	1,561,581	Santos, R	1,561,521
Ravasi, M	1,561,510	Ronda, G	1,561,264	Santosh, M	1,561,385
Ravelo-Cervantes, J	1,561,457	Rondon, M	1,561,786	Santra, A	1,561,572
Rayment, T	1,561,538	Ronen, S	1,561,456	Sao Carlos Federal Univ	1,561,442
Reales, O A M	1,561,601	Rong, H	1,561,257	Sao Paulo Univ	1,561,124
Reda, A	1,561,723	Rooney, A D	1,561,329	Sao Paulo Univ	1,561,442
Regina Univ	1,561,249	Roosevelt Univ	1,561,202	Sao Paulo Univ	1,561,700
Reinicke, C	1,561,465	Rosvall, M	1,561,202	Sardina, I	1,561,522
Remirez, M N	1,561,190	Rouget, I	1,561,128	Sarhan, M	1,561,481
Ren, C	1,561,409	Rout, T K	1,561,604	Sarker, P	1,561,686
Ren, H	1,561,466	Routh, P	1,561,423	Sarr, A C	1,561,109
Ren, H	1,561,867	Routh, P	1,561,425	Sarrasin, F	1,561,726
Ren, J	1,561,364	Rovelli, R	1,561,393	Saskatchewan Univ	1,561,401
Ren, K	1,561,650	Rovig, J	1,561,559	Sasputurru, N	1,561,101
Ren, N	1,561,728	Rowe, A	1,561,128	Satish-Kumar, M	1,561,155
Ren, Y	1,561,470	Rowe, M D	1,561,573	Saud Alothman, T	1,561,562
Ren, Y	1,561,471	Rowe, M D	1,561,580	Saudi Arabian Oil Co	1,561,556
Ren, Z	1,561,858	Roy Choudhury, T	1,561,394	Saudi Arabian Oil Co	1,561,557
Repetski, J E	1,561,142	Royal Belgian Inst	1,561,842	Saudi Arabian Oil Co	1,561,564
Repsol	1,561,565	Royal Ontario Museum	1,561,350	Saudi Arabian Oil Co	1,561,576
Repsol	1,561,756	Ruan, H	1,561,856	Saudi Arabian Oil Co	1,561,593
Repsol Exploracion SA	1,561,761	Ruan, Z	1,561,106	Saudi Arabian Oil Co	1,561,600
Repsol Sinopec Brasil	1,561,601	Rubinstein, C V	1,561,122	Saudi Arabian Oil Co	1,561,666
Res Inst Geol Mineral Rscs	1,561,369	Rudan, S	1,561,688	Saudi Arabian Oil Co	1,561,671
Res Inst Petrol Explor Dev	1,561,121	Ruhl, M	1,561,346	Saudi Arabian Oil Co	1,561,744
Res Inst Petrol Explor Dev	1,561,130	Ruiz-Fuentes, A	1,561,111	Saudi Arabian Oil Co	1,561,747
Res Inst Petrol Explor Dev	1,561,212	Russell, M C	1,561,560	Saudi Aramco	1,561,464
Res Inst Petrol Explor Dev	1,561,236	Russian Academy Sciences	1,561,216	Saudi Aramco	1,561,468
Res Inst Petrol Explor Dev	1,561,243	Russian Academy Sciences	1,561,495	Saudi Aramco	1,561,494
Res Inst Petrol Explor Dev	1,561,256	Russian Academy Sciences	1,561,555	Saudi Aramco	1,561,495
Res Inst Petrol Explor Dev	1,561,278	Russian Fed Financial Univ	1,561,804	Saudi Aramco	1,561,505
Res Inst Petrol Explor Dev	1,561,282	Rutherford, J	1,561,634	Saudi Aramco	1,561,520

Saulter, A	1,561,888	Schneider, S	1,561,265	Sharma, S	1,561,201
Saunders, B J	1,561,863	Schnitzler, E	1,561,632	Shchuplov, P	1,561,555
Sava, P	1,561,498	Schobben, M	1,561,104	She, J	1,561,317
Sava, P	1,561,501	Schobben, M	1,561,195	Shearwater GeoServices	1,561,475
Sava, P	1,561,527	Schobben, M	1,561,221	Sheffield Univ	1,561,372
Savatic, K	1,561,119	Schramm, K D	1,561,863	Shell Explor & Prod Co	1,561,456
Savioli, G B	1,561,525	Schwark, L	1,561,138	Shell Global Solut Int BV	1,561,162
Savoie Univ	1,561,264	Schwartz, T M	1,561,263	Shell Global Solut Int BV	1,561,456
Saxena, S	1,561,832	Schwarze, C O	1,561,246	Shell Global Solutions Int	1,561,518
Schiffbauer, J D	1,561,382	Scott, J M	1,561,234	Shell Int Explor & Prod	1,561,162
Schirrmeister, B E	1,561,149	Scott, L	1,561,449	Shen, B	1,561,757
Schlumberger	1,561,283	Second Inst Oceanography	1,561,400	Shen, C	1,561,177
Schlumberger	1,561,437	Seher, T	1,561,470	Shen, H	1,561,782
Schlumberger	1,561,445	Seher, T	1,561,471	Shen, J	1,561,390
Schlumberger	1,561,450	Seismic PPS	1,561,544	Shen, J	1,561,754
Schlumberger	1,561,453	Seisnetics	1,561,446	Shen, M	1,561,378
Schlumberger	1,561,457	Sekine, Y	1,561,408	Shen, S Z	1,561,304
Schlumberger	1,561,565	Sellars, S E	1,561,368	Shen, Y	1,561,176
Schlumberger Canada Ltd	1,561,592	Sen, A	1,561,396	Shen, Y	1,561,366
Schlumberger Canada Ltd	1,561,594	SENAI-CIMATEC	1,561,509	Shen, Y	1,561,646
Schlumberger Canada Ltd	1,561,618	SENAI-CIMATEC	1,561,532	Shen, Z	1,561,649
Schlumberger Canada Ltd	1,561,624	Senckenberg Res Center	1,561,181	Shengli Oilfield Co	1,561,722
Schlumberger Canada Ltd	1,561,627	Senger, H	1,561,442	Shengli Oilfield Co	1,561,784
Schlumberger Canada Ltd	1,561,629	Seo, D W	1,561,811	Shengli Oilfield Res Inst	1,561,395
Schlumberger Canada Ltd	1,561,636	Seo, J K	1,561,844	Shengli Oilfield Res Inst	1,561,517
Schlumberger Canada Ltd	1,561,664	Sequero, C	1,561,112	Shengli Oilfield Res Inst	1,561,722
Schlumberger Canada Ltd	1,561,743	Sercel	1,561,456	Shengli Oilfield Res Inst	1,561,782
Schlumberger Canada Ltd	1,561,768	Serpa, M	1,561,534	Shengli Oilfield Res Inst	1,561,784
Schlumberger Canada Ltd	1,561,875	Serra, J M S	1,561,756	Shengli Oilfield Technol Ltd	1,561,159
Schlumberger Canada Ltd	1,561,876	Serrano, O	1,561,101	Shenzhen Univ	1,561,712
Schlumberger Canada Ltd	1,561,878	Sevastopol State Univ	1,561,645	Sherrill, K V	1,561,692
Schlumberger Canada Ltd	1,561,884	Sevillano, L C	1,561,602	Sherrill, K V	1,561,881
Schlumberger Serv Petrol	1,561,592	Seward, D	1,561,337	Sherrit, S	1,561,692
Schlumberger Serv Petrol	1,561,594	Seymour, N	1,561,445	Shi, C	1,561,699
Schlumberger Serv Petrol	1,561,618	Sfax Nat Sch Engineering	1,561,391	Shi, G	1,561,177
Schlumberger Serv Petrol	1,561,624	Shaanxi Univ Sci & Technol	1,561,758	Shi, Q	1,561,242
Schlumberger Serv Petrol	1,561,627	Shah, J	1,561,566	Shi, W	1,561,240
Schlumberger Serv Petrol	1,561,629	Shah, N	1,561,192	Shi, W	1,561,651
Schlumberger Serv Petrol	1,561,636	Shaiek, S	1,561,786	Shi, X	1,561,242
Schlumberger Serv Petrol	1,561,664	Shaikh, A J	1,561,600	Shi, Y	1,561,651
Schlumberger Serv Petrol	1,561,743	Shakeel, A	1,561,579	Shi, Y	1,561,755
Schlumberger Serv Petrol	1,561,768	Shan, T	1,561,808	Shi, Z	1,561,121
Schlumberger Serv Petrol	1,561,875	Shan, X	1,561,378	Shi, Z	1,561,217
Schlumberger Serv Petrol	1,561,876	Shandong Power Eng Co Ltd	1,561,729	Shi, Z	1,561,403
Schlumberger Serv Petrol	1,561,878	Shandong Univ	1,561,367	Shi, Z	1,561,819
Schlumberger Serv Petrol	1,561,884	Shandong Univ	1,561,536	Shi, Z W	1,561,301
Schlumberger Technol BV	1,561,592	Shandong Univ	1,561,582	Shillito, A P	1,561,164
Schlumberger Technol BV	1,561,618	Shandong Univ Sci Technol	1,561,251	Shinn, Y J	1,561,207
Schlumberger Technol BV	1,561,624	Shandong Univ Sci Technol	1,561,356	Shiraishi, F	1,561,191
Schlumberger Technol BV	1,561,627	Shandong Univ Sci Technol	1,561,659	Shirley, B	1,561,142
Schlumberger Technol BV	1,561,629	Shandong Univ Sci Technol	1,561,755	Shirley, B	1,561,343
Schlumberger Technol BV	1,561,636	Shandong Univ Sci Technol	1,561,870	Shirota, A	1,561,447
Schlumberger Technol BV	1,561,664	Shang, J	1,561,108	Shragge, J	1,561,501
Schlumberger Technol BV	1,561,743	Shang, J	1,561,735	Shragge, J	1,561,504
Schlumberger Technol Corp	1,561,592	Shang, X	1,561,745	Shragge, J	1,561,527
Schlumberger Technol Corp	1,561,594	Shang, Y	1,561,656	Shragge, J	1,561,528
Schlumberger Technol Corp	1,561,618	Shanghai Jiao Tong Univ	1,561,539	Shu, H	1,561,326
Schlumberger Technol Corp	1,561,624	Shanghai Jiao Tong Univ	1,561,699	Shui, B	1,561,807
Schlumberger Technol Corp	1,561,627	Shanghai Maritime Univ	1,561,681	Shumway, W	1,561,721
Schlumberger Technol Corp	1,561,629	Shanghai Maritime Univ	1,561,802	Sichuan Agricultural Univ	1,561,843
Schlumberger Technol Corp	1,561,636	Shanghai Maritime Univ	1,561,818	Sichuan Univ	1,561,843
Schlumberger Technol Corp	1,561,664	Shanghai Maritime Univ	1,561,869	Sickmann, Z T	1,561,263
Schlumberger Technol Corp	1,561,743	Shanghai Univ	1,561,729	Siddorn, J	1,561,888
Schlumberger Technol Corp	1,561,768	Shanghai Univ Sci Technol	1,561,862	Siemens Energy AG	1,561,864
Schlumberger Technol Corp	1,561,875	Shantou Univ	1,561,754	Silva, D C	1,561,597
Schlumberger Technol Corp	1,561,876	Shanxi Geo-Environ Ctr	1,561,317	Silva, E	1,561,442
Schlumberger Technol Corp	1,561,878	Shao, B	1,561,796	Silva, M F	1,561,124
Schlumberger Technol Corp	1,561,884	Shao, G	1,561,858	Silva, P	1,561,534
Schlunegger, F	1,561,182	Shao, L	1,561,374	Silva, R B	1,561,432
Schmidtke, C	1,561,631	Shao, X	1,561,106	Silva, R L	1,561,346
Schmitt, S	1,561,538	Sharif Univ Technology	1,561,777	Silverio, G	1,561,145
Schmitz, L	1,561,880	Sharma, A	1,561,191	Silvestre-Albero, J	1,561,640
Schneider, J	1,561,164	Sharma, R	1,561,743	Silvestrov, I	1,561,495

Sima, L	1,561,307	Southern Univ Sci Technol	1,561,256	Su, W	1,561,806
Simmons, J	1,561,426	Southern Univ Sci Technol	1,561,473	Su, X	1,561,367
Simmons, J	1,561,438	Southwest Petroleum Univ	1,561,235	Su, Y	1,561,251
Simon Fraser Univ	1,561,331	Southwest Petroleum Univ	1,561,267	Su, Y	1,561,659
Simon Fraser Univ	1,561,368	Southwest Petroleum Univ	1,561,276	Su, Y	1,561,725
Simos, A N	1,561,700	Southwest Petroleum Univ	1,561,289	Suan, G	1,561,404
Singapore LNG Corp Pte Ltd	1,561,676	Southwest Petroleum Univ	1,561,307	Subbiah, S K	1,561,878
Singh, H	1,561,528	Southwest Petroleum Univ	1,561,357	Subsea 7	1,561,669
Sinopec	1,561,159	Southwest Petroleum Univ	1,561,373	Subudhi, B	1,561,647
Sinopec	1,561,198	Southwest Petroleum Univ	1,561,451	Suc, J P	1,561,135
Sinopec	1,561,213	Southwest Petroleum Univ	1,561,551	Sui, Y	1,561,656
Sinopec	1,561,305	Southwest Petroleum Univ	1,561,599	Sui, Z	1,561,813
Sinopec	1,561,779	Southwest Petroleum Univ	1,561,608	Sulaiman, S	1,561,429
Sinopec Int Petrol Corp	1,561,326	Southwest Petroleum Univ	1,561,661	Sultan Qaboos Univ	1,561,248
Sinopec Research Inst	1,561,198	Southwest Petroleum Univ	1,561,704	Sultan Qaboos Univ	1,561,249
Sinopec Research Inst	1,561,223	Southwest Petroleum Univ	1,561,762	Sumiko Rscs Explor & Dev	1,561,447
Sinopec Research Inst	1,561,254	Southwest Univ Sci Technol	1,561,847	Sumitomo Metal Co Ltd	1,561,447
Sinopec Research Inst	1,561,327	Souza, J	1,561,442	Sun, B	1,561,326
Sinopec Research Inst	1,561,759	Souza, J A B	1,561,285	Sun, C	1,561,333
Sinopec Research Inst	1,561,779	Souza Junior, F G	1,561,601	Sun, D	1,561,582
Sinopec Shengli Oil Co	1,561,463	Souza, M	1,561,521	Sun, G	1,561,185
Sitaworawet, P	1,561,863	Souza, M I L	1,561,724	Sun, G	1,561,259
Siveter, D J	1,561,197	Souza, R	1,561,532	Sun, G	1,561,739
Siveter, D J	1,561,345	S&P Global	1,561,835	Sun, H	1,561,424
Skelton, P W	1,561,266	Spano, A	1,561,841	Sun, H	1,561,454
Skivington, G	1,561,786	Speglich, J	1,561,509	Sun, H	1,561,536
Skopljak, F	1,561,117	Speglich, J	1,561,521	Sun, J	1,561,476
Skovsted, C	1,561,113	Speijer, R P	1,561,219	Sun, J	1,561,515
Skovsted, C	1,561,226	Spencer, B M	1,561,114	Sun, L	1,561,208
Slapnicar, V	1,561,688	Sperandio, E	1,561,521	Sun, L	1,561,540
Slater, B J	1,561,174	Sperling, E A	1,561,247	Sun, L	1,561,657
Slater, S M	1,561,372	SPH Engineering	1,561,436	Sun, M	1,561,731
Slob, E	1,561,433	Spire Engineering	1,561,687	Sun, N C	1,561,244
Slovenia Geological Survey	1,561,117	Split Univ	1,561,814	Sun, Q	1,561,582
Slovenia Geological Survey	1,561,311	Spong, R	1,561,687	Sun, Q	1,561,782
Smirnov, K	1,561,493	Sridhar, G	1,561,878	Sun, R	1,561,177
Smithson, T	1,561,342	Srinivasan, A	1,561,492	Sun, S	1,561,365
Smithson, T R	1,561,292	Srivastava, A	1,561,488	Sun, W	1,561,817
Snihur, K N	1,561,846	Srivastava, R K	1,561,859	Sun, X	1,561,789
Snyder, D	1,561,424	St Francis Xavier Univ	1,561,137	Sun, Y	1,561,236
Snyder, D	1,561,425	St Petersburg Marine Univ	1,561,804	Sun, Y	1,561,554
Snyder, D	1,561,490	St Petersburg State Univ	1,561,302	Sun, Y	1,561,731
Soares, C G	1,561,667	Stassen, P	1,561,219	Sun, Y	1,561,802
Sobhana, R	1,561,586	State Key Laboratory China	1,561,215	Sun Yat-sen Univ	1,561,540
Sofia Univ	1,561,684	State Key Laboratory China	1,561,306	Sun Yat-sen Univ	1,561,889
Solovyeva, V	1,561,744	State Key Laboratory China	1,561,582	Sun, Z	1,561,099
Somerville, I	1,561,103	State Key Laboratory China	1,561,757	Sunwin Intelligent Co Ltd	1,561,817
Son, S	1,561,853	State Key Laboratory China	1,561,776	Surge, D	1,561,349
Song, A	1,561,796	Stavanger Univ	1,561,861	Swedish Museum	1,561,135
Song, B	1,561,274	Stebbins, A	1,561,221	Swedish Museum	1,561,226
Song, C	1,561,276	Steel Space Drilling Ltd	1,561,585	Swedish Museum	1,561,325
Song, C	1,561,531	Steenmans, P	1,561,122	Swennen, R	1,561,760
Song, G	1,561,654	Steffen, R	1,561,427	Swenson, B	1,561,629
Song, G	1,561,796	Stepanek, C	1,561,389	Szabalyozott Tevekenysegek	1,561,415
Song, J	1,561,701	Stephane, O	1,561,441	Szekely, G	1,561,871
Song, J	1,561,740	Stevens, R F	1,561,711	Szlapeczynska, J	1,561,815
Song, J	1,561,882	Stewart, E M	1,561,111	Taboada, V M	1,561,428
Song, L	1,561,774	Stibbe, H C	1,561,736	Tachikawa, K	1,561,109
Song, Y Y	1,561,642	Stock, G	1,561,476	Tafur, M F	1,561,629
Song, Z	1,561,775	Stocker, C P	1,561,197	Tait, N	1,561,350
Songploy, S	1,561,863	Stokes, S	1,561,439	Taiyuan Univ Technology	1,561,850
Sorbonne Univ	1,561,128	Stowell, H H	1,561,114	Taiz Univ	1,561,397
Sorbonne Univ	1,561,894	Strauss, H	1,561,221	Tajikistan Academy Science	1,561,262
South China Sea Inst Ocean	1,561,892	Strauss, J V	1,561,329	Takeuchi, M	1,561,184
South China Univ Technol	1,561,621	Streng, M	1,561,120	Taleblian, S H	1,561,765
South China Univ Technol	1,561,713	Strogen, D P	1,561,337	Talha Qadri, S M	1,561,397
South China Univ Technol	1,561,728	Strotz, L	1,561,350	Tan, G	1,561,463
South China Univ Technol	1,561,823	Struck, U	1,561,104	Tan, S	1,561,423
South Florida Univ	1,561,866	Stukins, S	1,561,165	Tan, Z	1,561,554
Southampton Oceanogr Ctr	1,561,888	Su, C	1,561,713	Tanaka, G	1,561,197
Southampton Univ	1,561,219	Su, D X	1,561,750	Tang, C	1,561,650
Southeast Univ	1,561,796	Su, H	1,561,870	Tang, D	1,561,242
Southern California Univ	1,561,316	Su, P	1,561,108	Tang, H	1,561,267

Tang, H	1,561,314	Tomson Technologies LLC	1,561,639	Vajda, V	1,561,118
Tang, W	1,561,484	Tong, D	1,561,107	Vajda, V	1,561,119
Tang, X	1,561,377	Tong, L	1,561,660	Valcarce, G Z	1,561,761
Tang, Y	1,561,354	Tongji Univ	1,561,133	Valencia Univ	1,561,141
Tangshan Ship Tech Co Ltd	1,561,567	Tongji Univ	1,561,400	Valentine, A	1,561,349
Tao, B	1,561,537	Tongji Univ	1,561,403	Valiente, N G	1,561,888
Tao, L	1,561,466	Tongji Univ	1,561,466	Vallourec Oil & Gas France	1,561,589
Tao, R	1,561,867	Tongji Univ	1,561,548	Valverde, G R	1,561,321
Tao, Y	1,561,732	Topper, T P	1,561,113	Van Bakel, B	1,561,169
Tao, Z	1,561,257	Topper, T P	1,561,350	van Dalfsen, J	1,561,839
Tarim Oilfield Co	1,561,206	Topuz, F	1,561,871	van de Ven, D	1,561,822
Tata Inst Fundamental Res	1,561,518	Torino Univ	1,561,887	van Eeden, F	1,561,893
Tata Steel Ltd	1,561,604	Toronto Univ	1,561,227	Van Nguyen, V	1,561,319
Tateo, F	1,561,158	Toronto Univ	1,561,250	Van Roy, P	1,561,382
Tavares, F W	1,561,771	Torres De La Cruz, J G	1,561,581	van Tha, H	1,561,370
Taverna, M E	1,561,590	Torsvik, T H	1,561,288	van Wijk, J W	1,561,098
Tcholakova, S	1,561,684	Tosca, N J	1,561,329	Vanaverbeke, J	1,561,842
Tehran Univ	1,561,441	Tosi, L P	1,561,692	Vandenbroucke, T R A	1,561,399
Tehran Univ	1,561,503	Tran, C C	1,561,809	Vanderbilt Univ	1,561,227
Tekleva, M	1,561,216	Trentesaux, A	1,561,336	Vanderbilt Univ	1,561,232
Tengizchevroil	1,561,541	Trieste Univ	1,561,096	Vanderhaeghe, O	1,561,196
Tengizchevroil	1,561,542	Trieste Univ	1,561,308	VanderLeest, R A	1,561,263
Tenzer, R	1,561,427	Trieste Univ	1,561,324	Vanstone, L	1,561,560
Tertyshnikov, K	1,561,552	Trindade, R I	1,561,124	Vanzuilekom, A H	1,561,752
Tew, K S	1,561,886	Trinity Coll, Dublin	1,561,299	Vargas, D	1,561,496
Texas A&M Univ	1,561,401	Trinity Coll, Dublin	1,561,346	Vargas, D	1,561,510
Texas A&M Univ	1,561,422	Troch, P	1,561,893	Vasconcelos, D L	1,561,285
Texas Univ, Arlington	1,561,117	Trodden, D	1,561,734	Vasconcelos, I	1,561,510
Texas Univ, Arlington	1,561,167	Trofimuk Inst	1,561,302	Vaucher, R	1,561,331
Texas Univ, Austin	1,561,263	Tromba, G	1,561,272	Vazquez Carrizo, C	1,561,565
Texas Univ, Austin	1,561,352	Tsau, J S	1,561,598	Vazquez-Ortega, A	1,561,100
Texas Univ, Austin	1,561,511	Tsingas, C	1,561,464	Vdovina, T	1,561,424
Texas Univ, Austin	1,561,512	Tsinghua Univ	1,561,506	Veidt, M	1,561,689
Texas Univ, Austin	1,561,790	Tsukuba Univ	1,561,828	Velki, M	1,561,415
TGS	1,561,439	Tsvankin, I	1,561,528	Vendrasco, M J	1,561,175
TGS	1,561,470	Tu, Y	1,561,858	Venkataramana, K	1,561,821
TGS	1,561,471	Tuan, D M	1,561,370	Verbeurgt, J	1,561,893
TGS	1,561,476	Tuebingen Univ	1,561,389	Verde, W M	1,561,663
TGS	1,561,478	Tuha Drilling Co	1,561,599	Vergara, L	1,561,663
TGS	1,561,543	Tuha Oilfield Co	1,561,757	Verschuur, E	1,561,440
TGS	1,561,550	Tulane Univ	1,561,753	Verschuur, E	1,561,467
Thaemlitz, C	1,561,572	Tulsa Univ	1,561,546	Vertechs Oil & Gas Co Ltd	1,561,788
Thakur, R K	1,561,624	Tunisian National Oil Co	1,561,391	Vessey, C J	1,561,846
Thebaud, N	1,561,196	Turk, K A	1,561,227	Vick, J D Jr	1,561,706
Theurer, T	1,561,105	Turnbull, I M	1,561,234	Victoria Univ	1,561,351
Thiery, G	1,561,224	Twigg, J	1,561,439	Victoria Univ, BC	1,561,344
Thigpen, J R	1,561,114	Twitchett, R J	1,561,188	Victoria Univ, Wellington	1,561,337
Thompson, C	1,561,687	Ueno, Y	1,561,408	Vidal, A C	1,561,290
Thorson, A M	1,561,161	Ukraine State Univ	1,561,571	Vidan, P	1,561,814
Three Gorges Navigation	1,561,812	Ullmann, C V	1,561,104	Vienna Univ	1,561,325
Thu, H L T	1,561,319	Ulrich, S	1,561,325	Vienna Univ	1,561,343
Thurumella, H	1,561,851	Umea Univ	1,561,202	Vietnam National Univ	1,561,427
Tian, B	1,561,567	UMR-CNRS	1,561,224	Vietnam National Univ	1,561,809
Tian, J	1,561,400	UMR-CNRS	1,561,225	Viglietti, P A	1,561,202
Tian, J	1,561,413	UMR-CNRS	1,561,399	Villada, Y	1,561,578
Tian, K	1,561,237	UMR-CNRS	1,561,690	Villada, Y	1,561,590
Tian, S	1,561,858	und Polach, F B	1,561,880	Villier, L	1,561,128
Tian, Y	1,561,435	Underwood, C J	1,561,165	Vinogradov, J	1,561,894
Tianjin Research Inst	1,561,691	Underwood, L D	1,561,560	Vinta, B	1,561,875
Tianjin Univ	1,561,718	Unger, D	1,561,430	Vinta, B	1,561,876
Tianjin Univ	1,561,725	Universalmuseum Joanneum	1,561,325	Vinta, B	1,561,884
Tianjin Univ	1,561,824	Uppsala Univ	1,561,120	Vinther, J	1,561,268
Tileugabylov, A	1,561,136	Uppsala Univ	1,561,174	Virginia Tech	1,561,263
Tims, J F	1,561,692	Uppsala Univ	1,561,218	Vittur, B M	1,561,799
Tims, J F	1,561,881	Uppsala Univ	1,561,350	Vrbaski, S	1,561,272
Tinnin, T	1,561,628	Upton, G	1,561,834	Vuksa, S	1,561,814
Tkachenko, I	1,561,571	US Geological Survey	1,561,142	Wageningen Marine Res	1,561,842
Tocantins, J P	1,561,565	US Geological Survey	1,561,219	Waheed, U B	1,561,531
Tokyo Inst Technol	1,561,408	US Geological Survey	1,561,286	Waikato Univ	1,561,245
Tokyo Univ	1,561,191	US Geological Survey	1,561,399	Wakin, M	1,561,498
Toledo Filho, R D	1,561,601	Utrecht Univ	1,561,343	Walerianczyk, T J	1,561,585
Tomas, A	1,561,794	Utrecht Univ	1,561,496	Wallace, M W	1,561,095
Tomson, R	1,561,639	Utrecht Univ	1,561,510	Wallet, E	1,561,174

Author and Affiliation Index

Walther, B	1,561,629	Wang, P	1,561,866	Watson, A I	1,561,664
Wan, J	1,561,646	Wang, Q	1,561,508	Weatherford Technology LLC	1,561,609
Wan, S	1,561,187	Wang, Q	1,561,608	Weber, B	1,561,134
Wan, X	1,561,558	Wang, Q	1,561,774	Wedlake, G O	1,561,329
Wan, X	1,561,558	Wang, R	1,561,301	Wei, B	1,561,482
Wan, X	1,561,587	Wang, S	1,561,115	Wei, C	1,561,199
Wan, Y	1,561,276	Wang, S	1,561,185	Wei, C	1,561,740
Wan, Z	1,561,108	Wang, S	1,561,206	Wei, C	1,561,818
Wanderley Neto, A O	1,561,597	Wang, S	1,561,306	Wei, D	1,561,103
Wang, A	1,561,130	Wang, S	1,561,484	Wei, G	1,561,892
Wang, B	1,561,130	Wang, S	1,561,731	Wei, H	1,561,276
Wang, B	1,561,470	Wang, S	1,561,892	Wei, N	1,561,729
Wang, B	1,561,476	Wang, W	1,561,193	Wei, S	1,561,561
Wang, B	1,561,482	Wang, W	1,561,208	Wei, T	1,561,686
Wang, B	1,561,613	Wang, W	1,561,463	Wei, W	1,561,319
Wang, B	1,561,833	Wang, W M	1,561,170	Wei, W	1,561,364
Wang, B	1,561,846	Wang, X	1,561,178	Wei, W	1,561,682
Wang, C	1,561,230	Wang, X	1,561,243	Wei, X	1,561,198
Wang, C	1,561,274	Wang, X	1,561,354	Wei, X	1,561,359
Wang, C	1,561,652	Wang, X	1,561,371	Wei, Y	1,561,809
Wang, D	1,561,151	Wang, X	1,561,681	Wellman, C H	1,561,372
Wang, D	1,561,646	Wang, X	1,561,733	Welltec A/S	1,561,595
Wang, F	1,561,252	Wang, X	1,561,746	Welltec A/S	1,561,610
Wang, F	1,561,725	Wang, X	1,561,776	Wen, J	1,561,854
Wang, F	1,561,784	Wang, X	1,561,778	Wen, L	1,561,334
Wang, G	1,561,326	Wang, X	1,561,778	Wen, Q	1,561,379
Wang, G	1,561,339	Wang, X	1,561,797	Wen, Y	1,561,817
Wang, G	1,561,355	Wang, Y	1,561,166	Werkheiser, G T	1,561,685
Wang, G	1,561,359	Wang, Y	1,561,211	Werner, D	1,561,822
Wang, G	1,561,381	Wang, Y	1,561,223	Werner, M	1,561,389
Wang, G	1,561,431	Wang, Y	1,561,228	Western Sydney Univ	1,561,696
Wang, H	1,561,210	Wang, Y	1,561,319	Western Sydney Univ	1,561,824
Wang, H	1,561,243	Wang, Y	1,561,341	Westfaelische Wilhelm Univ	1,561,284
Wang, H	1,561,375	Wang, Y	1,561,371	Whittle, R J	1,561,293
Wang, H	1,561,423	Wang, Y	1,561,384	Wichern, N	1,561,284
Wang, H	1,561,459	Wang, Y	1,561,402	Wicklund & Associates	1,561,837
Wang, H	1,561,492	Wang, Y	1,561,420	Wicklund, J K	1,561,837
Wang, H	1,561,548	Wang, Y	1,561,619	Wiecek, B	1,561,751
Wang, H	1,561,682	Wang, Y	1,561,620	Wiedenbeck, M	1,561,104
Wang, H	1,561,718	Wang, Y	1,561,656	Wiederkehr, M	1,561,182
Wang, H	1,561,776	Wang, Y	1,561,740	Wignall, P B	1,561,277
Wang, H	1,561,801	Wang, Y	1,561,753	Wignall, P B	1,561,293
Wang, H	1,561,803	Wang, Y	1,561,759	Wignall, P B	1,561,323
Wang, H	1,561,808	Wang, Y	1,561,774	Wilby, P R	1,561,268
Wang, H	1,561,889	Wang, Y	1,561,789	Wilde, V	1,561,181
Wang, J	1,561,106	Wang, Y	1,561,797	Wildman, M R	1,561,673
Wang, J	1,561,166	Wang, Y	1,561,801	Wildman, S L Sr	1,561,673
Wang, J	1,561,200	Wang, Y	1,561,803	Wildman, W D	1,561,673
Wang, J	1,561,206	Wang, Y	1,561,843	Wilkinson, D	1,561,727
Wang, J	1,561,524	Wang, Z	1,561,107	Williams, M	1,561,197
Wang, J	1,561,536	Wang, Z	1,561,172	Williams, M	1,561,342
Wang, J	1,561,540	Wang, Z	1,561,215	Williams, M	1,561,345
Wang, J	1,561,607	Wang, Z	1,561,267	Williams, M	1,561,349
Wang, J	1,561,607	Wang, Z	1,561,333	Willman, S	1,561,174
Wang, K	1,561,710	Wang, Z	1,561,416	Wilson, S A	1,561,846
Wang, L	1,561,121	Wang, Z	1,561,444	Winguth, A	1,561,118
Wang, L	1,561,307	Wang, Z	1,561,682	Winguth, A	1,561,119
Wang, L	1,561,433	Wang, Z	1,561,714	Winguth, C	1,561,118
Wang, L	1,561,648	Wang, Z	1,561,746	Winguth, C	1,561,119
Wang, L	1,561,659	Wang, Z	1,561,812	Winklbauer, M	1,561,631
Wang, L	1,561,791	Wang, Z	1,561,818	Witts, J D	1,561,293
Wang, L	1,561,802	Wang, Z	1,561,825	Witts, J D	1,561,393
Wang, L W	1,561,369	Wang, Z	1,561,869	Wlodarczyk, S	1,561,594
Wang, M	1,561,546	Wapenaar, K	1,561,465	Wo, Y	1,561,551
Wang, M	1,561,661	Ward, A E M	1,561,165	Wolferstetter, L	1,561,631
Wang, M	1,561,757	Ward, D J	1,561,165	Woo, D	1,561,844
Wang, M	1,561,790	Warnock, R C M	1,561,271	Wood Envir Infrastructure	1,561,872
Wang, M	1,561,870	Warren, X	1,561,141	Wood plc	1,561,845
Wang, N	1,561,251	Warsaw Univ	1,561,370	Worley, J E	1,561,683
Wang, P	1,561,313	Warsaw Univ	1,561,405	Wu, B	1,561,602
Wang, P	1,561,746	Warsaw Univ Technology	1,561,698	Wu, C	1,561,554
Wang, P	1,561,780	Waseda Univ	1,561,348	Wu, F	1,561,484
Wang, P	1,561,862	Waskom, M	1,561,275	Wu, G	1,561,769

Author and Affiliation Index

Wu, G	1,561,802	Xie, J	1,561,892	Yanfang, Z	1,561,486
Wu, H	1,561,298	Xie, P	1,561,387	Yang, B	1,561,473
Wu, H	1,561,728	Xie, Q	1,561,774	Yang, C	1,561,471
Wu, H	1,561,760	Xie, S	1,561,833	Yang, D	1,561,620
Wu, H	1,561,818	Xie, T	1,561,847	Yang, F	1,561,739
Wu, J	1,561,740	Xijing Univ	1,561,641	Yang, F	1,561,852
Wu, K	1,561,187	Xing, T	1,561,444	Yang, G	1,561,384
Wu, K	1,561,482	Xinjiang Oilfield Res Inst	1,561,354	Yang, H	1,561,317
Wu, L	1,561,177	Xiong, B	1,561,434	Yang, H	1,561,545
Wu, L	1,561,257	Xiong, Z	1,561,473	Yang, H	1,561,784
Wu, L	1,561,694	Xu, B	1,561,796	Yang, H	1,561,808
Wu, N	1,561,435	Xu, B	1,561,796	Yang, H	1,561,889
Wu, P	1,561,654	Xu, C	1,561,160	Yang, J	1,561,199
Wu, Q	1,561,185	Xu, C	1,561,378	Yang, J	1,561,364
Wu, Q	1,561,410	Xu, C	1,561,792	Yang, J	1,561,402
Wu, R S	1,561,466	Xu, F	1,561,789	Yang, J	1,561,515
Wu, S	1,561,152	Xu, G	1,561,776	Yang, K	1,561,541
Wu, S	1,561,154	Xu, G	1,561,778	Yang, K	1,561,542
Wu, S	1,561,163	Xu, H	1,561,407	Yang, L	1,561,187
Wu, W	1,561,506	Xu, H	1,561,715	Yang, L	1,561,715
Wu, X	1,561,179	Xu, H	1,561,733	Yang, M	1,561,782
Wu, X	1,561,215	Xu, H	1,561,843	Yang, P	1,561,668
Wu, X	1,561,277	Xu, J	1,561,256	Yang, R	1,561,148
Wu, X	1,561,420	Xu, J	1,561,341	Yang, R	1,561,356
Wu, X	1,561,506	Xu, J	1,561,508	Yang, S	1,561,251
Wu, X	1,561,705	Xu, J	1,561,515	Yang, S	1,561,354
Wu, Y	1,561,156	Xu, M	1,561,889	Yang, S	1,561,411
Wu, Y	1,561,214	Xu, P	1,561,482	Yang, S	1,561,757
Wu, Y	1,561,482	Xu, T	1,561,702	Yang, X	1,561,608
Wu, Y	1,561,611	Xu, W	1,561,346	Yang, X	1,561,722
Wu, Y	1,561,847	Xu, X	1,561,729	Yang, X	1,561,843
Wu, Z	1,561,210	Xu, X	1,561,862	Yang, X Q	1,561,750
Wu, Z	1,561,451	Xu, Y	1,561,259	Yang, Y	1,561,166
Wu, Z	1,561,707	Xu, Y	1,561,274	Yang, Y	1,561,170
Wuhan Univ	1,561,654	Xu, Y	1,561,722	Yang, Y	1,561,211
Wuhan Univ Technology	1,561,805	Xu, Y	1,561,735	Yang, Y	1,561,296
Wuhan Univ Technology	1,561,807	Xu, Y	1,561,774	Yang, Y	1,561,297
Wuhan Univ Technology	1,561,812	Xu, Y	1,561,852	Yang, Y	1,561,459
Wuhan Univ Technology	1,561,813	Xu, Z	1,561,154	Yang, Y	1,561,477
Wuhan Univ Technology	1,561,817	Xu, Z	1,561,507	Yang, Y	1,561,536
Wuhan Univ Technology	1,561,819	Xu, Z	1,561,558	Yang, Y	1,561,537
Wuhan Univ Technology	1,561,890	Xu, Z	1,561,582	Yang, Y	1,561,641
Wuxi Inst Technology	1,561,806	Xu, Z	1,561,587	Yang, Y	1,561,651
Wysocka, A	1,561,370	Xu, Z	1,561,749	Yang, Y	1,561,652
Xavier-de-Souza, S	1,561,522	Xu, Z J	1,561,244	Yang, Y	1,561,702
Xcalibur Multiphysics	1,561,447	Xuan, K	1,561,856	Yang, Y	1,561,770
Xi, K	1,561,380	Xuan, P	1,561,892	Yang, Z	1,561,159
Xi, Y	1,561,519	Xue, C	1,561,144	Yang, Z	1,561,252
Xia, G	1,561,237	Xue, J	1,561,608	Yang, Z	1,561,256
Xia, J	1,561,704	Xue, J	1,561,650	Yang, Z	1,561,367
Xia, M	1,561,735	Xue, L	1,561,121	Yang, Z	1,561,473
Xia, W	1,561,773	Xue, M	1,561,421	Yang, Z	1,561,558
Xia, X	1,561,739	Xue, R	1,561,213	Yang, Z	1,561,587
Xia, Y	1,561,660	Yabuta, S	1,561,184	Yang, Z	1,561,661
Xia, Z	1,561,186	Yahnker, C	1,561,692	Yangtze Univ	1,561,154
Xiamen Univ	1,561,654	Yakovlev, I	1,561,493	Yangtze Univ	1,561,251
Xi'an Jiaotong Univ	1,561,416	Yale Univ	1,561,140	Yangtze Univ	1,561,300
Xi'an Jiaotong Univ	1,561,526	Yale Univ	1,561,194	Yangtze Univ	1,561,309
Xi'an Jiaotong Univ	1,561,530	Yamada, T	1,561,345	Yangtze Univ	1,561,489
Xi'an Jiaotong Univ	1,561,745	Yamada, T	1,561,848	Yangtze Univ	1,561,619
Xi'an Shiyou Univ	1,561,252	Yamashita, Y	1,561,828	Yangtze Univ	1,561,626
Xi'an Shiyou Univ	1,561,679	Yan, B	1,561,358	Yangzhou Univ	1,561,652
Xi'an Univ Architecture	1,561,650	Yan, D	1,561,375	Yantai Jereh Petrol Co Ltd	1,561,606
Xi'an Univ Sci & Technol	1,561,253	Yan, D	1,561,701	Yantai Jereh Petrol Co Ltd	1,561,607
Xiang, B	1,561,827	Yan, G	1,561,359	Yantai Jereh Petrol Co Ltd	1,561,612
Xiang, W	1,561,860	Yan, G	1,561,658	Yantai Jereh Petrol Co Ltd	1,561,613
Xiang, Y	1,561,458	Yan, K	1,561,811	Yantai Jereh Petrol Co Ltd	1,561,614
Xiao, G	1,561,661	Yan, P	1,561,755	Yao, B	1,561,739
Xiao, G	1,561,823	Yan, S	1,561,809	Yao, C	1,561,708
Xiao, J	1,561,671	Yan, X	1,561,254	Yao, S	1,561,160
Xiao, W	1,561,722	Yan, X	1,561,687	Yao, W	1,561,729
Xiao, Y	1,561,791	Yan, Y	1,561,333	Yao, X	1,561,833
Xie, D	1,561,788	Yan, Y	1,561,679	Yao, Y	1,561,479

Author and Affiliation Index

Yao, Y	1,561,760	Yusuf, T I	1,561,636	Zhang, J	1,561,163
Yaoude Univ	1,561,427	Zachariah, D	1,561,672	Zhang, J	1,561,421
Yarranton, H W	1,561,741	Zachos, J C	1,561,219	Zhang, J	1,561,455
Ye, Q	1,561,806	ZAG Consulting	1,561,478	Zhang, J	1,561,484
Ye, X	1,561,115	Zagreb Univ	1,561,117	Zhang, J	1,561,641
Ye, X	1,561,354	Zagreb Univ	1,561,415	Zhang, J	1,561,642
Ye, Y	1,561,602	Zagreb Univ	1,561,688	Zhang, J	1,561,650
Ye, Z	1,561,665	Zagreb Univ	1,561,814	Zhang, J	1,561,769
Yeates, D W	1,561,161	Zalan, P V	1,561,478	Zhang, J	1,561,776
Yfantis, E A	1,561,865	Zammuto, V	1,561,841	Zhang, J	1,561,824
Yi, H	1,561,237	Zand, T	1,561,503	Zhang, J	1,561,884
Yi, J	1,561,378	Zang, C	1,561,797	Zhang, K	1,561,437
Yi, J	1,561,626	Zang, Z	1,561,824	Zhang, K	1,561,541
Yi, J	1,561,670	Zaszewski, D	1,561,370	Zhang, K	1,561,542
Yi, J T	1,561,714	Zeeden, C	1,561,331	Zhang, L	1,561,115
Yi, M	1,561,411	Zein El-Din, T	1,561,677	Zhang, L	1,561,333
Yi, P	1,561,620	Zeng, D	1,561,879	Zhang, L	1,561,341
Yilmaz, O	1,561,502	Zeng, F	1,561,691	Zhang, L	1,561,508
Yin, C	1,561,434	Zeng, H	1,561,626	Zhang, L	1,561,544
Yin, H	1,561,252	Zeng, J	1,561,373	Zhang, L	1,561,586
Yin, K	1,561,274	Zeng, Q	1,561,788	Zhang, L	1,561,774
Yin, L	1,561,769	Zeng, Q Z	1,561,750	Zhang, L	1,561,784
Yin, Q	1,561,735	Zeng, S	1,561,276	Zhang, L	1,561,789
Yin, R	1,561,392	Zeng, X	1,561,130	Zhang, M	1,561,277
Yin, S	1,561,300	Zeng, X	1,561,177	Zhang, M	1,561,473
Yin, X	1,561,519	Zeng, X	1,561,735	Zhang, M	1,561,619
Yin, X	1,561,769	Zeng, X	1,561,852	Zhang, M	1,561,862
Yin, Z Y	1,561,703	Zeng, Y	1,561,875	Zhang, N	1,561,691
Yinson Production	1,561,861	Zeng, Y	1,561,876	Zhang, N	1,561,806
Yobo, L N	1,561,401	Zeng, Y	1,561,884	Zhang, P	1,561,130
Yong, S G	1,561,131	Zeng, Z	1,561,856	Zhang, P	1,561,251
Yoo, J	1,561,480	Zetter, R	1,561,135	Zhang, P	1,561,479
Young, J R	1,561,165	Zetter, R	1,561,325	Zhang, P	1,561,606
Young, R T	1,561,140	Zeyen, N	1,561,846	Zhang, P	1,561,607
Yousef, A	1,561,747	Zhai, X	1,561,759	Zhang, P	1,561,773
Ysaccis, R	1,561,457	Zhan, B	1,561,648	Zhang, Q	1,561,133
Yu, D	1,561,808	Zhan, B	1,561,655	Zhang, Q	1,561,166
Yu, D G	1,561,862	Zhan, G	1,561,556	Zhang, Q	1,561,708
Yu, F	1,561,228	Zhan, G	1,561,557	Zhang, Q	1,561,749
Yu, F	1,561,229	Zhan, L	1,561,443	Zhang, Q	1,561,807
Yu, F	1,561,374	Zhan, L	1,561,763	Zhang, Q	1,561,833
Yu, F	1,561,376	Zhan, Y	1,561,890	Zhang, Q	1,561,879
Yu, H	1,561,517	Zhang, B	1,561,126	Zhang, R	1,561,607
Yu, J	1,561,107	Zhang, B	1,561,160	Zhang, S	1,561,198
Yu, J	1,561,229	Zhang, B	1,561,209	Zhang, S	1,561,243
Yu, J	1,561,725	Zhang, B	1,561,387	Zhang, S	1,561,298
Yu, J	1,561,757	Zhang, B	1,561,548	Zhang, S	1,561,387
Yu, L	1,561,627	Zhang, C	1,561,154	Zhang, S	1,561,614
Yu, Q	1,561,386	Zhang, C	1,561,335	Zhang, S	1,561,660
Yu, S	1,561,454	Zhang, C	1,561,371	Zhang, S	1,561,710
Yu, T	1,561,313	Zhang, C	1,561,642	Zhang, S	1,561,715
Yu, W	1,561,327	Zhang, C	1,561,738	Zhang, S	1,561,755
Yu, W	1,561,605	Zhang, C	1,561,760	Zhang, S	1,561,779
Yu, Y	1,561,283	Zhang, C	1,561,824	Zhang, S	1,561,795
Yu, Y	1,561,377	Zhang, D	1,561,306	Zhang, S	1,561,811
Yu, Y	1,561,423	Zhang, D	1,561,464	Zhang, S S	1,561,549
Yu, Y	1,561,712	Zhang, D	1,561,473	Zhang, T	1,561,366
Yu, Y	1,561,725	Zhang, D	1,561,733	Zhang, T	1,561,373
Yu, Z	1,561,535	Zhang, F	1,561,240	Zhang, T	1,561,412
Yuan, C	1,561,241	Zhang, F	1,561,315	Zhang, T	1,561,654
Yuan, D X	1,561,304	Zhang, F	1,561,354	Zhang, T	1,561,762
Yuan, W	1,561,371	Zhang, F	1,561,499	Zhang, W	1,561,108
Yuan, Y	1,561,242	Zhang, F	1,561,769	Zhang, W	1,561,213
Yuan, Y	1,561,750	Zhang, F	1,561,858	Zhang, W	1,561,254
Yuan, Y	1,561,758	Zhang, G	1,561,334	Zhang, W	1,561,341
Yuan, Y	1,561,758	Zhang, G	1,561,619	Zhang, W	1,561,434
Yue, D	1,561,152	Zhang, G	1,561,769	Zhang, W	1,561,482
Yue, H	1,561,185	Zhang, H	1,561,536	Zhang, W	1,561,822
Yue, X	1,561,451	Zhang, H	1,561,608	Zhang, X	1,561,373
Yufei, S	1,561,486	Zhang, H	1,561,722	Zhang, X	1,561,387
Yukhimets, D	1,561,645	Zhang, H	1,561,870	Zhang, X	1,561,431
Yun, L	1,561,126	Zhang, H	1,561,890	Zhang, X	1,561,473
Yurikov, A	1,561,552	Zhang, J	1,561,126	Zhang, X	1,561,649

Author and Affiliation Index

Zhang, X	1,561,773	Zhen, R	1,561,819	Zou, G	1,561,317
Zhang, Y	1,561,236	Zhen, Y Y	1,561,369	Zou, R	1,561,661
Zhang, Y	1,561,313	Zheng, C	1,561,177	Zou, Y	1,561,187
Zhang, Y	1,561,360	Zheng, D	1,561,334	Zucali, M	1,561,262
Zhang, Y	1,561,443	Zheng, D	1,561,654	Zuhlsdorff, L	1,561,460
Zhang, Y	1,561,454	Zheng, J	1,561,133	Zuo, S	1,561,708
Zhang, Y	1,561,526	Zheng, J	1,561,791		
Zhang, Y	1,561,705	Zheng, K	1,561,587		
Zhang, Y	1,561,705	Zheng, L	1,561,749		
Zhang, Y	1,561,806	Zheng, R	1,561,126		
Zhang, Y D	1,561,369	Zheng, S	1,561,779		
Zhang, Y Q	1,561,240	Zheng, W	1,561,722		
Zhang, Z	1,561,120	Zheng, Z	1,561,178		
Zhang, Z	1,561,218	Zheng, Z	1,561,294		
Zhang, Z	1,561,230	Zhilenkov, A	1,561,804		
Zhang, Z	1,561,278	Zhong, A	1,561,617		
Zhang, Z	1,561,350	Zhong, F	1,561,661		
Zhang, Z	1,561,380	Zhongyuan Oilfield Co	1,561,305		
Zhang, Z	1,561,387	Zhou, C	1,561,536		
Zhang, Z	1,561,421	Zhou, D	1,561,728		
Zhang, Z	1,561,561	Zhou, F	1,561,602		
Zhang, Z	1,561,643	Zhou, G	1,561,818		
Zhang, Z	1,561,659	Zhou, H	1,561,334		
Zhang, Z	1,561,729	Zhou, H	1,561,523		
Zhang, Z	1,561,801	Zhou, H	1,561,524		
Zhang, Z	1,561,830	Zhou, J	1,561,789		
Zhao, C	1,561,274	Zhou, J B	1,561,244		
Zhao, C	1,561,582	Zhou, L	1,561,879		
Zhao, C	1,561,869	Zhou, R	1,561,409		
Zhao, D	1,561,177	Zhou, S	1,561,236		
Zhao, D	1,561,185	Zhou, S	1,561,375		
Zhao, D	1,561,606	Zhou, S	1,561,620		
Zhao, D	1,561,612	Zhou, W	1,561,108		
Zhao, F Y	1,561,339	Zhou, W	1,561,655		
Zhao, H	1,561,106	Zhou, W	1,561,717		
Zhao, H	1,561,126	Zhou, X	1,561,599		
Zhao, H	1,561,305	Zhou, Y	1,561,106		
Zhao, H	1,561,315	Zhou, Y	1,561,407		
Zhao, H	1,561,454	Zhou, Y	1,561,409		
Zhao, H	1,561,636	Zhou, Y	1,561,620		
Zhao, J	1,561,444	Zhou, Y	1,561,795		
Zhao, J	1,561,812	Zhou, Y	1,561,867		
Zhao, K	1,561,294	Zhou, Z	1,561,858		
Zhao, L	1,561,416	Zhu, B	1,561,309		
Zhao, L	1,561,847	Zhu, B	1,561,846		
Zhao, M	1,561,611	Zhu, C	1,561,295		
Zhao, M	1,561,696	Zhu, C	1,561,770		
Zhao, M	1,561,824	Zhu, D	1,561,473		
Zhao, P	1,561,567	Zhu, F	1,561,316		
Zhao, S	1,561,778	Zhu, H	1,561,807		
Zhao, T	1,561,768	Zhu, J	1,561,151		
Zhao, W	1,561,444	Zhu, J	1,561,452		
Zhao, W	1,561,801	Zhu, J	1,561,485		
Zhao, X	1,561,235	Zhu, M	1,561,159		
Zhao, X	1,561,289	Zhu, M	1,561,817		
Zhao, X	1,561,802	Zhu, R	1,561,282		
Zhao, Y	1,561,334	Zhu, W	1,561,133		
Zhao, Y	1,561,489	Zhu, W	1,561,206		
Zhao, Z	1,561,435	Zhu, W	1,561,775		
Zhao, Z	1,561,546	Zhu, X	1,561,358		
Zhao, Z	1,561,739	Zhu, X	1,561,539		
Zhe, L	1,561,486	Zhu, Y X	1,561,339		
Zhejiang LBX Pump Ind Ltd	1,561,651	Zhu, Z	1,561,255		
Zhejiang Ocean Univ	1,561,882	Zhu, Z	1,561,694		
Zhejiang Petroleum Co Ltd	1,561,833	Zhuang, L	1,561,830		
Zhejiang Univ	1,561,466	Zhuang, X	1,561,135		
Zhejiang Univ	1,561,487	Ziauddin, M	1,561,636		
Zhejiang Univ	1,561,694	Zid, W	1,561,786		
Zhejiang Univ	1,561,717	Zong, K	1,561,366		
Zhejiang Univ	1,561,745	Zong, Z	1,561,769		
Zhejiang Univ	1,561,746	Zorina, S	1,561,287		
Zhejiang Univ	1,561,882	Zou, D	1,561,561		
Zhejiang Univ Sci Technol	1,561,732	Zou, D	1,561,803		

PUBLICATIONS COVERED IN THIS ISSUE

(Volume 63, Number 01

January 7, 2023

Abstract Nos. 1,561,095 - 1,561,894)

The numbers following the date of each publication are the last three digits of the abstract number assigned to each article selected from the publication.

American Journal Of Science (Sept. 2022) 126, 336	312, 313, 314, 318, 320, 331, 332, 333, 338, 341, 346, 353, 355, 356, 357, 361, 362, 363, 364, 365, 373, 374,
Applied Geochemistry (Aug. 2022) 375, 386, 411, 826, 846	376, 377, 378, 379, 380, 381, 390, 392, 394, 396, 400, 402, 403, 404, 405, 407, 410, 412, 413, 414
Carbon Capture Technology Expo - North America (Houston, TX, 6/14-15/2022) Proceedings 840	Journal Of Applied Geophysics (Dec. 2022) 116, 279, 315, 418, 434, 435, 451, 454, 473, 484, 489, 508, 535, 536, 547
Chemical Geology (10/20/2022) 384, 406, 408, 409	Journal Of Asian Earth Sciences (Jan. 2023) 108, 160, 184, 256, 276, 334, 335, 354, 397, 847
Colloids And Surfaces A: Physicochemical And Engineering Aspects (10/5/2022) 590, 599, 608, 611, 653, 654, 658, 777, 787, 829, 843, 850, 852, 859, 860, 862, 894	Journal Of Marine Science And Engineering (April 2021) 367, 588, 643, 644, 651, 688, 694, 709, 713, 714, 728, 763, 801, 802, 803, 804, 805, 823, 844, 853, 865, 866, 882, 887, 888
Colloids And Surfaces A: Physicochemical And Engineering Aspects (10/20/2022) 582, 619, 650, 659, 741, 749, 771, 856	Journal Of Marine Science And Engineering (Aug. 2022) 387, 443, 444, 539, 555, 641, 645, 646, 649, 652, 695, 696, 703, 712, 723, 729, 731, 733, 754, 755, 770, 793, 794, 806, 807, 808, 809, 810, 811, 812, 813, 814, 815, 824, 833, 841, 854, 867, 886, 889, 890, 892, 893
Colloids And Surfaces A: Physicochemical And Engineering Aspects (11/5/2022) 578, 597, 640, 655, 660, 683, 710, 739, 750, 753, 757, 790	Journal Of Marine Science And Engineering (Sept. 2022) 388, 540, 571, 647, 648, 657, 667, 681, 682, 689, 715, 716, 726, 732, 734, 735, 816, 817, 818, 819, 825, 855, 857, 868, 869, 873, 883
Colloids And Surfaces A: Physicochemical And Engineering Aspects (11/20/2022) 598, 604, 626, 656, 661, 679, 684, 686, 746, 758, 760, 764, 772, 773, 774, 775, 776, 778, 791, 827, 828, 830, 870	Journal Of Petroleum Geology (Oct. 2022) 248, 251, 290, 340, 391
Colloids And Surfaces A: Physicochemical And Engineering Aspects (12/5/2022) 579, 620, 621, 704, 745, 759, 762, 858	Marine Environmental Research (June 2022) 839, 842
83rd Annual EAGE Conference (Online And Madrid, Spain, 6/6-9/2022) Abstracts 201, 283, 321, 416, 417, 433, 439, 441, 447, 459, 463, 474, 485, 531, 537, 552, 756, 761, 765, 785	Marine Environmental Research (Sept. 2022) 863, 872
3rd EAGE HPC In Americas Workshop (Online, 5/17-18/2022) Abstracts 442, 446, 486, 509, 521, 522, 532, 533, 534	Micropaleontology (v.68, no.6, 2022) 167, 328
First Break (Nov. 2022) 448, 449, 453, 456, 460, 475, 478	New Zealand Journal Of Geology And Geophysics (v.62, no.3, 2019) 234, 245, 337
First Break (Dec. 2022) 436, 469, 472, 477, 480, 493, 553	Ocean Engineering (9/1/2022) 668, 690, 691, 697, 698, 699, 700, 701, 702, 717, 718, 795, 820, 821, 879, 880, 891
Geochimica Et Cosmochimica Acta (9/1/2022) 401	Offshore Technology Conference [OTC] (Houston, TX, 5/2-5/2022) Proceedings 428, 562, 565, 566, 583, 601, 602, 617, 632, 663, 669, 670, 687, 711, 719, 725, 727, 786, 831, 836, 845, 851, 861, 864
Geological Journal (Oct. 2022) 106, 130, 191, 212, 244, 249, 317, 326, 327, 339, 370, 385, 427	Palaeogeography, Palaeoclimatology, Palaeoecology (12/15/2022) 100, 211, 241, 303, 348, 351
Annual IADC General Meeting (New Orleans, LA, 11/2-4/2022) Proceedings 559, 832, 834, 835, 837, 838	58th Annual Palaeontological Association Meeting (Leeds, UK, 12/16-19/2014) Abstracts 120, 129, 139, 140, 147, 149, 157, 168, 169, 175, 188, 194, 195, 218, 221, 222, 225, 226, 233, 247, 265, 266, 269, 270, 291, 292, 293, 299, 322, 323, 342, 347, 349, 350, 372, 382, 383, 399
Industrial & Engineering Chemistry Research (6/29/2022) 708, 797, 871	65th Annual Palaeontological Association Meeting (Manches- ter, UK, 12/18-20/2021) Programme And Abstracts 102, 110, 113, 127, 128, 138, 141, 142, 164, 165, 174, 192, 197, 227, 231, 232, 250, 260, 268, 271, 272, 273, 275, 281, 288, 329, 345, 393
International Geology Review (v.58, no.16, 2016) 134, 207	Palaeontology (Sept./Oct. 2022) 104, 202, 239
21st International Sedimentological Congress [ISC] (Beijing, China, 8/22-26/2022) Abstract Book 096, 105, 107, 112, 115, 118, 119, 121, 131, 132, 133, 136, 137, 148, 150, 151, 152, 154, 156, 158, 162, 163, 170, 172, 173, 176, 177, 181, 183, 185, 186, 190, 193, 198, 199, 200, 203, 205, 206, 208, 209, 210, 213, 215, 217, 220, 223, 228, 229, 230, 235, 237, 238, 243, 253, 254, 255, 257, 258, 259, 261, 267, 274, 278, 282, 284, 287, 289, 294, 295, 296, 297, 298, 300, 301, 308, 309,	Paleoceanography And Paleoclimatology (Oct. 2022) 109, 219, 316, 389
	Petroleum Geology And Recovery Efficiency (Youqi Dizhi Yu Caishoulu) (Nov. 2022) 159, 252, 305, 306, 307, 371, 395, 517, 722, 740, 779, 780, 781, 782, 783, 784

Precambrian Research (v.382, Nov. 2022)
095, 124, 155, 178, 196, 242, 286, 302, 358, 366

Review Of Palaeobotany And Palynology (Dec. 2022)
122, 135, 214, 216, 325

2nd Annual SEG/AAPG Applied Geoscience And Energy
International Meeting [IMAGE] (Houston, TX,
8/28/2022-9/1/2022) Abstracts
419, 420, 421, 422, 423, 424, 425, 426, 429, 430, 432,
437, 438, 440, 445, 450, 452, 455, 457, 458, 461, 464,
465, 466, 467, 468, 470, 471, 476, 479, 481, 483, 487,
488, 490, 491, 492, 494, 495, 496, 497, 498, 499, 500,
501, 502, 503, 504, 505, 506, 507, 510, 511, 512, 513,
514, 515, 518, 519, 520, 523, 524, 525, 526, 527, 528,
529, 530, 538, 541, 542, 543, 544, 545, 546, 548, 549,
550, 551, 554

Tectonics (Oct. 2022)
097, 098, 111, 114, 153, 180, 204, 262, 263, 264, 280,
285, 344, 368, 482

Tectonophysics (11/20/2022)
101, 182, 189, 319, 415, 431, 462

Tectonophysics (12/5/2022)
103, 123, 166, 240, 246

The Mountain Geologist (Oct. 2022)
161, 352, 398

West Texas Geological Society Bulletin (Nov.-Dec. 2022)
849